BARC Newsletter
Founder's Day Special Issue 2015

Bhabha Atomic Research Centre

From the Editor's Desk

The Founder's day Special Issue of the BARC Newsletter published every year on Founder's Day, carries award winning work of our Scientists and Engineers. DAE Awards 2013 received in 2014 and Merit Awards for R&D work in 2014 are being published in this issue.

This year Forty Seven papers have been published. Apart from DAE Awards, BARC Scientists and Engineers received several awards for their R&D work, which was presented at various national and international fora (Merit Awardees). Some of the R&D work received special awards instituted by the sponsoring organizations. Some included oral presentations and others were Poster presentations.

This CD contains all the Forty Seven papers which are grouped under 1.DAE Awards and 2. Merit Awards. Individual papers can be accessed from the Contents as well as from the Author index by clicking on the hyperlinks.

Dr. G. Ravi Kumar
On behalf of the Editorial Committee

CONTENTS

Abhijit Tillu[1], Vivek Yadav[1], Hemant Sarukte[1], Shiv Chandan[1], Ramchandra Chavan[1], Kavita P Dixit[1], R.K. Rajawat[1] and K. Dasgupta[2]
[1] Accelerator & Pulse Power Division & [2] BTDG
Shri Abhijit Tillu is the Recipient of the DAE Young Applied Scientist /Technologist Award for the year 2013

DAE Young Engineer Awards

DAE Young Scientist Awards

MERIT AWARDS

BARC NEWSLETTER
FOUNDER'S DAY SPECIAL ISSUE 2015

MOLECULAR MECHANISMS UNDERLYING GAMMA RADIATION RESISTANCE IN *DEINOCOCCUS RADIODURANS*

H. S. Misra
Molecular Biology Division

Dr. H.S. Misra is the Recipient of the DAE Homi Bhabha Science & Technology Award for the year 2013

Abstract

Gamma radiation damages biomolecules by direct energy deposition and breaking of covalent bonds, and also indirectly by producing reactive oxygen species through water radiolysis. An organism that survives the higher doses of γ radiation would have to have the efficient mechanisms for combating the deleterious effects of ionizing radiations. Deinococcus radiodurans is a bacterium known for its extreme resistance to γ radiation. We have been studying the molecular basis to its extreme phenotypes by understanding both DNA damage and repair, and the mechanisms that protect biomolecules from oxidative damage in this bacterium. Using the technological and intellectual capabilities developed in house, we demonstrated that there is no single but several protective and repair mechanisms that work together for providing radiation resistance in this bacterium. A summary of our significant findings related to radiation resistance in D. radiodurans has been presented.

Introduction

DNA damage occurs in all organisms as a consequence of ultraviolet (UV) light emanating from the sun and ionizing radiation (γ rays & X-rays) from natural sources, medical treatment and contaminated land. The repair of DNA damage is crucial for life and defects in DNA repair pathways can lead to genetic disease and cancer in mammals. Unlike eukaryotes, the cellular and molecular responses to DNA damage have not been fully characterized in prokaryotes except UV induced SOS response in certain bacteria, possibly because bacteria differ from higher organisms into both cellular complexity and tolerance to DNA damage. *Deinococcus radiodurans* is a Gram-positive bacterium primarily known for its extraordinary resistance to both ionizing and non-ionizing radiations [1, 2]. It can tolerate up to 6.5kGy γ radiation without a measurable loss of cell viability [3, 4]. The extraordinary tolerance of *D. radiodurans* (hereafter referred as *Deinococcus*), to other abiotic stresses including radiation and desiccation, has attracted both radiation biotechnologist and molecular geneticists for using it (i) for bioremediation of radioactive waste and, (ii) as a model organism for understanding the molecular basis of its extreme radioresistance. The radiobiotechnological use of this bacterium however, suffers a major setback because this microorganism is yet to be known for any

desirable traits for its use in bioremediation of radioactive waste, except that it is resistant to both chronic as well as acute exposures of γ radiation, and has a number of proteins that needs to be characterized for their usefulness. On contrary, there are microorganisms that do not confer such a magnitude of radiation resistance but have numerous features that are useful in bioremediation of hazardous waste mixed with metals and aromatic compounds. Therefore, the basic understanding of mechanisms underlying the radiation resistance and at least the identification of molecules required for the usefulness of this bacterium in radio-biotechnological applications would come under the core areas of basic research and would be worth pursuing. Further, both basic and applied research using this bacterium would have required the development of technology for its genetic modification and for the introduction of desirable characters in this bacterium. Our laboratory has been focusing on both of these aspects i.e. the development of both technological and intellectual capabilities for carrying out advanced research in this bacterium and the basic research on understanding the molecular basis of the extraordinary radiation resistance. Using in house expertise in these areas, we have significantly contributed in the global efforts on the subject where our findings have been used for discussing the findings from the renowned laboratories working in this area of research. Some of our works are summarized below.

Development of technological expertise for easy manipulation of Deinococcus radiodurans

Genetic manipulation of any organism requires the organism specific genetic tools. These are developed depending upon the need of researchers. We were in need of technology for genetic manipulations of *Deinococcus* mainly on two aspects (i) the synthesis of proteins from other bacteria as well as over production of this bacterial proteins itself, and (ii) the inactivation of any gene of interest for studying their contributions in radiation resistance of *Deinococcus*. We developed many constructs for this work using the resources available in our laboratory. The notable ones were pRADgro (Fig 1a) and pNOKOUT (Fig 1b). For the development of pRADgro, a 261bp DNA fragment containing regulatory sequences of *groESL* genes of *Deinococcus* (*P*gro), Shine-Delgarno (SD) sequences for ribosome binding and five codons of GroE along with four new unique restriction enzyme sites for providing correct translation frame for recombinant protein synthesis, was cloned in pRAD1 [5] cloning vector. The pRADgro was checked for its nature as a shuttle expression vector between *Deinococcus* and *Escherichia coli*, another model organism mostly used for gene cloning and recombinant proteins synthesis and the expression of transgenes on this vector was ascertained in both the hosts [6, 7]. Similarly, pNOKOUT was constructed by cloning the neomycin phosphoryltransferase II (*npt*II) selection marker cassette into pBluescript SK+ an *E. coli* cloning vector. The *nptII* cassette was earlier known for the expression of kanamycin resistance in *Deinococcus* and pBluescript SK+ should not be surviving in *Deinococcus*. Thus pNOKOUT was anticipated to carry an expressing *nptII* cassette into *Deinococcus* but would not be maintaining in it. This will make pNOKOUT a suicidal vector and the replacement of desired gene with *nptII* would take place through genetic recombination. These features of pNOKOUT were confirmed again in both *E. coli* and *Deinococcus*. The results showed the integration of *nptII* into *Deinococcus* R1 genome and expression of kanamycin resistance in these cells. So far, we were expressing recombinant proteins in *Deinococcus* under constitutive and a relatively weaker promoter, pGroES. For many experiments, both high levels and controlled expression of recombinant proteins is required. For

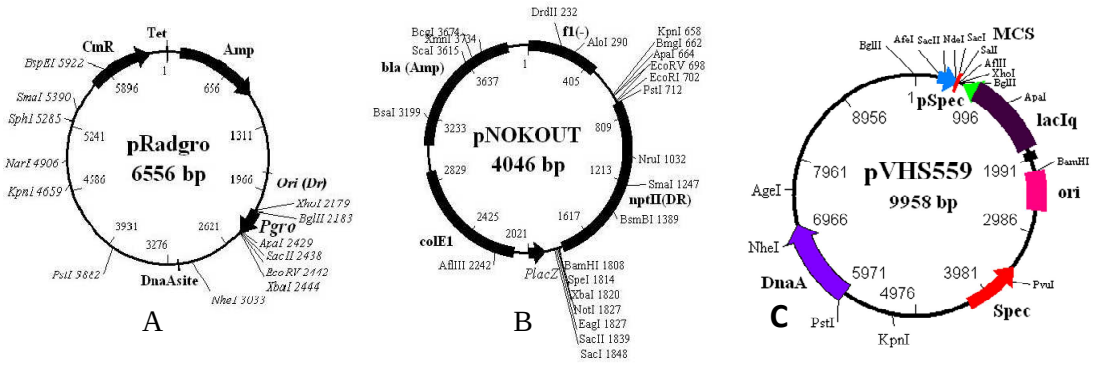

Fig. 1: Partial restriction map of pRadgro and pNOKOUT constructs. The 261bp *BglII-XbaI* fragment containing promoter (*Pgro*) was cloned in pRAD1 to get pRadgro (A) and 937bp an expressing cassette of *nptII* (*nptII* (DR) was cloned at *SmaI* site of pBluescript SK+ to get pNOKOUT (B). Similarly, another deinocccal shuttle expression vector pVHS559, for the controlled expression of desired proteins in *Deinococcus* was constructed (C).

that, a new vector pVHS559, having IPTG inducible promoter backbone was modified for providing additional cloning sites and inducible expression of recombinant in *Deinococcus* (Fig 1c) and being used for localization of deinococcal proteins fused with fluorescent tag. Using these constructs a large number of proteins from both *E. coli* and *Deinococcus* have been expressed and a number of genetic knockout strains have been generated, localization of both host as well as external proteins, and the roles of various proteins in radiation resistance have been ascertained in this bacterium. These vectors have also been provided several laboratories abroad on material transfer agreement (MTA) and being used for basic research in *Deinococcus*. This allowed us to have the complete autonomy in any kind of genetic manipulation required for making *Deinococcus* suitable for both basic and applied work.

Functional significance of macromolecular interactions in radioresistance of *D. radiodurans*

Proteins are ultimate functional units that contribute to different characteristics in a living system. The protein's functions are intimately regulated by the microenvironment around these molecules and therefore, the different organisms surviving in different environment would be expected to have different microenvironment inside the cells. Although, different organisms having similar array of proteins, might exhibit different characteristics due to change in microenvironment in which these proteins are functioning in a particular living system. With these existing paradigm, we hypothesized a possibly of DNA metabolic proteins required for extreme phenotypes in this bacterium might be interacting in a different microenvironment and thus functioning differently in this bacterium. This assumption got further support when we observed that *Deinococcus* with *E. coli*, which exhibit just opposite response to γ radiation, have nearly similar protein complements for DNA recombination and repair pathways. Therefore, to test our hypothesis, the possible existence of these proteins in form of macromolecular complex was first checked. The multiprotein complexes were isolated from stationary phase cells of *Deinococcus* and *E. coli* and compared for different DNA metabolic activities and the presence

of recombination repair proteins as detected by immune blotting [8]. Multiprotein complexes from both these organisms although have several of the DNA metabolic activities common, they differ grossly on some of the crucial functions. For example unlike *E. coli*, the multiprotein complex from *Deinococcus* did not contain RecA but it had some of the other important DNA repair function like ATP sensitive nuclease (Fig 2a) and ATP stimulated DNA ligase (Fig 2b). The protein components of this complex were identified by mass spectrometry and 24 different polypeptides were detected that include PprA, ATP type DNA repair ligase (DRB0100) and a 5' nucleotidase (DR0505).

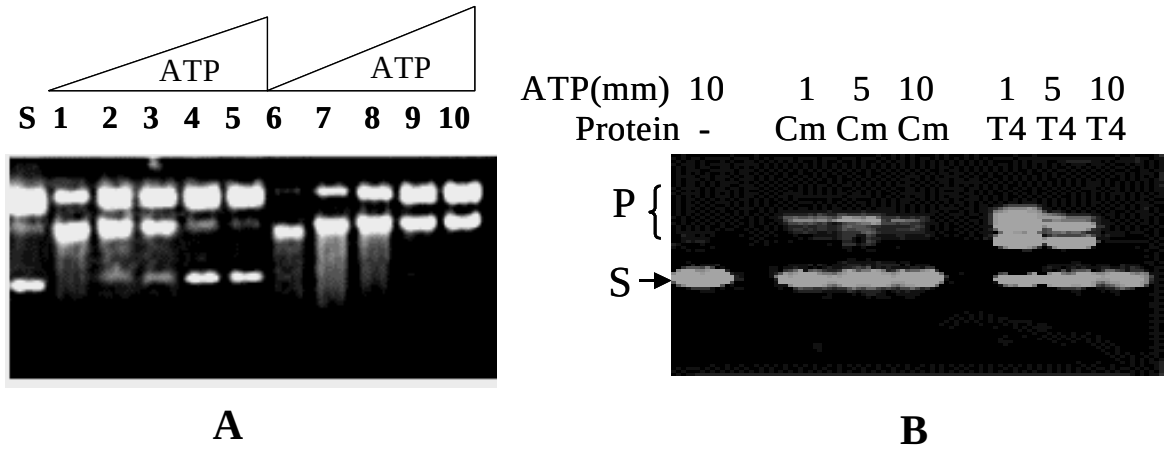

Fig. 2: Regulation of two incompatible functions in multiprotein complex. Multiprotein complex isolated from *D. radiodurans* was checked for nuclease activity on dsDNA in presence of Mg2+ (1-5) and Mn2+ (6-10) with increasing concentration of ATP (A). The DNA ligase activity of complex (Cm) was compared with T4 DNA ligase (T4) in presence of different concentration of ATP (B).

The functional significance of some of these proteins like PprA, DRB0100 and DR0505 in γ radiation resistance of this bacterium was further studied. We deleted *dr0505*, *pprA* and *drb0100* genes from *Deinococcus* genome as well as the recombinant proteins were made in *E. coli* and purified. By checking the γ radiation effect on the survival of these mutants and activity characterization of recombinant proteins, we demonstrated the roles of these proteins in γ radiation resistance of *Deinococcus* and the possible mechanisms of action were shown.

Interestingly, the activity of recombinant DRB0100 ligase compulsorily required PprA and DRB0098, another protein of this bacterium for its enhanced activity (Fig. 3). Further DRB0100 supported radiation resistance in *Deinococcus* only when PprA, DRB0098 and DRB0099 were present [9]. These results suggested the functional significance of protein-protein interaction in macromolecular complex for its efficient functioning in γ radiation resistance in *Deinococcus*. Similarly, the recombinant DR0505 is characterized as an ATP sensitive nuclease with a novel thermostable phosphoesterase activity, which could withstand up to 65^{o}C *in vitro* [10] and implicated for its role in nucleotide recycling.

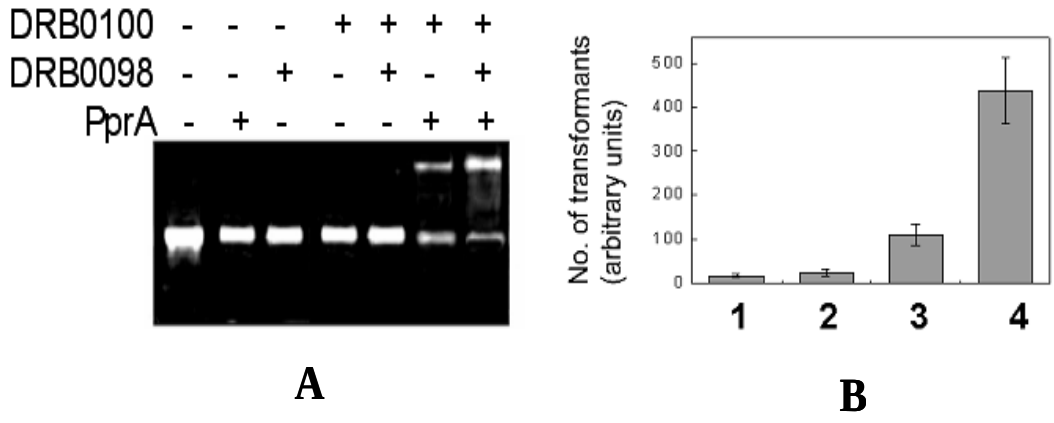

Fig.3: DNA end joining activity assay of DRB0100 identified from multiprotein complex. Purified proteins were incubated with PCR amplified linear DNA and checked on agarose gel (A) and linearised plasmid DNA ligated samples were checked for transformation in *E. coli* (B). Ligation efficiency directly correlates with the number of transformants obtained with each samples

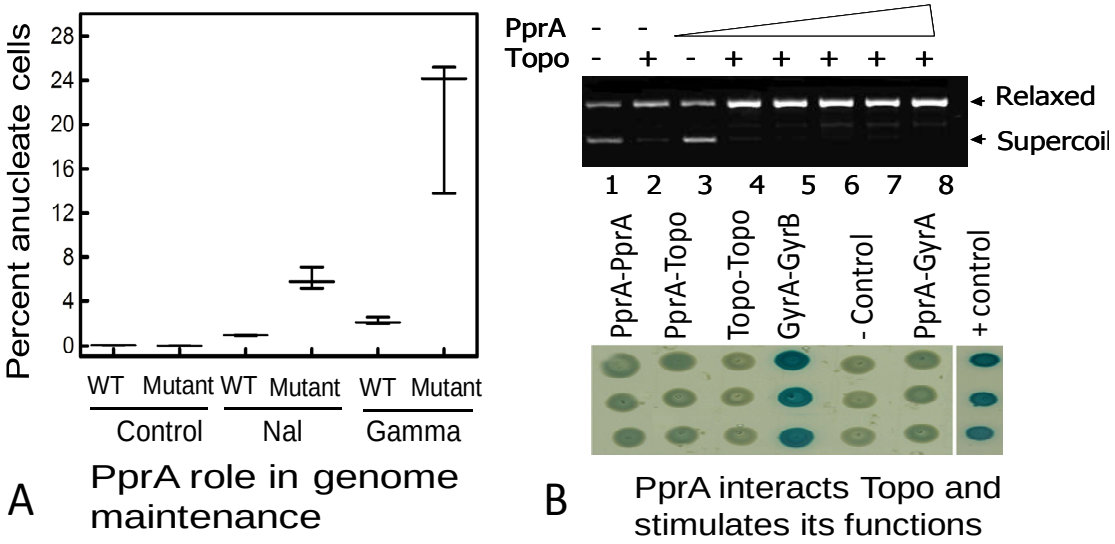

Fig 4. Protein-protein interaction studies leading to reveal hitherto unknown function of a DNA repair protein. A. The wild type (WT) and *pprA* mutant (Mutant) cells were treated with nalidixic acid (Nal) and gamma radiation (Gamma) separately. These cells were compared with untreated controls (Control) for the loss of nucleoid as estimated microscopically. B. The recombinant TopoIB was assayed for relaxation activity in the presence and absence of its complex partner PprA (Top panel) and in vivo interaction using bacterial two hybrid system (Bottom panel)

In vivo localization of PprA and other components of multiprotein complex were proposed in *D. radiodirans*. PprA-GFP cellular localization studies showed that PprA binds to septum trapped nucleoid. Further studies on this observation resulted in deciphering a hitherto unknown function of this protein in genome maintenance and cell division [11, 12]. When we generated *pprA*

mutant of *D. radiodurans* and measured the genome stability of mutant and wild type cells treated with nalidixic acid and gamma radiation (Fig. 4). We provided evidence on the mechanism of action of PprA and showed that PprA interacts with both TopoIB and DNA gyrase *in vivo* and modulates deinococcal TopoIB and DNA Gyrase activities *in vitro* (Fig. 4).

Functional significance of known DNA recombination / repair proteins in radioresistance of *Deinococcus*

There are two major DNA recombination pathways like RecF and RecBC, which have been implicated in the repair of radiation-induced DNA damage in most of the bacteria. RecBC enzyme complex has been characterized for their roles in DNA double strand break repair in many radiation sensitive bacteria as well. Surprisingly, the genome of *Deinococcus* encodes all the components of RecF recombination pathway but lacks the components of classical RecBC pathway. How does this bacterium mend its shattered genome in the absence of RecBC enzymes was intriguing. First the possibility of RecF contributing to efficient DNA strand break repair was checked by *in-trans* expression of SbcB, an exonuclease I, a known inhibitor of RecF pathway, and then by over expression of RecBC from *E. coli* into *Deinococcus*. *Deinococcus* cells expressing these proteins separately become sensitive to radiation but the levels of radiation sensitivity was more in SbcB expressing cells than RecBC suggesting the involvement of RecF pathway in radiation resistance of this bacterium [6] and less significance of RecBC to these phenotypes at least in *Deinococcus* [13]. The role of RecF recombination pathway in radiation resistance of this bacterium was further supported from the observation where the functions of other suppressors like SbcCD of RecBC pathway is required for higher radioresistance [14]. Similarly, a protein (PolX) of unknown function was predicted for its DNA polymerase activity and characterized *in vitro* as a short patch base excision repair (SPBER) polymerase [15] (Fig 5).

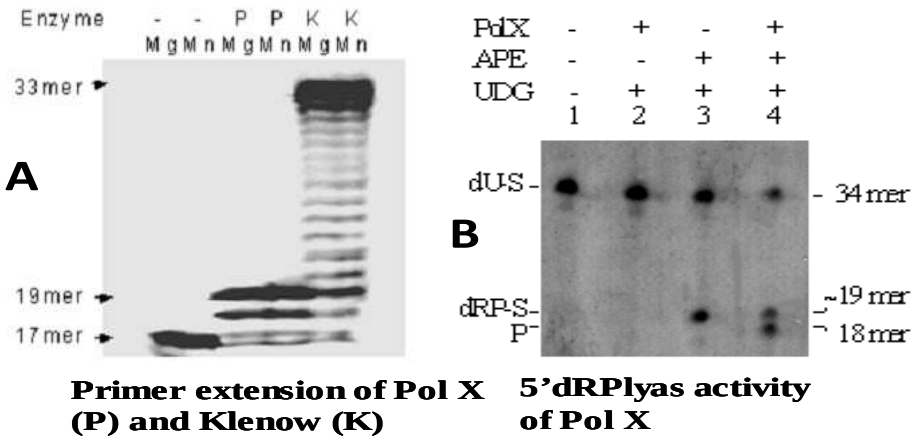

Fig 5. Functional characterization of PolX from *D. radiodurans*. Purified recombinant PolX (P) was assayed for primer extension activity using normal template – primer and compared with a replicative DNA polymerase Klenow fragment (K) and products were analysed on UREA-PAGE gel (A). Base excision repair activity was assayed on oxidative damage DNA template in the presence of DNA glycosylase and AP endonuclease (B)

Characterization of a novel oxidative stress and DNA damage response mechanism in *Deinococcus*

Living cells exposed to various stress exhibit a rapid change in cellular and molecular processes to counteract the deleterious effect of stressors. For example, the cells exposed to γ radiation respond to both oxidative stress and DNA damage effects leading to in genome functions both at the levels of gene expression and functional modulation of proteins associated with DNA repair and cell division. The DNA damage response in prokaryotes has been termed as SOS response. *Deinococcus* does not exhibit classical SOS response [16]. Despite, it shows DNA damage induced gene expression and protein turnover. The molecular mechanisms underlying the regulation of the synthesis and activity modulation of various proteins by γ radiation induced DNA damage are not known. The systematic studies on the changes occurring in *Deinococcus* cells exposed to γ radiation were carried out at both cellular and molecular levels. It showed that cells exposed to γ radiation, rapidly synthesized very high levels of signaling nucleotides including ATP, AMP and cyclic AMP etc. and stress responsive enzymes like adenylyle cyclase, phosphodiesterase, protein kinases [17]. These molecules are well known for their roles in regulation of various cellular and molecular processes, suggesting that *Deinococcus* does respond to γ radiation induced DNA damage. If it does not confer classical SOS response mechanism, the possibility of some alternate mechanisms could be hypothesized.

Since gamma radiation kills living cells by directly damaging biomolecules and indirectly through oxidative stress, we studied both these components for understanding the gamma radiation response in *Deinococcus*. We searched the genome of this bacterium for metabolic pathways associated with antioxidant synthesis in bacterial system. We observed that the genome of this bacterium confers a gene (we hereby designate as *pqqE*) that encodes an enzyme responsible for pyrroloquinoline quinone (PQQ) biosynthesis in bacterial system. This gene was cloned and expressed in *E. coli*. Transgenic *E. coli* producing PQQ showed several fold higher tolerance to oxidative stress *in vivo* and protected biomolecules from γ radiation damage *in vitro* [18]. PQQ was subsequently shown as strong antioxidant as vitamin C and Trolox [19] and could neutralize superoxide, hydroxyl and oxygen free radicals *in solution* without any indication of its consequential effect [19]. PQQ was subsequently shown as pro-oxidant in mammalian cells by depleting the redox equivalents that acts as antioxidants in mammalian cells. It showed higher rates of apoptotic cell death in tumor cells as compared to normal cells [20].

The role of PQQ in radiation resistance phenotypes of *Deinococcus* was investigated. For that, *pqqE* gene was deleted from genome of *Deinococcus* and the effect of different DNA damaging agents including γ radiation, on cell survival and DSB repair ability of mutant cells were investigated. Results showed that the absence of PQQ makes this bacterium incompetent to withstand higher doses of DNA damage and γ radiation in particular (Fig 6A). Molecular mechanisms contributing to this phenotype of PQQ was checked and found that PQQ has a role in DNA strand break repair (Fig 6B) [21]. Subsequently, a PQQ inducible putative protein kinase encoded from *dr2518* gene was identified from this bacterium and its role in γ radiation resistance of *Deinococcus* through DNA strand break repair was demonstrated [22].

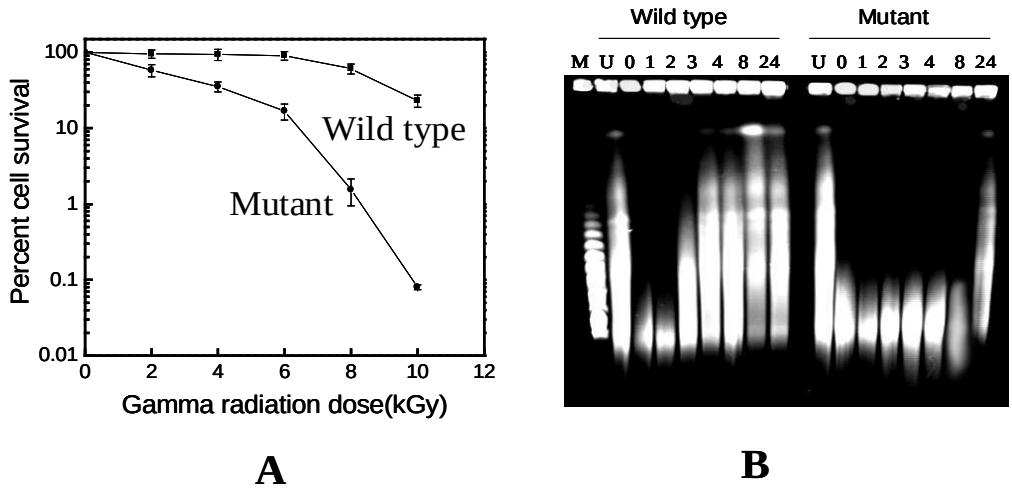

Fig. 6: Involvement of PQQ in radiation resistance of *D. radiodurans* through its role in DSB repair. *D. radiodurans* cells devoid of PQQ were generated and the effect of γ radiation on survival of these cells (mutant) was compared with wild type (wild type) (A). The cells recovering from γ radiation effects were collected at different time interval (1-24 h) and analyzed for shattered genome reassembly on pulsed field gel electrophoresis (B) and compared with unirradiated (U) controls.

DR2518 was earlier shown as a PQQ inducible protein kinase having a role in radiation resistance in *Deinococcus*. The effect of γ radiation induced DNA damage on expression and activity of DR2518 protein kinase was checked. Results showed that both synthesis and activity of this kinase are regulated by γ radiation induced changes in the cells, which indicated that this kinase could be a typical candidate of an alternate DNA damage response mechanism in this bacterium. The ability of this kinase phosphorylating several important DNA repair proteins of *Deinococcus* and regulating the differential expression of genes in response to radiation induced DNA damage (Fig. 7) strengthened its role in radioresistance. The results obtained from this particular study suggested that unlike other bacteria that confer SOS response, *Deinococcus* might have an alternate mechanism of DNA damage response and DR2518 kinase seems to be a candidate protein kinase playing crucial role in this process. Recombinant DR2518 has been characterized as a radiation and quinone responsive protein kinase and named as RqkA [22]. Further we showed it contribution in radioresistance of this bacterium through phosphorylation of important DNA repair proteins like PprA and RecA and those involved in bacterial cell division. Phosphorylation sites in PprA and RecA of *D. radiodurans* were mapped mass spectrometrically and confirmed by site directed mutagenesis. Both *in vivo* and *in vitro* phosphorylation of PprA and RecA by RqkA kinase have been demonstrated. Importance of PprA and RecA phosphorylation in the regulation of these proteins functions *in vivo* and their respective roles in radioresistance have been demonstrated [23]. For instance, the phosphorylation of PprA by RqkA kinase had increased the DNA binding activity of PprA and its ability to stimulate intermolecular ligation activity of T4 DNA ligase was stimulated by ~ 6 fold. Similarly, RecA phosphorylation by RqkA kinase showed enhanced strand exchange

reaction activity of RecA in the presence of dATP as compared to ATP and non-phosphorylated RecA *in vitro* (Fig. 8). The phsophorylation also affected RecA roles in radioresistance in *D. radiodurans*.

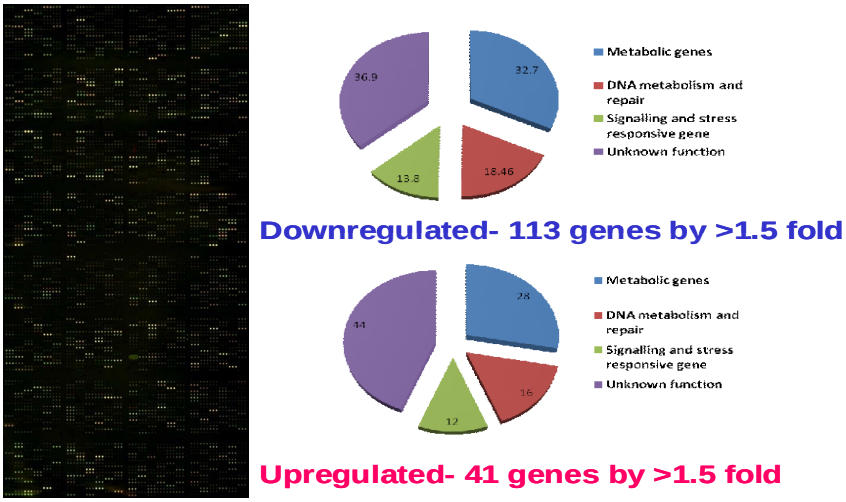

Fig. 7: Involvement of a radiation responsive serine/ threonine protein kinase (STPK) in regulation of gene expression in *D. radiodurans*. *Deinococcus* cells devoid of STPK were exposed with 6.5kGy radiation and global change in gene expression was measured by microarray analysis (Microarrayer) in collaboration with Prof. Yeujin Hua, Zhejiang University, Hangzhou China. Different numbers of genes showing reduced expression (donwregulated) and increased expression (upregulated) by 15 fold or more were taken into consideration for making conclusions.

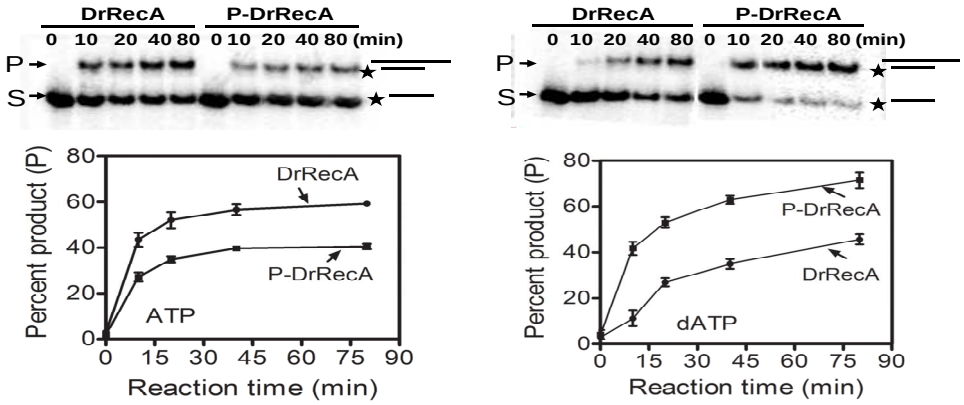

Fig 8. Effect of phosphorylation on strand exchange reaction of RecA from *D. radiodurans*. Purified recombinant RecA was phosphorylated by RqkA kinase and assayed for strand exchange activity in the presence of ATP and dATP, respectively.

Multipartite genome system and cell division regulation in *D. radiodurans*

Apart from the extreme radioresistance, the cytogenetic features of *Deinococcus* are equally interesting. It has multipartite genome system and ploidy. All genome elements are held together producing a toroidal ring shaped nucleoid structure. Genome maintenance and cell division regulation in cells recovering from gamma radiation effects would be worth investigating. Here, we demonstrated that chromosome I encodes proteins that regulate its partitioning by following the Type IB mechanism (Pulling mechanism) of genome segregation [24].

For the first time, we identified centromereic sequences in chromosome I and showed that ParB1 binds to these centromeric elements both *in vivo* and *in vitro*. ParA1 is a non-specific DNA binding protein, it showed oscillation on nucleoid of the bacterium from one pole to other, and once ParA1 encountered the ParB1 bound to centromere, the depolymerization of ParA1 is triggered leading to the pulling of two daughter chromosomes in opposite direction followed by cytokinesis.

In order to ascertain the involvement of ParB proteins of *D. radiodurans* in genome maintenance and in the radioresistance, the genes encoding ParBs on different genome elements were deleted. These deletion mutants were checked for various stressors response and anucleation phenotype. Interestingly, it is observed that *parB1* deletion produces the high frequency of anucleate cells, growth retardation and sensitivity to nalidixic acid. It showed a little less effect on gamma radiation resistance as compared to *parB2* and *parB3* deletion mutants.

The *parB2* deletion also showed effect on normal growth while *parB3* mutant grew similar to wild type. Both *parB2* and *parB3* mutants showed the high frequency of anucleate cells and higher sensitivity to DNA damaging agents but not to nalidixic acid. Thus we provided evidence that the 'ParB' proteins encoded on different genome elements are not functionally redundant and these are specifically responsible for maintenance of respective genome elements during cell division. Further, the chromosome II and megaplasmid seem encoding complements responsible for gamma radiation resistance of this bacterium.

Further in order to understand the effect of gamma radiation cell growth, the molecular mechanisms underlying cell division regulation is investigated. FtsZ a protein centre to the entire bacterial cell division complex was characterized both *in vitro* and *in vivo*. This protein is found to be different from its homologues known in other bacteria in terms of its kinetics, rate of polymerization/ depolymerization.

These characteristics determine the growth rate, and the requirements of other divisome components for a productive cellular localization and FtsZ ring formation in *Deinococcus* [25]. FtsZ-GFP expressing in *Deinococcus* produced typical FtsZ ring perpendicular to first plane of cell division (Fig.9).

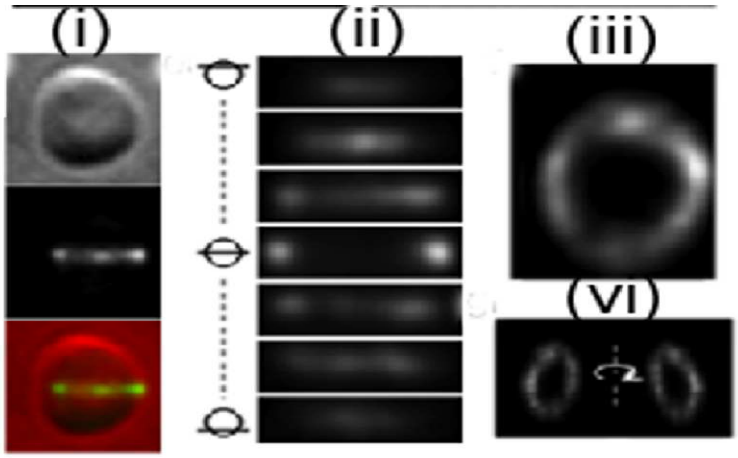

Fig. 9. In vivo localization of FtsZ in the dividing cells of *D. radiodurans*. FtsZ-GFP was expressed in *D. radiodurans* on plasmid and the localization of FtsZ tagged with GFP was carried out using confocal fluorescence microscope. FtsZ ring was constructed using Z stacks of images generated in three dimensional planes.

Molecular mechanism underlying extraordinary radioresistance of *Deinococcus* is being progressively unfurled. Several laboratories globally, working on various aspects leading to a single question on how this bacterium confers unthinkable and unbelievable tolerance to radiation effect. Our work from Bhabha Atomic Research Centre has contributed significantly to the global efforts on this aspect. Some of our notable contributions that are being used for explaining and in the discussion of the work from other laboratories are (i) the RecF recombination pathway in absence of RecBC enzymes, contributes to efficient DSB repair and radiation resistance (ii) an antioxidant metabolite PQQ has a role in both oxidative stress tolerance and DSB repair, (iii) the multiple proteins having greater significance in DSB repair and radiation resistance, are present and function together in a multiprotein complex, (iv) the bacteria do not confer classical SOS response but have eukaryotic type serine /threonine protein kinase might have a different DNA damage response mechanism as an alternate to SOS response and (vi) the involvement of a eukaryotic type Ser/Thr protein kinase in DSB repair and radiation resistance was reported first time in any bacteria.

Acknowledgements

I am grateful to Dr. Subrato Chattopadhyay, AD(B), BSG and Dr S. K. Apte, Ex-Director, BSG for their keen interest in the subject as well as moral and intellectual supports. I am thankful to Drs Hari Mohan, Indira K Priyadarshini, Atanu Barik, V.P. Joshi, Roja Gopalakrishnan, Raghvendra Tewari and many others as my short term or long term collaborators for their knowledge sharing and for accepting my intellectual inputs in their projects. My special appreciations and sincere gratitude to my colleagues Drs N. P. Khairnar, Vidya Kamble, Shruti Desai and Swathi Kota and Y. S Rajpurohit, A. D. Das, C. Vijay Kumar and Kruti Mehta and Shri Ganesh Kumar Maurya, for keeping the pace in their research progress uninterrupted, in spite of many hurdles, and for their outstanding research output. Sincere efforts of Shri Sunil D.

Dhotre Sr Tech/H and Shri Priyoda Abhishek Tech/D for their commendable supports to other colleagues are highly appreciated. I am grateful to Professor Yuejin Hua, Professor John Battista Professor Matthew Waldor, Professor I Narumi and Dr Sangyong Lim and Dr. Dongho Kim for their collaborative supports.

References

[1]. Makarova, K. S., Aravind, L., Wolf, Y. I., Tatusov, R. L., Minton, K. W., Koonin, E. V. and Daly, M. J. "Genome of extremely radiation-resistant bacterium *Deinococcus radiodurans* viewed from the perspectives of comparative genomics". *Microbiology and Molecular Biology Reviews* 65 (2001): 44-79.

[2]. Slade, D. and Radman, M. "Oxidative stress resistance in *Deinococcus radiodurans"*. *Microbiology and Molecular Biology Reviews* 75 (2011): 133-191.

[3]. Battista, J.R. "Radiation resistance: the fragment that remain". *Current Biology* 10 (2000): R204-205.

[4]. Misra, H. S. Rajpurohit, Y. S. and Kota, S. "Physiological and molecular basis of extreme radioresistance in *Deinococcus radiodurans*". *Current Science* 104 (2013):194-205.

[5]. Meima, R. Lidstrom, M.E. "Characterization of the minimal replicon of a cryptic *Deinococcus radiodurans* SARK plasmid and development of versatile *Escherichia coli-D. radiodurans* shuttle vectors". *Applied and Environmental Microbiology* 66 (2000): 3856–3867.

[6]. Misra, H.S., Khairnar, N.P., Kota, S., Srivastava, S., Joshi. V.P. and Apte, S.K. "An exonuclease I sensitive DNA repair pathways in *Deinococcus radiodurans*: a major determinant of radiation resistance". *Molecular Microbiology* 59 (2006*)*:1308-1316.

[7]. Kota,S. and Misra, H.S. "PprA: a protein implicated in radioresistance of *Deinococcus radiodurans* stimulates catalase activity in *Escherichia coli*". *Applied Microbiology and Biotechnology* 72 (2006): 790-796.

[8]. Kota,S. and Misra,H.S. "Identification of a DNA processing complex from *Deinococcus radiodurans"*. *Biochemistry and Cell Biology* 86 (2008): 448-458.

[9]. Kota, S., Kamble, V. A., Rajpurohit, Y. S. and Misra, H. S. "ATP-type DNA ligase requires other proteins for its activity *in vitro* and its operon components for radiation resistance in *Deinococcus radioduransin vivo"*. *Biochemistry and Cell Biology* 88 (2010) :783-90.

[10]. Kota,S., Kumar,C.V. and Misra,H.S. "Characterization of an ATP-regulated DNA-processing enzyme and thermotolerant phosphoesterase in the radioresistant bacterium *Deinococcus radiodurans*". *Biochemical Journal* 431 (2010): 149-157.

[11]. Kota, S. Charaka, V.K. Ringgaard, S. Waldor, M.K. and Misra, H.S. "PprA contributes to *Deinococcus radiodurans* resistance to nalidixic acid, genome maintenance after DNA damage and interacts with deinococcal topoisomerases". *PLoS One* 9 (2014):e85288

[12]. Kota, S. Charaka, V.K. and Misra, H.S. "PprA shows growth dependent dynamics in cellular localization during post irradiation recovery of *Deinococcus radiodurans"*. *Journal of Genetics* 93 (2014):349-354.

[13]. Khairnar,N.P., Kamble,V.A. and Misra,H.S. (2008) RecBC enzyme overproduction affects UV and gamma radiation survival of *Deinococcus radiodurans*. *DNA Repair (Amst)* 7:40-47.

[14]. Kamble,V.A. and Misra,H.S. "The SbcCD complex of *Deinococcus radiodurans* contributes to radioresistance and DNA strand break repair *in vivo* and exhibits Mre11-Rad50 type activity *in vitro*". *DNA Repair (Amst)*, 9 (2010): 488-494.

[15]. Khairnar, N. P. and Misra, H. S. "DNA polymerase X from *Deinococcus radiodurans* implicated in bacterial tolerance to DNA damage is characterized as a short patch base excision repair polymerase". *Microbiology* (UK) 155 (2009):3005-3014.
[16]. Narumi, I., et al. "The LexA protein from *Deinococcus radiodurans* is not involved in RecA induction following gamma irradiation". *Journal of Bacteriology* 183 (2001):6951-6956.
[17]. Kamble,V.A., Rajpurohit,Y.S., Srivastava,A.K. and Misra,H.S. "Increased synthesis of signaling molecules coincides with reversible inhibition of nucleolytic activity during postirradiation recovery of *Deinococcus radiodurans*". *FEMS Microbiology Letters* 303 (2010): 18-25.
[18]. Khairnar, N. P., Misra, H. S. and Apte, S. K. "Pyrroloquinoline-quinone synthesized in *Escherichia coli* by pyrroloquinoline-quinone synthase of *Deinococcus radiodurans* plays a role beyond mineral phosphate solubilization". *Biochemical Biophysical Research Communications* 312 (2003): 303-308
[19]. Misra, H.S., Khairnar, N.P., Atanu, B., Priyadarshin,i K. I., Mohan, H. and Apte, S. K. "Pyrroloquinoline-quinone: a reactive oxygen species scavenger in bacteria". *FEBS Letters* 578 (2004) :26-30.
[20]. Shankar, B., Pandey, R., Amin, P., Misra, H. S. and Sainis, K. B. "Role of glutathione in augmenting the anticancer activity of pyrroloquinoline quinone (PQQ)". *Redox Report* 15 (2010): 146-154
[21]. Rajpurohit, Y.S., Gopalakrishnan, R. and Misra, H.S. "Involvement of a protein kinase activity inducer in DNA double strand break repair and radioresistance of *Deinococcus radiodurans"*. *Journal of Bacteriology* 190 (2008): 3948-3954.
[22]. Rajpurohit,Y.S. and Misra, H.S. "Characterization of a DNA damage-inducible membrane protein kinase from *Deinococcus radiodurans* and its role in bacterial radioresistance and DNA strand break repair". *Molecular Microbiology* 77 (2010): 1470-1482.
[23]. Rajpurohit, Y.S. and Misra, H.S. "Structure-function study of deinococcal serine/threonine protein kinase implicates its kinase activity and DNA repair protein phosphorylation roles in radioresistance of *Deinococcus radiodurans". International Journal of Biochemistry and Cell Biology* 45 (2013):2541-2552.
[24]. Charaka, V, K. and Misra, H.S. "Functional characterization of the role of the chromosome I partitioning system in genome segregation in *Deinococcus radiodurans*". *Journal of Bacteriology* 194 (2012):5739-5748.
[25]. Modi, K.M. Tewari, R. and Misra, H.S. "FtsZDr, a tubulin homologue in radioresistant bacterium *Deinococcus radiodurans* is characterized as a GTPase exhibiting polymerization/depolymerisation dynamics in vitro and FtsZ ring formation in vivo". *International Journal of Biochemistry and Cell Biology* 50 (2014):38-46.

BARC NEWSLETTER
FOUNDER'S DAY SPECIAL ISSUE 2015

PREDICTIVE ABILITY OF THEORETICAL AND COMPUTATIONAL CHEMISTRY IN DESIGNING NOVEL COMPOUNDS OF LANTHANIDES AND ACTINIDES

Tapan K. Ghanty
Theoretical Chemistry Section, Chemistry Group

Dr. T.K. Ghanty is the Recipient of the DAE Homi Bhabha Science & Technology Award for the year 2013

Abstract

First-principles based theoretical and computational techniques are of immense importance in providing invaluable insights into the experimental observations, proposing new experiments, and designing molecules and materials for specific applications. In fact, the potential role of theoretical and computational chemistry to design new molecules and novel materials through prediction of their structure and various physico-chemical properties is well recognized throughout the globe as is evident from the award of 1998 Nobel Prize in chemistry to Walter Kohn "for his development of the density-functional theory" and John A. Pople "for his development of computational methods in quantum chemistry". Interestingly, the Nobel Prize in Chemistry for the year 2013 has also been awarded jointly to Martin Karplus, Michael Levitt and Arieh Warshel "for the development of multiscale models for complex chemical systems". In the present article an overview of some of our recent works, which are carried out using various theoretical and computational techniques is provided, with a special emphasis on the chemistry of lanthanides and actinides directly relevant to the back-end nuclear fuel cycle. In particular, our very recent work dealing with the introduction of a new chemical concept, "Intra-ligand Synergism" followed by design of novel ligands for the separation of trivalent actinides from lanthanides is presented briefly. Moreover, our recent theoretical prediction on the design of actinide-lanthanide encapsulated small-size new metallofullerenes, which are associated with very high stability and high symmetry because of the effect of geometric and electronic shell closing, is reviewed briefly. Finally, experimental validations of some of our theoretical predictions on the lanthanide-actinide separation that have been carried out at BARC through syntheses of the predicted ligands followed by solvent extraction experiments are also presented here.

Keywords

Actinide-Lanthanide Separation; Metallofullerenes; Theoretical and Computational Chemistry; Density Functional Calculations; Magic Clusters; 32-electron Principle

Introduction

In the past century many physico-chemical concepts and popular electron counting rules that have been introduced in chemistry are highly successful in rationalizing the stability of many

chemical systems and to explain various chemical reactions and processes. Among them, some of the notable ones are the concept of electronegativity,[1] hard-soft-acid-base-principle (HSAB),[2] frontier molecular orbital (FMO) theory of chemical reactivity,[3] Lewis octet rule,[4] 18-electron rule,[5] 32-electron principle [5] etc. Of late, particularly in the 1980's and 1990's density functional theory (DFT)[6] has provided rigorous physical foundation to some of these concepts; for instances, identification of the chemical potential of the electron cloud in density functional theory with the negative of the electronegativity,[7] quantification of the hardness parameter as the second order energy derivative with respect to the number of electrons,[8] defining Fukui function within the framework of FMO,[9] introduction of the principle of maximum hardness,[10] and the concept of spin-polarized electronegativity,[11] proposition of hardness-polarizability relationship within the FMO approach[12] etc. At the same time computational chemistry gained popularity because of the advent of high-speed computers, development of new theoretical formalisms and various new theoretical tools in the domains of DFT and the post-Hartree Fock based approaches.[13] In fact, in recent times, the theoretical and computational chemistry have been proven to be quite versatile in providing meaningful insights to explain the behavior of various chemical systems and processes.

Among the available theoretical methods, the density functional theory (DFT)[6] has become one of the most popular computational methods for large systems because of its computational economy and good accuracy, and its ability to treat the electron correlation effect quite accurately. As a consequence, it is now possible to compute the properties of various chemical systems and processes quite accurately using DFT based techniques. Moreover, DFT is not only computationally cheaper but also conceptually simpler because it involves single particle electron density as the basic variable. Apart from being interpretative, theoretical and computational chemistry is able to design new chemical systems through predicting the structures and properties of hitherto unknown systems with good accuracy. In fact there are many instances in the literature where theoretical predictions are followed by experimental investigations.[14]

In this account we describe some of our recent works, which falls under this category. Thus, the present article provides a brief description of our recent achievements in the areas of lanthanide-actinide separation[15-16] and lanthanide-actinide encapsulated small size metallofullerenes,[17-20] where large scale electronic structure calculations are involved for predicting the structures, energetics, and many physico-chemical properties including infrared and electronic spectra. We have used various conventional physico-chemical concepts and adopted first-principle based DFT approach for all our investigations, as discussed in our recent works.[15-20] It is well known that relativistic effects are very important for high Z elements such as lanthanides and actinides. Therefore we have taken into account the relativistic effects by using both scalar as well as spin-orbit approaches within the framework of zeroth order regular approximations. Finally, we have discussed some of the experimental results that have confirmed our theoretical predictions on the design of actinide selective new ligands.

The article is organized as follows: Some of our recent works involving lanthanides and actinides have been presented in the next two sections, and finally in the last section concluding remarks have been provided.

Lanthanide-Actinide Separation

Design of suitable ligands for selective complexation of metal ions in solution is of enormous importance in various fields like medicinal biology, environmental sciences, hydrometallurgy, and nuclear waste management as well as for different industrial applications. In recent years, considerable attention has been given to understand the chemistry of actinides because of its close link with the nuclear waste management processes. It is well known that the radiotoxicity of high level liquid wastes can be reduced to a great extent through removal of long-lived α emitting actinides under partitioning and transmutation option and hence it is considered to be an important step in the back-end nuclear fuel cycle.

Thus, selective extraction of actinides (An) from the lanthanides (Ln) is one of the important steps in the back-end nuclear fuel cycle. However, it is a challenging and difficult task because of very similar chemical properties of these two series of ions as they are associated with similar ionic radii and same coordination numbers. The HSAB principle classifies the trivalent lanthanides (Ln(III)) and trivalent actinides (An(III)) cations as hard Lewis acids; consequently their bonding is mainly ionic and primarily governed by charge density.

In spite of this, there is a modest enhancement of covalency in the bonding of An(III) with various ligands as compared to that of Ln(III) complexes due to the larger spatial extent of the 5*f* orbitals of actinides as compared to the 4*f* orbitals of lanthanides. Because of this, An(III) are considered softer than Ln(III), and an advantageous discrimination between An(III) and Ln(III) ions is possible while using ligands with soft donor atoms like sulfur and nitrogen.

Here it is important to note that efficiency of complex formation of either Ln(III) or An(III) with hard donors like oxygen is much better as compared to nitrogen or sulfur donors because both the set of metal ions are hard Lewis acids, and it is in agreement with the HSAB principle, which states that "hard likes hard" and "soft likes soft". However, no selectivity is observed with oxygen donor ligands. Although actinide selective ligand with hard donor atom like oxygen seems highly unusual in a conventional solvent extraction based approach, we have made an attempt to design actinide selective new ligands associated with hard donor atoms.

To accomplish our objective, we have considered[15] two valence isoelectronic metal ions, viz., Am(III) and Eu(III) along with two other metal ions, i.e. U(III) and Ce(III) and investigated the complex formation process with 1,10-phenanthroline (PHEN) and its di-acid derivative, 1,10-phenanthroline-2,9-dicarboxylic acid (PDA) (Figure 1).

Consequently, both soft (nitrogen) as well as hard (oxygen) donor centers are available in the PDA ligand. We have also considered other ligands through functionalization of PDA with soft donor atom such as sulfur viz., 1,10-phenanthroline-2,9-mono-thio-dicarboxylic acid (binding through oxygen atoms, TCA1), 1,10-phenanthroline-2,9-mono-thio-dicarboxylic acid (binding through sulfur atoms, TCA) and 1,10-phenanthroline-2,9-di-thio-dicarboxylic acid (THIO).

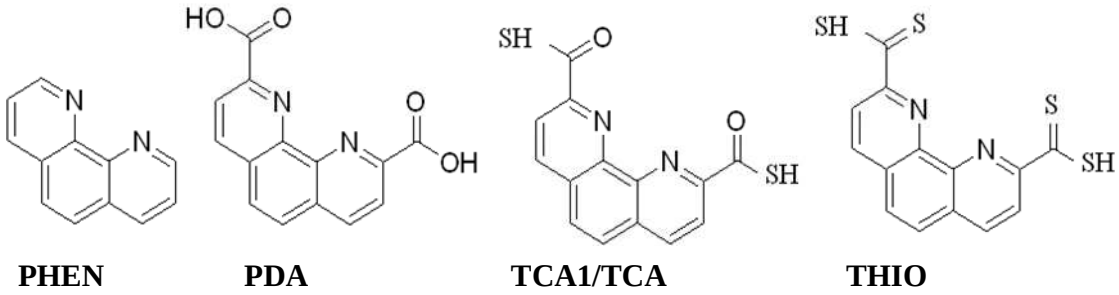

PHEN **PDA** **TCA1/TCA** **THIO**

Fig. 1: Structures of 1,10-phenanthroline (PHEN) and its different derivatives: 1,10-phenanthroline-2,9-dicarboxylic acid (PDA), 1,10-phenanthroline-2,9-mono-thio-dicarboxylic acid (TCA/TCA1) and 1,10-phenanthroline-2,9-di-thio-dicarboxylic acid (THIO).

Comparing the calculated bond length values and the complexation energies (Figure 2) it has been found that the Am(III) is selective towards sulfur donor ligands (TCA and THIO), which is rather expected from the fact that 5*f* orbitals of actinides are more diffused in nature as compared to the 4*f* orbitals of lanthanides. However, the interesting point to be noted here is that the bonding interaction of Am(III) is found to be higher with PDA and TCA1 ligands as compared to Eu(III), where the metal-ligand binding is mainly through the hard donor oxygen atoms. Similar trend is also observed for U(III) and Ce(III). A higher complexation energy of the softer Am(III) ion with the hard donor ligands is quite unusual and it is in sharp contrast to the conventional ligand design methodology, where soft donors are generally used to achieve actinide selectivity. Nevertheless, we have rationalized the selective complex formation of An(III) over Ln(III) with oxygen donor ligands through providing an in-depth insight within the framework of HSAB principle and FMO theory of chemical reactivity.

The calculated hardness value (η) for the bare Eu^{3+} and Am^{3+} ions is found to be 0.395 au and 0.270 au, respectively, which indicate that Am^{3+} ion is softer than Eu^{3+} ion. However, η values of $[Eu\text{-}PHEN]^{3+}$ and $[Am\text{-}PHEN]^{3+}$ complexes are found to be 0.072 and 0.077 au. In other words, the $[Am\text{-}PHEN]^{3+}$ complex is calculated to be slightly harder than the $[Eu\text{-}PHEN]^{3+}$ complex, which is in contrast to the hardness values of the respective bare metal ions. Thus, the nature of the metal ion is changed dramatically after coordination with nitrogen donors present in the PHEN moiety, and Am^{3+} in $[Am\text{-}PHEN]^{3+}$ moiety can be considered as harder as compared to Eu^{3+} in $[Eu\text{-}PHEN]^{3+}$ fragment. Consequently, Am^{3+} in $[Am\text{-}PHEN]^{3+}$ fragment is able to bind to harder oxygen donor atoms present in the two –COOH groups of PDA in a stronger way. It is further supported by the calculated values of Fukui reactivity indices, which reveal that the interaction of oxygen donor is favorable with Am^{3+} in $[Am\text{-}PHEN]^{3+}$ complex as compared with Eu^{3+} in $[Eu\text{-}PHEN]^{3+}$ complex.[15]

From the calculated results it is quite clear that the interaction of the metal ion (An/Ln) with the oxygen donors in the PDA ligand is much stronger than that with the nitrogen atoms present in the same ligand. Therefore, to ascertain the effect of nitrogen atoms on the coordinating behavior of oxygen donors present in phenanthroline derivatives further, we have considered the ligand PDA with nitrogen atoms replaced with -CH groups. With this modification one can investigate

the behavior of the oxygen binding towards the metal ion in absence of nitrogen donors. The calculated results revealed that the modified ligand is devoid of any selectivity towards trivalent actinides. It has also been observed that the metal-nitrogen interaction is much weaker than the metal-oxygen interaction in the An/Ln-PDA complexes. Thus, all the calculated results clearly indicate that in presence of nitrogen atom as another donor center, the PDA ligand becomes selective towards actinides as compared to lanthanides.

Based on all the calculated results, we have introduced the concept of "Intra-ligand Synergism",[15] and shown that selective complexation of actinides with hard donors in presence of soft donors, available in the same ligand is indeed favorable. The nitrogen atoms act as a synergistic agent to facilitate the preferential interaction between the softer actinide ion and the hard donor oxygen atoms, which are present in the same PDA ligand. In fact, in separation science intermolecular synergistic agents are used extensively for an efficient extraction of a particular metal ion where a second ligand known as co-extractant works in a synergistic way with the first ligand in presence of each other. In the literature several such investigations are reported where it has been demonstrated that synergistic effect plays an important role for an efficient and selective extraction of a particular metal ion. However, we have used synergistic donor atoms, which are present in the same primary ligand, and therefore coined the term, "Intra-ligand Synergism". Syntheses of some of the theoretically designed ligands followed by their solvent extraction study have also been performed to validate our theoretical predictions.

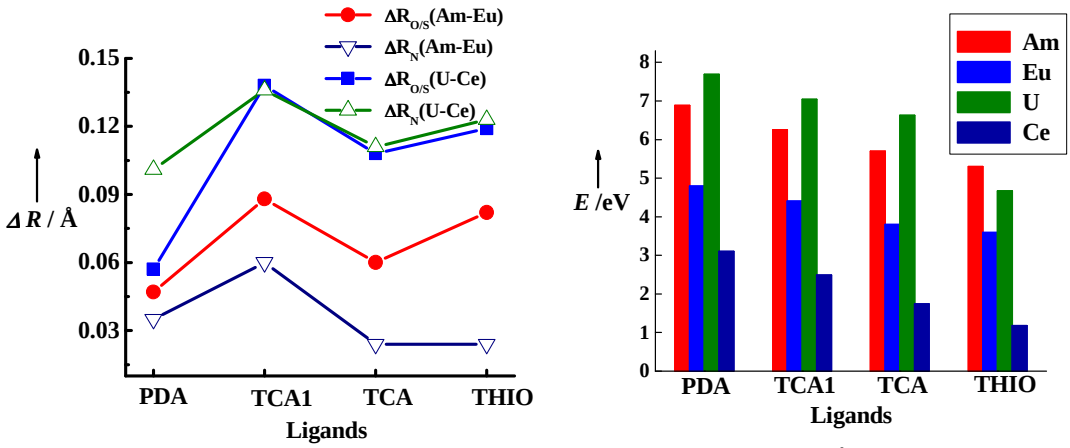

Fig. 2: Difference in the optimized M-N and M-O/S bond distance values (ΔR in Å) between Am(III) , Eu(III) and U(III), Ce(III) in presence of solvent, and Complexation energies (E/eV) of metal complexes, $[ML]^+$, where M= Am/Eu/U/Ce, and Ligand=PDA, TCA1, TCA and THIO in presence of solvent

Although PDA may be considered as a promising ligand for the purpose of actinide-lanthanide separation, it is limited by its low solubility in aqueous solution as well as in organic medium. However, it has been emphasized that solubility of PDA in organic medium can be enhanced through conversion of carboxylate groups into carboxyamides, to make it suitable for actinide-lanthanide separation. Therefore, two valence isoelectronic metal ions, viz., Am(III) and Eu(III) have been considered to investigate the complex formation process with 1,10-phenanthroline-2,9-carboxyamide (PDAM) based ligands, viz., PDAM, N,N-di-isobutyl PDAM (PDAM-Isobutyl), and N-decyl PDAM (PDAM-Decyl), which are derived from the 1,10-

phenanthroline-2,9-dicarboxylic acid. The calculated values of difference in the metal-ligand bond lengths (Figure 3) clearly indicate that the carboxyamide based ligands are Am(III) selective. It is further supported by the calculated values of the complexation energies where it has been found that the Am-Ligand complexes are more stable as compared to the corresponding Eu-Ligand complexes, with a difference in the complexation energies of 3.19, 2.93 and 3.08 eV with the PDAM, PDAM-Isobutyl and PDAM-Decyl ligands, respectively.

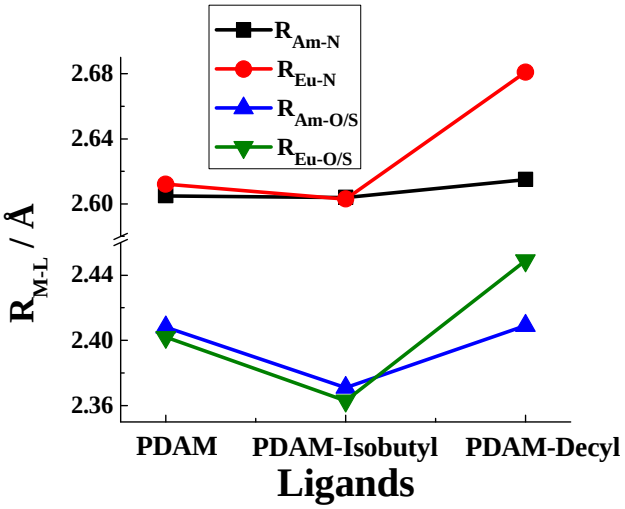

Fig. 3: Calculated M-L bond distances (Å) for Am^{3+} and Eu^{3+} complexes with PDAM, PDAM-Isobutyl and PDAM-Decyl ligands in presence of solvent

Due to very low solubility of the PDAM ligand in the organic diluents, we have alkylated the amide groups of PDAM through which its solubility in organic medium has been enhanced. Therefore, three amide-based ligands viz, PDAM (**3**), N,N-di-isobutyl PDAM (PDAM-Isobutyl, **5**) and N-decyl PDAM (PDAM-Decyl, **6**) have been synthesized (Figure 4) and the extraction efficiency of these ligands have been investigated using solvent extraction technique, the details of which are given in our recent publication.[16] It has been found that all the alkyl derivatives of PDAM ligand are Am^{3+} selective.

The experimentally observed distribution ratio values are found to be 21.4, 4.62 and 10.3 for the Am^{3+} ion with PDAM, PDAM-Isobutyl and PDAM-Decyl ligands, respectively, and the corresponding values for the Eu^{3+} ion are 2.9, 1.05 and 0.2. Therefore, a maximum extraction efficiency and separation of Am^{3+} over Eu^{3+} with a separation factor (S.F.) of 51 has been observed experimentally using the ligand PDAM-Decyl as compared to the other ligands (Figure 5) investigated by us. It is interesting to note that the separation factor is found to be the maximum at pH 1. Thus, all the experimental results confirm our theoretical predictions on the selectivity of hard donor containing ligands towards Am^{3+} ion.

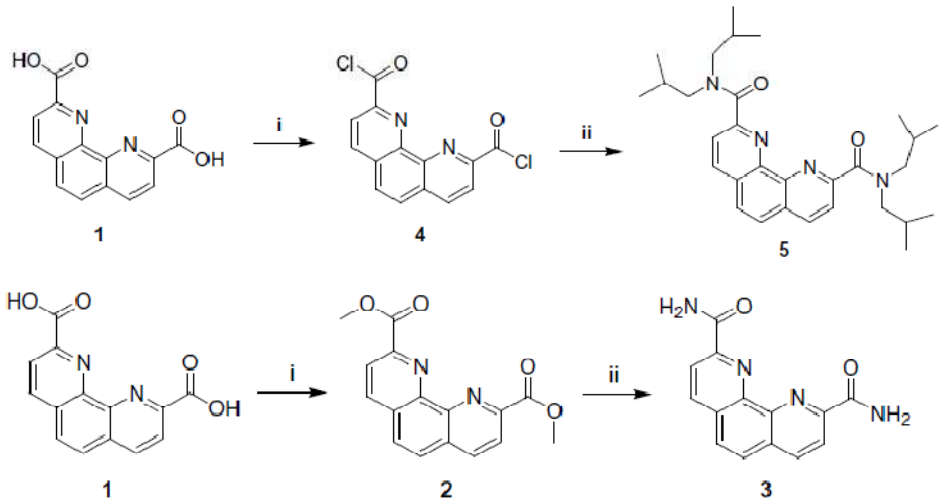

Scheme 1: i) MeOH, dry HCl, reflux, 2.5 h; ii) NH_3, NH_4Cl, 25 ^oC, 15 h.

Scheme 2:i) $SOCl_2$, reflux, 24 h; ii) Diisobutylamine, DMF, 25 ^oC, 24 h

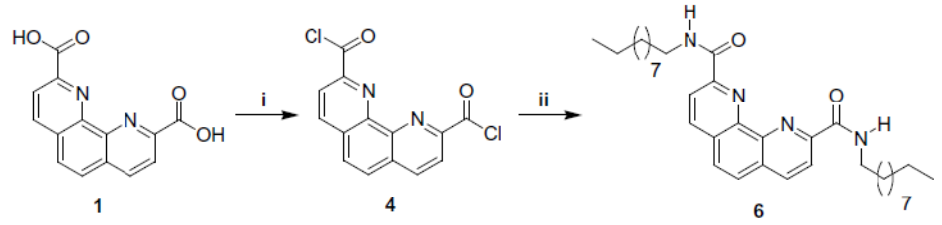

Scheme 3:i) $SOCl_2$, reflux, 24 h; ii) Decylamine, DMF, 25 ^oC, 24 h.

Fig. 4: Synthesis Schemes of PDAM (3), PDAM-Isobutyl (5) and PDAM-Decyl (6)

Predictions of New Metallofullerenes

The radioactive isotopes doped endohedral metallofullerenes are of considerable recent interests because of their potential applications in various fields including nuclear medicines.[21-25] Therefore, we have been interested to investigate the selective encapsulation of radioactive metal atom/ions using suitable fullerene. Moreover, it has been indicated that fullerene might act as nanoscale absorbent materials for radionuclide immobilization and it may be possible to entrap different actinides into carbon nanostructures, resulting into chemically stable radionuclide encapsulated biocompatible fullerenes for various applications including safe

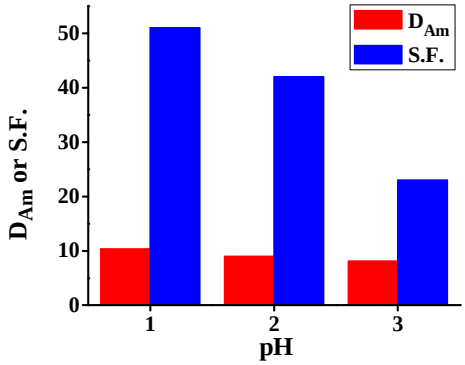

Fig. 5: Effect of pH on the Distribution Ratio (D_{Am}) and Separation Factor (S.F.) of Am^{3+} and Eu^{3+} using PDAM-Decyl. Org. Phase: 8 x 10^{-3} M PDAM-Decyl in dodecane:octanol (5:1) mixture; Aq. Phase: 2M $LiClO_4$ at different pH

management of nuclear wastes and designing cluster-assembled novel materials. The physical and chemical properties of a metallofullerene can be easily tuned by altering the encapsulated species, which in turn can act as a promising functional material. Smaller fullerenes are of special interest due to the presence of high curvature and huge strain energy owing to the presence of adjacent pentagonal rings, which lead to clusters with unusual intra and inter - molecular bonding and electronic properties. Among the smaller fullerenes (n < 60) only C_{36} have been isolated in solid form,[26] although other smaller fullerenes have been identified in various gas phase experiments.

The smaller fullerenes, which are generally formed during the production of stable fullerenes, are difficult to isolate because of their extremely high chemical reactivity and very low stability. However, encapsulation of a suitable dopant atom or ion (metal or nonmetal) may lead to the stabilization of smaller fullerenes. We have shown that the stability of the smaller fullerenes can be increased considerably through encapsulation of an appropriate metal atom or ion so that experimental preparation of such smaller size fullerenes may be possible. This stability gain has been rationalized using some fundamental electronic structure principles, viz., electronic shell closing, geometrical shell closing, the concept of magic number etc. We have chosen four different small fullerenes, viz., C_{20}, C_{24}, C_{26} and C_{36}, and encapsulated lanthanide /actinide (Ln / An) atoms/ions with specific number of valence electrons to attain magic number electronic configuration for the central metal atom/ion (Figure 6). Here, we have provided in-depth insights into the process of encapsulation of various metal atoms/ions within different fullerene cages using computational techniques. A complete discussion of structural, electronic, bonding, aromatic and spectroscopic properties for all the clusters has been provided in our recent publications.[17-20]

First we have considered[17] one of the smallest fullerenes, C_{20} to investigate the encapsulation of a Ln/An atom/ion into it. On encapsulation of a lanthanide/actinide atom/ion with six valence electrons, C_{20} fullerene with C_{2h}/D_{3d} symmetry has been found to be transformed to highly symmetric icosahedral structure. It is important to note that the HOMO-LUMO gap of the bare C_{20} fullerene is increased from 1.9 eV to 2.5-4.9 eV after encapsulation of various Ln/An atom/ion into it (Figure 7). The calculated values of high binding energy per atom (6.0-7.4 eV)

indicate that the $M@C_{20}$ clusters (M = Pr^{-}, Pa^{-}, Nd, U, Pm^{+}, Np^{+}, Sm^{2+}, Pu^{2+}, Eu^{3+}, Am^{3+}, Gd^{4+}, Cm^{4+}) are associated with very high stability as compared to the bare C_{20} cage. Similar to Pb_{12}^{2-} and Sn_{12}^{2-} species,[28] all the predicted organometallic icosahedral $M@C_{20}$ systems with 26-valence electrons occupying the metal-carbon hybrid orbitals (Figure 8), can be considered as highly stable clusters with "intermediate magic numbers". The most important aspect to be noted here is that the bare C_{20} fullerene with C_{2h}/D_{3d} symmetry is transformed to highly symmetric I_h structure after encapsulation of an atom/ion with 6-valence electrons, which is rather counter-intuitive from the fact that symmetry of a chemical system is generally lowered after doping with an impurity atom. Preparation of the $M@C_{20}$ clusters using laser ablation techniques may be one of the possible ways of detecting the elusive I_h structure of C_{20} cage by mass spectroscopy or photoelectron spectroscopy.

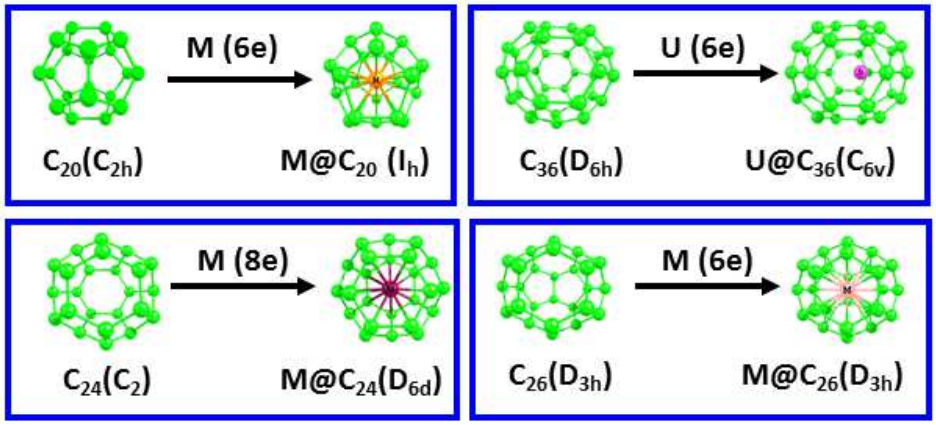

Fig. 6: Structure of bare C_{2n} Fullerenes and $M@C_{2n}$ Metallofullerenes with M as Ln /An atom or ion with specific number of valence electrons. Molecular Point Group Symmetry is given within the parenthesis

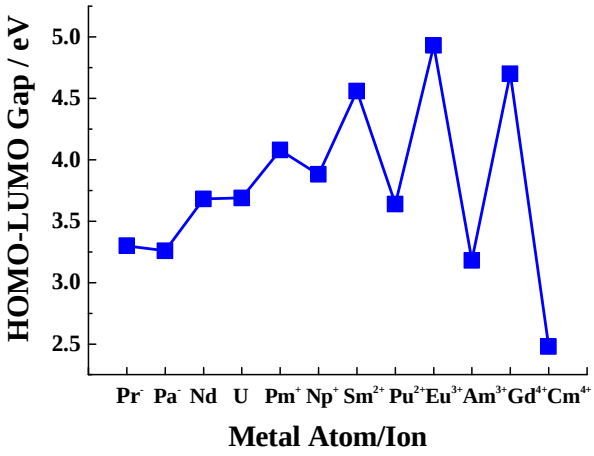

Fig. 7: Calculated values of HOMO-LUMO gap of $M@C_{20}$ Metallofullerenes, M= Pr^{-}, Pa^{-}, Nd, U, Pm^{+}, Np^{+}, Sm^{2+}, Pu^{2+}, Eu^{3+}, Am^{3+}, Gd^{4+} and Cm^{4+}

Subsequently, we have considered C_{36} fullerene, which was prepared experimentally in solid form[26] in the past. In this case we have investigated[19] different classical cage structures of C_{36} fullerene with an objective to investigate the possibility of enhancing the stability of the C_{36} cage through encapsulation of a uranium atom. We have studied fifteen $U@C_{36}$ isomers associated with various symmetries. Two competitive isomers are found to exist for the C_{36} cage, viz., D_{2d} and D_{6h}, whereas, for the $U@C_{36}$ metallofullerene, the C_{6v} isomer, which is derived from the D_{6h} cage, is the most stable one and significantly lower in energy as compared to the other isomers. The stability of the most stable $U@C_{36}$ metallofullerene has been rationalized through geometric and energetic criteria.

The stability of the $U@C_{36}$ metallofullerene has also been explained in terms of larger HOMO-LUMO gap (1.8-2.5 eV as compared to 1.34 eV for bare C_{36} fullerene), higher binding energy per atom (~6.5 eV) and more compact structure, as compared to the bare C_{36} cage. For the $U@C_{36}$ metallofullerene the 50 valence electrons are contributed by metal atom/ion (14 electrons from U) and the C_{36} cage (36 π electrons) (Figure 9).

The stability and the magic nature of the uranium encapsulated 36-atom fullerene cage, as evident from our calculated results, clearly indicate a possibility of formation of cluster-assembled material consisting of $U@C_{36}$ cluster as building block. The origin of the higher intensity peak corresponding to the $U@C_{36}$ metallofullerene in the experimentally observed[27] FT-ICR mass spectrum of cluster cations formed from the vaporization of a UO_2-graphite target may be attributed to the highly stable C_{6v} structure, derived from the C_{36} cage with D_{6h} symmetry.

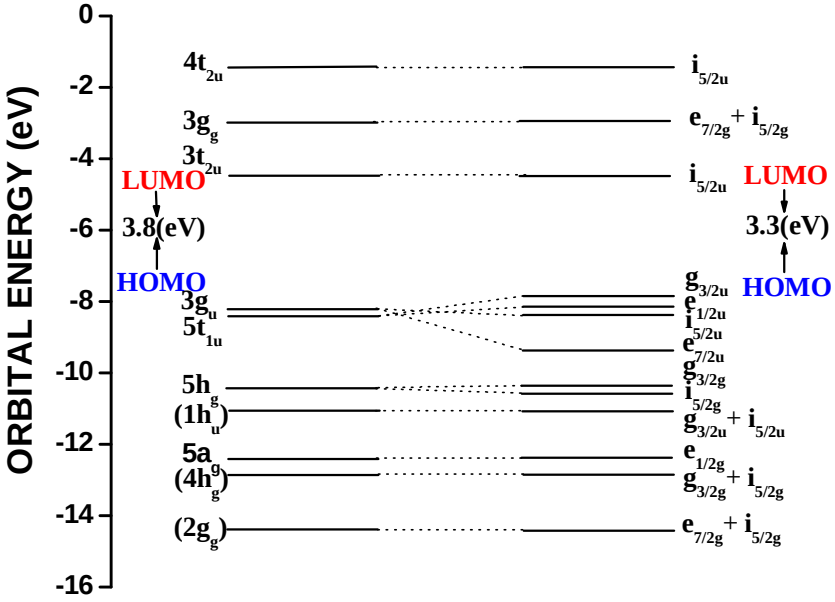

Fig. 8: Molecular Orbital Diagram for the $U@C_{20}$ Metallofullerene without (left) and with (right) Spin-Orbit Coupling

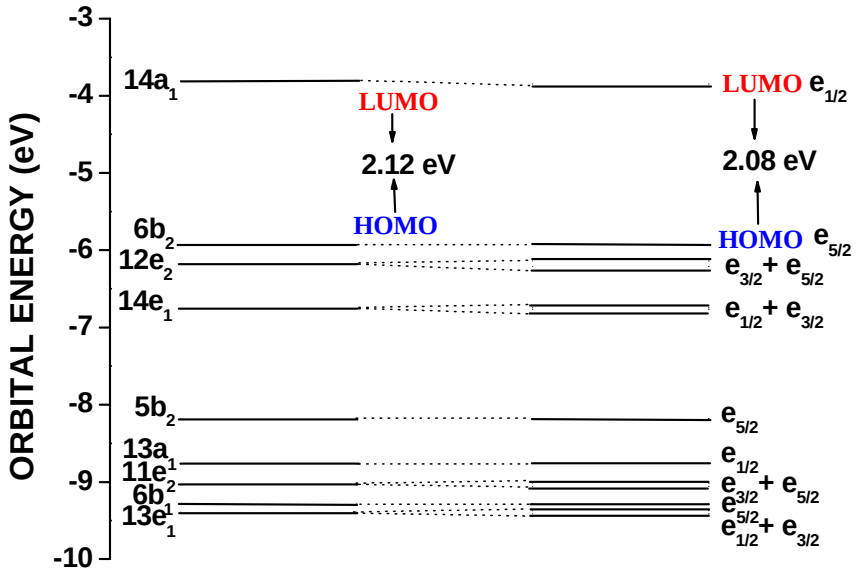

Fig. 9: Molecular Orbital Diagram for the U@C_{36} Metallofullerene without (left) and with (right) spin-orbit coupling

Apart from the M@C_{20} and U@C_{36} metallofullerenes, two new series of metal atom/ion encapsulated "superatoms" fulfilling the 32-electron principle have been proposed by us. Here we have considered two fullerenes, viz., C_{24} and C_{26}. In the case of C_{24} fullerene, the non-classical C_2 symmetry isomer is the most stable one for the bare cluster. However, after encapsulation of an atom/ion with 8 valance electrons inside the bare C_{24} cage, the sole classical isomer achieves high symmetry (D_{6d}) and stability along with high HOMO-LUMO gap. The elevation of symmetry from C_2 to D_{6d} point group and gain in stability can be attributed through fulfillment of 32-electron principle for the central actinide/lanthanide metal atom/ion (Figure 10), where 32-electrons are contributed by the actinide atom (8 valence electrons) and C_{24} fullerene (24 π electrons). The calculated values of HOMO-LUMO gap and binding energy indicate that the encapsulation of 8-valance actinide metal atom/ion is energetically more favorable as compared to encapsulation of 8-valance lanthanide metal atom/ion. The calculated results show that, Pu@C_{24} is the most stable metallofullerene among all the M@C_{24} clusters (M= Sm, Pu, Gd^{2+}, Cm^{2+}) reported by us.[18]

Next we have investigated the encapsulation of various lanthanide/actinide atom/ion with 6 valence electrons into the C_{26} fullerene. It has been found that the electronically open-shell C_{26} cluster with quintet ground state is transformed to a closed-shell singlet system on encapsulation with an actinide/lanthanide atom/ion with 6-valence electrons. High stability of the M@C_{26} metallofullerens (M = Pr^-, Pa^-, Nd, U, Pm^+, Np^+, Sm^{2+}, Pu^{2+}, Eu^{3+}, Am^{3+}, Gd^{4+}, Cm^{4+}) for all the actinides and few of the lanthanides has been rationalized in terms of larger HOMO-LUMO gap (2.6-4.0 eV as compared to 1.6 eV for the bare C_{26} cage) and higher binding energy per atom (5.8-6.8 eV). Thus, the M@C_{26} systems with 32 valence electrons occupying the metal-carbon hybrid orbitals, can be considered as highly stable clusters with "magic number" of electronic configuration (Figure 11). Thus, in addition to the recently predicted Pu@Pb_{12}, M@C_{28} and

$[U@Si_{20}]^{6-}$ systems,[28,29] the new series of metallofullerens reported by us[18,20] strongly suggest that the 32-electron principle might have important implications in the chemistry of lanthanide and actinide compounds. Moreover, all the calculated structural, energetic and spectroscopic properties indicate[18,20] that it may be possible to observe the $M@C_{24}$ and $M@C_{26}$ metallofullerenes through suitable experimental technique.

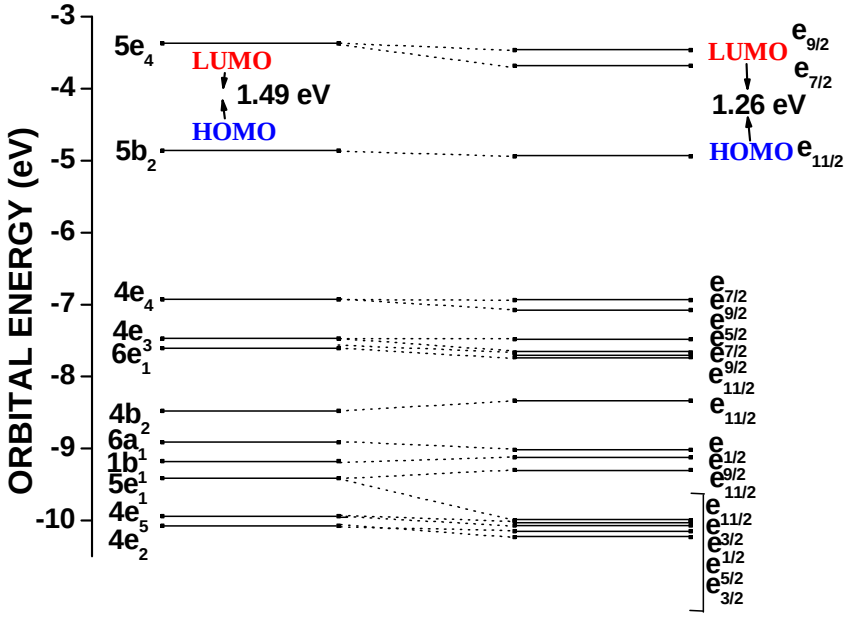

Fig. 10: Molecular Orbital Diagram for the $Pu@C_{24}$ Metallofullerene without (left) and with (right) spin-orbit coupling

Conclusion

A brief overview on the predictive ability of theoretical and computational chemistry in designing new compounds containing lanthanide and actinide atom/ion has been given in this article. Particularly, the importance of theoretical techniques in proposing new concept, viz., "Intra-ligand Synergism" and its role in predicting trivalent actinide selective new ligand associated with hard-donor atoms has been emphasized. However, idea of using hard-soft mixed donor ligands in achieving actinide selectivity is very new and therefore more collaborative and concerted efforts involving theoreticians, experimentalists and technologist are required to utilize this concept for future applications, which would indeed be interesting as well as challenging. Importance of stabilizing the smaller fullerenes through fulfillment of geometric and electronic shell closing through encapsulation of a lanthanide/actinide atom/ion within small-size fullerene has been highlighted, which are otherwise associated with very low stability for experimental preparation. Till now only limited number of investigations has been reported on the radionuclide encapsulated small-size metallofullerenes, and the stabilization strategy proposed by us might be very useful in designing new metallofullerenes involving various radionuclides. Entrapment of radioactive noble gas atoms is considered to be another important area of research in any nuclear energy establishment, and hence prediction of novel compounds involving noble

gas atoms is equally important. Recently we have contributed along this direction and predicted few chemically bonded noble gas compounds,[30] however, they are stable only at cryogenic conditions. Further studies for the prediction of stable noble gas compound at ambient conditions are in progress in our group.

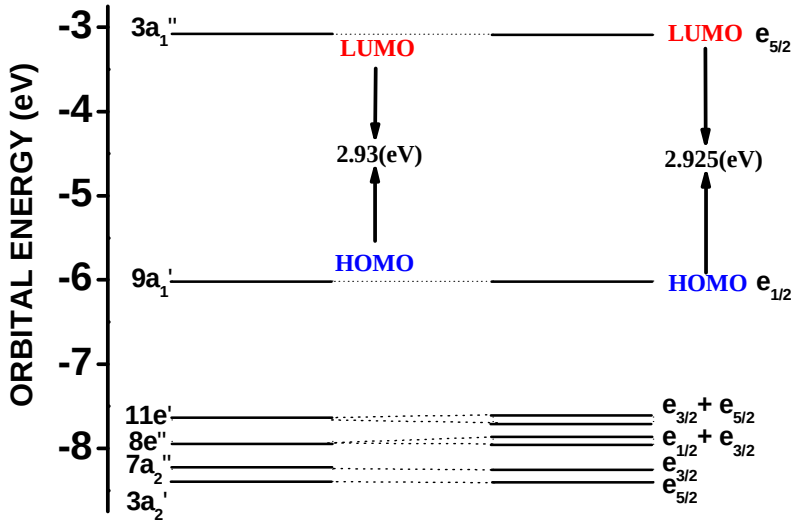

Fig. 11: Molecular Orbital Diagram for the U@C_{26} Metallofullerene without (left) and with (right) spin-orbit coupling

Acknowledgements

It is a pleasure to thank my coworker Dr. Debashree Manna for her significant contributions in all the works discussed in the present article. I am very much thankful to my experimental collaborators, Dr. Soumyaditya Mula, Dr. Arunasis Bhattacharyya and Dr. Subrata Chattopadhyay for their sincere efforts in experimental validation of our theoretical predictions. Shri Ayan Ghosh is gratefully acknowledged for many fruitful discussions and for critically going through the manuscript. I would like to thank Dr. Swapan K. Ghosh and Dr. B. N. Jagatap for their support and encouragement. Computer Division, BARC is thankfully acknowledged for providing parallel computational facility.

References

1. Pauling, L. *The Nature of Chemical Bond*; 3rd Eds.; Cornell University Press: Ithaca, New York, **1960**.
2. Pearson, R. G. *J. Am. Chem. Soc.* **1963**, *85*, 3533–3539.
3. Fukui, K. Science **1982**, *218*, 747–754.
4. Lewis, G. N. *J. Am. Chem. Soc.* **1916**, *38*, 762–785.
5. Langmuir, I. *Science* **1921**, *54*, 59–67.
6. Parr, R. G.; Yang, W. *Density Functional Theory of Atoms and Molecules*; Oxford University Press: New York, **1989**.

7. Parr, R. G.; Donnelly, R. A.; Levy, M.; Palke, W. E. *J. Chem. Phys.* **1978**, *68*, 3801–3807.
8. Parr, R. G.; Pearson, R. G. *J. Am. Chem. Soc.* **1983**, *105*, 7512–7516.
9. Parr, R. G.; Yang, W. *J. Am. Chem. Soc.* **1984**, *106*, 4049-4050.
10. Parr, R. G.; Chattaraj,P. K. *J. Am. Chem. Soc.* **1991**, *113*, 1854–1855.
11. Ghanty, T. K.; Ghosh, S. K. *J. Am. Chem. Soc.* **1994**, *116*, 3943–3948.
12. Ghanty, T. K.; Ghosh, S. K. *J. Am. Chem. Soc.* **1994**, *116*, 8801–8802.
13. Cramer, C. J. *Essentials of Computational Chemistry: Theories and Models*; 2nd Eds.; John Wiley, **2004**.
14. (a) Pyykkö, P.; Runeberg, N. *Angew. Chem. Int. Ed.* **2002**, *41*, 2174–2176; (b) Li, X.; Kiran, B.; Li, J.; Zhai, H-J; Wang, L-S. *Angew. Chem. Int. Ed.* **2002**, *41*, 4786–4789.
15. Manna, D.; Ghanty, T. K. *Phys. Chem. Chem. Phys.* **2012**, *14*, 11060–11069.
16. Manna, D.; Mula, S.; Bhattacharyya, A.; Chattopadhyay S.; Ghanty, T. K. *Dalton Trans.* **2015**, *44*, 1332–1340.
17. Manna, D.; Ghanty, T. K. *J. Phys. Chem. C* **2012**, *116*, 16716–16725.
18. Manna, D.; Ghanty, T. K. *J. Phys. Chem. C* **2012**, *116*, 25630–25641.
19. Manna, D.; Ghanty, T. K. *J. Phys. Chem. C* **2013**, *117*, 17859–17869.
20. Manna, D.; Sirohiwal A.; Ghanty, T. K. *J. Phys. Chem. C* **2014**, *118*, 7211–7221.
21. (a) Mikawa, M.; Kato, H.; Okumura, M.; Narazaki, M.; Kanazawa, Y.; Miwa, N.; Shinohara, H. *Bioconjugate Chem.* **2001**, *12*, 510–514; (b) Bolskar, R. D.; Benedetto, A. F.; Husebo, L. O.; Price, R. E.; Jackson, E. F.; Wallace, S.; Wilson, L. J.; Alford, J. M. *J. Am. Chem. Soc.* **2003**, *125*, 5471–5478.
22. Iezzi, E. B.; Duchamp, J. C.; Fletcher, K. R.; Glass, T. E.; Dorn, H. C. *Nano Lett.* **2002**, *2*, 1187–1190.
23. Cagle, D. W.; Kennel, S. J.; Mirzadeh, S. et al. *Proc. Natl. Acad. Sci.* U S A. **1999,** *96*, 5182–5187.
24. Ross, R. B.; Cardona, C. M.; Guldi, D. M.; Sankaranarayanan, S. G.; Reese, M. O.; Kopidakis, N.; Peet, J.; Walker, B.; Bazan, G. C.; Van Keuren, E.; Holloway, B. C.; Drees, M. *Nat. Mater.* **2009**, *8*, 208–212.
25. Rudolf, M.; Feng, L.; Slanina, Z.; Akasaka, T.; Nagase, S.; Guldi D. M. *J. Am. Chem. Soc.* **2013**, *135*, 11165–11174.
26. Piskoti, C.; Yarger, J.; Zettl, A. *Nature* **1998**, *393*, 771–774.
27. Dunk, P. W.; Kaiser, N. K.; Mulet-Gas, M.; Rodriguez-Fortea, A.; Poblet, J. M.; Shinohara, H.; Hendrickson, C. L.; Marshall, A. G.; Kroto, H. W. *J. Am. Chem. Soc.* **2012,** *134*, 9380–9389.
28. Dognon, J. P.; Clavaguéra, C.; Pyykkö, P. *Angew. Chem. Int. Ed.* **2007**, *46*, 1427–1430.
29. Dognon, J. P.; Clavaguéra, C.; Pyykkö, P. *J. Am. Chem. Soc.* **2009**, *131*, 238–243; Dognon, J. P.; Clavaguéra, C.; Pyykkö, P. *Ch*em. *Sci.* **2012**, *3*, 2843–2848.
30. (a) Ghosh, A.; Manna, D.; Ghanty, T. K. *J. Chem. Phys.* **2013**, *138*, 194308; (b) Ghosh, A.; Manna, D.; Ghanty, T. K. *J. Phys. Chem. A* **2015**, *119*, 2233–2243; (c) Manna, D.; Ghosh, A.; Ghanty, T. K. *Chem. Eur. J* **2015**, *21*, 8290–8296.

PROCESS DEVELOPMENT FOR SEPARATION OF CESIUM FROM ACIDIC NUCLEAR WASTE SOLUTION USING 1,3-DIOCTYLOXYCALIX[4]ARENE-CROWN-6 + ISODECYL ALCOHOL / *n*-DODECANE SOLVENT

J.N. Sharma
Process Development Division

Shri J.N. Sharma is the Recipient of the DAE Homi Bhabha Science & Technology Award for the year 2013

Abstract

A new process for selective separation of cesium from acidic nuclear waste solution has been described using 1,3-dioctyloxycalix[4]arene-crown-6 (CC6)/n-dodecane modified with isodecyl alcohol. The solvent has shown strong extraction ability for cesium between 1 to 6.0 M nitric acid. Stoichiometry of the extracted complex determined by slope analysis method reveals 1:1:1 molar ratio for Cs^+, CC6 and HNO_3. Extraction of cesium was found to be independent of nitrate ion concentration, due to formation of solvated free ions $Cs^+CC6.HNO_3$ and NO_3^- in the organic medium. Lab scale mixer-settler experiments with four extraction, two scrubbing and four stripping stages removed about 99% of cesium with very high selectivity from high level waste (HLW) solution. Plant scale operation with 12 extraction and 12 stripping stages gave 99.97 % recovery of cesium from sulphate bearing legacy HLW.

Introduction

Safe management of high level radioactive waste (HLW) solution is one of the most important technological challenges faced by the nuclear industries. Development of efficient separation processes for removal of harmful radiotoxic elements from waste solutions will be the key for success and public acceptance of nuclear energy program. The toxicity of the waste is mainly due to the presence of unrecovered U and Pu, long-lived minor actinides such as Np, Am, Cm and radioactive fission products, mainly rare earths, ^{99}Tc, ^{90}Sr and isotopes of cesium (^{135}Cs, ^{134}Cs and ^{137}Cs). Removal of residual Uranium and Plutonium from the waste can be done by employing TBP as a solvent. Actinide partitioning and Transmutation (P&T) is the proposed strategy for safe management of minor actinides, where they will be separated from the waste and converted to short-lived or stable nuclides in a high energy flux reactors. It is known that, ^{137}Cs ($t_{1/2}$ = 30.1 years) and ^{90}Sr ($t_{1/2}$ = 28.9 years) are major heat emitting nuclides contributing largely on heat and radiation load of HLW and ^{135}Cs ($t_{1/2}$ = 2.3 x 10^6 years) has a long term adverse impact on ecology due to its mobility in repository [1]. Removal of ^{137}Cs and ^{90}Sr provides several advantages, like, significant reduction in the need for redundant cooling of the waste solution, reduction in time of vitrified waste storage before disposal in geological

formation, increases the stability of vitrified waste which results in increase in capacity of geological repository, facilitates the handling and transport of waste, and also the separated ^{137}Cs can be used as gamma source in medical and industrial applications. It is, therefore, imperative to develop an efficient separation process for recovery of cesium from HLW. In fact, its selective separation from HLW solution, containing large content of sodium and other competing ions, has long been one of the most challenging goals [2].

The calix[4]arene-crown-6 ethers are one of the most widely investigated class of calix-crown ring system for their application as host molecules for selective separation of cesium ion from acidic and alkaline nuclear waste solutions. These calix-crown-6 ethers, when fixed in 1, 3 alternated conformation posses a cavity which is highly complementary to cesium ion and serve as potential extractants for selective separation of cesium ion in liquid-liquid extraction processes from solution containing large amount of Na^+, H^+ and other metal ions. This property has enabled their exploitation in selective separation of radioactive cesium from acidic nuclear fuel reprocessing solutions containing much large amount of sodium compared to cesium. However, difficulty in synthesis of calix-crown-6 molecules at larger scale and their incompatibility with PUREX based diluents (*n*-dodecane) complicates the attempt to develop a process for separation of cesium from HLW at industrial scale [3]. In an effort to recover cesium from HLW solution, we have successfully synthesized 1,3-dioctyloxycalix[4]arene-crown-6 at larger scale indigenously and also developed diluent system based on *n*-dodecane and isodecyl alcohol (IDA), which is our existing diluent system for on-going program on separation of minor actinides and strontium from HLW solution [4].

In this report, results of batch and continuous counter-current extraction of cesium from controlled and sulphate bearing legacy HLW solutions at lab and plant scale runs are presented.

Experimental

CC6 (Fig.1) was synthesized and purified according to procedure described by Casnati et al. [2]. The product was obtained as white needle crystals with a sharp melting point of 94-96 ^oC. The composition of HLW solution is listed in Table 1, it is a high salt content historical waste called legacy HLW, stored in our waste tank farm.

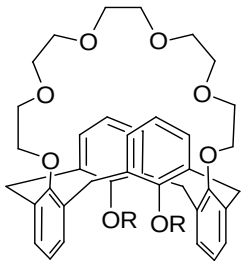

R = C_8H_{17}

Fig.1: Structure of 1,3-dioctyloxycalix[4]arene-crown-6

Table1: Batch extraction of metal ions from legacy HLW solution

Organic phase: 0.03 M CC6 + 30% IDA / *n*-dodecane
Aqueous phase: HLW solution, HNO_3 = 3.6 M, Sulphate = 8 g/L, O/A = 1
Gross β = 5.4 Ci/L, Gross α = 3.66 mCi/L
^{137}Cs = 1.75 Ci/L, ^{90}Sr = 1.5 Ci/L, ^{106}Ru = 1.2 mCi/L, ^{125}Sb = 1.12 mCi/L, ^{144}Ce = 0.97 mCi/L

Elements	Concentration (mg/L)	D_M	Separation factor (SF) D_{Cs}/D_M	$[HNO_3]$ in loaded organic
Cs	---	5.2	---	0.065 M
Sr	---	1.0E-04	52000	
Mo	130	2.0E-02	260	
Zr	86	1.0E-02	520	
Ru	---	2.0E-02	260	
Ca	1120	1.0E-03	5200	
Ba	375	5.0E-03	1040	
Fe	7600	1.0E-03	5200	
Na	30,602	1.0E-04	52000	
K	215	1.0E-02	520	
Al	5750	1.0E-04	52000	
La	300	ND	very high	
Ce	---	ND*	very high	
Nd	750	ND	very high	
Y	60	1.0E-03	5200	
U	18000	5.0E-03	1040	
Pu	---	< 1.0E-03	>5200	
Am	---	< 1.0E-03	>5200	

**ND: Not detected*

For the determination of distribution ratio (D_M), equal volume of organic phase constituted with CC6, isodecyl alcohol/*n*-dodecane and aqueous phase containing metal ions was equilibrated for 10 minutes in a 5 mL glass vial. After the phase separation by centrifugation, the organic and aqueous phases were separated and analyzed for metal ions, the D_M was calculated as the ratio of concentration (or radioactivity) of metal ion in the organic phase to the aqueous phase.

Results and discussion

Extraction of cesium

Preliminary studies on dissolution of CC6 in *n*-dodecane at 25 ±1°C has shown that a solution up to 0.03 M is stable for more than two months, above this concentration the dissolution was assisted by sonication, however after standing for 48 hours, a powdery white solid was precipitated out. CC6 was found to have good solubility in isodecyl alcohol + *n*-dodecane mixture, the solubility increases with increase in isodecyl alcohol content in the mixture. Extraction of cesium with CC6 + IDA/*n*-dodecane solutions was carried out and the results in variation of D_{Cs} as a function of isodecyl alcohol concentration at different CC6 molarities (0.01-

0.03 M) were shown in Fig.2. There was almost no extraction of cesium when CC6 was dissolved only in *n*-dodecane, extraction was observed only on addition of isodecyl alcohol to the solvent. Extraction of cesium increases with increase in concentration of isodecyl alcohol for all the concentrations of CC6. Isodecyl alcohol, being a polar molecule, helps in solvating the polar calix-crown-cesium complex, therefore, with increase in isodecyl alcohol concentration, D_{Cs} increases. From the results, it is clear that a higher concentration of isodecyl alcohol is more suitable for effective extraction of cesium. 0.03 M CC6/*n*-dodecane containing 30% and above isodecyl alcohol content was considered as appropriate process solvent for effective separation of cesium from acidic HLW. The relation between D_{Cs} and $HNO_{3\ (initial)}$ concentration for 0.03 M CC6 + 30% IDA/*n*-dodecane is shown in Fig.3. A very small increase in D_{Cs} was observed in lower region of nitric acid, up to 1 M nitric acid concentration D_{Cs} was 0.58, and above it the increase was significant up to 6 M nitric acid ($D_{Cs} \sim 6.6$) and then decreases with further increase in nitric acid concentration. Thus, indicating a significant role of nitric acid in extraction process. The acid dependency on the extraction of cesium was determined from nitric acid solutions of constant nitrate concentrations or at fixed ionic strength of 4.0 M $(H,Na)NO_3$. The observed slope of 0.976 ± 0.035 suggests the presence of one molecule of HNO_3 in the extracted complex.

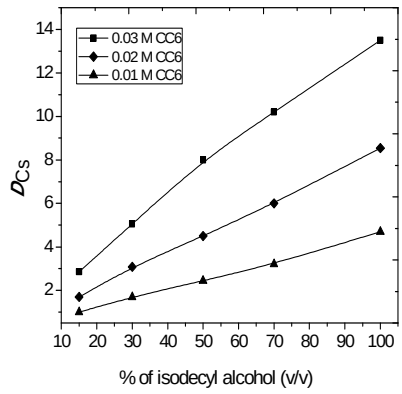

Fig.2: Variation of D_{Cs} at 3.5 M HNO_3 with isodecyl alcohol concentration

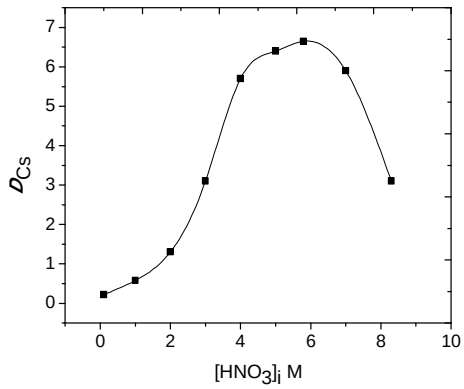

Fig.3: Extraction dependency of cesium on initial nitric acid concentration

The increase in nitric acid concentration favors the formation of organic soluble $Cs^+.CC6.HNO_3$ adduct, thus, resulting in increase in D_{Cs}. However, beyond 6 M nitric acid, decrease in D_{Cs} is attributed to the competitive extraction of nitric acid by CC6. The existence of nitric acid in the complex is likely due to hydrogen bonding between HNO_3 and etheric group of crown ether moiety of CC6. It is interesting to note that extraction of cesium is almost negligible at lower nitric acid concentrations (≤ 0.1 M), therefore this important property is used for stripping cesium with deionized water. The extractant dependency plot is a straight line with a slope of 0.99 ± 0.02, indicating participation of one molecule of CC6 in the extracted complex. Role of counter anion on the extraction was determined from D_{Cs} variation with $[NO_3^-]_{initi}$ at constant initial nitric acid concentrations. The results show no change in D_{Cs} with increase in nitrate ion

concentration. Contrary to extraction behavior of most of the neutral extractants, this result suggests that nitrate ion is not participating in the cesium-CC6 complex formation.
The stoichiometry of the complex indicated one cesium ion bonded with one molecule each of CC6 and HNO_3 to give a cationic complex of type $CsCC6^+.HNO_3$. This complex either remains ion paired with NO_3^- ion to give $CsCC6.HNO_3.NO_3$, or may remains dissociated from NO_3^- ion to give free ions $CsCC6^+.HNO_3$ and NO_3^-.

The extraction process may be thus represented as:

$$Cs^+_{aq} + NO_3^-{}_{aq} + CC6_{org} + HNO_{3\,aq} \rightleftharpoons CsCC6.NO_3.HNO_{3\,org} \quad (1)$$

$$Cs^+_{aq} + NO_3^-{}_{aq} + CC6_{org} + HNO_{3\,aq} \rightleftharpoons CsCC6^+.HNO_{3\,org} + NO_3^-{}_{org} \quad (2)$$

A non-polar diluents with low dielectric constant such as alkanes and aromatic hydrocarbons favor ion-pairing as shown in equation 1, whereas, in polar diluents like o-nitrophenyl alkyl ethers, nitrobenzene, ion-pair dissociation is favorable following equation 2. Since, in the present case the diluent used is *n*-dodecane with relatively high concentration (30% v/v) of polar phase modifier, isodecyl alcohol, it is therefore, expected that the diluent will have fairly high dielectric constant to favor ion-dissociation mechanism as shown in equation 2. Also, due to hydrogen bonding and electron pair donating ability of isodecyl alcohol, it can stabilize the complex cation and anion by solvation, thereby, increasing internuclear separations and preventing their close contact. Thus, the anomalous behavior of independency of D_{Cs} on NO_3^- ion concentration may be attributed to extraction mechanism following equation 2, where the ionic species are predominantly dissociated ions as $CsCC6^+.HNO_3$ and NO_3^- in the solvent [5].

Batch extraction test of cesium from HLW solution

The extraction behavior of cesium and other metal ions present in HLW solution was investigated using 0.03 M CC6 + 30% IDA/*n*-dodecane. The distribution ratios of all the elements (D_M) and separation factors with respect to cesium are tabulated (Table 1). The results showed that D_{Cs} is much higher compared to other elements, thus, indicating a very high selectivity for cesium extraction over other elements. Radiolysis of the process solvent up to an absorbed γ-dose of 0.6 MGy produces essentially no deterioration in its performance

Lab scale counter-current mixer-settler studies

The main objective for counter-current mixer-settler runs was to optimize flow sheet parameters for maximum recovery of cesium at high purity from HLW solution. Uranium was separated using TBP prior to the runs. Taking into account of reasonably high D_{Cs}, and good stripping with deionized water, four stages each of extraction and stripping at A/O of 1:1 was thought suitable for generating extraction and stripping data. Considering very low distribution ratios of other elements, only two stage of scrubbing unit was employed. Scrubbing of clear loaded organic phase was then carried out with 3.5 M nitric acid at O/A ratio of 2:1. Fig.4 shows the concentration profile of cesium in cpm/ml (after suitable dilution) across the extraction,

scrubbing and stripping stages, since the extraction of other elements were very low, therefore, their concentrations were only analyzed in the final strip aqueous solution. The results showed a good material balance with 99% extraction of cesium from HLW solution, four stages of stripping was found adequate to strip cesium from loaded organic, the discharged solvent contained less than 0.5% cesium. The total concentration of impurities in the cesium strip solution was found to be less than 1mg/l. The trials were repeated ten times with recycled solvent, the efficiency of the solvent was retained in all the runs.

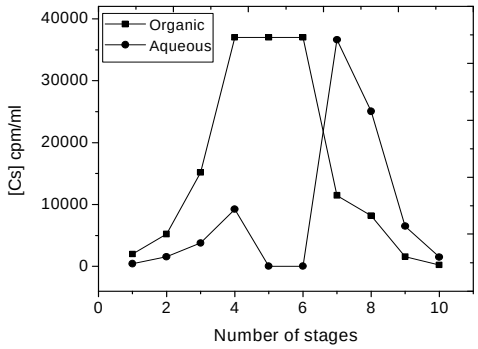

Fig. 4: Cesium concentration profile. Stages: 1-4 Extraction, 5-6 Scrubbing and 7-10 stripping

Fig.5: In cell view of cesium separation facility at WIP, Trombay

Plant scale counter-current mixer-settler run

To meet the requirements of maximum possible recovery of cesium from HLW at plant scale, few changes were made in the composition of the solvent and in the number of stages of mixer-settler. Solvent was constituted with higher percentage of the phase modifier, 50% IDA instead of 30% to obtain better extraction efficiency (D_{Cs} = 9), total number of extraction and stripping stages were increased to 12 x 2 from of 4 x 2. As the extraction of competing ions is negligible, therefore, no scrubbing section was kept. The extraction and stripping efficiencies obtained were more than 99.95 %, the ^{137}Cs mass balance was good with less than 0.1mCi/L ^{137}Cs left in the stripped solvent phase. Solvent retained the extraction and stripping properties throughout the run which lasted for continuous 20 days. This run processed about 30,000 liter of legacy HLW and 45,000 Ci of ^{137}Cs has been separated. The separated cesium was made as vitrified radiation source (pencils) and supplied to BRIT for commercial utilizations. In-cell view of the plant is shown in Fig.5. Following are the results of plant scale run:

Solvent: 0.03 M CC6 + 50% IDA/*n*-dodecane
Feed: Sulphate bearing HLW, HNO_3= 3.8 M
Strippant: 0.01 M HNO_3
Flow rates: Feed = 80 L/h, Solvent: 60 L/h, Strippant: 60 L/h
HLW processed: 30,000 L
^{137}Cs in HLW = 1.8 Ci/L, ^{137}Cs in raffinate = 0.5 mCi/L, ^{137}Cs in product = 2.5 Ci/L
% Recovery = 99.97
^{137}Cs Recovered: 45,000 Ci
Cs ($DF_{feed/raff}$) = 3600

Conclusions

CC6 constituted with a mixture of isodecyl alcohol and *n*-dodecane is found to be highly efficient solvent for separation of cesium from acidic high level waste solutions. Plant scale mixer-settler runs were smooth without any hydrodynamic problems, the extraction and stripping efficiencies were very high with 99.97% recovery of cesium from legacy HLW solution.

Acknowledgement

The author is thankful to P.K.Wattal, Ex-Director, NRG and A.K.Suri, Ex-Director, MG, for their continuous support in development the solvents for back-end processes. He is also thankful to all the members of the team for taking up the process of cesium separation to plant scale.

References

1. Radioactive waste management and disposal, L. Cecille, Ed., Elsevier Science Publisher: London, New York, 1991.
2. A. Casnati, Pochini, R. Ungaro, F. Ugozzoli, F. Arnaud, S. Fanni, M.-J. Schwing, Richard J.M. Egberink, F.de Jong, David N. Reinhoudt, Synthesis, complexation, and membrane transport studies of 1,3-alternate calix[4]arene-crown-6 conformers: A new class of cesium selective ionophores, J. Am. Chem. Soc. 117 (1995) 2767-2777.
3. W. Jianchen, Z. Xiaowen, S. Chongli, Extracting performance of cesium by 25,27-bis(2-propyloxy) calix[4]-26,28-crown-6 (iPr-C[4]C-6) in n-octanol, Sep. Sci. Technol. 40 (2005) 3381-3392.
4. J.N.Sharma, R. Ruhela, K.K. Singh, M. Kumar, C. Janardhanan, P.V. Achutan, S. Manohar, P.K. Wattal and A.K. Suri, Studies on hydrolysis and radiolysis of TEHDGA / isodecyl alcohol / *n*-dodecane solvent system, Radiochim. Acta 98 (2010) 485-491.
5. J.N.Sharma, Amar Kumar, Vikas Kumar, S.Pahan, C.Janardanan, V.Tessi, P.K.Wattal, Process development for separation of cesium from acidic nuclear waste solution using 1,3-dioctyloxycalix[4]arene-crown-6 + isodecyl alcohol/*n*-dodecane solvent. Sep. Purif. Technol., 135 (2014) 176-182.

PULSED POWER DRIVEN SYSTEMS AND APPLICATIONS TO MATERIAL STUDIES

T. C. Kaushik
Applied Physics Division

Dr. T.C. Kaushik is the Recipient of the DAE Homi Bhabha Science & Technology Award for the year 2013

Abstract

Pulsed Power based devices have been developed and utilized to study matter under pressure or in high temperature plasma states. These include "Electric Gun" to accelerate flyers to >6 km/s which are impacted on samples like tantalum, aluminum, iron and tin to obtain pressures up to 70 GPa with on-line observation of phase transitions. Capacitor banks have been used to drive "Rail Gun" to accelerate projectiles to >3 km/s or ultra-high pulsed magnetic fields of >260 Tesla compress targets as also to produce and characterize "pinch" plasmas. Inductive Energy systems have been developed to obtain current amplification of >70. Exploding conductor based opening switch schemes have been devised to shape short and fast current pulses. Systems and diagnostics have been applied to monitor fissile materials especially the high efficiency neutron detectors passive monitoring of waste hull.

Introduction

Capacitor bank and inductive storage systems are potential energy drivers for various devices used in basic studies of matter at high pressures, density or temperatures. A number of research and development activities related to Pulsed Power Sources and their use in strategic as well as in basic science studies have been developed, characterized and utilized by us. Salient features of some of these facilities are noted in Table-1.

Electrically Exploding Foil (Electric Gun) Accelerators

Electrically exploding foil accelerator (EEFA, also known as electric gun) works on the principle of electrical explosion of conductors by discharge of energy stored in a fast capacitor bank. Discharge of current ohmically heats and explodes a thin metallic bridge foil like a super high explosive, sandwiched between two dielectric sheets backed by a heavy tamper on one side and an appropriate size barrel on the other. These systems find applications in high pressure shock studies of materials especially energetic and hazardous (such as actinides) in nature. In our laboratory EEFA of various energies have been developed for different applications. This

include[1] a portable 1.6 kJ (ELG-2) set up for initiation studies of high explosives, 8 kJ (ELG-8) system for high pressure impact studies and a miniaturized low energy (up to 100J) system.

The ELG-2 system (see Fig .1.) has been developed and commissioned to carry out shock initiation studies on high explosives. An important aspect of system design is its portability. A flyer velocity ofto 4.0 km/s have been measured in Kapton flyers of thickness 125 µm and diameter 8 mm. Experiments carried out on wax bounded RDX pellets measure detonation and its simultaneity at free surface using optical fibers connected to fast photodiodes. The values are found to be in good agreement with the theoretical estimations.

Fig.1: ELG-2 System

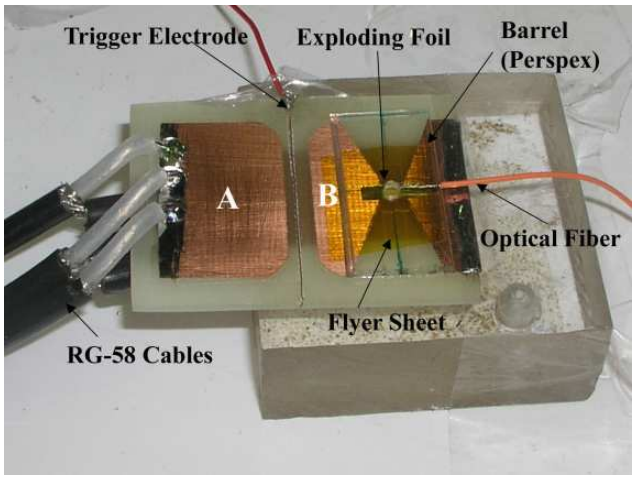

Fig.2: PCB Mounted Spark gap and EEFA

ELG-8 system (Fig.2.) is designed to accelerate larger diameter flyers (~10 mm) to higher velocities and conduct shock studies at relatively high pressures with better accuracies. In experiments a maximum velocity of 6.3 km/s has been registered in 125 µm thick x 6 mm diameter Kapton flyers with planarity in the range of a few milliradians.

The performance of these systems have been characterized with an in house developed Fabry-Perot velocimeter (FPV), which measures the Doppler shift in the light reflected from the moving surface and can measure velocities in the range of 0.2-10 km/s with a resolution of 0.2 km/s. This interferometer was recently improvized[2] with dual beam configuration to yield information from two moving surfaces in same shot, Different metals like aluminum, copper, tin, tantalum, tin, titanium and zirconium in the form of thin foils have been subjected to impacts with peak shock pressures of up to 70 GPa being attained in tantalum. Peak particle velocities at the target-glass interface measured by FPV have been found in good agreement with the reported equation of state data. A fiber optic based technique has been implemented to measure the shock velocity in stepped copper targets based on measuring the time delay in the shock breakouts at the consecutive steps. Measured shock velocity has again been in reasonable agreement with the reported equation of state data. In-situ measurement of projectile as well as particle or shock wave velocity in impacted targets has also been carried out[3] wherein phase transition in Ti and Zr

foils has been recorded at pressures well in agreement with reported data. Typical record for the case of impact on Zn foil is shown in Fig. 3.

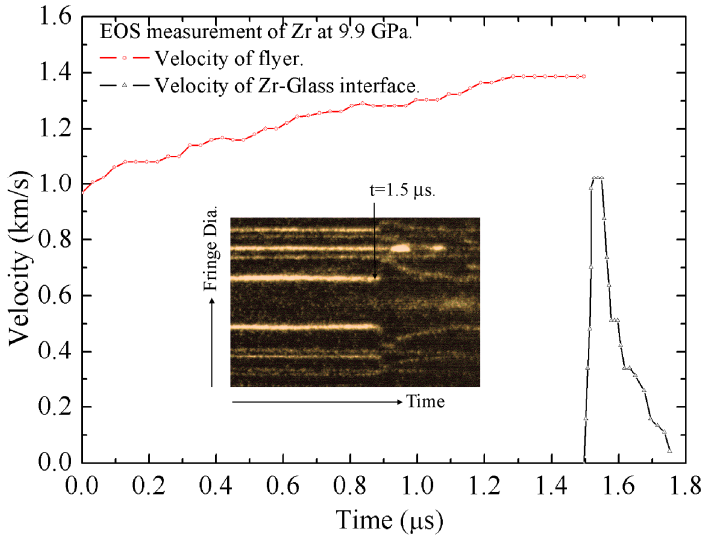

Fig.3: Streak Photograph and Corresponding Velocity Profile in Zn Sample

Initiation studies carried out on ELG-2 system have been extended to develop miniaturized and flexible assemblies. To achieve compactness, exploding foil assembly has been designed over a printed circuit board with an arrangement to safely hold an explosive pellet over it. To provide flexibility and low inductance, this assembly has been connected to high voltage capacitor using 2 meter long bunch of RG-174 coaxial cables. This arrangement helps in placing this assembly at a desired location away from the capacitor bank, spark gap and high voltage charging unit. With capacitor of 100J energy the velocities up to 3.0 km/s has been achieved on Mylar flyers diameter 3.0 mm and thickness 75 µm. Later the exploding foil assembly and spark gap, designed and characterized over a small piece of printed circuit board, were integrated together (Fig.9). This integrated assembly has been found to accelerate 3 mm diameter flyers up to a velocity of 1.6 km/s with a 40 J capacitor.A numerical scheme based on 1D Lagrangian finite difference formulation has been also developed for theoretical modeling of such systems. The developed numerical scheme is validated against experimental and simulation data reported in literature on systems of different energies. Numerically computed flyer velocity profiles and final flyer velocities have been found in close agreement with the reported experimental data and also with the results measured in our laboratory.

Rail Gun

Rail gun essentially consists of two parallel metal bars (rails) separated by suitably sized insulator blocks to form its barrel. Projectile is placed between the rails and backed by an armature (metal or plasma) to complete the current path. As a high current is passed through the rails and armature, the latter is accelerated by the electromagnetic force to push the projectile. In our lab, we have developed a 60cm long; 6mm square bore rail gun. The rails consist of two 12x

12 mm^2 ETC grade copper bars. A 4mm deep step was introduced on either side of the rails to get a bore size of 6mm x 6mm. The rail gun is fired by a 38 kJ capacitor bank with peak current of 150kA with a quarter cycle rise time 0.12ms**.** A velocity of 3.1 km/s has been obtained which matches well with theoretically expected value of 3.2 km/s Assembly and typical signals in a shot are shown in Fig.4. Another 200 kJ capacitor bank has been commissioned for enhancing the velocity further with a new rail gun set up.

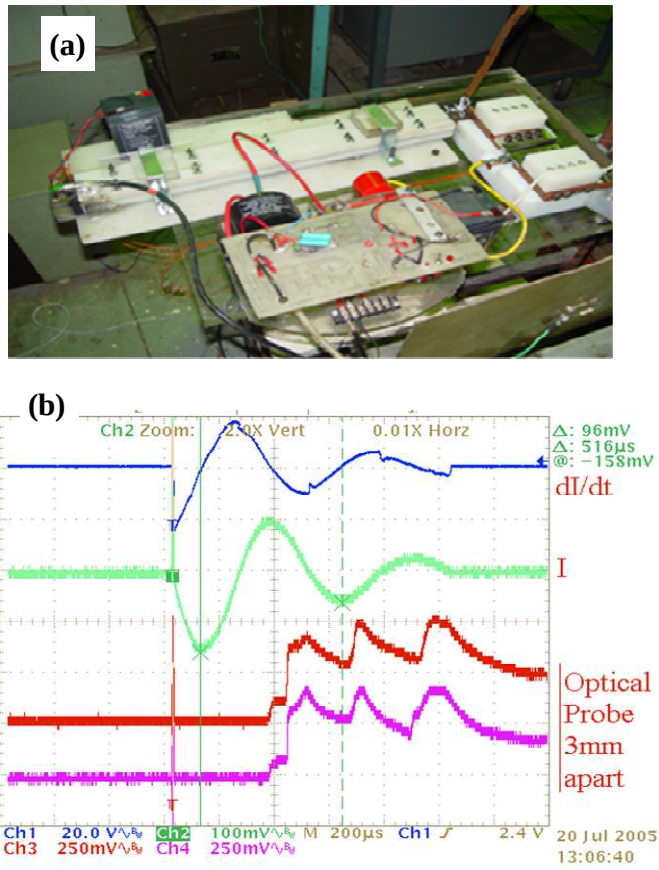

Fig.4. (a) System Photograph &
(b) Experimental Results with 38 KJ Rail Gun Assembly

Ultra-High Magnetic Field Generation Devices

With an aim is to develop a facility to generate high (multi mega gauss) magnetic field, two different schemes[4] have been implemented in our lab. These are inertial magnets and electromagnetically driven flux compression generators, briefly described below.

Inertial magnets

Inertial magnets are single turn coils made out of copper with 12 to 15mm thickness as shown in Fig. 5. These have been powered by MAGIC capacitor bank. The current flowing through the coil results in corresponding magnetic field at the coil center. The coil generates high magnetic

field by virtue of its inertia. Experiments have been carried with various coil dimensions and a maximum peak magnetic field of 257 T has been realized[4], using a copper coil with 3.6mm inner diameter, 35mm outer diameter and 5mm length. A compact B-dot probe has been used to measure this transient magnetic field with an estimated error of ±25 T.

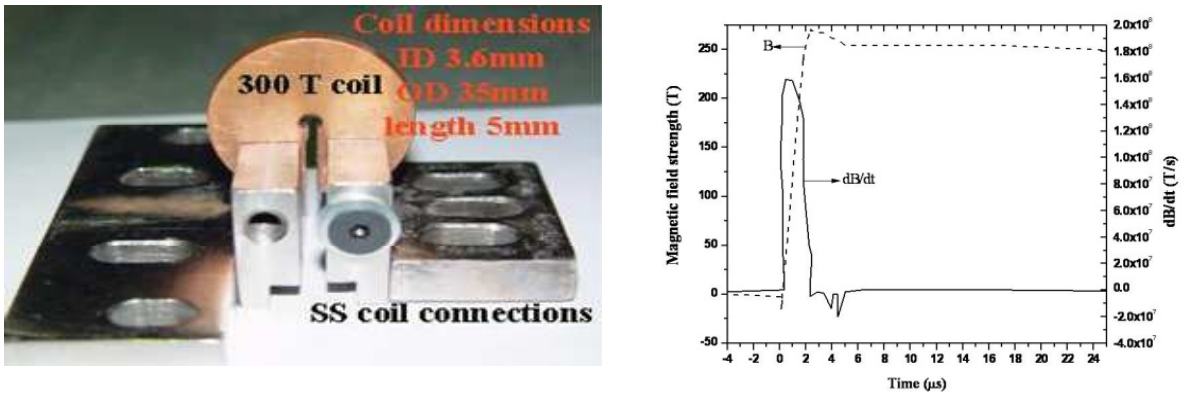

Fig.5. (a) Photograph of a Single Turn Coil and (b) Experimentally Measured Rate Change of Magnetic Field and Its Strength

Electromagnetic flux compression generators

Experimental investigation on the electromagnetically driven flux compression generators have been carried out with the aim to generate high magnetic field and to use the magnetic pressure associated with these high magnetic field for high pressure study in materials. The device includes a primary coil and a co-axial liner imploded to the central axis, by the Lorentz force (J_θ x B_Z), where J_θ is the induced current in the liner and B_Z is the primary coil magnetic field strength. Fig 6 shows the experimental set up. A peak magnetic field of 120T has been obtained utilizing 49kJ of MAGIC capacitor bank energy to accelerate a 0.5mm thick aluminum liner. A time rate of change of 0.9 x 10^8T/s has been obtained, which indicates the possibility of using this device as dynamic transformer generating high voltage pulses.

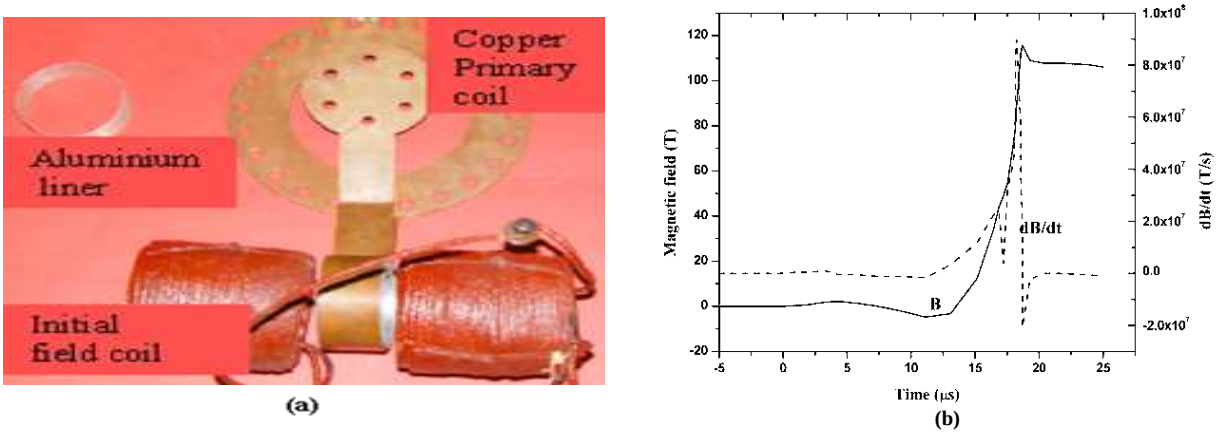

Fig.6: (a) EMFC Coil Assembly and (b) Experimentally Measured Magnetic Field and its Rate Change

Experiments on Explosively Driven Flux Compression Generators

Explosively driven magnetic flux compression generators are essentially the high current, compact and disposable pulsed power systems with energy density much larger than capacitor driven systems. Invented in the 1950's, such generators are capable of delivering ultra-high currents and voltages (up to tens of MA) in the time duration of few tens of microseconds. In order to have such generators for single shot applications especially to generate ultra-high magnetic field, which can be used to compress matter in an isentropic manner, devices and experiments have been carried out using 500 gm Comp-B explosive filled helical coils. So far a gain of about 70 has been achieved in these experiments with an initial current of 3 kA. Typically recorded signal is shown in Fig. 7.

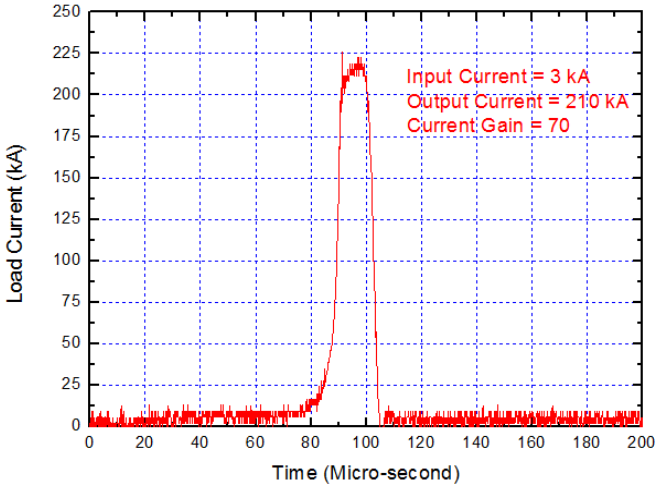

Fig. 7: Current Signal in an FCG Experiment

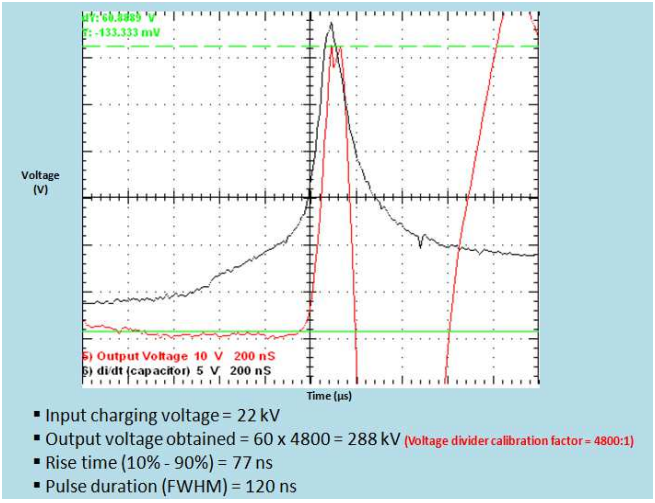

Fig. 8. Fast High Voltage Pulse using Opening Switch

Opening Switch Development

Opening switch is one of the possible components for power conditioning system which couples low impedance magnetic flux compression devices to the high impedance loads like high power microwave diodes. For this purpose, thin wires and foils which transform from a low impedance to high impedance in a short time upon explosion due to passage of fast currents function as opening switches. Work has carried out in our lab using low energy systems such as 7.1µF/ 40kV capacitor, charged to 15-25 kV. With a 5 mm wide, 125 micron thick aluminum foil, a 280 kV, <80 ns rise time and 120 ns FWHM pulse across 30 ohm could be generated with 22 kV sinusoidal capacitive discharge input as shown in Fig. 8. Such pulses have been used to drive a HPM device[5] earlier. To generate fast and high current pulses, considerations need to be different than for voltage and if used with another opening switch a single pulse can be generated. Accordingly, current pulse of about 400 ns rise time and 1.3 µs width have successfully been generated from 7.5 µs half cycle capacitive discharges. Work is in progress to obtain a few hundred ns, MA level current pulse which should be suitable to magnetically drive metallic flyers to high velocities or yield isentropic compressions in metallic samples.

Use of in-house Developed Neutron Detectors to Assay Fissile Materials

Plutonium and Uranium based nuclear materials need to be assayed for the purpose of nuclear material accounting, owing to strategic importance as well as radiological safety implications. Such characterization and assaying is also essential for safe disposal of nuclear waste and safeguards against proliferation. Thus interrogation and assay of plutonium/ uranium and other transuranic components, the so called special nuclear materials (SNM) is highly relevant for scientific and technical research and developments. In this direction work has been carried out both on active[6-7] i.e. induced fission reactions; and passive i.e. self emitted radiations techniques. In the latter, characteristic γ-rays from fissile or fertile components and their daughter products is one of the well known methods but being of low energy (a few hundred keVs), these can be attenuated and shielded by a few cm thick high Z material. Thus monitoring of the neutrons emitted due to spontaneous fission and (α,n) reactions in such materials or compounds can prove to be a simple and effective way especially for Pu based systems.

We have a long programme of preparing high sensitivity He^3 gas based proportional detector systems. Such detectors have now been deployed for the purpose of monitoring Pu content in waste hull drums. The method involves establishing correlation between the amount of Pu in the hull with the neutron emission from Pu from spontaneous fission as well as from α-n reactions, and the knowledge of the isotopic composition of the fuel. This correlation has been established by measurement of the passive neutron signal from the hull drum using He^3 detectors, in conjunction with the extensive Monte Carlo simulations. A set up based on such a method has been installed[8] in one of the reprocessing plants.

Acknowledgements

It is pleasure to acknowledge Dr. Satish C. Gupta, AD, MRG for his continuous support and keen interest in this work. I would also like to sincerely thank all colleagues of this division especially Dr. R K Rout, A. K. Saxena, Gaurav Pandey, Amit Sur, Amit Rav, S P Nayak, Sanjay Singh and Sanjay Andola, who have been involved in these works as well as collaborators from other divisions including Dr. B S Tomar, Head, RACD and Shri Kailash Agarwal, GM, NRPSED, NRB, for fruitful interactions and outcomes.

References

1. A.K. Saxena, T.C. Kaushik and S.C. Gupta, Shock Experiments and Numerical Simulations on Low Energy Portable Electrically Exploding Foil Accelerator, Rev. Sci. Instrum. **81**, 033508 (2010).
2. AK Saxena, T C Kaushik, A M Rawool & Satish C Gupta, "Equation of State Measurements Using Single Fabry-Perot Velocimeter", J. Phys.: Conf. Ser. **377**, 012049 (2012).
3. A.K. Saxena, T.C. Kaushik, A.M. Rawool and Satish C. Gupta, "Shock Loading Characteristics of Zr And Ti Metals using Dual Beam Velocimeter," J. Appl. Phys., Under Communication (2015).
4. N Nalini, T C Kaushik, and S C Gupta, "Generation and Measurement of Multi Megagauss Fields in Inertial Magnets", Sadhna **35** (5), 547-556 (2010).

5. S P Nayak, Nalini N, Mahesh Kale, T C Kaushik, S C Gupta, Archana Sharma, Senthil K., Rakhee Menon, Amitava Roy, K V Nagesh, and D P Chakravarthy, "Electrically Exploding Wire Opening Switch For Direct Driving of HPM Load", XII IEEE International Vacuum Electronics Conference (IVEC-2011, Banglore India) 497, (2011).
6. B.S. Tomar, T.C. Kaushik, Sanjay Andola, Ram Niranjan, R.K. Rout, Ashwani Kumar, D.B.Paranjape, Pradeep Kumar, K.L. Ramakumar, S. C. Gupta, and R. K. Sinha, "Non Destructive Assay of Fissile Materials through Active Neutron Interrogation Technique using Pulsed Neutron (Plasma Focus) Device", Nucl. Instr. and Meth **A703**, 11-15 (2013).
7. Sanjay Andola, Ram Niranjan, T.C. Kaushik, R.K. Rout, Ashwani Kumar, D. B. Paranjape, Pradeep Kumar, B.S. Tomar, K.L. Ramakumar, and Satish C. Gupta, "Use of Delayed Gamma Rays for Active Non Destructive Assay of ^{235}U Irradiated by Pulsed Neutron Source (Plasma Focus)", Nucl. Instr. and Meth **A753**, 138-142 (2014).
8. T. C. Kaushik, K. Agrawal, S. C. Andola, Raman Kumar, F. T. Qureshi, Satish C. Gupta and Sekhar Basu, "Quantitative Determination of Plutonium in Waste Hull Drums using Passive Neutron Technique", Bhabha Atomic Research Centre Report BARC/2013/R/006 (2013).

INDIGENOUS DEVELOPMENT OF THERAPEUTIC RADIOPHARMACEUTICALS USING ^{177}LU PRODUCED IN DHRUVA REACTOR: TRANSLATION FROM BENCH TO BED

Sudipta Chakraborty
Isotope Production and Applications Division

Dr. Sudipta Chakraborty is the recipient of the DAE Scientific & Technical Excellence Award for the year 2013

Introduction

Targeted cancer therapy using cancer seeking molecules tagged with particulate emitting radioisotopes is being practiced for last six decades. This particular therapeutic modality was dominated by treatment of thyroid cancer using radioiodine ($Na^{131}I$). Clearer understanding of cancer biology coupled with significant advancements in molecular biology and biotechnology in the last couple of decades have brought about tremendous prospect in the development of radiotherapeutic agents for the treatment of cancers other than that of the thyroid as well as for certain other diseased states, such as arthritis. The success of radionuclide therapy also emerged from the availability of suitable radionculides in large quantities and with high specific activity for radiolabeling biomolecules targeted to receptors which are up-regulated in cancer cells.

Among the wide spectrum of radionuclides proposed for *in vivo* therapeutic use, ^{177}Lu has emerged as one of the pivotal radionuclide in therapeutic nuclear medicine during the last decade by virtue of its attractive nuclear decay properties, favourable production logistics and straightforward coordination chemistry [1-5]. Lutetium-177 decays to stable ^{177}Hf with a half-life of 6.65 d by emission of β^- particles with E_{max} of 497 keV (78.6%), 384 keV (9.1%) and 176 keV (12.2%). The emission of low-energy gamma photons [E_γ=113 keV (6.6%), 208 keV (11%)] enable imaging and therapy with the same radiolabeled preparation and allow dosimetry to be performed before and during treatment as well.

The moderate energy beta emission of ^{177}Lu is effective in destroying small tumors and metastatic lesions (typically less than 3 mm diameter) while sparing the surrounding normal tissue. In this respect, ^{177}Lu is complementary to ^{90}Y [$T_{½}$ = 64.2 h, $E_{\beta(max)}$ = 2282 keV]. Moreover, the relatively longer half-life of ^{177}Lu provides logistic advantage for shipment to places far away from the reactors. While the physical half-life and energy of β^- emission of ^{177}Lu are very similar to that of ^{131}I [$T_{½}$ = 8.02 d, $E_{\beta(max)}$ = 606 keV (89.9%), 333 keV(7.3%); E_γ = 364 keV (81.2%), 636 (7.3%)], the emission of imageable gamma photons with significantly lower abundance compared to that of ^{131}I offers a distinct advantage. Indigenous cost-effective sourcing of the radioisotope with adequate quantity and specific activity required for saturable receptor targeting usign medium flux reactor facility was a challenge. Extensive optimization studies on irradiation time, target burn-up etc. finally resulted a standardized protocol for

production of ^{177}Lu with adequate specific activity in the highest available neutron flux position Dhruva reactor. Based on this protocol, ^{177}Lu in adequate specific activity, radionuclidic purity radiochemical purity is being routinely produced and supplied to at least ten leading nuclear medicine centres across India as a pharmaceutical ingredient. Three different therapeutic radiopharmaceuticals, namely, ^{177}Lu-DOTA-TATE (DOTA-TATE = DOTA^{0}-Tyr^{3}-Octreotate), ^{177}Lu-EDTMP (EDTMP = Ethylenediamminetetramethylene phosphonic acid).

Production of ^{177}Lu

Two different production strategies, namely, direct thermal neutron activation of enriched (in ^{176}Lu) lutetium target and thermal neutron activation enriched (in ^{176}Yb) ytterbium target leading to the formation of ^{177}Lu from the β^- decay of the short-lived activation product ^{177}Yb ($T_{½}$ = 1.9 h) have been explored in order to obtain ^{177}Lu suitable for therapeutic applications, particularly targeted cancer therapy using receptor targeting carriers [6-8].

Production ^{177}Lu using enriched ^{176}Yb as target provides no-carrier-added (NCA) form (theoretical specific activity 40.33 TBq/mg, 1090 Ci/mg), however, the need of a radiochemical separation procedure to isolate ^{177}Lu of >99.9% radionuclide purity as well as recovery of expensive enriched ^{176}Yb targets pose major impediments for its regular utilization. Moreover, irradiation of 1 mg of 99% enriched (in ^{176}Yb) Yb_2O_3 at a thermal neutron flux of 5×10^{14} n/cm^2.s produce only ~5.55 GBq (~150 mCi) of ^{177}Lu. Therefore reliable and sustainable large-scale production of ^{177}Lu to meet its emerging global demand through indirect route is not only challenging but also a capital intensive task.

In BARC, production of ^{177}Lu with specific activity adequate for preparing receptor-specific therapeutic radiopharmaceuticals by direct (n,γ) route was realized in medium flux Dhruva reactor by using lutetium target enriched in ^{176}Lu (80% or more). Two reasons contributing to this unique advantage are, (i) ^{176}Lu has very high thermal neutron capture cross section (σ = 2090 b, I_0 = 1087 b) for formation of ^{177}Lu and (ii) neutron capture cross section of ^{176}Lu do not follow 1/v law and has a strong resonance very close to the thermal region [9]. In the optimized protocol for production of ^{177}Lu, Lu_2O_3 (84.6% enriched in ^{176}Lu) was used as the target.

A stock solution of the target was prepared by dissolving it in 0.1 M suprapure HCl (1 mg/mL Lu). Measured aliquot of this solution was dispensed in a quartz ampoule and carefully evaporated to dryness. The ampoule was subsequently flame sealed, placed inside the irradiation can made of 1S aluminum [22 mm (ϕ) × 44 mm (l)] and irradiated in the Dhruva at a thermal neutron flux of ~1.2×10^{14} n/cm^{2}s for duration of 21 d.

To sustain weekly supply of ^{177}Lu to the nuclear medicine centers, three lutetium targets are used at three different irradiation positions receiving similar thermal neutron flux. Each lutetium target undergoes thermal neutron irradiation for a duration of 21 d and is subsequently replaced by a freshly prepared ^{176}Lu target. The 21 d irradiation period was decided based on extensive theoretical calculations and practical experiments which showed that specific activity of ^{177}Lu would be maximum at 21 d for 1.2×10^{14} n/cm^{2}s flux due to target burn up as shown in Fig. 1.

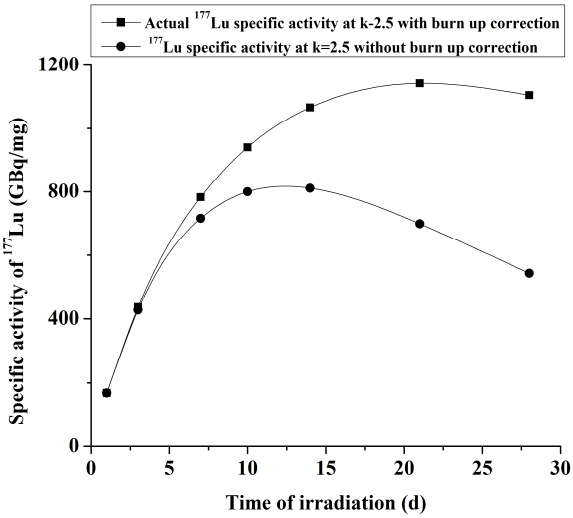

Fig. 1: Variation of specific activity of ^{177}Lu with irradiation time at 1.2×10^{14} n/cm^{2}s thermal neutron flux calculated with and without burn-up correction

Lu-177 is produced with a specific activity of 1126 ± 36 GBq/mg and high radionuclidic purity of 99.98 ± 0.05% suitable for clinical use as a pharmaceutical ingredient. Radiochemical processing of irradiated target to convert it to $^{177}LuCl_3$ solution, amenable for radiopharmaceutical preparation, is done in lead-shielded isotope processing plant facility as shown in Fig. 2 below.

Fig.2: 100 mm lead-shielded isotope processing plant for radiochemical processing of ^{177}Lu at IP & AD, BARC

^{177}Lu-DOTA-TATE for peptide receptor radionuclide therapy (PRRT): Peptide receptor radionuclide therapy (PRRT) using radiolabeled somatostatin analogues is a novel therapeutic modality for patients with somatostatin receptor-positive tumors. Lu-177 has emerged as one of the most effective candidates for PRRT, which is particularly useful for targeted therapy of smaller lesions owing to the small tissue penetration range of β^- particles of ^{177}Lu (maximum range ~ 2mm) [5,10]. ^{177}Lu-labeled DOTA-TATE, the ^{177}Lu complex of the somatostatin analog octapeptide, Tyr^3-Octreotate conjugated to DOTA, was envisaged as a promising agent for the treatment of patients suffering from inoperable neuro-endocrine originated tumors over-expressing somatostatin receptors. ^{177}Lu labeled DOTA-Tyr^3-Octreotate (^{177}Lu-DOTA-TATE) (Fig. 3) was synthesized in high radiochemical purity and with maximum achievable specific activity by varying various reaction parameters [11].

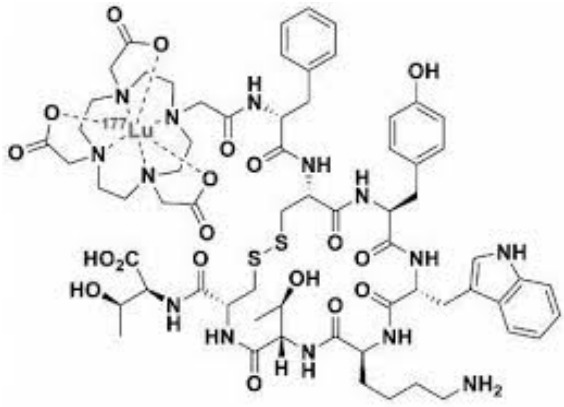

Fig. 3: Structure of ^{177}Lu-DOTA-TATE

The preparation demonstrated encouraging results in *in vitro* cell binding studies as well as HT29 tumor bearing nude mice model. Subsequently, human clinical trials of ^{177}Lu-DOTA-TATE were initiated in patients suffering from various forms inoperable neuroendocrine originated tumors.

One of the challenges involved in carrying out targeted tumor therapy using ^{177}Lu-DOTA-TATE is to prepare the radiolabeled agent with adequately high specific activity in order that sufficient activity can be deposited in the cancerous lesions without saturating the limited number of receptors present in the cancerous site. As the specific activity of ^{177}Lu available at the time of preparation of the agent at hospital radiopharmacy may vary considerably, it is crucial to optimize the labeling protocol, more importantly with respect to the amount of peptide, in order that it can be prepared with high radiochemical purity using minimum amount of DOTA-TATE.

Therefore, an optimized protocol for the preparation of therapeutic dose (5.55-7.4 GBq, 150-200 mCi) with maximum achievable specific activity and stability was developed in our laboratory by extensive variation of several parameters [11]. More than 1000 patients suffering from various types of neuroendocrine originated tumors have been treated in fifteen major nuclear medicine centers across the country using ^{177}Lu-DOTA-TATE prepared following the developed protocol and using ^{177}Lu activity supplied from BARC.

Fig 4 shows the scintigraphic images of (a) patient with neuroendocrine tumor having extensive liver metastases recorded at 24 h post-administration of 7.4 GBq (200 mCi) of ^{177}Lu-DOTA-TATE. Available clinical data shows excellent symptomatic relief for the most of the patients who have undergone ^{177}Lu-DOTA-TATE therapy. On the other hand, prolonged follow-up study shows either complete to partial remission or stable disease conditions in > 60% of the patients suffering from various kinds of neuroendcrine originated tumors in our country.

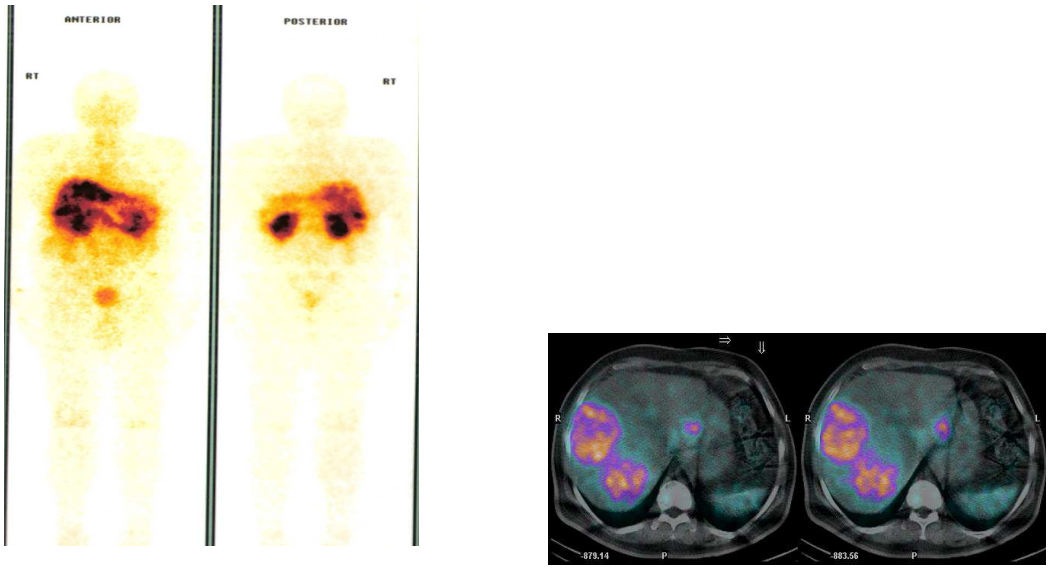

Fig. 4: A representative post-therapy whole body planar image and SPECT-CT of liver recorded 24 h post-administration of 7.4 GBq dose of ^{177}Lu-DOTA-TATE to a patient suffering from NET with extensive hepatic metastases

^{177}Lu-EDTMP for palliative care of painful skeletal metastasis

Skeletal metastases or secondary cancerous lesions in bone are common in patients suffering from breast, lung and prostate cancer in the advanced stage of their diseases. These metastatic lesions in skeleton often lead to excruciating pain and other related symptoms, such as lack of mobility, neurological deficits, depression etc., which adversely affect the quality of life. Radionuclide therapy employing radiopharmaceuticals labeled with β^-/conversion electron emitting radionuclides is an effective option for bone pain palliation and could provide significant improvement in quality of life of patients. The major challenge in developing effective agents for palliative treatment of bone pain arising from skeletal metastases is to ensure the delivery of adequate dose of ionizing radiation at the site of skeletal lesions with minimum radiation induced bone marrow suppression. Lu-177 is considered as a potential radionuclide for developing the palliative agents for bone pain arising due to skeletal metastases. The tissue penetration range of the β^- particles from ^{177}Lu are adequately low which ensures minimum bone marrow suppression, a major advantage of this radiotherapeutic application. Multidentate

polyaminopolyphosphonic acid ligands are reported to have high affinity towards skeletal lesions and known form stable chelates with many metals, particularly with lanthanides. Ethylenediaminetetramethylene phosphonic acid (EDTMP) is one of the most widely used polyaminophosphonate ligands for developing radiolabeled agents for bone pain palliation. ^{153}Sm-EDTMP (Quadramet®) is currently being used extensively for pain palliation due to skeletal metastases. Working in this direction, ^{177}Lu-EDTMP complex and was synthesized and studied with an objective to develop a suitable ^{177}Lu-based viable alternative of ^{153}Sm-EDTMP. ^{177}Lu-EDTMP complex (Fig. 5) was prepared in high yield and excellent radiochemical purity (>99%) and with desirable *in vitro* stability in our laboratory. Biological studies in Wistar rats and New Zeland White rabbits showed selective skeletal uptake of the agent with rapid blood clearance and minimum uptake in any of the major organs/tissue [12]. Subsequently, the radiolabeled formulation was evaluated in dogs with osteosarcoma and bone metastases with favourable outcome [13].

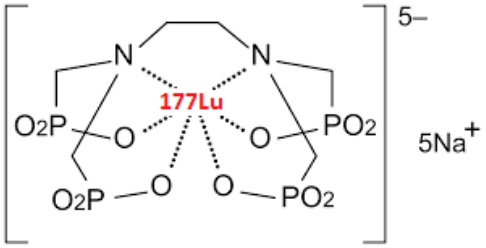

Fig. 5: Structure of ^{177}Lu-EDTMP

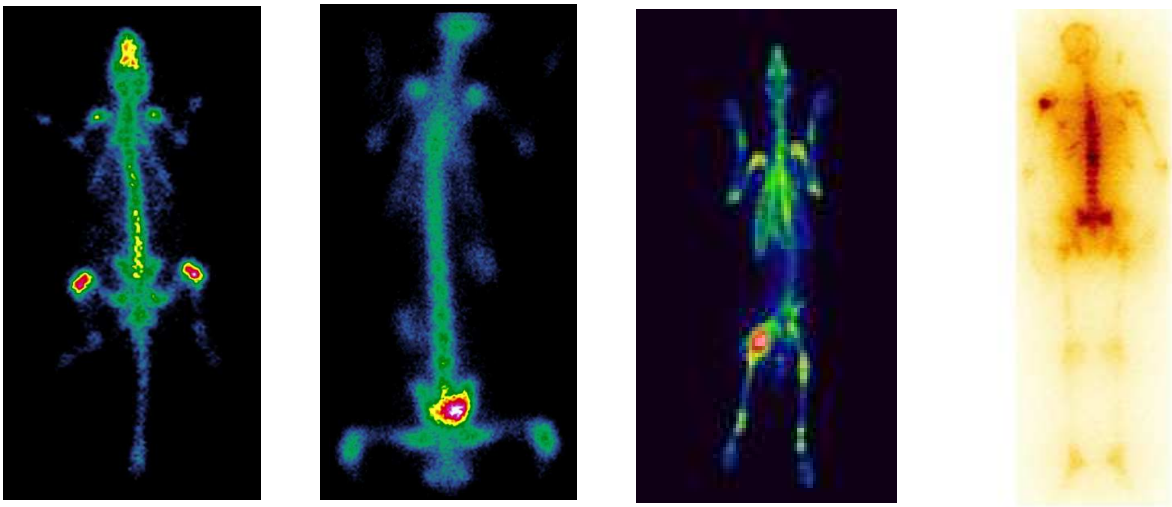

(a) (b) (c) (d)

Fig. 6: Scintigraphic images of ^{177}Lu-EDTMP in (a) Wistar rat (b) New Zealand white rabbits (c) dog with bone cancer and (d) human cancer patient with bone metastases recorded at 24 h post administration

^{177}Lu-HA for arthritis treatment

Approximately 2% of the adult population worldwide is affected by some form of arthritis which is manifested in pain, joint immobility and disability. Radiation synovectomy is a radiotherapeutic modality for the treatment of rheumatoid arthritis wherein a β^- emitting radionuclide is administered locally by intra-articular injection in the form of colloid or radiolabeled particulate. Hyroxyapatite microparticles (HA) [$Ca_{10}(PO_4)_6(OH)_2$], regarded as one of the most suitable carrier for applications radiolanthanides, have been envisaged for labeling with ^{177}Lu to develop a suitable radiopharmaceutical for arthritis treatment. Working in this direction, ^{177}Lu labeled HA particles were synthesized in high radiochemical purity (~99%) and excellent *in vitro* stability. Biological efficacy of the radiolabeled preparation was tested by both in normal as well as arthritis-affected knee joints of Wistar rats [14,15]. Based on the promising outcome these investigatons, ~20 patients having arthritis in different joints such as, knee, elbow and shoulder, were treated with 185-740 MBq doses of ^{177}Lu-HA. In the follow-up studiy, the patients reported significant pain relief, improved mobility and almost no side effects [15].

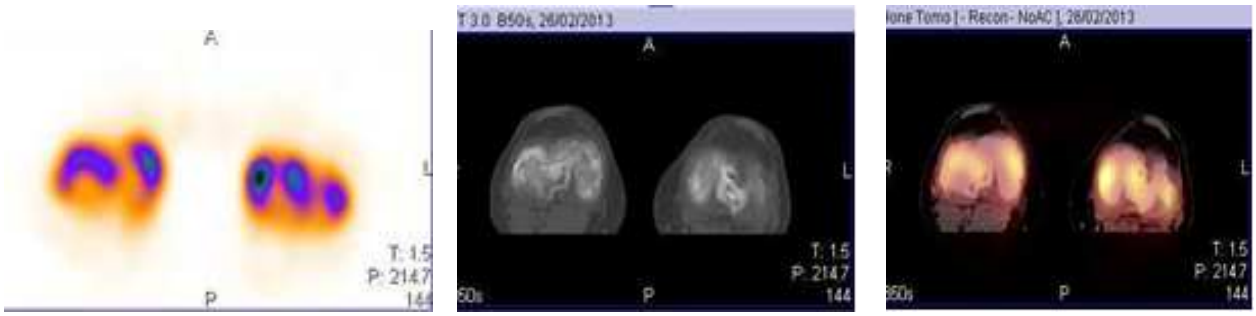

Fig. 7: (a) SPECT (b) CT and (c) SPECT-CT of arthritis affected knee joints of a patient recorded at 24 h post administration of 740 MBq of ^{177}Lu-HA

Acknowledgements

The author gratefully acknowledges Dr. K. L. Ramakumar, Director, Radiochemistry and Isotope Group, BARC and Dr. Ashutosh Dash, Head, Isotope Production and Applications Division, BARC for their support and encouragement. The author expresses his gratitude to all his collegues at Isotope Production and Applications Division and Radiopharmaceutical Chemistry Section, BARC, who were associted with him in the work reported in this article. The author is especially thankful to Dr. H.D. Sarma and staff members of Laboratory Animal House Facility of RB & HSD, BARC for carrying out the animal studies. Sincere thanks are due to all the clinical collaborators for carrying out evaluation of the developed agents in human patients.

References

[1]. Banerjee S, Pillai MRA, Knapp (Russ) FF. Chem Rev 2015, 115, 2934-2974.
[2]. Banerjee S, Das T, Chakraborty S, Venkatesh M. Radiochim Acta 2012, 100, 115-126.

[3]. Cutler CS, Hennkens HM, Sisay N, Huclier-Markai S, Jurisson SS. Chem Rev 2013, 113, 858-883.
[4]. Das T, Pillai MRA. Nucl Med Biol 2013, 40, 23-32.
[5]. Kam BLR, Teunissen JJM, Krenning EP, de Herder WW, Khan S, van Vliet EI, Kwekkeboom DJ. Eur J Nucl Med Mol Imaging 2012, 39(Suppl 1), S103–S112.
[6]. Pillai MRA, Chakraborty S, Das T, Venkatesh M, Ramamoorthy N. Appl Radiat Isot 2003, 59, 109-118.
[7]. Chakraborty S, Vimalnath KV, Lohar SP, Shetty PS, Dash A. J Radioanal Nucl Chem 2014, 302, 233-243.
[8]. Chakravarty R, Das T, Dash A, Venkatesh M Nucl Med Biol 2010, 37, 811-820.
[9]. Atlas of neutron capture cross sections. IAEA Nuclear Data Section, Vienna, 1997.
[10]. Kwekkeboom DJ, Bakker WH, Kam BL, Teunissen JJM, Kooij PPM, Herder WW, Feelders RA, Eijck CHJ, Jong M, Srinivisan A, Erion JL, Krenning EP. Eur J Nucl Med Mol Img 2003, 30, 417-422.
[11]. Das T, Chakraborty S, Kallur KG, Venkatesh M, Banerjee S. Cancer Biother Radiopharm 2011, 26, 395-400.
[12]. Chakraborty S**,** Das T, Banerjee S, Balogh L, Chaudhari PR, Sarma HD, Polyák A, Máthé D, Venkatesh M, Janoki GA, Pillai MRA. Cancer Biother Radiopharm 2008, 23, 202-213.
[13]. Chakraborty S, Balogh L, Das T, Polyak A, Andocs G, Mathe D, Kiraly R, Thuroczy J, Chaudhari PR, Janoki GA, Banerjee S, Pillai MRA. **Curr Radiopharm**, 2015, In press.
[14]. Chakraborty S, Das T, Banerjee S, Sarma HD, Venkatesh M. Nucl Med Commun 2006, 27, 661-668.
[15]. Chakraborty S, Vimalnath KV, Rajeswari A, Shinto A, Sarma HD, Kamaleshwaran KK, Thirumalaisamy P, Dash A. J Label Compd Radiopharm 2014, 57, 453-462.

BARC NEWSLETTER
FOUNDER'S DAY SPECIAL ISSUE 2015

GAS FILLED NEUTRON AND GAMMA RADIATION DETECTOR DEVELOPMENT FOR REACTORS AND ACCELERATORS

Priyamvada M. Dighe
Electronics Division

Smt. Priyamvada M. Dighe is the recipient of the DAE Scientific & Technical Excellence Award for the year 2013

Abstract

Mechanically rugged and radiation tolerant neutron and gamma detectors are indigenously developed for reactor control instrumentation and accelerator area monitoring applications. ^{10}B lined proportional counters of neutron sensitivity ranging from 1 cps/nv to 20 cps/nv are developed for reactor control and safety applications. Boron counters capable of operating at elevated temperatures upto 250°C are developed for monitoring neutron flux during fuel loading and approach to first criticality at Fast Breeder Reactor. All welded high sensitivity ^{3}He proportional counter of neutron sensitivity 235 cps/nv developed and characterized for reactor neutron flux monitoring. For measuring the yield of pulsed neutron source and pulsed neutron area monitoring at high energy accelerators first of its kind silver lined proportional counter is developed in cylindrical and annular shape and calibrated for pulsed neutron source yield measurement. High pressure gamma detectors have been developed for low energy pulsed X-ray area monitoring at high energy electron accelerators. Ionization chambers with multiple electrode configurations developed with enhanced collection efficiency for gamma monitoring at hot cell facilities and high intensity pulsed X-ray area monitoring inside shield at accelerators. Extensive parametric optimization studies, theoretical simulations, functional, nuclear and climatic tests have been carried out on the detectors developed. Long term signal stability tests are carried out under radiation and environmental conditions of reactor applications. Present article gives brief review on the development of above mentioned neutron and gamma detectors.

Introduction

Thermal neutron monitoring and gamma radiation monitoring is carried out in almost all nuclear facilities for control and health and safety applications. Gas filled detectors are oldest and most widely used radiation detectors which are based on sensing the ionization created by passage of radiation through the detector. Gas filled neutron and gamma detectors are simple in design and are mechanically rugged and therefore are used in nuclear reactors. Neutrons are neutral in nature and therefore can be detected only by causing them to interact with some target material and detecting the charged particles produced. The present paper compiles the work carried out on design development of gas filled neutron and gamma detectors. The detectors developed have innovative electrode configurations to meet challenging requirement of special applications. ^{10}B lined and ^{3}He filled proportional counters are developed for thermal neutron monitoring in reactors, silver lined proportional counters are developed for pulsed neutron monitoring and high pressure ionization chambers are developed for gamma and pulsed X-ray measurements in reactors and accelerators.

^{10}B lined proportional counters

There are strong needs of high sensitivity, high temperature tolerant and mechanically rugged neutron detectors for nuclear reactor related fields. Some such requirements are reactor start-up, failed fuel detection and nuclear fuel reprocessing. In all such requirements detectors with neutron sensitivities ranging from 1 cps/nv to 20 cps/nv or more are required with suitable gamma and temperature tolerances. Boron lined proportional counters are the most popular choices for monitoring low thermal neutron flux at reactors because of their high sensitivity to thermal neutrons, better tolerance to ambient gamma background and ease of fabrication, as boron is non-toxic and non-radioactive and its reaction products are also non-radioactive and can work in hostile reactor environment.

^{10}B coated counters for reactor applications

Boron lined proportional counters of varying neutron sensitivities are developed for reactor applications [1,2,3]. Fig. 1 gives the picture of the detectors developed and table 1 gives main specifications. The detectors developed were characterized for reactor applications by subjecting them to following functional and endurance tests.

- Functional tests: Insulation resistance, capacitance, output pulse characteristics, HV plateau characteristics, discriminator bias characteristics, neutron sensitivity, count rate linearity over desired operation range and tests in gamma radiation.
- Endurance tests: Vibration test, damp heat cycle tests, temperature cycling test, seismic tests, long term signal stability tests and nvt life test with HV bias "OFF" and "ON".

(A) (B)

Fig. 1: Photograph of B-10 lined (A) out core and (B) in core proportional counters respectively

Studies were also conducted on boron coating methods. The standard geometry detectors were developed with commercial ^{10}B powder. This boron as suspension in mineral oil was coated manually on cathode surface and baked in an electrical furnace at temperature about 350°C and rotating the cathode in a suitable fixture at slow speeds. A multiple dip coating method was tried out using indigenously available boron powder. This method gave flexibility of developing boron counters with baffle structure cathode [4]. Baffle structure enhanced the neutron

sensitivity without much altering the gamma tolerance. The detectors developed were successfully installed in various reactors and used for monitoring thermal neutron flux during startup and first criticality.

High temperature ^{10}B coated counters

High sensitivity high temperature ^{10}B coated proportional counters (HTBCCs) which can operate at continuous 250°C environment are developed for Fast Breeder Reactor. HTBCCs with sensitivity of 12 cps/nv, are required in control plug during initial core loading and first approach to criticality experiments. For flux monitoring in start-up range after long shutdown, HTBCCs of neutron sensitivity 4 cps/nv are required. Fig. 2 gives the picture of HTBCCs developed [5] and Table 1 includes the main specifications. The functional tests and qualification tests were carried out on these detectors at 250°C temperature and established the design specifications. The challenge of operation of detector in high temperatures is overcome by advanced mechanical design and proper selection of construction materials. Following challenges were incurred in development of these detectors to function upto 250°C temperature.

- Electrical breakdown observed during thermal cycling tests: Novel anode wire mounting technique developed [6].
- Gas leakage: Pinching tool modified, qualified and commissioned.
- Study of detector characteristics at high temperature: Large number of experiments conducted at variable temperatures and with neutron and gamma sources.

Table 1: Specifications of Boron-10 lined proportional counters

Detector	Out-core Detector	In-core Detector	Start-up detector	Start-up detector	Cold start-up FBR	Start-up FBR
Cathode Outer diameter	63 mm	13mm	34mm	30mm	54mm	25.4mm
Anode wire diameter	25 µm diameter tungsten					
Overall length	930mm	330mm	450mm	200mm	1000mm	735mm
Sensitive length	740mm	190mm	300mm	100mm	700mm	378mm
Gas fill and pressure	Ar (95%) + CO2 (5%) gas mixture at 20 cm Hg					
Neutron sensitivity	17 cps/nv	1.0 cps/nv	4 cps/nv	1.1 cps/nv	12 cps/nv	4 cps/nv
Gamma tolerance	1 R/h	3000R/h	500R/h	2000 R/h	200mR/h	200R/h
Temperature tolerance	60°C	60°C	60°C	60°C	250°C	250°C

(A) (B)

Fig. 2: Picture of 12 cps/nv (A) and 4 cps/nv (B) HTBCCs

^{3}He proportional counters

All welded ^{3}He proportional counters of neutron sensitivities ranging from 6 cps/nv to 235 cps/nv are developed for the first time in India. The main specifications are given in table 2 and Fig. 3 gives the picture of the detectors. The detectors are made out of SS 304 L and have all welded robust construction for reactor environment.
The high sensitivity (235 cps/nv) ^{3}He detector developed was characterized for low thermal neutron flux monitoring in reactors [7] by subjecting to following tests.

- Signal linearity: observed within ±10% up to a count rate of 30K cps.
- Gamma tolerance tests: No change in signal count rate in gamma radiation of 10 mR/h.
- Irradiation to high neutron flux: The response of the detector after being exposed to high neutron flux ($4x10^{6}$ nv) and high gamma field (about 10R/hr) was found to be repeatable within ±10%.
- Signal stability tests: The detector signal was found to be stable within 1 % when tested in 23.5 nv thermal neutron flux for 1800 s.
- nvt test: The detector performance remained stable and unchanged after exposure to high neutron flux of 1.44×10^{10} nvt.

This in-house developed detector has been used for the first time in the country to measure the fission power by monitoring the reactor core neutron flux at extremely low power of reactor.

(A) **(B)**

Fig. 3: (A) Medium sensitivity (A) High sensitivity all welded Helium-3 proportional counters

Table 2: Mechanical specifications of ^{3}He counters

Detector	High sensitivity	Medium sensitivity	Low sensitivity
Overall dimensions	SS Dia 54 mm X 1 m long	S.S. 25.3mm OD x 490mm	S.S. 25.5mm OD x 230mm
Sensitive dimensions	Dia 51 mm X 908 mm long	23.8mmID x 440mm length	23.8mmID x 160mm length
Gas fill	65% He3 + 35%Kr at 3.6 bar (g)	50% He3 + 50%Kr at 2 bar (g)	50% He3 + 50%Kr at 2 bar (g)
Operating voltage	1500V – 1800V	1500V-1800V	1000V-1200V
Neutron sensitivity	235 cps/nv	25 cps/nv	6 cps/nv

Silver lined proportional counters

Pulsed fast neutrons are generated in the form of short bursts in many facilities such as in the vicinity of electron accelerators, spallation sources, fusion experimental facilities or in plasma focus devices. The duration of these pulses can range between microseconds to nanoseconds and yields can range from 10^{2}neutrons to 10^{13} neutrons per pulse. Due to pulsed nature of the neutrons, devices that employ conventional neutron sensitive detectors such as ^{10}B lined, $^{10}BF_3$ or ^{3}He filled counters cannot resolve the neutron pulses and loss in the counting efficiency is observed due to inherent resolving time of detectors. Extensive research is undergoing to evolve instruments to measure the yield of pulsed neutron radiation. The oldest technique is utilization of Geiger-Mueller (GM) counter surrounded by silver foil. To overcome the inherent large dead time of GM counter based systems, silver lined proportional counters with standard cylindrical design and annular shape were developed and calibrated for pulsed neutron radiation measurements. Table 3 gives the main specifications and fig. 4 gives pictures of the detectors developed.

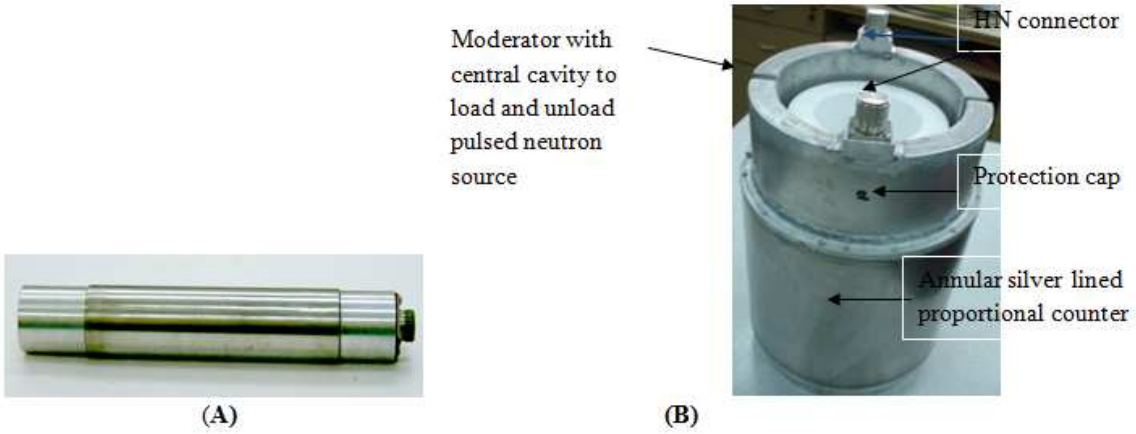

Fig. 4: Picture of cylindrical (A) and annular shape (B) silver lined proportional counters

Table 3: Main specifications of the silver lined proportional counter

Detector type	Cylindrical geometry	Annular geometry
Cathode (SS)	26mmID x 110mm length	235mm OD X 150 mm ID x 314mm length
Anode	25µ tungsten wire	25µ tungsten wires (10 nos.)
Neutron sensing material	0.025cm thick silver foil (23.6g)	0.025cm thick silver foil (23.6g)
Gas-fill	A (90%) + CH_4 (10%) at 20 cm Hg	A (90%) + CH_4 (10%) at 30 cm Hg
Insulators	Ceramic-to-metal feedthroughs	Ceramic-to-metal feedthroughs
Pulsed neutron calibration factor	$1.2x10^6$neutrons/pulse counts	$7.6x10^4$ neutrons/pulse counts
Application	REM dose monitoring	Pulsed neutron source calibration

The cylindrical detector [8] is designed to use in conventional REM meter developed for neutron dose monitoring. Thus this device can be used to measure neutron dose in pulsed neutron radiation. The annular shape detector is developed [9] to calibrate neutron yield of the pulsed neutron sources. The detector is fabricated in two halves with each half as an independent detector. The two halves are joined together for experiments. The source can be placed inside cavity of the detector. Due to annular shape, the detector covers more than 3π solid angle of the source hence gives enhanced sensitivity compared to conventional cylindrical detectors.

Low energy pulsed X-ray ionization chamber

Pulsed X-rays of small duty factor are produced in the vicinity of electron accelerators due to scattering of electrons by the molecules of the residual gas in the vacuum chambers of accelerators which are the main constituents of background radiations around electron accelerators and need to be monitored for personnel safety. Instruments that ordinarily respond well to the continuous radiation, fail to work in pulsed radiation because of high peak dose rate delivered during the pulse exposure. Detectors that have dead time problem such as GM counters saturate in pulsed fields and measure one count per pulse irrespective of dose. Ion chambers are most suitable, common and convenient method of on-line radiation area monitoring in continuous as well as in pulsed radiation since they are simple in design, works on average current measurement mode. These are mechanically rugged, have long life and good linearity in signal over a broad range. The Indus-1 and Indus-2 electron accelerator facilities of Raja Ramanna Centre for Advanced Technology, Indore require area monitors in the working areas. X-ray radiation suffers multiple scattering in the labyrinths and the shielding walls due to which the energy in the working area can be well below 100 keV. Conventional monitors available commercially underestimate the X-ray background because of pulsed nature of the radiation and are not sensitive to X-rays below 100 keV. For this purpose, a high pressure ion chamber made of aluminium with all welded construction has been developed [10] and tested for use in pulsed X-ray background. The main specifications of the ion chamber are given in Table 4. The detector has standard cylindrical geometry with top dome shape. The welded construction was possible because of use of special explosion welded clad plates obtained from the Explosives Research and Development Laboratories (ERDL), Pune, India, as shown in Fig. 5. All the weld joints have

been subjected to pneumatic pressure tests and helium leak tests up to 10^{-9}std. cc/sec to ensure the integrity of construction.

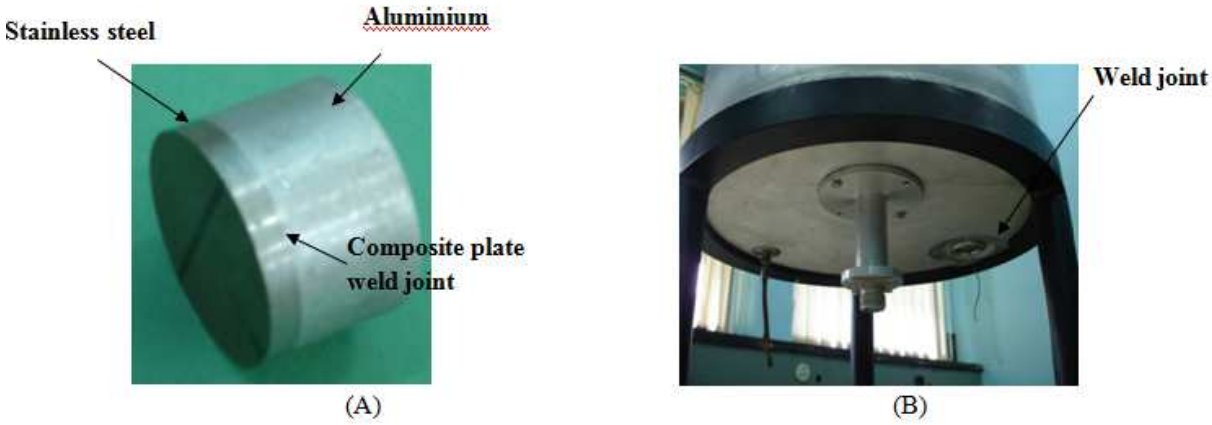

Fig. 5: Picture of SS-Al clad plate (A) and weld joint (B)

Table 4: Main specifications of the low energy pulsed X-ray ion chamber

Outer housing	Al 320 mm dia × 560 mm ht
Sensitive volume	25 ltr
Spacing between the HT and signal electrode	100 mm
Gas fill	Nitrogen at 6 bar
Sensitivity	12 pA/mR/h
Measuring range	20 µR/h-100 mR/h
Energy response	±12% from 35 keV to 1.25 MeV X-ray energy
Ion collection efficiency	86% at 100 mR/h for 500V HV

Multi-electrode ionization chamber

Ionization chambers were developed with multiple electrode geometry instead of conventional two electrode design. Special guard rings were designed to define the sensitive volume and the detector performance was enhanced for three additional decades of range of operation. Table 5 gives the main specifications of the multi-electrode ion chambers developed for high range gamma area monitoring at hot cell facilities and in space constrained areas. Fig. 6 gives the schematic of the multielectrode configuration of high range gamma monitor and miniature multielectrode ion chamber.

The high range ion chamber is developed [11] for pulsed X-ray background measurements at the INDUS-I facility under normal as well as beam loss conditions and for measurement of gamma radiation during movement of intense gamma sources in hot cell facilities. Standard ion chambers of identical dimensions with two electrode configuration can measure gamma radiation from 100µR/h to 1R/h. The detector with multielectrode configuration enhances the performance

and measures gamma radiation from 100µR/h to 10^3 R/h with more than 90% collection efficiency for $3x10^3$R/h gamma radiation at 500V HV.

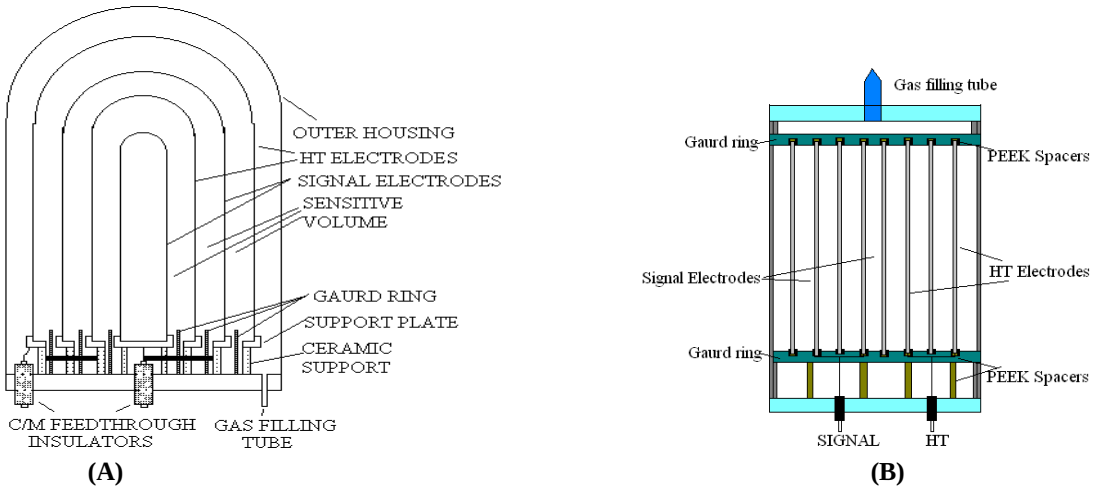

Fig. 6: Schematic of multi electrode configuration of ionization chamber

Table 5: Main specifications of multielectrode ionization chambers

Detector	High range gamma monitor	Miniature ion chamber
Outer housing	SS 178mm dia x 300mm	SS 46 mm dia x 120 mm length
Electrode dia	162mm, 128mm, 94mm & 58mm	35mm, 25mm, 15mm, 5mm
Spacing	15.5mm	5mm
Sensitive volume	4.5ltr	64cc
Gas fill	Argon at 10 atmospheric pressure	Argon at 10 atmospheric pressure
Sensitivity	4.6nA/R/h	8.2 pA/100 mR/h
Measuring range	100µR/h-1x10^3R/h	100 mR/h – 10^4 R/h

Summary

A wide range of gas filled neutron proportional counters and high pressure ionization chambers have been developed for various applications. The detectors developed were extensively characterized and installed at nuclear facilities for control and safety applications. The experience gained on the development and characterization of these detectors has helped in accurately determining the neutron, gamma and X-ray radiation intensity. Listed references give details of the detectors describes in the article.

Acknowledgements

The author expresses gratitude towards Shri C.K. Pithawa, Director E&I Group for providing encouragement and support in the work presented. Sincere thanks to Shri Debashis Das, Head, Electronics Division for providing technical guidance in the detector development. The work presented in the article is the support, guidance, assistance and collaboration of colleagues from

Electronics Division, Reactor Operations Division, Radiation Standards and Safety Division, Radiation Standards Section, Health Physics Division and Electronics Corporation of India Ltd., Hyderabad.

References

1. Neutron sensitivity improvement in boron-lined proportional counter, P.M. Dighe et al, *Indian Journal of Engineering and Material Sciences*, Vol. 9, April 2002, pp. 91-97.
2. Boron-lined proportional counters with improved neutron sensitivity, P.M. Dighe et al, *Nuclear Instruments and Methods in Physics Research (A)*, 496, 1 pp 154 - 161, January 2003
3. New cathode design boron lined proportional counters for neutron area monitoring applications, P.M. Dighe, *Nuclear Instruments and Methods in Physics Research A* 575 (2007) 461–465.
4. Anode wire mounting technique for high temperature Boron -10 lined proportional counter, P.M. Dighe et al, *Nuclear Instruments and Methods in Physics Research* A 621 (2010) 713–715.
5. Performance studies of boron lined proportional counters for reactor applications, P.M. Dighe, D. Das, *Nuclear Instruments and Methods in Physics Research A* 770 (2015) 29–35.
6. Design and Development of High Temperature ^{10}B Coated Proportional Counters for PFBR, P.M. Dighe et al, *BARC NEWSLETTER*, Jan-Feb 2015.
7. Design, Development and Characterization of ^{3}He Proportional Counters for Reactor Applications, P.M. Dighe et al, *3rd National Symposium on Advances in Control & Instrumentation* 24-26 November, 2014 Mumbai.
8. Silver lined proportional counter for detection of pulsed neutrons, P.M. Dighe et al, *Nuclear Instruments and Methods in Physics Research (A)* **523**, Issues 1-2, 1 May 2004, 158
9. Annular shape silver lined proportional counter for on-line pulsed Neutron yield measurement P.M. Dighe et al, *Nuclear Instruments and Methods in Physics Research A* 778 (2015)115–119.
10. Low energy pulsed X-ray ion chamber monitor for accelerator radiation safety, P.M. Dighe et al, *Indian Journal of Pure & Applied Physics*, Vol. 50, July 2012, pp. 458-46.
11. Ion chamber monitors for pulsed X-ray background at electron accelerator facilities, P.M. Dighe et al, *Nuclear Instruments and Methods in Physics Research A* 578 (2007) 246–252
12. Design and development of a wide range ion chamber for reactor instrumentation, P.M. Dighe et al, *Nuclear Instruments and Methods in Physics Research A*, 614 (2010) 449–452.

STUDY OF QUANTUM CHROMO DYNAMICS IN RELATIVISTIC HEAVY ION COLLISIONS WITH CMS EXPERIMENT IN LHC AT CERN

Dipanwita Dutta
Nuclear Physics Division

Dr. Dipanwita Dutta is the Recipient of the DAE Scientific & Technical Excellence Award for the year 2013

Abstract

Quantum Chromo Dynamics (QCD) predicts the existence of a new phase of matter, Quark Gluon Plasma (QGP), at high temperature and energy density. CMS (Compact Muon Solenoid) experiment in Large Hadron Collider (LHC) at CERN with its heavy ion program started exploring QGP phase in PbPb collisions at energy 2.76 TeV in 2010. We will discuss the measurement of quenching of jets in heavy ion collisions, an important probe of QGP, by looking into the momentum dependence of the momentum imbalance of jets. The striking results from isolated photon + jet study in PbPb collisions which reveals that, jets really lose energy compared to associated photon production which is unaffected by the QGP medium, and thus make it an excellent probe to quantitative assessment of jet energy loss in QGP, will be reported. We will also discuss the first measurement of production of Z boson in heavy ion collisions, which serve as candle to study the initial state of collision.

The CMS experiment

The Compact Muon Solenoid (CMS) detector operates at the Large Hadron Collider (LHC) at CERN is designed to see a wide range of particles and phenomena produced in high-energy collisions in the LHC. Though prime motivation of LHC is the detection of Higgs boson, but CMS experiment has an elaborate program to study the heavy ion collisions to study QCD and explore QGP phase. At the core of the CMS detector sits a superconducting solenoid provides a uniform magnetic field of 3.8 T. The inner tracking system is composed of a silicon pixel detector and a silicon strip tracker.

Charged particles follow spiralling paths in the CMS magnetic field and the curvature of their paths reveals their momenta. The tracker is surrounded by a lead-tungstate scintillating crystals electromagnetic calorimeter, is designed to measure the energies of electrons and photons with great precision. Particles that interact by the strong force, hadrons, deposit most of their energy in the next layer, the hadronic calorimeter (HCAL) which is a brass scintillator sampling calorimeter. The only known particles to penetrate beyond the HCAL are muons and weakly interacting particles such as neutrinos.

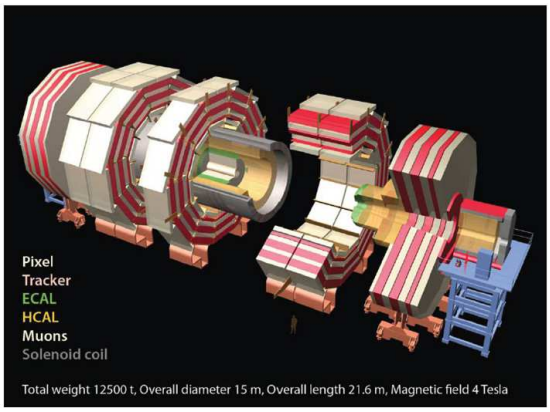

Fig.1: The CMS detector with its sub detector systems

As the name suggest, CMS is designed to measure muons with great accuracy. Muons are tracked in the $|\eta| < 2.4$ range ($\eta = -\ln[\tan(\theta/2)]$, where θ is the polar angle w.r.t. the beam axis) with four detection planes made of three different technologies which are interleaved with the iron yoke. The transverse momentum of the muons matched to silicon tracks is measured with a resolution better than 1.5%. The neutrinos escape from CMS undetected, although their presence can be indirectly inferred from the "missing transverse energy" in the event. The overall dimensions of the CMS detector are a length of 21.6 m,a diameter of 14.6 m and a total weight of 12500 t [1], Fig.1.

High energy collisions and QGP:

High-energy collisions of heavy ions allow the fundamental theory of the strong interaction, Quantum Chromodynamics (QCD)to be studied under extreme temperature and densityconditions. A new form of matter[2] formed at energy densities above1 GeV/fm^3 is predicted in Lattice QCD calculations. This quark-gluon plasma (QGP) consists of an extendedvolume of deconfined quarks and gluons. Heavy ion collisions at the Large Hadron Collider (LHC) are expected to produce matter at energy densities exceeding any previously explored in experiments conducted at particle accelerators.

Jet momentum dependence of jet quenching in PbPb collisions

Scattering of partons (quarks and gluons) from colliding nuclei with large momentum transfer produce energetic particles, known as "jets", which is used to probe the properties of the medium formed in heavy-ion collisions. More specifically, these higher-p_T jets have sufficient energy to stand out very clearly from the background of soft particles created in the heavy ion collision. The yields and correlations of high momentum particles are modified due to the energy loss of hard scattered partons while passing through the medium (Fig. 2). This effect is known as "jet quenching" [3], an important signature of QGP. The jet quenching effect on partons traversing the medium with different path lengths will lead to modifications in the observed dijetenergy

balance. Such unbalanced events are easy to detect visually even atthe level of event displays, Fig. 2.

The Compact Muon Solenoid (CMS) detector at the LHC is particularly well suited for these types of studies. Its high-precisions calorimetry and tracking allow very accurate reconstruction of both jets and charged particle tracks. Dijet production in PbPb collisions at a nucleon–nucleon center-of-mass energy of 2.76 TeV is studied with the CMS. A data sample corresponding to an integrated luminosity of 150 μb^{-1} is analyzed.

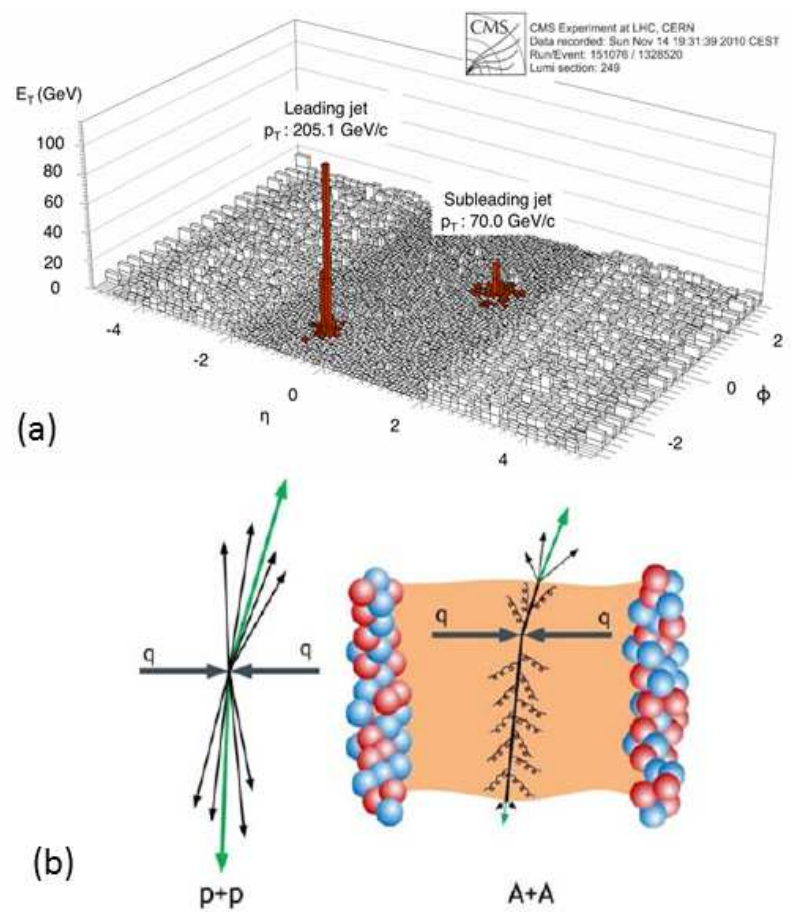

Fig. 2: (a) Example of unbalanced dijet in PbPb collision event at $\sqrt{s_{NN}}$=2.76 TeV. (b) Jet quenching of back-to-back jet pair in the medium in heavy ion collisions (right) in comparison to pp collisions (left)

Jets are reconstructed using the CMS "particle-flow" algorithm. This algorithm attempts to identify all stable particles in an event (electrons, muons, photons, charged and neutral hadrons) by combining information from all sub-detector systems. The anti-k_T sequential recombination algorithm is used tocombine the particle-flow candidates into jets using a radius parameter R = 0.3.

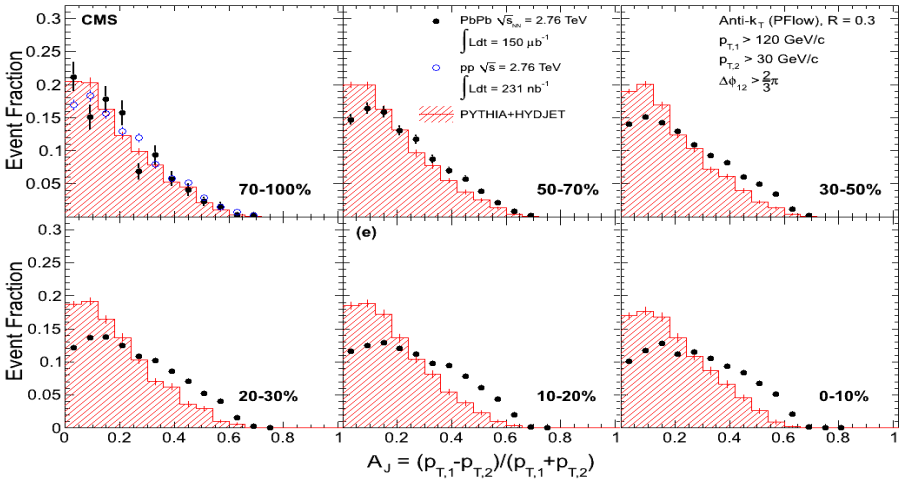

Fig. 3: Dijet asymmetry ratio, A_J, for six bins of collision centrality

The goal of the analysis is to characterize the possible modification of dijet event properties as a function of collision centrality and leading jet transverse momentum. Events containing a leading jet with $p_{T,1}$>120 GeV/*c* and a subleading jet with $p_{T,2}$ >30 GeV/*c* in the pseudorapidity range $|\eta|$ <2 are analyzed. The analysis is performed in six bins of collision centrality: 0–10%, 10–20%, 20–30%, 30–50%, 50–70%, and 70–100%, the latter being the most peripheral bin. The centrality of AA collisions, i.e., the geometrical overlap of the incoming nuclei, is related to the energy released in the collisions. In CMS, centrality is defined as percentiles of the distribution of the energy deposited in Hadron Forward calorimeter (HF).

The momentum imbalance between pairs of back-to-back jets, A_J, is studied with collision centrality and leading jet momentum. Dijets are selected with $\Delta\varphi_{1,2}>2\pi/3$. The contribution of background fluctuations is estimated from the events with dijets of $\Delta\varphi_{1,2}< \pi/3$, and the distributions obtained from these events are subtracted from the results. The centrality dependence of momentum imbalance of dijets$A_J$for PbPb collisions is shown in Fig. 3, in comparison to results from PYTHIA+HYDJET[4] Monte Carlo simulations at the same collision energy which include the effect of underlying PbPb event but no energy loss. The most peripheralevents are also compared to results from pp collisions at $\sqrt{s}$ = 2.76 TeV, where the same jet algorithm is used. The shape of the dijet momentum balance distribution experiences a gradual change with the collision centrality, towards more imbalance in more central collisions than in either pp or peripheral collisions [5].

The ratio of transverse momenta of the two jets is also studied as a function of centrality and the transverse momentum ofthe leading jet and shown in Fig. 4. This ratio rises smoothly with increasing leading-jet p_T in pp collisions. The same pattern is found in PbPb at all centralities, except that the ratio is systematically shifted down, i.e. the p_T of the sub-leading jet is smaller or more quenched [5].

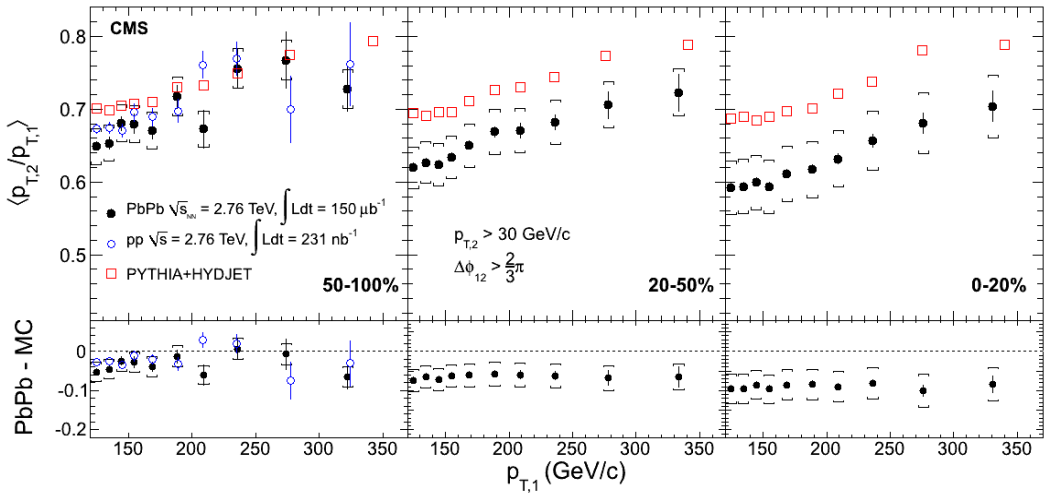

Fig. 4: Average dijet momentum ratio $p_{T,2}$ / $p_{T,1}$ as a function of leading jet $p_{T,1}$ for three bins of collision centrality

Jet quenching with isolated photon + jet correlations

To overcome the disadvantage of using dijet events to study parton energy loss where both the partons are traversing the medium and only difference in energy loss can be measured, an alternative way is considered to study the photon-jet events. At leading order (LO), photons are produced back-to-back with an associated parton (jet) having close to the same transverse momentum. Moreover, these photons do not strongly interact with the medium. The p_T spectrum of photons, even in central PbPb events, is identical within uncertainties to that found in pp at the same centre-of-mass energy. Furthermore, the yield of high p_T photons matches the prediction based on pp data and the number of nucleon-nucleon collisions for a given PbPb centrality. Hence photon+jetis an ideal probe to study the energy loss of partons in the medium.

The first study of isolated photon + jet correlations in PbPb collisions at a centre-of-mass energy of 2.76 TeV per nucleon pair corresponding to an integrated luminosity of 150 μb^{-1} is performed [6]. Events containing an isolated photon with transverse momentum p_T^{γ}>60 GeV/*c* and an associated jet with p_T^{Jet}>30 GeV/*c*, are considered. The photon+ jet *p*T imbalance is studied as a function of collision centrality and compared to pp data and PYTHIA+HYDJET calculations at the same collision energy.

The asymmetry ratio $x_{J\gamma}= p_T^{Jet}/p_T^{\gamma}$ is used to quantify the photon+jet momentum imbalance. In addition to the jet and photon selections, we further impose a strict $\Delta\varphi_{J\gamma}>7\pi/8$cut to suppress contributions from background jets. To study the quantitative centrality evolution of the energy loss, the average ratio of the jet and photon transverse momenta, $\langle x_{J\gamma}\rangle$, is shown in Fig. 5(a). Here solid red circle corresponds to CMS PbPb data at 2.76 TeV centre-of-mass energy,open black

circle toPYTHIA+HYDJET and solid black square to pp data at same centre of mass energy.While the photon + jet mean momentum ratio in the PYTHIA + HYDJET simulation exhibits a roughly centrality-independent value is $\langle x_{J\gamma} \rangle$ = 0.847 ± 0.004(stat.) to0.859 ± 0.005(stat.),the ratio $\langle x_{J\gamma} \rangle$= 0.73 ± 0.02 (stat.) ± 0.04(syst.) in the most central PbPb data, indicating that the presence of the medium, results in a more unbalanced photon + jet pairs.

Figure 5(b) shows R_j, the fraction of events containing a high-pT photon in which a jet was also found as a function of centrality. The value of $R_J^\gamma$is also found to decrease, from R_J^γ= 0.685 ± 0.008 (stat.) - 0.698 ± 0.006 (stat.) for the PYTHIA+HYDJET reference, as well as pp and peripheral PbPb data, to the significantly lowerR_J^γ= 0.49 ± 0.03 (stat.) ± 0.02 (syst.) to 0.54 ± 0.05 (stat.) ± 0.02 (syst.) for the three PbPb bins above 50% centrality.

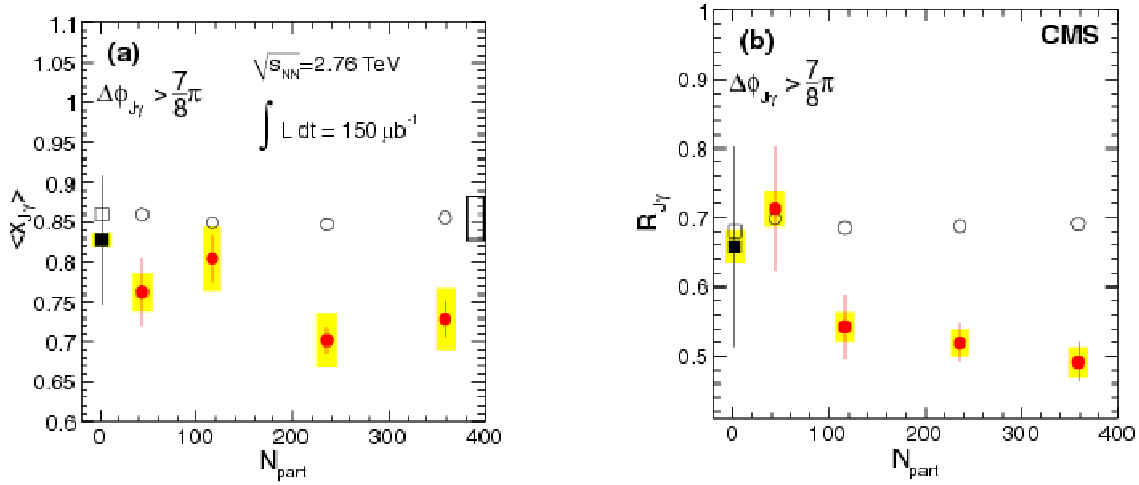

Fig. 5: (a) Average ratio of jet transverse momentum to photon transverse momentum as a function of N_{part}. (b) Average fraction of isolated photons with an associated jet above 30 GeV/*c* as a function of N_{part}

Z boson production in PbPb collisions

The first measurement of the production of Z boson in the $\mu^+\mu^-$ decay channel is performed in PbPb collisions at 2.76 TeV energy with the CMS detector at LHC with 7.2 μb^{-1} data sample [7,8]. Dileptons from Z decay, lose negligible energy in the strongly interacting QGP medium. Therefore, Z boson ideally suited to serve as candle to study the initial state in heavy ion collisions.

At 7 TeV pp collisions, the production of Z boson can well described by higher order perturbative QCD (pQCD) with recent parton distribution functions (PDFs). The PDFs however get modified in nuclei and depletion of Z boson yield is expected as much as 20% due to nuclear shadowing of PDFs. Precise measurements of Z production in heavy ion collisions can therefore help to constrain nuclear PDFs.

The dimuon invariant mass spectrum is shown in Fig. 6. Thirty-nine Z candidates are observed in the mass interval of 60-120 GeV/c^2. Their distribution is consistent with the one from the pp data at 7 TeV with CMS, scaled down to 39 counts and limited to the 60-120 GeV/c^2 mass range, which is displayed by the histogram in Fig. 6.

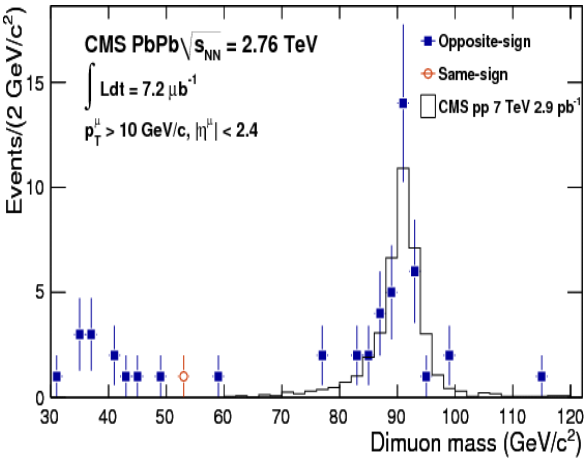

Fig. 6: Dimuon invariant mass spectra

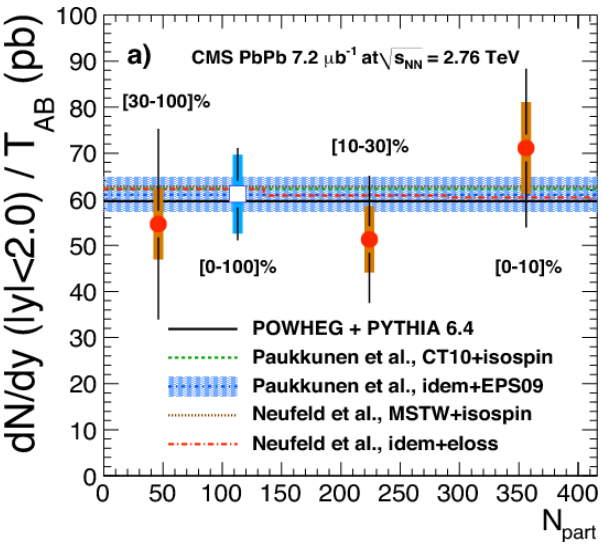

Fig. 7: The yields of Z to $\mu^+\mu^-$ per event: dN/dy divided by the expected nuclear overlap function T_{AB} and as a function of event centrality parameterised as the number of participating nucleons N_{part}.

The yield of $Z \rightarrow \mu^+\mu^-$ decays is estimated from the number of dimuons counted in the mass window of 60–120 GeV/c^2 and found to be dN/dy (|y|<2.0) = (33:8 ± 5:5± 4:4) × 10^{-8}, where the first uncertainty is statistical and the second is systematic. The analysis described above is repeated after subdividing the data into three bins for each of the following variables: event centrality and Z boson y and p_T. The total systematic uncertainty does not vary significantly with these variables and is considered to be constant and dominantly uncorrelated.

Without the in-medium modifications, the production of Z boson from perturbative processes, supposed to scale with the number of incoherent binary collisions. To compare the measured yield in PbPb to the available pp cross-sections, it is scaled with nuclear overlap factor T_{AB} which is estimated from Glauber model. The full circles in Fig. 7 show the centrality dependence of the Z yield divided by T_{AB}, while the open square is for MB events (integrated yield). The variable used on the abscissa is the average number of participating nucleons N_{part} computed in the same Glauber model. No centrality dependence of the binary-scaled Z yields is observed in data.

The normalized yields (dN/dy)/T_{AB} are compared to various theoretical calculations: (1) using the nucleon CT10 pusing MSTW08 PDFs and modeling incoming parton energy loss, and (3) provided by the POWHEG generator interfaced with the PYTHIA parton-shower generator

using CTEQ6.6 PDFs. Within uncertainties, no modification is observed with respect to theoretical next-to-leading order perturbative quantum chromodynamics proton-proton cross sections scaled by the number of elementary nucleon-nucleon collisions.

This measurement establishes the feasibility of carrying out detailed Z physics studies in heavy-ion collisions with the CMS detector. With upcoming PbPb collisions at higher luminosity and higher energy, the Z boson promises to be a powerful reference tool for final-state heavy-ion related signatures as well as providing a means to study the modifications of the parton distribution functions.

Acknowledgement

We are thankful to DAE for funding the CMS project at CERN. We are thankful to Heavy Ion Group and High p_T Physics Group of CERN for their continuous support for the analysis. I would like to thank Dr. S. Kailasand Dr. A. K. Mohanty for their guidance and continuous support. I would also like to thank my NPD colleagues from HENP section (CMS collaborators) who are involved in some of these works.

References

1. The CMS experiment at the CERN LHC, 2008, JINST 3, S08004.
2.E. V. Shuryak, "Theory of Hadronic Plasma", Sov. Phys. JETP 47 (1978) 212.
3. D. d'Enterria, "Jet quenching", Landolt-Boernstein, Springer-Verlag Vol. 1-23A (2010) 99,arXiv:0902.2011.
4. I.P. Lokhtin, A.M. Snigirev, Eur. Phys. J. C 45 (2006) 211, arXiv:hep-ph/0506189.
5. Jet momentum dependence of jet quenching in PbPb collisions at $\sqrt{s_{NN}}$=2.76 TeV, CMS Collaboration, Phys. Lett. B 712, 176 (2012).
6. Studies of jet quenching using isolated-photon+jet correlations in PbPb and pp collisions at $\sqrt{s_{NN}}$= 2.76 TeV, CMS Collaboration, Phys. Lett. B718,773 (2013).
7.Study of Z boson production in PbPb collisions at nucleon-nucleon centre of mass energy $\sqrt{s_{NN}}$= 2.76 TeV,CMS Collaboration, Phys. Rev. Lett. 106, 212301 (2011).
8. High mass dimuon resonances in Pb-Pb collisions at 5.5. TeV in CMS,CMS Collaboration (Dipanwita Dutta for the collaboration),Indian J. Phys. 85, 45, 2011.

A QUICK ACTING DEVICE FOR ARRESTING ACCIDENTAL GROSS LEAKAGE OF COOLANT FROM PRESSURE TUBES IN CANDU TYPE REACTORS DURING SHUTDOWN IN-SERVICE INSPECTION

Amit Kumar Haruray, Manojit Bandyopadhyay and D.N. Badodkar
Division of Remote Handling and Robotics

This design was awarded a patent in Canada (Patent No CA 2545993) and also in South Korea (Patent No 1012021310000)

Shri A.K. Haruray is the Recipient of the DAE Scientific & Technical Excellence Award for the year 2013

Abstract

The paper discusses design of an innovative device that can quickly arrest gross leakage of coolant heavy water in the event of accidental ejection/drifting of Special Sealing Plug during in-service inspection of coolant channels in Indian PHWRs (Pressurized Heavy Water Reactors) in reactor shutdown time. A Special Sealing Plug (installed inside the End Fitting of coolant channel assembly) forms the pressure boundary in the Primary Heat Transport system (PHT) of reactor for carrying out in-service inspection of coolant channels. It is designed to permit entry and movement of an Inspection Head inside the coolant channel. The accidental ejection of Special Sealing plug may result in gross leakage of heavy water coolant. A special leakage arresting device has been developed for arresting gross leakage quickly in such a situation. This paper discusses the design and functioning of this device in detail.

Introduction

In-service inspection of coolant channels is an important activity during shutdown period of the reactor. This is necessary to provide assurance about the structural integrity of the reactor for continued operation. The inspection is done with the help of an inspection Head that houses a variety of NDE sensors. The pressure boundary of the reactor is penetrated from outside dry environment to drive the inspection Head inside the wet environment of coolant channel. This necessitates use of a Special Sealing plug that has a central sealed opening through which the drive links can be inserted. The Special Sealing Plug remains installed in the End Fitting of the coolant channel while the Inspection Head is driven inside the coolant channel.

We visualize an event of accidental ejection of Special Sealing Plug that will expose the entire bore (full bore) of the coolant channel resulting in a gross leakage of heavy water. A loss in the capacity to remove the decay heat from the fuel bundles due to loss of coolant may have serious consequences and hence there is a strong requirement of arresting the leakage as soon as possible.

Coolant Channel in a PHWR (CANDU Type Reactor)

An Indian Pressurized Heavy Water Reactor consists of 306 coolant channels in a 220 MWe Indian PHWR reactor core. There are 392 fuel channels in a 540MWe Indian PHWR.

A typical coolant channel assembly has an inlet and an outlet connection for coolant heavy water at the north and south ends. A schematic given below shows the general layout of the coolant channel and inspection system while doing in-service inspection. It shows a Special Sealing Plug installed at one end from where the Inspection Head is driven inside the coolant channel.

Scheme and Layout of Inspection

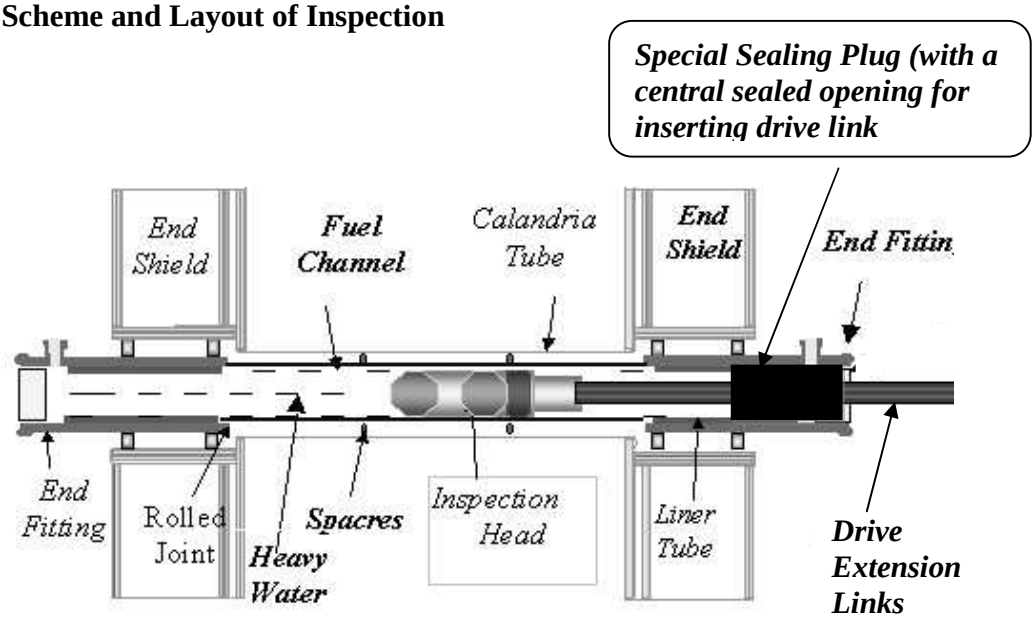

Fig. 1: Coolant Channel Schematic for In Service Inspection

This is a typical layout of the coolant channel assembly of an Indian Pressurized Heavy Water Reactor. The Special Sealing plug (shown as black color block on the right end of the assembly) has a central opening through which the drive extension links are inserted penetrating the pressure boundary from dry environment outside.

Inspection Head and Special Sealing Plug

All the NDE sensors are housed in the Inspection Head. This Inspection Head is assembled with Special Sealing Plug for installation into the coolant channel that has to be inspected. The Fueling Machine then installs the combined assembly in the End Fitting of the chosen coolant channel for inspection.

Penetration of Pressure Boundary for In-Service Inspection

The Inspection Head rear end is a stainless steel tube which passes through the central opening in the centre of the Special Sealing Plug. This rear end of the Inspection Head penetrates the pressure boundary and is connected to the BARCIS drive system placed in dry vault area (Drive system is placed on the Fueling Machine bridge).

The in-service inspection system consists of following:

1) Inspection Head (ref.[2]): Carries ultrasonic and Eddy current sensors for measuring critical coolant channel parameters.
2) Special Sealing Plug: With a central opening (with seals) for pressure boundary penetration, the Special Sealing Plug forms critical part of the whole inspection scheme.
3) Drive Extension Links:The drive extension links join Inspection Head's rear end with the BARCIS Drive System. Multiple extension drive links are required as the drive system has a limited linear stroke
4) Drive System:BARCIS drive system pushes the Inspection Head linearly with extension drive links passing through the seals of Special Sealing plug.

Event of Accidental Ejection of Special Sealing Plug (Emergency Preparedness)

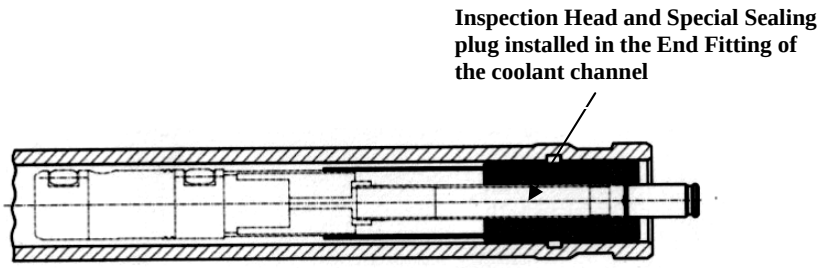

Fig. 2: Special Sealing plug and Inspection Head installed

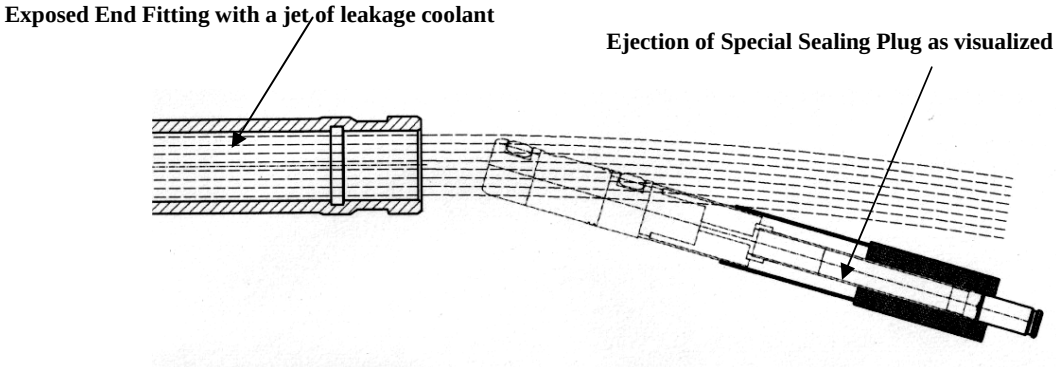

Fig. 3: Gross leakage due to accidental ejection of Special Sealing Plug

In the visualized event of ejection of Special Sealing plug gross leakage may occur because the end of the coolant channel will be left exposed with no means to block the flow. There are no fuel bundles in the coolant channel when the in-service inspection is taken up and hence the bore will be fully exposed as shown in Figure 3. Though the Special Sealing plug design and installation methodology is extremely strong in safe installation and operation, emergency preparedness is necessary from comprehensive safety standpoint.

Key Design Features of Quick Acting Leakage Arresting Device

Following are the *key design features* of the 'Emergency leakage Arresting Device'.

- Semi cylindrical shape / design of the Primary component of leakage arresting device
- Use of the 'End Fitting Collar' feature
- Special Ball valve attachment with End Fitting ID sealing arrangement

The construction of this device is discussed as following.

The innovative use of semi *cylindrical shape* (half cup design) enables simple and quick installation of the device on the coolant channel End Fitting. The design makes it possible for mounting or placing the device from top while standing sideways.

Semi cylindrical shape of the primary component of the Device

This helps the operator in avoiding facing the jet of water head-on. The primary component has a half cup shape on the front side and full cylinder at the rear side which has internal threading. This internal threading is used for assembling it with ball valve attachment (see Fig 7 and Fig.8). The assembly can be manually installed onto the End Fitting by a single person for arresting the gross leakage.

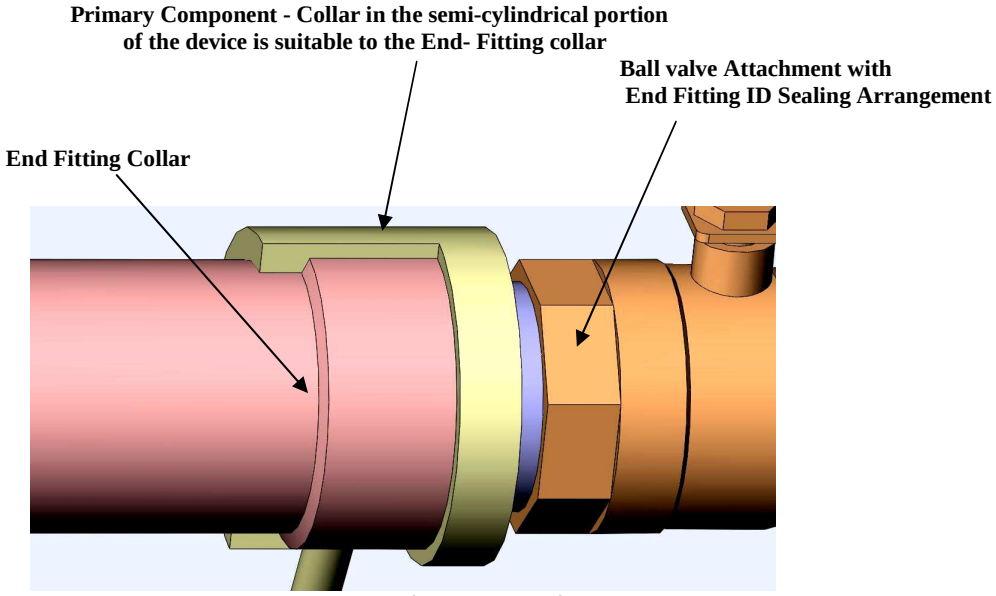

Fig. 4: A representation of the design of the Device

In the snap-shots shown below it becomes clear how the device is placed onto the End Fitting collar from top.

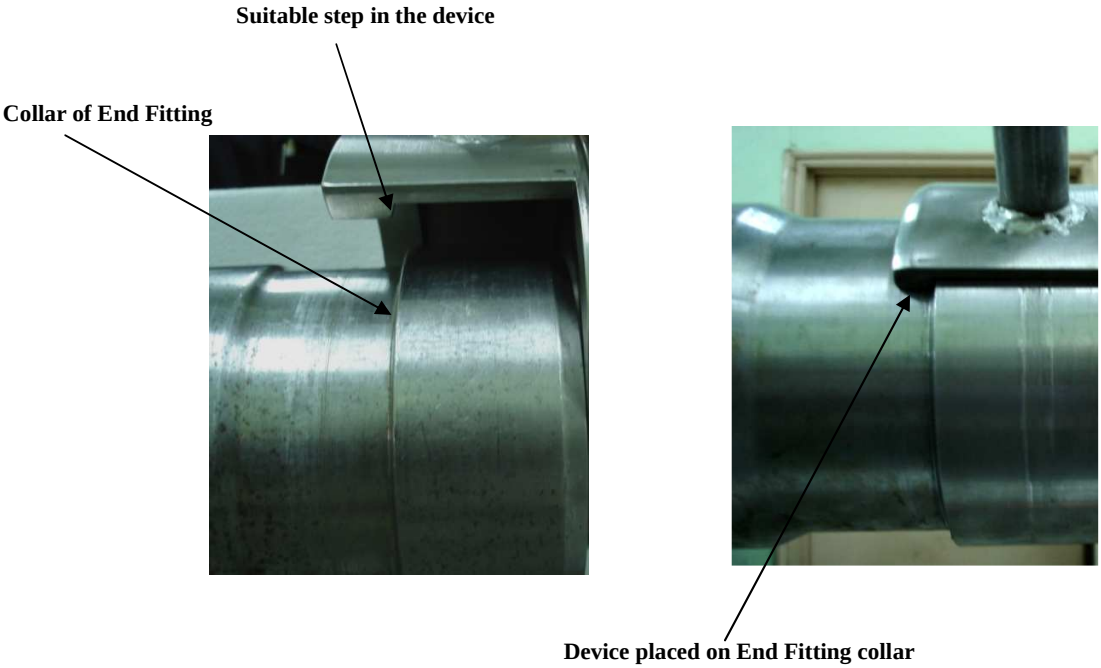

Fig. 5: Snapshots of the device getting placed onto the End Fitting

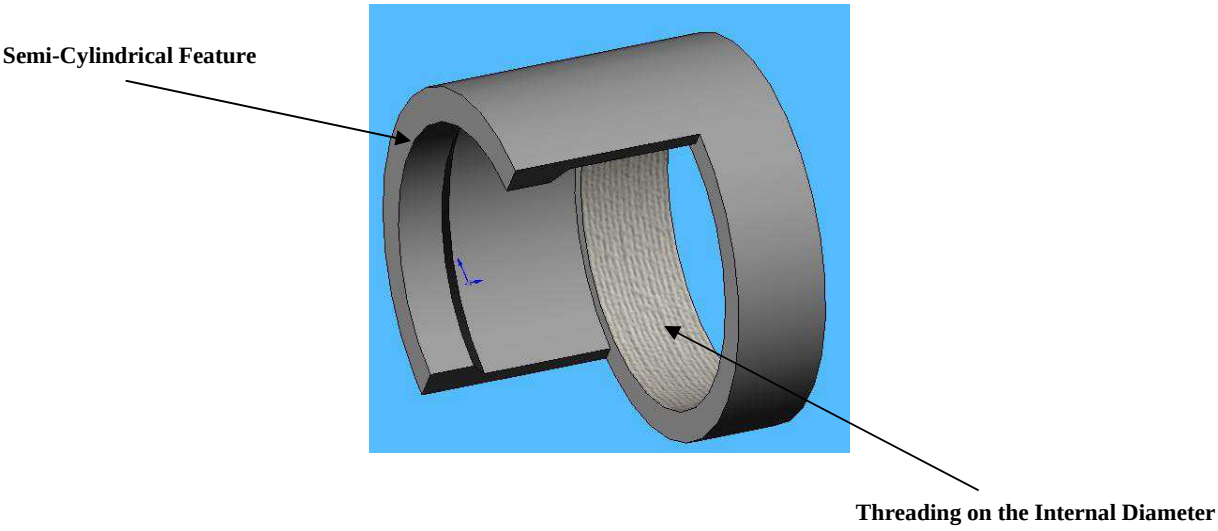

Fig. 6: Primary Component showing semi-cylindrical shape feature

Functioning of the device

First step is to place the assembly on the End Fitting collar such that the step in the semi cylindrical component matches the step of the End Fitting collar. Once the assembly is placed, other operations can follow. A ball valve is used to block the flow. Ball valve alone however, is not enough to arrest the leakage fully. The ball valve attachment is equipped with an O' ring that enters the ID (internal diameter) of the End Fitting when the Ball valve attachment is threaded inside the primary semi-cylindrical component. As the ball valve attachment O' ring enters the internal diameter of End fitting, the leakage path from that area is sealed. This directs the entire leakage flow towards the ball valve opening. Once it has been made sure that Ball Valve Attachment O' ring has entered the ID of the End Fitting, the ball valve can be closed by operating the lever. Fig.7 and Fig.8 display the operation and functioning of the device clearer.

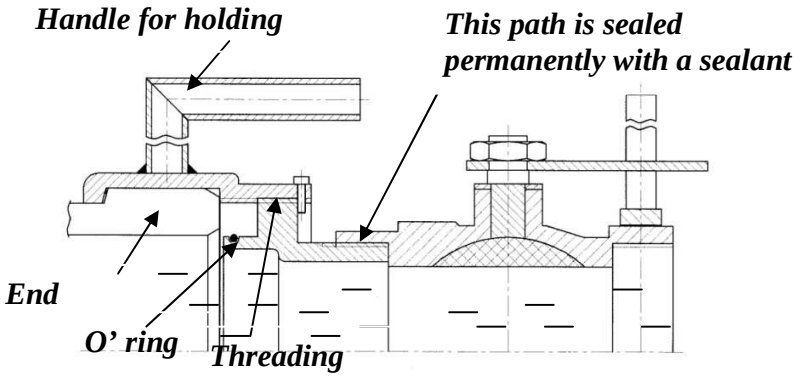

Fig. 7: Device placed onto the End Fitting, O' ring is out of the End Fitting

The ball valve attachment is rotated by turning the lever at the ends so that it threads into the primary semi-cylindrical component and advances as per the threading pitch.

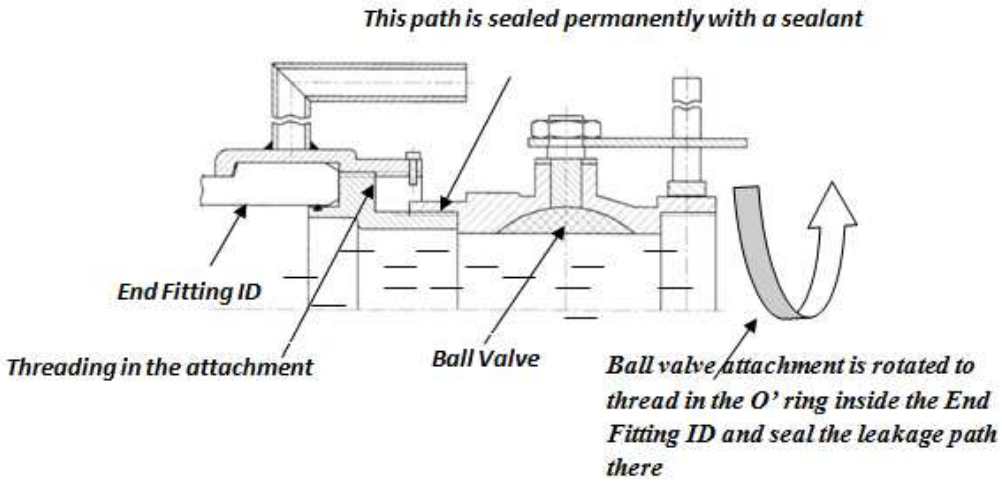

Fig. 8: O' ring enters inside the End Fitting ID, components butt with E-face

A representation of the entire assembly is shown in the following model. The operating lever for rotating the ball valve attachment (that has an O' ring to enter the End Fitting ID) is at the end of the ball valve (lever shown in blue green color). It may be noted that while placing the device onto the End Fitting collar and threading in the ball valve attachment the ball valve must. be kept open to vent off the water. Once it is ensured that O' ring has entered the ID of the End Fitting (components butt) the ball valve can be closed. This will completely arrest the leakage. Entire process of performing this operation takes about 10 seconds for a single person to arrest the leakage completely.

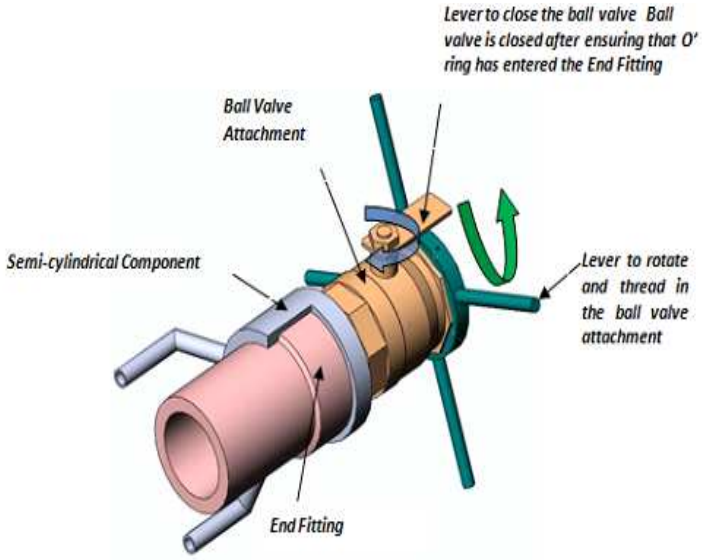

Fig. 9: Quick Acting Gross Leakage Arresting Device - Features

Testing and Qualification

The device was tested extensively for arresting the leakage in the simulated conditions. An experiment test set up was used to simulate the test conditions. During testing the coolant channel was kept completely empty as is be the case in the in-service inspection of coolant channels. It takes about 10 seconds to completely arrest the leakage. Following results have been noted.

The estimated worst leakage rate in the event under discussion is below 400 liters per minute (in 220 MWe as well as 540 MWe PHWRs). The device is suitable for arresting such leakages comfortably and very quickly (within 10 seconds).

Leakage Arresting Exercise & Estimated Worst Leakage Rates

Fig.11 shows the facility where the leakage is simulated and the exercise to arrest the leakage was taken up. A 9-channel lattice simulation is built to simulate the conditions at the reactor site. The central channel was provided with the leakage flow of the order mentioned in the Table 1.

Table 1

Sr. No.	Simulated Flow Rate (litres per minute-LPM)	Pressure in Coolant Channel after installation of Device and arresting of the leakage completely	Remarks
1	500	13 Kgf/cm2	Device installed & leakage arrested completely(by a single operator)
2	1000	13 Kgf/cm2	Device installed & leakage arrested completely(by a single operator)
3	1500	13 Kgf/cm2	Device installed & leakage arrested completely (by a single operator)
4	2000	13 Kgf/cm2	Device installed & leakage arrested completely (by a single operator)
5	2500	Device difficult to install due to heavy outflow	Not easy to install due to heavy outflow

The exercise was carried out by the personnel with proper wearing gear required in the emergency situation in the accidental conditions. Estimated worst gross leakage in the event of ejection of Special Sealing plug for a 220 MWe PHWR is about 250 liters per minute. For a 540MWe PHWR the estimated worst leakage rate is around 350 liters per minute. Following are the pictures of the exercise taken up at the leakage simulation facility. These pictures show the operations to arrest the leakage.

Fig. 10: Leakage Simulation

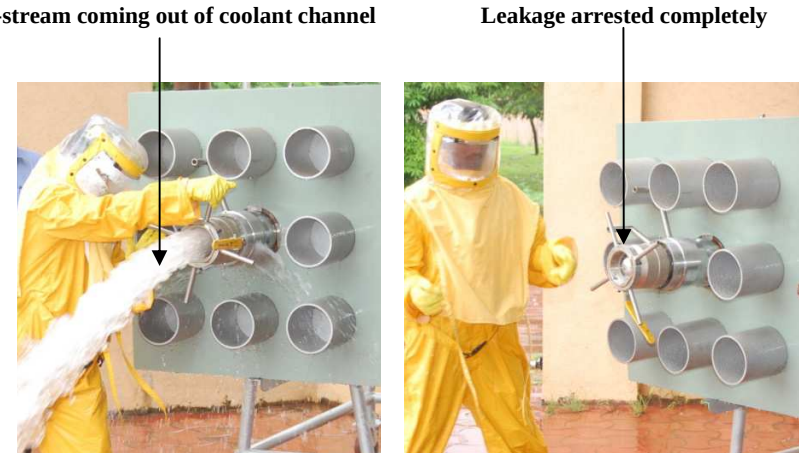

Figs. 11 & 12: Operating the device and arresting the leakage

It may be noted that the operator does not have to face the leakage water straight-on (see Fig.11). Leakage can be arrested standing sideways. The device is placed from the top onto the End Fitting collar and installed by rotating the ball valve attachment till components butt - followed by closing the ball valve to arrest the leakage completely. In Fig.12 the component is completely

threaded in and then the operator has closed the ball valve that has arrested the leakage completely.

Fig. 13: Quick Acting Gross Leakage Arresting Device

Leakage of the order of 2000 liters per minute with a line pressure up to 13Kgf/cm^2 can be arrested comfortably by using this device. It takes about 10 seconds to arrest the leakage completely.

Comprehensive Safety

This design is the inspiration behind a series of additional devices for attending to different types of accidental leakage scenarios. Coolant Channel inspection in Indian PHWRs is now equipped with safety devices based on this design. This safety methodology has been implemented at all Indian PHWR sites during shutdown ISI activity.

Conclusion & Acknowledgements

The 'Quick Acting Leakage Arresting Device' has critical contribution in generating enhanced confidence in plant crew for ensuring safety against accident leakages during in-service inspection. This device is also known as 'Full Bore Leakage Arresting Device and it takes about 10 seconds to arrest the leakage completely. It is an integral part of contingency measures at all PHWR sites in India during shut down In-Service Inspection activity.

This design was awarded patent in Canada and South Korea.

A number of other designs which are 'End Fitting' mountable are inspired from this work.
Authors are thankful to the support of Bhabha Atomic Research Centre and Nuclear Power Corporation of India Ltd. in this development.

References

[1] R K Puri, Manjit Singh , 'In-Service Inspection System for Coolant Channels of Indian PHWRs' (Seventh CNS Conference on CANDU Maintenance, Toronto, Canada,November 2005)

[2] Amit Kumar Haruray, R.D. Veerapur, R.K. Puri, Manjit Singh, 'Inspection Head Design for In-Service Inspection of Fuel Channels of PHWRs' June-2006, International Congress on the Advances in Nuclear Power Plants 2006 (ICAPP06) organized by American Nuclear Society at Reno, Nevada-USA.

BARC NEWSLETTER
FOUNDER'S DAY SPECIAL ISSUE 2015

EXPERIMENTAL AND THEORETICAL STUDIES ON RESPONSE OF MATERIALS UNDER HIGH PRESSURE AND HIGH TEMPERATURES

K.D. Joshi, Amit Rav, Amit Sur and Satish C. Gupta
Applied Physics Division

Dr. K.D. Joshi is the recipient of the DAE Scientific & Technical Excellence Award for the year 2013

Abstract

The applied physics division, BARC is involved in various research and development activities related to understanding of high pressure and high temperature behavior of materials. Using gas gun we have carried out a number of shock wave experiments in various materials and examined their response to rapid loading and unloading. These experimental studies required development of various sophisticated diagnostic techniques, the optical interferometry system named VISAR is one of them. This instrument developed by us indigenously has been used to measure the particle/free surface velocity history of target material during high strain rate loading. This instrument capable of measuring velocity in the range 100 m/s to 5000 m/s with time resolution of a few nanoseconds during few microseconds shock compression process has been integrated with the gas gun at our laboratory and is in continuous use for measurement of the yield strength and fracture strength of many important materials e.g. aluminum alloys Al2014-T4, Al2024-T4, SS304, alumina ceramics etc., subjected to impulsive loading with strain rates of ~ 10^4/s. Apart from experimental work, we have carried out theoretical investigations on various important materials, e.g. thorium, uranium carbide, Ti, Zr and Hf, osmium and LiH using ab-initio band structure method. In these materials, we have examined structural stability and determined equation of state under high pressure. For example, on thorium our theoretical analysis suggests that the fcc phase transforms to bct structure at 67 GPa (experimental value is 70 GPa) and this transition is driven by softening of the tetragonal shear modulus. Also, we have theoretically determined the thermal expansivity and melting of thorium at ambient pressure.

Introduction

The high-pressure research has contributed significantly to modern science and technology. Discovery of various important pressure induced phase transitions, determination of the high pressure equation of state (EOS), shock Hugoniot (pressure-volume, pressure-temperature relation obtained from shock compression), pressure dependent elastic constants and strength properties of materials have been proved very useful in both applied and basis sciences. For example, in applied science, the high pressure EOS, shock Hugoniot, elastic constants and pressure induced phase transitions serve as key inputs for hydrodynamic codes used for simulation of various situations such as reactor accidents, effect of missile attacks or meteorite impacts on installations and geological media, fission/fusion energy systems and analysis of

many problems pertaining to geophysics, astrophysics, planetology. For such applications, in addition to these properties the mechanical properties such as yield strength and fracture strength (hence elastic constants) of materials in the negative pressure regime also become important because in each of the above mentioned events the high compressive stresses generated in materials are always followed by high tensile stresses. In basic sciences the knowledge of high pressure EOS, shock Hugoniot, elastic constants and pressure induced phase transitions has played an important role in understanding various aspects of the physics of materials.

The high pressures in materials can be generated by two ways, namely, static compression technique and shock compression technique. In static compression method the sample placed between the two anvils of a hard material is compressed by pressing these anvils against each other [1,2], however, in shock compression, the sample gets compressed by high pressure pulse of microsecond duration generated by a rapid release of high energy into a small region [3,4]. In the static compression technique [1,2] the material is squeezed slowly, hence, temperature inside the sample during the experiment remains constant *i.e.* the static compression is an isothermal process, however, the rapid compression of materials under shock loading is accompanied by rise in temperature and entropy.

As far characterization of material subjected to high pressure is concerned, the x-ray diffraction, neutron diffraction, Raman scattering, IR scattering and Brillouin scattering [2, 5-7] are some of the commonly used microscopic techniques. In case of shock compression of materials it is quite difficult to perform in-situ microscopic measurement due to very short duration of the pressure in the material, however, time resolved measurements of some continuum properties such as such as particle velocity and stress are possible with application of diagnostic techniques such as optical velocimetry and piezoresistive gauges [8-10]. These measurements in conjunction with mass, momentum and energy conservation equations can be utilized to derive information about various physical and mechanical properties of materials subjected to shock loading.

In addition to experiments, modern density functional theory based *ab-initio* electronic band structure calculation methods are also used for understanding the response of materials under high pressures [11-18]. The modern *ab-initio* theoretical methods which can calculate the total energy reliably and accurately for any kind of strain, have facilitated the theoretical determination of pressure induced phase transitions, high pressure EOS, pressure dependent elastic constants and mechanical properties of the material in compressive as well as in negative pressure regime [11, 12, 19, 20]. Due to the increased accuracy and precision in calculating the total energy, the modern band structure methods have got even predictive capability on pressure induced phase transformations [12, 21, 20]. The theoretical methods have been proved to be very useful tool in circumstances when configuring a well defined experiment becomes difficult due to limitation posed by the instrument used for pressurization or undesirable properties of the sample. For example, osmium metal which exhibits extreme hardness, brittleness and toxicity is very difficult to fabricate in well defined shape and size due to which it is not possible to perform controlled shock wave experiment on it. In past few years, we have developed various diagnostic techniques for shock wave experiments and used them to examine the response of materials to high strain rate compression and tension [23-25] generated in plate impact experiments carried out in gas gun. Apart from experimental work, we have carried out *ab-initio*

electronic band structure calculations on various materials to examine their high pressure and high temperature behaviour. Highlights of few of the experimental and theoretical studies performed in past few years will be presented in this paper.

Development of VISAR instrument

The velocity interferometer system for any reflector (VISAR) is one of the important diagnostic techniques used in shock wave experiments. We have developed this instrument indigenously and integrated with the single stage gas gun existing in our laboratory at BARC [26]. Fig. 1 displays the photograph of this instrument.

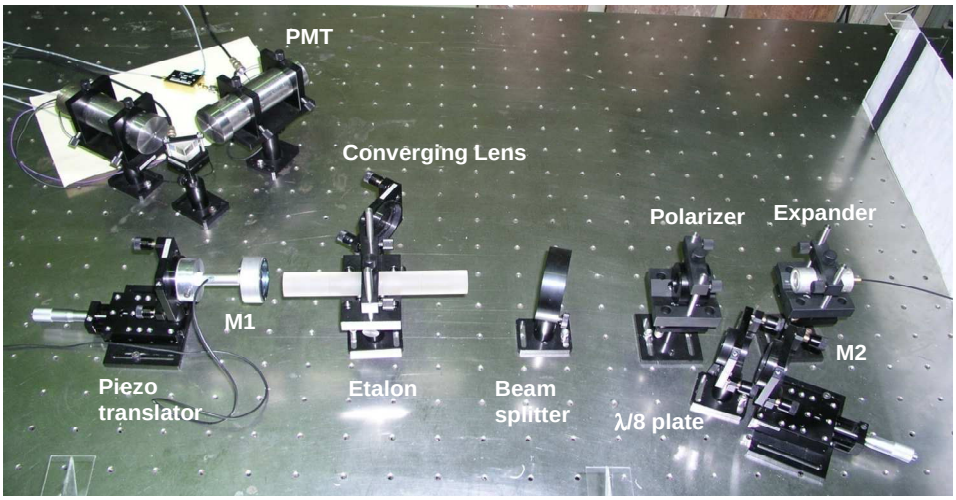

Fig.1: Photograph of VISAR instrument

This instrument is essentially a wide angle Michelson interferometer used for measuring the Doppler shift of the monochromatic light from a laser (in our case λ_0 = 532 nm) after it gets reflected off the free surface of the moving target [9, 10]. A fiber optical arrangement directs the laser beam to the target and transports the scattered light signal into the interferometer.

The interferometer beats the light signals reflected from the target at the two different instant of time separated by the delay (τ) decided by the length of the etalon in one of the leg of the interferometer. The interferometer signal is fed to the photomultiplier tube, the output of which is recorded in a digital storage oscilloscope. The free surface velocity and the interference fringe shift due to free surface motion are related as:

$$U_{fs}\left(t-\frac{\tau}{2}\right)=\frac{\lambda_0}{2\tau}F(t) \qquad (1)$$

Where, *F(t)* is the fringe count as a function of time. This recorded fringe shift pattern is used to derive the free surface velocity history of the target material. The free surface velocity profile so derived contains several features related to the elastic to plastic transition, phase transitions and tensile fracture strength at high strain rates.

Measurement of yield strength and spall strength of aluminium alloys

As mentioned in the starting paragraph, the yield strength and fracture strength of materials are of practical importance. In many situations such as hypervelocity impacts and armor applications, the generated strains are dynamic in nature with strain rates in the range ~ 10^4/s to 10^9/s. For such high strain rates, the yield strength and fracture strength are different than those in static measurements.

So it is essential to determine these properties under high strain rates. We have carried out measurements of these quantities in various materials such as alloys of aluminium, SS304 and alumina ceramics in plate impact experiments carried out using gas gun [23-25]. For example, Fig. 2 (left panel) shows, the free surface velocity history of Al2014-T4 alloy of aluminium measured in shock wave experiments carried out at three different impact velocities of 180 m/s, 290m/s and 500m/s, respectively [25].

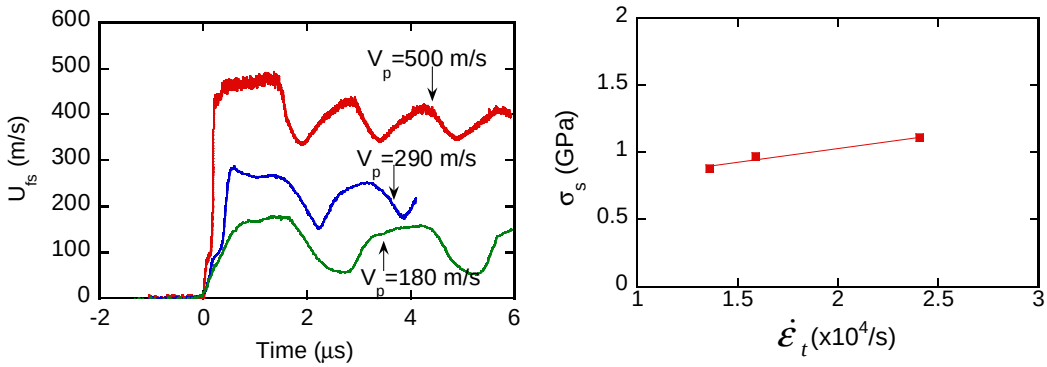

Fig.2: Free surface velocity history of Al2014-T4alloy measured for three impact velocities (left panel). The spall strength of Al2014-T4 alloy as a function of strain rate (right panel)

The stress σ_{HEL} corresponding to Hugoniot elastic limit, tensile stress σ_s just before the spall fracture and yield strength Y from measured free surface velocity history in different experiments is derived using following expressions [24]:

$$\sigma_{HEL} = \frac{1}{2} U_H \rho_0 c_l \qquad \dot{\varepsilon}_c = \frac{U_H}{2\Delta t_1}\frac{1}{c_l} \qquad (2)$$

$$\sigma_s = \frac{1}{2}\Delta U_{fs} \rho_0 c_b \qquad \dot{\varepsilon}_t = \frac{\Delta U_{fs}}{2\Delta t_2}\frac{1}{c_b} \qquad (3)$$

$$Y = \sigma_{HEL}\frac{(1-2\nu)}{(1-\nu)} \qquad (4)$$

Here $\dot{\varepsilon}_c$ and $\dot{\varepsilon}_c$ are average strain rates corresponding to Hugoniot elastic limit and spall fracture. The, U_H is free surface velocity at σ_{HEL}. The Δt_1 is the time taken for free surface to reach a

velocity of U_H. The $\Delta U_{fs}, c_b, c_l$ and ν correspond to pull back velocity of free surface, bulk sound speed, longitudinal sound speed and Poisson ratio, respectively. The pull back velocity is defined as $U_f - U_m$ where U_f is the peak free surface velocity and U_m is free surface velocity just ahead of spall pulse. The Δt_2 is the time taken by the free surface to retard from the peak velocity U_f to U_m.

Table 1 lists the value of peak compressive stress σ_{impact}, stress corresponding to Hugoniot elastic limit and tensile stress just before the spall fracture. Also, displayed are corresponding average strain rates. The Table also shows the yield strength Y derived from the Hugoniot elastic limit. For comparison, also listed are the yield strength and ultimate tensile strength measured under quasi-static loading conditions. It is clear from the Table 1 that the effect of strain rates is to increase tensile fracture strength of Al2014-T4 alloy significantly.

Table 1: The dynamic yield strength, spall strength and corresponding average strain rates measured in the Al2014-T4 alloy in the present work. A comparison also made with data measured under quasi static loading conditions

Properties	High strain rate loading impact velocity Vp (m/s)			Quasi static values
	500	290	180	
σ_{impact}(GPa)	3.61	2.13	1.32	
σ_{HEL}(GPa)	0.79	0.77		
$\dot{\varepsilon}_c$ (s^{-1})×10^4	9.4	3.6		
Y(GPa)	0.400	0.395		0.355
σ_s(GPa)	1.11	0.97	0.87	0.511
$\dot{\varepsilon}_t$ (s^{-1})×10^4	2.41	1.59	1.36	

This increase in tensile fracture strength at high strain rates is associated to the overstressing caused by rapid loading due to the slow response of material flaws to the loading. As displayed in the Fig. 2 (right panel), the increase in spall strength with the impact velocity is more or less linear at least up to impact velocity of ~500m/s. Though, the yield strength at high strain rates is slightly higher than the value measured under quasi static loading, it do not display significant increase with strain rates at least up to strain rates of ~9.4×10^4/s. The similar results have been obtained in another alloy Al2024-T4 of this metal.

Thorium having fcc structure is the first element of the light actinide series and it occurs naturally as fertile material besides natural uranium. Like uranium, Th^{232} can be transmuted in to nuclear fuel by absorption of slow neutrons, where the U^{233} formed after nuclear reactions acts as fissile material. A good understanding of the response of thorium to high temperatures and high pressures is an important need for its efficient conversion to fissile material in fast reactors and for the analysis of its behavior under extreme conditions in severe accident scenario. For

conversion of thorium to fissile U^{233}, the thorium blanket in the fast reactors needs to maintain its shape and integrity under high temperatures, therefore, the knowledge of its thermal expansion behaviour and melting property is very useful. Further, for accident analysis of the advanced nuclear power systems, the behaviour of thorium under rapid pressurization is an essential input.

In view of the technological and academic importance of this metal, we have determined thermal expansivity, thermal vibrations and room pressure melting of thorium employing the first principles method [27]. Further, the structural stability under pressure, isotherm and shock Hugoniot, have also been determined [28]. In order to derive thermal expansivity, the theoretically calculated potential energy has been fitted as a quasi-harmonic function of fourth order in interatomic spacing. The average thermal displacement $<u> = <r-r_0>$ is then obtained using Boltzmann distribution function [27]. Here r and r_0 is Wigner Seitz radius at any arbitrary volume and at equilibrium volume. The linear thermal expansion coefficient (α) is then obtained using expression $\alpha = \frac{1}{r_0}\frac{\partial < u >}{\partial T}$

The value of α obtained from temperature derivative of $<u>$ is 1.427×10^{-5}/K as compared to the experimental value of 1.23×10^{-5}/K [29]. Fig. 3 shows the reduced lattice constant ($a(T)/a_0$) so determined as a function of temperature. Also plotted is the experimentally measured data of Lawson et al. [29]. The theoretical values of reduced lattice constant at different temperature agree reasonably well with the experimental data. The mean square vibrational amplitude $<u^2>$ at a given temperature has been determined using expression $< u^2 >= \frac{3\hbar^2 T}{mk_B\theta^2}$ within Debye Model

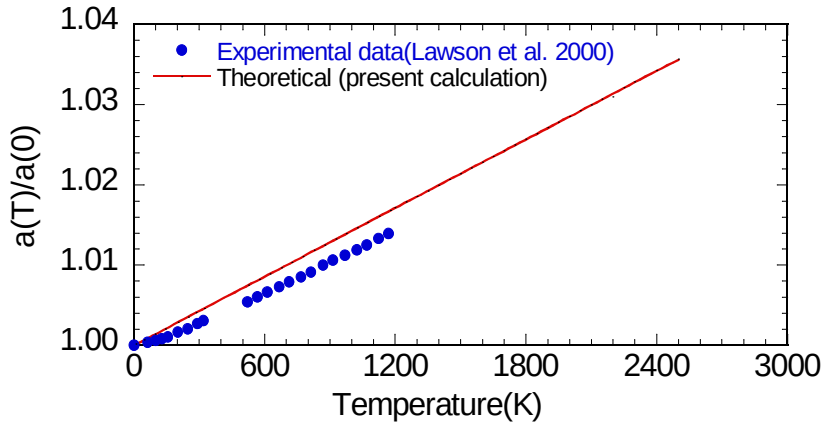

Fig.3: Reduced lattice constant of fcc thorium as a function temperature

The Debye temperature (θ) has been evaluated from volume dependent elastic constants obtained by finding the second order derivative of potential energy as a function of corresponding distortions [27].

Fig. 4 displays the mean square vibrational amplitude as a function of temperature. Also, plotted is the same derived from neutron diffraction experiments carried out by Lawson *et al.* [29] at various temperatures.

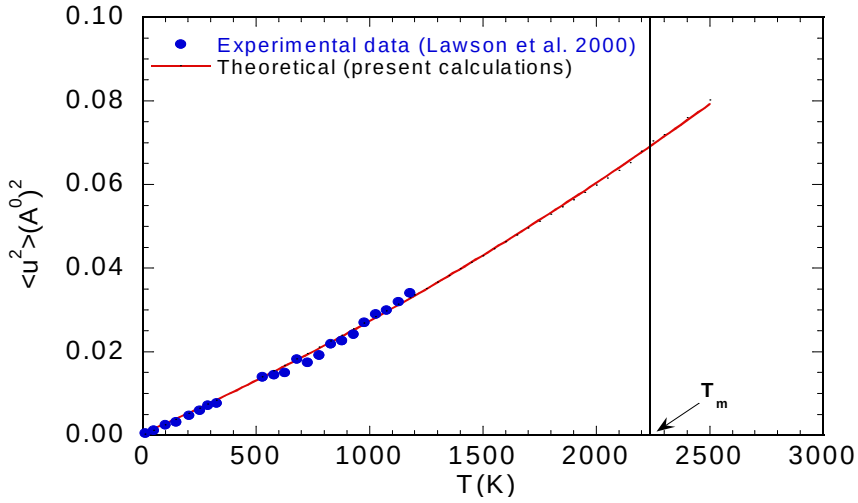

Fig.4: Mean square atomic displacement for fcc thorium as a function of temperature

The agreement between theory and experiment is quite well. Further, the melting point of thorium is determined using Lindemann melting criteria, which states that a solid will melt when the ratio of the square root of the $\langle u^2 \rangle$ with the equilibrium interatomic distance exceeds certain fraction (x_m). The value of this parameter for actinides has been reported to be ~ 0.083 from experiments [29]. Our calculations show that this value of x_m will occur at T= 2234 K, suggesting that the thorium will melt at this temperature, which agrees with experimental value of 2120 K within ~10%.

In diamond anvil cell experiment, Vohra *et al.* [30] have reported that thorium undergoes fcc to bct phase transition at ~ 70 GPa. The later calculations by Rao *et al.* [31] reported this transition to occur at ~ 80 GPa and related it with transfer of *spd* electrons to initially unoccupied *f* level. To understand the behaviour of this metal in more detail and to understand its response to high strain rate compressions generated by shock waves, we have carried out detailed theoretical analysis using first principles method.

The total energy calculations have been carried out at various unit cell volumes in bct cell. At each volume the c/a ratio of bct cell is optimized and the corresponding minimum energy is obtained. Up to the V/V_0 of ~ 0.61 (corresponding pressure ~ 67 GPa) it has been found that the optimum c/a ratio is ~ 1.414 and above this compression the optimum c/a ratio starts increasing and continues to increase till it reaches the maximum value of ~ 1.63 at V/V_0 ~ 0.47 with corresponding pressure of ~ 169 GPa.

This theoretical analysis suggests that fcc to bct transition in thorium starts at ~ 67 GPa and completes at ~ 169 GPa. The theoretically optimized c/a ratios along with experimental data [29] have been plotted as a function of compression in Fig.5. The theoretically derived pressure dependent elastic moduli have also been plotted in the same figure. As can be seen from the figure, the shear modulus C′displays anomalous behaviour as it starts softening around the

transition point and continues to decrease till it vanishes at V/V_0~ 0.51. This indicates that the fcc to bct transition in thorium under high pressure is shear driven.

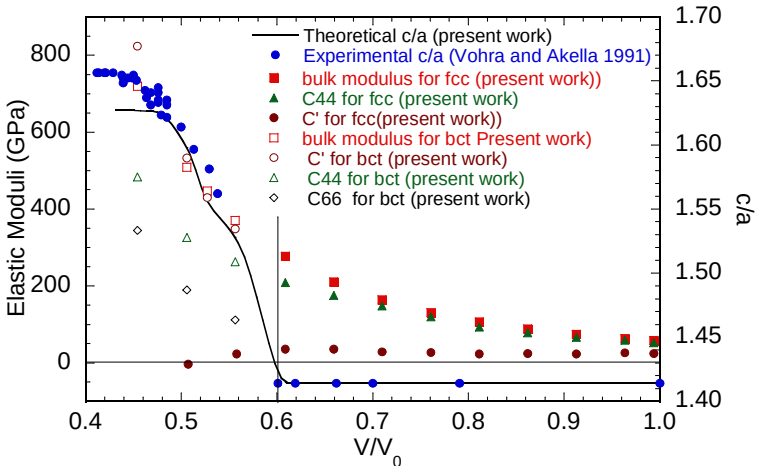

Fig.5: Elastic moduli of thorium and equilibrium c/a ratio as a function of specific volume

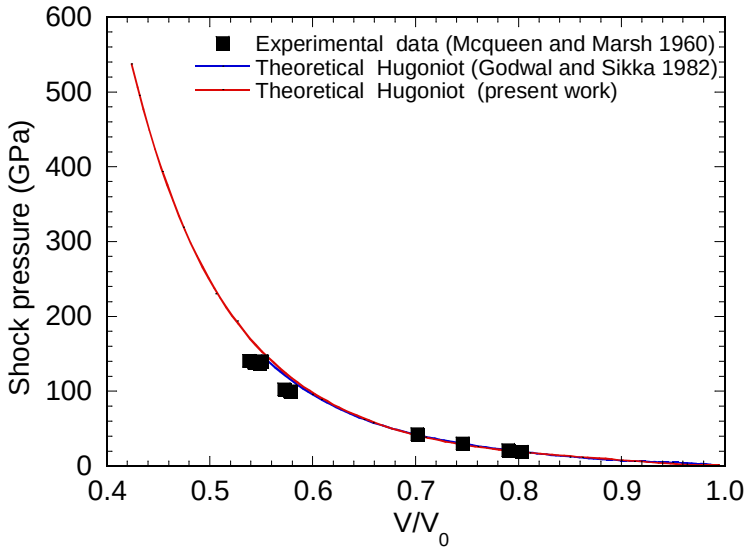

Fig.6: Comparison of theoretically deduced shock Hugoniot for thorium with available experimental Hugoniot data [32].

Finally, the 0 K calculations have been utilized to derive the 0 K isotherm, which after adding the thermal corrections has been used to derive the shock Hugoniot and 300K isotherm. In order to derive Hugoniot from 0 K isotherms, the thermal corrections have been used in conjunction with the Rankine Hugoniot condition. The Hugoniot so derived is displayed in Fig. 6. As is clear

from the figure the theoretical Hugoniot displays reasonably good agreement with experimental data [32] and theoretical values from other sources.

Summary

To summarize, in this paper we have presented the diagnostic technique VISAR developed in our laboratory at BARC. Using this technique in plate impact experiments carried out employing gas gun, we have measured various important mechanical properties such as yield strength and fracture strength of aluminum alloys subjected to high strain rate loading and unloading. This development has facilitated the measurement of various mechanical and physical properties of materials subjected to to high strain rate compressive and tensile loading. In theoretical front, we have developed capability of analysis of structural and elastic stability and generating equation of state of materials from first principles. For example, in thorium, we have determined high pressure induced phase transitions and pressure dependent elastic properties. Also derived are the isotherm and shock Hugoniot of this metal. Apart from this, we have presented our results on theoretical determination of room pressure thermal expansivity and melting of thorium.

References

1. A P.W. Bridgeman, *The Physics of High Pressure*, (Bell, London, 1952)
2. Jayaraman, *Rev. Mod. Phys*., 55, 65, (1983); *Rev. Sci. Instrum.*, 57, 1013 (1986)
3. Lee Davison, *Fundamentals of shockwave propagation in solids*, Springer Verlag, 2008, p. 38
4. G.E. Duval and R.A. Graham, *Rev. of Modern Phys*., 49, 523 (1977); G.E. Duvall and G R. Fowles 1963 *Shock Waves in High Pressure Physics and Chemistry* Vol 2, (Ed: R S Bradley) New York: Academic, p. 2
5. Anil K. Singh, H.K. Mao, J. Shu, Russel J. Hemley, *Phys. Rev. Lett.*, 80, 2157 (1998)
6. Thomas S. Duffy, Guoyin Shen, Jinfu Shu, H.K. Mao, R.J. Hemley and Anil K. Singh, *J. Appl. Phys*., 86, 6729 (1999)
7. E.S. Zouboulis, M. Grimsditch., A. K. Ramdas and S. Rodriguez, *Phys. Rev. B* 57, 2889 (1998).
8. Satish C. Gupta and Y. Gupta, *J. Appl. Phys*.57, 2464 (1985); *J. Appl. Phys*.62, 2605 (1987)
9. L.M. Barker and R.E. Hollenbach, *J. Appl. Phys.*, 43, 4669 (1972).
10. D.D. Bloomquist and S.A. Sheffield, *J. Appl. Phys*., 54, 1717 (1983)
11. M. Cerny, M. Sob, J. Pokluda and P. Sandera, *J. Phys. Cond. Matter* 16, 1045 (2004)
12. Satish C. Gupta, Jyoti M. Daswani, S.K. Sikka and R. Chidambaram, *Current Science* 65 399 (1993)
13. K. D. Joshi, G. Jyoti, Satish C. Gupta and S.K. Sikka, *Phys. Rev. B* 65**,** 052106 (2002)
14. M. Marcus, F. Jona and S.L. Qiu, *Phys. Rev. B* 66, 064111 (2002)
15. F. Jona and P.M. Marcus, *Phys. Rev. B* 63**,** 094113 (2001)
16. H.L. Skriver, *LMTO Method* (Berlin: Springer, 1984)
17. P. Blaha, K. Schwarz and J. Luitz, *WIEN97* (Technical University of Vienna)
18. A.R. Oganov and C.W. Glass, J. Chem. Phys. 124**,** 244704 (2006)
19. K.D. Joshi and Satish C. Gupta, *High Press. Res.*, 27, 259 (2007)
20. Sinko and N.A. Smirnov, *JETP Letters* 75, 184 (2002)

21. Jyoti S. Gyanchandani, Satish C Gupta, S.K. Sikka and R. Chidambaram, *High Press. Res.* 4, 472 (1990); *J. Phys. Cond. Matter* 2, 6457 (1990)
22. B.D. Sahoo, K.D. Joshi and Satish C. Gupta, *J. Appl. Phys.* 117, 185903 (2015)
23. Anoop K. Mukhopadhyay, Keshaw D. Joshi,, Arjun Dey, Riya Chakraborty , Amit Rav, Sampad K. Biswas, Satish C. Gupta, *J. Mater. Sci.* 45, 3635 (2010)
24. K.D. Joshi, Amit. S. Rav, Satish C. Gupta and S. Banerjee, *J. Phys.Conf. Series* 215 012149 (2010)
25. K.D. Joshi, Amit S. RaV, Amit Sur, P.C. Das and Satish C. Gupta, AIP Conf. Proc., 1665, 060024 (2015)
26. K.D. Joshi, Amit S. Rav and Satish C. Gupta, BARC Report No. BARC/2011/E/002
27. K.D. Joshi, Satish C. Gupta and S. Banerjee, *Phil. Mag. B*, 88, 3145 (2008)
28. Satish C. Gupta, K.D. Joshi and S. Banerjee, *Metall. Mater. Trans. A*, 39A, 1585 (2008)
29. A.C. Lawson, B. Martinez and J.A. Roberts, *Phil. Mag. B* 80, 53 (2000)
30. Y.K. Vohra and J. Akella, *Phys. Rev. Lett*., 67, 3563 (1991)
31. R.S. Rao, B.K. Godwal and S.K. Sikka, *Phys. Rev. B*, 46, 5780 (1992)
32. R.G. McQueen, S.P. Marsh, *J. appl. Phys*, 31, 1253 (1960)
33. B.K. Godwal and S.K. Sikka, *J. Phys. F: Met. Phys*., 12, 655 (1982).

DEVELOPMENT OF SINGLE SOURCE MOLECULAR PRECURSORS FOR ADVANCED SEMICONDUCTING METAL CHALCOGENIDE MATERIALS

G. Kedarnath and Vimal K. Jain
Chemistry Division

Dr. G. Kedarnath is the recipient of the DAE Scientific & Technical Excellence Award for the year 2013

Growing energy demand worldwide has directed research in renewable energy sources. Semiconducting materials both in bulk and nanoform showed immense potential in photovoltaic and thermoelectric applications [1,2]. However, properties of bulk materials can be improved by tailoring the size and shape of the material either in the form of colloidal solution or thin films. Controlling the size of materials facilitates tuning electronic, optical, magnetic properties, etc. [3]. Such types of tunable semiconducting materials are of great interest in technological advances.

A wide range of methods for the preparation of nanomaterials and for deposition of thin films have been evolved over the years. The synthetic ways for the preparation of nanomaterials involve physical (top-down, *e.g.* ion sputtering), chemical (bottom-up *e.g.* solvothermal synthesis) or hybrid methods.

Although there are number of routes available for the preparation of nanomaterials and thin films, single source molecular precursor route has emerged as a versatile method which can be used not only for the synthesis of phase pure and narrowly distributed materials but also for the deposition of thin films using aerosol assisted chemical vapor deposition (AACVD) method.

Single source molecular precursors for I-VI nanomaterials

For I-VI materials, novel tetrameric copper, $[Cu\{EC_5H_3(R\text{-}3)N\}]_4$ (E/R = Se/Me or Te/R; R = H or Me) [4] and hexameric, $[M\{SeC_4H(Me\text{-}4,6)_2N_2\}]_6$ (M = Cu, Ag) complexes using pyridyl/pyrimidyl chalcogenolate ligands have been synthesized and characterized structurally [5].

Structural analysis revealed that the complexes, $[Cu\{EC_5H_3(R\text{-}3)N\}]_4$ are tetrameric in nature where each copper atom lies at the vertex of the tetrahedron and each face of the tetrahedron is capped by the bridging pyridylchalcogenolate ligand. Similarly, the structures of $[Cu\{SeC_4H(Me\text{-}4,6)_2N_2\}]_6.H_2O$ and $[Ag\{SeC_4H(Me\text{-}4,6)_2N_2\}]_6.6MeOH.H_2O$ (Figure 1) revealed that the respective metal centre adopt distorted tetrahedral and trigonal geometries.

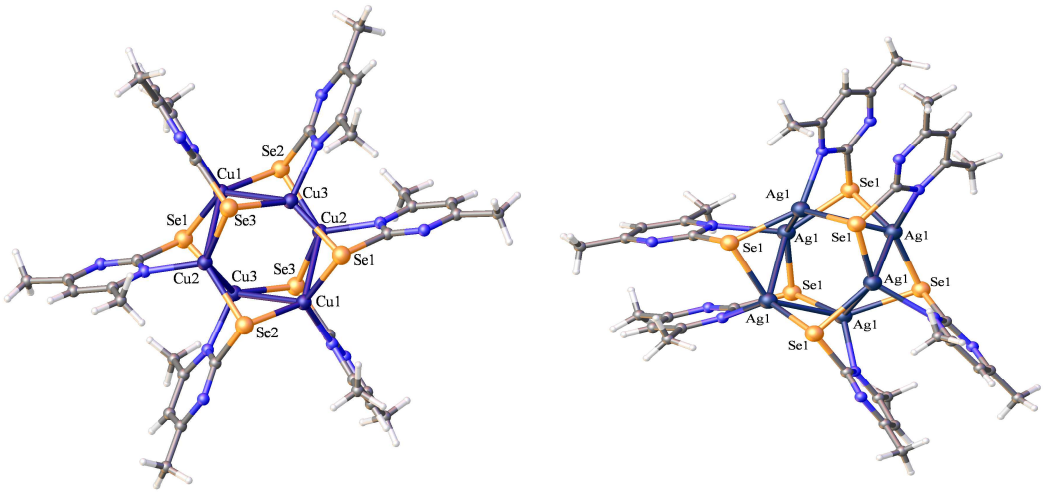

Fig. 1: Crystal structures of a) $[Cu\{SeC_4H(Me\text{-}4,6)_2N_2\}]_6.H_2O$ and b) $[Ag\{SeC_4H(Me\text{-}4,6)_2N_2\}]_6.6MeOH.H_2O$.

The tetrameric copper complexes have been used for the synthesis of copper chalcogenide (CuE) nanoparticles and for deposition of thin films by AACVD. Depending on reaction conditions, thermolysis gave both stoichiometric and non-stoichiometric copper chalcogenides. For instance, thermolysis of $[Cu\{SeC_5H_3(Me\text{-}3)N\}]_4$ in TOPO and HDA/TOPO at 170 and 150 ^oC, respectively afforded cubic phase of Cu_7Se_4 spherical (average diameter 125 nm) and cubic phase of $Cu_{1.8}Se$ polygon shaped nanoparticles, respectively. The former precursor has also been used for the deposition of orthorhombic phase of Cu_5Se_4 thin films at 400 ^oC using AACVD. Thermolysis of $[M\{SeC_4H(Me\text{-}4,6)_2N_2\}]_6$ (M = Cu or Ag) in DDT (1-dodecanethiol) at 150 ^oC afforded cubic phase of Cu_7Se_4 and orthorhombic phase of Ag_2Se, respectively.

Single source molecular precursors for II-VI nanomaterials

Synthesis, characterization and properties of II-VI semiconductor nanostructures have been probed and reviewed extensively [6,7]. Accordingly, a wide range of synthetic routes have been developed for utilizing their potential. Of them, single source molecular precursor route delivers monodispersed and phase pure materials.

Several single source molecular precursors for II-VI materials have been designed and studied by spectroscopic techniques using different ligand systems. Dithiocarboxylates of zinc triad, $[M(S_2CAr)_2]$ (M = Zn, Cd, Hg; Ar = Phenyl or Tolyl) and $[M(S_2CAr)_2(tmeda)]$ have been synthesized and used for the preparation of phase pure metal sulfide quantum dots under different pyrolytic conditions [8]. HgS nanoparticles could be isolated at low temperature (57 ^oC). Different phases (cubic/hexagonal) can be obtained under different experimental conditions. Similarly, a range of precursors for metal selenides have been developed. Among them monomeric metal selenocarboxylates, $[M(SeCOAr)_2(tmeda)]$ containing easily cleavable C-Se bond help in the formation of metal selenides at low temperatures [9]. For instance, HgSe nanoparticles of uniform size and shape have been prepared in good yields at room temperature. Another family of single source precursors of the type, $[M(Se(CH_2)_nNMe_2)_2]$ (M = Zn or Cd for

n =2; M = Zn, Cd and Hg for n =3) have been developed using internally functionalized selenolate ligand, $[Se(CH_2)_nNMe_2)_2]$ [10]. Phase pure and luminescent CdSe (Figure 2) quantum dots have been prepared by pyrolysis of $[Cd(SeCH_2CH_2NMe_2)_2]$ in coordinating solvents.

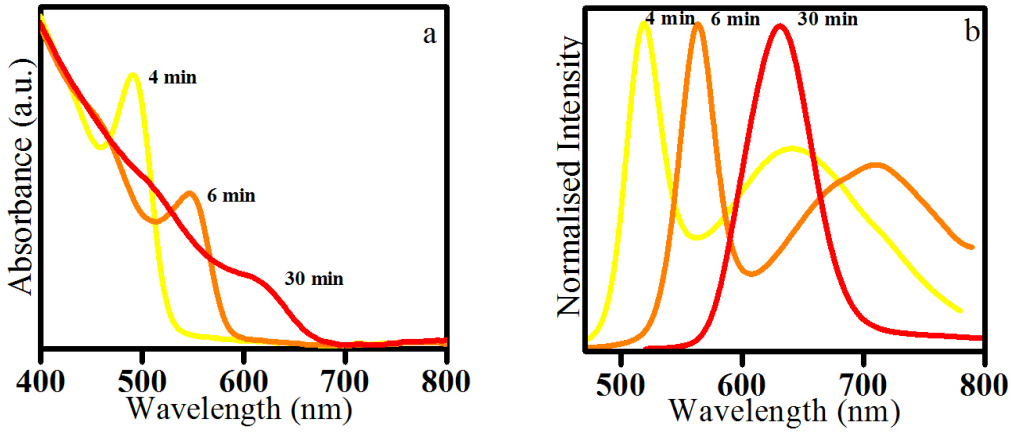

Fig.2.a) Absorption and b) emission spectra of CdSe nanoparticles obtained by thermolysis of $[Cd(SeCH_2CH_2NMe_2)_2]$ at 187 ^oC in HDA/TOPO recorded at 4, 6 and 30 minutes of preparation

In addition to above complexes, a number of precursors without M-E linkages have also been developed as chalcogenolates of zinc and cadmium often hydrolyze by atmospheric moisture or polymerize on ageing. Accordingly, heterocyclic diselenides and ditellurides with nitrogen donors such as $(EC_5H_4N)_2$ (E = Se or Te) have been utilized to synthesize zinc and cadmium complexes where nitrogen atom of the ligands coordinate to the metal atom [11]. Thermolyses of the resulting complexes yield metal chalcogenides.

Unlike group II metal sulfide and selenide nanomaterials, synthetic routes for analogous tellurides are relatively unexplored due to the difficulty in obtaining phase pure products. Recently, we have prepared $[Hg(TeCH_2CH_2NMe_2)_2]$ and utilized for the preparation of undoped and doped HgTe quantum dots by pyrolysis of $[Hg(TeCH_2CH_2NMe_2)_2]$ in HDA at ~100^oC in the size range of 5-10 nm [12]. Although doping of HgTe is a challenging problem due to labile nature of Hg-Te bond, a paramagnetic ion (Mn^{2+}) in the HgTe lattice could be introduced successfully. The Mn doped HgTe nanoparticles show ferromagnetism at room temperature.

Single source molecular precursors for III-VI nanomaterials

The III-VI chalcogenides find applications in solar cell absorbers, opto-electronics, photodetectors and photovoltaic devices. Among III-VI materials, indium chalcogenide have received considerable attention due to their photovoltaic properties. Thus for indium chalcogenides, indium complexes with 2-seleno- and -telluro pyridines, $[In(EpyR)_3]$ (E = Se or Te; R = H and Me) have been synthesized which on pyrolysis/solvothermolysis gave In_2E_3. $CuInSe_2$ nanomaterials have also been prepared by decomposing precursors, $[In(SepyR)_3]$ and

$[CuSepyR]_4$ together in high boiling coordinating solvents and have been characterized by electron microscopic techniques [14].

Single source molecular precursors for IV-VI nanomaterials

The IV-VI binary semiconductors like SnE, SnTe, PbE (E = S, Se, Te) show distinctive properties such as larger bulk Bohr radius and narrow band gaps which is helpful in thorough understanding of quantum confinement and their applications IR detectors and thermoelectrics [2,15]. Therefore, a number of methods have been explored both in solution and in gas phase leading to the preparation of different morphologies of IV-VI materials. Of them, the least investigated method is single source precursor route and hence, a number of thio- and seleno-pyridyl/pyrimidyl derivatives of organotin(IV) have been synthesized and structurally characterized.

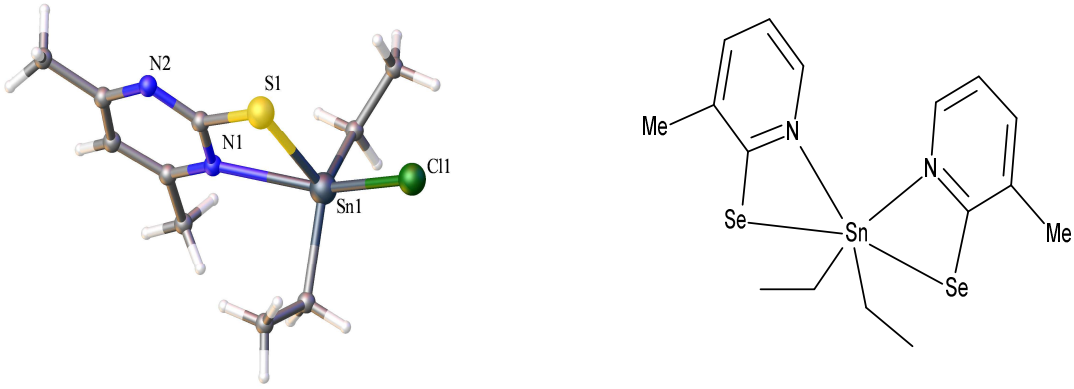

Fig. 3: a) Crystal and b) schematic structures of $[Et_2SnCl\{SC_4H(Me\text{-}4,6)_2N_2\}]$ and $[Et_2Sn\{2\text{-}SeC_5H_3(Me\text{-}3)N\}_2]$, respectively.

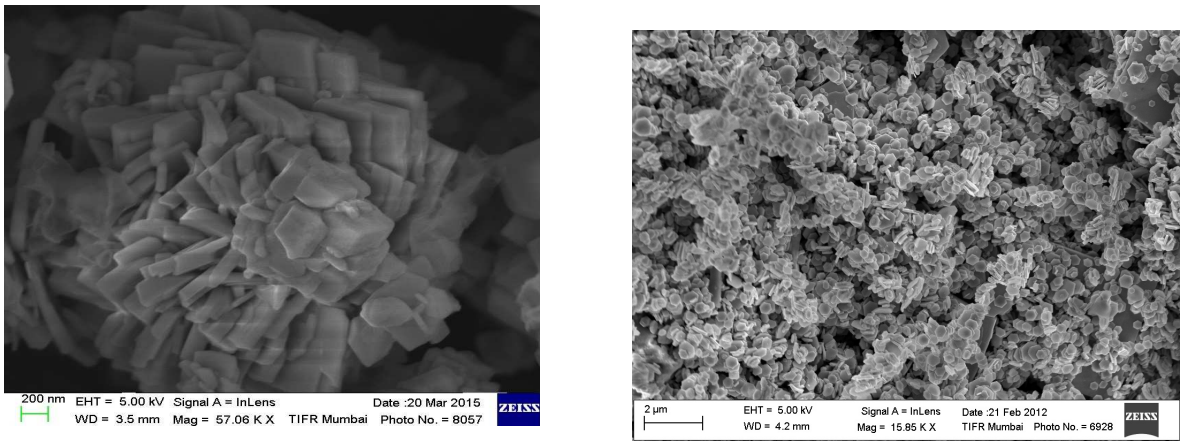

Fig. 4: SEM images of a) SnS sheets and b) SnSe hexagons obtained by thermolysis of $[Et_2SnCl\{SC_4H(Me\text{-}4,6)_2N_2\}]$ and $[Et_2Sn\{2\text{-}SeC_5H_3(Me\text{-}3)N\}_2]$ in OLA at 300 and 215 ^oC for 5 and 25 min, respectively

Further, the diorganotin complexes, $[Et_2Sn(2\text{-}SC_5H_4N)_2]$, $[Et_2SnCl\{SC_4H(Me\text{-}4,6)_2N_2\}]$ and $[R_2Sn\{2\text{-}SeC_5H_3(R'\text{-}3)N)_2\}]$ (R = Me, Et or ^{t}Bu; R' = H or Me) [16,17] on thermolysis in hot oleylamine produced different morphologies tin chalcogenide nanostructures at different temperatures. For instance, thermolysis of $[Et_2SnCl\{SC_4H(Me\text{-}4,6)_2N_2\}]$ (Figure 3a) and $[Et_2Sn\{2\text{-}SeC_5H_3(Me\text{-}3)N\}_2]$ (Figure 3b) in oleylamine (OLA) at 300 and 215 ^oC afforded rectangular SnS and hexagonal shaped SnSe sheets, respectively (Figures 4a and 4b). SnSe thin films have been deposited on glass and silicon substrates by AACVD of $[^tBu_2Sn(2\text{-}SeC_5H_4N)_2]$. The former have showed photo response. Other than tin chalcogenides, difficult to prepare PbE (E = S or Se) quantum dots have been synthesized by employing monomeric complexes, $[Pb(ECH_2CH_2NMe_2)_2]$ [18]. PbSe nanoparticles with an average diameter of 10 nm have been isolated. The complexes $[Pb(S_2CAr)_2]$ (Ar = Ph or Tol) in refluxing HDA afforded PbS nanoparticles at fairly low temperatures.

Single source molecular precursors for V-VI nanomaterials

The anisotropic and layered structured V-VI semiconducting materials, M_2E_3 (M = Sb or Bi, E = S, Se, Te) having direct band gap have drawn significant interest due to their potential applications in a variety of thermo-electric and optoelectronic devices, optical recording systems, television cameras and X-ray computed tomography [19-22].

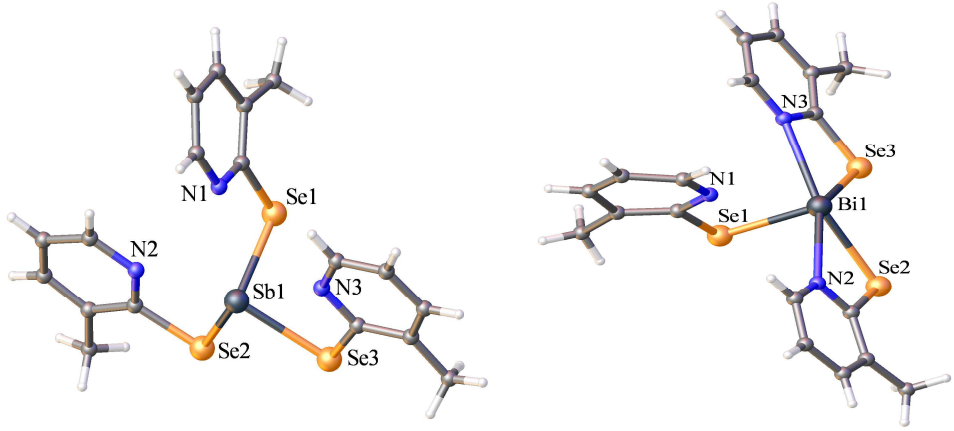

Fig. 5: Crystal structures of a) $[Sb\{SeC_5H_3(Me\text{-}3)N\}_3].1.5H_2O$ and b) $[Bi\{SeC_5H_3(Me\text{-}3)N\}_3].0.5H_2O$

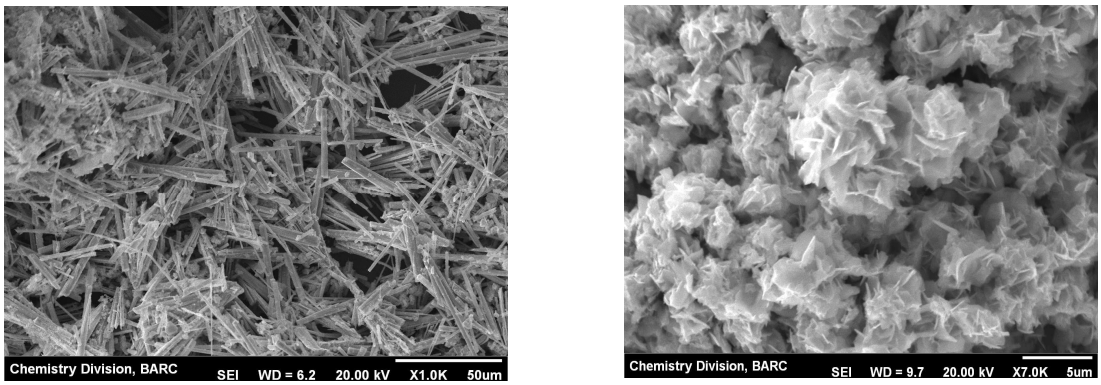

Fig. 6: SEM images of a) Sb_2Se_3 nanorods and b) BiSe nanoflowers obtained by pyrolysis of $[Sb\{Se\text{-}C_5H_3(Me\text{-}3)N\}_3]$ and $[Bi\{Se\text{-}C_5H_3(Me\text{-}3)N\}_3]$ in a furnace at 400 and 450 ^oC for 1 h.

Therefore, for V-VI materials, pyridylselenolate complexes of antimony and bismuth, $[M\{SeC_5H_3(R\text{-}3)N\}_3]$ (M = Sb or Bi; R = H or Me) have been developed and characterized structurally (Figure 5) [23]. The complexes either have been pyrolyzed in a furnace or thermolyzed in hexadecylamine (HDA) afforded a variety of M_2Se_3/MSe nanostructures [nanorods (Figure 6a) and nanoflowers (Figure 6b), *etc.*]. The precursors ave also been employed to deposit films of M_2Se_3 (M = Sb or Bi) by AACVD.

Acknowledgements

We thank Dr. B. N. Jagatap for encouragement of this work. We are grateful to all our collaborators, whose names appear in references for their sustained interest.

References

1. J. Li and J. Z. Zhang, *Coord. Chem. Rev.*, **253** (2009) 3015.
2. L. –D. Zhao, S. –H. Lo, Y. Zhang, H. Sun, G. Tan, C. Uher, C. Wolverton, V. P. Dravid and M. G. Kanatzidis, *Nature*, **508** (2014) 373.
3. E. Roduner, *Chem. Soc. Rev.*, **35** (2006) 583.
4. R. K. Sharma, G. Kedarnath, V. K. Jain, A. Wadawale, C. G. S. Pillai, M. Nalliath and B. Vishwanadh, *Dalton Trans.*, **40** (2011) 9194.
5. R. K. Sharma, A. Wadawale, G. Kedarnath, D. Manna, T. K. Ghanty, B. Vishwanadh and V. K. Jain, *Dalton Trans.*, 43 (2014) 6525.
6. X. Peng, *Chem. Eur. J.*, 8 (2002) 335.
7. T. Trindade, P. O'Brien and N. L. Pickett, *Chem. Mater.*, 13 (2001) 3843.
8. G. Kedarnath, V. K. Jain, S. Ghoshal, G. K. Dey, C. A. Ellis and E. R. T. Tiekink, *Eur. J. Inorg. Chem.*, (2007) 1566.
9. G. Kedarnath, L. B. Kumbhare, V. K. Jain, P. P. Phadnis and M. Nethaji, *Dalton Trans.*, (2006) 2714.
10. G. Kedarnath, S. Dey, V. K. Jain, G. K. Dey and B. Varghese, *Polyhedron*, **25** (2006) 2383.
11. G. Kedarnath, V. K. Jain, A. P. Wadawale and G. K. Dey, *Dalton Trans.*, (2009) 8378.
12. G. Kedarnath, S. Dey, V. K. Jain, G. K. Dey and R. M. Kadam, *J. Nanosci. Nanotechnol.*, **8** (2008) 4500.
13. A. R. Barron, *Adv. Materials for Optics & Electronics*, **5** (1995) 245.
14. R. K. Sharma, G. Kedarnath, N. Kushwah, M. K. Pal, A. Wadawale, B. Vishwanadh, B. Paul and V. K. Jain, *J. Organomet. Chem.*, **747** (2013) 113.
15. K. Szendrei, F. Cordella, M. V. Kovalenko, M. Böberl, G.Hesser, M. Yarema, D. Jarzab, O. V. Mikhnenko, A. Gocalinska, M. Saba, F. Quochi, A. Mura, G. Bongiovanni, P. W. M. Blom, W. Heiss, and M. A. Loi, *Adv. Mater.*, **21** (2009) 683.
16. A. Tyagi, G. Kedarnath, A. Wadawale, V. K. Jain, and B. Vishwanadh, *Unpublished Results*.
17. R. K. Sharma, G. Kedarnath, A. Wadawale, C. A. Betty, B. Vishwanadh and V. K. Jain, *Dalton Trans.*, **41** (2012) 12129.
18. G. Kedarnath, L. B. Kumbhare, S. Dey, A. P. Wadawale, G. K. Dey and V. K. Jain, *Polyhedron*, **28** (2009) 2749.

19. W. Wang, X. Lu, T. Zhang , G. Zhang , W. Jiang and X. Li, *J. Am. Chem. Soc.*, **129** (2007) 6702.
20. X. Zheng, Y. Xie, L. Zhu, X. Jiang, Y. Jia, W. Song and Y. Sun, *Inorg. Chem.*, **41** (2002) 455.
21. D. Cope, *U. S. Patent*, (1959) 2875359.
22. O. Rabin, J. M. Perez, J. Grimm, G. Wojtkiewicz and R. Weissleder, *Nature Materials*, **5** (2006) 118.
23. R. K. Sharma, G. Kedarnath, V. K. Jain, Amey Wadawale, Manoj Nalliath, C. G. S. Pillai and B. Vishwanadh, *Dalton Trans.*, **39** (2010) 8779.

LASER ASSISTED SURFACE CLEANING: A STUDY VIS-A-VIS INDIAN NUCLEAR FUEL CYCLE

Aniruddha Kumar
Advanced Fuel Fabrication Facility

Dr. Aniruddha Kumar is the Recipient of the DAE Scientific & Technical Excellence Award for the year 2013

Abstract

Occupational exposure to radiation occurs as a result of work associated with different stages of nuclear fuel cycle from mining to de-commissioning. The essential objective of radiation protection is to protect human health against the effects of radiation resulting from handling of radioactive materials. Although adoption of appropriate design of handling equipments and operational procedures offers protection but it cannot provide complete safeguard as the conventional methods often involve personnel coming into contact of the radioactive surfaces mainly with jobs involving cleaning of contaminated surfaces. To this end laser has proved to be an ideal tool as the entire cleaning operation with laser can be performed in a remote manner thus greatly reducing the possibility of exposure to the personnel. Further, the laser parameters can be carefully controlled to dramatically minimize the secondary wastes. No wonder that laser assisted surface cleaning has decided advantage as a decontamination tool when employed in nuclear industry. It has the potential to remove both loose and fixed contaminations from metallic as well as dielectric substrates without causing any harm to the surface underneath. This paper provides an insight to our work of employing a laser in multiple ways to affect surface cleaning in nuclear industry.

Introduction

India is persuading a three stage nuclear power programme to meet its future energy needs. This three stage program is based on a closed fuel cycle, wherein the spent fuel of one stage is reprocessed to produce the fuel for the next stage. The first stage of this programme involves using the natural uranium in Pressurized Heavy Water Reactors (PHWR's). The plutonium that is recovered from the reprocessing of the spent nuclear fuel from the first stage along with the non-fissile depleted uranium and thorium make the fuel for the second stage that essentially is a fast breeder reactor The depleted uranium and thorium can breed additional fissile material here viz., plutonium and uranium-233 respectively.

The third stage is based on the operation of thorium and uranium-233 fuelled nuclear reactors. Thus, fabrication of Plutonium and U-233 bearing MOX fuel and reprocessing of spent fuel plays a major role for successful implementation of the three stage nuclear power programme.

The major hazard in a plutonium / U-233 handling facility e.g. in a fuel reprocessing plant or a fuel fabrication plant arises from the possibility of inhalation or ingestion of the radio-toxic material by personnel or from the exposure of radiation caused primarily by gamma rays and neutrons. Storage and treatment of highly active alpha wastes is also another concern for these facilities. Thus plant design, equipment design and process flow sheet for these facilities should aim for minimising both *manrem* expenditure and generation of wastes. The high radio-toxicity and large biological half life associated with plutonium necessitates installation of all processing equipments inside leak tight glove boxes and heavily shielded glove boxes or hot cells for U-233 owing to the hard γ activity of daughter products of U-232 with remote operation and automated facilities.

In a MOX fuel fabrication plant, fuel pins are fabricated by loading fuel pellets, fabricated by conventional powder-pellet route using powder metallurgy techniques followed by encapsulation with a suitable technique. The pellet loading operation involving pushing the fuel pellets into the fuel tube, evacuation process during top end plug welding and in general handling the tubes inside glove boxes results in the presence of loose oxide particulates contamination on its surface, in general, and near the edges in particular. The loose contamination present on the outer surface of the fabricated fuel pins needs to be removed before their removal from the glove box for further processing and assembly. Conventional methods based on mechanical and chemical techniques are not suitable for decontamination of thin walled fuel pins as they are abrasive in nature leading to the possibility of clad damage. The manual method of decontaminating the fuel pins is most common and involves cleaning the pin surface inside the glove box with soft wet cloth and repeating the procedure after their removal from the glove box until the permissible level of activity is reached. This process is time consuming, leads to undue exposure of the personnel, generates large alpha active secondary waste and increases the possibility of air borne activity in the working area. Ultrasonic cleaning, an alternate technique currently adopted in many industrial facilities world-wide, requires submerging of the fuel pins in a specially designed water filled tank and subjecting them to ultra-sonic agitation. Although ultrasonic decontamination results in the dislodging of larger size loose particulates, it also generates large quantity of liquid waste necessitating an additional step of treating the active liquid for re-use / disposal.

Lasers can play an important role in surface decontamination of nuclear fuel pins as the process can be performed remotely with minimum generation of secondary wastes.

As discussed earlier, nuclear fuel fabrication plants and reprocessing plants handle bulk of plutonium material either in liquid form or in powder form inside glove boxes. The entire internal surfaces of the glove boxes get severely contaminated during handling of plutonium, more severely in the case where PuO_2 is handled as fine powder. These glove boxes need either renovation or disposal after several years of service primarily due to the build up of activity to an alarming level and deteriorated internal conditions. In case of disposal, the activity of the glove box needs to be reduced considerably so as to treat it as a low level waste that, in turn, reduces the disposal cost. On the other hand, the cleaning of the internal surfaces of the glove box will allow the renovation work to be performed at a lower radiation field. Conventionally the internal surfaces of the glove boxes are cleaned using strippable gels or chemicals. In the former case, the

gel is first applied to the contaminated surfaces and is allowed to cure. Later the layer so formed is peeled from the surface and stored as a solid waste. In the chemical process complex blends of acids and other chemicals are used manually in a multi-step process. There is prospect of cleaning the contamination from the inner surface of the glove box by locating the laser outside as there is enough literature to suggest that reverse cleaning is a possibility. Wherever the contamination is on the surface and fixed in nature the generated secondary waste can be greatly reduced by employing laser as the cleaning agent. This assumes larger significance as many reactors of the country are ageing and the prospect of decommissioning looms ahead. For recycling of precious materials and reduction of waste and exposure to personnel laser surface cleaning can be en efficient tool.

There are fundamentally three different approaches for laser assisted surface cleaning for removing particulate contamination from a substrate surface- 1) Dry laser cleaning, 2) Steam laser cleaning and 3) Laser shock cleaning. The dry laser cleaning involves direct interaction of the laser beam with either the contaminants or the surface or both. The micron /sub-micron sized particulates are adhered to the substrate by short range attractive forces e.g., Van der Waal's force that exists between both polar and non-polar substances. The magnitude of the adhesion force depends on the nature of the particle; its size, shape and contact area with the substrate. Absorption of energy from laser pulse either by the particulate or the substrate or by both can result in the rapid rise of temperature leading to the generation of a thermo-elastic force. The particulates can get dislodged from the substrate when the value of the generated force is more than the adhesion force. The steam cleaning approach is normally associated with the application of a thin liquid film on the surface prior to the interaction of the laser beam. The thrust generated by the explosive vaporisation of the liquid film under the action of the laser pulse dislodges the particulates from the surface. In laser shock cleaning, a shock wave is generated by focusing the laser beam at a specific distance above the surface to be cleaned in a gaseous or liquid environment. High electric field at the focal point results in dielectric breakdown and ionization of the medium generating rapidly expanding plasma at the point of focus. This results in the formation of a shock wave which moves outwardly at supersonic velocity. The resulting drag force acting on the particulates, if exceeds the van der Waal's binding force, can result in their expulsion.

In Advanced Fuel Fabrication Facility, Tarapur we have carried out experiments for decontamination of metallic and dielectric surfaces using dry laser cleaning and laser shock cleaning techniques. The dry laser cleaning technique has been successfully implemented in the decontamination of PFBR fuel pins. The following paragraphs will elaborate some of our experimental work and their results.

Experimental and results

Dry laser forward cleaning: Decontamination of PFBR fuel pins

The second stage of India's nuclear power programme is based on Fast Breeder Reactors. A Prototype Fast Breeder Reactor (PFBR) is under construction at Kalpakkam, Tamilnadu. The reactor is based on Uranium-Plutonium Mixed Oxide (MOX) fuel, 20% cold worked D9 stainless steel clad tube and liquid sodium coolant. Fabrication of fuel pins for this reactor is now

in progress at Advanced Fuel Fabrication Facility, Tarapur. Decontamination of fuel pins was carried out using a Q-switched Nd-YAG laser operating at 1.06 μm and capable of delivering a maximum energy of 1.6 J over a pulse of duration 6 ns (FWHM). The laser emits a multimode beam of cross section ~ 1 cm^2. A schematic diagram of the experimental set-up is shown in Figure 1. A work station capable of providing simultaneous rotational and translational motion to the fuel pin was made use of for this work and was installed inside a specially built fume-hood. The far end of the pin was held in a chuck, mounted on the shaft of the rotational stage. Proper supports were provided to hold the 2.60 meter long fuel pin horizontally. The linear and translational motions were effected through a programmable controller. The laser beam was steered into the fume hood through a narrow opening by means of appropriately arranged mirrors. A suction mechanism ensured that the ejected particulates from the interaction zone found their way into the HEPA filter attached with it. This mechanism along with the appropriate pressure gradient maintained inside the fume hood ensured that no airborne activity contaminated the working area. Further, usage of an inert purge gas prevents oxidation of the clad surface at the interaction zone as well as re-deposition of the ejected particulates. The pitch of rotation of the workstation, and the repetition rate of the laser were so adjusted as to irradiate

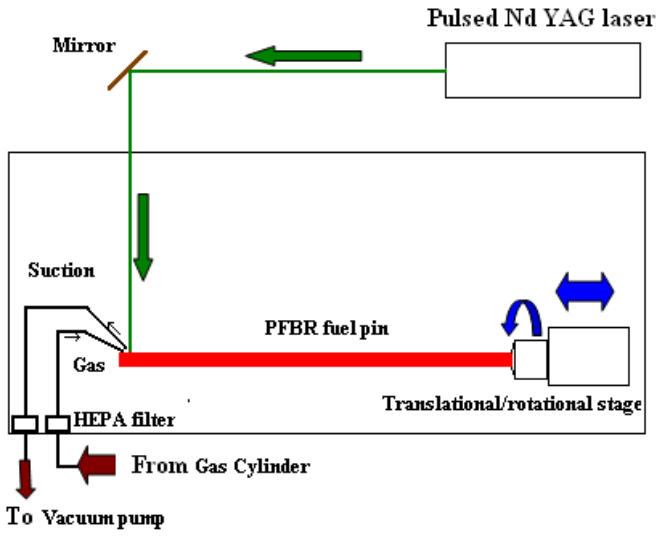

Fig. 1: Schematic of PFBR fuel pin decontamination setup

the entire active area of the fuel pin surface by the stationary laser beam with marginal overlap between the successive exposures. A number of precursory experiments on small contaminated samples were carried out to ascertain the laser parameters required to bring down the activity to the permissible level [1]. It was observed that exposing the sample surface to ~ eight laser pulses with a fluence value of ~700 mJ/cm^2 @1064nm could bring down the contamination level to the acceptable level. Following the optimization of laser parameters, laser assisted decontamination of the PFBR fuel pins was carried out. Figure 2 shows the activity per unit area (Bq/cm^2) of hundred fuel pins before and after laser decontamination. It is seen that laser cleaning could always bring down the activity significantly ensuring the removal of the loosely bound

contaminants from the fuel pin surface. Decontamination factor (ratio of the initial to the final activity) as high as 10^4 was achieved. The effect of laser exposure on the clad surface was then evaluated by carrying out SEM, EPMA and micro-hardness analysis. It was observed that this process does not alter the surface morphology and mechanical properties of the clad tube. Being a dry and non contact process, generation of solid waste and personnel exposure to radiation was also reduced. Figure 3 shows a typical comparison of radiation dose received by an individual radiation worker while carrying out decontamination of ten representative fuel pins by three different methods. It is observed that use of laser as the decontamination tool resulted in minimum exposure.

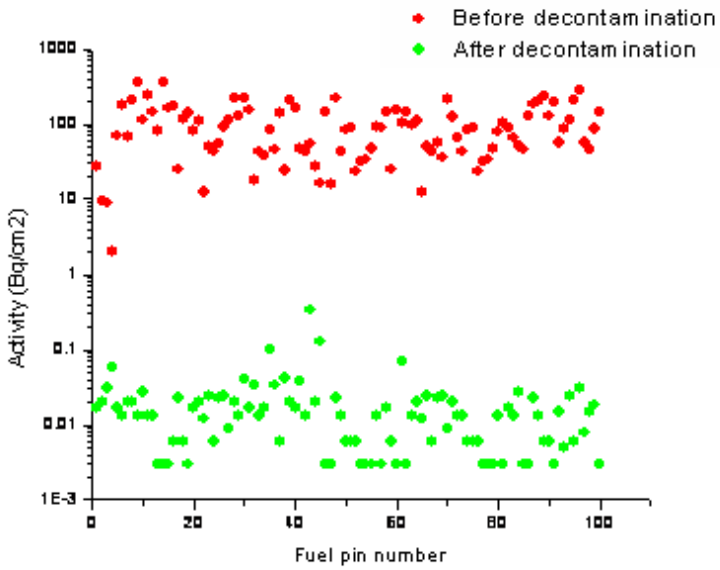

Fig. 2: Activity of hundred PFBR fuel pins before and after laser decontamination

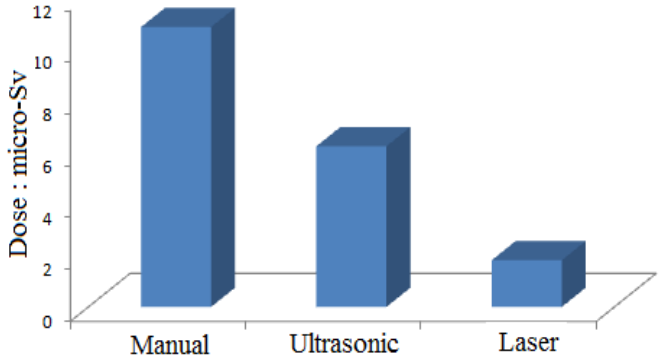

Fig. 3: Comparison of radiation exposure for three different methods of decontamination

Dry laser reverse cleaning - Cleaning of contaminated laminated glass

Our experiments were conducted on laminated glass pieces of size 2 inch x 2 inch and thickness ~ 6 mm. One of the clear surfaces of these glasses was contaminated by smearing UO_2 powder on it. A pulsed Nd-YAG laser capable of delivering a 6 ns pulse at 1064 nm and 532 nm wavelengths was used as the cleaning tool. The sample was scanned manually to clean the entire area. To estimate the decontamination efficiency, which is defined as the percentage of initial activity removed, alpha activity of the samples was measured before and after laser irradiation by making use of a ZnS(Ag) scintillation detector. The float glass is basically a soda lime glass which exhibits maximum transmission at @500nm wavelength.

Experimentally we found that the laminated glass slab used by us exhibits a maximum transmission of ~ 85% at 532 nm wave length and ~ 50 % for 1064 nm. Most of the earlier works on cleaning of contamination from glass surfaces have made use of UV radiation derived from either ArF or XeCl lasers. However for laminated glass panel cleaning, UV light cannot be used because the intermediate PVB layer blocks the transmission of UV photons through it. In our experiment we have irradiated the UO_2 contamination from the back side of the glass as the magnitude of the generated thermo elastic force will be more here in comparison to front side exposure. Practically too, it is an easy option as the laser beam in that case can be readily directed towards the glass panel. Figure 4 shows the percentage of decontamination efficiency as a function of fluence obtained after single pulse exposure.

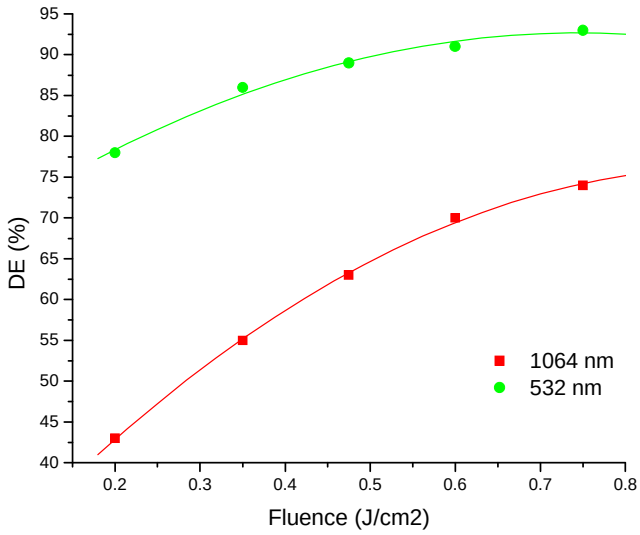

Fig. 4: Variation of single pulse decontamination efficiency with fluence

It is seen that very efficient cleaning at much lower fluence can be obtained with 532 nm wave length because of its better transmission through the laminated glass sheet as well as better absorption in UO_2. Although we have calculated DE after single pulse exposure, its value may

increase with more number of exposures for the fluence values used here. We have not observed any visual defects in the form of cracks or any marks on the glass surface as a result of the laser irradiation. Even though we have carried out initial experiments with UO_2 powder, this method of cleaning can be used for plutonium powders as well with an appropriate change in the fluence values. For practical application of this method, lasers with beam delivery through articulated arm will be preferred. Manually the beam can be scanned over the surface. For collection of dislodged particulates from the interaction zone the ventilation system of the glove box itself can be made use of, although, with an increased number of air changes. Other than renovation or disposal, cleaning of the inner surfaces of the glove boxes will increase the life of the glove boxes in addition to reducing the exposure to laboratory personnel.

Laser shock cleaning of contaminated samples

In dry laser cleaning, the contaminants are removed by exposing the contaminated substrate directly with a laser beam. However, direct exposure of the substrate to the intense laser beam may cause permanent damage to the substrate, especially if the substrate is brittle or has low melting point. As an alternative to the thermal stress induced cleaning, laser shock cleaning is a promising technique that allows removal of small particulates from the substrate surface without requiring it to be exposed directly to the laser beam. The shock wave is generated by focusing the laser beam at a specific distance above the surface to be cleaned in a gaseous or liquid environment. This results in dielectric breakdown and ionization of the medium generating rapidly expanding plasma at the point of focus. This results in the formation of a shock wave which moves outwardly at supersonic velocity. The resulting drag force acting on the particulates, if exceeds the van der Waal's binding force, can result in their expulsion. Experiments on cleaning of UO_2 particulates off metallic surface was carried out with shock waves induced by a Q-switched Nd-YAG laser (2^{nd} harmonic @532 nm) capable of generating pulses of 6 ns duration in air and water. Decontamination efficiency, defined as the percentage of initial activity removed, was evaluated by counting the alpha activity of the samples before and after laser exposure using a ZnS(Ag) scintillation detector. The laser treated samples were analyzed for any possible surface damage by optical and electron microscopy. In the first set of experiments the velocity of the shock waves as a function of laser energy at varying distances from the focal spot was estimated by beam deflection technique [2]. The shock pressure was then estimated using the Rankine-Hugoniot equations. The shock velocity was found to be varying between 2000 m/s to 800 m/s in air and between 3,500 m/s to 1800 m/s in water as the distance from the focal spot changed from 0.7mm to 2 mm respectively. The peak pressure of the shock wave at a distance of 0.7 mm was found to be ~ 3 MPa in air and ~ 3.5GPa in water and then decayed exponentially with increase in gap distance. Figure 5a to 5d shows the variation in decontamination efficiency (DE) obtained in water (5a and 5b) and in air (5c and 5d), as a function of laser pulse energy and number of exposures for two different orientations of the sample wrt the focal point i.e placing the sample horizontally and vertically at the same distance (0.7mm) from the laser focal spot. DE was seen to increase with increase in laser pulse energy and the number of exposures Under identical conditions of exposure DE was found to be always more for the samples treated holding vertically in comparison to the samples treated placing horizontally. The reduced DE in case of horizontally held samples was due to re-deposition of

the some of the removed particulates. Re-deposition was more in water than air due to higher density of water resulting inefficient cleaning in water particularly with laser pulses of lower energy and less number of exposures (Fig.5a).

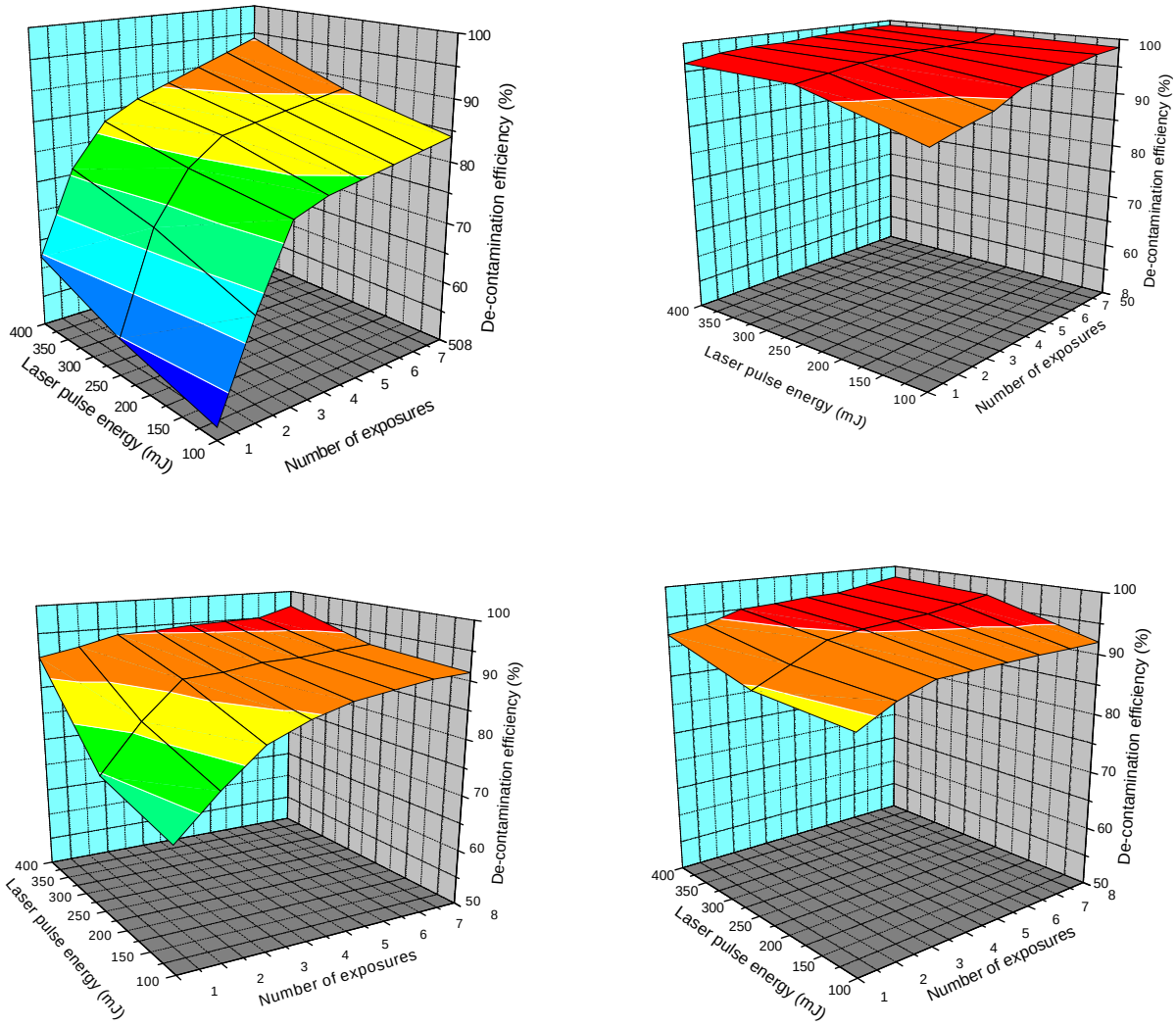

Fig. 5: Variation of DE with laser pulse energy and number of exposure. a) Sample placed horizontally in water, b) sample placed vertically in water, c) sample placed horizontally in air, d) sample placed vertically in air.

Most efficient cleaning was obtained when the samples were treated in water and was held vertically. DE of more than 99% was achieved when the samples were exposed to five laser shocks produced with laser pulses with energy more than 300 mJ (fig.5b). Cleaning under water resulted in higher efficiency because of the following reasons, 1) Greater magnitude of shock pressure due to confinement of plasma in water, 2) reduced adhesion force between the substrate

and the particulates by an order and 3) practically no redeposition when the samples were held vertically. The generation of cavitation bubbles inthe liquid due to the focussed laser beam also aids the cleaning process. Optical and electron microscopy of the cleaned surface revealed no damage on it.

Conclusion

Laser assisted surface cleaning has been implemented successfully in decontaminating metallic and dielectric contaminated substrates. This method is being used routinely in the AFFF fuel fabrication line for decontamination of PFBR fuel pins. Till date more than forty thousand fuel pins have been decontaminated using this technique. Other than removing loose contamination, lasers can play a dominant role in the decommissioning of aged nuclear reactors by ablating contaminated concretes and other metallic components. However, to exploit the full potential that lasers offers in surface cleaning a well directed research and development work is prerequisite.

References

1. Laser assisted decontamination of fuel pins for prototype fast breeder reactor, Aniruddha Kumar, R.B.Bhatt, Mohd. Afzal, J.Panakkal, D.J.Biswas, J.P.Nilaya and A.K.Das, Nuclear Technology, vol:182, 2013, 242-247.
2. Laser shock cleaning of radioactive particulates from glass surface. Aniruddha Kumar, Manisha Prasad, R.B.Bhatt, Mohd. Afzal, Arun Kumar, J.P.Nilaya D.J.Biswas. Optics and lasers in engineering, vol:57, 2014, 114-120.

BARC NEWSLETTER
FOUNDER'S DAY SPECIAL ISSUE 2015

MULTISOURCE REMOTE OPERATING DEVICE FOR CALIBRATION AND DOSIMETRY OF HIGH DOSE RATE BRACHYTHERAPY SOURCES

S. D. Sharma, R. K. Chaudhary, N. R. Kakade and D. A. R. Babu
Radiological Physics & Advisory Division

Dr. S.D. Sharma is the recipient of the DAE Scientific & Technical Excellence Award for the year 2013

Abstract

A fully computer controlled multisource storage cum source driving device was designed and fabricated locally. This device contains three major components, namely (i) a meticulously designed and properly shielded source container with proper mechanical support and coupling arrangement for connecting the source guiding tube, (ii) a specially designed electronic control system for driving the motors and position sensors, and (iii) a programmable graphical user interface (GUI) for operating the machine. The source container is a mild steel shell filled with sufficient amount of lead to keep the radiation leakage level within the prescribed limit. The device contains nine independent channels and hence it can store nine different high dose rate (HDR) brachytherapy sources. The objective of this development was to store the HDR brachytherapy sources of all the vendors so that the brachytherapy dosimeter of the hospital can be calibrated against the same source which used at the hospital in the clinical application. The performance characteristics of this multisource remote operating device (MROD) was thoroughly verified and found within the specified tolerance limit. For commissioning the MROD, a decayed HDR 192Ir source was loaded in the unit and its source strength was measured using the large volume brachytherapy reference standard.

Introduction

Beam therapy and brachytherapy are the two different approaches for delivering the prescribed radiation dose to a cancer patient. Brachytherapy uses sealed radioactive source(s) for dose delivery to the delineated tumour volume. On the basis of treatment site and method of placement of treatment applicator, brachytherapy is categorized as intracavitary, interstitial, intraluminal and surface mould applications. In this mode of cancer therapy, a high radiation dose is delivered locally to the tumor volume with rapid dose fall-off in the surrounding normal tissue region. Traditionally, brachytherapy was using preloaded applicators (treatment applicators loaded with a fixed activity of the radiation source) for insertion into the patient. This approach had the major drawback of higher occupational exposure and hence this approach of source placement was changed to manual afterloading technique. The manual afterloading brachytherapy allows loading of radioactive sources after the treatment applicators are put in place in the patient and have been checked radiographically for proper positioning using

radiopaque markers and source dummies. Even though, this technique of source placement requires manual handling of radioactive material during source preparation and loading of the sources into the previously inserted applicators, pose no greater risk to patients and personnel. From the last three decades, remote afterloading technique of source placement is used for delivering brachytherapy treatment. With the advancement in technology of source production/ fabrication and source storage and drive mechanism, brachytherapy is now practiced with relatively higher activity single stepping radiation source (^{192}Ir and ^{60}Co) that allow remote loading of radioactive sources after insertion of the treatment applicators into the patient. Remote controlled afterloading brachytherapy devices are now available that eliminate the direct handling of the radioactive sources. In this approach, the radiation source can be instantly loaded and unloaded, making it possible to provide patient care with the sources retracted into their shielded position. Commonly used brachytherapy remote afterloader is known as high dose rate (HDR) brachytherapy unit. It is well known that the biological effect of radiation on tumors and normal tissues is according to sigmoid shaped dose response relationships. Clinical dose response curves are recognized to be very steep, typically 5% change in dose causes 10 to 30% change in tumour control probability when looked at the steepest portion of such curves. On the basis of these considerations, the International Commission on Radiation Units and Measurements (ICRU) recommended that the overall accuracy in the radiation dose delivered to the patient should be within 5% (ICRU 24, 1976). The accurate calibration of the brachytherapy source plays an important role in achieving the required accuracy in treatment delivery (Nath et al 1997; Kubo et al 1998; IAEA, 2002; Podgorsak 2003). Reference Air Kerma Rate (RAKR) is used for specification of the strength of brachytherapy source by the various international agencies which is defined as the kerma rate to air, in air, at a reference distance of one meter, corrected for air attenuation and scattering. Air kerma strength (AKS) is also used for specifying the strength of brachytherapy source and is defined as the product of the air kerma rate in free space at a measurement distance r from the source center along the perpendicular bisector and the square of the distance r. RAKR or AKS calibration coefficient of brachytherapy dosimetry system depends on construction material, geometry and dimensions of the radiation source.

A variety of HDR brachytherapy sources are used in remote afterloading devices of different vendors. It will be appropriate to calibrate the brachytherapy dosimeter of a hospital against the same source which is available for the clinical use in that hospital. For achieving this goal, it is required that the calibration laboratory should have a remote operating device which can store HDR sources of all the vendors. To fulfill this requirement, a fully computer controlled brachytherapy multisource storage cum source driving device was designed and fabricated. This paper describes the salient technical features of this device as well as its performance aspects.

HDR Brachytherapy Sources

Majority of the HDR remote afterloading brachytherapy units contain a miniature Ir-192 source (nominal activity of about 10 Ci) as HDR brachytherapy source. Some of the vendors is also supplying miniature Co-60 source (nominal activity of about 2 Ci) in their HDR remote afterloading brachytherapy unit. Generally, an HDR brachytherapy source is a sealed radioactive source which contains a cylindrical source capsule and an active rod of the radioisotope concerned. Such sealed sources are identified by their total length and total diameter as well as

active length and active diameter. Commercially available HDR brachytherapy sources have total length in the range of about 4.5 mm to 10 mm and outer diameter of 0.4 to 1.1 mm. These sources are welded at one end of about 1.5 to 2.5 meter long multistrand drive cable having outer diameter approximately equal to source outer diameter. As an example, the dimensional details of old and new microSelectron (Nucletron, Netherlands) HDR Ir-192 source has been given in Table 1. The schematic internal configurations of microSelectron HDR Ir-192 old/ classic source is given in Fig. 1.

Table 1: Dimensional details of old and new microSelectron HDR ^{192}Ir brachytherapy sources

Parameters	Old/classic Source	New Source
Active length (mm)	3.50	3.60
Active diameter (mm)	0.60	0.65
Total length (mm)	5.00	4.50
Capsule diameter (mm)	1.10	0.90
Capsule thickness (mm)	0.25	0.125
Cap radius (mm)	0.55	0.40

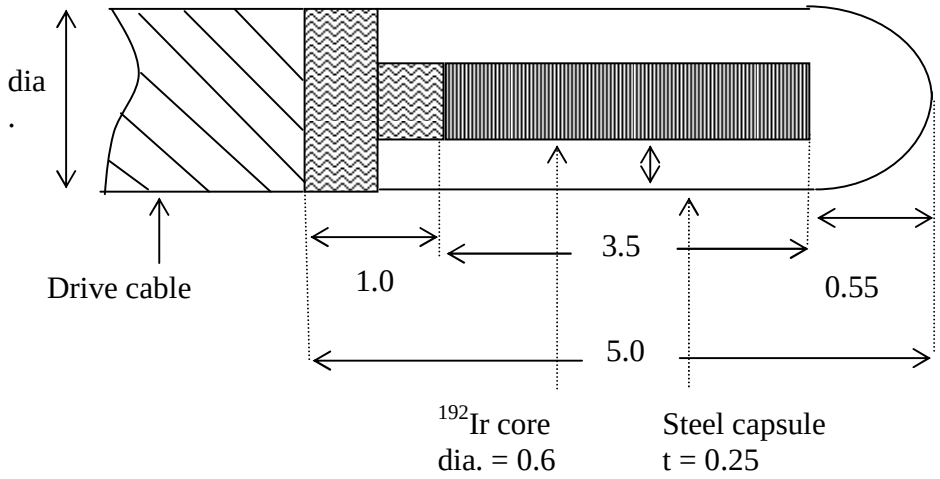

Fig. 1: Schematic internal configurations of microSelectron HDR ^{192}Ir old/ classic source. All dimensions are in mm.

Multisource Remote Operating Device

Multisource remote operating device (MROD) is a novel fully computer controlled brachytherapy source storage cum source driving device which can store nine high dose rate (HDR) ^{192}Ir/ ^{60}Co brachytherapy sources. This device contains three major components, namely (i) a meticulously designed and properly shielded source container with proper mechanical support and coupling arrangement for connecting the source guiding tube, (ii) a specially designed electronic control system for driving the motors and position sensors, and (iii) a programmable graphical user interface (GUI) for operating the machine. The source container is a mild steel shell filled with sufficient amount of lead to keep the radiation leakage level within

the prescribed limit. The source container consists of nine 'S' shape channels each of 2 mm conduit diameter which can store nine different HDR brachytherapy sources. During OFF condition of the MROD, the source is resting at the centre of its 'S' channel. The drive mechanism has the capability to allow the source travel by 100-150 cm from its resting point. Specially designed nine connectors are provided at the frontal end of the source container to couple the source channel with the guiding plastic tube. Electronic as well as mechanical provisions have been made to drive only one source at a time for the safety of the operator and accuracy of calibration. The intended source can be positioned in the plastic tube anywhere (between 40-150 cm) from the centre of the container at a movement step of 2 mm.

The distance of the source movement is counted from the frontal end of the container. The source cable moves out of the container and stop at the last irradiation position of the selected range of irradiation. From this position, the source moves in user selectable steps backward and stay at all assigned dwell positions for indicated irradiation duration. Dwell time (time of irradiation) at each dwell position (position of irradiation) can be selected in the range of 0 to 9999 seconds. The speed of the source movement is user selectable (0 to 600 cm/min).

The MROD is useful in calibration of the hospital dosimeters against the same source which is available to the hospital and will help in enhancing the accuracy of dose delivered to the patient during brachytherapy treatments. The MROD has been thoroughly evaluated using dummy as well as active HDR brachytherapy sources and its performance was found well within the specified tolerance. Fig. 2 shows the closed box photograph of the MROD and Fig. 3 shows its electronic drive and control systems. There are two sets of electronic drive and control systems mounted at left and right sides of the device. Only one side is visible in Fig. 3.

Fig. 2: Photograph of the multisource remote operating device (MROD)

Fig. 3: Photograph of the electronic drive and control systems of the MROD. There are two sets of electronic drive control systems mounted left and right sides of the device. Only one side is visible in this photograph

Two position sensors, one at the frontal part and the other at the rear part, of this device has been provided to monitor the movement of the source from its resting position. During irradiation by selecting a given source, the distance of the source movement is counted from the frontal end of the selected source channel. The provision has been made in the control software to limit the movement of the source within a specified limit of 2 mm. The control system has been customized to allow the movement of only one source at time at a pre-programmed position. In case of any obstacle in the path of source movement, the source returns to its resting position in the 'S' conduit. The option of homing has been provided to bring the source to its actual resting position and then start the movement which ensures the accurate positioning of the source at the pre-selected dwell position. The system for manual source retraction has also been provided to deal with the abnormal condition of operation of the MROD. For loading of a new source it is required to push the dummy end of the source up to the location of frontal position sensor and on selecting the homing action the active end of the source is brought the centre of the 'S' channel. Similarly, for unloading of the spent source, required movement range is selected for bringing the dummy end of the source out of the frontal sensor. Fig. 4 shows the arrangement of source drive mechanism. There are nine source drive systems. Each of the source drive system contains arrangements of wheel bearing system along with high duty conveyor belt. The frontal end of the source drive mechanism is coupled with the 'S' channel of the source storage container and its rear end is coupled with the wire storage tube which is mounted on a durable plastic sheet.

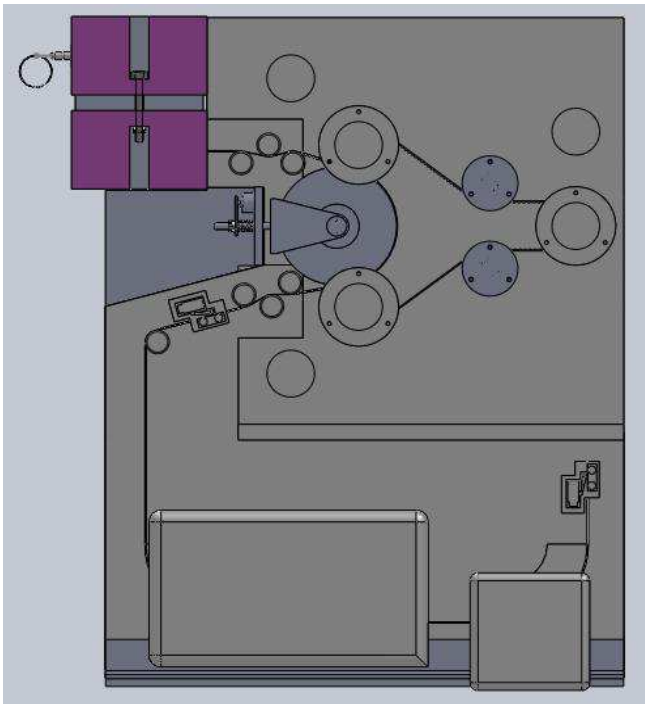

Fig. 4: Mechanical arrangements of source drive mechanism of the multisource remote operating device

Fig. 5 shows the snapshot of the operation and control screen of the MROD control system. This screen displays the pre-programmed location of the source along with the pre-programmed dwell position. The length of the source wire, movement speed, available and selected range of the source movement, current location of the source and elapsed irradiation duration, source type and radionuclide, loaded source strength and current source strength in Ci or user selectable units are also displayed on this screen. Salient technical features of the MROD and its control system has been listed in Table 2.

Table 2: Salient technical features of multisource remote operating device

Material of Source container	Mild steel and lead
Number of source to be stored	9
Shape of source storage channel	'S' type
Conduit diameter of 'S' channel	2 mm
Length of the 'S' channel	40 mm
Number of steps for source movement	50
Step size	2 mm
Length of source travel from the centre of 'S' channel	1500 mm
Positional accuracy of the source	±1 mm
Positional reproducibility of the source	±1 mm
Diameter of source guiding wire	1.6 mm
Dwell time	10 to 9999 sec
Channel inhibitor	9
Control system	GUI based programmable

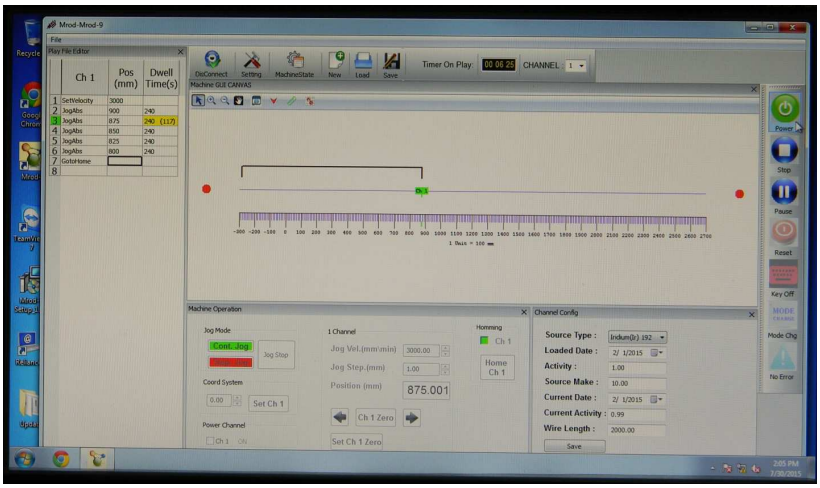

Fig.5: A snapshot of the operation and control screen of the multisource remote operating device showing the planned dwell positions and current location of the HDR ^{192}Ir brachytherapy source

Commissioning and Source Strength Measurements

The functional parameters of the MROD have been thoroughly verified and found within the stated tolerance. Strength of the HDR ^{192}Ir brachytherapy source stored in this unit was measured using locally designed brachytherapy reference standard (1000 cm3 graphite ionization chamber). Fig. 6 shows the experimental arrangement used for measuring the strength of HDR ^{192}Ir brachytherapy source stored in MROD using large volume graphite ionization chamber and specially designed PMMA source calibration jig. This experiment was conducted as part of the commissioning of the MROD for its intended purpose.

Fig. 6: Photograph of the experimental set up used for measuring the strength of HDR ^{192}Ir brachytherapy source stored in the multisource remote operating device. Large volume graphite ionization chamber and PMMA source calibration jig can also be seen in this photograph

Summary and Conclusions

A versatile fully computer controlled multisource remote operating device was designed and fabricated locally for storage of nine high dose rate brachytherapy sources. The performance characteristics of this device was checked thoroughly and found within the specified tolerance limit. The objective of this development was to make available an automated source storage and driving device for calibration and dosimetry of HDR 192Ir/ 60Co brachytherapy sources so that the dosimetry systems of the hospitals can be calibrated against the source which is used at the hospital for treatment of the patient. This approach of source calibration will further reduce the uncertainty in strength measurement of HDR brachytherapy sources which in turn will enhance the accuracy of physical dosimetry and hence the accuracy in delivery of prescribed dose to the patient.

References

1. International Commission on Radiation Units and Measurements (ICRU) **1976**. Determination of absorbed dose in a patient irradiated by beams of x or gamma rays in radiotherapy procedures. ICRU Report 24, Washington, USA.
2. Nath R, Anderson LL, Meli JA, Olch AJ, Stitt JA and Williamson JF **1997**. Code of practice for brachytherapy physics: Report of the AAPM Radiation Therapy Committee Task Group No. 56. Med. Phys. 24(10), 1557-98.
3. Kubo HD, Glasgow GP, Pethel TD, Thomdsen BR, Williamson JF **1998**. High dose rate brachytherapy treatment delivery: Report of the AAPM Radiation Therapy Committee Task Group No. 59. Med. Phys. 25, 375-403.
4. International Atomic Energy Agency (IAEA) **2002**. Calibration of photon and beta ray sources used in brachytherapy, TECDOC-1274, Vienna, Austria.
5. Podgorsak EB (editor) **2003**. Review of radiation oncology physics: A handbook for teachers and students. International Atomic Energy Agency, Vienna, Austria.

INDIAN R&D PROGRAMME RELATED TO LIFE MANAGEMENT OF COOLANT CHANNELS OF INDIAN PHWRS: AN OVERVIEW

S.K. Sinha
Reactor Engineering Division

Shri S.K. Sinha is the Recipient of the DAE Scientific & Technical Excellence Award for the year 2013

History of Growth of Pressurised Heavy Water Reactors (PHWRs) India

The pressurised heavy water reactor (PHWR) traces its history way back in year 1962 when 22MWe Nuclear Power Demonstration (NPD) reactor was commissioned in Canada. Horizontal pressure tube along with half a meter long multiple bundles to facilitate online refuelling and heavy water as coolant and moderator to facilitate use of natural uranium fuel were chosen as design features for NPD reactor and the same has been continued in all the CANDU reactors and Indian PHWRs designed later for commercial power generations.

India took its first step in the commercial power generation from Nuclear energy way back in the year 1964 to build two units of 200 MWe each at Rawatbhata, Rajasthan with the help of Atomic Energy of Canada Limited (AECL). These units were to be similar in design to the Douglas Point reactor - the first natural uranium fuelled commercial heavy water reactor built in Ontario, Canada. The first unit at Rawatbhata was commissioned in 1972 with eighty percent of equipments used in the construction sourced from Canada. With the Indian nuclear test in year 1974 and consequent withdrawal of support by Canadian, the construction of 2nd unit was completed with much delay with the help of Indian manufacturers and commissioned in the year 1980. Experience and confidence gained in this project encouraged Indian Nuclear Industry to design and build wholly indigenous nuclear power station of nearly same capacity at Kalpakkam, Madras. Thereafter, with the construction of 220 MWe power stations at Narora, Kakrapar, Kaiga, Rawatbhata and 540 MWe power stations at Tarapur, Indian Nuclear Industry has attained its maturity in all the aspects involving design, manufacturing, construction, commissioning and operation.

Reasons for Evolution in Pressure tube related technology

The pressure tube starting its journey from NPD in 1962 has been in service in different reactor units worldwide for the last 53 years. During these periods, it has met with a few uncalled for incidences in CANDU Units and one in Indian Unit – like failure of G16 pressure tube in Pickering-2 in 1983, heavy water coolant leakages from cracks developed in over-rolled pressure tubes in the Pickering and Bruce reactors (1974-75, 1982), sudden rupture of N16 pressure tube of Bruce (1986), and a few others. Analyses of these incidences led to extensive independent research in pressure tube related technology both in Canada and India. These efforts resulted into

evolution in design, development of better alloy, improved rolled joint fabrication procedure, development of analytical models for assessment of degradations, design of inspection tools and methodology for inspection during manufacturing and during service, and evolution of life management programme for older generation of reactors.
With all the indigenous developments, India has attained self reliance in designing, constructing, operating and managing the Pressurised Heavy Water type Reactors and is contributing to global R&D activities in making Nuclear energy much safer.

Subsequent paragraphs give details of the development of pressure tube technology in Indian perspective.

Coolant Channel Assembly Design

The coolant channel assembly of PHWR comprises mainly of a pressure tube (PT) concentrically located inside a calandria tube (CT) with the help of garter springs spacers supports evenly spaced along its length. All these components are made up of zirconium alloys. There are 306 assemblies in a 220 MWe PHWR and nearly 392 assemblies in a 540/700 MWe PHWR. The calandria tube is surrounded by heavy water moderator maintained at 65^{o}C. A gas of low thermal conductivity flows through the annulus to thermally insulate the hot pressure tube from the cold calandria tube. These assemblies form individual pressure boundaries inside the calandria vessel. The pressure tube houses the fuel bundles and, heavy water coolant flows through it at 10.0 MPa pressure to extract the heat of fission reaction. Temperatures of heavy water at the inlet and the outlet are approximately 250 C and 300 C respectively. Fig. 1 shows schematic of PHWR coolant channel.

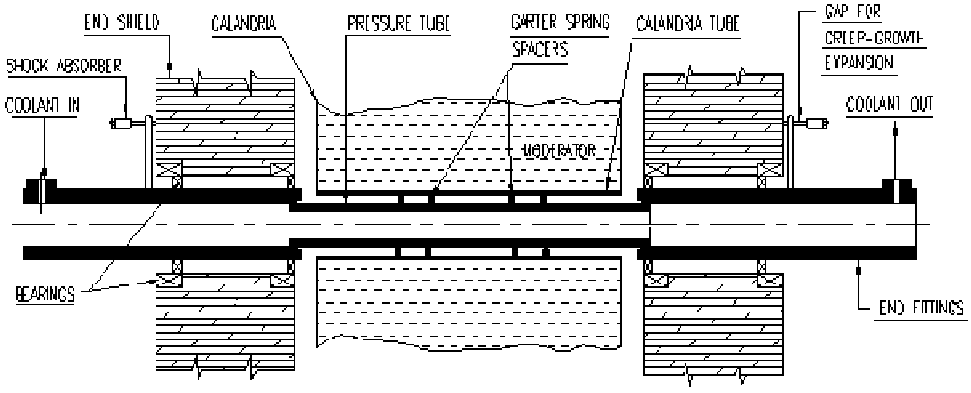

Fig. 1: Schematic of PHWR Coolant Channel

Amongst various components of the coolant channel assembly, it is the pressure tube which operates under the most vulnerable environment of fluid pressure, temperature and neutron flux. As a result, the service life of a coolant channel is dictated by the service life of the pressure tube.

Zircaloy-2 Pressure tubes : the Drivers for Pressure tube Related Indian R&D Programme

The first seven Indian PHWRs (RAPS-1 to KAPS-1) had pressure tubes made of cold worked Zircaloy-2 and loose fit garter springs. India had operated these reactors for a period ranging between 8.5 – 12.0 years. The new reactors built after KAPS-1 and the old reactors after retubing have Zr-2.5%Nb pressure tubes and four tight fit garter spring spacers.

The pressure tube R&D programme in India has evolved over last 20 years. The focus in the early period was on safe operation of reactors with Zircaloy-2 pressure tubes. The contact between pressure tubes and calandria tubes as a result of shifting loose-fit garter springs and, the accelerated corrosion and hydrogen pick-up were the main concerns. Addressing the safety of pressure tubes arising from these issues along with life extension was a challenging task because of its multidisciplinary and ever evolving nature of tools and technologies. A self evolving life management strategy based on the results of analytical assessment studies, in-service inspection (ISI), health diagnosis, post-irradiation examination and life extension helped in operating these units with safety. As a part of the life management strategy health diagnostic tools, in-service inspection tools, life extension tools, analytical models for simulating in-reactor degradations were developed. Simultaneously, tools and technologies for post-irradiation examination of irradiated components and their materials were also developed.

With the era of Zircaloy-2 pressure tubes coming to an end in the year 2010, the focus is now shifted to addressing life limiting issues of Zr-2.5%Nb pressure tubes. The experience gained from the life management programme of Zircaloy-2 pressure tubes has been helpful in planning similar R&D programme for Zr-2.5%Nb pressure tubes as well.

Key Elements of Life Management Programme

Computer models for the degradation mechanisms affecting the service life of pressure tubes, health diagnostic tools, in-service inspection and life extension tool, and evolving an effective life management strategy were identified as the key elements of the life management programme. These have been elaborated in the ensuing paragraphs.

Computer Codes developed for monitoring of Fitness for Service of pressure tubes

Separate computer codes for simulating each of the in-reactor degradation mechanisms were developed and validated using results of inspection of coolant channels. These codes were used extensively for taking safety related decisions. The codes developed have the following acronyms and the expanded form:

SCAPCA:	**Static and Creep Analysis for Pressure tube and Calandria tube**
HYCON:	**Estimation of Hydrogen Concentration (HYCON)**
BLIST:	**Estimation of Blister Depth (BLIST)**
CEAL:	**Assurance of Leak Before Break (CEAL)**

SCAPCA was used to estimate time and location at which PT would contact CT based on current garter spring positions. SCAPCA was used for life extension activity. It was used to estimate the parameters for relocation of garter spring spacers. HYCON was used to estimate hydrogen

ingress in the pressure tube at a given operating period. Using the contact location, contact time and hydrogen ingress, BLIST used to estimate the possibility of nucleation and growth of allowable and critical size of hydride blisters. While arriving at the safe residual service life of a coolant channel, strategy was to ensure a margin of 1 year at least between the time for growth of allowable blister size and the critical blister size. Alternatively, safe residual service life was arrived at by subtracting 1 year from the time for growth of critical blister. The computer code CEAL was used to confirm the possibility of satisfying Leak Before Break (LBB) criteria. Figs. 2-4 give the glimpses of comparison between the measurement and the prediction for gap profile, hydrogen pick-up and size of blister in a pressure tube.

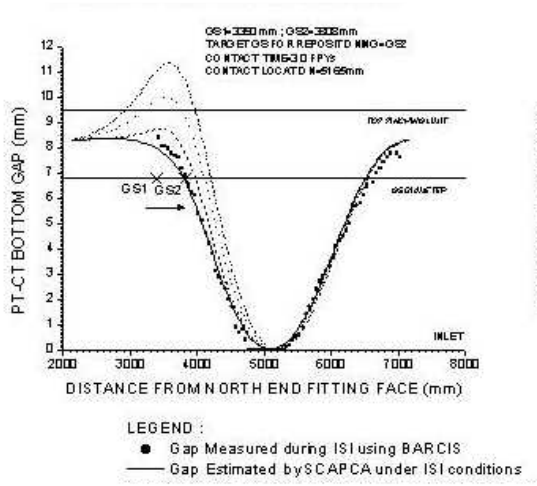

Fig. 2: Comparison between measured and predicted CT-PT gap

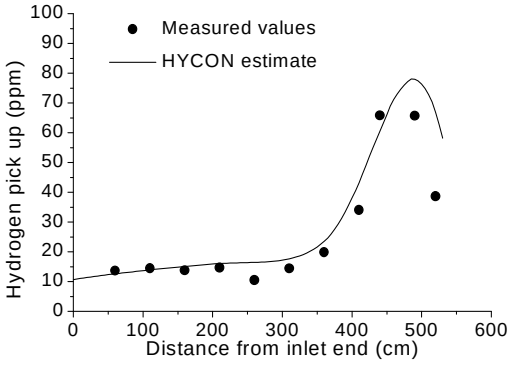

Fig. 3: Comparison between measured hydrogen pick-up and HYCON estimate for RAPS-2 J07

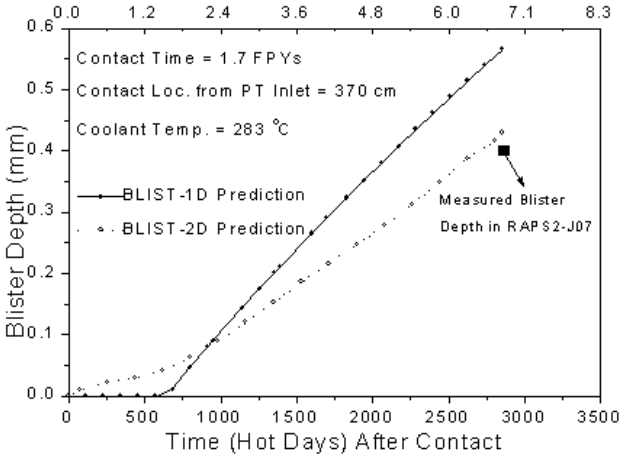

Fig. 4: Comparison between measured hydrogen pick-up and HYCON estimate for RAPS-2 J07

Tools for Health Diagnosis, In-service Inspection, Life Extension

Non Intrusive Vibration Diagnostic Tool (NIVDT), Sliver Scrape Sampling Tool (SSST), BARC channel Inspection System (BARCIS), Integrated Garter Spring Repositioning System (INGRES) etc. were developed and used extensively for life management of Zircaloy-2 pressure tubes. The specific purpose for which these tools were developed are described below:

NIVDT: was used to nondestructively identify the channels with PT and CT contact.
SSST: was used to obtain material sample from the operating pressure tubes for hydrogen concentration measurement.
BARCIS: was used to carry out inspection for garter spring location, PT-CT gap, wall thickness and flaw detection
INGRES: was used to relocate the garter spring in a channel to the locations decided by SCAPCA code for extension of life of coolant channel.

Life Management Strategy for the Zircaloy-2 Pressure Tubes

In view of the loose fit garter springs, a large number of channels PT-CT contact were expected in the reactor core of the early generation reactors. It was anticipated that extensive in-service inspection programme would be required to deal with the large volume of work. But, in-house developed analytical models and health diagnosis tools helped in the life management strategy to prioritize the vulnerable pressure tubes. Thus an optimum balance between inspection load and safety of coolant channel could be maintained over a realistic interval of operating period (shown in Fig. 5).

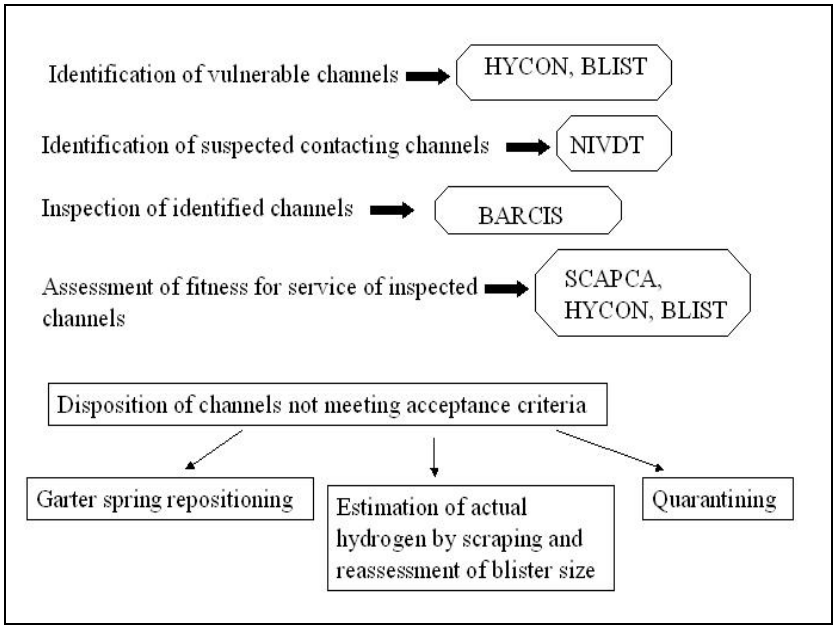

Fig. 5: Life management strategy followed for Zircaloy-2 pressure tubes

Life limiting Issues Specific to Zr-2.5%Nb Pressure tubes used in current reactors

Zr-2.5%Nb pressure tubes are used in all the currently operating reactors. The life is limited mainly by reduced room temperature fracture toughness due to high hydrogen concentration near rolled joint region of pressure tube and high diametral expansion rate caused by irradiation induced creep & growth.

High hydrogen ingress near the rolled joint region is due to galvanic corrosion occurring at dissimilar metals joint between stainless steel end fitting and Zr-2.5%Nb pressure tube. The hydrogen concentration in excess of solubility limit precipitates as hydrides which may be radially oriented at the places of high stresses. The toughness of material in this region is seriously affected and so is its critical crack length (CCL). Material in such condition provides restricted scope for varying pressure and temperature during start-up/shutdown. Additionally, it may also cause a flaw generated during service to propagate by Delayed Hydride Cracking (DHC) mechanism under favourable conditions of temperature and pressure.

The solution to this problem lies in nurturing safety culture (to ensure PHT free from debris created during routine maintenance) to avoid generation of service induced flaw and provision of highly sensitive annulus gas monitoring system (AGMS) to detect any leakage in the event of through wall crack. A computer code Delayed Hydride Cracking (DelHyC) has been developed to evaluate the crack propagation rate by DHC mechanism so as to estimate allowable time limit for safe shutdown of reactor in the event of leakage into annulus. The computer code DelHyC has been validated with respect to experimental data (Fig. 6).

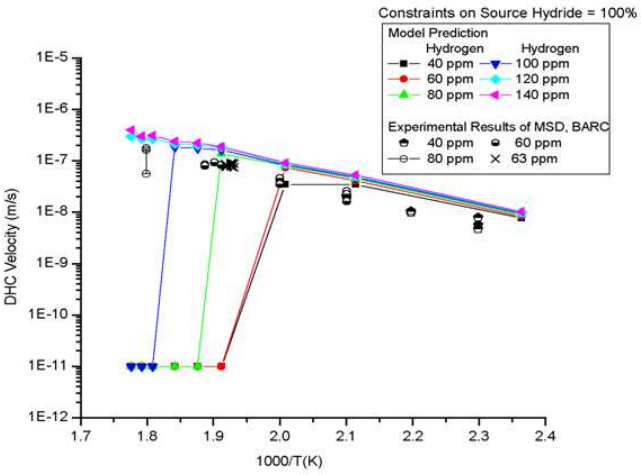

Fig. 6: Comparison of DelHyC prediction with experimental results

High diametral expansion caused by neuron induced irradiation creep and growth will reduce the clearances between garter spring spacer and the calandria tube at a faster rate ultimately leading to pinching of garter spring spacer between pressure tube and calandria tube (Fig. 7) much early in the service life. Additionally, it may also cause coolant bypass to occur at the maximum creep location which may lead to fuel failure (Fig. 8). None of the foregoing situations pertain to

normal operation as they affect the design functionality of the component. This problem is more pronounced in 220 MWe PHWRs than in 540 MWe PHWRs as the use of garter spring spacer with larger coil outer diameter provides comparatively much lower gap between the garter spring spacer and the calandria tube.

This situation may also pose requirements of in-service inspection of large number of pressure tubes and derating of reactor power. A computer code "In-reactor Diametral Expansion and Axial Elongation of Pressure tube (IDEAELP)" has been developed to predict the in-reactor diametral expansion and axial elongation of the pressure tubes (Fig. 9). This has helped in identification of vulnerable pressure tubes requiring inspection on priority basis.

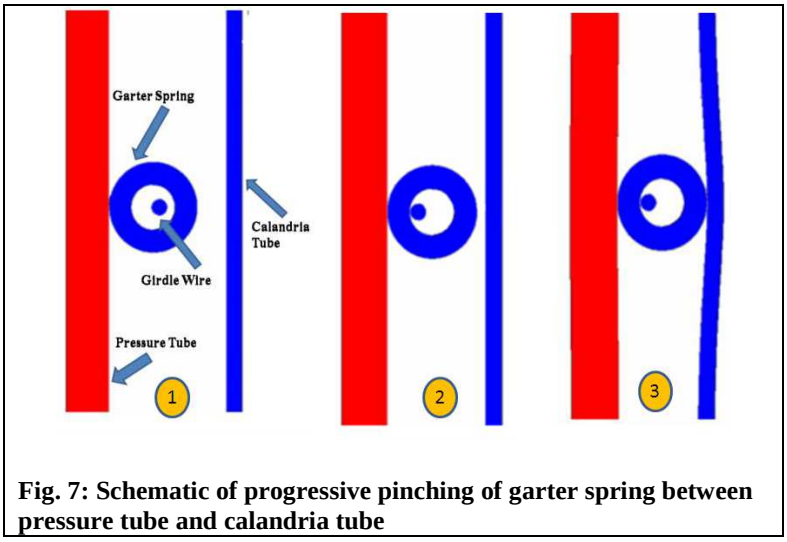

Fig. 7: Schematic of progressive pinching of garter spring between pressure tube and calandria tube

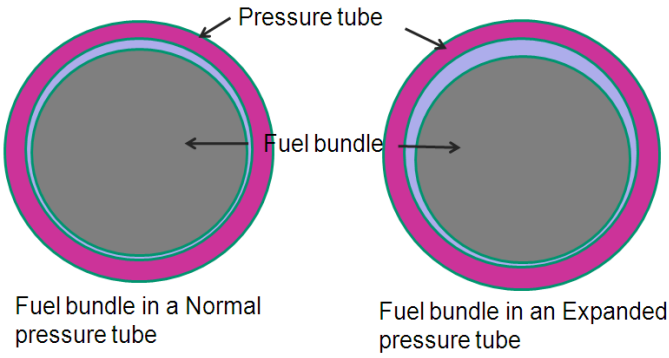

Fig. 8: Schematic of coolant bypass in a diametrically expanded pressure tube

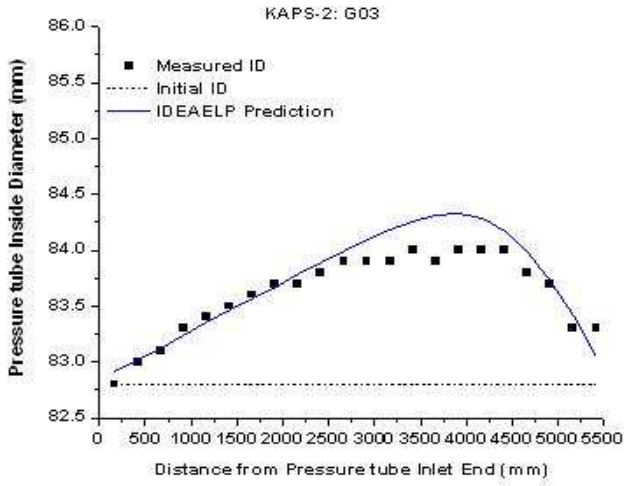

Fig. 9: Comparison of IDEAELP prediction with measurement

The possible engineering solutions to this problem lies in the altering the alloy texture so as to get reduced creep rate, use of bundles with larger inter pin gap at the bottom than at the top and use of garter spring with lower coil outer diameter. The first two options require development and demonstration of performance before the actual implementation and therefore have long gestation period. The last option is not only quick and easy to implement but also has assured outcome. In-house developed computer code for Garter spring Spacer Optimised Design (GSOD) has been used to arrive at an optimised design which will help in accommodating ~6% of diameter creep which is 2% higher than achievable using the current design (Figs. 10-12).

Fig. 10: Garter Spring Spacer

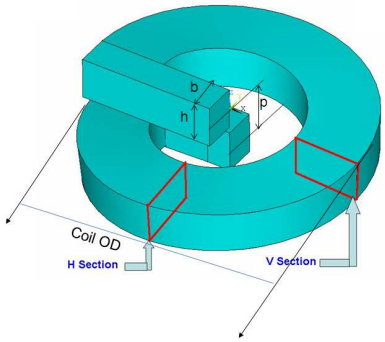

Fig. 11: Basic dimensions of a coil of garter spring

DIMENSIONS	Width(b) (mm)	Thickness (h) (mm)	Pitch (p) (mm)	Outer diameter (d_o) (mm)	Remark
VALUES	0.9	1.4	1.1	5.8	Optimised design
	1.04	1.73	1.25	6.8	Existing design

Fig. 12: Dimensions of optimized and existing design of garter spring

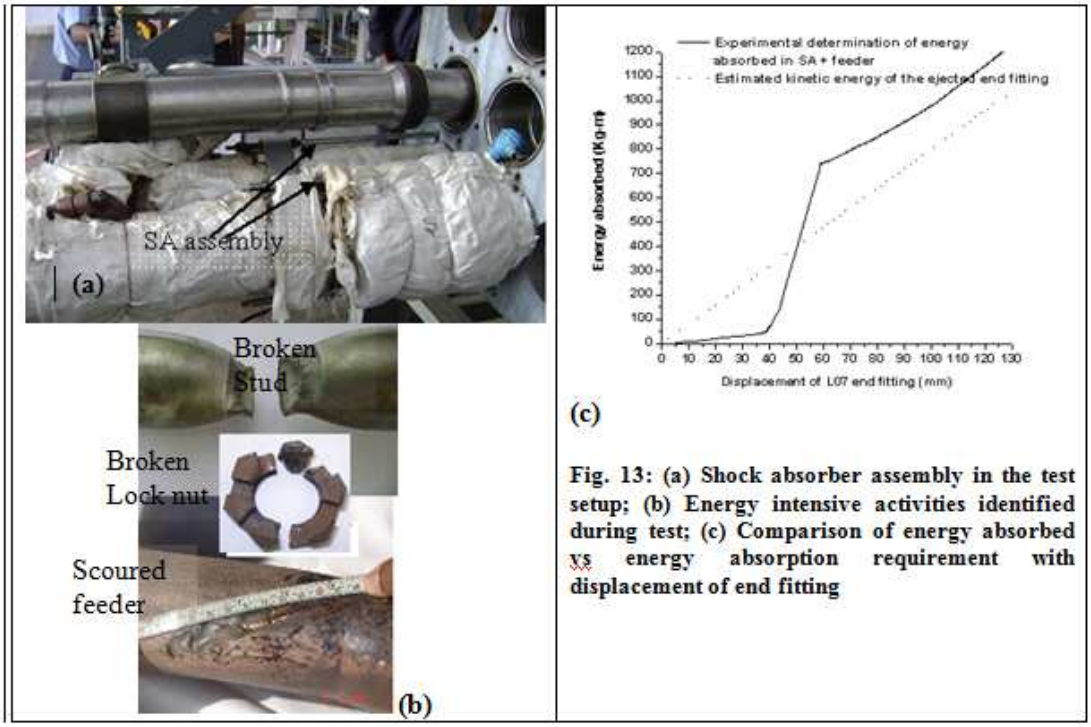

Fig. 13: (a) Shock absorber assembly in the test setup; (b) Energy intensive activities identified during test; (c) Comparison of energy absorbed vs energy absorption requirement with displacement of end fitting

Future of Coolant Channel Design

In present design of coolant channel the pressure tube can operate up to a maximum of 25 years. The degradation mechanisms – like diametral creep, axial creep and hydrogen induced embrittlement would compete with each other to limit the service life. If a reactor system is designed for 60 years, pressure tubes and associated components need to be replaced at least once. Though this exercise is very much possible today, it is mandays and manrem intensive.
A system working infinitely and efficiently without demanding any maintenance and without losing design functionality is the most ideal design. Extensive multidisciplinary research and development efforts over a long period are to be put to realise such design. Coolant channel design is also going through such churning process. The rates of all the degradation mechanisms discussed in the previous paragraphs and found to be affecting the service life of the pressure tube are required to be lowered so as to a attain a significantly long design life.

A new design of coolant channel has been conceptualised in which the pressure tube is shielded from the hot coolant by an insulator (Fig. 14). The low operating temperature of the pressure tube in this design not only makes calandria tube redundant but also provides opportunity to explore the possibility of keeping pressure tube in direct contact with cold moderator. Fuel bundles would be housed inside the insulator backed with a thin perforated metallic tube on the inside. The coolant flows through the insulator pipe to carry the heat of fission. In this arrangement, the operating temperature of the pressure tube is expected to be around 100 C.

The low operating temperature achieved in this design significantly reduces the temperature dependent contribution to the overall rates of the degradation mechanisms affecting the service life of the pressure tube. One such estimate is that this arrangement will give a service life as long as two tenure of previous design life.

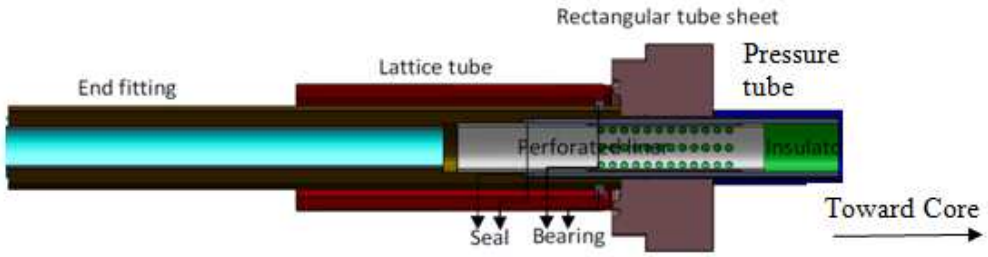

Fig. 14: Schematic of Future Coolant Channel Design

Acknowledgement

Author would like to express his special gratitude to Dr. R.K. Sinha, Chairman, Atomic Energy Commission and Secretary, Department of Atomic Energy, India for all his valuable advice and constant encouragement. The author would also like to thank Dr. P.K. Vijayan, Director RD&DG and Shri K.K. Vaze, Ex. Director, RD&DG for their unquestionable support during all this developmental work. Further, He would like to thank all his colleagues in the Reactor Engineering Division & Post-Irradiation Examination Division, BARC and in the Nuclear Power Corporation of India Ltd. for valuable suggestions and support during interactions and for providing valuable information.

BARC NEWSLETTER
FOUNDER'S DAY SPECIAL ISSUE 2015

NUCLEAR SAFETY STUDIES RELATED TO CONTAINMENT THERMAL HYDRAULICS, SOURCE TERM ANALYSIS AND NUCLEAR SYSTEMS/COMPONENTS

Vishnu Verma, I. Thangamani, P. Goyal and R. K. Singh
Reactor Safety Division

Shri Vishnu Verma is the recipient of the DAE Scientific & Technical Excellence Award for the year 2013

Abstract

This paper briefly describes studies related to containment thermal hydraulics in nuclear reactor containments, source term evaluation, flow accelerated corrosion study, thermo-mechanical analysis of metallic fuel, containment safety related study in experimental facility, heat load analysis of ADSS components and fire test analysis in transportation cask.

Keywords

Containment Thermal Hydraulic, FAC, Metallic Fuel, Joule Heated Ceramic Melter, ADSS components

Comprehensive Nuclear Safety Studies related to containment thermal hydraulics, Source Term Analysis and Nuclear Systems/Components have been carried out for Indian nuclear program and are briefly described in the subsequent sections.

Containment Thermal Hydraulics

AHWR Containment Analysis for DBA

Containment thermal hydraulics analysis for AHWR containment has been carried out for evaluating containment peak pressure and temperature under Design Basis Accident (DBA) condition i.e. 200% break LOCA in Reactor Inlet Header (RIH) [1]. Results were compared with the containment having no liner (i.e. only concrete structure) and containment peak pressures found to be almost the same as obtained for the case of lined containment. An optimisation study for peak pressure variation with respect to Blow Out Panel area (see figure-1) has been carried out. BOP panels are required to limit the load generating on the walls due to differential pressure arising between two compartments in case of accident. Performance of Passive Containment Isolation System (PCIS) through Inclined Fuel Transfer Machine has been assessed for LOCA conditions [2]. Level variations in Transfer Fuel Storage Bay (TFSB) pool (see figure-2) and in primary ramp were evaluated during the transient for 200% break LOCA in RIH. It was found

that remaining water left in TFSB pool is sufficient to maintain the shielding requirements for pool and containment isolation.

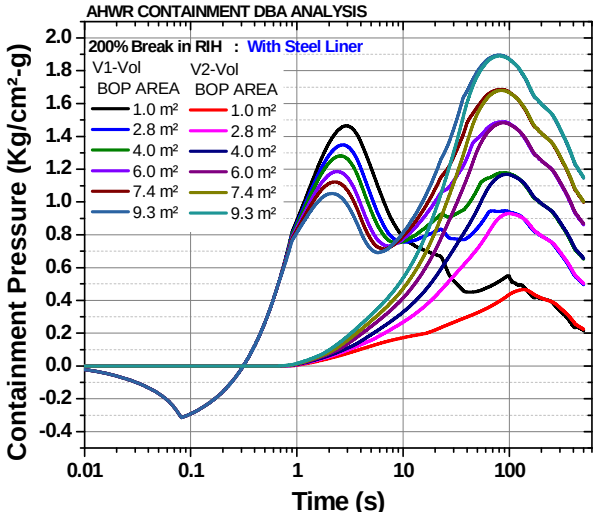

Fig.1: Variation of pressure in V1 and V2 volume for various BOP areas

PCIS analysis was also carried out for containment isolation from the environment in case of accident condition LOCA by forming U tube water seal due to pressure differential between V1 and V2 volume. Performance of PCIS has been evaluated for LOCA covering the entire range of RIH break sizes from 2 % to 200 %. It is observed from the analysis that the PCIS will perform its intended function within 15 seconds for all the break sizes.

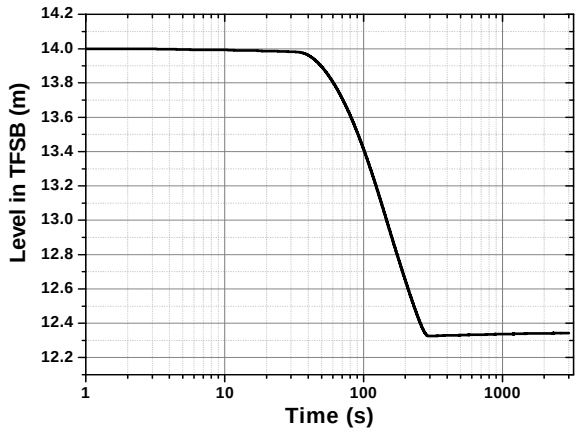

Fig.2: Level transient in TFSB for 200% break LOCA condition

Experiments Studies related to Containment Thermal Hydraulics

Containment Studies Facility (CSF) is designed to study containment performance under DBA and beyond DBA conditions for Indian PHWRs. The CSF (see figure-3) consists of a PHTM, a Containment System (CM) model and a Control and Instrumentation room.

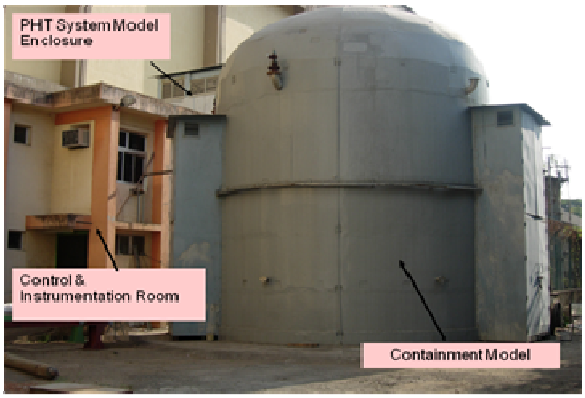

Fig.3: Containment Studies Facility

The containment model is approximately 1:250 volumetrically scaled down model of the prototype 220 MWe PHWR containment of Kaiga NPP. Like Indian PHWR containment system, the CM is also divided into V1 volume (dry well) and V2 volume (wet well). The V1 volume is further divided into many compartments to simulate the various rooms such as pump room, fuelling machine vault etc. present in actual reactor containment. The V2 volume is connected to V1 volume through vent pipes and suppression pool. The containment model is a cylindrical structure with an ellipsoidal dome, made out of RCC with epoxy painting on the inner surface. The outer diameter of the model is 6.9 m and its height is 10.95 m. Containment thermal hydraulics experiments have been performed for Blowdown pressure of 30, 50 and 75 kg/cm^2(g) [3]. The experimental data [3] were compared with the results of in-house containment code CONTRAN and ASTEC codes, for simulated blow down conditions and results were found to be in good agreement (see figure 4).

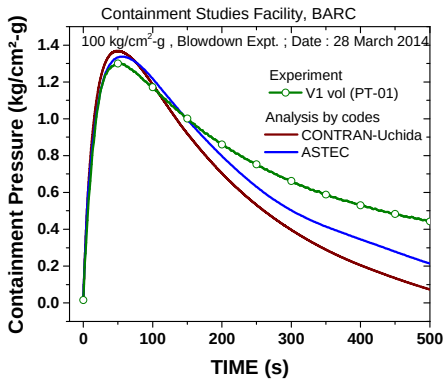

Fig.4: Comparison: Experiment Vs. Analytical (100 kg/cm^2-g)

Suitable condensation model has been identified for the thermal hydraulic codes through this study. The present experiment and its validation have given requisite confidence on the PHWR / AHWR containment pressure and temperature transient evaluation with in-house CONTRAN and French code ASTEC. Besides with a systematic evaluation of various condensation models, the adequacy of Uchida model for containment transient calculations has been demonstrated.

Source Term Analysis

Fukushima Daichi Unit –1

Severe accident analysis of Fukushima Daichi Unit -1 has been carried under Station Black Out (SBO) condition initiated by Seismic and Tsunami events. In the analysis, containment thermal hydraulics, Molten Corium Concrete Interaction and Fission product (FP) transport analysis has been considered using ASTEC code. Analysis was carried out up to hydrogen detonation time in unit-1. For fission product transport in the containment, 18 species including Xe, Kr, Cs and Iodine and corresponding cases of decay heat have been modelled. Except Xe and Kr all other FPs including Iodine have been taken as aerosol form in the numerical model.
Containment pressure & temperature transients and deposited and suspended mass of the FPs with time have been evaluated in all the zones. Hard vent opening and enhanced leakage at containment high pressure has been considered. Source term (ground and stack level release from containment to Environment) is evaluated up to H_2 detonation. Inert atmosphere as initial condition has been considered in Primary Containment Vessel and in suppression chamber. Continuous release of corium from Reactor Pressure Vessel in case of vessel failure and external water injection were modelled. A large relocation of the molten corium on the floor of reactor cavity and consequent Molten Corium Concrete Interaction (MCCI) was observed releasing large amount of hydrogen and carbon monoxide, making primary containment to further pressurize and the reactor building susceptible to explosion. H_2 and CO concentration has been plotted on Shapiro diagram for deflagration/detonation limits. It was found that containment pressure (see figure-5) reaches up to twice the containment design pressure and top region of reactor building enters into deflagration zone. Fig. 6 shows cavity erosion due to MCCI at the end of one day transient in Unit-1.

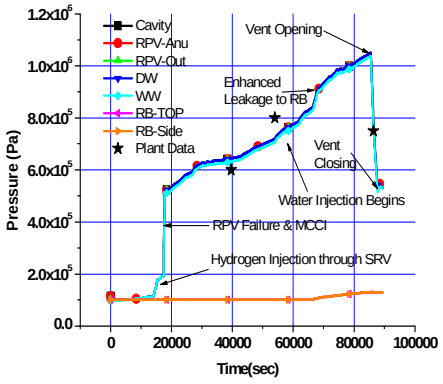

Fig. 5: Containment Pressure Transient

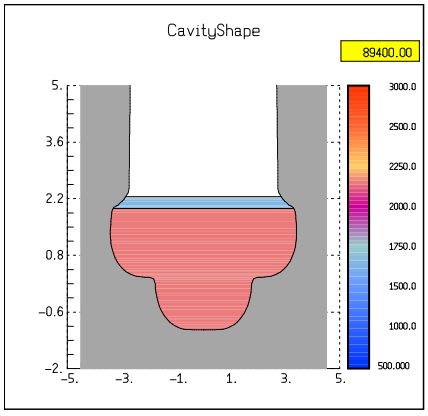

Fig. 6: Cavity Erosion due to MCCI

By and large, the present analysis [4] predictions agree well with the event chronology, recorded plant parameters and measured activity and with the analysis prediction of Nuclear and Industrial Safety Agency, Japan.

IAEA- Benchmarking of severe accident computer codes for PHWR

Containment analysis for severe accident conditions was carried out for 700 MWe CANDU reactor under IAEA Coordinated Research Project (CRP) [5]. Objective of this CRP was benchmarking of severe accident computer codes for Pressurized Heavy Water Reactor applications under prolonged Station Black Out conditions (SBO). Containment Pressure, Temperature transient, concrete ablation rate due to MCCI, hydrogen and CO distribution, fission product distribution in the containment have been evaluated using ASTEC code. Containment was divided into 14 zones. Flammability limits of H_2 and CO has been checked with time on Shapiro diagram. Results were compared among 7 International Participants from different countries and found to be in good agreement. Fig.7 shows comparison of time predicted by participant for different chronological events during progression of the severe accident. Figure 8 shows total amount of hydrogen generated during accident as predicted by all the participant.

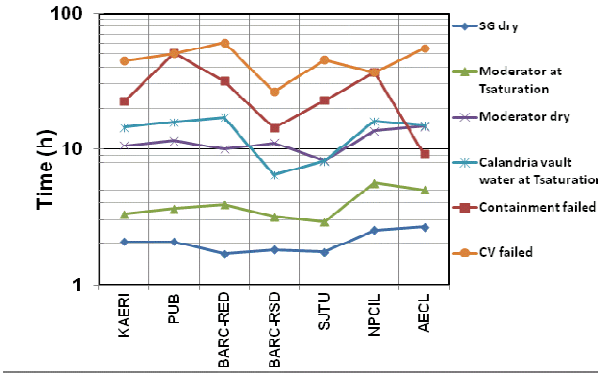

Fig.7: Comparison of time predicted by participant for different chronological events

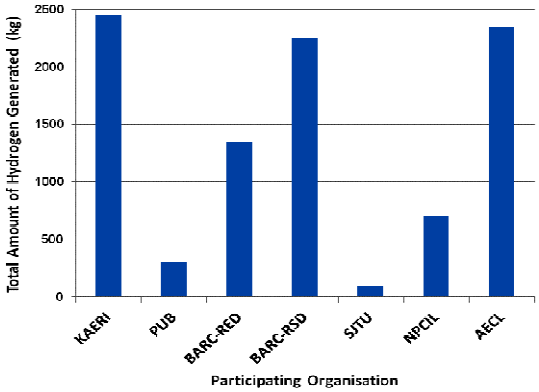

Fig. 8: Total amount of hydrogen generated during accident

Thermal Analysis of VWSB-IP1 at Tarapur

Thermal Design and analysis of Vitrified Waste Storage Block-IP1 at Tarapur has been carried out [6]. The vitrified waste has high heat generation rate due to decay heat and needs interim storage under surveillance. The waste needs to be cooled continuously until major portion of the decay heat is dissipated. VWSB-IP1 is designed for interim storage of waste generated of 30yrs of Integrated Plant-1 under plant operation.VWSB-IP1 will be consisting of about 2192 canisters housed in 548 locations. Natural circulation air cooling was considered to cool the canisters. Canisters are placed in a storage vault and cooled by induced flow of air with the help of stack (Fig. 9). Each location houses four canisters stacked axially based on the parametric study.

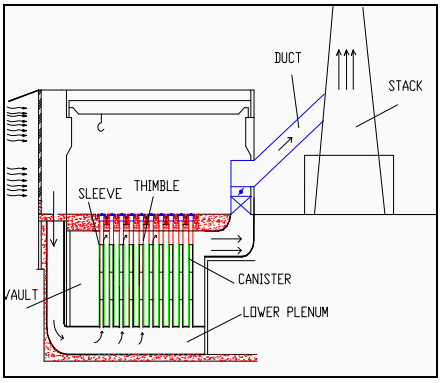

Fig. 9: Schematic view of the Facility

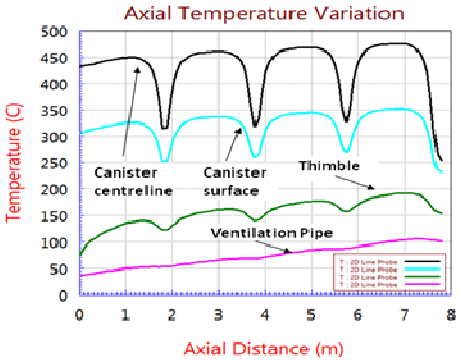

Fig. 10: Axial temperature variation along canister centre line, canister surface, Thimble and Ventilation pipe

Air from the inlet duct is introduced at the lower plenum of all the storage locations and flows axially through the annular gap between thimble and sleeve. The flow emerging from the top of each storage location is combined at the top plenum and goes to the stack. The air flow in the annular space between sleeve and thimble gets heated and rises due to buoyancy. The hot air rises through the stack due to chimney effect and maintains the flow through the vault.Through parametric study, stack dimensions, duct dimensions at inlet and outlet, plenum height, flow gap between sleeve and thimble etc. have been arrived based on concrete and canister temperature limitation. Analysis is divided in two steps; in first step converged flow rate has been obtained based on the 1-D flow model. Thereafter detail temperature field within the canister has been obtained using CFD code CFD ACE+ (Fig. 10). To validate results one miniature experimental facility was planned and the results were validated at IIT-Bombay.

Metallic fuel for future FBRs

2-D thermo-mechanical analysis of Metallic fuel (U+15 % Pu) for future fast Breeder Reactors have been carried out [7]. These metallic fuel have merit with high breeding ratio beside power production. The fuel consists of U-Pu binary alloy (containing 15 % Pu) cladded in T91 alloy with Zr layer between the fuel slug and cladding material and helium gas in semicircular groove

region. Two geometries (two and four groove, see figure 11) of fuel are considered for the analysis.

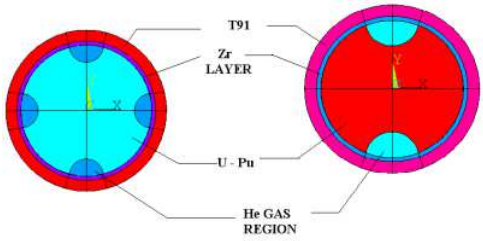

Fig. 11: Schematic diagram of the cross-section of (U-Pu) metallic fuel

Smeared density of fuel with these grooves is about 85 %. The length of the fuel slug is 1000 mm. Thermal performance of the fuel has been evaluated based on maximum allowable Linear Heat Rate depending on the maximum permissible fuel centerline and clad temperature. For closed gap condition various models were studied for gaseous conductance and solid to solid conductance. Parametric study has been done and effect of gas thermal conductivity and contact pressure on gap conduction (gaseous and solid to solid) has been studied. Detailed temperature distribution was estimated using Finite Element Method. Contact pressure between clad and fuel slug due to differential thermal expansion was also evaluated with the help of finite element method and gap conductance was modified accordingly. Contact elements were used in-between clad and fuel slug. It was found that LHR limitation is first reached based on maximum clad temperature rather than fuel centerline temperature (see figure-12). Input data required for gap conductance was obtained from various models available for gaseous and solid to solid conductance.

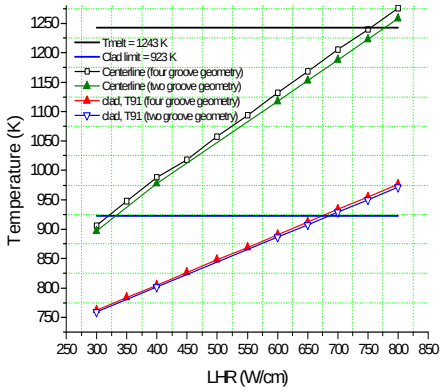

Fig. 12: Variation of fuel centerline and clad inner temperature with LHR (FEM analysis for geometry with four semicircular groove)

Flow Accelerated Corrosion Study

Flow Accelerated Corrosion (FAC) studies in Pipes and Elbows have been carried out for number of geometries. Analysis was done using CFD software. In each case wall shear stress has

been evaluated. Wear rate can be obtained by knowing shear stress with the help of correlation. FAC rate has been evaluated for RAPS-2 outlet feeders and Surry unit-2 feed water pipe failure (Incident occurred in Virginia, USA) using Colburn analogy and compared with the Lister model based on shear stress. Exact location of the pipe failure has also been predicted by CFD analysis [8]. Fig. 13 shows location of the pipe failure which occurred on the intrados of the second elbow of the feeders.

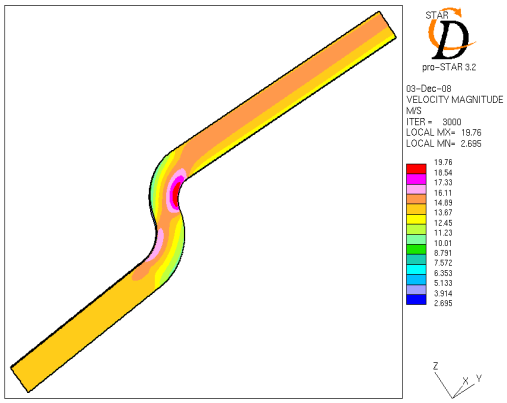

Fig.13: Velocity contour plot

Thermal Test Analysis of Radioactive Transportation Cask

The transportation cask/packages are used to transport of radioactive material from one place to other. The design of packages should satisfy the regulatory requirements for safe transport of radioactive material. Different types of packages are used for transport of radioactive material. The package should demonstrate its compliance to various tests under normal and accident conditions, and in addition to the general design qualifications as required by regulatory authority. The overall objectives of all these tests are to demonstrate that the loss of radioactive contents or dose to the public do not exceed the respective limits specified by the regulatory guides. For thermal test, package should be tested on fully engulfed fire for at least of 30 minutes. A fire should be controlled to an extent that it sufficiently engulfs a test package and develops at least the required minimum heat flux (based on the temperature of 800 ^{o}C to ambient temperature) to the package.

A package may be thermally tested in a furnace if acceptable conditions in the furnace can be achieved. Alternately, the same can be achieved by carrying out requisite thermal analysis. The thermal analyses of a number of casks such as cask for transportation of Cesium source for irradiation, calibration lab for calibrating wide range of radiation monitoring instruments, marine product irradiator, and transportation of a coolant tube of PHWR etc. have been carried out in RSD in the recent past as per IAEA/AERB guidelines. Temperature distribution and lead melting if any have been evaluated for normal and accidental fire conditions. Analysis has been done using CFD ACE^{+} software. The analysis covers normal transport conditions, half an hour external conditions representing fire and also the post fire cool down period. Fig.14 shows temperature contour plot for Portable Research Irradiator (PRI) cask at the end of fire test.

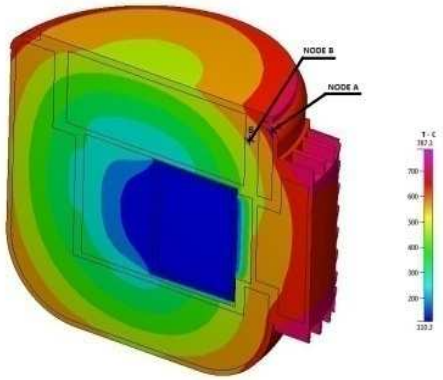

Fig. 14: Temperature Contours in the PRI Cask at the end of fire test (30 minutes)

Joule heated Ceramic Melter

Thermal analysis of Joule Heated Ceramic Melter (JHCM) has been carried out for AVS-1 (Advance Vitrifiaction System) and AVS-2 at Tarapur. In AVS, concentrated high level liquid waste and glass former (in the form of granules) is fed into JHCM, where electrodes immersed in the glass generates heat by the Joule heating due to electric current passing between electrodes through glass. The vitrified product glass melted in the furnace is withdrawn periodically by using a bottom freeze valve (central or side drain) consisting of Joule heated section followed by induction heated section into the stainless steel canister. Temperature at selected location were compared for both types the melter for normal condition (without draining), and different melt draining conditions (main drain and side draining). A temperature contour plot for side draining case is shown in figure-15. This analysis had given insight for further improvement in the JHCM design.

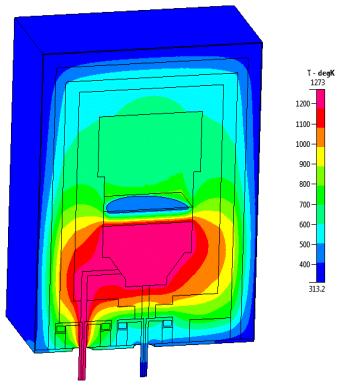

Fig. 15: Temperature contour plot of AVS2 for side draining of glass

ADSS components

A linear accelerator comprising of Radio frequency quadruple (RFQ) and drift tube linac (DTL) is being developed by BARC under LEHIPA (Low Energy High Intensity Proton Accelerator) as

front end injector of the 1 GeV accelerator for the ADS programme. This DTL accelerates protons from energy of 3 MeV to 20 MeV. In DTL particles are accelerated by longitudinal electric fields at the gap crossings between drift tubes. The permanent magnet quad-poles are placed inside the hermetically sealed drift tubes and provide a constant magnetic field gradient in the beam aperture. The drift tubes are mounted concentrically inside the resonating DTL tank and are attached to the tank body with stems. Heat is generated in each drift tube due to Joule losses because of RF heating. Hence drift tubes should be continuously cooled to limit the temperature and resulting thermal deflection. Thermal deflection is required to evaluate frequency shift in the cavity. Analysis was done using CFD code CFD-ACE$^+$ as thermo-mechanical coupled analysis simulating conjugate heat transfer and thermal deflection. Each drift tube have different geometry (higher length in axial direction) and heat generation rate. A number of drift tubes for different tanks have been analyzed for thermal deflection, pressure drop and temperature distribution [9]. Effect of flow velocity and change in the outer channel flow gap has also been studied on drift tube temperatures. Based on feedback from thermal analysis, outer channel size was suggested and the design was modified. Fig. 16 shows velocity vector plot in inner and outer channel of drift tube.

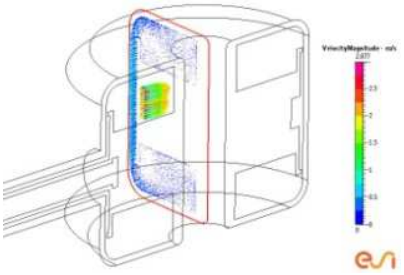

Fig. 16: Velocity vector plot in a Drift Tube

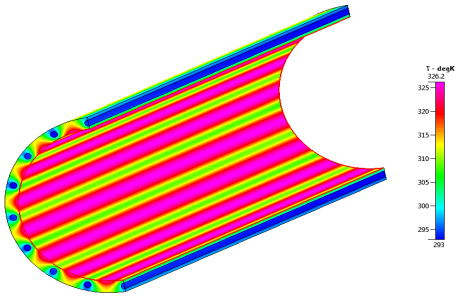

Fig. 17: Temperature contour plot for DTL tank

DTL tank is a very complex structure having opening for waveguide, vacuum port, cooling channels etc. About 115 kW of power is dissipated due to RF heating which is to be removed to limit the temperature and frequency shift due to cavity expansion. The incident heat flux on the wall is about 24 kW/m^2. Heat transfer analysis was carried out for 3-D geometry and minimum flow rate required to limit the temperature below the acceptable limit has been evaluated. Before detail 3-D analysis coolant channels size optimization was done with the help of 2-D analysis and modification were suggested. Fig. 17 shows temperature contour plot for the case of DTL tank.

Closing Remarks

With thermal analysis, CFD and suitably designed experiments, the relevant design and safety issues related to nuclear reactor containment thermal hydraulics, flow accelerated corrosion, thermo-mechanical analysis of metallic fuel, thermal analysis of ADSS components and fire test analysis in transportation cask have been addressed as presented in this paper.

References

1. Thermal Hydraulic Analysis Of AHWR Containment, I.Thangamani, Vishnu Verma, R.K.Singh, K.K.Vaze, 4th National Conference on Nuclear Reactor Technology (NRT-4), paper no. TH-55, 4-6 March 2011, Mumbai, India.
2. Performance Analysis Of Passive Containment Isolation System, I.Thangamani,Vishnu Verma, R.K.Singh, A.K.Ghosh, 37th International & 4th National conference on Fluid Mechanics and Fluid power FMFP2010, paper no. 254, December 16-18, 2010, IIT Madras, Chennai, India.
3. Containment Studies Facility : Experiments and Analytical Studies, Anu Dutta et.al., New Horizons in Nuclear Reactor Thermal Hydraulics and Safety, January 2014, Mumbai.
4. Ex-Vessel Severe Accident Analysis for Fukushima Dai-Ichi Unit-1 NPP, Vishnu Verma, I. Thangamani, R. K. Singh, K. K. Vaze and A. K. Ghosh, International workshop on New Horizons in Nuclear Reactor Thermal Hydraulic and Safety, Mumbai, January 13-15, 2014.
5. IAEA-TECDOC 1727, " Benchmarking Severe Accident Computer Codes for Heavy Water Reactor Applications", 2013. (IAEA -CRP on Heavy Water Reactor Applications).
6. Thermal Analysis of VWSB-IP1 at Tarapur, V. Verma, R. K. Singh and K. K. Vaze, Independent Journal of Nuclear Engineering, Kerntechnik, Vol. 78, No. 5, November 2013.
7. Thermal analysis of Metallic Fuel for Future FBRs, Vishnu Verma and A.K. Ghosh, 2nd International Conference on Asian Nuclear Prospects 2010 (ANUP2010), 11-13 October 2010, Chennai, India.
8. FAC Study in Feeder Pipes of 220 MWe Indian PHWR, P. Goyal, Vishnu Verma, Rohit Rostagi, Vivek Bhasin and A. K. Ghosh, International Conference on Flow Accelerated Corrosion, May 4th-7th, 2010, Lyon, France.
9. Thermal Analysis of Drift Tubes for LEHIPA, Vishnu Verma, P. Goyal, R. K. Singh and K. K. Vaze, Second International workshop on Acclerator driven Sub-Critical System and Thorium Utlization, December 11-14, 2011, Mumbai, India.

BARC NEWSLETTER
FOUNDER'S DAY SPECIAL ISSUE 2015

EQUATION OF STATE MODELING OF HIGH ENERGY DENSITY SYSTEMS

Chandrani Bhattacharya
Theoretical Physics Division

Dr. Chandrani Bhattacharya is the Recipient of the DAE Young Applied Scientist/Technologist Award for the year 2013

Introduction

The progress in material science today is characterized by dramatic advances in our understanding of the extreme states of matter. Development of advanced techniques like high power lasers and similar pulsed power systems - e.g. ion beams, electron beams, capacitor and inductive storage devices - have given rise to a new field of physics known as *high energy density physics* (HEDP) [1]. HEDP deals with properties of matter at very high energy densities ~ 10^{12} ergs/gm and very high pressures $\geq 10^6$ bars. Such systems occur in inertial confinement fusion, stellar and planetary interiors, pulsed power devices, impact loading for shock wave generation, nuclear weapons etc. In all these systems, a large amount of energy is concentrated in a very small region at a very fast rate leading to rapid motion of matter and generation of high temperatures and pressures. The entire phenomena occurring within a very short time period inside a typical HED system is very complex [1]. Highly sophisticated computer codes are needed for numerical simulation of the whole problem. Computer codes for these purposes are generally not available; commercially or otherwise. Most of the commercial codes available pertain to some specific area of application and are not intended for use in the HED regimes. So, these codes have to be developed ***in-house***.

The high speed motion of materials subjected to HED conditions are governed by the equations of hydrodynamics, which basically represent the conservation of mass, momentum and energy. These equations are solved in conjunction with the equation of state (EOS) of the material, which acts as a closure relation in solving the hydrodynamic equations. For simulating HED systems, EOS should be valid over wide ranges of density, temperature and pressure. Wide range EOS is essential because, under HED conditions, materials can get partially or completely ionized and exist in the plasma state. However, the entire temperature - density range spanned by HED systems cannot be modeled by a single generalized formula. It warrants development of different models in different regimes to account for all the effects properly [1].

We developed new models for the EOS which can be used to generate global EOS tables which will model the behavior of materials appropriately in various phases. These models were extensively verified against experimental data and hence can be used in hydrodynamic simulations. We discuss our work on hydrodynamic simulations and development of wide range EOS to study HED systems in the foregoing sections.

Hydrodynamic simulations

The hydrodynamic equations [1] in the Eulerian form can be written as follows:

$$\frac{\partial \rho}{\partial t} + \nabla.(\rho u) = 0 \qquad [1.1]$$

$$\frac{\partial (\rho u)}{\partial t} + \nabla.(\rho u u) = -\nabla p + \rho g \qquad [1.2]$$

$$\frac{\partial (\rho E)}{\partial t} + \nabla.(\rho E u) = -\nabla.(pu) - \nabla.H + \rho g.u \qquad [1.3]$$

$$p = p(\rho,\varepsilon); \varepsilon = E - \frac{u^2}{2} \qquad [1.4]$$

where, ρ(**r**,t), **u**(**r**,t), p(**r**,t), E(**r**,t), ε(**r**,t), H(**r**,t) and g(**r**,t) represent respectively, density, velocity, pressure, total and internal energy (per unit mass), energy flux and external body acceleration of the fluid at a given point **r** in space at a given time t. Equation [1.4] formally represents the EOS. We developed a two-dimensional Eulerian fluid code to simulate many problems for a single-fluid ICF system based on fluid in cell (**FLIC**) method [2,3].

Wide range Equation of state

In HED systems, rapid material motion generates huge pressure gradients which lead to formation of shock waves. The strength of shock waves is decided by the pressure rise across the shock front. Depending on the strength of the shock wave, various phase changes occur in materials which initially exist in the solid phase. For shocks of relatively lower strengths, solids may only undergo change in structure instead of going over to the liquid, vapor or plasma phase [1].

Properties of solids and dense fluids compressed by shock waves are primarily governed by strong inter-atomic interactions as one needs to overcome the repulsive forces which increase rapidly as atoms are brought close together. So, compression of solids require large amount of pressure even in the absence of heating. This non-thermal pressure also known as the "cold" pressure determines the basic behavior of materials in the condensed phase. Materials are also strongly heated by shock waves which results in appearance of a pressure associated with thermal motion of ions and electrons. For weak shocks of strength up to ~100 kilobars, cold pressure dominates over thermal pressure. As the strength of shock increases, thermal pressure becomes significantly large [1].

Electronic structure methods coupled with Molecular Dynamics and Monte Carlo simulation have evolved to an extent such that these phases can be accurately computed in principle. But, the computational effort required for these calculations being enormous, one needs to develop simple models that capture the physics underlying all these phenomena to generate global EOS libraries.

EOS in the compressive region

We developed the scaled binding energy formalism for the cold equation of state. This was a modification over the universal scaled binding energy formula proposed by Rose at al [4]. According to the authors, a universal relation exists between the binding energy and inter-atomic separation of a solid under condition of moderate expansion and compression. We introduced two modifications in the binding energy formula. The first was to include the equilibrium value of pressure derivative of bulk modulus in the original binding energy formula. Secondly, the universal binding energy formula was modified to make it applicable at high compressions. Ionic contribution to EOS was determined by Gruneisen EOS [1]. We derived a new expression for the Gruneisen parameter to account for the non-central part of the interatomic potential. To obtain the thermal electronic contribution to free energy, Somerfield model was used. Thus, a complete EOS was formulated which was verified against a large number of available experimental data viz. Hugoniot data, melting data etc. These were discussed in detail in reference [5, 6].

Shock Hugoniot data can be verified by solving the Rankine-Hugoniot (RH) relations in conjunction with the EOS. The RH equations represent the conservation of mass, momentum and energy across a shock wave and can be written as follows:

$$u = D\left(1-\frac{V}{V_0}\right)\ ;\ P_H - P_0 = Du/V_0\ ;\quad E_H - E_0 = \frac{1}{2}(P_H + P_0)(V_0 - V) \qquad [2]$$

where, V and V_0 represent the specific volumes of material, D is shock velocity and u is the gas velocity [1]. P_H, E_H and P_0, E_0 are pressure and internal energy behind and ahead of the shock front respectively. The Hugoniot curve is the locus of all thermodynamic states represented by P_H, E_H and V attained by shock compression. We present the Hugoniot curve for Al obtained using this model in Figure 1.

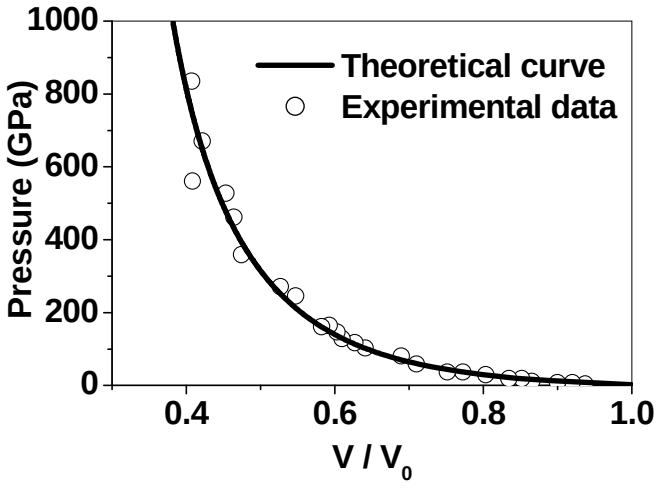

Fig. 1: Shock Hugoniot curve of Aluminum

The ion equation of state used in this work was based on a quasi-harmonic approximation. However, in realistic situations, anharmonicity in the inter-atomic potential should be accounted properly. So, we developed a mean field approach based on the scaled binding energy formula.

Mean field theory for anharmonicity

In this approach, we assume that volume V is divided into a simple cubic lattice consisting of N cells, with one ion in each cell. Each ion executes thermal motion independently in the cell in an effective potential g(s, V) generated by the neighboring ions. The variable,'s', denotes the displacement of ion from its equilibrium position. The vibrational part of the partition function is then given by:

$$Z_{ion} = \left[\frac{mk_BT}{2\pi\hbar^2}\right]^{3N/2} \left\{\int \exp[-g(s,V)/k_BT]^N d^3s\right\} \qquad [3]$$

where, m is mass of the lattice ion. This is also known as the cell theory approach. There are several methods to calculate g (s, V) based on pair wise additive inter-particle potential [7]. The proposal of Wang and Li [8] is to compute it using the 0-K isotherm, which can include even three particle or higher order interactions. The physical basis [8] of this mean field potential is that a lowest order Taylor expansion of g (s, V) in 's' provides the three well-known equations for the Gruneisen parameter 'γ'. In our work, we have used it in conjunction with scaled binding energy model to yield good agreement with experiments. The electronic contribution to free energy was calculated using the McClosky formula which interpolates between the ideal gas limit at high temperature and the Fermi Dirac degenerate gas at low temperature, and hence is suitable over a larger range of temperatures [9]. The complete EOS model was used to predict the Hugoniot curves of many metals [9]. Apart from this, some thermodynamic properties, viz. thermal expansion, ionic specific heat and temperature dependence of enthalpy of Al were also calculated. We present the thermal expansion curve for Al in Figure 2. This model was also used to study the stability of shock waves at very high pressures [10].

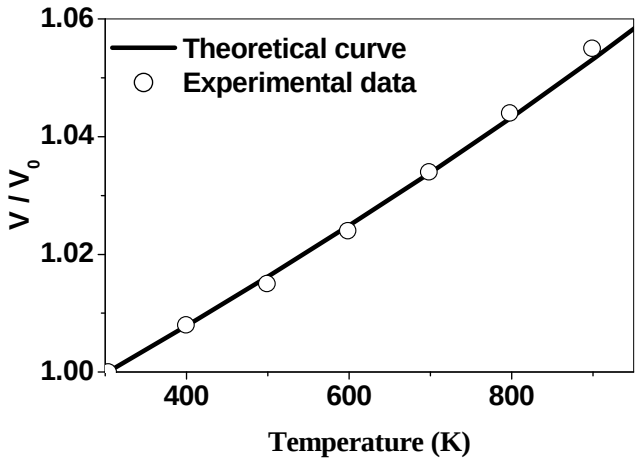

Fig. 2: Volume thermal expansion curve of Aluminum

Shock induced phase transformations

The EOS models discussed in earlier sections describe materials which exist in a single phase. These models were also used to predict phase boundaries between different solid phases which may occur during shock compression. We obtained the results for solid-solid structural phase transitions occurring in Fe, Zr, Hf, Ti etc. The phase boundaries and the shock Hugoniot for Zr are shown in Figure 3 and Figure 4 respectively. Phase transitions are characterized by the appearance of a kink in the Hugoniot curve. These kinks are observed in the computed Hugoniot curves of all the metals studied [5,6,9].

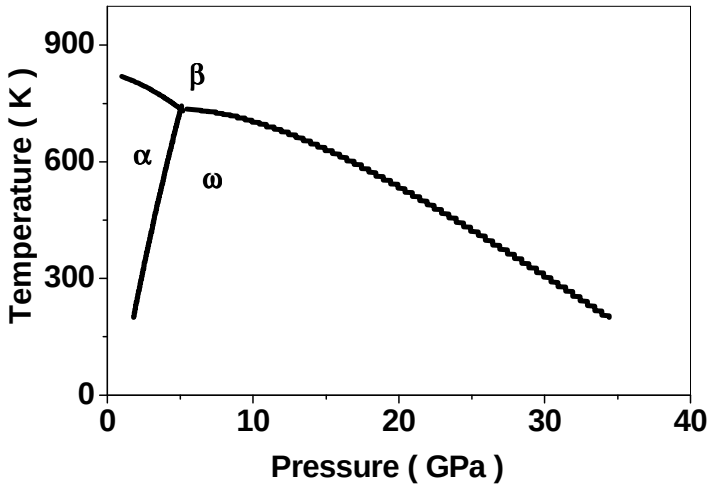

Fig. 3: Phase boundary of Zirconium

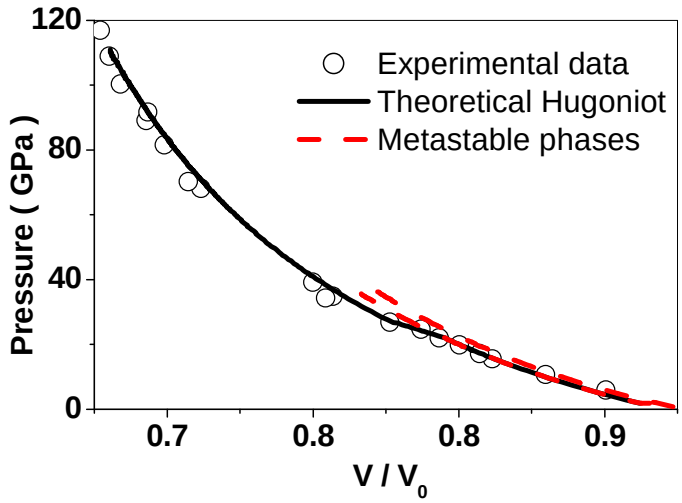

Fig. 4: Pressure Hugoniot curve of Zirconium

Melting curves

Melting curves represent the phase boundary between the solid and liquid phases. In our early work, we used the Lindemann's criterion to generate the melting curve [5,6,9]. According to this criterion, a solid is supposed to melt if the interatomic displacements are ~ 10% of interatomic distances [11]. But it is more appropriate to obtain melting curves by matching Gibbs free energy of the solid and liquid phases.

The phenomenon of melting is indicative of anharmonicity of interatomic potential. Although mean field approach described in the previous section could account for effects of anharmonicity, it did not have a strong theoretical basis. So, we developed the cell theory with embedded atom method (EAM) potential which incorporates presence of free electrons apart from ion-ion pair potential term [12,13].

Free energy of liquid phase was developed using a perturbation theory based approach known as the Corrected Rigid spheres (CRIS) model [14]. In this approach, the free energy of a liquid molecule trapped in a cage formed by nearest neighbours is expanded about a hard sphere reference system. Higher order terms in the perturbation expansion were obtained in terms of average of the cold curve instead of the pair potential. Then melting curve is calculated by matching the Gibbs free energies of the two phases [12,13]. The melt curve of Al is presented in Figure 5.

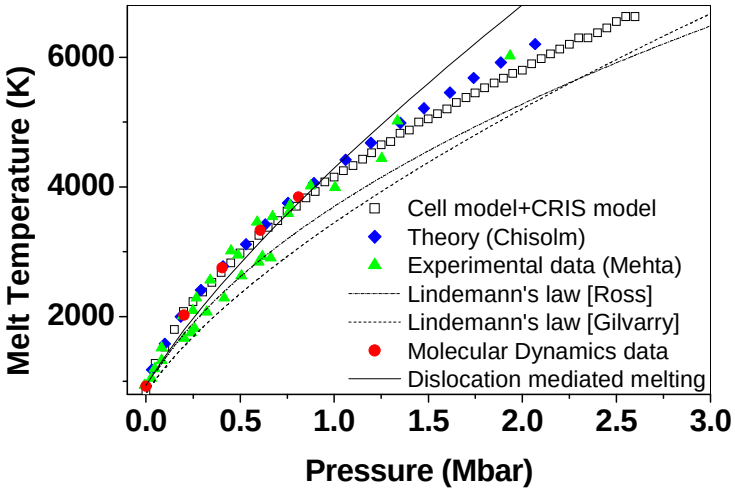

Fig. 5: Melting curve of Aluminum

EOS in expansion phase

The EOS models developed in the previous subsections pertain to the compressive phase only. However, for developing wide range EOS libraries for use in hydrodynamic simulations, one needs to explore the lower density regimes as well. This was done by extending the CRIS model

to lower densities. The EAM potential was used to predict critical parameters for Al and the entire low density phase diagram. Figure 6 represents the phase diagram of Al obtained using the EAM potential [15].

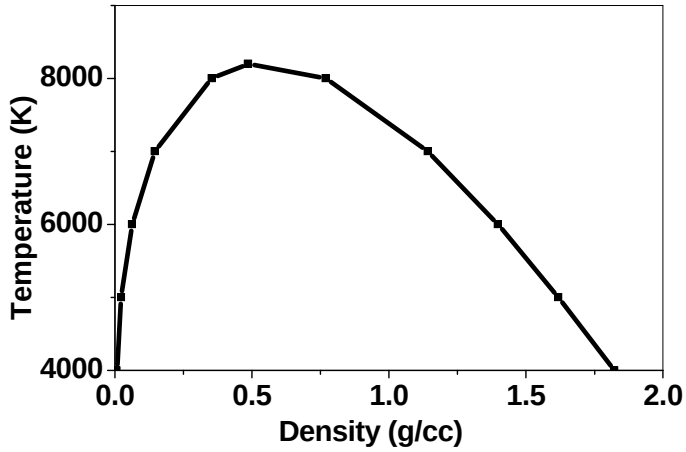

Fig. 6: Theoretical liquid-vapour phase diagram of Aluminum

The release isentropes of strongly compressed materials provide another way to characterize the liquid-vapor phase region. If the medium has a free surface, the shock will 'unload' on reaching the free surface. The EOS of the material, starting from the compressed state to the whole of expanded states is needed to obtain the release wave depending on the starting pressure and temperature on the Hugoniot. Comparison with the measured release wave parameters (pressure-velocity profiles) will allow one to validate the EOS in expanded states. The release curve of Al is presented in Figure 7 [16,17].

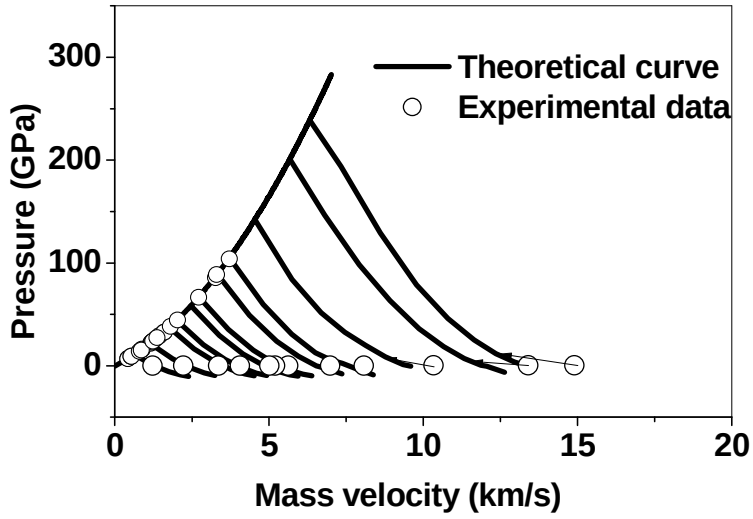

Fig. 7: Release isentrope of Aluminum

Conclusion

In this article, we presented a brief description of the various aspects involved in formulating the EOS of an HED system. We have improved and developed new models to obtain a wide range EOS. These models have been extensively verified using several available experimental data and can be used to generate global EOS libraries for use in hydrodynamic simulations at run time.

References

1. Ya. B. Zeldovich and Yu.P.Raiser, *Phys. Shock waves & High Temp Hydrodynamic Phenomena*, Academic Press, New York, Vol.-I&II(1966).
2. R. A. Gentry et al., *J. Comp. Phys.* 1, 87 (1966).
3. C. Bhattacharya, and M. K. Srivastava, INS conference (2005).
4. J. H. Rose, J. R. Smith, F. Guinea, J. Ferrante, *Phys. Rev. B* 29, 2963, (1984).
5. C. Bhattacharya and M. K. Srivastava, *J. App. Phys.*, 102, 64915 (2007).
6. C. Bhattacharya and M. K. Srivastava, *J.Phys:Conf. ser.*, 208, 012004 (2010).
7. T. L. Hill, *Stat. Mech.-Princ. & selec. App.*, McGraw-Hill, (1956).
8. L. Li, Y. Wang, *Phys. Rev. B* 63, 245108, (2001).
9. C. Bhattacharya & S. V. G. Menon, *J. App. Phys.*, 105, 064907 (2009).
10. M. Das, C. Bhattacharya, & S. V. G. Menon,. *J. App. Phys.*, 110, 083512 (2011).
11. F. A. Lindemann, *Z. Physik*, 11, 609-612, (1910).
12. C. Bhattacharya, M.K. Srivastava and S.V.G. Menon, *Phys. B*, 406, 4035 (2011).
13. C. Bhattacharya, *AIRAPT-23 conference proceedings*, P36, 254 (2011).
14. G. I. Kerley, *J. Chem. Phys.*, 73, (1,2,3), 469-494, (1980).
15. C. Bhattacharya, *AIP conference proceedings*, 1512, 52 (2013).
16. S. Jiuxun, *J. Phys.: Condensed matter*, 17, L103-L111, (2005).
17. C. Bhattacharya, *Computational Materials Science*, 82, 274 (2014).

BARC NEWSLETTER
FOUNDER'S DAY SPECIAL ISSUE 2015

ECONOMICAL ROUTE SYNTHESIS OF HALOGEN-FREE ORGANOSILICON PRECURSOR AND NANOCRYSTALLINE SILICON CARBIDE DEPOSITION BY LOW TEMPERATURE MOCVD

Jyoti Prakash
Powder Metallurgy Division

Shri Jyoti Prakash is the recipient of the DAE Young Applied Scientist/Technologist Award for the year 2013

Abstract

There is a huge requirement for development of a coating technique in nuclear industry, which is made of environmentally safe chemicals, should be easy and economical. In this view, halogen free, non toxic and non corrosive silicon carbide precursor was developed using a simple two step synthesis route. Uniform coating of SiC was obtained on graphite, C-C composite and zircaloy substrate at 900 °C using synthesized precursor. Optimized parameters used for coating were derived from the simulation of gas phase dynamics in specially designed chemical vapor deposition reactor. The X-ray diffraction and scanning electron microscopy analysis show that dense, adherent and impervious nanocrystalline SiC film was deposited using synthesized precursor.

Introduction

Silicon carbide is most widely used material especially for corrosion resistance applications such as in high temperature/nuclear reactors. In nuclear industry, it is of interest for use as a layer in tristructural isotropic (TRISO) fuels, layer on zircaloy, insulating material in nuclear fusion systems such as separators, or insulating flow channel inserts, between tritium breeding and neutron multiplier materials composing Li–Pb blanket modules. In addition, properties such as high thermal conductivity, high hardness and stiffness, mechanical strength at elevated temperature, low coefficient of thermal expansion, good dimensional stability under irradiation, small neutron capture cross sections, low density than other ceramics, and resistance to wear and abrasion make SiC ideally suited for a vast number of applications, especially in high temperature and nuclear reactors.

In past many SiC coating have been produced by the CVD technique, however, most SiC coating deposited have been grown at relatively high temperatures of 1300^{o}C- 1380^{o}C and at atmospheric pressure, using separate precursors for Si and C and single source precursor Methyltrichlorosilane (MTS). The high temperature deposition results in the introduction of structural defects in the layers and difficulties with using the system. Besides the above constraint, MTS decomposes under typical SiC CVD conditions producing corrosive HCl,

$SiHCl_3$, $SiCl_3$, $SiCl_4$, and CH_4 as well as other silanes and hydrocarbons. The MTS-CVD gas phase products of chlorine can migrate in layer and induce defects in layer. Therefore, it is worthy to employ a source that is not pyrophoric, halogen free, decomposes at low temperatures and contains only silicon, hydrogen and carbon atoms.

In the present study an economic and simple method for synthesis of potential organosilicon precursor of SiC has been reported. The process parameters have been optimized for bulk production of this precursor. SiC film was deposited on the zircaloy substrate using specially designed low temperature metallorganic chemical vapor deposition (MOCVD) process. A computational study was carried out to identify the onset of transverse buoyancy-driven recirculations during laminar flow of argon gas in vertical cylindrical reactor. The motivation for this work stems from the need to identify operating conditions maximizing the thickness uniformity, the interface abruptness and the precursor utilization during growth of films by MOCVD.

Materials and methods

Synthesis of organosilicon precursor

Silicon powder (Sigma Aldrich make, 99% purity, 120-200 µm size) and anhydrous methylene chloride (CH_2Cl_2, sigma Aldrich make) were used as the reagents. The direct synthesis procedure of organosilicon compounds by the reaction of methylene chloride with silicon was used in the current process. The methylene chloride was dried over sodium and silicon powder was charged in hydrogen atmosphere at 1100 °C for 2 hours prior to reaction. A fluidized bed reactor (quartz tube: 50mm Ø × 1000 mm L) was used to carry out the synthesis. The experiments were carried out in single stage (20 gm scale of silicon powder). The methyl chloride was passed through peristaltic pump to the pre-heater zone and the argon gas swept away the vapors of methylene chloride to the silicon powder fluidizing hot zone. After reaction, products were collected in liquid nitrogen cooled condenser. The process variables such as reaction temperature, methylene chloride flow rate, argon flow rate and reaction time were optimized for maximum yield of the organohalosilane product. The organohalosilane compounds were later on reduced with lithium aluminum hydride to obtain the organosilicon compounds. From this mixture of organosilicon compounds, volatile fraction was separated at 200ºC and used for SiC coating. The volatile fraction of compounds used for SiC coating is abbreviated as CVDP throughout paper.

Deposition of SiC solid film on Zircaloy sheet

SiC coating experiments were carried out using specially designed CVD reactor. The reactor consists of a vertical tube with a circular cross-section and a heated side wall as shown schematically in Fig. 1. The purpose of choosing vertical CVD reactor was to get uniform coating on all surfaces of a 3D object. Simulation of gas-phase behavior in specially designed CVD reactor was carried out using computational tool, COMSOL version 4.4. The axial temperature, gas velocity and precursor concentration profile were generated. The input data include the physical model parameters such as temperature, pressure, inlet velocity, and the mixture concentration at the inlet. The SiC coating on the different substrates were carried out using optimized parameters derived from the computational analysis.

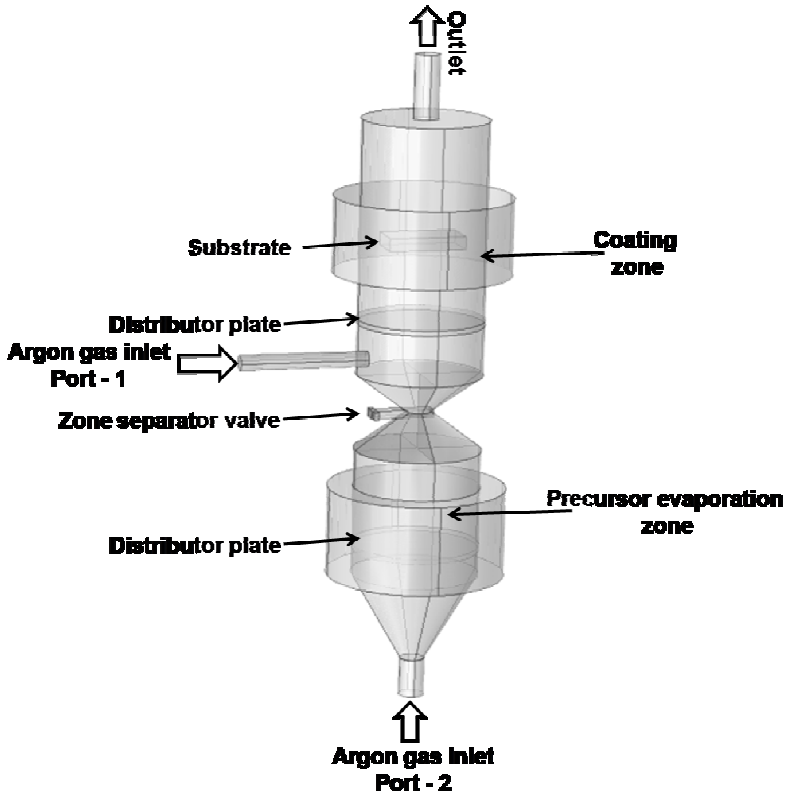

Fig. 1: The schematic of metalloorganic Fluidized bed CVD reactor used for SiC deposition

Results and Discussion

Synthesis of oraganosilicon compound

Two stage reaction occurred during synthesis of organosilicon compound is as follows

$$CH_2Cl_{2(g)} + Si_{(s)} \xrightarrow[T=400^oC]{} H_yCl_xSiCH_2SiH_yCl_x + H_yCl_xSiCH2SiCH2SiH_yCl_x + (Cl_2SiCH_2)_3 \text{ etc.}$$

where x+y=3

Lithium Aluminum Hydride (LAH)
(Butyl diglyme)
T = 50°C

$$H_3SiCH_2SiH_3 + H_3SiCH_2SiCH_2SiH_3 + (H_2SiCH_2)_3 \text{ etc.}$$

The first stage involves the reaction of vapor of methylene chloride with silicon powder. The organohalosilane produced in first stage were condensed and collected. The unreacted methylene chloride and other highly volatile silane products were removed by distilling the condensed product at 170 °C in atmospheric environment. The organohalosilane compounds were mixture of $H_yCl_xSiCH_2SiH_yCl_x$, $H_yCl_xSiCH_2SiCH_2SiH_yCl_x$, $(Cl_2SiCH_2)_3$ etc. The second stage involves

the reduction of organohalosilane compounds with lithium aluminum hydride (LAH) and the reduced compounds were mixture of $H_3SiCH_2SiH_3$, $H_3SiCH_2SiCH_2SiH_3$, $(H_2SiCH_2)_3$ etc and higher molecular weight polymer viscous compounds. The optimum parameters deduced for highest production rate were first stage reaction temperature: 400ºC, dicholoromethane flow rate: 0.25ml/min and argon flow rate (minimum fluidizing velocity for silicon particles of average particle size of 185 µm): 500 sccm. Organohalosilane compounds were synthesized using these optimized parameters in first stage and further reduced in second stage to get mixture of organosilicon compounds (CVDP). The IR spectra confirmed that the CVDP precursor was mixture of different organosilicon compounds such as $H_3SiCH_2SiH_3$, $H_3SiCH_2SiCH_2SiH_3$, $(H_2SiCH_2)_3$. The CVDP precursor was low viscous colorless liquid. This CVDP precursor was further used for SiC coating.

Coating studies using synthesized organosilicon compound

Computational analysis of specially designed MOCVD reactor

Computational simulation using COMSOL Multiphysics Version 4.4 were performed for a variety of operating conditions to observe the flow inside reactor and to predict the operating condition for uniform deposition and higher growth rate. The temperature profile and velocity profile inside tubular reactor at different fluid velocities (represented in terms of Reynolds number, *Re)* were simulated. The computations indicate that, for abrupt temperature changes along the reactor and substrate wall (worst-case scenario) will not occur if the following criterion is satisfied:

$$27 < Re < 270$$

The overall effect of fluid velocity, heat flow and concentration profile showed that Re = 54 is the optimum reaction condition for present MOCVD system.

Experimental studies on SiC coating using specially designed MOCVD reactor

SiC coating on the graphite, C/C composite and zircaloy substrates were carried out using computed optimized parameters. The experimental parameters used were: Temperature of deposition: 900 °C, Argon flow rate: 2 lpm, pre-heater temperature: 200°C and time: 30 min.

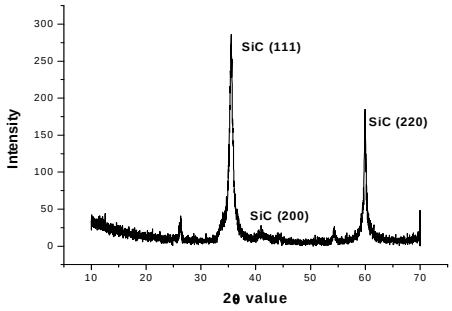

Fig. 2: XRD pattern of the dense SiC coating using CVDP precursor

The substrates were covered with a light gray color dense layer after coating. The XRD pattern (Fig. 2) showed the reflections from (111), (200) and (220) planes corresponding to β-SiC phase. The orientations and degrees of crystallinity in the SiC films were analyzed by XRD.

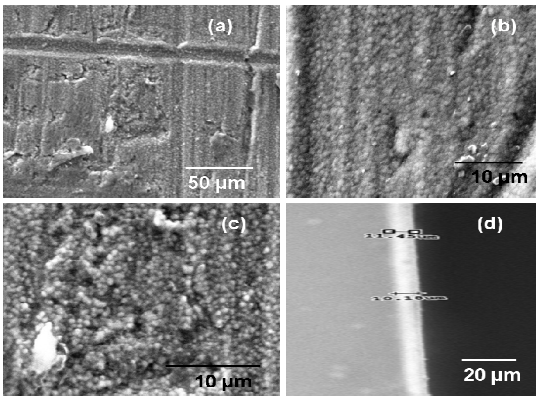

Fig. 3: SEM image of the dense nanocrystalline SiC deposit on zircaloy substrate (a)(b)(c) surface morphology at different magnification (d) cross sectional view of SiC coating

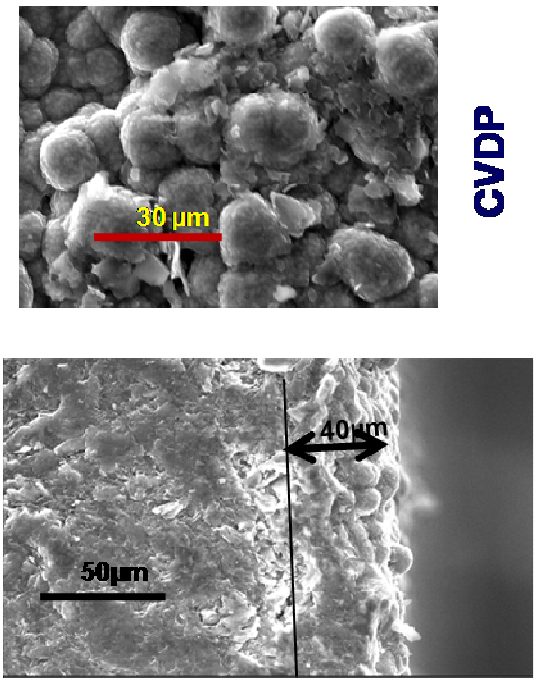

Fig. 4: SEM image of the dense SiC deposit on graphite substrate (a) surface morphology (b) cross sectional view of SiC coating

The deposited 10-12µm SiC film (Fig. 3d) on zircaloy sheet was crystalline, with (111) face growth having the most intense reflection at 2q value of 35.5 (Fig. 2). The full width at half maximum (FWHM), measured from the various reflections (111), (200) and (220) of SiC coated zircaloy sheet surface are 0.69, 0.508 and 1.112 respectively. The average crystallite size was evaluated using Scherrer's equation and was found to be 22.5 nm. This values of the grain size suggested that the coating is composed of nanocrystalline SiC. SEM micrographs of the coated zircaloy sheet at different magnifications are shown in Fig. 3. The SiC deposition on the zircaloy surface was homogeneous with dense grain deposition. The cross sectional SEM images show that the coating adhesion on the surface was strong, as no detachment of the coating was visible. SEM image (Fig. 4) of the dense SiC deposit on graphite substrate shows dense, adherent and uniform coating. The XRD and SEM results revealed that the use of CVDP precursor yielded dense SiC films.

Conclusion

An easy synthesis route has been reported for potential precursor of SiC. The potential SiC precursor is non toxic, non corrosive and easy to handle. It is stable in atmosphere and completely volatile upto 200°C. Dense nanocrystalline SiC film was deposited using this potential precursor on graphite, C/C composite and zircaloy sheet. The low temperature MOCVD coating has been developed to uniformly coat the substrate. The present report on the development of halogen free SiC precursors and deriving nanocrystalline SiC from such precursor has show a new path for the birth of a user-friendly and eco-friendly synthesis and deposition process. In near future the developed precursor will be used to coat the large and complex geometry nuclear structural materials. Further realistic modeling of the deposition process combining detailed chemical reaction kinetics with transport models will be developed.

References

1. "Catalyst-free chemical vapor deposition for synthesis of SiC nanowires with controlled morphology" Jyoti Prakash, Sunil Kumar Ghosh, Dakshinamoorthy Sathiyamoorthy, book chapter 9 in Book titled "Silicon based Nanomaterials", Chief Edi. Zhiming M. Wang, Springer, 2013.
2. "Low temperature coating deriving from Metal-Organic precursors: An economical and environmentally benign approach" Book chapter in Book" Jyoti Prakash, B. M. Tripathi, Sunil Kumar Ghosh, book chapter in Book titled "Inteligent coating for corrosion control, First edition", Edited by: Atul Tiwari, J.W.Rawlins and L.H.Hirara, Elsvier 2014.
3. "Chemistry of one dimensional silicon carbide materials: principle, production, application and future prospects" Jyoti Prakash, Ramani Venugopalan, B.M.Tripathi, S. K. Ghosh, J. K. Chakravartty, A.K.Tyagi, Progress in Solid State Chemistry, doi:10.1016/j.progsolidstchem.2015.06.001, 2015.
4. "Surface induced oxidation kinetics and mechanism of oxidation of 2-D carbon fabric in different oxidative environments" Jyoti Prakash, Kinshuk dasgupta, Brij Kumar, J.K. Chakravartty, International journal of Materials Research 106, 628-635 (2015).

5. "A new approach to fabricate SiC nanowire embedded-dense SiC matrix/carbon fiber composite" Jyoti Prakash, Kinshuk Dasgupta, B.M.Tripathi, J. Bahadur, Sunil Kumar Ghosh, J.K.Chakravartty, Journal of Materials Science, 49, 6784-6792 (2014).
6. "Role of SiC nanowire coating on oxidation behavior of carbon fibers: Kinetic and thermodynamic study" Jyoti Prakash, K. Dasgupta, Brij Kumar, Sunil Kumar Ghosh, J.K. Chakravartty, Surface & Coatings Technology, 259C, 637–646 (2014).
7. "Study of thermal degradation behavior of dense and nanostructured silicon carbide coated carbon fibers in oxidative environments", Jyoti Prakash, Ramani Venugopalan, Bhaskar Paul, Jitendra Bahadur, Sunil Kumar Ghosh, Dakshinamoorthy Sathiyamoorthy. Corrosion Science 67, 142-151 (2013).

NON-DESTRUCTIVE ASSAY OF NUCLEAR WASTE BARRELS USING ACTIVE AND PASSIVE COMPUTED TOMOGRAPHY

Tushar Roy
Neutron & X-Ray Physics Division

Shri Tushar Roy is the recipient of the DAE Young Applied Scientist/Technologist Award for the year 2013

Introduction

Assay of nuclear waste drums is required for decisions on its disposal, safe transportation, permanent storage as well as nuclear material accounting. Manual inspection of opened drums for an assay is a risky, time-consuming, and expensive proposition. Traditionally, the drums are inspected by conventional transmission radiography or tomography. However, these techniques do not yield information about the radioisotopes inside the drum, but just on the material density. Gamma spectroscopy in open geometry or segmented gamma scanning can be performed to this aim, but to improve accuracy and provide information about the spatial distribution of the radioisotopes, an active and passive computed tomography (A&PCT) technique is best suited.

Principle of Active & Passive CT

Active and Passive Computed Tomography (A&PCT) is one of the most efficient techniques for characterization (source strength estimation) and localization of radioisotopes in nuclear waste assay. It uses the decay of radioactive isotopes to image the spatial distribution of the isotope as well as to determine their source strength or activity. The A&PCT method consists of two steps to perform an assay: Active CT and Passive CT.

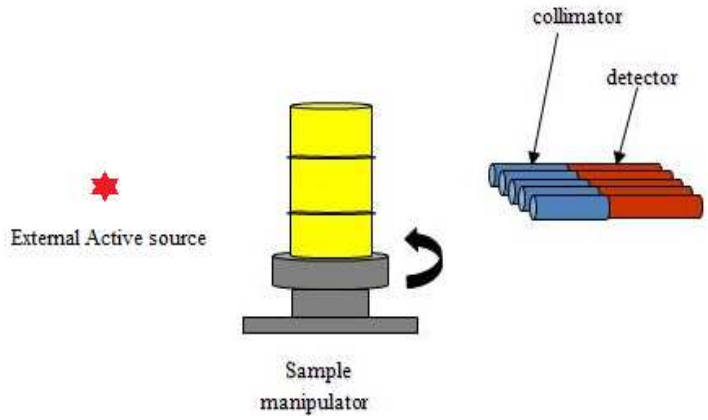

Fig.1: Schematic of A&PCT set-up for waste assay

In active CT, attenuation map of the object is obtained. This is similar to conventional X-ray CT but it uses an external gamma source (instead of X-ray) and the spectrum is recorded using multi channel analyzer (MCA). It differs from conventional CT scanners in that it discriminates between photons of different energies. The gamma source used for active CT has, generally, multiple emission energies. The reconstruction results are a discrete quantitative measurement of the linear attenuation coefficient at each energy measured, i.e., there has been no integration over the energy spectrum. Thus active CT images have pixels that represent the absolute measurement of attenuation at specific energies. For a waste drum, the attenuation due to its contents is accurately measured in three dimensions and displayed as a sequence of two dimensional images at different z-planes (or elevations) of the drum. Energy specific attenuation maps are then used to determine the attenuation map of the object corresponding to the emission energy of the radioisotope (inside the object) to be imaged by interpolating the above data.

Passive CT is used to measure and determine the location, identity, and strength of radioisotope sources within an object. The ray sum for passive CT (also called Single Photon Emission Computed Tomography (SPECT)) is the counts measured in disintegrations per unit volume per unit time of the passive source within the object. Therefore, a single-photon-emitted ray sum is the integrated radioisotope activity, modified by one or multiple of exponential attenuations, along the path from a source position within the object to the detector. The function that is imaged for passive CT is the measured gamma-ray activity at one or more energies of all detectable radioisotopes within the object. By combining active and passive measurements, corrections can be made to account for the effect that the waste contents have on the internal radioactive emissions. The corrected gamma-ray spectra can be used to identify, localize, and assay all measured radioisotopes present in the container.

Mathematics of SPECT

Consider a vector $\bar{x} = (x, y)$ in a two-dimensional Euclidean space (Fig.2). Let $f(\bar{x})$ denote the distribution of radioisotope activity and $\mu(\bar{x})$ denote the attenuation map of the surrounding object.

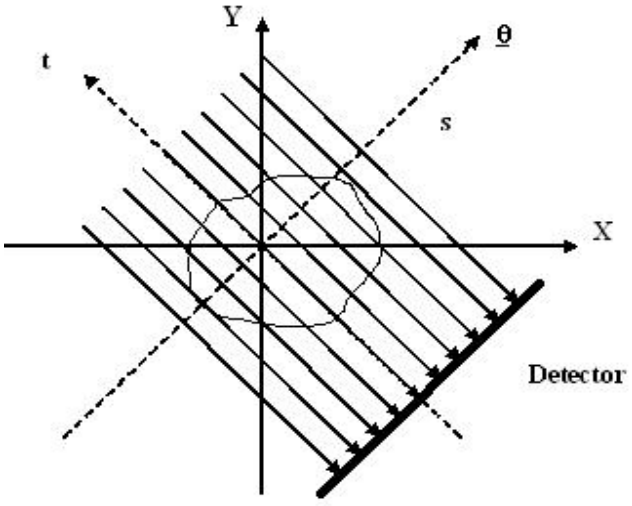

Fig.2: A typical SPECT set-up in parallel geometry

The attenuated 2D Radon transform at energy E for parallel beam geometry is of the form[1]

$$[\Re_{att} f](s,\theta;E) = g(s,\theta;E) = \int_{-\infty}^{\infty} f(s\underline{\theta} + t\underline{\theta}^{\perp};E) e^{-\int_{t}^{\infty} \mu(s\underline{\theta}+\tau\underline{\theta}^{\perp};E)d\tau} dt \quad (1)$$

where $\bar{\theta} = \begin{pmatrix} \cos\theta \\ \sin\theta \end{pmatrix}$, $\bar{\theta}^{\perp} = \begin{pmatrix} -\sin\theta \\ \cos\theta \end{pmatrix}$ and $D_{\mu}(\bar{x},\bar{\varphi};E)$ is the divergent beam transform of $\mu(\bar{x};E)$ in the direction of $\bar{\varphi} = \begin{pmatrix} \cos\varphi \\ \sin\varphi \end{pmatrix}$ defined as $D_{\mu}(\bar{x},\bar{\varphi};E) = \int_{0}^{\infty} \mu(\bar{x} + p\bar{\varphi};E)dp$ where $\mu(\bar{x};E)$ is the linear attenuation coefficient at energy E.

In matrix notation, the SPECT problem can be written as

$$g = Af \quad (2)$$

or,

$$\begin{pmatrix} g_1 \\ g_2 \\ . \\ . \\ g_M \end{pmatrix} = \begin{pmatrix} a_{11} & a_{12} & . & . & a_{1N} \\ a_{21} & . & . & . & . \\ . & . & . & . & . \\ . & . & . & . & . \\ a_{M1} & . & . & . & a_{MN} \end{pmatrix} \begin{pmatrix} f_1 \\ f_2 \\ . \\ . \\ f_N \end{pmatrix} \quad (3)$$

where $g \in \mathbb{R}^{M\times 1}$ is the observed projection data, $A \in \mathbb{R}^{M\times N}$ is the probability system matrix and $f \in \mathbb{R}^{N\times 1}$is the vector of unknown spatial density distribution of nuclear disintegration events resulting in gamma emission in the object. The system model can take into account various physical factors involved in the detection process – attenuation, collimation, scatter, distance-dependent fall in intensity, transmission through collimator, etc. All these factors can be modeled into the system matrix. The attenuation factor is modeled using the attenuation map obtained in the active CT step. The problem thus reduces to solving the linear system of equations (2).

Reconstruction Algorithms

Mathematically, reconstruction is an inverse problem: the aim is to find vector of unknowns from the measured observables by solving a system of linear equations. Reconstruction algorithms generally employed for solving SPECT problem can be divided into two classes: Analytical and Iterative Reconstruction Techniques.

The analytical approach assumes noiseless data, an ideal collimator, no attenuation and no scatter of gamma radiation. These assumptions can make the reconstruction result an inaccurate representation of the true activity distribution. Therefore, additional data filtering and post-processing are necessary. The most commonly used method is the Filtered Back Projection

(FBP) algorithm. In this approach, the projections are filtered in the frequency domain and the filtered projections are backprojected in the spatial domain. An analytical solution of Eq.1 was first provided by Novikov [1] as follows:

$$f(\bar{x}) = \frac{1}{4\pi} Re\left\{ \nabla . \int_0^{2\pi} \bar{\theta} \left\{ e^{-h(s,\theta)+D_\mu(\bar{x},-\bar{\theta}^\perp)} \mathcal{H} e^{h(s,\theta)} g(s,\theta) \right\} |_{s=\bar{x}.\bar{\theta}} \, d\theta \right\} \quad (4)$$

where $h(s,\theta) = \frac{1}{2}(I + i\mathcal{H})[\Re\mu](s,\theta)$ and $[\mathcal{H}\varphi](s,\theta) = \frac{1}{\pi} p.v. \int_{-\infty}^{\infty} \frac{\varphi(s',\theta)}{s-s'} ds'$

with $i^2 = -1$. I is the identity operator. $\mathcal{H}$ is the Hilbert transform with respect to the second parameter and *p.v.* denotes Cauchy principal value of the integral. ∇ is the divergence operator.

The iterative approach [79] allows a complex model of gamma radiation interaction to be taken into account including the effect of collimation and scatter as well as statistical variability of measured data. These are recommended for quantitative image analysis which is crucial, for example, in waste assay. The algebraic reconstruction techniques include simple ART, SART, SIRT, etc. The statistical reconstruction technique takes into account the Poisson statistics of radiation. The techniques include MLEM, OSEM, MAP-EM, etc.

One of the commonly used iterative techniques for reconstruction of Passive CT data is Maximum Likelihood Expectation Maximization (MLEM) technique. The MLEM formulation is mathematically stated as [2]:

$$\hat{f}_j^{k+1} = \frac{\hat{f}_j^k}{\sum_{i=1}^{M} a_{ij}} \sum_{i=1}^{M} \frac{g_i}{\sum_{j'=1}^{N} a_{ij'} \hat{f}_{j'}^k} a_{ij} \quad (5)$$

Experimental set-up

In order to demonstrate the capability of doing active and passive CT, an experimental system has been set-up at Purnima Labs (Fig.3). It consists of the following:

- Sample Stage
- Sample / object matrix with (passive) source
- Detector and associated electronics
- Collimator
- Data Acquisition system
- (External) Active source (for transmission measurement)

For the experiments, a mock-up waste drum (580mm diameter and 850mm height) filled with cotton waste/gloves/tissues is used and radionuclide samples are placed at different locations inside the drum.

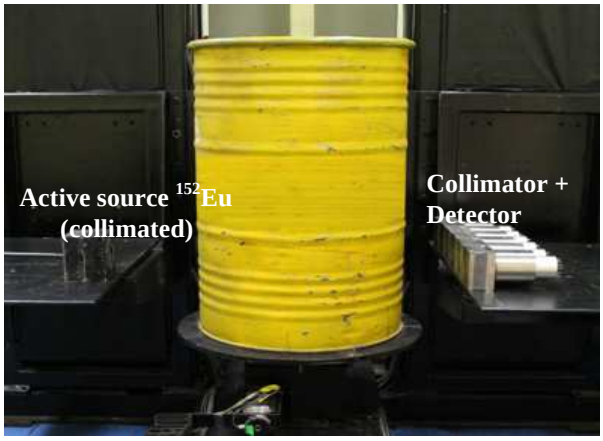

Fig.3: Experimental A&PCT set-up for waste assay

Experimental Results

Various experiments have been carried out using this set-up. Some of the results are presented below:

(a) Parallel Beam Geometry

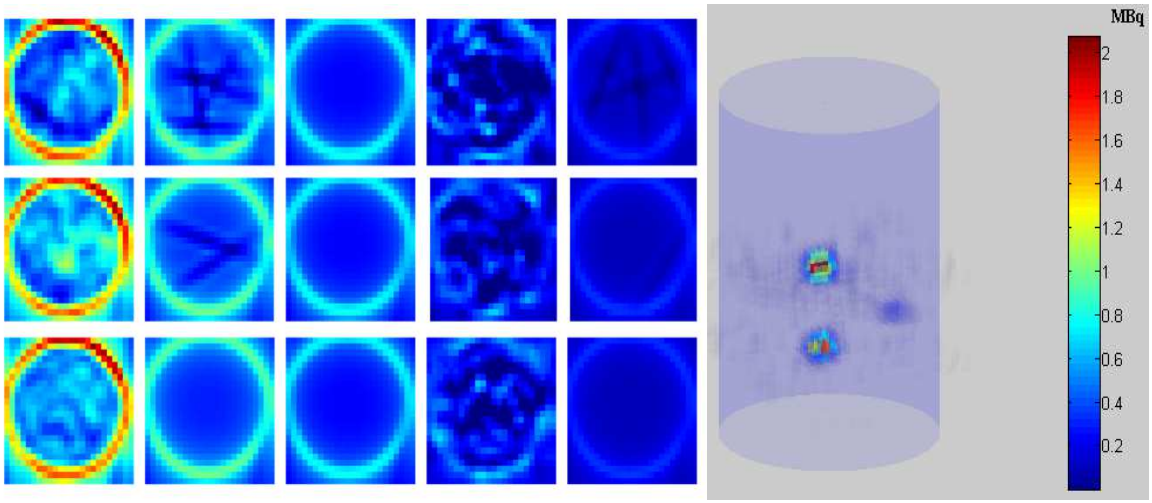

a **b**

Fig. 4: (a) Active CT data for three different slices (top to bottom) at different energies (from left to right) – 121 keV, 244 keV, 344 keV, 444 keV, 778 keV (b) 3D view of reconstructed ^{137}Cs activity

Three ^{137}Cs sources are placed inside the drum at different locations. Transmission computed tomography (TCT) of the drum is carried out using external ^{152}Eu source. The TCT data are acquired for different energies (121 keV, 244 keV, 344 keV, 444 keV, 778 keV and 867 keV). The attenuation map is reconstructed for each energy using Filtered Backprojection algorithm. Fig. 4(a) shows the reconstructed TCT data for three slices at different energies.

The attenuation map for 662 keV (emission energy in SPECT) is interpolated from these data. This attenuation map is then used for attenuation compensation. For Passive CT, projections are acquired with $LaBr_3$(Ce) detectors at 36 angular locations and 24 lateral positions for each z-position. In the vertical direction, 34 z-positions are scanned. Reconstruction is done using Filtered Backprojection scheme with attenuation compensation based on Novikov's Inversion Formula. The reconstructed 3D volume is shown in Fig. 4(b).

(b) Fan Beam Geometry

The schematic experimental arrangement for fan-beam geometry is shown in Fig. 5. It has the advantage of performing Active CT with single active source and multiple detectors.

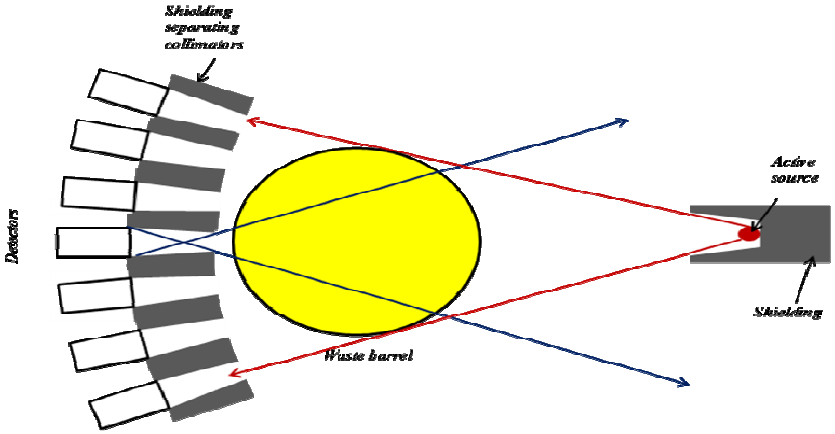

Fig. 5: Schematic arrangement for multiple detector A&PCT scan in Fan beam configurations

Fig. 6(a) shows the attenuation map of drum contents. Fig. 6(b) & 6(c) show the reconstructed 137Cs activity using Analytical and 2D MLEM techniques respectively.

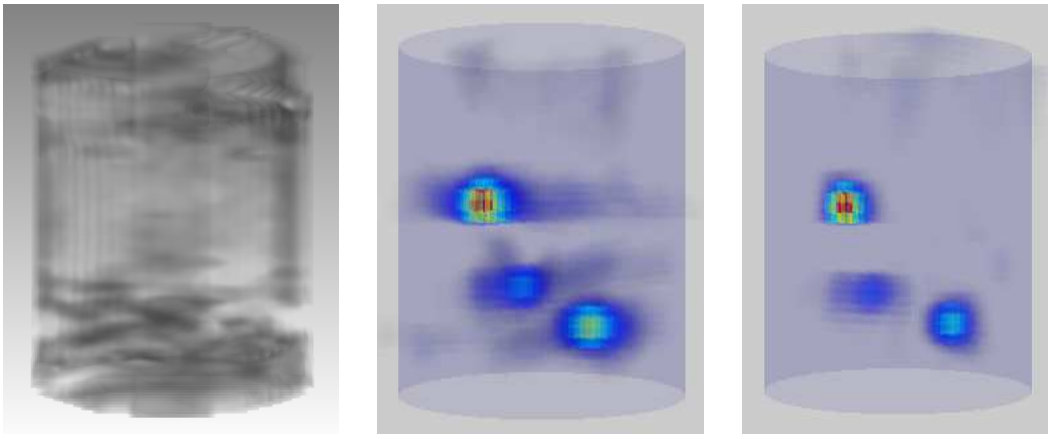

(a) (b) (c)

Fig. 6 (a): Reconstructed attenuation map (b) & (c) Analytical and 2D MLEM reconstructed volume showing ^{137}Cs activity respectively

(c) Imaging of ^{239}Pu

Experiments were performed for imaging of ^{239}Pu in waste drums using A&PCT technique.

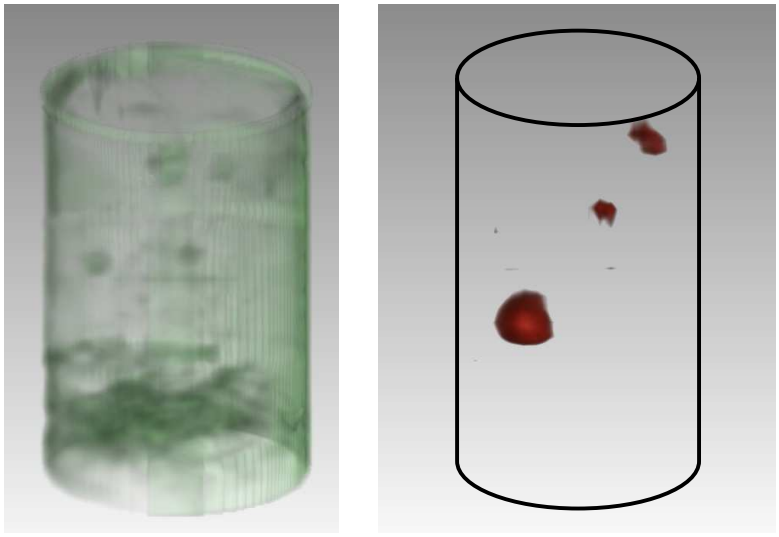

(a) (b)

Fig. 7 (a): Reconstructed 3D attenuation map (b) & (c) Reconstructed 3D activity map showing ^{137}Cs and ^{239}Pu activity respectively

For the ACT measurement, the external gamma source and a single $LaBr_3$(Ce) detector are used. The attenuation map (at 414 keV) is shown in Fig.7(a). For the PCT measurement, the external source is removed and gamma rays emitted from within the drum are recorded by three collimated $LaBr_3$(Ce) detectors. Data is acquired at 24 lateral positions and 12 angular positions over 360º for each z-position. In the vertical direction, 33 z-positions were scanned. Each slice thickness is 25mm. The 414 keV peak from ^{239}Pu is used for PCT reconstruction. Fig.10 (b) shows the reconstructed 3D volume. The radioisotope activity distribution can clearly be observed.

(d) Fully 3D Reconstruction

For 2D reconstruction, system matrix is constructed for a single slice and the corresponding slice is reconstructed. The 3D activity map is obtained by vertically stacking the respective 2D reconstructed slices. It is assumed that all photon counts in a particular row of the planar image are due to photons emitted from the slice at same height. However, the projection data has contribution from other voxels also which are located in other slices. In fact, each detector or projection bin accepts contributions from a cone whose dimensions depend on the shape and size of collimator holes.

For fully 3D reconstruction, 3D system matrix corresponding to 3D collimator is generated for the whole object. This method requires large storage space for matrices, is computationally quite

intensive and much harder to implement. However, fully 3D reconstruction should reduce both intra-slice and inter-slice blurring.

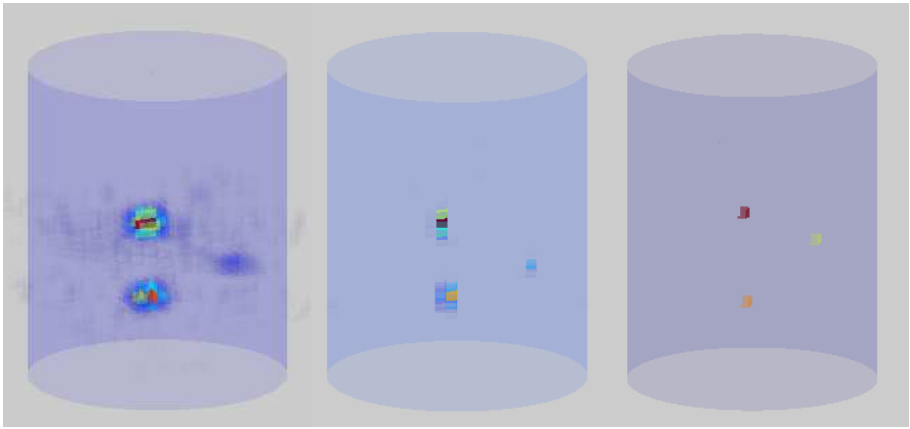

a **b** **c**

Fig. 8: Reconstructed activity for SS drum sample (a) FBP (b) 2D (Stacked) MLEM (c)

Fig. 8 (a), (b) and (c) show the 3D view of ^{137}Cs activity distribution using analytical, 2D MLEM and fully 3D MLEM reconstruction respectively (for the sample in Fig.4). The effect of collimator blurring is clearly evident from these images. For fully 3D MLEM reconstruction, (Fig. 8(c)), both inter- and intra-slice blurring are reduced considerably and the point source appear point-like.

Conclusion

The development of an active and passive gamma emission tomography technique has been reported. This technique can be used for non-destructive assay of nuclear waste barrels. Some experimental results with ^{137}Cs as well as ^{239}Pu sources have been presented.

References

[1] Novikov R G: "An inversion formula for the attenuated X-ray transformation" *Ark. Math.* **40** (2002) 145-167

[2] L. A. Shepp, Y. Vardi, "Maximum likelihood reconstruction for emission tomography", *IEEE Trans Med Imaging*; MI-1:113–122, (1982)

[3] Tushar Roy, Jilju Ratheesh, Amar Sinha, "Three-dimensional SPECT imaging with $LaBr_3$:Ce scintillator for characterization of nuclear waste", *Nuclear Instruments and Methods in Physics Research A* **735** (2013) 1-6.

[4] Tushar Roy, M. R. More, Jilju Ratheesh and Amar Sinha, "A practical fan-beam design and reconstruction algorithm for Active and Passive Computed Tomography of radioactive waste barrels", *Nuclear Instruments and Methods in Physics Research A*, doi: 10.1016/j.nima.2015.05.018 (2015).

BARC NEWSLETTER
FOUNDER'S DAY SPECIAL ISSUE 2015

HIGH POWER PULSE MODULATORS FOR KLYSTRONS/MAGNETRONS/ELECTRON GUNS FOR ELECTRON LINAC

Abhijit Tillu[1], Vivek Yadav[1], Hemant Sarukte[1], Shiv Chandan[1], Ramchandra Chavan[1], Kavita P Dixit[1], R.K. Rajawat[1] and K. Dasgupta[2]
[1] Accelerator & Pulse Power Division
[2] Beam Technology Development Group

Shri Abhijit Tillu is the Recipient of the DAE Young Applied Scientist /Technologist Award for the year 2013

Abstract

Pulsed Modulators required for RF sources, based on klystrons and magnetrons, for RF electron linacs have been designed and developed at Electron Beam Centre, APPD, BARC. Electron guns in these linacs have also been powered by pulsed modulators. Line-type modulators, as well as IGBT-based solid-state modulators have been developed for these applications. A 150 kV/100 A line-type modulator has been tested on klystron to generate 7.5 MW peak RF Power. Magnetron modulator rated for 50kV/120A has been tested for long term stability at full peak and average power ratings of the magnetron. A proof of principle Solid-state modulator, using fractional-turn pulse transformer has been designed, developed and tested successfully on magnetron load up to output power of 1.3 MW peak. In addition, line-type modulators for electron guns up to 85 kV have been successfully commissioned and are in operation in the linac systems. This paper activities of the APPD towards development of subsystems for the indigenous development of pulse modulators.

Introduction

Industrial electron RF linacs [1] including the 10 MeV RF Linac and 3 MeV DC Accelerator, have been indigenously designed and developed at the APPD, BARC. Several industrial applications such as plastic modification, semiconductor irradiation [2] have been demonstrated with these accelerators. A prototype 6 MeV & 9 MeV linacs as X-ray sources for cargo-scanning have been built for imaging experiments. These linacs operate in the pulsed mode, which requires the use of pulse modulators for the RF source as well as the electron guns. The design, development, testing and operation of various pulse modulators are presented in this paper.

Development of Line Type Magnetron Modulator

A magnetron modulator has been developed by APPD for conditioning of magnetrons being developed by CSIR-CEERI, Pilani. The modulator is designed for an output pulsed voltage of 50 kV (-ve pk) and current of 120 A (pk), with pulse width of 4 μs and repetition rate of 250 Hz.

The schematic of the magnetron modulator is shown in Fig.1. This is a line-type modulator, using a Pulse Forming Network (PFN). During the charging cycle, Constant Current Power supply (CCPS) is used to charge the PFN capacitors. During the discharge cycle, the thyratron is triggered and the PFN capacitors discharge through the step-up pulse transformer into the Magnetron. Magnetron is connected as load at the secondary of pulse-transformer. The VI characteristics of magnetron are highly nonlinear (equivalent to biased diode).Hence the output pulse voltage/ current range is very narrow. The modulator is tuned to have best performance for a load of 415 Ω.

The modulator has been tested on a equivalent magnetron load (Faza make MI456A) at 49kV/ 95A, 4 µs, 250 pps for a continuous period of 8 hours. Fig.2 shows the view of the modulator Rack and the HV Pulse transformer connected to the Magnetron.

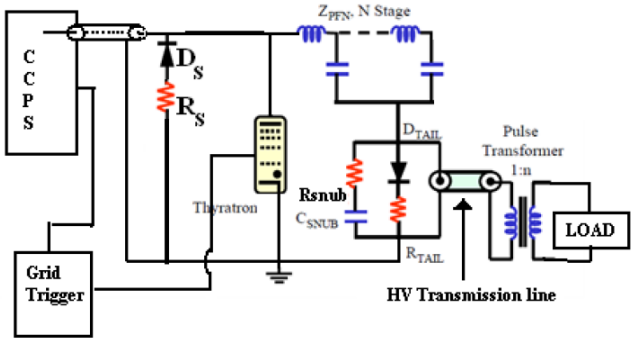

Fig. 1: Schematic of Line type Magnetron Modulator

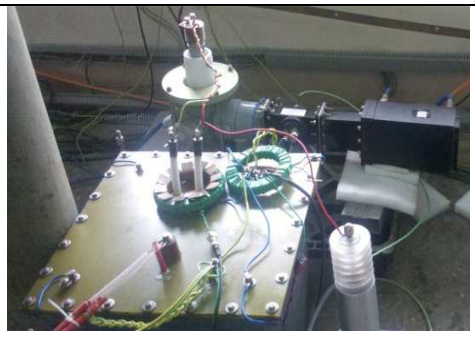

Fig. 2: View of Magnetron Modulator and Pulse Transformer Tank

The salient features of the development of magnetron modulator are listed below:

1. Design and Development of 1:5 HV pulse transformer with locally available Amorphous Cur C Cores (Fe based 2605SA1,Hitachi metglass).
2. Programmable sensitivity for ARC trip: It is possible to program the number of arcs that can be tolerated before tripping the modulator. For a well conditioned tube, the manufacture allows typically 25 consecutive arcs. This modulator will be used for

conditioning of the magnetron being developed at CSIR-CEERI Pilani. Hence the user has been given the option to set the number of allowed ARCs in 4 sec (1 arc- 40 arcs), hence the modulator sensitivity to arcing is user defined.

3. Two set point operation possible, enabling the magnetron to pulse at two different RF peak powers for alternate pulses. This feature will be useful for dual energy operation of the Cargo Scanning Linac (6/3MeV, for material discrimination).

Design and Development of 1:5 HV Pulse Transformer

The HV Pulse transformer shown in Fig. 1, is the major component affecting the pulse characteristics. These pulse transformers are traditionally implemented with 2mil or 1 mil Si Steel Cores. These cores are not readily available in the country. This Pulse transformer has been implemented with locally available Hitachi metglass 2605SA1 Fe based Amorphous Cut C cores (AMCC1000). Two pairs of this Cut C core are used in EE construction. Fig. 3 shows a view of the pulse transformer assembled in the Lid mounted fashion.

The primary consisting of 9 turns is implemented using a rectangular copper wire of ~ 4mm x 2mm cross section area. The 45 turns secondary is implemented in bifilar construction using enameled copper wire of SWG17. The primary has been tapered to minimize the leakage inductance. The measured leakage inductance as seen from the primary is 10uH, the magnetizing inductance as seen from the primary is 2.5mH. The distributed Capacitance is 60pF, as seen from the secondary. The rise time across a resistive load of 400 ohms was measured to be < 500ns.The transformer along with the filament heating transformer is housed in an oil tank as shown in Fig. 3, and is kept in the close vicinity of the magnetron as seen in Fig 2. The max rise in the oil temperature was < 10 deg C when the modulator was operated at full rated specifications for 8 hours.

Fig. 3: 1:5 HV Pulse Transformer

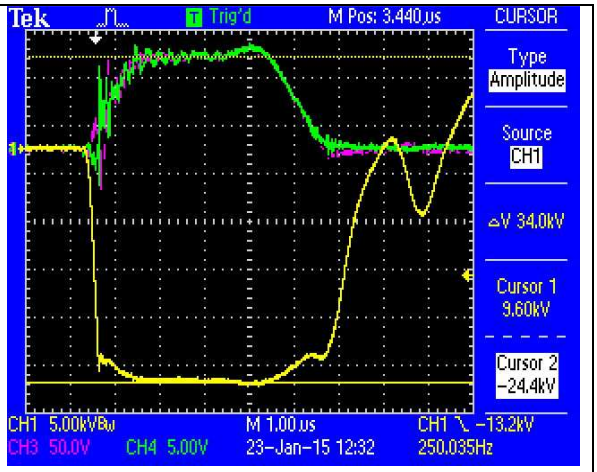

Fig. 4: V/I across magnetron at 250 pps

Fig. 4 shows the pulsed voltage and current waveforms. CH1 indicates a pulse voltage of 48.8kV. The probe used is Iwatsu make 2000X HVP-60 probe. The CH3 and CH4 show the pulsed current through the magnetron. This current has been measured in the HV side and the LV side, using a Current transformer as is seen in Fig. 2. The measurements indicate a pulsed current of 96A. The peak RF power from the magnetron was measured to be 2.7MW, and in agreement with the manufacturer's data sheet

Design studies of a prototype Solid state magnetron Modulator

A prototype solid state pulse modulator based on Induction Adder Topology has been designed and is currently being tested on an S Band Pulsed magnetron rated for 3.2MW Peak RF Power. After successful lab tests the modulator is intended for use in cargo scanning and radiography applications. Currently the topology consists of 4 nos. of single turn primaries driven independently at voltages of ~1000V. The secondary encircles all the four primaries to generate the desired pulsed voltage across the magnetron. The designed output pulse parameters are 50kV, 120A, 4 µs, at a pulse repetition rate of 250 pps. The peak electrical power delivered to the magnetron per pulse is ~6MW. The modulator is designed for at-least 8MW of pulse power. There Split core pulse transformer has four primaries independently driven by their respective power modules. Each module is a 1kV pulse source implemented as shown in Fig. 5. The IGBT used is a 1700V, 2400A IGBT. The 200µF/1100V energy storage capacitor is implemented by two Axial type Metalized polypropylene Capacitors. The electrical connections between the IGBT, Capacitors and diode are implemented by low inductance strip line geometry. The pulse transformer construction is oil free and uses epoxy casting.

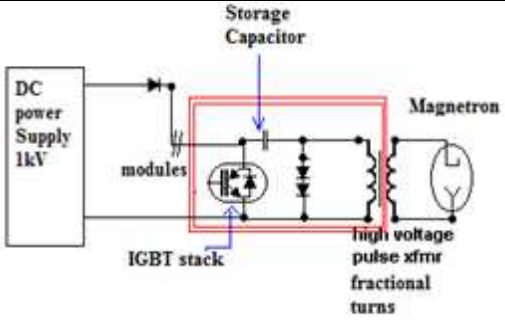

Fig. 5: Schematic of the split core Solid state Modulator

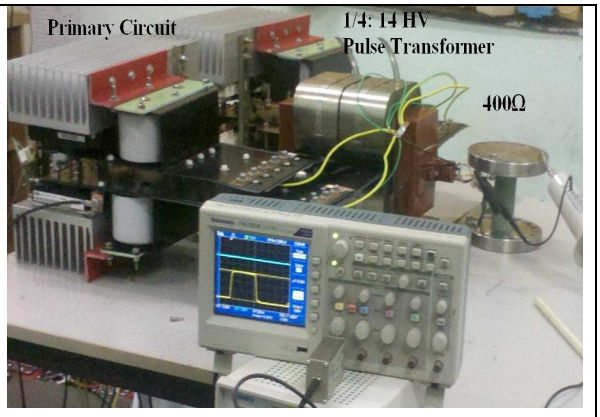

Fig. 6: Testing on Resistive Load

The split core pulse transformer also referred as fractional turns transformer has four primaries, each implemented by using a single turn foil winding of 0.3mm thick Copper. The secondary consists of 14 turns of SWG16. The secondary is in bifilar type, so as to allow filament heating power to the magnetron. The 8 turn Reset winding on the secondary is implemented by using SWG14 enamelled copper wire. The entire secondary is adequately screened and epoxy potted, so as to allow Oil Free construction of the pulse transformer. The pulse transformer core uses 4

pairs of Amorphous Cut C cores (2605SA1). Each core is excited by its own primary. The cores are arranged such the transformer is in E type configuration. The estimated flux swing is ~ 1.5T. Hence the cores are biased at ~ 0.75T, so as to get the best pulse permeability. The pulse permeability of the core was evaluated separately and was confirmed to be ~ 3500 for the required flux swing, if the core is biased at ~ -0.75T.

The Prototype pulse modulator was assembled and tested on a resistive load of 400Ω, with very low inductance of <1µH. Fig. 6 shows the view of the test setup. The Pulse Voltage was measured to be 30kV at DC voltage of 545V. The Rise time measured was < 300ns and the backswing is negligible, as shown in Fig.7. When the Pulsed voltage was increased from 10kV to 30kV the rise time did not change significantly. It was tested at higher voltages also, but the probe was removed as the limitation of the probe is 40kV. Fig. 7 shows the voltage across the load.

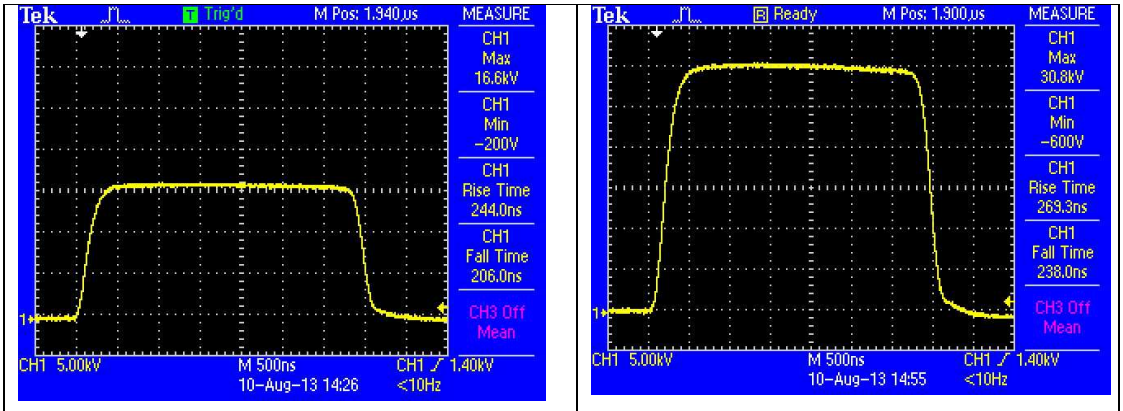

Fig. 7: Modulator output across resistive load at 15kV and 30kV pulse Voltage

After testing on Resistive Load, the modulator was connected to the e2v make magnetron MG5028. The electromagnet current of the magnetron was set for 130mT Field. This corresponds to the operating point of 38kV/ 168A. The magnetron output was terminated on a water load. The waveguide line consisting of one directional coupler was pressurized with ~ 20 psi of SF6. The filament was heated at the rated parameters and the pulse voltage was slowly increased. At Voltages much below the Hulls Cutoff, the magnetron offered very high impedance, and hence the output showed significant ringing, as shown in Fig. 8a. As the magnetron pulse voltage was increased further the magnetron current increased and the pulse shape improved significantly, as indicated in Fig. 8b. The magnetron was tested up-to ~34kV, 100 A and the peak RF Power was measured to be ~ 1.6MW maximum using Diode Detectors Fig. 8 indicates a rise time < 350ns and backswing of ~ 3kV. The e2v make magnetron was in regular use and hence well conditioned, hence there were no ARC events. The testing was done up-to 30pps for around 15 min and the pulse shape was stable. The yellow waveform (CH1) in Fig. 8a and 8b is the magnetron voltage and CH3 is the magnetron current. Fig. 9 shows the pulser being used for conditioning of buncher linac. The e2v make magnetron was disconnected and the FAZA make 2.7MW magnetron MI456A was connected to the modulator. It has an

operating point of 50kV/100A. With this magnetron testing was done up-to 43kV, 70A pulse. The magnetron required some conditioning and there were ~ 8 ARC events, but the modulator did-not indicate any damage.

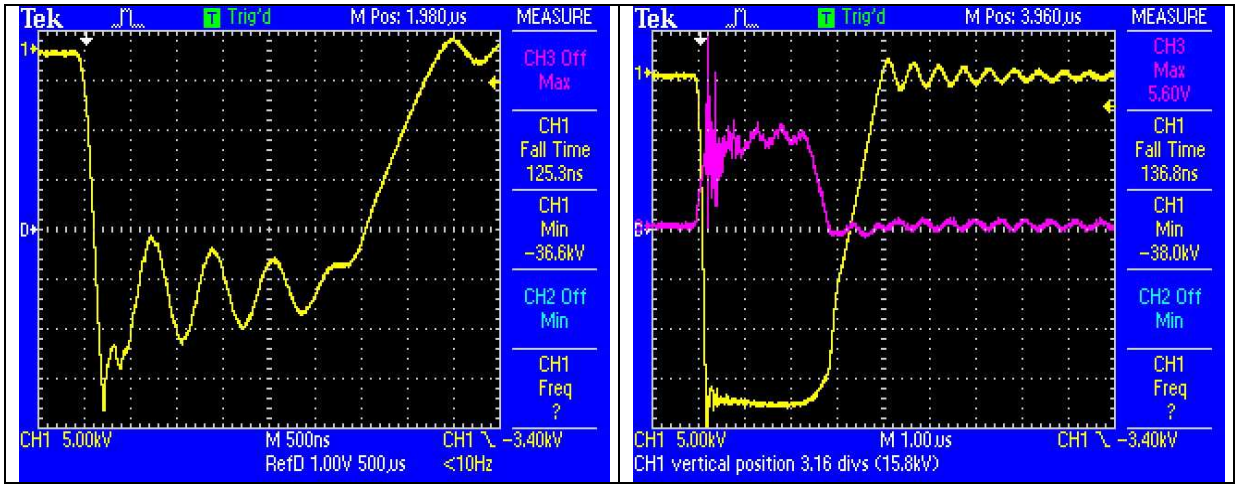

Fig. 8a: Modulator output at voltage much lower than Hulls Cutoff	Fig. 8b: Modulator Output on e2v magnetron MG5028

Fig. 9: Modulator used for powering the e2v make magnetron MG5028 used for buncher Linac Conditioning

Commercially available gate drives were used for this testing. These commercially available Gate drives were slightly modified to restrict the ARC current, however they are not suitable. An improved Gate Drive has been designed, fabricated and is being tested. The CCPS for the modulator has been designed and is under fabrication, Water cooled heat sinks will be used for more compactness.

Development of Line type klystron Modulators

Pulsed modulators have been designed and built for both single-beam and multi-beam klystrons. A 150kV/110A/7µs/250 Hz line-type modulator, shown in Fig.10, has been successfully tested on the klystron load. The indigenously developed pulse transformer for this modulator is shown in Fig. 11. Peak RF power of 7.5 MW and average power of 7.5kW has been achieved at the output of klystron. The pulse transformer along with the Blocking Inductance in the Core Biasing circuit have been indigenously developed using 2605SA1 Fe based Amorphous Cut C Cores. The transformer uses a bifilar winding topology with tapered Secondary so as to reduce the leakage Inductance.

Fig. 10: Modulator with single-beam klystron on test

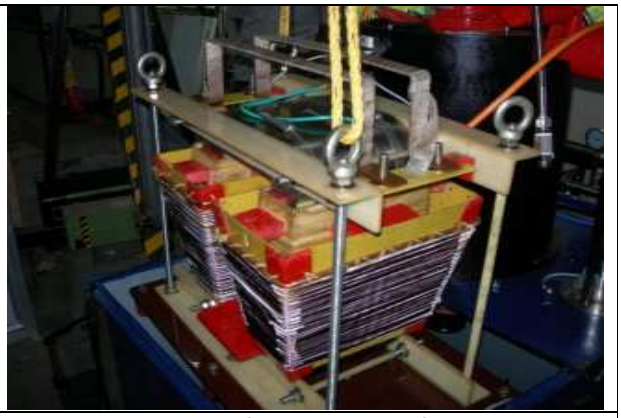

Fig. 11: Pulse transformer (1:10.7) for 150kV/110 A klystron modulator

Line type Modulators for Electron Gun

Line type modulators are regularly used for driving pulsed high power microwave tubes such as klystrons and magnetrons. The operating point of these devices is fairly fixed, hence the line type modulator is designed for a fixed impedance. However the case is far different in the line type modulator designed for a high impedance Electron gun. Line type electron gun modulators have been developed by APPD and being routinely used for powering the Triode Electron Gun of the linear accelerator. The beam parameters of such guns are user defined and the pulse current varies from few mA to 1 A (typ). The beam energies requirement varies from 40keV to 80 keV. Hence the impedance offered by the electron gun to the power source (modulator) is not well defined.

Table 1: Electron Gun requirements for 6MeV Compact Linac

Max Gun Voltage	85kV (- ve)
Peak current	0 - 800mA
Pulse width (flat top)	3.4µs
Rise time	< 2.5µs
Pulse repetition frequency	250 Hz

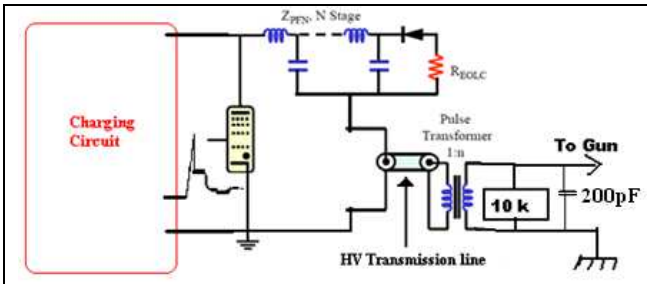

Fig. 12: Schematic of Gun Modulator

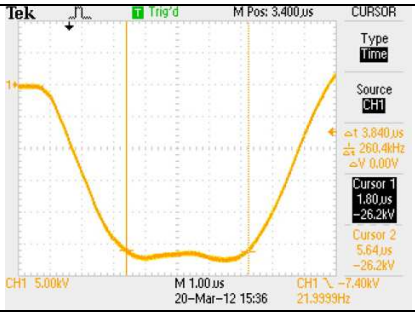

Fig. 13: 53kV Pulse across the electron gun

The load capacitance which is inclusive of the various stray capacitance along with the intrinsic gun capacitance is ~ 200-400 pF. This capacitance, which depends on the configuration, shunts the load and makes the effective load highly capacitive with the resistive part varying over a wide range. The equivalent impedance of the beam varies from 50k ohms to infinity. The gun capacitance, the transformer and other stray capacitance also need to be charged to the cathode potential. Hence the stored energy in these capacitance is equivalent to (if not more than) the useful beam energy per pulse. Table 1 describes the electrical parameters of the electron gun used in 6MeV Compact linac for which the line type modulator is designed. Fig. 12 shows the schematic of the same.

The pulse characteristic in case of line type modulator is strongly dependent on the impedance seen by the PFN. Hence the Gun is shunted by a dummy resistance which is much smaller than the beam impedance. The value of the dummy resistance is a compromise between the rise time and the power dissipation. A larger value of dummy resistance results in lesser dissipation but poorer rise time and load regulation. Fig. 13 shows the pulse output voltage at 53kV as measured by 2000X probe (Iwatsu make HVP-60).

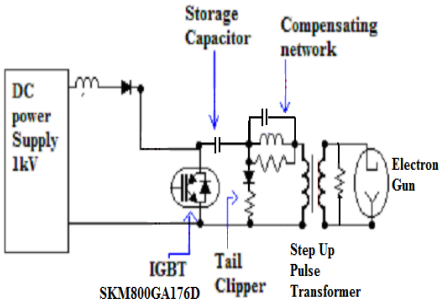

Fig. 14: Schematic of solid state gun modulator

Fig. 15: Photo of 1:90 pulse transformer

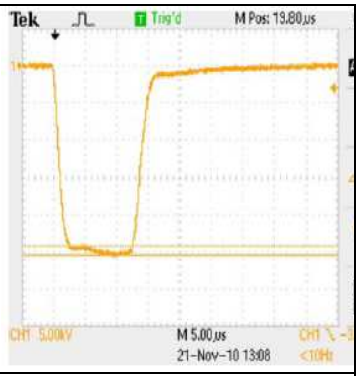

Fig. 16: 50kV Voltage across the electron gun

Solid State Electron Gun Modulators

Solid-state modulator uses a single-stage IGBT-based system with a 1:90 pulse transformer, shown in Fig. 14. A primary pulse of 1 kV is applied for obtaining an output pulse of 90 kV. the pulse transformer is shown in Fig 15, the 50kV pulse across the gun is shown in Fig. 16. The voltage was measured with 2000X probe. The modulator is regularly in use in the electron gun test setup for characterizing the e guns.

Conclusion

Indigenous design and development of line-type modulators for klystron, magnetron and electron gun has been successfully demonstrated. The design and implementation of oil insulated pulse transformers for the magnetron and klystron have been successfully demonstrated using locally available magnetic cores. The initial result of the prototype solid state magnetron modulator has been encouraging and work on full scale prototype is in process.

Acknowledgement

Authors wish to thank Dr L.M Gantayet, Dr A.K.Ray, Dr K.C Mittal and Shri D.P.Chakravarthy for their constant encouragement and support. The authors also thank the support provided by the entire team at Electron Beam Centre towards the development and testing of these modulators.

References

1. K.C.Mittal, et al., "High Power Electron Accelerator Programme at BARC", LINAC2014, CERN (2014)
2. D.Bhattacharjee, et al., "Design and development of compact electron gun and its performance with compact linac operation, Proc.InPAC 2013, Kolkata
3. [Shiv Chandan, et al, "Commissioning and beam trials of 6 MeV RF electron linac", Proc.InPAC 2013, Kolkata (2013)
4. A.R.Tillu, et al., "Design, development and initial results of solid state magnetron modulator", LINAC2014, CERN (2014)
5. V.Yadav, et al, "High Power testing of 7.5 MW S-Band pulsed klystron", Proc.InPAC 2013, Kolkata (2013)
6. K.P.Dixit, et al., "Design and development of Line type modulators for high impedance Electron gun", ISDEIV2014, Mumbai, Oct 2014
7. K.P.Dixit, et al., "Design & development of pulsed modulators for RF Electron Linacs" LINAC2014, CERN (2014).

BARC NEWSLETTER
FOUNDER'S DAY SPECIAL ISSUE 2015

DESIGN AND DEVELOPMENT OF CAPACITOR CHARGING POWER SUPPLY FOR PULSED POWER SYSTEMS

A. S. Patel
Accelerator and Pulse Power Division

Ankur Patel is the Recipient of the DAE Young Engineer Award for the year 2013

Abstract

Regulated power supplies are designed to operate at constant or nearly constant load, where as capacitor charging power supplies(CCPS) are designed to operate from nearly short circuit to low load condition. The CCPS is used to charge capacitor load. CCPS are generally used to charge the pulse power systems. Pulse power systems are consists of Marx generator, pulse forming line and high power microwave or flash X ray load. These loads are generally dynamic in nature, the load changes affects the power supply. If regulated power supplies to be used for this purpose then after charging the capacitor, the supply is removed and then capacitor can be discharged in the dynamic load. But this cannot be feasible in rep rate system. So ccps is designed to prevent against dynamic noise. APPD, BARC is working on the development of CCPS for pulse power systems. The 3kJ/s, 30kV, 200mA is commissioned with 40kJ electro- magnetic manufacturing machine. The ±50kV, 50kJ/s, 1A is commissioned with 1kJ reprate Marx based pulse power system.

3kJ/s, 30kV, 200mA CCPS

Series resonant converter (SRC) has been extensively used for capacitor charging power supply (CCPS) applications. However, SRC does not inherently behave as a constant-current source (except for operation in discontinuous mode with switching frequency below half the resonant frequency) and complex control methods such as dead-time control, variable frequency control and constant on-time variable frequency control are required for controlling the charging current. The circuit diagram is shown in Schema 1 and Figure 1.

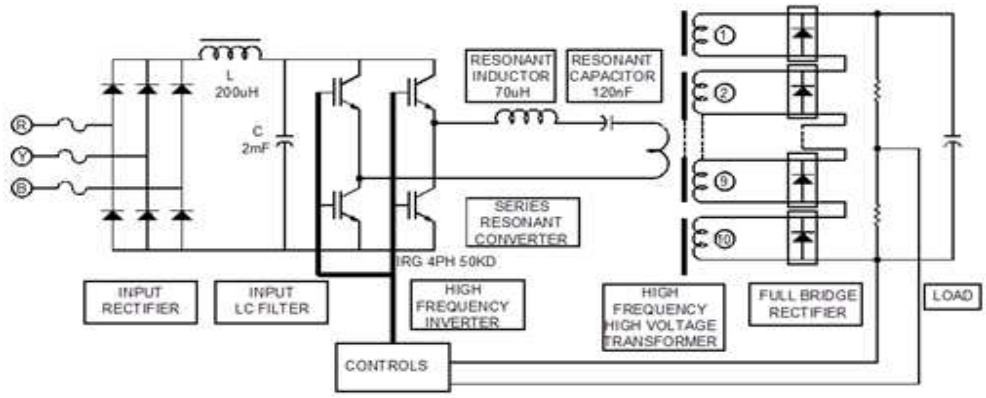

Schema1: Circuit diagram of series resonant CCPS

The supply operating frequency is 25kHz and resonant frequency is 55kHz. The inverter switches are operated in Zero current switching (ZCS) and it minimizes the switching load. The inductor is 70μH and resonant capacitor is 120nF. The most important design is transformer design, because the resonant topology is very sensitive to transformer parameters. These parameters will change the resonant frequency and change the operation of design. The high voltage high frequency transformer is modular type. We have selected ferrite toroidal cores (10 nos) having 5 turns common on primary. The transformer secondary's are individually rectified and added to get 30kV output. The cores are grounded to reduce the coupling capacitor between primary and secondary. This will reduce the common mode coupling from output to input. The maximum value of coupling capacitance is analysed to have low over voltage across inverter IGBT. This supply has been used to charge EMM having 40kJ system. The charging voltage varies from 16kV to 28kV and discharging through welding coil. The reversal comes across the power supply due to mismatched load, the resistive and diode combination is employed to prevent against the voltage reversal. The supply has been reliably operated with this system.

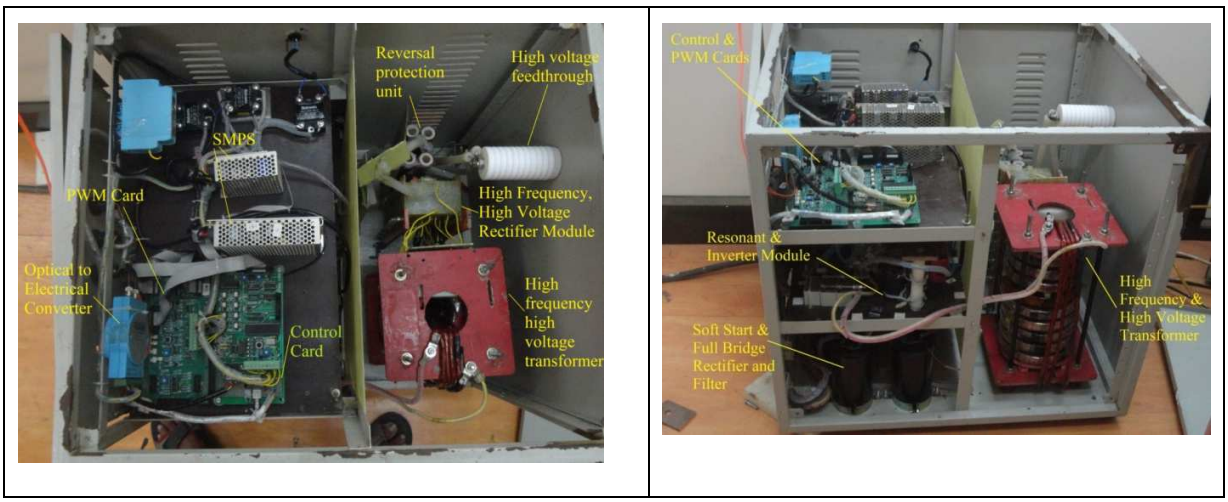

Fig.1: Top view and side view of 3kJ/s CCPS

Series resonant topology provides inherent zero current switching (ZCS) when it is operated under discontinuous conduction mode, since in discontinuous conduction mode, dead time in which the current flowing through the IGBT switches is zero. This time the switch over takes place in the inverter circuit. The discontinuous conduction mode of operation is possible when the resonant frequency is twice or more than twice the switching frequency (i.e. $f_r \geq 2f_s$).

Especially in capacitor charging power supply, since this power supply load is a capacitor and it is a dynamic pulsed power load. Protection against voltage reversal has been employed using Diode resistor combination. Short circuit Protection in switches: It has been employed by collector emitter de saturation technique. Protection against dv/dt and di/dt: In which we provided RCD snubber circuit across CE terminals of all switches and across input rectifier diode. Common mode noise: It has been mitigated by grounding the high voltage high frequency core. Fig.1 shows the top view and side view of CCPS. It shows the high frequency transformer,

control card, PWM card, softstart, full bridge rectifier and filter module, high frequency high voltage rectifier module.

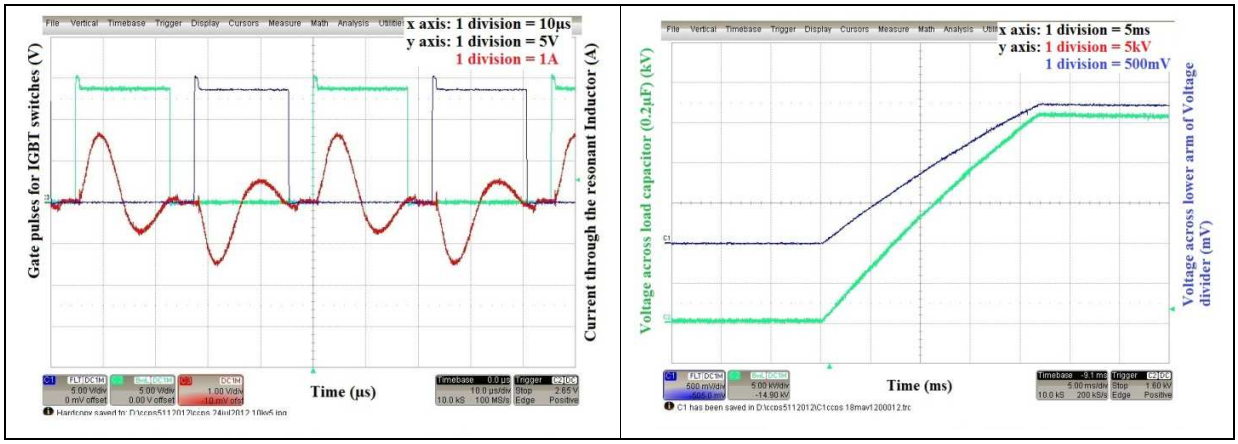

Fig.2: Experimental results (a) Current through I_{Lr} to verify ZCS (b) Voltage across load capacitor (0.2µF

Experimental results shown in Figures .2(a) and 2(b) are confirms the charging voltage across load capacitor (0.2µF) and soft switching (ZCS). The load capacitor charged to 27kV in 22ms which matches with simulation. Achieved ZCS at 22 kHz in experimental.

50kJ/s, ±50kV, 1A bipolar CCPS for 1kJ Marx based pulsed power system

Basic block diagram of CCPS along with pulsed power system is shown in Figure.3. It consists of charging source followed by pulse power system, where energy storage capacitors are located then followed by pulsed load, where total energy has to be dumped across the pulsed load. The detailed circuit diagram has been shown in Figure.3. Starting from 3-phase supply to pulsed load hole circuit is divided into seven stages (i.e. S-1 to S-7).

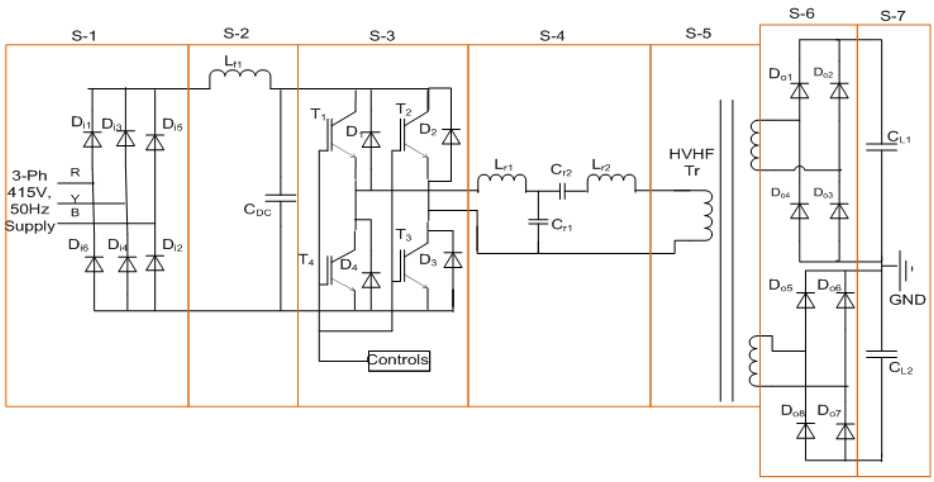

Fig.3: Circuit diagram of power supply and pulse system with pulse load

Topological structure of proposed 4th order LCLC resonant topology is shown in Figure.4. Mathematical analysis carried out to find out the conditions for load independent constant current and condition for ZCS switching. Inductance L_{r1}, C_{r1} and $L_{r2}C_{r2}$ are the resonant inductances and capacitances connected in T-fashion to form a 4th order resonant network. The input is a simple square wave voltage source, where as the load capacitor is shown is an equivalent capacitance reflected to primary of HFHV transformer to make circuit simple to carry out the mathematical analysis.

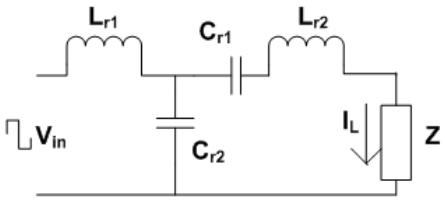

Fig.4: Topological structure for mathematical analysis

Where X_1=sL$_{r1}$, X_2= 1/sC$_{r1}$, X_3 = sL$_{r2}$+ (1/sC$_{r2}$) and Z = n^{2}C$_L$

On applying kirchoff's voltage law(KVL) and kirchoff' current law (KCL) in the circuit, the load current I_L has been calculated as

I_L Is independent of Z at ω_o and it is given by

$$\omega_o = \sqrt{\frac{xy}{2L_{r1}C_{r1}}} \quad (1)$$

Imaginary part of Z_{TOT} make to zero at ω_0 for ZCS

$$xy = 1+ y \quad (2)$$

Where $x=\frac{L_{r2}}{L_{r1}}$ and $y = \frac{C_{r2}}{C_{r1}}$

Current through resonant inductor L_{r1} at ω_0 is given by

$$I_{Lr1rms} = (Vrms/\omega_o L_{r1}) \text{ at } \omega_0 \quad (3)$$

Where $L_{r2} = 2L_{r1}$ and $C_{r2} = C_{r1}$

From the above equations, it is clear that this resonant topology is suited for the capacitor charging power supply with inherent property of short circuit proof, wherein it can provide constant current, ZCS switching or zero voltage switching.

Experimental setup

Rating of the capacitor charging power is given in the following table.

Table1: Rating of power supply

Input supply	**415V,3Phase**
Repetition rate	**10Hz**
Charging voltage	**±50kV**
Load capacitor	**0.9µF for +ve0.9µF for –ve**
Peak charging rate	**45kJ/s**

The current flowing through the load capacitor with the given data is shown in table. The equivalent RMS value of current flowing through the primary has been calculated. By using equations resonant inductors (L_{r1} and L_{r2}) and capacitors (C_{r1} and C_{r2}) and there values are 18µH, 36µH, 3.54µH and 3.54µH respectively.

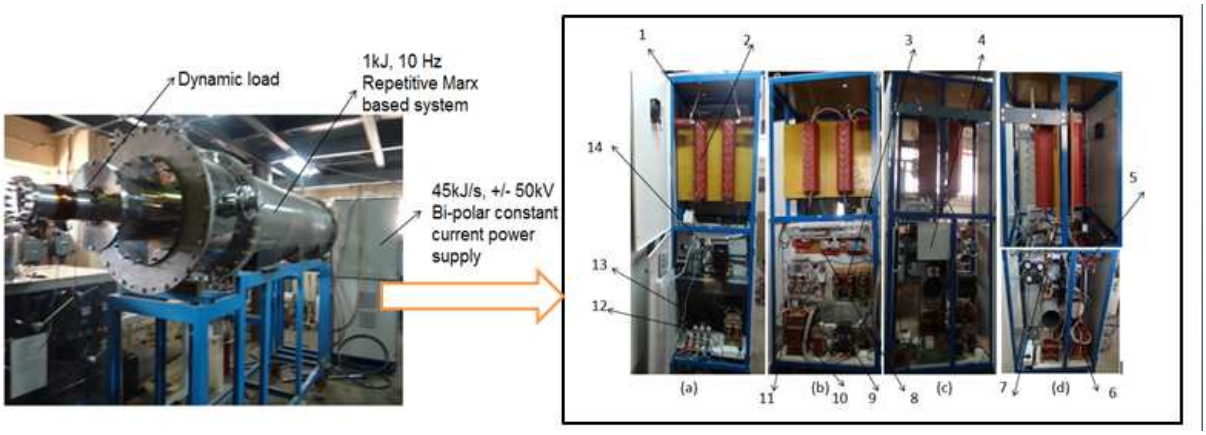

Fig.5: Experimental setup facility of 1kJ, 10Hz repetitive Marx based system along with CCPS (In box Front, Back, Left hand and Right hand side views of CCPS)

1. HVHF transformer. 2. HF diode rectifier. 3. Bleeder resistor of DC link capacitor. 4. Control and low power electronics box. 5. Resonant capacitors (3.54µH each). 6. Heat sink. 7. IGBTs. 8. Resonant inductors (18µH and 27µH). 10. Soft start. 10. 3-Phase line filters. 11. 3-Phase diode rectifier. 12. Input fuses. 13. DC Filter inductor. 14. DC link capacitors

Another important design in the power supply is development of high voltage high frequency ((HVHF) transformer. A HVHF transformer with a selected switching frequency of 20 kHz has been developed in the laboratory to provide ±50kV voltage. For the development utilized ferrite core with OD = 100mm, ID = 55mm, height = 20mm and effective core area = 436mm^2 with maximum flux density of 0.2wb. Experimental setup of 10 Hz repetitive pulse power system facility with dynamic load with the developed 45 kJ/s CCPS has been shown in Figure 5.

Results

Charging voltage across load capacitor (0.9µF) for both (+ve and –ve) are showed separately in Figure.6. The experimental set up has been tested with 0.9µF both for +ve and –ve to charge 38kV in 40ms. There is slight decrement in the charging voltage as per calculation due to the lead inductances. Positive voltage charging profile is shown in Figure.6(a) and negative voltage charging profile is shown in Fig. 4(b).

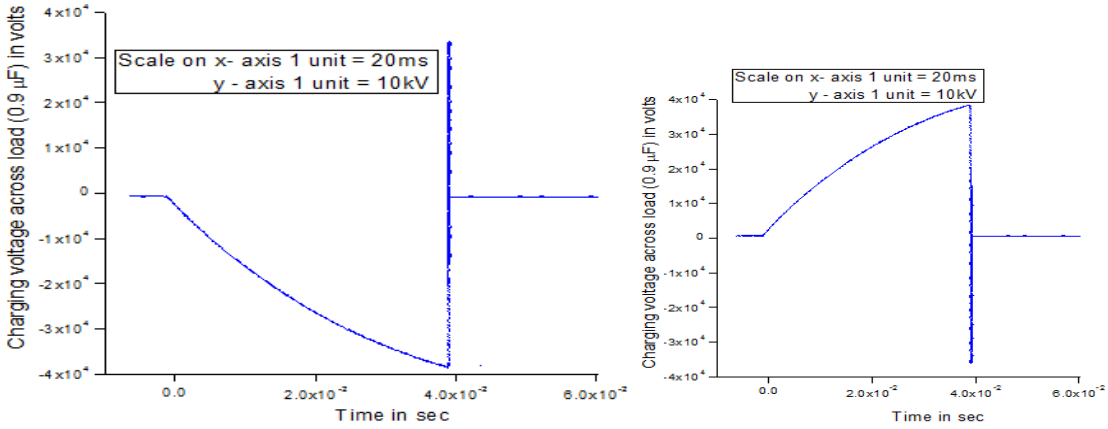

Fig. 6: Voltage across load capacitor (0.9µF) (a) +ve Charging (b) –ve Charging

Charging and discharging profile across load capacitor (0.9µF for +ve) with a repetition rate 5Hz has been in Figure.7.

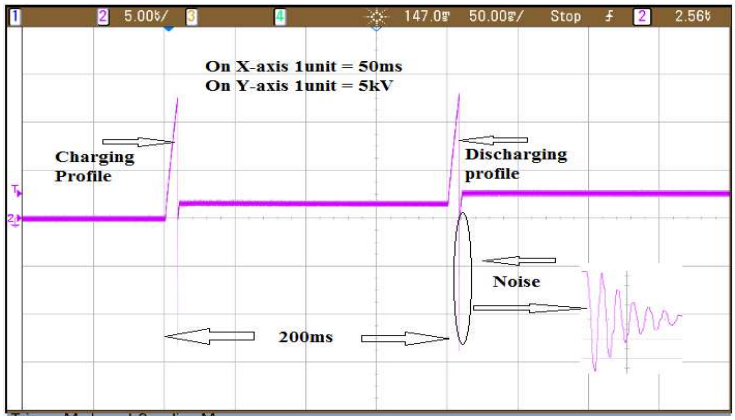

Fig.7: Voltage profile across 0.9µF capacitor (+ve) with 5Hz repetition rate

Zero current switching and zero voltage switching are achieved experimentally by adjusting switching frequency. At 21.5 kHz achieved ZCS and by adjusting dead time achieved the ZVS is presented in Figure 8.

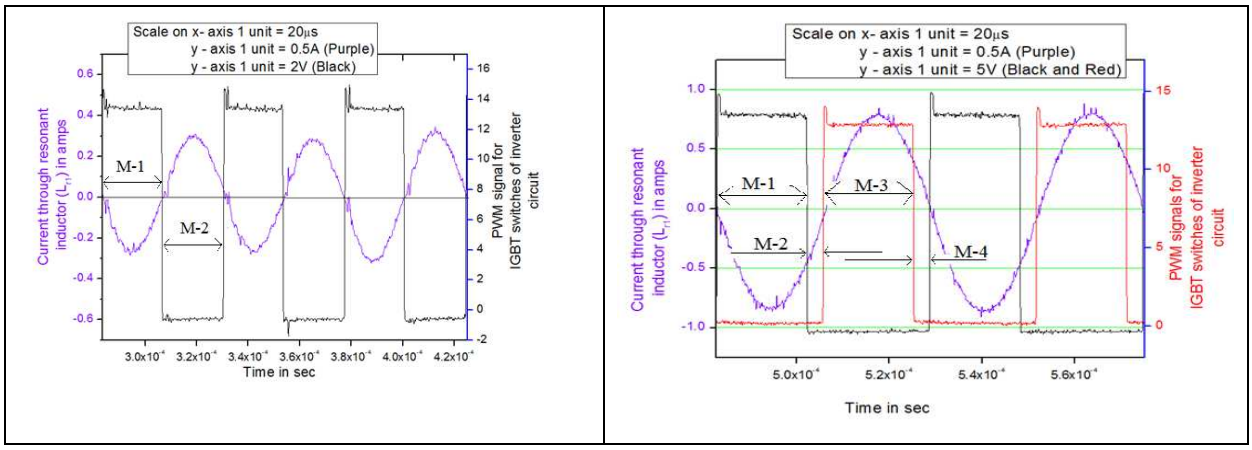

Fig.8: Soft switching (a) ZCS (b) ZVS

Conclusion

The capacitor charging power supplies (3kJ/s and bipoar 50kJ/s) are designed, developed and commisioned with pulse power systems. Protection circuits are working satisfactorily to avoid dynamic noise generated by pulsed power systems. The resonant converters were used for ZCS and ZVS operation of inverter IGBT's, so switching losses becoes negligible hence improve the efficiencies. The 3kJ/s and 50kJ/s power supplies has the efficiencies of 89% and 85% respectively.

DEVELOPMENT OF TECHNOLOGIES FOR REMOTE SURVEILLANCE AND RADIATION MEASUREMENT

S. S. Saini[1], U. Sarkar[1], T.Teja Swaroop[1], D. D. Ray[1], D. N. Badodkar[2]
Division of Remote Handling & Robotics,
[2]Design Manufacturing & Automation Group

Shri S.S. Saini is the Recipient of the DAE Young Engineer Award for the year 2013

Abstract

In view of recent nuclear accidents like that in Fukushima Daiichi, the necessity for remote radiation measurement, as a first step in crisis management has been felt in the nuclear technology community. Also, some regular maintenance works in nuclear facilities result in substantial radiation exposure to human workers. All these have provided an impetus to the development of robots capable of remote radiation mapping and visual surveillance inside nuclear installations; accordingly various prototype systems have been developed at DRHR, BARC. These robots have been designed to negotiate uneven terrain including staircases. The first prototype CTR01 included a single camera with night vision. The second prototype RAD01 is equipped with multiple cameras and a retractable radiation detector. The robots can be remotely controlled over wireless communication links with a computer. The control software, through its seamless interface, allows for easy viewing and logging of visual/radiation data in real time. Preliminary field trials have been taken for the robot with retractable Teletector.

Material and Methods

The basic structure of the first prototype was made of Mild Steel. Its wheels are made from engineering plastics and the drive belts are made up of rubber composites. Additionally, engineering plastic materials have been used to construct gears. The CTR01 is driven by four tracked belts in differential drive mode and it can climb a ramp/staircase up to 30 degrees. Effective staircase negotiation has been made possible by making remotely adjustable swing arms. The design of the robot has been advanced from the earlier developments by Kan Yoneda, Yusuke Ota and Shigeo Hirose[1]. The control software for the robot consists of a drive firmware in the robot's microcontroller and the supervisory firmware in the Hand Held Control Terminal (HHT). Figures 1 to 5 show the CTR01 in its various modes of operation.

Fig. 1: Climbing Stairs

Fig. 2: Down the Staircase

Fig. 3: Opening a door

Fig. 4: Going on a slope

Fig. 5: Hand Held Terminal

The RAD01 Robot is driven by six tracked belts with a differential drive and it can climb ramp/staircases up to 30 degrees with the help of Tele-operable swing arms. It has three cameras for navigation including infrared cameras for low light operation. The radiation detector is composed of two GM tube sensors[2]. One tube covers the range from 0.01µSv/h to 10mSv/h and the other tube covers the range from 0.01mSv/h to 10Sv/h. The radiation sensors are placed on a remote controlled electrically driven retractable telescopic mechanism with three degrees of freedom. Onboard batteries provide the robot a continuous run time of one hour.

Both the robot and the retractable telescopic mechanism can be controlled from a Joystick attached to remote computer via an RF link. A separate RF link is provided for collecting and logging the measurement data from the radiation sensors. The remote computer provides multiple camera view panes, graphical display of the robot pose, real time display of radiation measurement, video and data logging, remote range selection, sensor linearity calibration via keyboard and configurable alarm set points for dose as well as dose rate.

Results and Discussion

The first successful demonstration of the RAD01 robot has been carried out at WIP, BARC for measurement of radiation levels[3] inside one HEPA filter bank room as well as outside the pre filter bank area. The robot had been continuously run for one hour on site. The peak radiation level at the time of operation was found to be about 160mR/hr. The radiation level outside biological shield was about 20mR/hr. The radiation detector was used with removable booting for easy decontamination.

The trial run although successful revealed the necessity of stereoscopic vision for better navigation. This venture went on to prove that even in very cluttered environment, remote measurement of radiation can be done in a user friendly manner thereby reducing the exposure of human workers to harmful radiation.

Fig. 6: RAD01 Robot Side View

Fig. 7: Trials at HEPA Filter Room, WIP

Acknowledgements

We acknowledge the whole hearted industrial support from Shri P. Taktawala of M/S Zenn Systems Ahmedabad for making the fabrication of these application specific robots possible in a reasonable time span. We also acknowledge the motivation and support by our Ex. Group Director Shri Manjit Singh for without his visionary decisions, the development of these technologies would not have been possible.

References

1. Kan Yoneda, Yusuke Ota and Shigeo Hirose (2010), Stair Climbing Robots and High-Grip Crawler, Climbing and Walking Robots, Behnam Miripour (Ed.), ISBN: 978-953-307-030-8, InTech, DOI: 10.5772/8843.
2. ANSI/IEEE Std. 309-1999/N 42-3-1999 (R2006) "IEEE Standard Test Procedures and Basis for Geiger–Mueller Counters" U.S.A. 2006.
3. IAEA (2004), Workplace Monitoring For Radiation and Contamination: Practical Radiation Technical Manual. Vienna.

BARC NEWSLETTER
FOUNDER'S DAY SPECIAL ISSUE 2015

DEVELOPMENT OF COMPACT HIGH VOLTAGE LOW INDUCTANCE ENERGY STORAGE PULSE CAPACITORS

Ravindra Kumar Sharma
Advanced Technology Systems Section, Electronics and Instrumentation Group

Shri Ravindra K. Sharma is the Recipient of the DAE Young Engineer Award for the year 2013

Abstract

A research effort has been put to develop high voltage, high energy density, low inductance energy storage capacitors for high-current delivery capacity in sub micro seconds time. High voltage energy storage capacitor is the basic building block for any pulsed power system. This is true in systems such as fast Marx generators, Electromagnetic pulse (EMP) systems, lasers, Flash X-ray, High Power Microwave (HPM) generation, beam generation, Fusion research etc. Low inductance energy storage capacitors up to 50kV, and 25nH are being designed and developed for the different pulse power applications.

Introduction

World-wide, there is an urgent and unfulfilled need for reliable technique to develop oil-free, non-standard geometry, low inductance and high energy density (by volume and weight) energy storage capacitors. Energy storage capacitors are used extensively in pulsed power systems as primary or intermediate energy storage units. Internal construction of the capacitor can have significant effect on system performance in very fast low inductance high voltage pulse power systems.

Bi-axially oriented polypropylene (BOPP) film and the Aluminum foil with extended foil compact design is a combination which delivers moderately high power. This comes closest to fulfilling the need. Low viscosity, high dielectric constant, electrical grade thermally curable resin system has been used as impregnate of these pulse capacitors.

BOPP Film-foil design adoption in practice is made difficult by its weak points (volume electrical break down), relative permittivity and the edge gap margins to avoid the surface flash over discharge. A concept for implementing above combination in a less complex and costly manner has been developed in lab. This requires some novel design of the on-line impregnation capacitor machine, development process techniques to use thermally curable resin system (dielectric constant – 4, dielectric strength – 20kV/mm) and low inductance high current lead-less electrical connection technique. This paper concerns the development and testing process techniques for two quite different non-standard geometry configuration oil-free hollow cylindrical capacitor (5µF, 10kV, 20nH) and flat format pulse capacitor (4µF, 5.5kV, 10nH) with center rectangular hollow space for low inductance connection.

Design and Construction Challenges

The on-line impregnating capacitor winding machine

A special purpose capacitor winding machine has been custom designed to our specification and is in operation. Many layers of dielectric film (BOPP, 12µm) and aluminum foil (6 µm) are assembled and passed through an impregnating liquid, which is a thermoset low viscosity resin. The impregnated assembled stack of dielectric films and aluminum foils is wound up in application specific manner. Excess resin is removed, electrical connections are applied to the aluminum foils and resin is cured.

Processing of the uncured resin for the next winding

Unused excess resin was filtered and degassed to be used for the next on-line impregnating cycle. We have to take care that the resin system should be less exposed to the UV light as it has the inherent property of the curing at room temperature.

How to build low inductance connection in non-standard geometry capacitors

The advantage of the extended foil construction has a much higher current carrying capability and strong metal electrodes electrical connections directly seating on the aluminum foils. This confirms good mechanical strength against electromagnetic forces during high current discharges. This also ensures low equivalent series inductance (ESL) and equivalent series resistance connections for fast discharging pulsed power applications. There is a practical limit to how high in voltage; a single capacitor section can be operated. As the voltage increases, the field between the electrodes increases causing high areas of stress concentration particularly at the edges of the electrodes. While this practical limit varies with capacitor design and application, it is usually below 12kV for pulse power applications. Both flat-format and hollow cylindrical capacitors are of extended foil construction and the working voltage is less than 12kV as shown in Fig. 1 & 2. Because of the parallel plate transmission line geometry is maintained with large width and small gap between the strip lines, removal of bushing and oil metal Can in the capacitor design, we get very low self inductance of the capacitor elements.

Fig. 1: Flat format pulse capacitor 4µF, 5.5kV

Performance Data

Shot life (charge-discharge cycle) of 1000 has been experimentally performed on the capacitor test bed at its rated energy density level.

Fig. 2: Hollow cylindrical pulse capacitor 10kV

Insulation resistance of 2000MΩ and voltage reversal of 80% is also experimentally measured. Capacitance and dissipation factor change is confirmed less than 2% after testing at 11kV DC for 60seconds. The self inductances of these capacitors have been important. Inductive pick up for inductance measurement for 5µF, 10kV capacitor is shown in Fig. 3. The inductance values of 21nH and 10nH were measured for 10kV and 5.5kV capacitors respectively. The process and engineering techniques necessary for manufacturing and testing the BOPP based oil-free capacitors are now available and used.

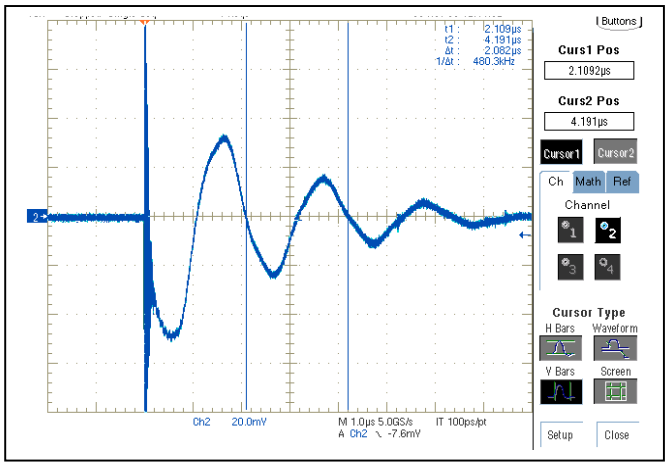

Fig. 3: Inductive pick up (T=2.0µs) for inductance measurement for 5µF, 10kV capacitor

Conclusion

Oil free capacitors with limited life often have higher capabilities than previous generation oil filled capacitors. Now, film-foil based low inductance energy storage capacitors can operate at higher energy density (> 0.1J/cc for flat format 4µF, 5.5kV, 10nH capacitor and 0.08J/cc for hollow cylindrical 5µF, 10kV, 20nH capacitor), which require less volume by 30% and less weight by 50% compare to market available capacitors. Voltage reversal of 80% was experimentally measured. New pulse power systems are now being developed taking into account the improved properties of the oil-free low inductance energy storage capacitors.

Acknowledgement

Author is grateful to Shri C. K. Pithawa, Director, E&I Group and Shri Y. S. Mayya, Associate Director, E&I Group for their continuous support, valuable suggestions and encouragement in development of this technology. The author also gratefully acknowledge & thank Shri Satish G Chavan and Shri Manoher A Gurav, ATSS, E&I Group, BARC for their assistance at various stages of the high voltage pulse capacitor development and testing.

BARC NEWSLETTER
FOUNDER'S DAY SPECIAL ISSUE 2015

SMALL ANGLE SCATTERING STUDIES ON ASSEMBLY OF COLLOIDS

Jitendra Bahadur
Solid State Physics Division

Dr Jitendra Bahadur is the recipient of the DAE Young Scientist Award for the year 2013

Abstract

The important aspects of assembly of colloids have been probed using small-angle X-ray and neutrons scattering. It has been shown that real time small-angle scattering measurement is very powerful method to study the assembly process. Nature of jamming of the colloids in the assembled grains has been described for various physicochemical parameters. The internal structure and overall morphology of the assembled grain has been investigated using small-angle scattering and electron microscopy, respectively.

Introduction

Small-angle scattering (SAS) using neutrons and X-rays has been utilized across all the discipline of science such as physics, chemistry, materials science, metallurgy, polymer, biology etc. [1-3]. SAS probes the density fluctuations from sub nanometer length scale to micrometer length scale [4]. Schematic -1 shows the various length scales and suitable techniques probing those length scales. The electron microscopy and neutron/x-ray scattering techniques appears to be most suitable techniques to probe mesoscopic (sub nanometer to sub-micron) length scales. Although electron microscopy provides direct morphology however it remains a local probe of the structure due to limited penetration power of electrons in the materials.

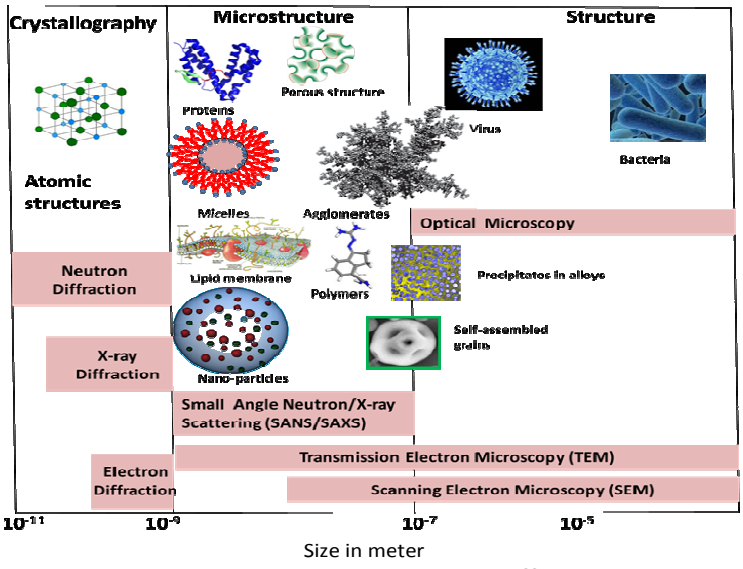

Schematic 1: Various techniques to probe the different length scales

X-ray and neutrons scattering gives statistically averaged information of the structure in reciprocal space and require model fitting for data interpretation. In general electron microscopy is used as a complementary technique in conjunction with small-angle X-rays scattering (SAXS) and small-angle neutron scattering (SANS). Due to wide range of applicability of this technique various SAS instruments have been developed at various synchrotron and neutron sources across the world. Due to high flux of the X-rays at the synchrotron sources, dynamic processes such as nucleation and growth in millisecond time scale can be studied. A synchrotron based SAXS instrument is under design and development stage at INDUS-II synchrotron at RRCAT, Indore.

Due to completely different scattering power of H and D for neutrons, SANS has special advantage. One can resolve complex structure especially using hydrogen and deuterium labeling. The contrast matching experiment is quite popular in soft matter and biology. Recently, hydration of cement has been studied quite extensively [5-7] using SANS due to high scattering cross-section of neutron for hydrogen which is otherwise not possible with X-rays. The real time measurements on hydration of cement with H_2O and D_2O show strikingly different behavior for the first time [5].

National facility for neutron beam research at Dhruva reactor managed by Solid State Physics Division of BARC operates two SANS instrument to cover wide length scales. To compliment the SANS data, a laboratory based SAXS facility is also available at SSPD, BARC. Laboratory based SAXS instrument has also been utilized extensively for investigating variety of systems such as polymer-nanocomposites, colloids, biomaterials, alloys etc.

In this article, we present a study on evaporation induced assembly (EISA) of colloids confined in the droplets. EISA finds its application in ink-jet printing, fuel injection, drug delivery and food industry. During drying of a colloidal droplet, various physico-mechanical processes take place, which in turn decide the morphology of resulting assembled grain. A dimensionless parameter, Peclet number Pe ($=R^2/D\tau_{dry}$, R is droplet radius, D is diffusion coefficient of the NPs and τ_{dry} is the drying time) can be defined to demarcate two drying regimes. If Pe >>1, the drying process is regarded as fast and there is a possibility of formation of hollow or doughnut/crumpled grains. However, if Pe<< 1, drying process is regarded as slow and droplet shrinks isotropically throughout drying process resulting uniformly jammed spherical grain.

Recently, spray drying experiments have been carried out in both the regimes, slow and fast, which led to spherical [8] and doughnut [9] grains, respectively. It has been shown that the tailored morphology such as buckball type structure [10] and porous microcapsules [11-12] can be achieved by modifying the physicochemical parameters during drying. Drying of the droplets containing mixture of two or more different type of colloids gives solid state dispersion of the nanoparticles [13]. The assembly of mixed colloids where one component is used as a template can provide porous grains for variety of applications [14,15].

Here, we present real time SAXS investigation on the drying of single droplet and studies on the assembled grain obtained using spray drying. The present work has been performed using the facilities at SSPD, BARC and abroad.

Real time SAXS experiment on assembly of colloids

The colloidal droplet was suspended with a narrow tip and initial size of the droplet was approximately 2 mm. In order to estimate the size of the colloids, SAXS experiment was performed using a laboratory based instrument.

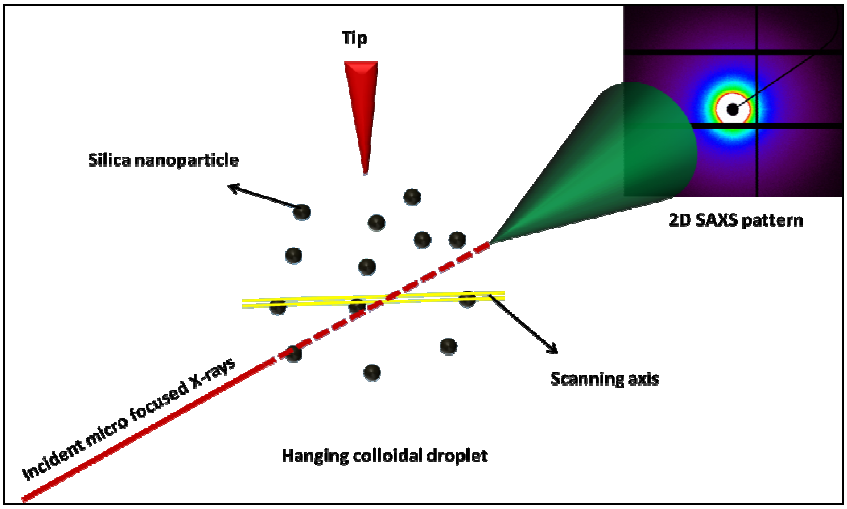

Fig. 1: The experimental set-up of the drying of single colloidal droplet

Figure. 1 shows the schematic of the experimental setup for an *in-situ* experiment on drying of single colloidal droplet using a micron size beam at a synchrotron source [16-17].

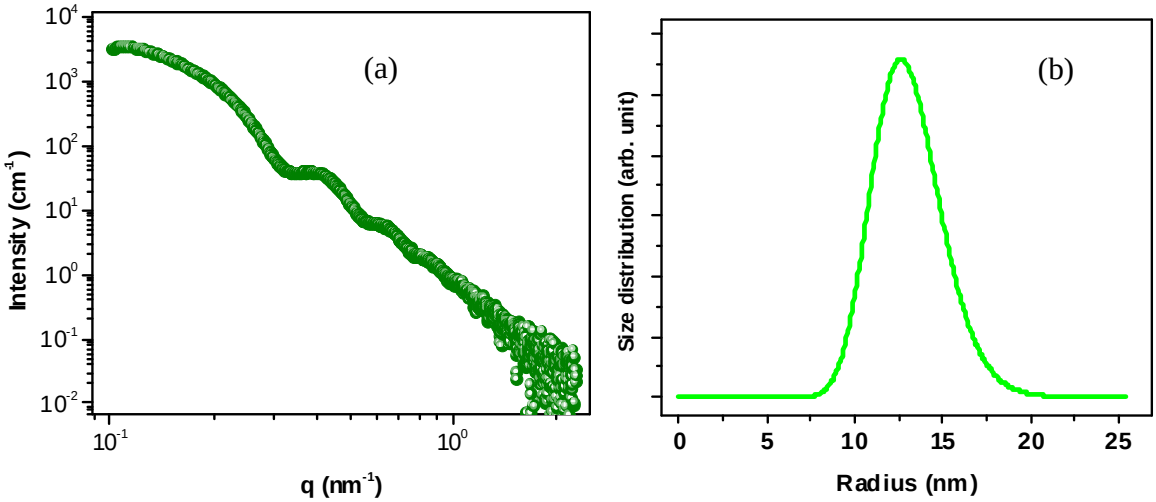

Fig. 2: The SAXS profile (left) of the colloids before assembly process and calculated size distribution (right)

Fig. 2a shows the scattering profile for a dilute silica colloid. The SAXS data was fitted using polydisperse sphere model to estimate the size distribution of the colloids. The size distribution of colloids is shown in Fig. 2b. The average radius of the silica colloids was found to be ~12 nm. The evolution of the scattering profiles during drying of the droplet containing the silica colloids

is shown in Fig. 3a. The scattering pattern shows a significant change during drying of the droplet. Initially, the concentration of nanoparticles in the droplet is small and we do not see any significant peak in the scattering profile. The droplet shrinks during drying and this leads to increase in the concentration of the nanoparticles in the droplet. We start to observe broad peak in the intermediate stage of drying and subsequently scattering profile possess sharp peak. The peak in the scattering profile in present case comes due to inter-particle structure factor. The peak position is inversely related to the distance between the colloids. The evolution of the peak position is shown in the Fig. 3b. The position of the peak increases with drying of droplet. This indicates that distance between the colloids decreases with drying, i.e. nanoparticles come closer as drying progress. The position of the peak reaches to a plateau region at the end of drying.

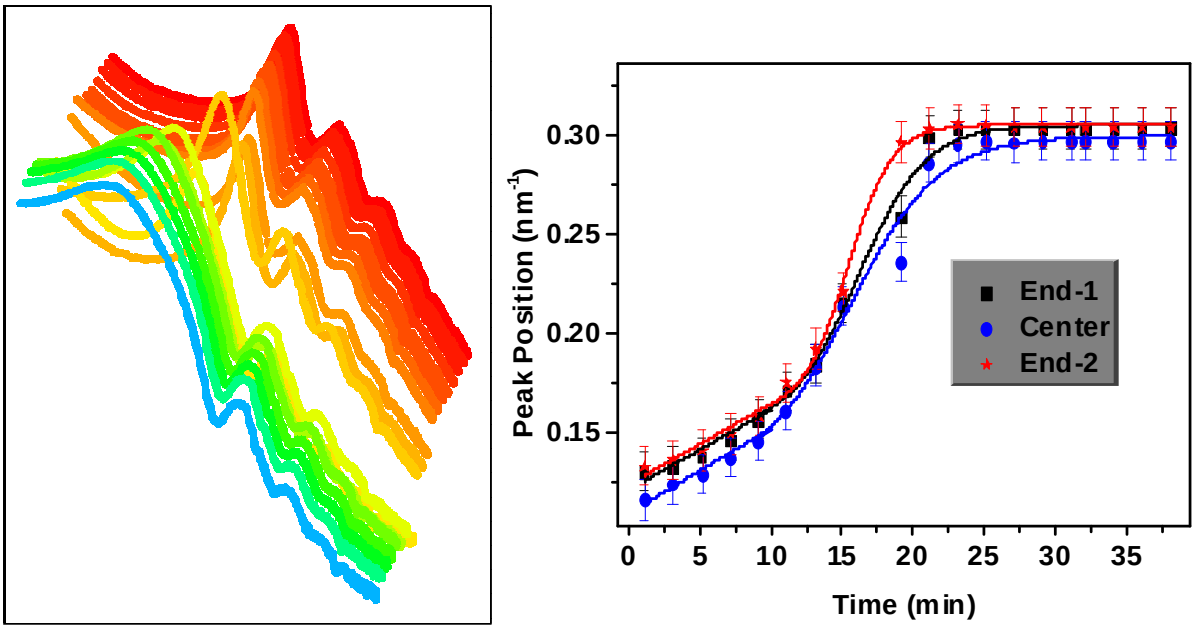

Fig. 3: Evolution of scattering intensity (left) and peak position (right) during assembly of colloids confined in a droplet.

Thus, it is clear that pathways of assembly of colloids can be tracked by real time SAXS measurements. Moreover, the shrinkage of the droplet and nature of jamming of colloids can be monitored using transmission as well as real time scanning SAXS experiments [16,17].

SAXS/SANS studies assembled grains

The drying of the colloidal droplets has been utilized to obtain the assembled grains of nanoparticles by spray drying. The assembled grains obtained using spray drying of silica colloids of ~12 nm radius is depicted in Fig. 4. The jamming of the colloids is also shown in the magnified view. It is evident from the micrograph that doughnut shaped assembled grains is achieved which is realized in fast drying regime. It is also clear from the zoomed view that silica nanoparticles are jammed in the ordered state; however the ordering of nanoparticles remains short range.

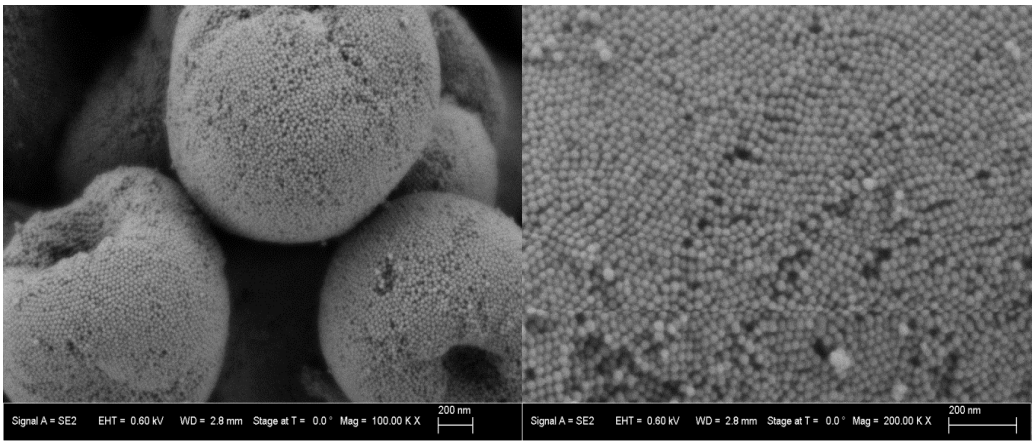

Fig. 4: The electron micrograph of the assembled grainsand low (left) and high magnification (right)

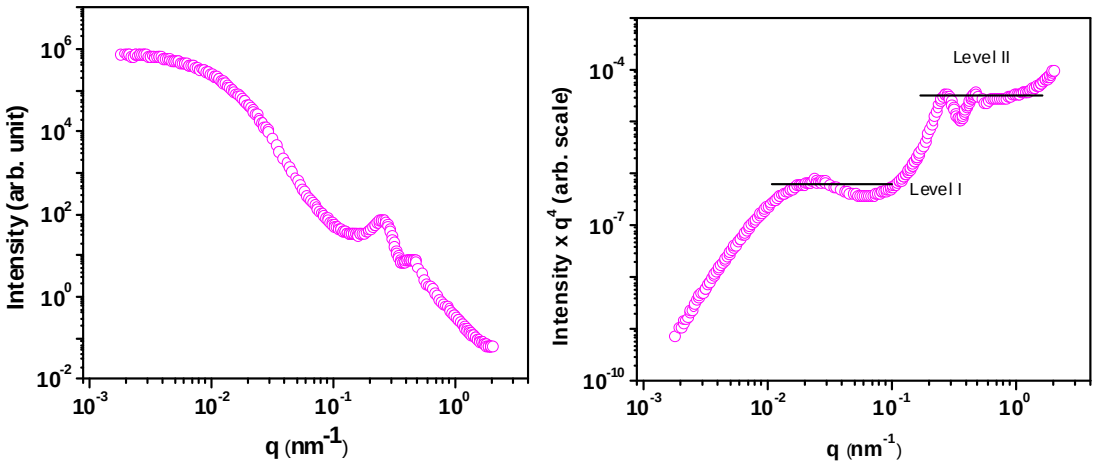

Fig. 5: The SANS profile of the assembled grains in (left) double logarithmic scale and (b) Porod representation

The packing fraction of the colloids and the specific surface area of the mesopores due to interstices between jammed colloids cannot be achieved from SEM micrograph. Although scanning electron microcopy can show overall morphology of the grains, it cannot probe the internal structure of the grains except the structure at the surface. In order to get the internal structure, SANS experiment has been carried out on these grains.

Fig. 5 shows the SANS profiles in double logarithmic scale (left) and in Porod representation ($I(q) \times q^4$ vs q) (right). The two constant levels in Porod representation are indicative of two length scales. The packing fraction of the nanoparticles is obtained by fitting of the SANS profiles and its value is found to be ~0.50 which is indicative of random jamming of the colloids. The specific surface area of themesopores can be estimated using the Porod level II and the aspect ratio of the particle can be calculated using the ratio of two Porod levels.

Conclusion

Small-angle scattering is a versatile technique to address the issues in mesoscopic scale in many branch of science. Real time SAXS/SANS technique is useful to study the kinetics, in particular, during assembly of colloids and hydration of cement. Evaporation induced assembly of colloids is an important tool to fabricate the porous, hollow and nano-composite micron sized grains. SANS and SAXS provides the internal structure such as packing fraction and mesopore surface area of the assembled grains.

Acknowledgements

The encouragement and support from Dr. S. Mazumder is greatly acknowledged. I would like to thank Dr. Debasis Sen for his support throughout the work. I am also thankful to my collaborators associated to the present work.

References

1. P. Fratzl *J. Appl. Cryst.*2003, 36, 397-404.
2. B. Chu and B. S. Hsiao *Chem. Rev.* 2001, 101, 1727−1761
3. C. E. Blanchet and D. I. Svergun *Ann. Rev. Phy. Chem.* 2013, 64, 37-54
4. A.Guinier, G. Fournet *Small-angle scattering of x-rays. New York: John Wiley & Sons*1955.
5. S. Mazumder, D. Sen, A.K. Patra, S.A. Khadilkar, R.M. Cursetji, R. Loidl, M. Baron, H. Rauch *Phys. Rev. Lett.* 2004, 93 (25), 255704
6. S. Mazumder, D. Sen, J. Bahadur, J. Klepp, H. Rauch, J. Teixeira *Phys. Rev. B* 2010, 82 (6), 064203.
7. D. Sen, S. Mazumder, J. Bahadur *Phys. Rev. B* 2009, 79 (13), 134207
8. J. Bahadur, D. Sen, S. Mazumder, B. Paul, A. Khan,G. Ghosh *J. Colloid and Interface Sci.* 2010, 351 357–364.
9. J. Bahadur, D. Sen, S. Mazumder, S. Bhattacharya, H. Frielinghaus, G. Goerigk*Langmuir* 2011, 27 (13), pp 8404–8414.
10. J. Bahadur, D. Sen, S. Mazumder, B. Paul, H. Bhatt, S. G. Singh*Langmuir*2012, 28, 1914−1923.
11. D. Sen, J. Bahadur, S. Mazumder, G. Verma, P. A. Hassan, S. Bhattacharya, K. Vijay and P. Doshi *Soft Matter* 2012, 8, 1955–1963.
12. D. Sen, J. Bahadur, S. Mazumder, S. Bhattacharya*Soft Matter*2012,8, 10036-10044.
13. J. Bahadur, D. Sen, S. Mazumder, P. U. Sastry, B. Paul, H. Bhatt, S. G. Singh *Langmuir* 2012, 28, 11343−11353.
14. D. Sen, J. S. Melo, J. Bahadur, S. Mazumder, S. Bhattacharya, S. F. D'Souza, H. Frielinghaus, G. Goerigk and R. Loidl *Soft Matter* 2011, 7 (11), 5423 – 5429.
15. D. Sen, J. Bahadur, A. Das, S. Mazumder, J.S. Melo, H. Frielinghaus, R. Loidl*Colloids and Surfaces B: Biointerfaces* 2015, 127, 164-171.
16. J. Bahadur, D. Sen, S. Mazumder, G. Santoro, S. Yu, S.V. Roth, Y.B. Melnichenko *Langmuir* 2015, 31(16) 4612-4618.

17. D. Sen, J. Bahadur, S. Mazumder, G. Santoro, S. Yu, S.V. Roth *Soft Matter* 2014,10, 1621-1627.

NRF-2: A NOVEL REGULATOR OF THE IMMUNE SYSTEM

Rahul Checker, Deepak Sharma and Santosh Kumar Sandur
Radiation Biology & Health Sciences Division

Dr. Rahul Checker is the recipient of the DAE Young Scientist Award for the year 2013

Abstract

Nuclear factor-erythroid 2-related factor-2 (Nrf-2) is a transcription factor that plays a central role in cellular defense against oxidative and electrophilic insults by induction of antioxidative and phase-2 detoxifying enzymes. Inhibition of Nrf-2 signaling renders the organism susceptible not only to oxidative and electrophilic stresses but also results in dysregulated inflammatory responses. Activation of Nrf-2 pathway has been shown to be helpful in protection against inflammatory and auto-immune disorders. Hence, induction of Nrf-2 using redox active agents could be considered as effective means for the prevention and treatment of inflammation associated diseases.

Introduction

The well-known hallmarks of inflammation i.e. redness, swelling, heat, pain were described over 2000 years ago by Celsus and are characteristic of any kind of infection or injury. During an immune response, these symptoms of acute inflammation dissipate swiftly after the infection is cleared and the damaged tissue is repaired. However, during chronic inflammation the immune system goes into overdrive because the stimulus that triggers the inflammation persists for long time and contributes substantially to chronic diseases. While acute inflammation is an important element of the organism's defense repertoire, persistent inflammation can contribute substantially to the pathogenesis of several age-related chronic diseases such as metabolic diseases, type 2 diabetes, cardiovascular diseases, and neurodegenerative diseases. Suppression of this superfluous and chronic activation of immune cells by using immunosuppressive agents is desirable to avoid occurrence of the aforementioned inflammation associated disorders. In addition to this, successful organ transplantation also requires the use of immunosuppressive drugs to prevent the host's immune system from rejecting the transplanted organ. Immunosuppressive agents involve many classes of drugs such as inhibitors of calcium signaling and translation (Cyclosporin A, tacrolimus), inhibitors of nucleotide synthesis (azathioprine, mycophenolate mofetil), inhibitors of growth factor signal transduction (sirolimus) and also antibody therapies that eliminate specific groups of cells. Each of these drugs induces a distinct set of side effects on normal tissues which limits their long term usage and hence there is a need for identification of novel targets for regulation of chronic inflammation. Over the last decade our lab has been working towards the identification of novel targets to manage uncontrolled inflammatory responses. We have now shown that redox sensitive immuno-regulatory transcription factors can be used as druggable targets for the development of new anti-inflammatory drugs.

Cellular redox and Nrf-2 as regulators of immune responses

Cellular redox status is the ratio of the inter-convertible oxidized and reduced form of intracellular redox couples (GSSG/GSH) that work together to maintain the redox environment which is important for a variety of cellular functions such as proliferation, apoptosis and intracellular signaling. Alteration in reactive oxygen species (ROS) levels and redox status leads to abberant immune functions. Nuclear factor erythroid 2-related factor 2 (Nrf-2) is a redox-sensitive, basic-leucine zipper transcription factor [1]. It is expressed in a variety of cell types where it contributes to maintenance of redox homeostasis by regulating key cytoprotective/antioxidant genes, including glutathione (GSH), heme oxygenase-1 (HO-1), NAD(P)H:quinine oxidoreductase 1, and superoxide dismutases. In addition, Nrf-2 is also reported to regulate innate immune response that dramatically improves survival during experimental sepsis by protecting against dysregulated inflammation [2]. Under resting conditions, Nrf-2 is sequestered in the cytoplasm by the cytoskeleton-associated protein, Kelch-like ECHassociated protein 1 (Keap1) which functions as a negative regulator of Nrf-2 by promoting the ubiquitination and proteasomal degradation of Nrf-2 [3]. When liberated from its repressor Keap1, Nrf-2 translocates into the nucleus and binds to its consensus sequence in the promoter region of many genes whose products are involved in cellular defence against toxins, oxidative stress and electrophiles. A widely accepted model for nuclear translocation and activation of Nrf-2 involves alteration of the Keap1 structure by oxidation or covalent modification of critical cysteines present in Keap1. We have shown that compounds which do not show cellular toxicity and yet modify Keap1 by inducing redox imbalance may prove to be important canditates for the development of novel anti-inflammatory drugs.

Cross-talk between Nrf-2 and NF-κB

NF-κB is a redox sensitive transcription factor and central regulator of many genes involved in immune response including cytokines, chemokines, cytokine/chemokine receptors, adhesion molecules, survival genes, cell cycle regulators, acute phase proteins, and inducible effector enzymes. Since Nrf-2 is an important transcription factor responsible for maintaining cellular antioxidant capacity, it has been shown that Nrf-2 may inactivate or counteract NF-κB signaling. Pro-inflammatory genes known to be regulated by NF-κB were highly expressed upon lipopolysaccharide stimulation in Nrf-2 knockout mice when compared with those in wild-type mice. Activity of IκB kinase (IKK) and IκBα degradation needed for NF-κB activation were more pronounced in Nrf-2$^{-/-}$ mouse embryo fibroblasts (MEFs) stimulated with LPS or TNF-α [2]. Hence, agents that activate Nrf-2 by directly modifying cysteine thiols of Keap1 may lead to suppression of NF-κB and in addition these agents may also target the critical cysteine residues of p50 or IKK, thereby blocking NF-κB pathway.

Redox active agents and Nrf-2 activators as putative anti-inflammatory drugs

Based on the studies carried out by us and several other investigators, we hypothesized that redox active agents may exhibit potent anti-inflammatory activity by perturbing cellular redox and by activating Nrf-2 pathway. The studies carried out in our laboratory provide convincing evidence for redox modulation as a novel strategy for regulating immune responses and for

development of new anti-inflammatory drugs. Further, we have also shown that phytochemicals can be used to modulate cellular redox balance which would find significant application towards management of immune responses for therapeutic benefits. We have used both synthetic and plant derived molecules like naphthoquinones (plumbagin, menadione, 1,4-naphthoquinone), ursolic acid, schisandrin B etc and studied their anti-inflammatory effects [4-10]. The detailed molecular mechanisms that may contribute to their immuno-modulatory activity were also elucidated. We have for the first time demonstrated that plumbagin, (5-hydroxy-2-methyl-1,4-naphthoquinone), acts as a pro-oxidant in normal lymphocytes and suppresses mitogen induced T-cell activation, proliferation, cell cycle progression and effector functions in vitro and in vivo.

The potent anti-inflammatory effects of plumbagin were attributed to its ability to suppress redox sensitive immuno-regulatory transcription factor NF-κB in lymphocytes and macrophages. It was further revealed that depletion of intracellular glutathione levels in lymphocytes by plumbagin is responsible for the observed oxidative stress. Our results for the first time demonstrated that plumbagin indeed interacts with and forms an adduct with intracellular free thiols. It was also established that plumbagin could modulate thiol groups on critical cysteine residues of proteins by inducing glutathionylation. Plumbagin inhibited nuclear translocation and activation of NF-κB through induction of p65 glutathionylation.

Further, the in vivo anti-inflammatory potential of plumbagin was also verified using mouse models of graft-versus-host-disease, allograft transplant and endotoxin induced septic shock. Our studies highlight the potential application of plumbagin as an anti-inflammatory agent which may be used in the treatment of inflammatory disorders. Further, we also demonstrated that glutathionylation can be an important mechanism by which inflammatory pathways and signalling mediators are regulated and provide new insights into novel anti-inflammatory strategies. In addition to plumbagin, menadione, ursolic acid and schisandrin B were also shown to act as a pro-oxidant in normal lymphocytes and suppresses mitogen induced T-cell activation, proliferation and effector functions in vitro and in vivo.

All the above mentioned agents have been shown to alter redox balance leading to activation of Nrf-2 pathway and upregulation of Nrf-2 dependent genes. In our studies, we have reported that the potent anti-inflammatory effects of these Nrf-2 activator molecules were also due to their ability to suppress redox sensitive immuno-regulatory transcription factor NF-κB in lymphocytes.

In addition to this, we have demonstrated the ability of redox active molecules to ameliorate radiation induced damage to normal cells and tissues. We have shown that, contrary to conventional wisdom of antioxidants acting as radioprotectors, even pro-oxidants which induce mild oxidative stress, could offer radioprotection to normal cells [11]. The ability of these molecules to upregulate intra-cellular anti-oxidant defences and induce multiple pro-survival signalling pathways like ERK and Nrf-2 was shown to be responsible for the observed radioprotection.

Conclusions and Future Direction

Our studies highlight a potential application of redox active molecules as anti-inflammatory agents which may find application in the treatment of inflammatory disorders. Since NF-κB is a central regulator of pro-inflammatory signaling pathways, suppression of NF-κB-mediated transcriptional activity by Nrf-2 is a promising strategy to control dysregulated immune responses.

Our future challenges include development of novel immunosuppressant strategies whereby a wider choice of immunosuppressive agents will probably help physicians to minimize the burden of drug induced toxicity (side effects) in patients. The use of redox active agents derived from natural sources which have a favorable toxicity profile unlike corticosteroids and cytotoxic agents (methotrexate, azathioprine, cyclosporine) will be particularly helpful in treatment of chronic inflammatory conditions.

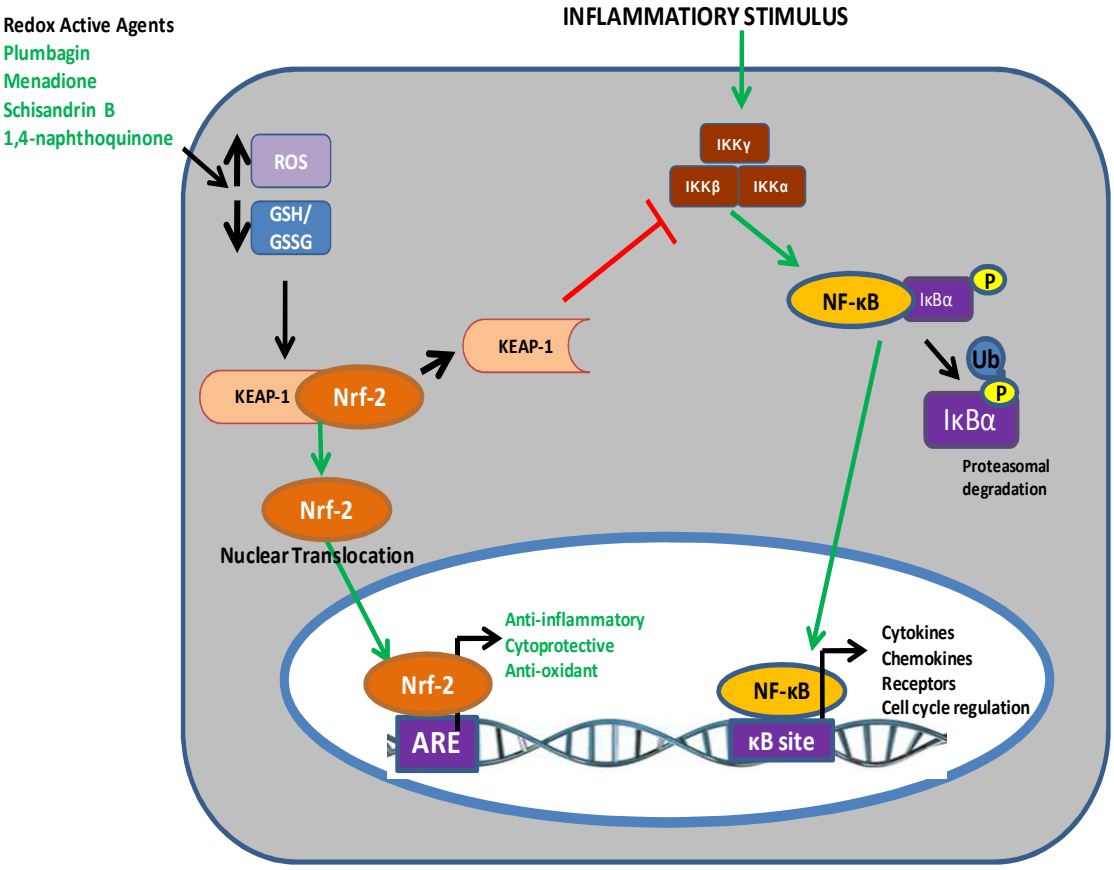

Scheme: Anti-inflammatory effects of redox active agents are mediated via activation of Nrf-2 and suppression of Nf-κB

References

1. Andrews NC, Erdjument-Bromage H, Davidson MB, Tempst P, Orkin SH. Erythroid transcription factor NF-E2 is a haematopoietic-specific basic-leucine zipper
2. protein. Nature. 1993 Apr 22;362(6422):722-8.
3. Thimmulappa RK, Lee H, Rangasamy T, Reddy SP, Yamamoto M, Kensler TW, Biswal S. Nrf2 is a critical regulator of the innate immune response and survival during experimental sepsis. J Clin Invest. 2006 Apr;116(4):984-95.
4. Kobayashi A, Kang MI, Okawa H, Ohtsuji M, Zenke Y, Chiba T, Igarashi K, Yamamoto M. Oxidative stress sensor Keap1 functions as an adaptor for Cul3-based
5. E3 ligase to regulate proteasomal degradation of Nrf2. Mol Cell Biol. 2004 Aug;24(16):7130-9.
6. Gambhir L, Checker R, Thoh M, Patwardhan RS, Sharma D, Kumar M, Sandur SK. 1,4-Naphthoquinone, a pro-oxidant, suppresses immune responses via KEAP-1
7. glutathionylation. Biochem Pharmacol. 2014 Mar 1;88(1):95-105.
8. Checker R, Patwardhan RS, Sharma D, Menon J, Thoh M, Bhilwade HN, Konishi T, Sandur SK. Schisandrin B exhibits anti-inflammatory activity through modulation of the redox-sensitive transcription factors Nrf2 and NF-κB. Free Radic Biol Med. 2012 Oct 1;53(7):1421-30.
9. Checker R, Sandur SK, Sharma D, Patwardhan RS, Jayakumar S, Kohli V, Sethi G, Aggarwal BB, Sainis KB. Potent anti-inflammatory activity of ursolic acid, a triterpenoid antioxidant, is mediated through suppression of NF-κB, AP-1 and NF-AT. PLoS One. 2012;7(2):e31318.
10. Checker R, Sharma D, Sandur SK, Khan NM, Patwardhan RS, Kohli V, Sainis KB.
11. Vitamin K3 suppressed inflammatory and immune responses in a redox-dependent manner. Free Radic Res. 2011 Aug; 45(8):975-85.
12. Checker R, Sharma D, Sandur SK, Subrahmanyam G, Krishnan S, Poduval TB, Sainis KB. Plumbagin inhibits proliferative and inflammatory responses of T cells independent of ROS generation but by modulating intracellular thiols. J Cell Biochem. 2010 Aug 1;110(5):1082-93. Checker R, Patwardhan RS, Sharma D, Menon J, Thoh M, Sandur SK, Sainis KB,
13. Poduval TB. Plumbagin, a vitamin K3 analogue, abrogates lipopolysaccharide-induced oxidative stress, inflammation and endotoxic shock via NF-κB suppression. Inflammation. 2014 Apr;37(2):542-54.
14. Checker R, Sharma D, Sandur SK, Khanam S, Poduval TB. Anti-inflammatory effects of plumbagin are mediated by inhibition of NF-kappaB activation in lymphocytes. Int Immunopharmacol. 2009 Jul;9(7-8):949-58.
15. Khan NM, Sandur SK, Checker R, Sharma D, Poduval TB, Sainis KB. Pro-oxidants ameliorate radiation-induced apoptosis through activation of the calcium-ERK1/2-Nrf2 pathway. Free Radic Biol Med. 2011 Jul 1;51(1):115-28.

BARC NEWSLETTER
FOUNDER'S DAY SPECIAL ISSUE 2015

PROBING THE RADIATION INDUCED CHANGES IN TROMBAY NUCLEAR WASTE GLASS BY SPECTROSCOPIC TECHNIQUES

M. Mohapatra[1,*] and B.S.Tomar[2]
[1]Radiochemistry Division, [2]Radioanalytical Chemistry Division

Dr. Manoj Mohapatra is the recipient of the DAE Young Scientist Award for the year 2013

Abstract

Borosilicate based glass formulations have been found suitable for vitrification of high level nuclear waste (HLW) generated during the reprocessing of spent nuclear fuel from nuclear reactors. These glasses possess desirable properties like high chemical, mechanical, thermal and radiation stability for HLW storage. Also, the amorphous nature of the glass helps to accommodate the waste containing a variety of elements easily. Because of the presence of the radioactive components, such as, fission /activation products and minor actinides present in the waste, the glass containment experiences radiation damage that can significantly alter the glass structure which may influence their long term leaching behavior. Spectroscopic techniques provide direct and non-invasive method for investigating this radiation induced changes in the glass. The present article gives a glimpse of our work on the radiation induced changes in the glass matrix as investigated by different spectroscopic techniques. It was found that although radiation causes a lot of structural changes including, breaking of bonds, formation of defect centers, modification of the glass network, unbinding, migration and segregation of ions etc. the overall glass network remains largely unaffected. Even at a cumulative radiation dose of 10^{11} Gy, no major changes were observed in the bulk glass network that can affect its long term integrity.

Introduction

Borosilicate based glass matrices have been found suitable for fixing the high level liquid waste (HLW) generated after the reprocessing of the spent nuclear fuel [1]. As the HLW composition varies according to the nature of fuel, its burn up, storage conditions, process flow sheet followed for reprocessing, so does the glass composition. In fact, for HLW generated from fast reactor fuel, iron phosphate glasses have been found suitable [2]. For the HLW generated from Indian PHWR, sodium borosilicate glass matrix containing TiO_2, MnO, BaO etc. are used for vitrification [3]. On the other hand, suitable glass formulations for thorium rich HLWs, which are likely to be generated during reprocessing of spent fuel containing thorium based fuel (from AHWR), are yet to be developed [4]. At BARC, Trombay, the historic HLW from the research reactors using metallic fuel is characterized by high sulfate content. Since sulfate solubility is very low in borosilicate glasses, a barium oxide containing alkali borosilicate glass has been developed and is routinely being used for fixing this historic waste [5]. It is well known that HLW contains the major portion of the radioactivity of the entire nuclear fuel cycle. The

radioactivity comes from major and minor actinides such as unrecovered U, Pu, ^{237}Np, $^{241, 243}$Am, $^{244, 245}$Cm (mostly alpha emitters) and have very long half lives. In addition, fission and activation products such as ^{90}Sr, ^{99}Tc, ^{106}Ru, ^{129}I, $^{135, 137}$Cs , ^{144}Ce, ^{147}Pm etc. (primarily beta emitters) also contribute to this. Because of these radioactive components present in the HLW, the glass experiences constant irradiation by α, β and γ. For the first few years of waste storage, the β decay, primarily from the short lived fission products (such as ^{90}Sr, $t_{1/2}$ = 28 years and ^{137}Cs, $t_{1/2}$ = 30 years) plays a predominant role in radiation induced changes.

After which the radiation damage due to alpha, recoil heavy ions and gamma takes over. According to Weber, the radioactive decay results in volume changes of up to ± 1.2 %, radiolytic decomposition, bubble formation along with increase in the leach rate with a factor of 3 [6]. In another review article Weber et al. have discussed about these changes in the glass matrix after radiation damage by alpha, beta, gamma, neutron and heavy ion irradiation [7]. Since the final destination of the nuclear waste glass is the geosphere (inside waste repositories), it is pivotal to assess the long term integrity and radiation damage of the glass matrix.

In this context, a systematic approach was initiated to establish the radiation stability of the Trombay nuclear waste glass matrix used for fixing the research reactor nuclear waste. The glasses were irradiated with gamma rays, electron beam and heavy ions. The electron beam can simulate the effects of beta irradiation. On the other hand heavy ion irradiation can simulate the effects of recoil damage taking place in the system. It is well known that the optimal engineering performance of a glass is dominated by its structure. Hence, the knowledge of the glass structure before and after irradiation is a prerequisite for understanding the structural evolution of glasses under long term irradiation. In addition, these studies on the borosilicate glasses will lead to an understanding of the nature of the damage which can further lead to fabrication of materials in which the deleterious effects of radiation can be minimized. Moreover, careful study of radiation induced defects can help elucidate certain structural aspects of the glassy state which are not readily accessible by other means.

Spectroscopic techniques provide direct and noninvasive method for characterization of the irradiated glass. Through these techniques one can obtain extensive information with minimal sample handling. In literature one can find various spectroscopic techniques being used for these investigations as discussed above. As no single spectroscopic technique is capable of answering all the questions related to the radiation damage of glasses, use of multiple techniques becomes imperative. For example, Electron Spin Resonance (ESR) can give information regarding the chemical nature of defect centers formed in the irradiated glass and quantify them.

On the other hand, FTIR (Fourier Transform Infra Red) and Raman spectroscopy can give information about the changes in the bulk glass network. In the present paper, highlights of some of our work are presented where radiation induced changes in these glass matrices were evaluated using conventional photon based techniques, such as photoluminescence spectroscopy (PL), FTIR and Raman. Also the usefulness of novel techniques like positron annihilation spectroscopy (PAS) and ESR in understanding the radiation damage in these glass matrices is discussed.

Glass preparation, irradiation and characterization

All the glass samples were prepared by conventional melt quench technique at Waste Management Division (WMD), BARC adopting standard procedure. The base glass compositions used for the present set of investigations are given in table-1. Gamma irradiation of the samples was done in two ^{60}Co gamma chambers with dose rates of 1 kGy/hr and 8 kGy/hr. Electron beam irradiations were done at ILU-6 (BRIT, Vashi) Navi Mumbai and EBC (Kharghar) Navi Mumbai. Heavy ion irradiations (helium and carbon ion beam) were done at BARC-TIFR Pelletron facility located at TIFR, Mumbai. PL experiments on the samples were done on an Edinburgh FLS-900 unit (Edinburgh Analytical Instruments, Livingston, UK).

ESR data were recorded on a Bruker ESP 300 spectrometer operating at X band frequency (9.5 GHz) using 100 kHz field modulation with di-phenyl picryl hydrazyl (DPPH) as the field marker. ESR data acquisition and analysis was done by WIN-EPR software and the ESR simulation studies were carried by Simfonia software from Bruker, Germany. PAS measurements were carried out with ^{22}Na positron source in the form of NaCl. FTIR data was obtained in the range 400-4000 cm^{-1} using a Bruker Vertex 80V spectrometer. Raman experiments were done on a Jobin Yvon micro instrument using Ar ion laser.

Table 1: Composition of the Trombay base glass (SB 44)

Chemical	Mol %
SiO_2	47.34
Na_2O	14.30
B_2O_3	26.80
BaO	11.56

Results and Discussion

Investigations by PL Technique

Like other glasses, the nuclear waste glasses also develop color centers when exposed to external radiation sources. The mechanism of the formation of these color centers is well known. During preparation of these glasses, several defects and impurities are formed inside the glass matrix. These defects are mostly vacancies or voids in the glass structure due to absence of an atom at regular site. When exposed to radiation, electrons and holes are produced few of which get trapped by these defects and/or impurities. A large fraction of the centers formed in this way are optically active, that is, they absorb, and in many cases, emit light (luminescence) like the commonly observed F-center which is formed by trapping of electron in a single mono valent negative ion vacancy.

Earlier it has been reported that the generation of these point defects is independent of the nature of the radiation rather it depends on the radiation dose [8].

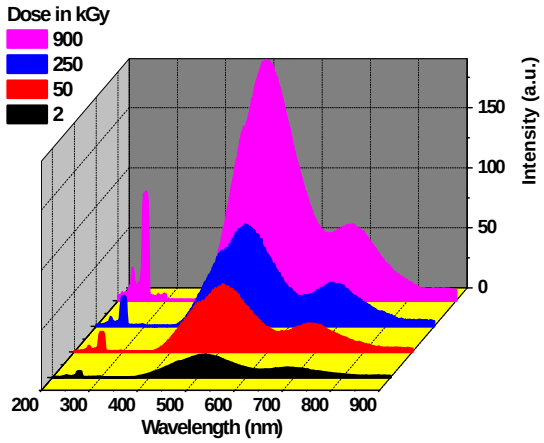

Fig. 1: PL spectrum of the gamma irradiated borosilicate base glass with varying dose

We have investigated the formation of different radicals in gamma/electron beam irradiated Trombay base glass by PL technique [9, 10]. The PL data of the electron beam irradiated glass samples with 171 nm excitation is presented in figure 1. The spectrum is characterized by the presence of weak but broad peaks at 229, 257, 507 and 687 nm and a shoulder at 457 nm. It was observed from the figure that the PL peak intensities increased with increase in the radiation dose. The defect centers were mainly assigned to the non-bridging-oxygen hole centers (NBOHC), oxygen deficient centers (ODC) and E′ center. The generation of NBOHC and E′ centers was attributed to the bond cleavage occurring at regular Si–O sites due to the impinging electron beam on the glass. In addition, to understand the changes taking place in the glass because of irradiation, Eu ion was used as a local probe. We had presented a brief overview regarding the irradiation induced changes in local site symmetry and oxidation state of Eu ion in the glass matrix by PL and ESR techniques [11, 12]. Our investigations suggested that upon irradiation, the ion preferentially moved to asymmetric sites without change in the valence state.

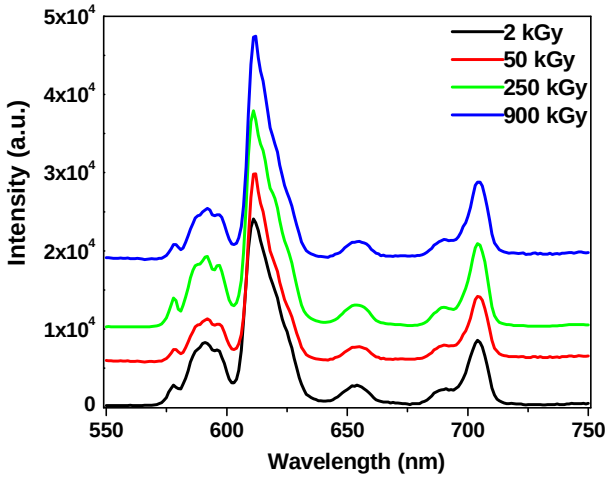

Fig. 2: PL spectrum of the Eu doped irradiated borosilicate base glass with varying gamma dose

Investigations using FTIR spectroscopy

Figure 2 shows the PL spectrum of the glass samples doped with Eu^{3+} ions as a function of gamma dose. It may be noted here that, the defect centre signal observed in case of base glass on gamma irradiation, could not be observed in the PL spectra of Eu-doped glasses. This could be due to the masking of the defect centre signal by the highly intense signal due to Eu.
FTIR technique is capable of detecting the radiation induced changes in the nuclear waste glass at macroscopic as well as microscopic level (through ATR-FTIR). The FTIR spectra of the Trombay nuclear waste glass, irradiated with gamma rays in the dose range 2-900 kGy are presented in figure 3. All spectra are base line corrected and normalized with respect to the highest intensity. From the spectra it can be seen that upon irradiation the main peak position, due to the silicate and borate network, shifts from ~1550 cm^{-1} (corresponding to 2 kGy sample) to ~1380 cm^{-1}(corresponding to 900 kGy sample) along with broadening. Significant broadening is also observed at the wave number region 3300 cm^{-1}. This is attributed to the modification in the glass network due to breaking of Si-O bonds leading to the formation of super structural units with non bridging oxygen atoms (NBOs). The intensities of the bands were also enhanced after irradiation indicating the increase in the formation of NBOs.

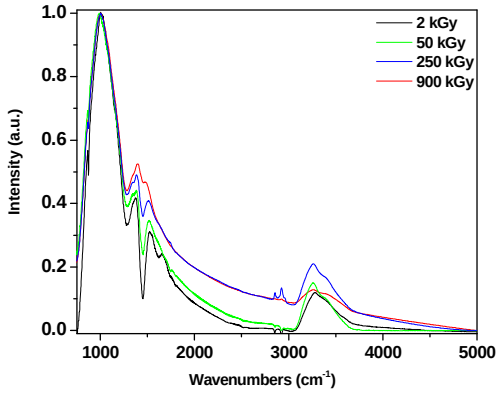

Fig.3: Base line corrected and normalized FTIR data for the gamma irradiated Trombay glass as a function of dose

We had also reported similar results for the electron beam irradiated Trombay nuclear waste glasses in the dose range 10^5 to 10^8Gy [13]. In this case, it was reported that the main peak position, due to the silicate and borate network, shifted from ~1050 cm^{-1} to ~950 cm^{-1} with broadening in the band suggesting significant changes in the glass network as shown in figure 4. It is believed that because of gamma irradiation, more and more alkali ions get unbound and get incorporated in the network.

This makes the structure more distorted and hence decreases the local symmetry [14]. Although earlier it has been reported that alkali borosilicate glasses show a shift in the Q_n (Q_n = Si-O/B-O network with n bridging oxygen) positions due to network polymerisation in the Trombay glass we did not see any significant changes in the band positions which was attributed to the presence of iron in the glass matrix that helps in reducing the extent of radiation damage.

Investigations using ESR technique

Upon irradiation, the defect centers formed in the nuclear waste glasses are often paramagnetic in nature due to the presence of the extra electron/hole. Therefore, ESR becomes an important tool in characterizing the exact chemical nature of the defect centers formed because of radiation. It was observed that for the gamma irradiated Trombay glass, the ESR signals due to defect centers decreased with increase in the iron content in the glass as given in figure 5 [15]. Explanation for this type of reduction in the number of defect centers has been given by Debnath [16], who had suggested that a hopping process between ferrous and ferric ions in the glass is mainly responsible for this reduction in defects. Due to this hopping, the excitons produced during the electronic excitation are consumed and are not available for defect production.

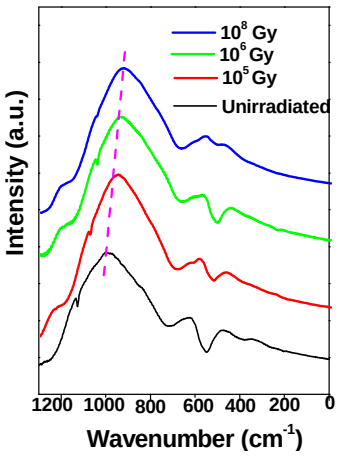

Fig.4: FTIR spectra for the un-irradiated and electron beam irradiated sodium-barium borosilicate glass samples; the change in the band position is marked by the dotted line

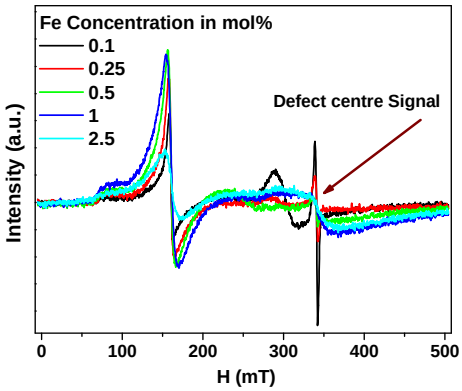

Fig.5: EPR spectra of the Trombay nuclear waste glass irradiated with gamma dose of 2.5 MGy as a function of iron content

In the ESR study of electron beam and gamma irradiated glasses [13, 15], we had provided a detailed analysis of the radiation induced radicals in the Trombay glasses. In this particular glass

composition it was observed that at least four different defect centers were generated as a result of irradiation. These were the common boron oxygen hole trapped species (BOHC), silicon hole trapped species, electron trapped species (F centers) and Oxy radicals [12, 13, 15]. In addition, an ESR spin counting technique was used to quantify the number of defect centers formed in the glass [13]. This study concluded that even with 10^9 Gy of electron dose the total number of defect centers were few hundreds of ppm indicating the stability of the glass.

Investigations by positron annihilation spectroscopy (PAS)

Through PAS technique, the free volumes/defects/ porosity of materials can be characterized in a non destructive manner. PAS has been utilized to investigate the changes taking place in electron beam irradiated Trombay nuclear waste glasses [13]. Figure 6 shows the PAS lifetime results for the electron beam irradiated glasses as a function of dose. Here, the lower graph (A) shows the variation of the ortho-positronium pick-off life time and the upper graph(B) shows the variation in the pick-off intensity.

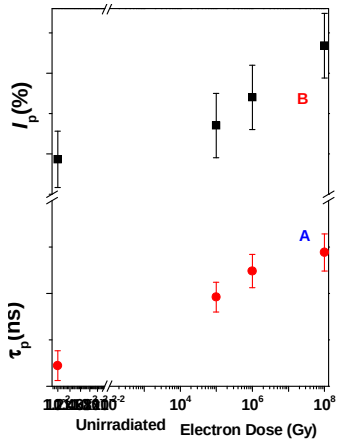

Fig.6: Variation of the pick off life time and pick off intensity for the electron beam irradiated Trombay nuclear waste glass samples as a function of dose

The results showed that, the o-Ps pick-off lifetime (τ_p) and the pick-off intensity (I_p) in electron-irradiated samples are higher than that in the un-irradiated ones and the values increase with the dose. The increase in lifetime is related to the increase in free volume size inside the borosilicate glass samples due to the effect of electron irradiation. The free volume size of the glass sample (R) was calculated from pick-off lifetime (τ_p) using the following equation.

$$\tau_p = \frac{1}{2}\left(1 - \frac{R}{R+\Delta R} + \frac{1}{2\pi}\sin\frac{2\pi R}{R+\Delta R}\right)^{-1}$$

Here τ_p is measured in ns and R (radius of the spherical free/defect volume) is in Å. The ΔR (1.66 Å) is the electron layer thickness inside the wall of the spherical free volume. The increase in the positron life time with irradiation suggested that the positron annihilation process gets delayed because of its trapping in voids, also referred to as free volume. As a result of

irradiation, more and more such type of voids or defects traps the positron and inhibits the annihilation process thus increasing the life time.

Investigations by Raman Spectroscopy

Using high power lasers as excitation sources, micro Raman spectroscopic technique can be used to investigate the changes occurring at surface level also. Earlier it has been reported that upon irradiation, the Si–O–Si bending vibration modes and the Q_2 species (Q_n species correspond to SiO_4 units with 'n' bridging oxygen) in glass matrix are shifted to higher wave number along with a change in the Q_3/Q_2 ratio. Raman spectra of the alpha irradiated glasses as a function of radiation dose are given in figure 7. It was observed that, all the peaks of the irradiated sample were shifted by 10-25 cm^{-1} towards the higher wave numbers. This was more prominent in the vibrations of the Si-O-Si group (400 cm^{-1}).

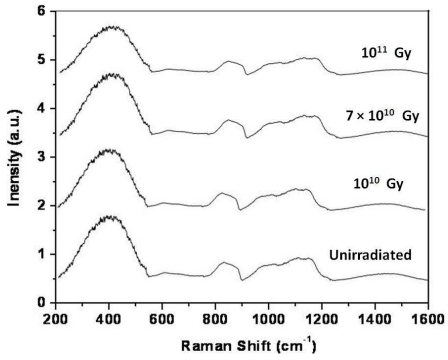

Fig.7: Raman spectra of the Trombay waste glass samples irradiated with ^{4}He as a function of dose

This shift is because of the reduction in the mean angle of the Si-O-Si bonds as a result of the alpha irradiation. It was also observed that, with increasing dose, the Q_n mean band position shifted towards a higher 'n' value indicating increase of the silicate network polymerization under alpha irradiation. This type of structural evolution has been attributed to the migration and aggregation of alkali ions during the irradiation [18, 19]. It is thus inferred from the above Raman spectroscopic results that, alpha irradiation of the Trombay nuclear waste glass, modifies the glass network enhancing the alkali migration and higher extent of polymerization.

Summary

Our study concludes that with the help of different spectroscopic techniques, it is possible to exactly pin point the nature of radiation damage occurring in the glass samples. Techniques such as EPR, PAS provide information about the microstructural changes in the glass matrix. On the other hand, PL, IR and to some extent Raman spectroscopy are macroscopic in nature where they give information regarding the bulk nature of the sample. From the above discussion it is clear that, indeed, the borosilicate glass samples, used for nuclear waste vitrification, undergo a lot of structural modification on irradiation. However, the overall glass network remains unaffected to a large extent by the irradiation. The glass composition was found to be stable at a cummulative

radiation dose of 10^{11} Gy. Considering 20% loading of the nuclear waste in the glass, this radiation dose is equivalent to a storage period of few thousands of years. In addition, the "self healing" effect of the Trombay glass was demonstatred where incorporation of iron, increases the radiation stability and reduces the radiation damge in the glass.

Acknowledgements

Authors thank a large number of collaborators, who were associated with this work by way of sample preparation, providing the facilities, such as the gamma chamber, electron accelerator (ILU-6 and EBC Staff), heavy ion beams (BARC-TIFR Pelletron facility) for irradiation and instruments for spectroscopic investigations. Special thanks are due to Dr.C.P.Kaushik and Dr.R.K.Mishra from WMD, BARC for the sample preparation. The authors gratefully acknowledge the support from Dr.R.M.Kadam and Dr.P.K.Pujari from Radiochemistry Division (RCD), BARC for their help in the EPR and PAS work, respectively. One of the authors (MM) is thankful to Dr. S. V. Godbole, Head, Spectroscopy section, RCD; Dr. A. Goswami, Head, RCD and Dr.V.K.Manchanda, former Head, RCD for their valuable suggestions, constant support and encouragement for the work.

References

1. C. M. Jantzen, K. G. Brown, J. B. Pickett, Int. J. App. Glass Sci. 1 (2010) 38
2. K. Joseph, R. Asuvathraman, R. Venkata Krishnan, T.R. Ravindran, R. Govindaraj, K.V. Govindan Kutty, P.R. Vasudeva Rao, J. Nucl. Mater. 452 (2014) 273
3. A. M. Bevilacqua, N. B. Messi de Bernasconi, D. O. Russo, M. A. Audero, M. E. Sterba, A. D. Heredia, J. Nucl. Mater. 229(1996) 187
4. V.S. Yalmali, D.S. Deshingkar, P.K. Wattal and S.R. Bharadwaj, J. Non Cryst. Solids 353 (2007) 4647
5. C.P. Kaushik, R.K. Mishra, P. Sengupta, A. Kumar, D. Das, G.B. Kale, K. Raj, J. Nucl. Mater. 358 (2006) 129
6. W.J. Weber, Nucl. Instrum. Meth. B 32 (1988) 471
7. W.J. Weber, R.C. Ewing, C.A. Angell, G.W. Arnold, A.N. Cormack, J.M. Delaye, D.L. Griscom, L.W. Hobbs, A. Navrotsky, D.L. Price, A.M. Stoneham, M.C. Weinberg, J. Mater. Res. 12 (1997) 1946
8. L. Nuccio, S. Agnello, R. Boscaino, B. Boizot, A. Parlato, J. Non-Cryst. Solid 353 (2007) 581
9. M. Mohapatra, V.K. Manchanda, IOP Conf. Series: Mater. Sci. Engg. 2 (2009) 012006
10. M. Mohapatra, R.K.Mishra, C.P.Kaushik and B.S.Tomar, Procedia Materials Science 7 (2014) 247
11. M. Mohapatra, R.K. Mishra, C.P. Kaushik, S.V. Godbole, Physica B 405 (2010) 4790
12. M. Mohapatra, R.M. Kadam, R.K. Mishra, C.P. Kaushik, B.S. Tomar and S.V. Godbole, Physica B406 (2011) 3980
13. M. Mohapatra, R.M. Kadam, R.K. Mishra, D. Dutta, P.K. Pujari, C.P. Kaushik, R.J. Kshirsagar, B.S. Tomar and S.V. Godbole, Nucl. Instrum. Methods B 269 (2011) 2057
14. O. J. McGann, P. A. Bingham, R. J. Hand, A. S. Gandy, M. Kavčič, M. Žitnik, K. Bučar, R. Edge, N. C. Hyatt, J. Nucl. Mater. 429 (2012) 353.

15. M. Mohapatra, R.M. Kadam, R.K. Mishra, C.P. Kaushik, B.S. Tomar and S.V. Godbole, Int. J. App. Glass Sci. 4 (2013) 53
16. R. Debnath, J.Mater.Res.16 (2001) 127
17. S.V.Raman, Philos. Mag. A, 82 (2002) 3055
18. F.Y. Olivier, B. Boizot, D. Ghaleb, G. Petite, J. Non Cryst. Solids, 351 (2005) 1061
19. M.Mohapatra and B.S.Tomar, Defects and Diffusion Forum 341 (2013) 107.

PHOTOPHYSICAL STUDIES OF AN AMYLOID SENSING DYE IN CONFINED ENVIRONMENT

Prabhat K. Singh
Radiation & Photochemistry Division

Dr. Prabhat K. Singh is the recipient of the DAE Young Scientist Award for the year 2013

Thioflavin T (ThT), a benzothiazole-based cationic dye, belongs to the "gold standard" for selective staining and identifying amyloid fibrils both in vitro and vivo. Amyloid fibrils are denatured filamentous form of protein responsible for several neurodegenerative diseases, such as Alzheimer's and Parkinson's diseases.[1] On association with amyloid fibril, ThT shows a remarkable enhancement in emission yield, whereas in water, ThT is very weakly fluorescent. ThT binds specifically with the amyloid form of the protein, without any significant interaction with the protein in its native form. This makes it a highly selective and efficient reporter for the real time observation of fibrilation in solution. However, despite its widespread use in detecting amyloid fibrils, the basic molecular mechanism behind its fluorescence sensing activity of amyloid fibril was not properly understood. So we took up a detailed investigation of the photophysical behavior of ThT in homogeneous solvents, and in several confined micro-heterogeneous environments, to gain a better understanding of the factors responsible for the fluorescence sensing ability of ThT.

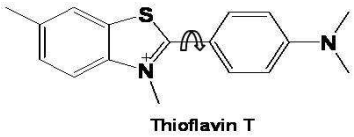

Thioflavin T

Scheme 1: Chemical structure of Thioflavin-T

The emission yield (Φ_f) of ThT in water is very low (~ 10^{-4})[2] suggesting that ThT bears a very efficient non-radiative process in its electronic excited state. Using fluorescence up-conversion spectroscopy, which is capable of reporting the excited-state dynamics down to sub-picosecond time-regime, we have observed that the excited state of ThT decays on picoseconds (ps) time scale in water.[3] The excited sate decay trace displays a multi-exponential kinetics at any given emission wavelength, and also shows a very rich emission wavelength dependent dynamics. The detailed analysis of the wavelength dependent transient decay traces reveals that, upon photoexcitation, ThT undergoes an efficient non-radiative process with a time constant of 0.57 ps.[3] Thus, due to the presence of such ultrafast non-radiative process, the emission quantum yield of ThT in water is very low.

With an aim to understand the origin of this very efficient non-radiative process, we carried out detailed investigation of the photo-physical properties of ThT in various homogeneous and confined micro-heterogeneous media. In homogeneous solvents, it was found that the emission

quantum yield and the excited state lifetime are very sensitive to the viscosity of the medium. For example, the excited state lifetime varied from 0.6 ps in acetonitrile (η=0.35 cP) to 17.6 ps in ethylene glycol (η=17.6 cP).[4] This prominent effect of viscosity on the non-radiative relaxation of ThT, suggests the presence of a large amplitude torsional motion in the excited state of ThT. By detailed investigation of the excited-state dynamics of ThT, and with the aid of quantum chemical calculations, we have established that, upon electronic excitation in solution, a large amplitude non-radiative torsional relaxation around central C—C bond of ThT takes place on a barrier-less potential energy surface. This torsional relaxation leads to the rapid conversion of initially populated strongly emissive locally excited state (LE) state to a very weakly emissive twisted intramolecular charge transfer (TICT) state, which quenches its emission in water and other low viscosity solvents (Figure 1).[3-4] It is believed that the dramatic increase in the ThT emission, on association with the amyloid fibril, results from the restriction of an ultrafast torsional relaxation around central C-C bond in the excited electronic state of ThT.

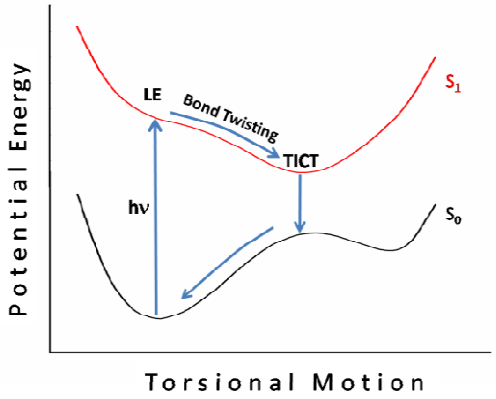

Fig. 1: Schematic presentation of the excited state relaxation pathways of ThT

Thus, knowledge of the photo-physical behavior of the photo-excited ThT molecule under different restricted environments is very essential in order to understand the underlying mechanism for the enhancement of the fluorescence emission yield of ThT in amyloid fibril. With this aim, we have investigated the behavior of photo-excited ThT in several confined media such as nanopool of reverse micelles, nanocavity of cyclodextrins, etc.

Water/aerosol-OT (AOT)/oil reverse micelles is one of the systems that can provide nanometer-size confined water pool and has been extensively studied as a model system to mimic the water in biological systems. Interestingly, the size of the water pool, and hence the extent of confinement, in the AOT reverse micelle can be changed systematically, in a controlled manner, just by changing the water to surfactant ratio (W_0). We have demonstrated that, due to the confinement, torsional dynamics in ThT becomes very sluggish. Due to this sluggish torsional motion, fluorescence enhancements of about 250 times have been observed in the AOT reverse micelle as compared to bulk water.[2] However, with increase in the water pool size, both fluorescence quantum yield and excited-state lifetime decreases non-monotonically (Figure 2). Such a decrease in the fluorescence quantum yield and excited-state lifetime has been attributed to the faster torsional motion in the larger water pools of the reverse micelles.[2] However, we also observed that the torsional motion does not reach the situation prevailing in bulk water and remains restricted even in a very large water pool. This result has been rationalized in terms of

electrostatic interaction between the probe and the surfactant head groups, and also the effect of the bound water, which move unusually slow even in a large water pool of the reverse micelle.

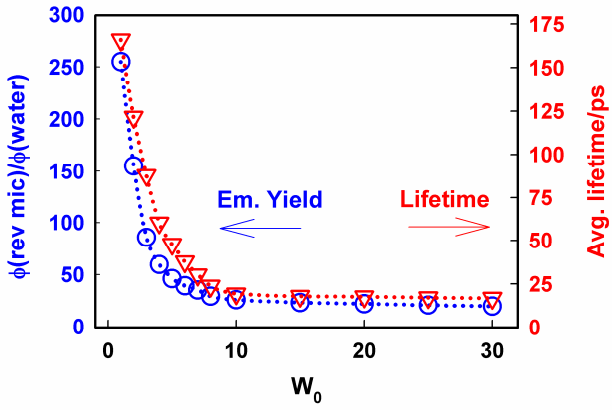

Fig. 2: Variation in the relative φ values of ThT in the reverse micelle with respect to that in water (○), and average fluorescence lifetime (▽) of ThT with the W_0 value of AOT reverse micelle

The effect of the head group of the surfactants on the photophysical properties of ThT in the reverse micelle was also investigated. However, surprisingly, in a reverse micelle, with the cationic head group of the surfactant (BHDC/benzene/water) system, the nano-confinement shows quite extraordinary electrostatic behavior as compared to other normal charged surfaces.[5] ThT was found to be associated with the cationic head group, despite bearing the similar charge. This unusual behavior in the nano-confined water pool of cationic reverse micelle was attributed to the possibility of stronger electrostatic screening of the repulsive interaction of the ThT and the surfactant head group, due to the presence of large number of counter ions in the small confined water pool. Other contributing forces, towards this unusual attractive interaction, could be the hydrophobic interaction between the probe and the surfactant molecules, π–π and π–cation interaction between the aromatic ring of the BHDC surfactant and the ThT molecule.[5] In a neutral reverse micelle, consisting of TX-100 surfactant, a considerable increase in the emission intensity and the fluorescence lifetime of Thioflavin-T was noted as compared to bulk water, which indicates the effect of confinement on the photophysical properties of ThT, in these self assembled systems.[6] However, the photophysical parameters of Thioflavin-T in Triton X-100 reverse micelle remained almost invariant with the increasing water content, which is in sharp contrast to its behavior in ionic reverse micelles. This behavior has been rationalized on the basis of the differences in the localization sites of the probe in the nonionic and ionic reverse micelles.[6] Thus, our results on ThT in reverse micelles suggest that the reaction dynamics of the probe in the nano-confined water pools of reverse micelle are strongly influenced by interfacial charge, which in fact control the location of the probe in the reverse micellar systems.

The effect of supramolecular confinement on the photophysical behavior of ThT was also investigated in both neutral β-Cyclodextrin (β-CD) and its charged derivative, Sulphobutylether β-cyclodextrin (SBE-β-CD).[7-8] The encapsulation of ThT inside the nanocavity of SBE-β-CD results in a significant increase in the emission intensity and the excited state lifetime of ThT (Figure 3), when compared with native β-CD. Detailed analysis of the time-resolved emission spectra (TRES) shows that the confinement inside the nanocavities of cyclodextrin derivatives

significantly affects the torsional dynamics of ThT as compared to bulk water. The ionic strength of the medium significantly affects the complexation of ThT with SBE-β-CD, which indicates that the interaction between the host and the guest is predominantly electrostatic in nature.

The results further suggest that the hydrophobic interaction in SBE-β-CD is comparatively stronger than the native β-CD.[8] Thus, our results on the supramolecular confinement of ThT inside the cyclodextrin nanocavities infer that, besides other factors that are operative in the ThT-fibrilar system, confinement might be one that is mainly responsible for the observed fluorescence enhancement of ThT in amyloid fibrils.

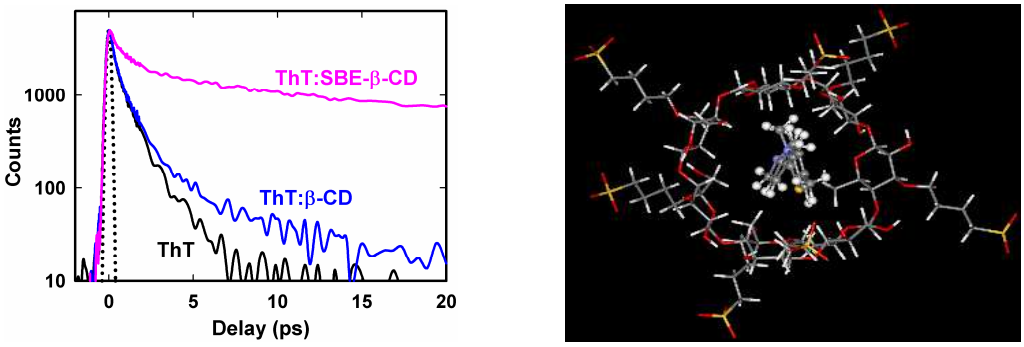

Fig. 3: (Left) The transient fluorescence decay trace of Thioflavin- T water (black), β-CD (blue), and SBE-β-CD (pink).The dotted line represents the instrument response function (IRF).(Right): Optimized geometry for the ThT-SBE-β-CD 1:1 complex

Considering the extreme sensitivity of ThT towards the restricted environment, we exploited its potential to detect small structural changes in nucleic acids in the premelting region.[9] These small structural changes play an important role in the biological activity of DNA at physiological temperature. It needs to be stressed that conventional optical spectroscopic techniques, such as UV absorption, circular dichroism, etc., has been found to be inadequate to measure small structural changes in the premelting region, especially for large natural DNA.

We have demonstrated that ThT can act as an extrinsic fluorescence sensor to sensitively detect small structural changes in natural DNA at the premelting temperature region, and is superior than most commonly used DNA stains.[9] We also demonstrated that ThT acts as an excellent probe to monitor the interaction between the ionic liquid (IL) and DNA.[10] The better understanding of such biomolecule–IL interaction mechanism will lead to efficient application of ILs in different biological research.

Finally, we investigated the photo-physical behavior of ThT in the insulin fibrils. The association of ThT with the insulin fibrils causes an enhancement of ~ 160 times in its emission yield, and the excited state lifetime was found to increase from ~1 picosecond in bulk water to ~ 1.3 nanosecond in insulin fibrils. Thus these data suggests that the torsional relaxation in ThT is strongly inhibited on association with insulin fibrils.[3]

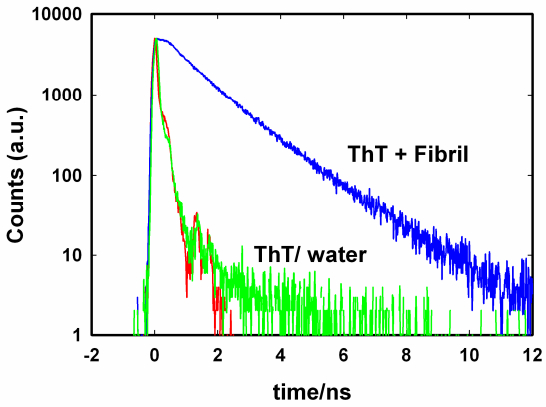

Fig. 4: Transient decay traces for ThT in insulin amyloid fibril (blue solid line) in the nanosecond time regime. The decay trace for ThT in bulk water (green) is also shown for comparison which is (shown in red) limited by instrument response function

Thus, we have experimentally demonstrated, for the first time, that the low emission yield of Thioflavin-T in low viscosity solvent is caused by an efficient torsional relaxation in its excited state. We also demonstrated that the restriction of the torsional relaxation of ThT causes large changes in its emission properties, which makes it a sensitive reporter for several confined environments including amyloid fibrils.

Acknowledgement

I sincerely thank all my coauthors for their significant contribution in the reserach work described here. I also acknowledge the constant support and encouragement from Dr. D. K. Palit and Dr. B. N. Jagtap.

References

1. F. Chiti and C. M. Dobson, *Annu. Rev. Biochem.*, 2006, **75**, 333-366.
2. P. K. Singh, M. Kumbhakar, H. Pal and S. Nath, *J. Phys. Chem. B*, 2009, **113**, 8532-8538.
3. P. K. Singh, M. Kumbhakar, H. Pal and S. Nath, *J. Phys. Chem. B* 2010, **114**, 2541-2546.
4. P. K. Singh, M. Kumbhakar, H. Pal and S. Nath, *J. Phys. Chem. B*, 2010, **114**, 5920-5927.
5. P. K. Singh, M. Kumbhakar, H. Pal and S. Nath, *Chem. Commun.*, 2011, **47**, 6912–6914.
6. P. K. Singh and S. Nath, *J. Photochem. Photobiol., A* 2012, **248**, 42-49.
7. P. K. Singh, M. Kumbhakar, H. Pal and S. Nath, *Phys. Chem. Chem. Phys.*, 2011, **13**, 80088014.
8. P. K. Singh, S. Murudkar, A. K. Mora and S. Nath, *J. Photochem. Photobio., A*, 2015, **298**, 40-48.
9. S. Murudkar, A. K. Mora, P. K. Singh and S. Nath, *Chem. Commun.*, 2012, **48**, 5301-5303.
10. P. K. Singh, J. Sujana, A. K. Mora and S. Nath, *J. Photochem. Photobiol., A*, 2012, **246**, 16-22.

BARC NEWSLETTER
FOUNDER'S DAY SPECIAL ISSUE 2015

VOLUME REDUCTION AND SAFE STORAGE OF PRESSURE TUBES (FROM EMCCR OF MAPS-I) FOR FUTURE RECYCLING OF PRECIOUS HAFNIUM-FREE ZIRCONIUM

D. Anji Reddy*, G. Chenna Keshavulu and Biplob Paul
Centralised Waste Management Facility, Kalpakkam
*Corresponding author email: anji@igcar.gov.in

Shri Biplob Paul, Nuclear Recycle Board and his team received the DAE Group Achievement Award for the year 2013

Abstract

At Centralised Waste Management Facility (CWMF), Pressure Tubes (PTs) were received from MAPS Unit–I & II during en-masse replacement of coolant channels as part of life extension. In 2002 campaign, Unit–II PTs were received as waste; cut into two half's and permanently disposed in Tile Holes (TH) at CWMF. But in 2005 campaign, Unit–I PTs were stored in an SS lined pool under DM water for further processing for the recovery of hafnium free zirconium. At the end of the pool storage period, a process was evolved to reduce the volume of the PTs and store in dry condition in Tile Holes on campaign basis in a retrievable manner till a process for the recovery of zirconium is available in plant scale. A detailed process flow sheet was prepared; sub-systems were designed, fabricated and erected. Inactive trials were carried out successfully. Active operations involving retrieval of pressure tubes, removal of shield plugs, compaction & shearing into small size pieces, collection of the pieces in SS drum and storage of the drum in Tile Holes were demonstrated to safety committee. After obtaining clearance, campaign of processing of 300 Pressure Tubes was completed successfully. This campaign was executed with due consideration to safety, minimization of radiation exposure and minimum use of precious waste disposal space. This paper outlines the design, erection and commissioning of the system and its component equipment. It also summarizes the challenges overcome and experiences gained during this maiden campaign for storage of a wealth of 11 tons of zircalloy for future retrieval of Hf-free zirconium.

Introduction

The MAPS is a heavy water cooled and heavy water moderated Pressure Tube type CANDU reactor. Each pressure tube is inside an outer tube called Calandria tube. Pressure tubes play an important role by isolating the high pressure primary coolant and the moderator. During 2005, the PTs of the MAPS-1 reactor were replaced *enmasse* due to various factors like induced neutron / hydride embrittlement, creep / growth, fatigue & corrosion etc. After their removal from the reactor, the PTs (contact dose ~1000s of R/h) were transported to CWMF in shielded casks as Category-III radioactive solid waste[1] and stored in an SS lined pool in racks under DM water. Figure-1 shows the view of the pool before and after storing of PTs.

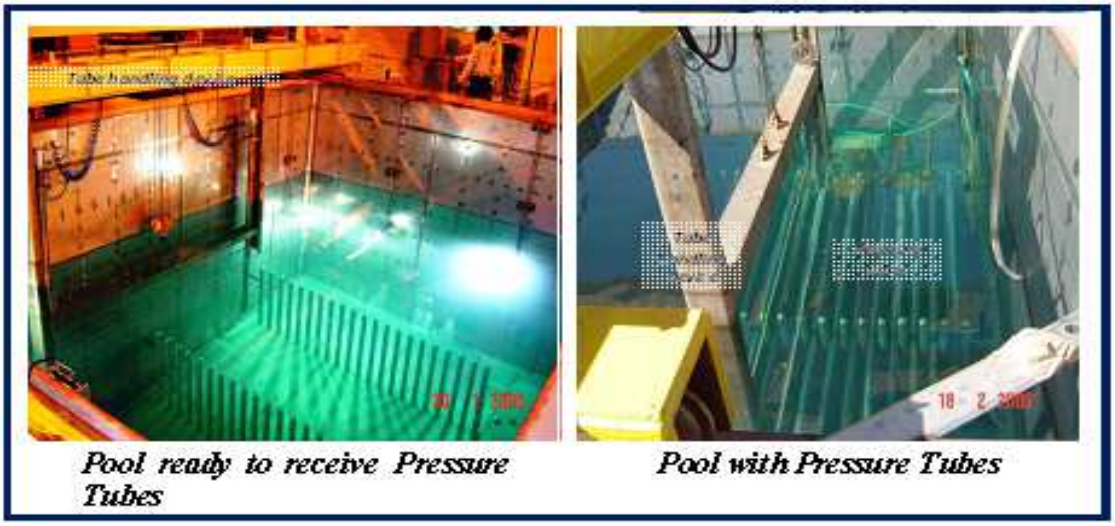

Fig.1: View of the pool before and after storing of PTs

The irradiated pressure tubes with shield plugs had a large inventory of activation product radionuclides; namely Cr-51, Co-58, Fe-59, Co-60, Zr-95, Nb-95, Hf-181, Zn-65, Sb-124, Sb-125. The longest half life amongst these radionuclides was of Co-60 i.e.5.3 years. The radioactive wastes inventory as on 2010 [2] measured before the campaign for design requirements were as given in Table-1.

Table 1: **Inventory of Radioactivity as on 2010**

Item	***Qty(Nos.)***	***Activity content***	***Dose rate on contact***
PT with shield plugs inside	*298*	*441040 TBq (11920 Ci)*	*250 -300 R/h*
Calandria tube	*2*	*2960 TBq (80 Ci)*	

At the end of the pool storage, it was decided to reduce their volume and store them retrievably in tile holes for future recovery of zirconium. A detailed process flow sheet was prepared for these operations. The sub-systems were designed, fabricated, erected and commissioned. Safety committee approval obtained for campaign on the retrieval of pressure tubes (PT) from pool, their volume reduction and storage of the drums in Tile holes.

The Campaign

In each cycle of the campaign, one pressure tube, now with surface dose of 100-150 R/h (reduced from 1000s of R/h due to decay of short lived radionuclides), was retrieved from the

pool using a split cask and processed. The following paragraphs describe the equipment used and operations carried out during the various steps of the campaign.

Retrieval of PTs from Storage Pool

The specialty of the split cask is that it is split horizontally with a removable top-half and at the same time, has ports at both ends for axial movement of the PT. To retrieve the PT from the pool, the bottom piece of split cask was lowered using 20 Te gantry crane and placed on the pad provided inside the pool. A pressure tube was taken out from the rack using a pneumatic tube handling device and placed in the cavity of the split cask. Split cask cover was next placed over the lower portion. The entire assembly of split cask was then lifted out of water and held over the pool for sufficient time to allow the water to drain completely. The cask was then shifted to Shield Plug Removal Station (SPRS) which is a 150 mm MS shielded and ventilated enclosure. Figure-2 shows the operation carried out in the storage pool.

Fig.2: Operation carried out in the storage pool

Removal of Shield Plugs from PTs

Before transfer of pressure tubes from MAPS, two shield plugs on either ends were pushed into the tubes. So, prior to taking up compaction and cutting of PTs, the shield plugs were to be removed and it was carried out in Shield Plug Removal Station (SPRS). The split cask, with the pressure tube inside, was placed on a trolley at one end of SPRS with the help of the crane and mated with enclosure port. A shield plug collection device was placed on its trolley on the other side of the enclosure, aligned and sliding doors of the ports were opened. The tube was fed into the enclosure using pusher ram.

It was held there with clamps and burr on ID of the PT removed using wedge shaped conical cutter. Next, the shield plug was pulled out of the PT into the cask with a special shield plug removal tool. After closing the ports, the shield plug was transferred to a drum and disposed in RCC Trenches. The pressure tube was retracted into split cask, sliding door closed and the split cask was rotated by 180°. The other shield plug was also removed similarly and the cask with

PT was next transferred to Compaction and Cutting Station (CCS). Figure-3 shows the view of Shield Plug Removal.

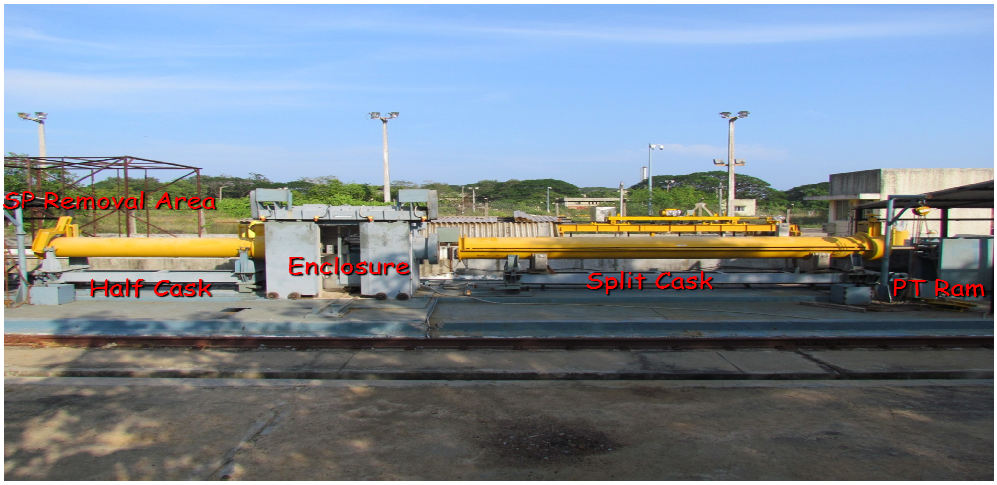

Fig.3: Shield Plug Removal Station

Volume Reduction of Pressure Tubes

Compaction and Cutting Station (CCS) was also a 150 mm MS shielded and ventilated enclosure. Compaction and cutting machine was housed in the enclosure. It also had a manipulator to collect the PT pieces which get dislocated from the intended position. For taking up cutting, the split cask was aligned to the enclosure port of CCS, sliding door was opened and the tube was fed into CCS in incremental movements of 200 mm by operating the feeding ram. After each feed, the length of 200 mm was flattened using the 150 Te compaction ram and sheared with 100 Te ram. The operation was controlled using a PLC based control system supported by view through a CCTV camera. The chopped pieces were collected through hopper in an SS drum located on the trolley below the hopper. Five tubes were cut and the drum was retrieved into the drum disposal cask through bottom opening door. Figure-4 shows the views of volume reduction operations at CCS.

Fig. 4: Views of Volume Reduction Operations

Storage of PT pieces in Tile Holes

The SS drum with five PTs cut pieces in the disposal cask was transported to Near Surface Disposal Facility and stored retrievably in tile holes for future recovery of zirconium.

Obstacles Overcome During Inactive Trails

After completion of fabrication and erection works, trials were carried out with inactive zirconium alloy tubes to validate operating and maintenance procedures. This resulted in the following improvements:

- ✓ Compensatory shielding was provided at enclosure ports of CCS minimizing radiation field in the working area during the actual campaign.
- ✓ Chamfering was carried out on split cask door port for smooth movement of the shield plug from PT into the cask.
- ✓ PT guiding unit was modified to fully encase the Pressure tube to prevent fragments from spilling out (and remain in guiding unit) & for smooth retraction of PT into the cask.
- ✓ Machine base and hopper was modified so that the cut pieces fall automatically into the SS drum.
- ✓ Modification was carried out on SS drum lid hinges to limit the angle of rotation of lid and automatic closing during its movement to cask bottom position.

Active Trails – Further Challenges Faced

Active operations with actual 5.2 meter long pressure tubes with surface dose rate of few hundreds of R/h were demonstrated to safety committee representatives. During the trials following difficulties were faced and overcome successfully.

- Shield plugs could not be taken out of the tubes due to presence of burr on inner diameter of the PT. This was because PT's were cut out from their original location at MAPS using a chip-less cutting machine with a disk cutter feeding from ID to OD. Due to this, deformation occurred on the inner surface of the PT, reducing its ID by about 1mm at cut ends. Hence, an additional step of removal of burr using a wedged shaped cutting tool was introduced in the procedure for the removal of shield plugs. With this modification in the SP removal procedure, all the shield plugs could be removed without any difficulty during actual operations.

- In Compaction and Cutting Chamber, after flattening of the PT, while shearing it was observed that a few pieces are travelling like projectiles and falling outside the chute provided for collecting the pieces. The shortcoming was overcome by providing a hood to the cutting ram.

Operational Experiences

Some interesting experiences are shared below:

- ✓ During the campaign, the burr removal tool wore out twice i.e. after processing about 60 and 220 tubes; the tool was changed with new tool and operation continued.
- ✓ During the campaign, the shearing tool was changed after processing 29 PTs. Since the available shearing tools were found to wear out too soon, after a review of the tool material, shock resistant tool steel was selected and tool fabricated. The new tool needed replacement only once i.e. after processing 222 PTs.
- ✓ Replacement of HEPA Filters: First and Second filters were replaced during processing of 23rd and 43rd PTs. To reduce the load and to prevent contamination of ducting, a pre-filter was installed at enclosure exhaust. The third & fourth HEPA filters needed replacement at 154th & 252nd PTs. Final HEPA filter was disposed after completion of campaign.
- ✓ Cut pieces of only 5 PTs were placed in one drum against envisaged 10. About 60 drums have been stored in 12 Tile Holes

Conclusion

- ➢ The campaign of retrieval, volume reduction and storage of high active pressure tubes involving their handling in heavy lead shielded casks and enclosure was completed successfully.
- ➢ About 11 tones of pressure tubes could be reduced to a minimum volume and safely stored retrievably in Tile Holes from where these can be taken out at a later date for recycle & reuse of precious zirconium.
- ➢ The NSDF area consumption was about three times less when compared to the MAPS Unit–II PTs disposal that was carried out in 2002.
- ➢ No overexposure or internal contamination reported in the campaign.

Post-Campaign Activities And Campaign Closure

The campaign was closed after completing the following Post-campaign activities:

- ✓ The Pre-filter (dose rate~3.5 R/h) & HEPA filter (dose rate~1.5 R/h) of the Compaction & Cutting Enclosure were removed and disposed in RCC trenches.
- ✓ The clear liquid from the PTs storage pool was transported to liquid effluent treatment plant for further processing.
- ✓ The slurry was collected in four drums (each with ~100 l slurry) and fixed in cement matrix. The CWP drums were disposed in RCC Trench.
- ✓ The PTs storage pool was decontaminated.
- ✓ The decontaminated SS lined pool has been kept for future use.

Before Decontamination

After Decontamination

Fig.5: Storage pool before & after Decontamination

Acknowledgement

The authors are grateful to Shri R C Sharma, Director, Reactor Group & Chairman, ULSC-NRG for his valuable guidance provided at crucial points during the campaign. We also acknowledge the contribution of Shri B Madhu, HP, CWMF who played a very important role by not only ensuring radiological safety during the entire campaign but also by working closely with the engineers in solving the problems encountered. The authors also would like to thank the core team of CWMF for their support during the campaign, especially Shri G J M Coelho, Smt S Chitra, Shri V. Subba Rao and Shri K. Paramasivan.

References

1. International Atomic Energy Agency, Standardization of radioactive waste categories, Technical Report Series No. 101, IAEA, Vienna, 1970
2. Safety Report on Retrieval, Volume Reduction and Storage of Pressure Tubes from EMCCR- 2005 (MAPS-1) campaign.

BARC NEWSLETTER
FOUNDER'S DAY SPECIAL ISSUE 2015

DEVELOPMENT OF ENERGY SCANNING EXAFS BEAMLINE (BL-09) AT INDUS-2 SYNCHROTRON SOURCE

C. Nayak, A. K.Yadav, Sohini Basu, P. Rajput, A. Agrawal, A. K. Poswal, D. Bhattachryya, S. N. Jha and N. K. Sahoo*
Atomic and Molecular Physics Division

Dr. N.K. Sahoo, Physics Group and his team received the DAE Group Achievement Award for the year 2013

Introduction

X-ray Absorption Fine Structure (XAFS) generally deals with measurement of the fine structure oscillations present in the absorption spectrum beyond the X-ray absorption edge of an element in a material and proper analysis of these oscillations can give precise information regarding the short range order and local structure around the particular atomic species in the material [1]. The experimental X-ray absorption spectrum of a sample consists of two regions: X-ray Absorption Near Edge Structure (XANES) (-50 eV to +50 eV around the absorption edge) and Extended X-ray Absorption Fine Structure (EXAFS) (from 50 eV to 700 – 1000 eV above the absorption edge). The former gives information on the oxidation state of the central atom in a compound whereas the latter gives relevant information regarding the bond length and the coordination number around the probed atom as well as disorder factor in the system. The detection of these fine oscillations requires a tunable and bright X-ray source like synchrotron in which radiation is emitted by high energy accelerated electrons. With the advent of modern bright synchrotron radiation sources, EXAFS has emerged out to be one of the most powerful techniques for local structure determination, which can be applied to any type of material viz. amorphous, polycrystalline, polymers, surfaces and solutions under different ambient and extreme environmental conditions. EXAFS beamlines are one of the most significant and extensively used experimental facilities at Synchrotron radiation sources all over the world. At INDUS-2 SRS at RRCAT, Indore, earlier an energy dispersive type EXAFS beamline at BL-08 port was established and it is operational since 2009 [2]. This beamline covers the photon energy range of 5-20 keV and in this beamline, the entire EXAFS spectrum of the samples can be recorded in a single shot within a time scale of ~300 msec. Hence this is best suited for studying in-situ fast and time-resolved processes. However, in the dispersive beamline (BL08), the spectra can be recorded in the transmission mode only and this requires uniformly thick and very thin samples for artifact-free results. Hence samples with very low concentrations or thin films deposited on thick substrates cannot be studied in the above beamline. So it was very much needed to develop another EXAFS beamline where measurements in both transmission and fluorescence modes are possible. With this goal in mind an Energy Scanning type EXAFS beamline has been developed at BL-09 port of INDUS-2 synchrotron source and has been commissioned recently [3,4]

Beamline Description

The specifications of the Energy Scanning EXAFS beamline (BL-09) are given in Table-1 and the optical layout of the beamline is shown in Fig. 1.

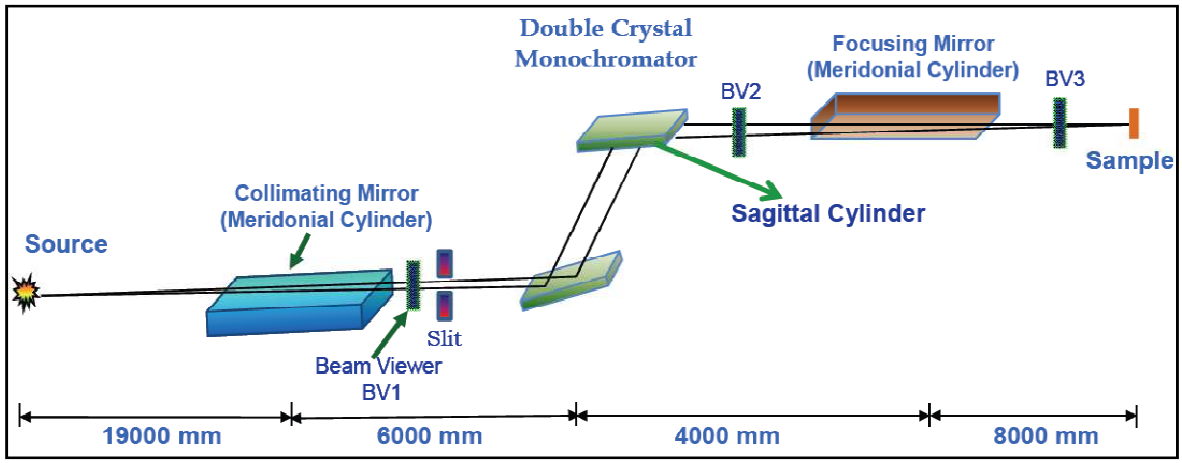

Fig.1: Optical layout of the BL-09 EXAFS beamline

Table 1: Important specifications of the BL-09 beamline

Energy range	**4-25 keV**
Energy Resolution (E/ΔE)	**10^4 @ 10keV**
Flux@ Focus	**1011 ph/sec/0.1% band width @2.5 GeV, 300mA**
Focal spot size	**0.50 mm x 0.50 mm**

The beamline uses a 1.3 m long meridonial cylindrical mirror with radius of curvature 11.2 Kms for vertical collimation of the beam. This mirror is followed by a fixed exit type double crystal monochromator (DCM). The DCM consists of two Si (111) crystals with 2d=6.2709Å and narrow Darwin widths. The fixed exit is realized by varying the relative lateral and vertical distances between the two crystals at each energy setting, maintaining parallelism between them. The second crystal of the DCM is a saggital cylinder with variable radius of curvature in the range 1.2 m to flat, which provides horizontal focusing to the beam. A post mirror with meridonial curvature is used upside-down for bending the beam path to horizontal direction again as well as for vertical focusing of the beam at the sample position. Higher harmonics are rejected by changing the angle of incidence at the second mirror. Each of the two cylindrical mirrors has two coating strips, viz., of Platinum (Pt) and Rhodium (Rh). Rhodium has the absorption edge at 23.2 KeV (K-edge) and Pt has L1, L2 and L3 absorption edges between 11.5 KeV to 13.9 KeV. So to cover the energy range of 4-25 keV, coatings of Rh and Pt are used. The beamline has been installed in two main parts namely optics hutch and experimental hutch.

The optics hutch consists of the optical components e.g., slit system, grazing incidence X-ray mirrors, beam viewer, double crystal monochromator (DCM) and Beryllium window. The entire optics hutch is at 10^{-9} torr vacuum and separated by front end and experimental hutch using 200μm thick beryllium windows.The experimental hutch is equipped to record EXAFS spectra of the samples. For measurements in the transmission mode, the sample is placed between two ionization chamber detectors. The first ionization chamber measures the incident flux (I_0) and the second ionization chamber measures the transmitted intensity (I_t).

Absorption (μ) is calculated using formula, $\mu = \log I_0/I_t$. A third ionization chamber is also used where reference metal foils are measured for energy calibration. For low concentration or dilute samples, fluorescence is recorded using Lytle or silicon drift detectors, which are placed in front of the sample in 45º degree geometry. The photographs of the Optics and Experimental hutches of the beamline are shown in Figs. 2 and 3.

Fig.2: Photograph of the Optics hutch of the beamline

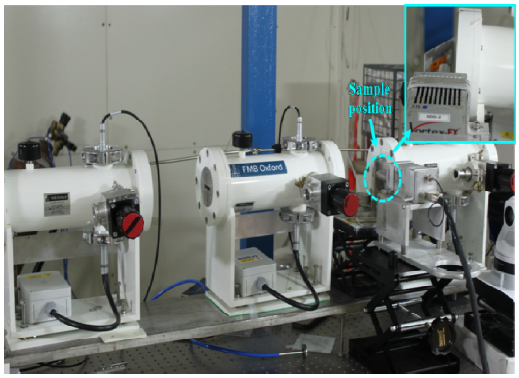

Fig. 3: Photograph of the Experimental hutch of the beamline

To cater to different users several auxiliary facilities have also been set up in the above beamline. These include two high temperature cells that can go up to 700K and 1000K respectively (in collaboration with Ch.D & FCD, BARC) in which it is possible to carry out measurements under various gaseous environments viz. Cl_2, H_2S, inert gases etc. The sample can also be handled in different forms such as powdered solid compressed to pellet form and sample on tape. A special quartz cell fitted with kapton window is also available for measurement of liquid samples.

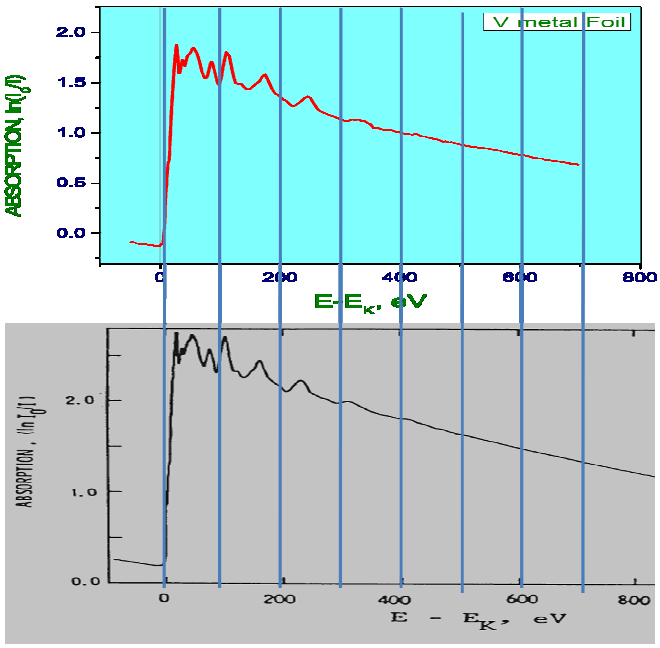

Fig. 4: (a) Comparison of K-edge EXAFS spectra of a Vanadium metal foil measured at BL-09 of INDUS-2 with the one measured at Stanford Synchrotron Radiation Light source (SSRL) USA.

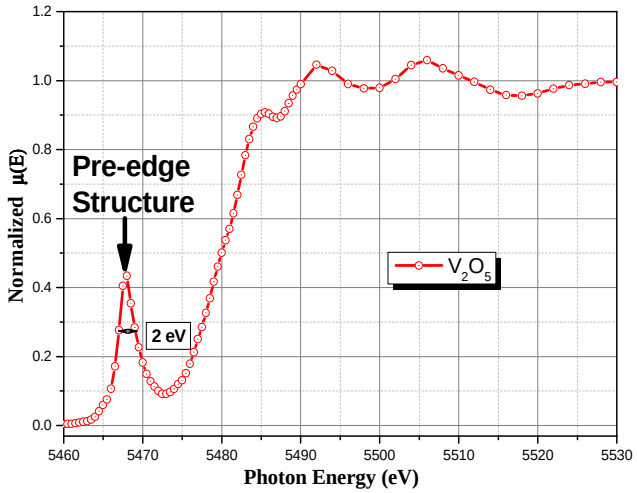

Fig.4: (b) X-ray absorption near edge spectrum (XANES) for commercial Vanadium Pentoxide (V_2O_5) powder measured at BL-09 of INDUS-2

The experimental station is also equipped with a low temperature He-gas cooled closed cycle cryostat which can go down to 4.2 K (in collaboration with HP&SRPD, BARC). The specialized software of the beamline, which controls the various diagnostic components and also the data acquisition software that collects data from the ionization chambers or solid state detectors in synchronization with the movement of the double crystal monochromator have been indigenously developed on a lab-view platform. The software has been made in a menu driven user-friendly mode so that non-expert users can also operate the beamline with a short training. After commissioning, the performance of the beamline has been tested by carrying out several measurements of standard metal foils and oxide powders. The K-edge EXAFS spectrum of a Vanadium metal foil measured at BL-09 of INDUS-2 along with one measured at Stanford Synchrotron Radiation Light source (SSRL) USA is shown in Fig. 4(a). Both the spectra measured in transmission mode matches quite well showing the extent of the satisfactory performance of the beamline. Fig. 4(b) shows the X-ray absorption near edge spectra (XANES) for commercial Vanadium pentoxide (V_2O_5) powder measured at BL-09. The pre-edge structure shows FWHM of 2eV with very good resolution achievable in the beamline.

Important Results

Since commissioning the beamline has been extensively used by a large number of users from various institutes and universities across the country and many of the results have been published in reputed international journals. Few of the important works carried out in this beamline recently are described below

Effects of Ni Concentration on the Structural and Magnetic Properties of $NiZnFe_2O_4$ Ferrites Synthesized via a Polymer Precursor [5]

Fig. 5 shows the XANES spectra at Fe K-edge of $Ni_xZn_{1-x}Fe_2O_4$ (x=0.2-0.8) nanoparticles prepared through chemical route.

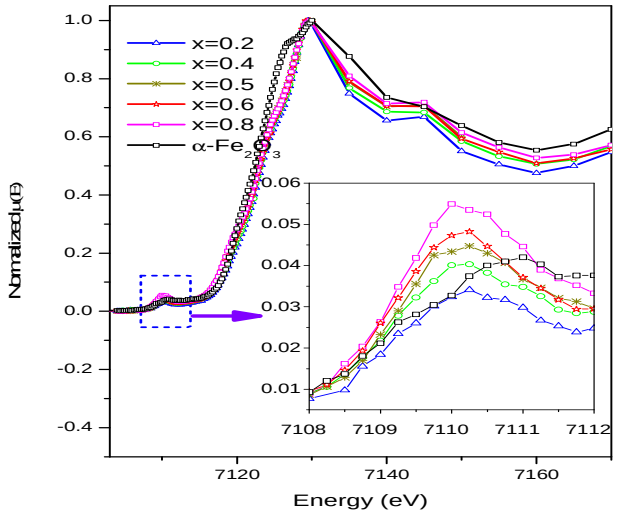

Fig. 5: XANES spectra at Fe K-edge of $Ni_xZn_{1-x}Fe_2O_4$ (x=0.2-0.8) nanoparticles

Sample	Octahedral	Tetrahedral
$Ni_{0.2}Zn_{0.8}Fe_2O_4$	87%	13%
$Ni_{0.4}Zn_{0.6}Fe_2O_4$	79%	21%
$Ni_{0.5}Zn_{0.5}Fe_2O_4$	73%	27%
$Ni_{0.6}Zn_{0.4}Fe_2O_4$	69%	31%
$Ni_{0.8}Zn_{0.2}Fe_2O_4$	61%	39%

Table 2: Percentage of cations in octahedral and tetrahedral sites

The pre-edge feature of the XANES spectra is mainly due to the 1*s* to 3*d* (electric dipole forbidden) quadrupole transition inside the crystal lattice and is attributed to the local mixing of 4*p* and 3*d* atomic orbitals, which is allowed in the tetrahedral symmetry but forbidden in the octahedral symmetry.Therefore, the enhancement of the pre-edge peak is due to increase in Fe^{3+} ion occupancy at the tetrahedral sites with the increase in Ni concentration in the samples. It was reported that in $NiFe_2O_4$, Ni^{2+} ions have favorable occupancy at the octahedral sites and any increase in Ni concentration at octahedral sites enhances the Fe occupancy in tetrahedral sites. The increase in tetrahedral coordination of Fe has also been quantitatively estimated from the relative increase in the pre-edge peaks and is shown in Table-2.

EXAFS measurements on Asymmetric Bipolar Pulse DC magnetron sputtered Ta_2O_5 thin films [6]

Tantalum pentoxide (Ta_2O_5) thin films have been deposited on fused silica substrates using a novel Asymmetric Bipolar DC (ABPDC) magnetron sputtering technique under a mixed ambient of oxygen and argon. Films have been prepared at different oxygen to argon ratios in the sputtering ambient and the EXAFS measurements on the films have been carried out at BL-09 in fluorescence mode. Fig. 6(a) shows the variation of the average Ta-O bond lengths for the first three Ta-O shells (R_{avg}) as a function of oxygen partial pressure used during preparation of the samples as obtained from EXAFS measurements, while Fig. 6(b) shows similar variation of total oxygen co-ordination numbers (N_{total}) around Ta atom in the three shells. It has been observed that the trend of variation in oxygen co-ordination as estimated from EXAFS measurements follows the variation in oxygen to tantalum ratio in the films as estimated from RBS measurement as shown in Fig.7(a), while the variation in physical density of the films obtained from RBS measurements, as shown in Fig.7(b), is found to be opposite to the variation in Ta-O bond lengths obtained from EXAFS measurements.

Finally these results have been useful to explain the variation of macroscopic optical properties of the films viz., intrinsic refractive index and band gap as a function of oxygen partial pressure.

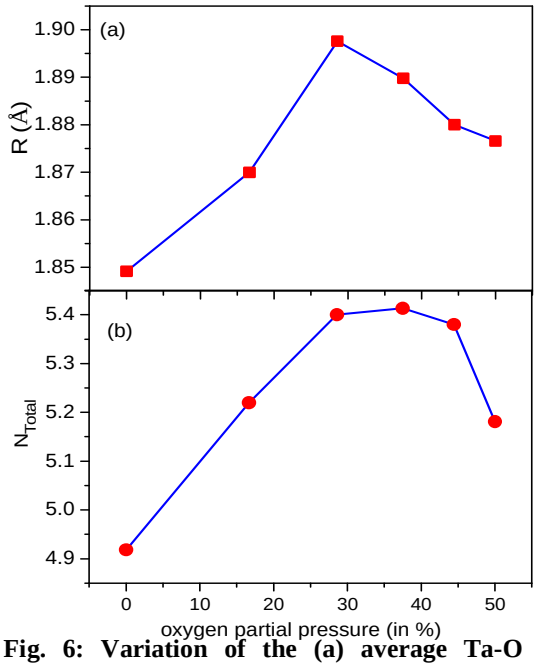

Fig. 6: Variation of the (a) average Ta-O bond lengths and (b) total oxygen co-ordination numbers (N_{total}) around Ta atoms as a function of oxygen partial pressure used during deposition

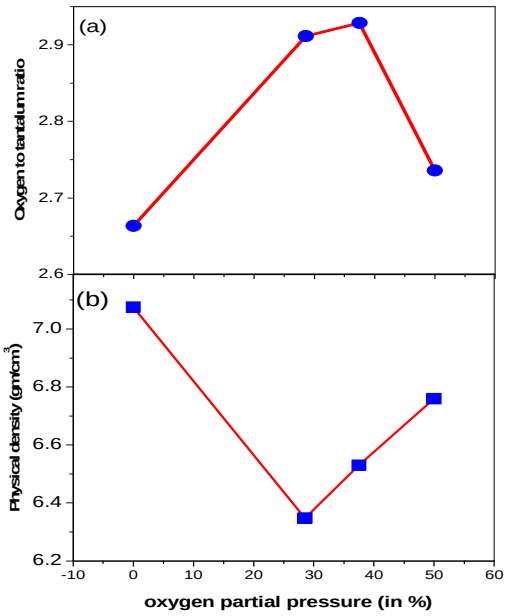

Fig. 7: Variation in (a) oxygen to tantalum ratio and (b) physical density of the films as obtained from RBS measurements as a function of oxygen partial pressure used during deposition

Local structure investigation of (Co, Cu) co-doped ZnO nanocrystals and its correlation with magnetic properties

Pure, Co doped and (2.5% Co, 2.5% Cu) co-doped ZnO nanocrystals have been prepared by wet chemical route to study the possible enhancement in magnetization of Co doped ZnO system due to an increase in carrier concentration by Cu doping. Fig. 8 shows the magnetization (M) vs. applied field (H) curves of 2.5% Co doped, 2.5% Cu doped and (2.5% Co, 2.5% Cu) doped ZnO samples measured at 300 K.

It can be seen that though the Cu doped sample does not show any magnetic hysteresis behavior, whereas 2.5% Co doped sample reveals magnetic hysteresis behavior with saturation magnetization (M_S) close to 0.095 emu/gm. It is also found that the (Co,Cu) co-doped sample shows a non-saturation trend, with almost a linear increase in magnetization with magnetic field and its magnetic moment value is less than the Co doped sample. The decrease in magnetization in the (2.5% Co, 2.5% Cu) co-doped sample compared to the 2.5% Co doped sample has been investigated by EXAFS measurements. Fig. 9(a) represents FT-EXAFS $\chi(R)$ versus R spectra of 2.5% Cu doped ZnO samples measured at Cu K-edge along with the best fit theoretical spectra where the fitting has been carried out by using CuO structure while Fig.

9(b) shows the fitting obtained by assuming wurtzite ZnO structure and replacing the central Zn atom with Cu. Comparison of the above spectra shows that the local structure of Cu ions resembles that of cubic CuO rather than ZnO tetrahedra, or in other words it proves the presence of CuO phase in the co-doped ZnO NCs. The presence of CuO phase is detrimental to the magnetic properties of the sample which causes the reduction in the magnetisation of the (Co,Cu) co-doped sample compared to the Co doped sample.

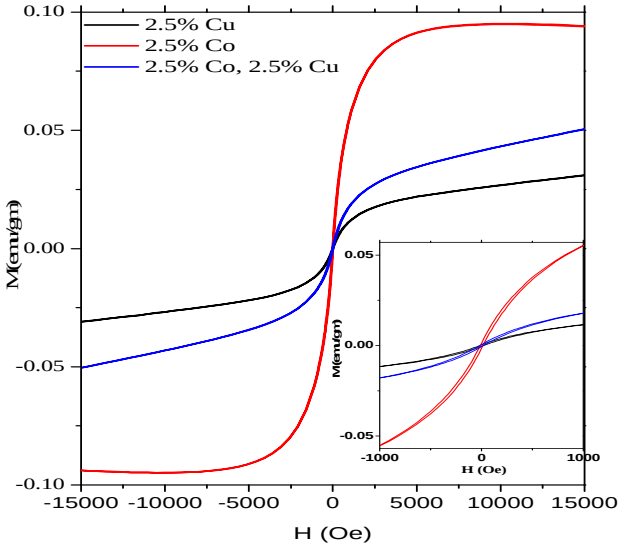

Fig. 8: Magnetization (M) vs. applied field (H) curves of 2.5% Co doped, 2.5% Cu doped and (2.5% Co, 2.5% Cu) doped ZnO samples measured at 300 K

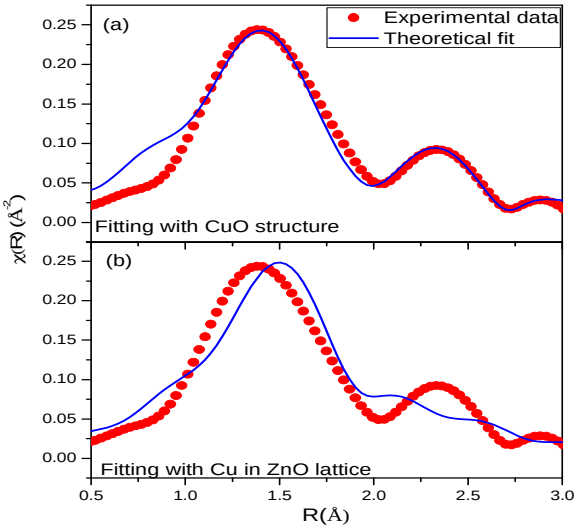

Fig. 9: FT-EXAFS spectra of 2.5% Cu doped ZnO samples measured at Cu K-edge along with the best fit theoretical spectra where the fitting has been carried out (a) by using CuO structure and (b) by assuming wurtzite ZnO structure and replacing the central Zn atom with Cu

Acknowledgement

The valuable contributions of each individual participated in this Group Award Winning Activity is greatly acknowledged.

References

[1] X-Ray Absorption: Principles, Applications, Techniques of EXAFS, SEXAFS and XANES, edited by D.C. Konigsberger and R. Prince (Wiley, New York, 1988).
[2] D. Bhattacharyya, A.K. Poswal, S.N. Jha, Sangeeta and S.C.Sabharwal, Nuclear Instruments and Methods in Physics Research A, **609** (2009) 286.
[3] S. Basu, C. Nayak, A. K. Yadav, A. Agrawal, A. K. Poswal, D. Bhattacharyya, S. N. Jha and N. K. Sahoo, J. Phys.: Conf. Ser.**, 493** (2014) 012032.
[4] K. Poswal, A. Agrawal, A. K. Yadav, C. Nayak, S. Basu, S. R. Kane, C. K. Garg, D. Bhattachryya, S. N. Jha and N. K. Sahoo, AIP Conf. Proc., **1591** (2014) 649.

[5] J. Jadhav, S. Biswas, A. K. Yadav, S. N. Jha, D. Bhattacharyya and N. K. Sahoo, Journal of Nano Research, **34** (2015) 9.

[6] S. Maidul Haque, Pankaj R. Sagdeo, D. D. Shinde, J. S. Misal, S. N. Jha, D. Bhattacharyya and N. K. Sahoo, Applied Optics, **54** (2015), 6744.

BARC NEWSLETTER
FOUNDER'S DAY SPECIAL ISSUE 2015

DESIGN, DEVELOPMENT AND COMMISSIONING OF 350 MHZ FOUR-VANE RADIO FREQUENCY QUADRUPOLE (RFQ) AND ITS HIGH POWER RF SYSTEM

P. Singh
Ion Accelerator Development Division

Dr. Pitamber Singh, Physics Group and his team received the DAE Group Achievement Award for the year 2013

Abstract

A 400 keV deuteron Radio-frequency quadrupole (RFQ) has been designed, developed and commissioned at BARC, Mumbai. In order to ease the fabrication a conventional (LANL) design procedure was adopted, where the vane voltage and cross section of RFQ are kept constant. The complete beam dynamics, 2D and 3D cavity dynamics were studied using the computer codes LIDOS, SUPERFISH and CST Microwave studio. The 1.1 m long RFQ operating at a frequency of 350 MHz required RF power of 60 kW to accelerate the deuteron beam to a final energy of 400 keV with beam transmission of ~ 95%.

Introduction

Radio frequency quadrupole (RFQ) accelerators are extensively used as injectors in the high current linacs because of their remarkable capability of simultaneously focusing, bunching and accelerating the low-energy ion beams with high transmission and minimum emittance growth [1]. In a conventional accelerator such as the drift tube linac (DTL), bunching is accomplished prior to injection into the linac using RF bunching cavities. In buncher cavities, RF electric fields are applied to the DC input beam to produce a velocity modulation in which early particles are decelerated and late particles are accelerated. For high-current beams, the bunching is not very efficient because of the high space-charge forces at low energies. In high intensity beams, the bunching process causes an increase in the beam density, which increases the space-charge forces further resulting in an increase of the transverse beam emittance. The conventional DTL linacs, in order to make the efficient use of DTL structures, the extraction voltage of the ion source was increased to about 0.70 MV, generated using the Cockcroft Walton generators. The fundamental limitations of the conventional linacs was not only in terms of beam current, but also the reliable operation of HV columns, which was responsible for the large fraction of the machine downtime. Beams were also lost during their focusing and bunching before injection into the linac.A RFQ uses the velocity independent transverse electric focusing at low energies which gives a significant strong focusing as compared to conventional linacs that normally use velocity dependent magnetic lenses.This allows one to extend the practical range of operation of RFQs to

low velocities, thus eliminating the need for large, high voltage dc accelerators. The RFQ accelerators are well suited for acceleration of beams with low velocities in the range of about 0.01 to 0.1 times the speed of light. Since RFQs bunch the beam adiabatically, by proper choice of parameters one can achieve a high beam transmission (> 90%).

Brief description of the work

The front-end of the proton linac driver for an Accelerator-Driven System (ADS) has been conceptualized as a 20 MeV, 30 mA, CW proton linac, and has been implemented as the Low Energy High Intensity Proton Accelerator (LEHIPA) project at BARC [2]. This will consist of a 50 keV ion source, a 3 MeV, 4 m long, radio-frequency quadrupole (RFQ) and a 3-20 MeV, 12 m long, drift-tube linac (DTL).Since RFQ technology is challenging, it was decided to design and build, as a precursor, a 400 keV, 1.1 m long deuteron RFQ, which can also be used for 14 MeV neutron generation [3,4] using D-T reaction. After considerable design efforts, and after ascending a steep technological curve, this RFQ was developed and successfully commissioned [5,6]. The system consists of: (i) an ion-source that can deliver deuteron beams at energies up to 50 keV, (ii) a Low Energy Beam Transport (LEBT) line consisting of two solenoids [7], two steerers, and various diagnostic elements, (iii) the 400 keV RFQ [6], (iv) a 90^0-analyzing magnet (v) a 60 kW RF system at 350 MHz [8], and (vi) a 50 kW power-coupler [9] that couples the power into the RFQ with better than 99.5% efficiency.
Based on the simulation studies, the RFQ made of OFE copper was machined and vacuum brazed at BATL, Trivandrum. For an RFQ to work efficiently, it must be made with high level of geometric precision. A series of measures were taken to achieve the desired level of accuracies. While brazing we adopted a two stage brazing process, in the first stage RFQ vanes were brazed, using Palcusil 5(68% Ag+27% Cu+5% Pd), in a horizontal vacuum furnace. In the second stage the ports and end flanges are brazed using Cusil (28% Cu+ 72% Ag) as a filler material. The RFQ after 1st and 2nd brazing is shown in Figs. 1 & 2. The various tolerances achieved during fabrication were: (1) vane position within ± 30 μm, (2) vane modulations within ± 20 μm, (3) vane thickness within ± 10 μm, (4) vane flatness within ± 20 μm.

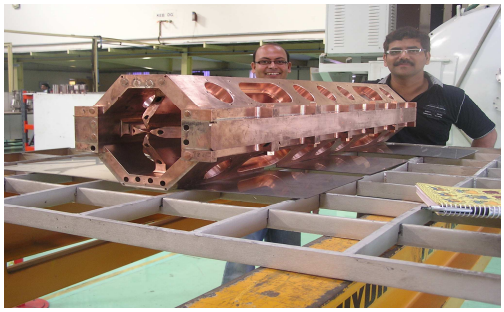

Fig. 1: RFQ after 1st Brazing

Fig. 2: RFQ after 2nd Brazing

After brazing, the RF characterization was done, this mainly involved frequency measurements, field tuning and quality factor measurements. Field distribution studies were done using the bead pull measurement setup developed in the lab [Fig. 3].

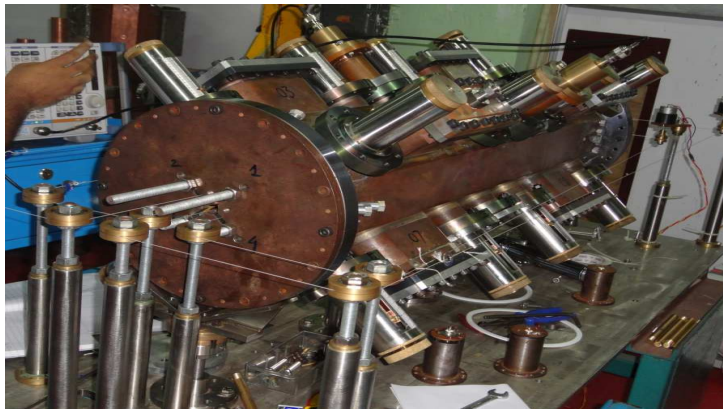

Fig. 3: Bead-pull measurement setup

Initially, the magnetic measurements were done using a metallic bead made of brass of Φ6 mm for the flush tuner conditions. In order to achieve the required field distribution the perturbative analysis of the RFQ has been studied and an algorithm was written to tune the cavity. With the help of this algorthm, the quadrupole field levels were tuned within 5% (dQ/Q_0) and dipole contribution < 4% (d_1/Q_0, d_2/Q_0) [Fig.4]

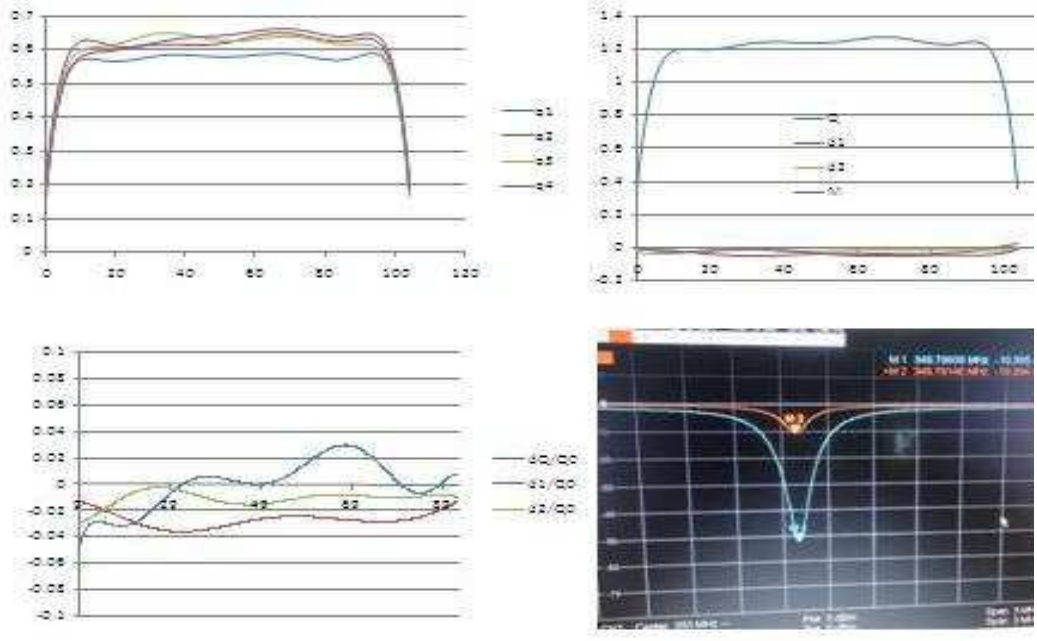

Fig. 4: Final field distribution and dipole and quadrupole contributions

The tuners were adjusted to get the required field distribution as well as resonant frequency of 350 MHz. After the low power testing and cleaning the quality factor (Q_0) was measured to be 6384 shown in Fig. 5, which is 73 % of the simulated value.

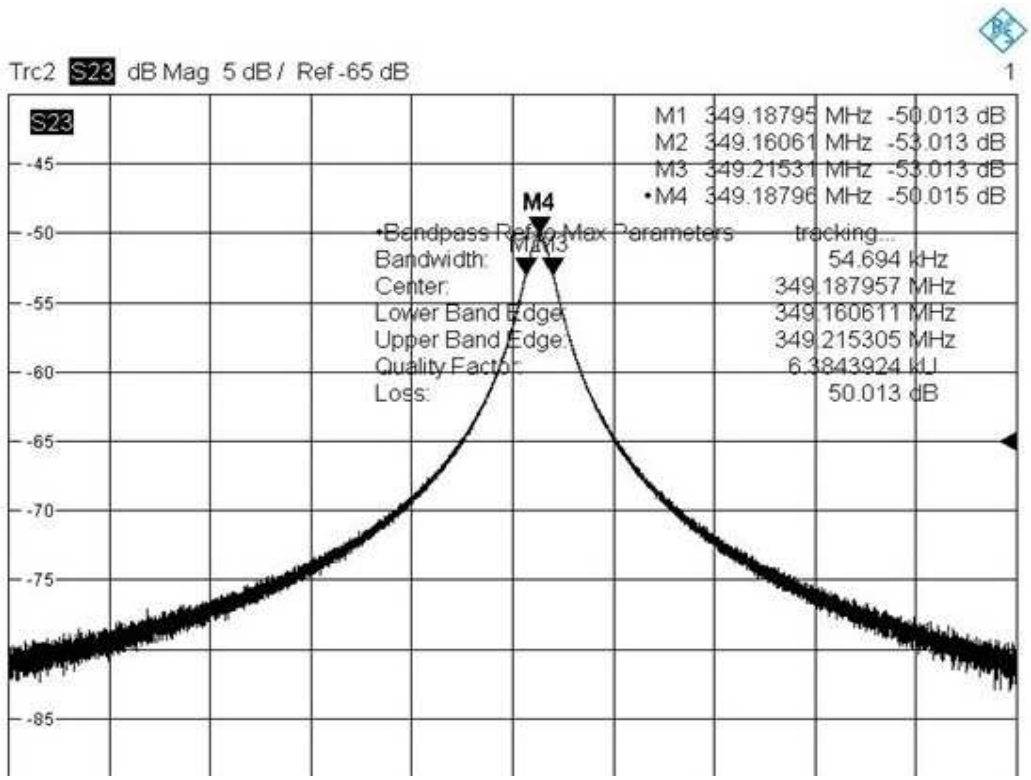

Fig. 5: Quality factor (Q_0)

After the successful completion of cold testing, the high power RF conditioning of the RFQ was done. The RFQ required around 60 kW of RF power to compensate for beam acceleration, vane voltage generation and power dissipation across the RFQ cavity. Therefore, a 60 kW tetrode based RF system at 350 MHz fulfilling all the critical parameters required for the accelerator, like high reliability, ruggedness, good wall plug efficiency, high gain and maximum voltage standing wave ratio (VSWR) withstanding capability, RF radiation limit below IEEE standard, low harmonic contents, was designed, developed and tested [Fig.6].

The RF system comprises of many subsystems such as tetrode based high power amplifier of 60 kW, its driver and pre-driver amplifiers, directional couplers, rigid transmission lines, crowbar based fast protection circuit, 80 kW RF load, a junction circulator, programmable logic controller (PLC) based interlock and protection system, low conductivity cooling subsystems and many other bias supplies of low and high voltage ratings.

The power was fed into the RFQ through 60 kW RF coupler [Fig.7].

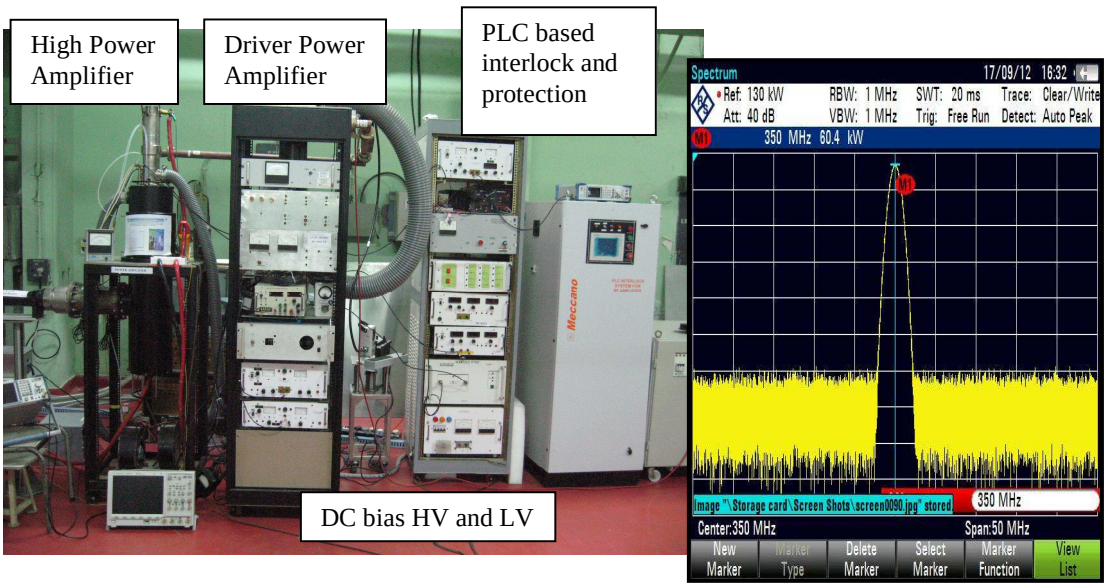

Fig. 6: 60 kW tetrode based RF Amplifier

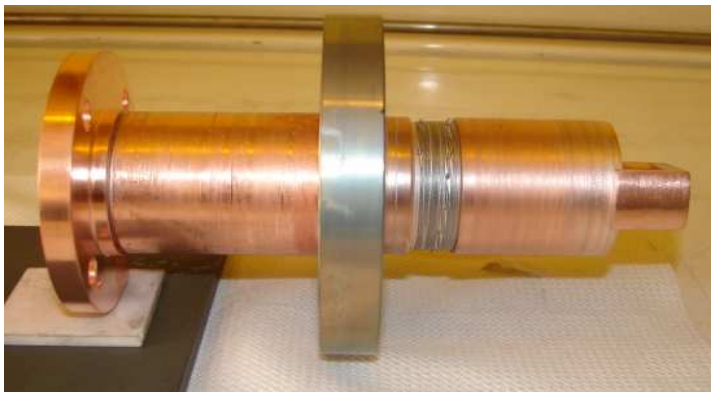

Fig. 7: 60 kW RF loop coupler

The RFQ was conditioned to a peak power of 60 kW with a duty cycle of 0.1 % (1 ms pulse width and 1 Hz rep rate). Once the RFQ was conditioned successfully at a peak power of 60 kW the beam was injected. In order to accelerate the beam through the RFQ a beam line was set up shown in Fig.8.

It mainly consists of a RF ion source (Alphatros), two solenoids, two steering magnets, one bending magnet and two Faraday cups. The ion source along with the accelerating

column used to accelerate the beam to 50 keV is installed in high voltage deck. This high voltage deck was tested up to a voltage of 75 kV, so the input beam energy can be varied from 0-75 keV.

Fig.8: Beam line of 400 keV RFQ

The emittance measurements of the injected beam is important for obtaining the emittance of the input beam within the accepted limit of the RFQ and also in optimizing the LEBT line that matches the beam from the ion source to the RFQ. A slit-wire scanner based emittance measurement setup was developed [Fig.9] for the transverse emittance measurements of H^+ and D^+ beams [Fig. 10]. The emittance measurement setup consists of movable slits of 0.3 mm width and movable tungsten wire of 0.05 mm diameter as shown in Figure 1.

The spatial beam distribution is scanned by the slit while the angular distribution is scanned by the wire scanner located at a distance of 140 mm downstream the beam line. A 1 µm precision linear motion mechanism is used for slit and wire holder movement. The beam emittance can be measured simultaneously in both transverse directions in this setup. The beam dynamics simulation of the RFQ with injector line was performed using TRACEWIN with the measured input beam emittance parameters. The measured Twiss parameters for 100 µA, 50 keV, D+ beam are α = -0.29, β = 1.28 mm/mrad with an rms emittance, ε_{yrms} = 2.5 π.mm.mrad [10, 11]. Figure 2 shows the variation of normalized rms emittance of H+ and D+ beams as a function of beam current. The emittance of the input beam is well within the acceptance value of RFQ.

Results and conclusions

We accelerated both the proton (H^+) and deuteron (D^+) beams through this RFQ. In order to accelerate the H^+ beam the RF power needed was ~ 15 kW and input beam energy should be 25 keV. The H+ beam was accelerated to 200 keV with a transmission of 70%. The output beam energy and beam current are measured using the 90^0 bending magnet and a faraday cup. The variation of transmission with input beam energy and with the RF power was also measured. After successful acceleration of H+ beam the D+ beam at an input energy of 50 keV was accelerated to 400 keV at a peak power of 60 kW. The transmission of 95 % was measured. The output D^+ beam energy and its energy spread were measured using 90^0 bending magnet and the results are shown in Fig.11. The results are in good agreement with the simulations.

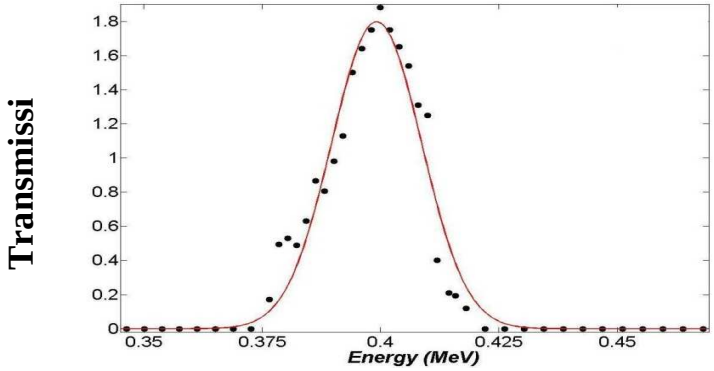

Fig.11: Output energy of D^+ beam

Acknowledgement

Following members of the RFQ team (P. Singh, Shrikrishna Gupta, S. Krishnagopal, Manjiri Pande, A. Agarwal, Rajesh Kumar, S.K. Singh, B.M. Kukreti, S.V.L.S. Rao, Rajni Pande, A. Basu, Shweta Roy, Piyush Jain, S.D. Shrotriya, Sapna P., Sonal Sharma, Jose V. Mathew, N.R. Patel, N.B.V. Subrahmanyam, J.P. Bhatt, S.V. Ware, Shiju A., M.R. Mishra, G.N. Singh, Pravin R. Parate, Laxman D. Tayade, Prashant P. Gorule, H.K. Sane, N.J. Koli, N.R. Dalvi, Mukesh Thapad, Gopal Joshi, N.K. Prasad) made excellent contributions towards design, development and commissioning of the 350 MHz four vane Radio Frequency Quadrupole (RFQ) and its high power RF system and we thank them all.

Publications

[1] Design studies of a high current radio frequency quadrupole for accelerator driven systems prohramme, S.V.L.S. Rao and P. Singh, Pramana –J Physics **74** 247 (2010), I.M Kapchinskii and V A Tepliakov, Prib. Tekh. Eksp **2**, 19 (1970).

[2] Accelerator Development in India for ADS programme, P. Singh, S. V. L. S. Rao, Rajni Pande, T. Basak, Shweta Roy, M. Aslam, P. Jain, S. C. L. Srivastava, Rajesh Kumar, P. K. Nema, S. Kailas and V. C. Sahni, Pramana- J Phys. **68**, 331 (2007), Status of the LEHIPA Project at BARC, InPAC-2006, Nov 1-4, 2006, BARC, Mumbai, p50.

[3] Physics Design of a 400 keV D^+ RFQ for PURNIMA Sub-Critical Facility, Shweta Roy, T. Basak, Rajni Pande, S. V. L. S. Rao, M. Aslam, P. Jain, P. Singh, P.K. Nema, S. Kailas and V.C. Sahni, BARC Report-BARC/2005/I/005

[4] Design of a RFQ based 14 MeV Neutron Generator for Studying Neutron Multiplication in a Sub-Critical Assembly, R. P. Anand, T. K. Basu, B.K. Godwal, V.K. Handu, S. Kailas, P.K. Nema, Manjiri Pande, B. V. Rama Rao, M. K.V. Rao, V.C. Sahni and P. Singh, Proc. DAE Symp. Nucl. Phys. (India) 46B, 574 (2003).

[5] Design, Development and Acceleration Experiments of a Four-Vane RFQ at BARC, S. V. L. S. Rao, Piyush Jain, Jose V. Mathew, Rajni Pande, Shweta Roy, S. Shrotriya, N. Patel, A. Shiju, , M. R. Mishra, Gireesh N. Singh,L. Tayade, Praveen Parate, B M Kukreti, Rajesh Kumar, Manjiri Pande, S. Krishnagopal, S. K. Gupta, P. Singh, InPAC 2013 at VECC, Kolkata, Nov.19-22, 2013

[6] Design, development and acceleration trials of Radio-frequency quadrupole, S V L S Rao, Piyush Jain, Rajni Pande, Shweta Roy, Jose Mathew, Rajesh kumar, Manjiri Pande, Srinivas Krishnagopal, S K Gupta and P Singh, Review of Scientific Instruments **85**, 043304 (2014).

[7] A LEBT for the 400 keV RFQ Based Neutron Generator at BARC, Rajni Pande, S. V. L. S. Rao, Shweta Roy, Manas Mishra, L.D Tayade, P.R Parate, Sapna P., Shailaja Ware, S. K Singh, A. Agarwal, S. K Gupta, P. Singh, Proc. Indian Particle Accelerator Conference (InPAC-2011), Feb 15-18, 2011, IUAC, New Delhi.

[8] Design and development of 60 kW, 350 MHz RF system in CW and Pulse mode for 400 keV RFQ accelerator, Manjiri Pande, Sandip Shrotriya, Niranjan Patel, Shiju A, Sonal Sharma and P.Singh, IEEE-MTTS-IMARC 2013, Dec 14-16, 2013, New Delhi.

[9] Development of a 50 kW, 350 MHz Pulsed Power Coupler for RFQ conditioning, Rajesh Kumar, P. Singh, L.M. Joshi, Proc. Indian Particle Accelerator Conf.(InPAC 2011), Feb 15-18, 2011, IUAC, New Delhi.

[10] Transverse Emittance Measurement Studies of a Deuteron Ion Source Beam, Jose V. Mathew, S.V.L S. Rao, Rajni Pande, M.R. Mishra, L.D. Tayade, P.R. Parate, P. Singh, InPAC 2013 at VECC, Kolkata, Nov.19-22, 2013.

[11] Beam emittance measurements and simulations of injector line of RFQ, Jose Mathew, S V L S Rao, Rajni Pande and P. Singh, Review Scientific Instruments **86**, 073306 (2015).

DEVELOPMENT OF CRYSTAL GROWTH SYSTEM TO GROW Tl DOPED CsI AND NaI SINGLE CRYSTALS FOR APPLICATIONS IN NUCLEAR RADIATION DETECTION

S.G. Singh, D.G. Desai, A.K. Singh, S. Pitale, G.D. Patra, M. Ghosh, M. Tyagi, B. Tiwari, S. Sen and S.C. Gadkari*
Technical Physics Division

Dr. Sanjay C. Gadkari, Physics Group and his team received the DAE Group Achievement Award for the year 2013

Abstract

Crystal growth systems based on the vertical Bridgman-Stockberger technique have been developed to grow Tl doped CsI and NaI single crystals of size up to 50 mm diameter and 80 mm length. The growth parameters for each material have been optimized to obtain the device-grade single crystals for high energy radiation detection. The expertise has been developed to process the grown crystals and to fabricate gamma-ray detectors. The entire technology starting from initial chemical powders to finished scintillator detectors coupled to photo-detectors (both PMTs and photo-diodes) has been developed and the know-how is ready for transfer to industry.

Introduction

Doped halides are the oldest and most widely used scintillator materials to date. Some of these (NaI:Tl, CsI:Tl, CsI:Na, etc.) have been deployed in various applications for over 60 years, however, the research on these materials to improve their scintillation properties is still at the forefront [1]. Alkali halide scintillator crystals, in particular, NaI(Tl), CsI(Tl), CsI(Na), are produced usually using directional crystallization of the corresponding melt in a crucible employing the Bridgman/Stockbarger method. The Bridgman technique is useful to grow small to medium size crystals (10 mm – 80 mm diameter). The growth of crystals using the Bridgman method is relatively simple, however, sticking of the grown crystal to the crucible wall and hence its recovery after the growth and thermal/mechanical stresses generated are important issues of considerable interest [2]. Luminescence and scintillation properties of grown crystals depend on various crystal growth parameters including starting material preparation, growth process and post growth treatments [3]. In the present work we report the growth of device-grade single crystals of Tl doped CsI and NaI using a modified vertical Bridgman crystal growth technique. The design and construction of the modified Bridgeman system and specially designed crucible employed for the growth of Tl doped CsI and NaI crystals are elaborated.

Furnace and crucible design

The crystal growth system is based on the Bridgman technique. This method is based on the work of Bridgman in 1925 [4]. This is a popular technique to grow single crystals of various

halides. In this method temperature gradient moves slowly relative to a crucible (vertically or horizontally) until the melt in the crucible solidifies.

The main economic advantage of the method is simple basic apparatus, and little operator attention. Disadvantages arise from the contact between container and melt/solid which can give spurious nucleation, sticking of the crystal ingot inside the crucible and consequently generating thermal and mechanical stresses.Therefore, the furnace design, appropriate crucible material and shape take the central stage in designing a crystal growth system.The crystal growth system, designed by us consists of two heating zones controlled independently and separated from each other using a baffle to increase the temperature gradient and minimize temperature fluctuations. The furnace, developed for the crystal growth, consists of four independently controlled resistive heating elements. The top isothermal zone consisting of two heating elements is separated from the bottom isothermal zone by a 50 mm thick baffle (adiabatic zone). Four temperature controllers (Eurotherm, Model no. 2416) are used to set and control necessary temperature profiles in the furnace. Fig.1 shows the schematic diagram of the furnace along with photographs of the complete crystal growth system. A servo motor with an appropriate gear assembly is used for lowering the crucible. A translational speed from 0.1 to 10 mm/h for crystal growth and 150 mm/min for coarse setting can be set form a touch screen panel mounted at the top of the furnace. Further, the furnace can be rotated at elevated temperatures around a horizontal axis passing through the middle of the furnace. There is a provision to lock the crucible assembly while rotating the furnace whenever required. A temperature gradient up to 20^{o}C/cm can be set in the adiabatic zone. The axial and radial temperature profiles of the furnace are shown in Fig. 2.

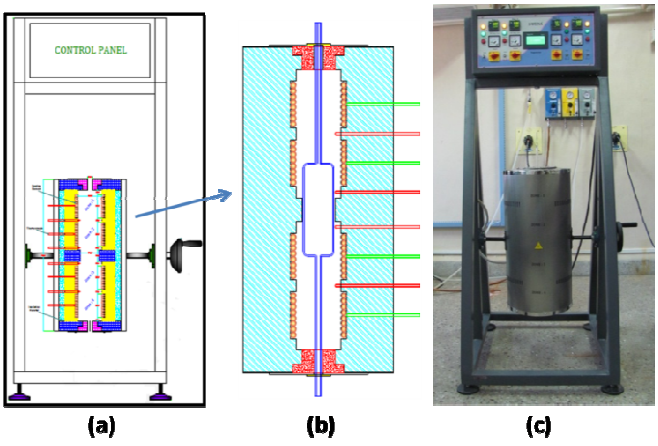

Fig.1: Modified Bridgman furnace (a) schematic diagram of the crystal growth system, (b) enlarged view of the furnace showing the position of control and monitoring thermocouples and (c) photograph of the crystal growth system

The crucible used in the modified Bridgman furnace was specially designed. It consists of two parts of approximately equal lengths (as shown in Fig.3). The lower part has a conical shape with a slightly less diameter (ID: 55 mm) than the upper cylindrical part (ID: 60 mm). The crystals grow in the lower part of the crucible while after the growth the crystal is retrieved in

the upper part by a definite process involving the rotation of the furnace along with the crucible at elevated temperatures. The detailed description of the growth is given in the next section.

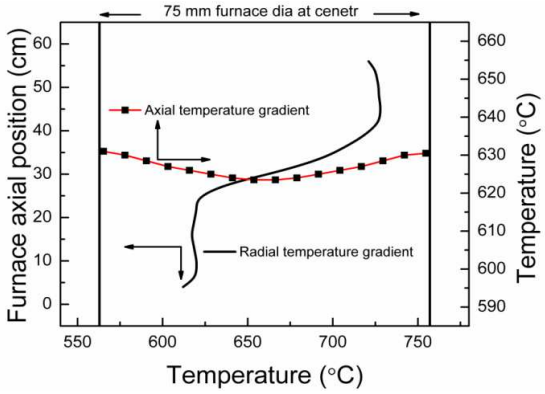

Fig.2: Radial and axial temperature profiles of the crystal growth furnace

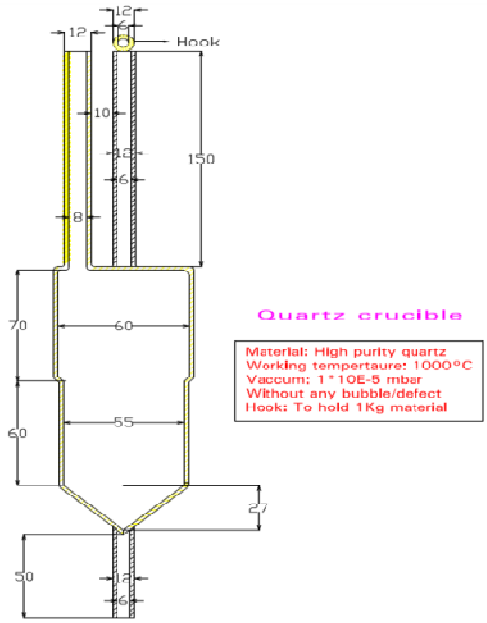

Fig.3: Schematic drawing of the crucible used for the growth of crystals using the modified Bridgman furnace

Material preparation and dehydration

High purity CsI (99.99%, 500 g) is taken in clean and dry crucibles. The loaded crucible is placed in an oven (already at 50°C) and connected to a vacuum system consisting of rotary and cryo-sorption pumps. The crucible is evacuated to $5x10^{-3}$ mbar pressure. After this, the temperature of the oven is increased up to 300°C in steps of 50°C under vacuum. A one hour

dwell is given at each step and the crucible is thoroughly shaken in between temperature steps to avoid the formation of lumps during the dehydration process. After the completion of dehydration the crucible temperature is brought down to 50°C and 1.275 g of TlI (0.2 mol%) (0.1 mol% TlI for NaI) is mixed in the dehydrated material in a manner that the dehydrated material is least exposed to ambient moisture. Again the crucible is connected to the vacuum system and evacuated gradually to $5x10^{-3}$ mbar pressure. The furnace temperature is increased to 150°C in the step of 50°C with a dwell of 30 minutes at each step. This completes the dehydration process of the material though finally a proper visual inspection of the material is required to ensure a complete dehydration of the material. The crucible is sealed using an LPG gas torch under a running vacuum condition and at about $5x10^{-3}$ mbar pressure of Ar (The crucible is flushed with Ar 3-4 times). During the Ar flushing crucible is kept at 100°C.

Crystal growth

The silica crucible containing the material (discussed in section-3) is located in the upper zone of the furnace for a complete melting. The temperatures of all the zones are raised in such a manner that the temperature of the upper zone is about 50°C above the melting point (MP) while the lower zone temperature is about 50°C lower than the MP (Fig.4-1). Once the material inside the crucible melts completely it is allowed to thermalize for 4 h. The crucible is then lowered at a rate of 0.5-2 mm/h to the bottom zone of the furnace through the temperature gradient (adiabatic zone) for a complete solidification of the melt into single crystal (Fig.4-2). The crucible is locked inside the furnace using a locking mechanism and the furnace together with the crucible is inverted (rotated through 180° about a horizontal axis) (Fig.4-3).

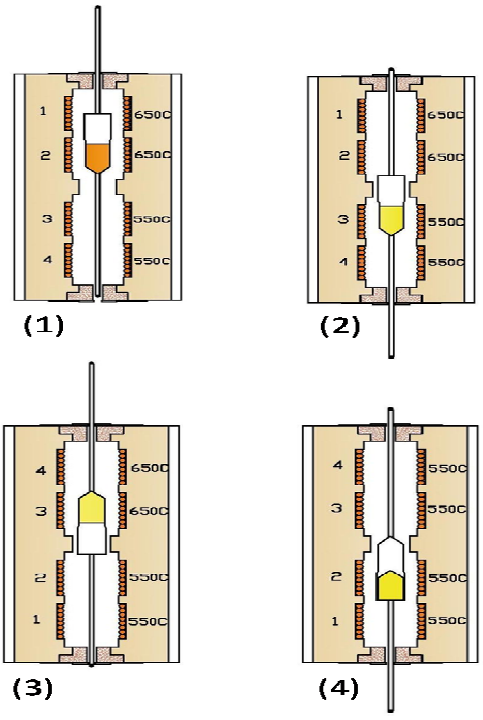

Fig. 4: The schematic diagram of the complete growth process of the single crystal in the modified Bridgman furnace, (1) Loading of the crucible and melting of the material, (2) lowering of the crucible to lower zone and solidification, (3) locking of the crucible in the furnace and rotation by 180° and (4) retrieval of the crystal

Now the temperature of the zone 3 and 4 containing the grown crystal is raised so that the temperature of the zone containing the grown crystal becomes slightly higher than the MP of the material and the grown crystal slides down in the lower zone of the crucible that has a slightly larger diameter. Temperatures of the all the zones are then lowered quickly to the same temperature (MP - 50°C) to achieve a uniform temperature in the furnace (Fig. 4- 4). The crystal is annealed at this temperature for 4 h. Finally the furnace is cooled down to room temperature at a uniform rate of 30°C/h. Afterwards the silica glass crucible is cut open to retrieve the grown crystal.

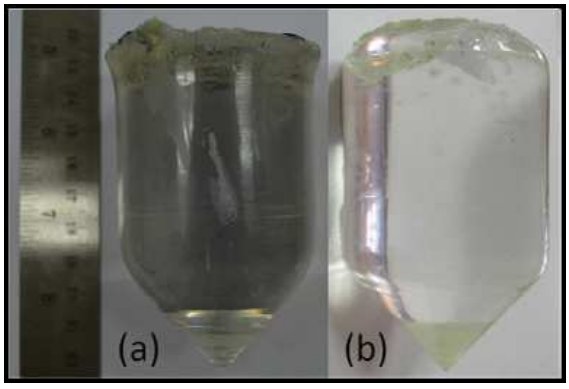

Fig.5: Photographs of (a) CsI:Tl (0.2 mol%) (b) NaI:Tl (0.1 mol%) single crystals

Scintillation characterization of grown crystals

To test the scintillation properties a detector element of size 18x18x18 mm^3 (for CsI:Tl) and 45 mm ϕ x 45 mm L were fabricated by processing of crystal ingot (50 mm diameter and 50 mm length). About 6 layers of 0.1 mm thick Teflon tape were used as reflectors. Silica based optical grease was used for the optical coupling. The fabricated CsI:Tl detector element of size 18x18x18 mm^3 was tested for scintillation performance using different readout system (i) P-I-N diode read out (Hamamatsu: S3204-8 18x18 mm^2 active area for CsI:Tl only) and (ii) Photomultiplier tube (Hamamatsu: R6095 25 mm diameter). In case of P-I-N photodiode 10-12 μs pulse shaping was used while in case of PMT read out it was kept as 5μs. To check the performance of the scintillator with the standard 50 mm diameter head-on PMT (Hamamatsu: R1306), scintillator detector elements of 45 mm diameter and 45 mm length were fabricated from the crystal ingots and mounted on the PMT. Reflector and mounting arrangement were similar to the detector described earlier. Different gamma-ray sources (^{60}Co, ^{57}Co, ^{137}Cs, ^{134}Cs, ^{22}Na) were used to check the energy dependence of scintillation characteristics.

Discussion

The main advantage of the present growth process over the conventional Bridgman system is that the grown crystal is subjected to minimum thermal and mechanical shocks during the retrieval of the crystal. After the growth crystal could be annealed for varying durations in the sealed ampoule to improve the properties without any contamination or stress as in this mncondition the grown crystal is free from the crucible walls. Photographs of grown crystals are shown in Fig.5.

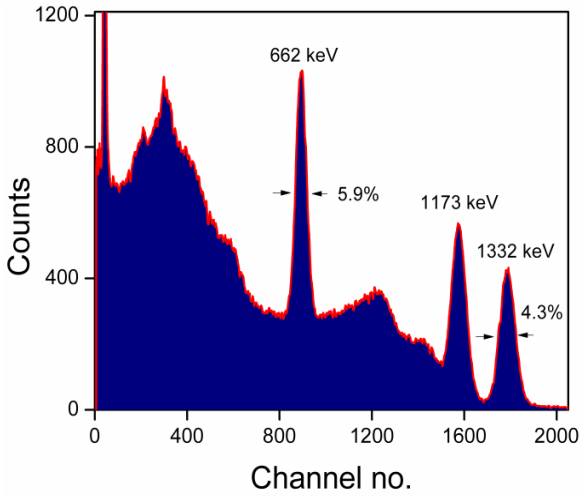

Fig.6: Gamma-ray spectrum of ^{137}Cs and ^{60}Co recorded using a CsI:Tl crystal (18x18x18 mm^3) coupled to a PMT

Typical gamma-ray spectrum recorded using the CsI:TL (18x18x18 mm^3) + PMT detector for different gamma sources (^{137}Cs and ^{60}Co) is shown in Fig.6. The fabricated detectors show an energy resolution of 6.0 ±0.2% at 662 keV. The detector performance of 45 mm diameter and 45 length scintillator was tested using a 50 mm diameter PMT. A schematic of detector assembly is shown in Fig.7. The typical gamma spectrum is shown in Fig.8. The energy resolution at 662 keV was found to be 6.5 ±0.2% that is remarkable for the CsI detectors of this size. The resolution obtained from this detector was comparable to the best quoted values for the NaI based detectors despite the mismatch of the PMT response with the emission profile of CsI:Tl (550 nm), this indicated the excellent quality of the grown crystals. The emission from the CsI:Tl at 550 nm matches well with the photodiode response, the CsI:Tl and P-I-N photodiode combination would have several advantages over the conventional PMT based detectors. Low voltage operation, magnetic insensitivity, rugged and compact size, economical, etc. are a few advantages to be mentioned here.

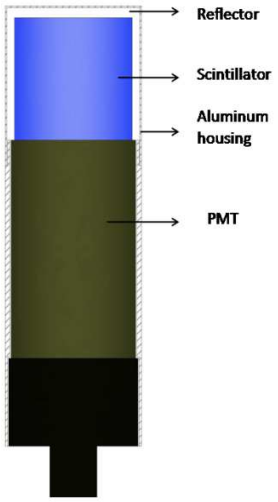

Fig.7: Schematic diagram of the scintillation detector assembly

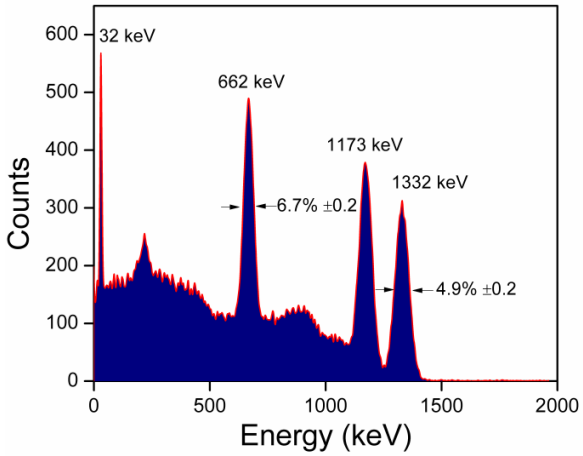

Fig.8: Gamma-ray spectrum of ^{137}Cs and ^{60}Co recorded using a CsI:Tl crystal (45 mm ϕ x 45 mm L) coupled to a PMT

A detector of size 18x18x18 mm^3 was coupled to a photodiode with the same active area. As in this case the time response of detector also depends upon the junction capacitance of the photodiode, the integration time was set at 10-15 μs while in case of PMT it was 4-5 μs. Gamma-ray spectrum recorded using a CsI:Tl+P-I-N detector is shown in Fig.9. An energy resolution of 8±0.2% could be achieved at 662 keV while at 1332 keV it was 5±0.2%. Though, in this case, the energy resolution at higher energies (>1 MeV) was comparable to the resolution obtained from the PMT based detector, at lower energies the resolution was poor. This is due to the fact that the P-I-N photodiodes have no gain and the electronic noise generated in various components like pre-amplifier, connecting pins/wire etc dominants at lower energies. This is the reason that to detect gamma energy below 100 keV special low noise electronics is required [5].

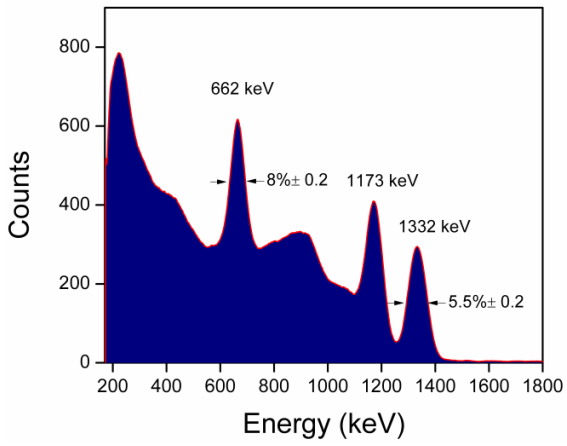

Fig.9: Gamma-ray spectrum of ^{137}Cs and ^{60}Co recorded using a CsI:Tl crystal (18x18x18 mm^3) coupled to a P-I-N photodiode

Though the crystal growth system was designed for the growth of CsI:Tl it can be used to grow any halide crystals having melting point up to 900°C. To demonstrate the versatility of the system single crystals of NaI:Tl were grown and characterized. All the growth parameters were the same as for the CsI except that the material was handled in a glove-box with reduced moisture and oxygen content. The material was dehydrated following the same procedure as described in the section 3. The TlI doping level was kept at 0.1-0.12 mol%. After the growth the crystal is annealed at 600°C for 4 h and finally the furnace was cooled down to room temperature at a uniform rate of 20°C/h. A photograph of an as-grown crystal is shown in Fig. 5(b).

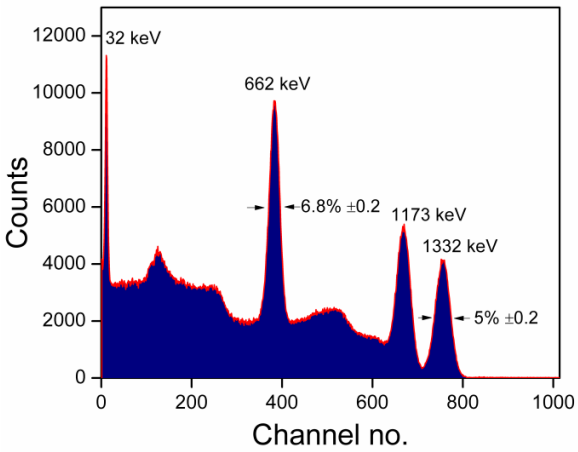

Fig.10: Gamma-ray spectrum of ^{137}Cs and ^{60}Co recorded using a NaI:Tl (45 mm ϕ x 45 mm L) coupled to a PMT

The scintillator performance was checked by processing the crystal to fabricate a detector of 45 mm diameter and 45 mm length. All the processing was done inside the glove-box to avoid any moisture contamination. The scintillator was coupled to a 2 inch diameter PMT (ADIT: B51D01S) and a gamma-ray spectrometer consisting of a pre-amplifier, a shaping amplifier with 1 μs time constant and 1k MCA was used for the pulse height analysis. The detector was hermitically sealed prior to testing. Gamma-ray spectrum recorded using the system is shown in Fig.10. An energy resolution of 6.8±0.2% has been achieved at 662 keV which is at par with the commercial NaI detectors [6,7].

References

[1] Robert Hofstadter, *Phys. Rev.* **75** (1949) 796-810.
[2] V.I. Goriletsky, L.G. Eidelman, V.A. Nemenov, V.G. Protsenko, A.V. Radkevich, J. Crystal Growth 52 (2) (1981) 509-513.
[3] S.G. Singh, D.G.Desai, A.K.Singh, M.Tyagi, ShashwatiSen, A.K.Sinha, S.C.Gadkari, S.K.Gupta , Journal of Crystal Growth 351 (2012) 88–92.
[4] P.W. Bridgman, *Proc. Amer. Acad. Arts Sci.* **60** (1925) 303-383.
[5] D.V. Dementyev et al. Nuclear Instruments and Methods in Physics Research A 440 (2000) 151-171.

[6] Intrinsic energy resolution of NaI(Tl), M. Moszyński, J. Zalipska, M. Balcerzyk, M. Kapusta, W. Mengesha, J.D. Valenti, Nucl. Instrum. Methods A, 484 (2002) 259-269.

[7] Energy resolution improvement of NaI(Tl) scintillation detectorsby means of a timing discrimination method, C. Celiktas, E. E. Ermis, M. Bayburt, J Radioanal Nucl Chem, 293 (2012) 377–382.

HOT COMMISSIONING OF AN ACTINIDE SEPARATION DEMONSTRATION FACILITY

Smitha Manohar, V.P.Patel, U. Dani, M.R. Venugopal & P.K.Wattal
Nuclear Recycle Group & Nuclear Recycle Board

Smt. Smitha Manohar, Nuclear Recycle Group and her team received the DAE Group Achievement Award for the year 2013

Introduction

Partitioning of minor actinides from high level waste could have a substantial impact in lowering the radiotoxicity associated with High Level Waste (HLW). This, when coupled with separation of long lived fission products like cesium-137 and strontium-90 could ease the management of high level liquid waste to a great extent. In the Indian context, the partitioned minor actinides could be routed into the fast breeder reactor systems scheduled for commissioning in the near time frame.

The technological breakthrough in solvent development has catalyzed the partitioning programme in India, leading to the setting up and hot commissioning of the Actinide Separation Demonstration Facility (ASDF) at BARC, Tarapur. The ASDF facility comprises of three distinct solvent extraction cycles, facilitating the use of three different solvents to typically address separation of residual U & Pu from concentrated HLW, separation of bulk minor actinides along with rare earths & separation of trivalent actinides from lanthanides [1]. In line with matching vitrification throughputs, the cycles have been designed for an average throughput of 30 l/hr of high level waste and have been provided with flexibility to try out various options for optimizing the overall partitioning process.

It is well recognized that operation of such a facility will lead to generation of secondary streams, including spent solvents, which have to be suitably addressed. In this regard, ASDF Facility has a spent solvent management facility co-located with it to address management of PUREX solvent and to serve as a test facility for other solvent systems (including their decontamination & reuse).

The ASDF Facility

Radiological Cell & Overall layout

The engineering scale Actinide Separation Demonstration Facility (ASDF) has been retrofitted in an available radiological hot cell situated adjacent to the Advanced Vitrification Facility (AVS) and has a processing capacity to match the vitrification throughput. This location advantage ensures an uninterrupted supply of high level waste and also facilitates the vitrification of the high level waste after separation of minor actinides. While the ASDF has its own dedicated chemical makeup area, all other services are shared with that of AVS. The

radiological cell housing the ASDF (before closure) is as shown in Fig.1 along with the remote operations of both the facilities from the control room.

Fig. 1: **The radiological cell housing ASDF and its remote operations from control room**

Various equipments, piping & staging in the facility are made of SS 304 L material and they have been designed in accordance with ASME Sec.VIII div.1. The plant has been built with all the mandatory requirements of ventilation and off-gas system applicable to radioactive facilities and is remotely operable from the control room. In line with the requirement of handling radioactive liquids, the plant has adopted a wet sampling system, which has been extensively used during the commissioning runs. Purge method has been adopted for the measurement of level, pressure, density and interface.

Contacting Devices Deployed at ASDF

The ASDF facility comprises of three distinct cycles, facilitating the use of three different solvents to typically address the separation of residual U & Pu from concentrated HLW, separation of bulk minor actinides along with rare earths & separation of trivalent actinides from lanthanides. As the ASDF had to be retrofitted in one of the existing hot cells, the choice of the contactors had to account for the limited head room available and relatively larger

number of stage requirements for the separation process. Suitably designed Combined Air Lift based mixer settler contactors (CALmsu) have been therefore deployed in the facility. These mixer-settler units are designed with static mixing element CALMIX (Combined Air Lifting and MIXing), which uses air to create mixing, effecting the intimate contact of the two phases i.e aqueous and organic. These units are provided with end-settlers to take care of any entrained phases in the terminal streams.

In order to have stable operations of mixer-settler, it is important to maintain the interface and the level gradient appropriate for stable operation. Unlike in the case of pulsed column, the available range for maintaining interface is very limited, hence the need for precise control. This has been achieved by measuring interface in both sides of the mixer-settler unit. The terminal streams are routed via density pots, which give on-line measurement of the density of the streams leaving/entering the mixer-settler. This data helps in estimating the real interface position in the mixer-settler. In addition, the density pots have been so designed to separate the entrained phase that no entrained phase goes with the main phase. It also provides flow rate measuring capability for occasional use.

Once the interface is detected, it also has to be controlled to avoid entrainment. This has been carried out by integrating an interface control pot which works on the principle of increasing or decreasing the hydraulic head by external application of pneumatic pressure. These instrumentation & controls features incorporated in the design have facilitated remote operation of this facility. Fig. 2 gives a typical photograph of the actinide separation demonstration facility and Fig. 3 shows the control screen depicting mixer-settler operations from control room.

Fig. 2: Actinide Separation Demonstration Facility, BARC, Tarapur

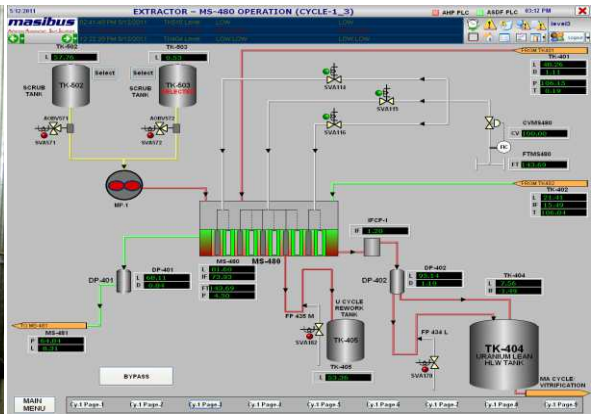

Fig. 3: Typical operating screen of ASDF depicting mixer-settler operations

Engineering Features of the facility

The three independent cycles have been engineered for simultaneous operation of extractor and stripper with the solvent in recycle mode. The equipment layout has been carried out to effect maximum number of gravity transfers. Other transfer/metering systems include air lift pump

devices and steam jets. No mechanical pumps and valves have been used inside the radiological cell to eliminate the need for any mechanical maintenance. All the secondary streams including spent solvents have been suitably addressed in this facility. Fig. 4 gives the overall block diagram of the integrated facility.

Overall Process Description

Solvent Extraction Cycles

As a pretreatment step, HLW is contacted with 30% TBP in n-dodecane to separate the residual uranium and plutonium from HLW. The recovered uranium and plutonium is recycled back to the reprocessing facility. The raffinate of the first cycle, namely, U lean HLW is contacted with diglycol amide based solvent TEHDGA solvent system, resulting in separation of the trivalent actinides along with lanthanides from HLW [2]. The loaded TEHDGA solvent is stripped with a tailor made strippant comprising of 0.05 M DTPA in 1 Molar lactic acid. The stripped product from this cycle containing all the lanthanides and actinides associated with HLW is taken up for further processing in the third cycle after suitable pH adjustment.

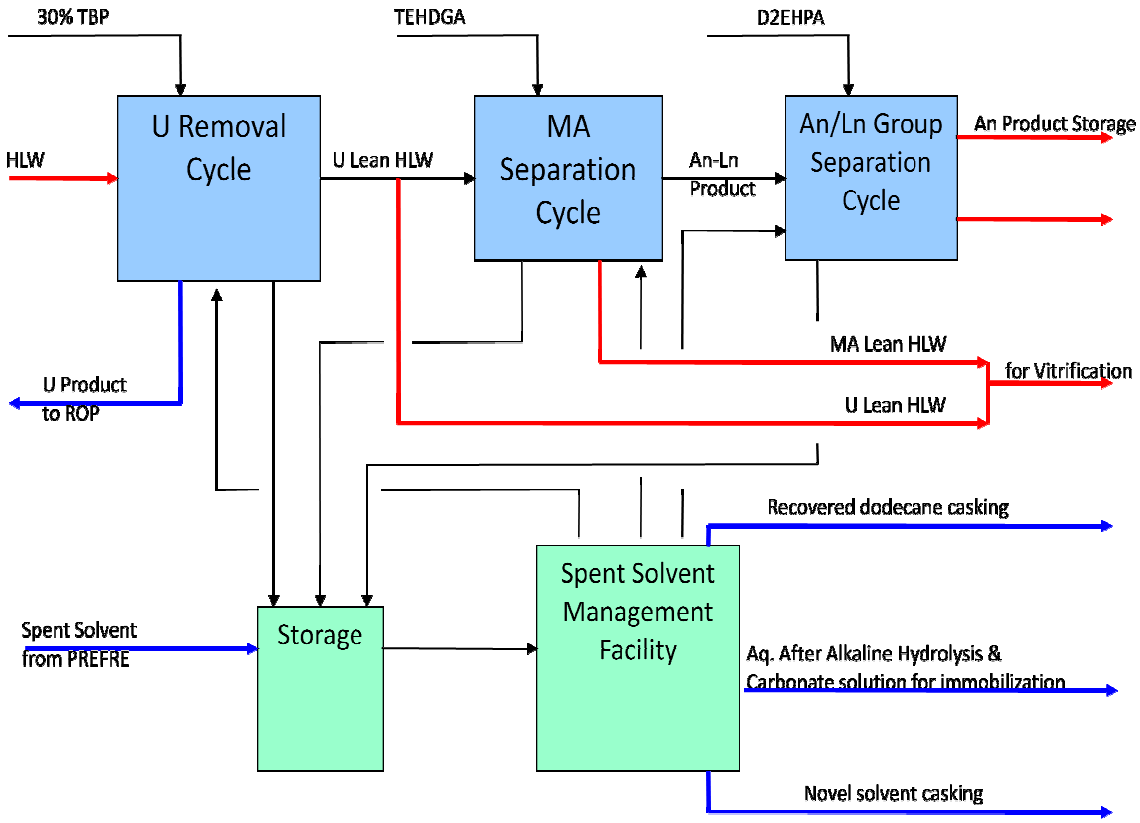

Fig.4: Overall Block diagram of the integrated facilities at ASDF

The actinide and lanthanide depleted HLW which forms the raffinate of the second cycle is sent back for vitrification. The stripped product of the second cycle rich in minor actinides & lanthanides forms the feed for the third cycle, where it is contacted with D2EHPA solvent in n-dodecane [3]. This results in preferential extraction of lanthanides in the organic phase leaving the actinides in the aqueous phase. The loaded D2EHPA solvent is stripped using 2 M nitric acid, and the solvent is recycled into the extractor after giving a water wash. Description of the three cycles is given in Table 1.

The above processes were conceived and optimized based on the indigenous availability of the solvent system and other chemicals required. Recognizing, the fact that adjustment and maintaining of pH on engineering scale would pose problems, a holistic approach was adopted with emphasis given on following points.

[1] The engineering detailing was carried out with special focus on pH adjustment by providing suitable chemical addition lines, air spargers for thorough mixing and sampling provisions for ascertaining the pH of the feed stream.

[2] Some of the process factors that were considered were that D2EHPA as a solvent has an advantage of not extracting acid from the aqueous feed and hence pH across the mixer settler remains steady. Moreover, the buffering action of the lactic acid in the system allows the conditioning of the third cycle feed with respect to pH (2-3).

[3] The presence of DTPA minimizes chances of precipitation of actinides in the system. All of these together aided in the successful demonstration of the modified TALSPEAK process (Trivalent Actinide_Lanthanide Separation by Phosphorus reagent Extraction from Aqueous Komplexes).

Table 1: Description of Three Cycles of ASDF

Cycle No.	Use	Feed	Extractant	Strippant
1	Residual uranium & plutonium separation	Stored HLW (3.5-4.5 M HNO3)	TBP	Acidified water
2	Bulk separation of An + Ln	U lean HLW	TEHDGA	0.05 M DTPA in 1 M Lactic acid
3	An/Ln Group Separation	Stripped product of second cycle after conditioning for pH (2.5-3.0)	D2EHPA	2 M Nitric acid

TBP : Tributyl phosphate; TEHDGA: Tetra ethylhexyl diglycolamide; D2EHPA: Di 2-ethylhexyl phosphoric acid; DTPA: Diethylene triamine pentaacetic acid

Solvent Management

Looking at the limited space available for accommodating all the above three cycles in a single cell at Tarapur, it was quite challenging to use three different solvents in the same cell. This has been duly addressed by providing separate feed tanks (chemical makeup area) to the in-cell organic tank. Subsequent to the useful life of the solvents, they are required to be drained into designated spent solvent tanks provided separately for the three cycles (Fig. 5).

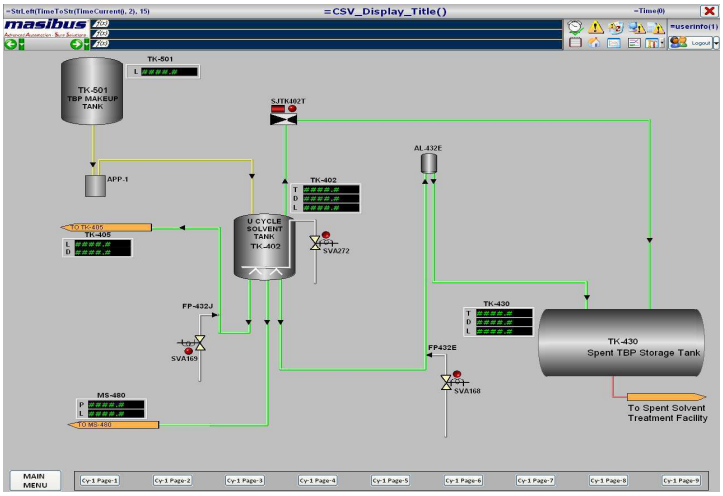

Fig. 5: Solvent Handling and its segregation

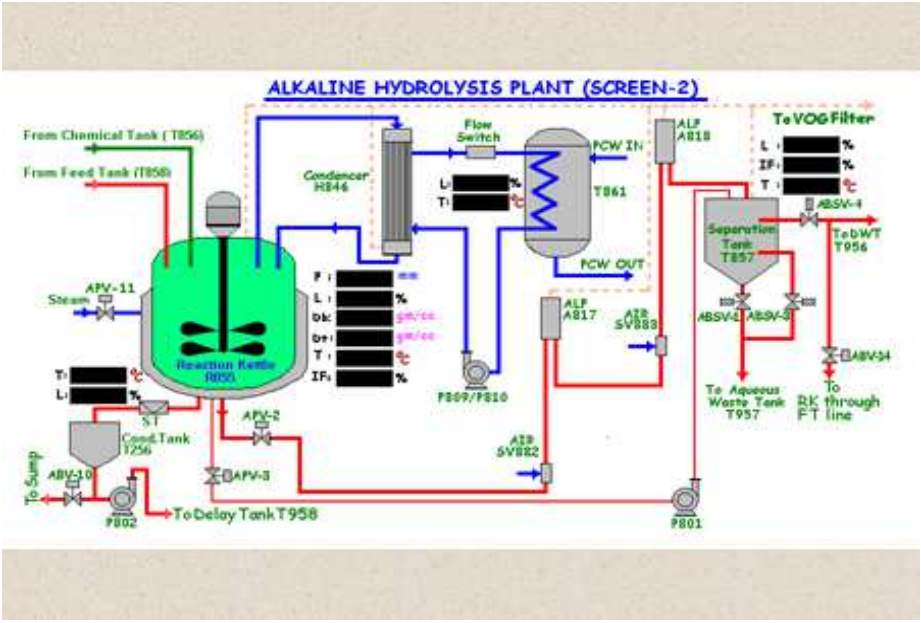

Fig. 6: Alkaline hydrolysis process schematic for First cycle solvent (30% TBP in n-dodecane)

Table 2: Solvents and their treatment scheme

Sr No	Solvent	Treatment scheme
1	TBP Solvent system	Carbonate wash for solvent reuse. Established Alkaline hydrolysis process for spent solvents.
2	TEHDGA Solvent System	Decontamination with suitable wash reagents for its reuse. Incineration of spent solvents
3	D2EHPA Solvent System	Neutralization followed by cementation of Na form of D2EHPA.

These are further connected to the solvent management facility which has provisions to either recycle the solvent after appropriate washings or finally manage the spent solvents as wastes. A typical schematic is shown in the Fig. 6 for the case of 1st cycle solvent. Table 2 gives the solvent management route envisaged for this facility.

Commissioning of the Actinide Separation Demonstration Facility

Commissioning of the facility was taken up in two stages viz., cold commissioning followed by hot commissioning.

Cold commissioning

Cold commissioning activities included pre-commissioning activities, individual cycle testing, followed by an integrated testing of the three cycles. These trials aided in establishing the performance of the three cycles with regard to the engineering and process efficiencies. The chemical markers used for evaluating the process performance are given in the Table 3 below:

Table 3: Markers for the Three Cycles of ASDF

Cycle	Markers
Cycle 1	Nitric acid, Uranium
Cycle 2	Rare earths (La, Ce,Nd, Sm)
Cycle 3	Nd as a marker for Am-241 in TALSPEAK environment La, Ce etc are markers for lanthanides

Typical results of the cold commissioning trials are as given in Tables 3 & 4 with respect to flow rates and separation efficiencies respectively.

Table 4: Inactive/Warm Commissioning of ASDF: Flow Rates for the Three Cycles

	Ist cycle Avg. Flow rates (L/hr) A/O/S	2nd cycle avg. Flow rates (L/hr) A/O/S	3rd cycle Avg. Flow rated (L/hr) A/O/S
Simulated HLW	40/14/16	40/20/20	42/28/17

A: Aqueous; O: Organic: S: Scrub Total Throughput: 2000 L (50 Hrs. of operation)

**Table 5: Inactive/Warm Commissioning of ASDF –
Mass Transfer Performance based on Concentrations of Markers**

	HLW	U Lean HLW (Ist cycle)	MA Lean HLW (IInd Cycle)	MA + RE Product (IInd cycle)	Actinide product (IIIrd Cycle)	RE Rafinate (IIIrd Cycle)
U mg/L	3260	14.7	ND	25.3	ND	19.1
Ce mg/L	332	320	0.22	700	8.95	1250
La mg/L	157	153	ND	332	ND	597
Nd mg/L	194	190	ND	390	69.3	552
Sm mg/L	35.4	31.1	ND	64.1	18.9	73.6

HLW: High Level Waste; MA: Minor Actinide ; RE: Rare Earth

Hot Commissioning

After successful completion of cold commissioning trials, the facility was prepared for hot commissioning specially with regard to off-gas & ventilation hook up to the existing systems. The facility further underwent stage wise active commissioning trials with increasing levels of activity and was hot commissioned using actual HLW. Tables 6 & 7 give hot commissioning trial results with respect to flow rates and separation efficiencies respectively (α, βγ). Along with the analysis of alpha and beta activities in the various streams, concentration of the various rare earths present in HLW were also analyzed. The rare earth concentrations in the various streams were found in perfect agreement with the inactive results. These results have validated the choice of inactive markers for such facilities.

Table 6: Hot Commissioning Trial results - Flow Rates

	1st cycle Avg. Flow rates	2nd cycle Avg. Flow rates	3rd cycle Avg. Flow rated
Natural Uranium (1800 L – 45 + 25 hrs of operation)	**40/14/14.5**	**40/19/19**	**35/35/16**
0.2 mCi/L (1700 L- 42 + 24 hr of operation)	**40/14/14.5**	**40/19/20**	**42/32/17**
2 Ci/L (2000 L – 50 + 25 hr of operation)	**40/14/16**	**40/20/20**	**35/35/17**
Actual HLW (1800 L – 45 + 24 hr of operation)	**40/14/16**	**40/33/20**	**42/28/17**

Table 7: Hot Commissioning Trial results - Separation Efficiencies

	1st cycle performance	2nd cycle performance	3rd cycle performance
Natural Uranium	**99.8% w.r.t U**	**99.9 % w.r.t RE**	**91.3% w.r.t RE; 75% w.r.t Nd (marker for Am-241)**
0.2 mCi/L	**99.7% w.r.t U**	**99.7% w.r.t RE (α : 10^{-3} to 10^{-5} mCi/L)**	**85% w.r.t RE 67.5% w.r.t Nd**
2 Ci/L	**99.23%**	**99.8% w.r.t to α (α : ~10^{-2} mCi/L)**	**96% w.r.t α (93% wrt RE)**
Actual HLW (2 m3)	**99.65%**	**99.85% w.r.t α (α : ~10^{-2} mCi/L)**	**97 % w.r.t α (92% wrt RE)**

Stable operating conditions could be maintained for runs lasting about 48 hrs – 115 hrs at an average throughput of 40 l/hr of high level liquid waste. Separation efficiencies for the first and second cycles were observed to be ~99.5% & 99.85% respectively with regard to uranium for first cycle and alpha activity for the second cycle. In line with inactive commissioning results, Neodymium was observed as the main impurity associated with the alpha product emanating from the third cycle during active operations with a separation efficiency of 97% with regard to alpha activity. In order to increase the decontamination factor with respect to alpha, further trials have been carried out with THEDGA solvent in both second and third cycle and separation efficiencies of greater than 99.9% were achieved. Analytical investigations have indicated that the residual activity in HLW was on account of Pu in organic colloidal form. Developmental efforts are in progress to achieve the desired separation efficiencies >99% by development of specific solvent systems for An-Ln Separation.

These trials have verified and established safe operating procedures including start up, cycle operations & shut down conditions for all the three cycles involving mixer-settler operations. It has been demonstrated that all the aqueous solutions can be suitably managed by evaporation /vitrification. Complete separation/consolidation of organic solvent from a particular cycle and its storage has been demonstrated.

Future Program

The successful hot commissioning of the Actinide Separation Demonstration Facility (ASDF) has demonstrated the separation of minor actinides from high level liquid waste followed by its separation from co-extracted lanthanides. Setting up and operation of ASDF has yielded valuable experience for inducting this technology into the back end of the fuel cycle. Based on these experiences, the new Solvent Extraction Plant at WIP, Trombay has been set up and operated successfully. In addition, the Integrated Nuclear Recycle Plant (INRP, Tarapur) is designed to have an industrial scale high level waste partitioning facility, being designed based on ASDF experiences. The partitioning technology has the potential to reduce the vitrified waste volumes requiring geological disposal to a great extent.

Future program encompasses conversion of Americium product into solidified source for use as targets in fast spectrum reactor or use as thermal source in RTG. It is therefore proposed to integrate the shielded glove boxes to the ASDF facility, and demonstrate the conversion of the alpha product solution into solidified product in the near time frame. Recognizing the limitation of TALSPEAK process with respect to separation efficiency of An-Ln, R&D efforts are presently being directed towards development of new solvent system for An-Ln separation directly from the acidic medium (0.5 to 1 M). This will also mitigate addition of DTPA-Lactic acid salt in the TALSPEAK process.

Conclusions

Design, construction and operation of the actinide separation demonstration facility has resulted in valuable experience for inducting this technology in the back end of the fuel cycle, which has the potential to reduce the vitrified waste volume requiring geological disposal to a great extent.

Acknowledgement

This work detailed out is a consolidation of efforts undertaken in Nuclear Recycle Group and Nuclear Recycle Board. Working as a team member, the contribution of Shri.J.N.Sharma, SO/G, PSDD, in the synthesis and development of novel solvents is noteworthy. Acknowledgements are due to FRD laboratories, PP, Trombay and NRB laboratories at Tarapur where the active lab. studies & analysis work have been carried out.

The entire ASDF team wishes to express their deep sense of gratitude to Shri.S.Basu, CE, NRB & Director BARC for his valuable guidance and support during this entire work. Our thanks are also due to Shri R.S.Soni, Head, PSDD for his active support in the preparation of this article.

References

[1] Smitha Manohar, V.P.Patel, U.Dani, M.R.Venugopal and P.K.Wattal '*Engineering Scale Demonstration Facility for Actinide Partitioning of High Level Waste*' Issue no. 332 May-June 2013, BARC Newsletter

[2] Smitha Manohar, J.N.Sharma, B.V.Shah, P.K.Wattal *'Process Development for Bulk Separation of Trivalent Actinides and Lanthanides from Radioactive High level Liquid Waste'*, Vol 156, No 1 May 2007, Nuclear Science & Engineering, American Nuclear Society

[3] Nilssona, Kenneth L. Nash 'Review Article: *A Review of the Developmental and Operational Characteristics of the TALSPEAK process*', Solvent Extraction and Ion Exchange, 25: 665–701, 2007.

TROMBAY PROGRAMMABLE LOGIC CONTROLLER TPLC-32

Uday W.Vaidya
Reactor Control Division

Shri Uday W.Vaidya, Electronics & Instrumentation Group and his team received the DAE Group Achievement Award for the year 2013

Abstract

Control and instrumentation systems of Nuclear Reactors and all critical infrastructures are built using Computer based programmable systems. These play a vital role in ensuring safety and availability of the plant. PLCs are the workhorses for modern automation- offering benefits of modular hardware, reusable design and graphical programming. Commercially available PLCs are mostly of foreign origin, subject to end-use restrictions and not amenable to full Verification & Validation as required for a safety Class IA and IB system of Nuclear power plant. In recent past, PLCs have been the target of Cyber security attacks, requiring need for high degree of trust in these equipments. Full transparency and visibility of design goes a long way in fostering this trust. Reactor Control Division has designed and developed Trombay Programmable Logic controller TPLC-32, to mitigate these problems. High quality and reliability required for safety class IA and IB systems, is ensured by following a systematic and well documented methodology based on AERB D-25 and international standards like IEC 60880. TPLC-32 platform has been successfully used for Up-gradation of Dhruva C&I systems and deploying C&I system of LEHIPA. TPLC-32 platform will be used developing C&I system of APSARA-II, cryogenic plant, AHWR, upcoming HFRR.

Introduction

Trombay Programmable Logic controller TPLC-32 is a qualified automation platform designed and developed by Reactor Control Division, BARC to build safety class IA and IB control and instrumentation systems for Nuclear Reactors and other nuclear utilities. It is based on in-house designed 32 bit processor based CPU board and FPGA based intelligent I/O boards.

Platform Architecture and Design

TPLC-32 platform consists PC based Engineering Console (EC) connected to TPLC-32 system hardware over Ethernet. The In-house developed software package "Application Development Environment (ADE)" facilitates GUI and functionalities at par with commercially available similar tools. The ADE allows defining complete system

configuration and application program development in the form of Function Block Diagrams (FBDs). FBD Editor, a graphical programming tool of ADE provides a library of function blocks based on IEC 61131-3 standard to develop, compile and test the application programs. The ADE facilitates downloading the developed application on to TPLC-32 hardware. The real time embedded system software executing on the processor board of TPLC-32, acquires all the configured inputs as defined in system configuration, executes the application logics and generates control outputs.

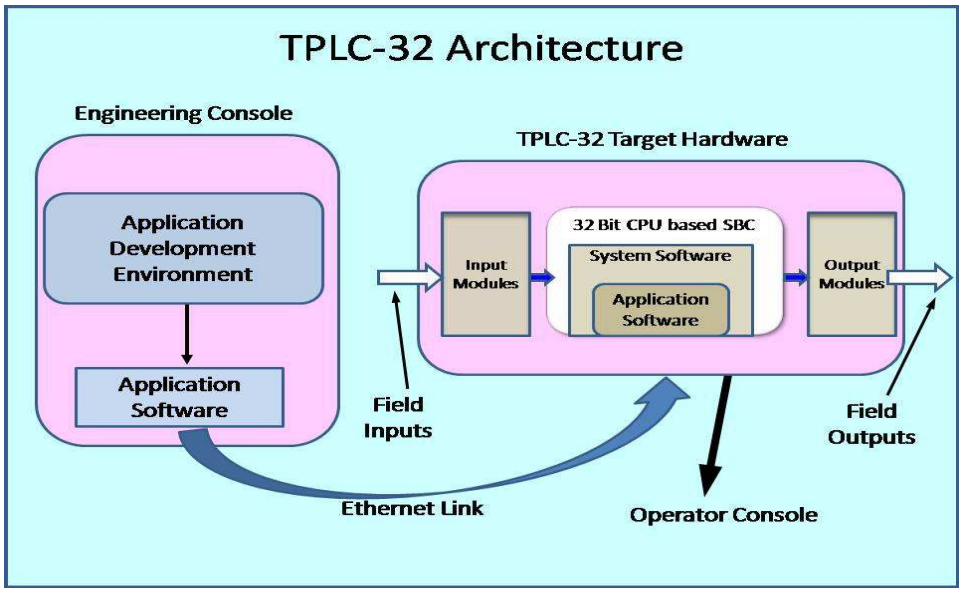

Fig.1: Architecture of TPLC-32 platform

Fig.2: TPLC-32 Based Distributed control system

Figure-1 shows architecture of TPLC-32. Figure-2 TPLC-32 based Distributed C&I System.

Programming guidelines derived based on IEC and MISRA C rules were strictly followed during software development. To ensure correct implementation of requirements implemented in software, each software unit was subjected rigorous unit testing followed by module and integrated testing. The software was subjected to static analysis and critical code walk through by members of independent software V&V team. Use of in-house designed small foot print Real Time Kernel ESOS ensures deterministic execution of all important functions and efficient handling of asynchronous events .The electronic hardware used for TPLC-32 was developed based on specifications prepared by a working Group for Electronic Hardware Standardization (EHS). The hardware design has been carried out as per IEC60987 and DO-254 standards. The hardware design has also been subjected to rigorous verification and validation by independent team. The hardware has been manufactured at ECIL as per approved Quality Assurance Plan. The Hardware modules have successfully passed qualification tests as per ECIL/CSG standards applied to all the electronic hardware used in Indian NPPs. The modular and scalable design of TPLC-32 enables creation of variants to suit requirements of scaling, fault tolerance, performance and cost. Salient features of TPLC-32 platform are described below.

Design based on Systematic Development Process

The complete design and development is carried out following a Systematically Controlled well documented development process based on AERB SG D25 and IEC 60880. Total 27 Design Documents (8000 pages) were produced as part of the design process. A matrix showing compliance of the development process to IEC 60880 guidelines was prepared .The Verification and Validation was carried out by an independent team of engineers from E&I group as per the Verification and Validation Plan.

Structured and Simple Design

Simple, User friendly, tree control based GUI facilitates quick design of System configuration. The graphical application programming environment in the form of Function block diagram editor with associated help and error detection features simplifies application software development. The Software design is highly modular based on TOP-DOWN design approach with high cohesion and low coupling among the modules. The system software uses in-house developed small footprint pre-emptive multitasking kernel having predefined static task priority structure. There is no memory allocation at run time. In the software implementation usage of interrupts is restricted, only for essential activities like time keeping in kernel and handling of bus errors. The design facilitates hardware redundancy at System level and embedding fault tolerant

features during system configuration and Application development. If facilitates easy maintenance with built-in automated on line fault detection and annunciation.

Cycle Time Estimation

The ADE estimates cycle time of the application to be executed on the TPLC-32 target hardware. The system developer gets the time estimates on ADE well before buying the hardware. In case the estimated time is not meeting the timing requirements of application, the developer can optimize the developed application if possible or the deployment can be done in distributed manner on multiple nodes. The time estimation functionality is very useful in early design phase, to plan the hardware architecture and resources to meet application timing requirements.

Deterministic Performance

TPLC-32 system Software sequentially executes all processing, control and safety functions at specified fixed cycle time under all load conditions without any jitter. It also ensures deterministic execution of diagnostics on hardware and Software.

Robust Diagnostics

Diagnostics is carried out on all I/O hardware modules at 1 second periodicity. A module is declared as faulty if fault persists for two consecutive cycles. On failure detection, time stamped Diagnostics message is generated detailing failure in the board. Check on integrity of System software, application software & alterable parameters at is carried out periodicity of 30 seconds. Health of hardware watchdog is also checked as part of diagnostics. Gross health status is displayed on 4 character alphanumeric display on CPU board.

Software Self Supervision

It has built-in software self-supervision functionality. It checks timely execution of control task and diagnostics task at programmed periodicity. Any delay in execution beyond programmed periodicity is detected. In such a case the system generates failsafe output and execution of software is halted. The software program monitored to check that all the functions of control task are executed every cycle in required sequence If any discrepancy is detected the system generates failsafe outputs and execution of software is halted.

Memory Protection

The ESOS provides task-to-task memory protection. Within the task space, code and static data are write-protected. Any write operation on write protected space is captured and software execution is halted. The memory protection feature is used to guard

against stack overflow. In case of stack overflow the software execution is halted. In such circumstances system generates failsafe outputs.

Fail safe Design

On detection of input module failure, for all further processing, it uses predefined failsafe values for input signals assigned to the failed module. On Output board failure, it uses the predefined safe output values. On failure detection, the system stops accessing failed digital output modules and on non access these modules generate de-energized output. In case of software integrity check failure and self supervision, the system generates failsafe outputs. Watchdog detects Gross software failure and generates predefined failsafe outputs. Health status every IO module is available for use in application program. Under such conditions Special node trip function block facilitates generation of failsafe output.

Cyber Safety and Access Control

The TPLC-32 platform software has been fully reviewed through independent V&V process. It does not contain any malicious code. The System and Application software is stored in Flash memory on processor board and checked for integrity at part of diagnostics. Access to the project on ADE is privileged and protected through password. For changing the software, physical access is required to the cabinets which are located in secured area in the plant. Further the flash memory is programmed through special in-house developed robust proprietary software which also has password and hardwired pass key checks. Access to on line alterable parameter change function is based on password and hardwired pass key. The TPLC-32 based systems provide only one way communication via intelligent Ethernet boards to Operator Console. Further the TPLC-32 system software has no software component to pickup data packets from Ethernet board making it completely immune against any network attack.

Modular and Scalable

A Single Node of TPLC can be configured for up to three 19 Inch Bins accommodating up to 43 I/O modules. Any Combination of I/O modules as per the application need can be configured.

Benefits of TPLC-Platform

- No need to develop low level complex system software (which is already available as part of the platform) for C& I systems.
- System configuration & application development by process / C&I engineer trained on the platform.

- Reduced application development time with help of simple and user-friendly graphical programming environment i.e. Function Block Diagrams.
- Inbuilt testing functions in the platform facilitate detailed testing of the application without going for target hardware.
- Application Cycle time estimations in early design stage before procurement of hardware.
- One time V&V efforts for the Qualified Platform by the Platform Designer.
- V&V to be carried out only for the configured Application.
- Time required to develop and qualify the system is drastically reduced.
- Ease in implementation of requirement change during system development and after deployment in plant

- Modernization of legacy C&I systems with platform based development offer lot of benefits.
- Complete in-house design with associated documentation assures long term support, scalability and solutions against continuous changes in technology.

Deployment

As a part of up-gradation of C&I systems of Dhruva Reactor, Reactor Trip Logic System (RTLS) and Alarm Annunciation System (AAS) haven been successfully developed, installed and commissioned in Dhruva and the reported performance is satisfactory. The development of Reactor Start-up Logic System (SULS) and system for Emergency Core Cooling Logics based on TPLC-32 has been completed and these will be commissioned soon. Vacuum control interlock system, Search and Secure Interlock System for LEHIPA accelerator have been developed using TPLC-32. Up gradation of Reactor Regulating System (RRS), Monitoring of Electrical Power Supply System for of Dhruva, C&I systems of NFNS, Cryogenic plant and prototype Distributed Control system for AHWR are being developed with TPLC-32. Variants of TPLC will be used for developing computer based C&I systems of upcoming research reactors.

Conclusion

Commercial PLCs are subject to denials and end-use restrictions, vulnerable to security hazards and inaccessible for full verification & validation. Life cycle management is complicated by high rate of obsolescence and intrusive O&M methods, compromising security. Development of TPLC 32 heralds a safe and secure control platform for building C&I applications using industry standard approach of re-usable functional blocks and proven hardware modules.

PRODUCTION OF HEAVY METAL TETRAFLUORIDE BY SINGLE STAGE DRY PROCESS

K C Guha
Chemical Technology Group

Shri K.C. Guha, Chemical Technology Group and his team received the DAE Group Achievement Award for the year 2013

Abstract

Development of a process technology has been accomplished to convert PG to heavy metal tetrafluoride in a batch reactor achieving an acceptable quality, yield and material accountability. Given the types of challenges ranging from handling toxic gases to constraints of criticality, the recourse to process development demanded conscientious planning, careful design and safe execution, which was delivered to the satisfaction of the ultimate users. The process details and design, safety & operation philosophies adopted during the execution of the above work has been discussed in the present report.

Introduction

Process Gas (PG) is highly reactive and therefore, should not be stored for long periods after processing. Furthermore, PG from processing facility needs to be converted into a material which can conveniently be used for onward fabrication of nuclear fuel. Heavy Metal Tetrafluoride (MTF), a stable material at ambient conditions, provides such an option if metallic fuel is the requirement. Besides, in case there is a pressing need in future to convert back to PG, MTF is the one which is used as the raw material in the extant established process. Process technologies for conversion of PG to MTF have been developed by the department using a H_2-F_2 flame reactor and also by using a thermal plasma reactor technology. However, they are found to be better suited for operations in continuous mode and larger throughputs. Additionally, processing requirement of special process gas adds another dimension of criticality consideration which significantly limits the mass of material that can be handled at a given time. This translates into development of an alternate system where small batches can be treated giving practically 100% yield or near zero Material Unaccounted For (MUF). In order to achieve the above mentioned objective, the process technology is developed and, a set-up comprising of a batch reactor for reduction of PG to MTF by a single step reduction using H_2 has been established. The materials handled in the reactor being only gases and solid, the process qualifies to be a dry process.

Challenges involved

The main challenges involved in selection and development of process and setting up of the facility included: criticality & radiation hazard, chemical hazard, fire/explosion hazard from

hydrogen and, requirement of high product yield or low MUF. The following were the other challenges.

- Space constraint: Since the facility was to be erected within a limited space in an existing building housing another operating plant, freezing the plant & equipment layout and subsequent execution during the installation was an exigent task.
- Utilization of existing utilities: Utility services such a cooling water, compressed air, dry nitrogen, ventilation etc., as existing in the extant system were to be extended for the newly set-up facility without affecting the operating plant. It was by itself an involved job because of very limited freedom for the layout.
- Strict time schedule: Because of stringent time schedules for meeting the delivery targets of the product material, the facility was conceived & planned, equipment & piping were fabricated, control & instrumentation schemes were finalized, design approvals were obtained from the safety committee, installation, testing & commissioning were carried out, and, finally conducting the experimental trials were expedited and accomplished within a short time period of nearly six months.

The above challenges were effectively addressed during the selection of the process and finalizing the design & the operation philosophy of the plant.

Process description and operation methodology

The chemical reaction involved in the process is given as:

$$PG(g) + H_2(g) \xrightarrow{550^{\circ}C} MTF(s) + 2HF(g) \qquad \Delta H^{o} = -69.8 \text{ kcal/g.mole}$$

The set-up used for conducting trials comprises of gas feed surge tanks, a reactor, a storage bin for collection of product, a sparger tank and a venturi scrubber system. A rupture disc opening into a containment vessel is also provided for the safety. Method of operation includes charging mixture of PG and hydrogen into the evacuated batch reactor in a predetermined ratio such that, hydrogen is in excess.

Subsequently, the gaseous mixture is gradually heated to the desired temperature. Adequate soaking period at the elevated temperature is provided to the mixture such that the reaction goes to completion.

After reaction, the byproduct, mainly HF gas, is let out of the reactor by depressurizing followed by purging with nitrogen. It goes to a venturi scrubber system for scrubbing, through an alkali seal (sparger tank). In order to get rid of the trapped HF in MTF, before collection, the solid product received in the bin attached to the reactor is subjected to desmoking with evacuation through the scrubber system. After purging and desmoking, the reactor is cooled and the product is collected from the bin. The block diagram of the process is given in Fig.1.

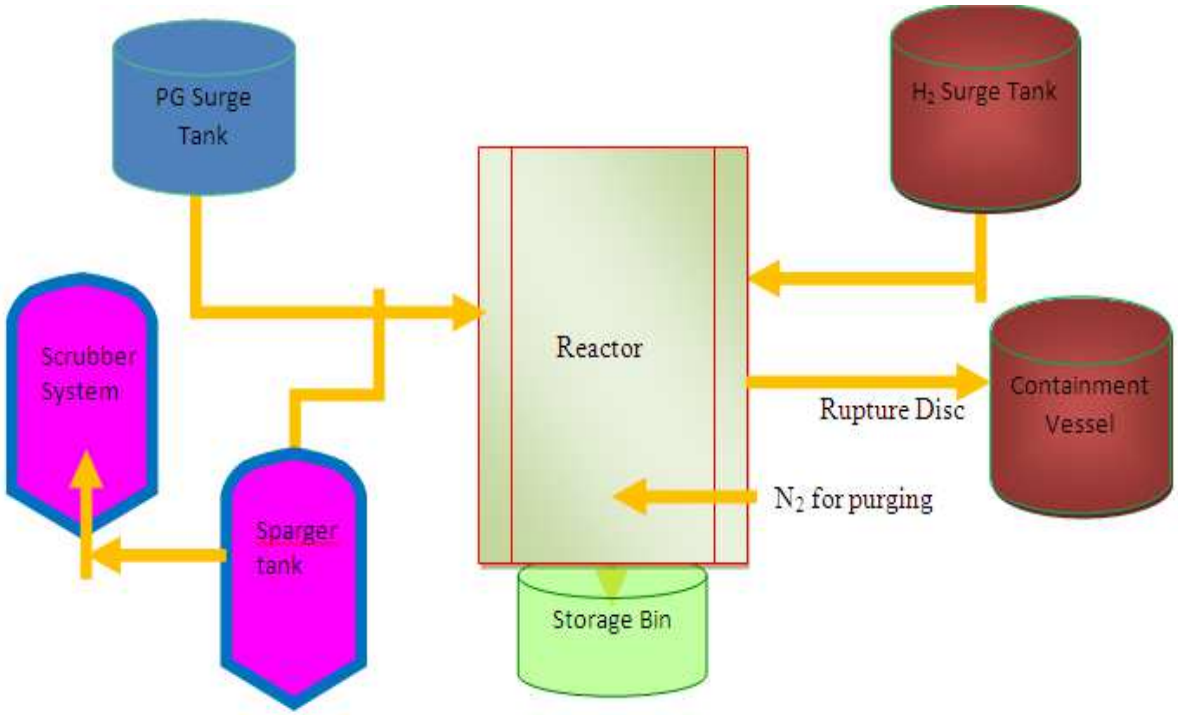

Fig. 1: Block diagram for PG to MTF conversion facility

Product quality

The powder produced in the batch reactor has been analyzed both chemically and optically using XRD and, it was found to be pure containing only the MTF phase. Fig.2 shows the product powder and its XRD pattern.

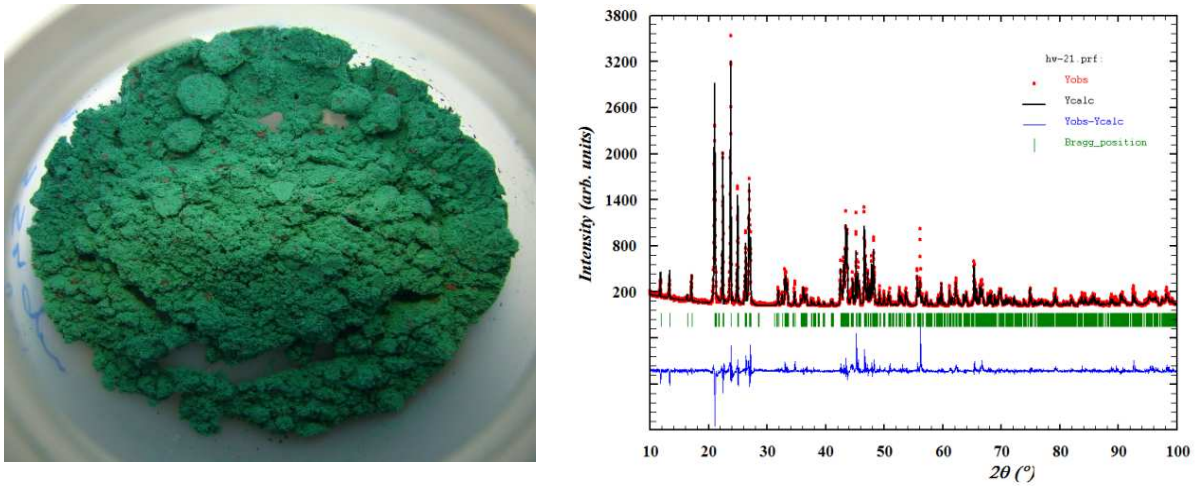

(a) (b)

Fig. 2: a) MTF powder and b) XRD results of MTF sample

Design philosophy & safety

Process, equipment & instrument selection/designs have been made with the objective of achieving the following safety functions.

- Prevention of criticality,
- Confinement for prevention of chemical releases and,
- Protection from fire/explosion hazard from hydrogen

Prevention of criticality

For prevention of criticality by means of design, the following measures are adopted.

- Limit the mass of the nuclear material in the process: Total inventory of PG processed in the reactor, PG surge tank & other equipments is maintained to a level such that it is well below the prescribed critical mass even under accidental conditions.
- Control of the geometry and/or interaction of processing equipment: All as built equipments handling PG, such as surge tank, reactor, sparger tank and scrubber have been critically evaluated by competent agencies for criticality conditions under full moderation/worst possible condition.

Confinement for prevention of chemical releases

Since materials handled during the process are both in gaseous as well as powder form, design of proper confinement/barriers for prevention & mitigation of accidental releases in gaseous form or release in the form of particulate/air borne activity is of primary importance. The following approach has been adopted in the design to ensure safety to the working personnel as well as the environment.

Protection of personnel

- All the process equipments have been designed for both vacuum & high pressure conditions and, operating temperature. Additionally, the design basis also ascertains a critically safe design for handling special PG even under accidental conditions of full moderation.
- A rupture disc is provided in the reactor for safe venting of the gases to a containment vessel in case of a pressure excursion.
- The reactor which operates at above atmospheric pressure is enclosed in a glove box as a secondary enclosure to contain an accidental gas leakage and spreading of solid particulates during draining/collection of the product material. Further, a negative pressure is maintained inside the glove box by connecting it to an exclusively dedicated scrubber system.

- A cascade of reducing absolute pressures has been established between the outside environment and the process area by exhaust and supply ventilation system, enforcing a minimum of 8 air changes per hour.
- With the help of a health physicist, a continuous monitoring for release of toxic gases and the radiotoxic gases in ensured during the operation trials.

Protection of environment

The chances of release of radioactive or chemical substances to the environment is minimized by adopting a multiple barrier approach in the design of the facility. The physical barriers installed in the set-up include:

- Sparger tank in the evacuation line of the reactor to prevent carryover of MTF powder and also for neutralization of HF generated during the reduction reaction. Since hydrogen is used in excess for the reaction, the sparger vessel also acts as a liquid seal to restrain back propagation of hydrogen flame towards the reactor.
- A venturi scrubber is deployed to scrub the gases before being finally released to the environment through a stack.
- The gases of the exhaust ventilation are routed through a wet precipitator and a spray scrubber and, are finally discharged to the atmosphere through the stack.

Protection from fire/explosion hazard from hydrogen

The chances of fire/explosion due to hydrogen are minimized by incorporating the following features in design:

- Minimizing the inventory of hydrogen in the plant.
- Use of explosion proof electrical fittings in the process area.
- Hydrogen sensor & alarm system for detection of hydrogen leakage.

Operation Philosophy

The following features have been considered in the operation philosophy to ensure safe operation of the plant.

- Batch size is small ensuing a low inventory of special nuclear material.
- Operations are carried out from a remote location through PLC based control system. All the important parameters are logged and stored for future retrieval and study. Safety interlocks are enforced for a smooth and safe operation.
- All other equipments outside the glove box, except hydrogen surge tank are maintained at sub atmospheric pressures. Hydrogen cylinder is kept in a open shaded area outside the plant room to evade unnecessary presence of hydrogen source in the plant area.
- The reactor is heated by induction heating.

- Proper safety checklists & administrative controls are ensured before the start of all important plant operations.
- Only trained personnel are authorized to operate the plant under strict access and administrative control of competent authorities.

Conclusion

A process for single step production of MTF from PG has been developed. The entire facility, right from conceptualization to operation has been set up in a very short period of time without bypassing any established safety protocol stipulated by the Department. The plant has been operating in batches adequately meeting the demands of the end users in terms of quantity and quality of the MTF. A high yield and a low MUF is achieved through stringent operational & administrative controls.

BARC NEWSLETTER
FOUNDER'S DAY SPECIAL ISSUE 2015

DEVELOPMENT AND PRODUCTION OF ^{10}B ENRICHED BORON CARBIDE (B_4C) PELLETS FOR CONTROL ROD APPLICATION IN PFBR

J.K.Sonber, T.S.R.Ch.Murthy*, K. Sairam, R. D Bedse, R.C. Hubli[#] and J.K. Chakravartty
Materials Group

Dr. R.C. Hubli, Materials Group and his team received the DAE Group Achievement Award for the year 2013

Abstract

This paper presents a brief account of the programme for the process development and production of ^{10}B enriched boron carbide pellets for control rod application in PFBR. At Materials Group, BARC a processing scheme has been developed for the preparation of enriched boron carbide pellets through powder metallurgy route. Using this process, 11,180 pellets of required specification for PFBR was manufactured and supplied to BHAVINI for control and diverse safety rod (CSR and DSR) applications.

Introduction

Boron carbide (B_4C) enriched with ^{10}B isotope has been selected for control rod application in Prototype Fast Breeder Reactor (PFBR), which is being constructed at Kalpakkam. Neutron absorption property of boron is due mainly to the presence of ^{10}B, which undergoes the main capture reaction [1-3]

$$_5B^{10} + _0n^1 \rightarrow _3Li^7 + _2He^4 + 2.6\ MeV$$

The cross section of this reaction varies from 3850 barns for thermal neutrons to a few barns for fast neutrons. At higher energies, the cross section of most other elements becomes very small, where as that of ^{10}B decreases monotonically with the energy and even at higher neutron energies of >1MeV, ^{10}B exhibits sufficient absorption cross section values. Natural boron that contains 19.8% of ^{10}B atoms can be enriched up to 99% and hence the use of boron is very attractive in the entire neutron energy spectrum [2-5]. The products of (n,α) reaction of ^{10}B namely helium and lithium are stable and non-radioactive isotopes. Boron carbide is extensively used for control rod and neutron shielding applications in nuclear reactors. High boron content, high melting point, high temperature strength, resistance to radiation damage, chemical inertness and low density are the key properties which make boron carbide suitable for control rod application in fast reactors [1-9]. The major issue in boron carbide is processing difficulties. Due to refractory nature and brittleness, only powder metallurgy route is used for fabrication of solid shapes. Sintering of boron carbide is extremely difficult due to its high melting point (2450^oC), strong covalent bonding and low intrinsic self-diffusivity. At lower temperatures, surface diffusion and evaporation - condensation mechanism are favoured which result in mass transfer without densification. At higher temperature, exaggerated grain growth

takes place which results in poor mechanical properties [1-10]. In order to overcome these issues, dense monolithic B_4C can be prepared by applying external pressure at high temperatures. This process is called hot pressing.

Development of Processing Scheme

The pellet fabrication has primarily two steps, synthesis of boron carbide powder and fabrication of dense pellets of B_4C by hot pressing. Flow sheet for fabrication of enriched boron carbide is presented in Fig.1. Before starting the production of enriched boron carbide pellets, studies were carried out on synthesis and densification of boron carbide. Effect of process parameters on product quality was investigated and all the process parameters were optimized for fabrication of pellets with desired specification.

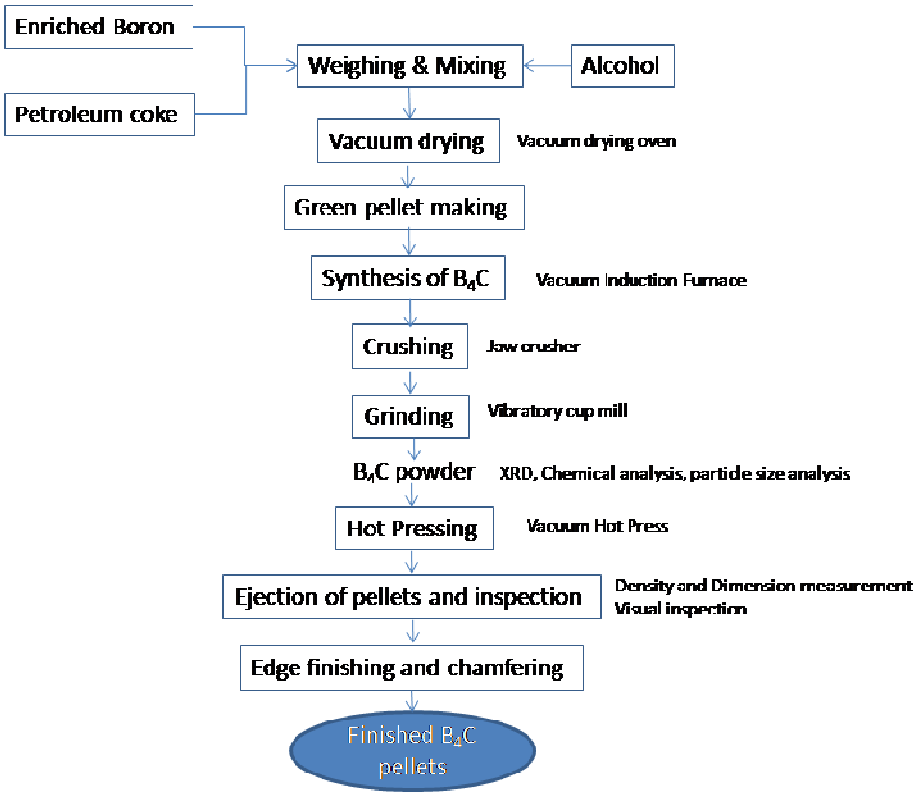

Fig. 1: Process flow sheet for fabrication of enriched boron carbide pellets

For synthesis of B_4C, elemental synthesis route was selected as it involves minimum loss of boron and also gives better control over purity & homogeneity of B_4C powder. Amorphous boron and petroleum coke were taken as starting materials. Boron and carbon were wet mixed in planetary ball mill using alcohol as medium. The mixed powder was dried in vacuum oven and then converted to green pellets by cold pressing. These green pellets were heated in vacuum induction furnace in the temperature range of 1800-1900^oC under vacuum to synthesize B_4C. The synthesized B_4C was in the form of loosely sintered mass, which was subjected to energy intensive grinding operations to obtain micron sized particles.

Effect of process parameters for synthesis and grinding, like temperature, time, charge composition, rpm were studied and the optimized processing parameters were established in order to get the required powder specifications.For fabrication of pellets, the synthesized B_4C powder was filled in a multi-cavity graphite die and hot pressed in vacuum at high temperature (~1950^oC). The required density of pellets was achieved by optimising the hot pressing temperature, pressure, holding time, particle size and length to diameter ratio of pellet. The final pellets are machined for finishing and chamfering as per the given specifications. More scientific details on synthesis and consolidation of boron carbide can be found elsewhere [10].
After optimizing the processing parameters, few experiments were conducted to ascertain the reproducibility and it was found that the processing route has good reproducibility. The creation of appropriate infrastructure and establishment of extended laboratory scale production and processing facilities and testing of the methodologies for making boron carbide pellets, have been key factors in asserting indigenous capabilities in the department for the production and supply of control rods for PFBR. The developmental work to establish the process flow sheet and operating parameters for synthesis of boron carbide and consolidation to high density shapes was completed first using natural boron. After achieving the required material purity, density and properties, trial production work has been initiated with ^{10} B enriched material.

Production and supply of enriched boron carbide pellets for PFBR

The developed processing scheme was used for production of 11,180 pellets of enriched boron carbide and loaded in the first core of PFBR. There are two types of control rods in PFBR (1) Control safety rods (CSR) and (2) Diverse safety rods (DSR). There was a requirement of 7355 pellets for CSR and 3821 pellets for DSR. Enriched boron was received from Heavy Water Plant, Manuguru. Boron carbide powder was synthesized using batch size of 1 Kg. During hot pressing, 62 pellets were made in one batch using multi-cavity graphite die. For quality control, the following checks were carried after every unit operation to account for the purity of the charge and contamination picked up during grinding operations.

- Chemical analysis for all the specified elements and compounds at different stages.
- Particle size & its distribution and specific surface area of boron, carbon and B_4C powders.
- Monitor the change in weight in each step (synthesis, grinding, drying, and densification).
- Phase identification by XRD (to be carried out after synthesis of B_4C)

Required machining, grinding and chamfering of the pellets were carried out by Centre for Design and Manufacture (CDM), BARC. Inspection was carried out for all the finished pellets by dimensional and visual inspection as per specification in supplied drawings in the presence of QA-CDM, QA-NFC and QA-BHAVINI. Visual Inspection (VI) of all the pellets has been carried out using 5x magnifier to check the presence of (a) end chips, (b) circumferential chips and (c) cracks as per ASTM-C-751-07. The pellets were critically examined and found to be within the acceptable maximum permissible values. Pellets have been verified for perpendicularity (Orthogonality) using V-block & Dial indicator set-up. The measured values (0.13 mm) were within the permissible value. Density of the samples was found to be within the acceptable limits. Chamfer angle was measured with "Profile Projector". Pellet stack length

was measured with "digital Vernier Calipers". All the measuring instruments are having calibration validity. Visually acceptable pellets have been used to make the stacks. The required stack length was achieved by selecting the appropriate pellets combination without the need to cut/grind the last pellet. A total of 171 nos. of acceptable pellet stack lengths (710 mm) were prepared for CSR applications and 60 stack lengths (1010 mm) were prepared for DSR. Each pellet stack length has been packed in specially designed thermocol containers and sealed in specially designed lockers in the presence of BHAVINI & NFC Quality Control Team. Each stack was designated with a code number. Each box was labeled with pellet Stack number, BHAVINI seal & signed by QA team members from NFC and BHAVINI. Fig. 2&3 show the major facilities used for synthesis and consolidation of enriched B_4C respectively. Fig.4&5 show the photograph of enriched boron carbide pellets and shipping of DSR stacks.

Fig. 2: Induction furnace for synthesis of powders carbide

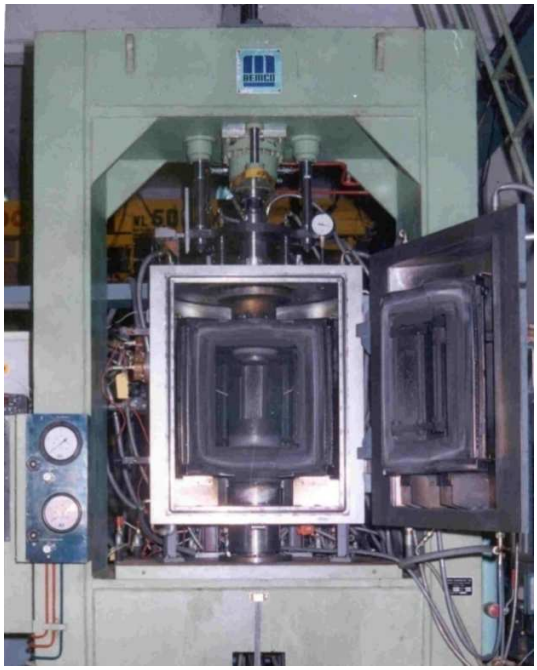

Fig. 3: Hot Press for fabrication of enriched boron pellets

Fig. 4: Enriched boron carbide pellets for PFBR

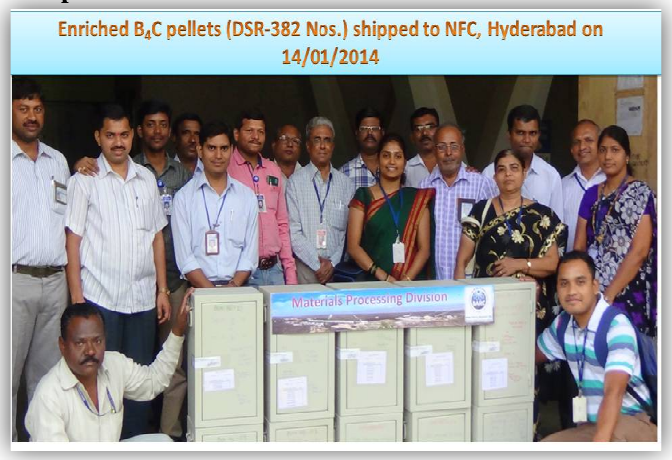

Fig. 5: Shipping of DSR stacks

Summary

Enriched Boron carbide pellets were fabricated by powder metallurgy route, which involves the following intermediate steps:

- Preparation of B_4C from elements with controlled composition. Starting powder chemistry, particle size and morphology have been tuned in order to get the desired quality.
- Micron size powders of B_4C without any significant contamination from grinding media were prepared by energy intensive grinding operations.
- Dense enriched boron carbide pellets were fabrication by hot pressing without using any sinter additives.
- Density, hardness, fractures toughness, compressive strength, flexural strength, thermal conductivity, coefficient of thermal expansion properties were evaluated for finished pellets.
- Microstructural characterization (XRD, SEM-EDS) were carried also out.

Acknowledgements

The authors would like to acknowledge the contributions of Dr. A.K. Suri, Dr. N.Krishnamurthy, Shri R.K.Fotedar and Shri C. Subramanian during the initial stages of this developmental activity.

References

[1] T S R Ch Murthy and A Mukherjee; "Densification of Boron Carbide and Titanium Diboride", *Metals Materials and Processes* 18[2] 151-158 (2006)

[2] A.K. Suri, C. Subramanian, J. K. Sonber and T. S. R. Ch. Murthy; "Synthesis and consolidation of boron carbide: A Review"; (Full critical review) *International Materials Review*, 55[1],4-40 (2010).

[3] C Subramanian, A. K. Suri and T. S. R. Ch. Murthy, "Development of Boron – based Materials for Nuclear Applications", (Technology Development Article) *BARC Newsletter*, 313, 14-22 (2010)

[4] C Subramanian., T.K. Roy, T.S.R.Ch.Murthy, P. Sengupta, G. B. Kale, M. V. Krishnaiah, A. K. Suri, "Effect of Zirconia addition on Pressureless Sintering of Boron Carbide"; *Ceram. Int.* 34[6] 1543-1549 (2008)

[5] J.K.Sonber, P.K.Limaye, T.S.R.Ch.Murthy, K. Sairam, A Nagaraj, N.L. Soni, R.J. Patel and J.K.Chakravartty. "Tribological properties of Boron Carbide in sliding against WC ball", *Int. J. Refract. Met. Hard Mater.*51, 110-117 (2015)

[6] K. Sairam,T. S. R. Ch. Murthy, J. K. Sonber, C. Subramanian, R. C. Hubli, A. K. Suri; "Mechanical properties of HfB_2 reinforced B_4C matrix ceramics processed by in situ reaction of B_4C, HfO_2 and CNT"; Book Title: Materials Challenges and Testing for Manufacturing, Mobility, Biomedical Applications and Climate, Chapter: Reliable manufacturing with advanced Materials, Publisher: Springer

International Publishing, Editors: Udomkichdecha, W, Böllinghaus, Th, Manonukul, A, Lexow, J., pp.87-96 DOI: 10.1007/978-3-319-11340-1_9 (2014).

[7] K. Sairam, J.K. Sonber, T.S.R.Ch. Murthy, C. Subramanian, R.K. Fotedar, P. Nanekar and R.C.Hubli, "Influence of Spark Plasma Sintering Parameters on Densification and Mechanical properties of Boron Carbide", *Int. J. Refract. Met. Hard Mater.* 42, 185-192 (2014)

[8] Shankar Kumar, K. Sairam, J.K. Sonber, T.S.R.Ch. Murthy, Vidhyasagar Reddy, G.V. S. Nageswara Rao, and T. Srinivasa Rao; "Hot-Pressing of $MoSi_2$ reinforced B_4C Composites", *Ceram. Int.* 40,16099-16105 (2014)

[9] K. Sairam, J.K.Sonber, T.S.R.Ch.Murthy, C.Subramanian, R.C. Hubli and A.K.Suri, "Development of B_4C-HfB_2 Composites by Reaction Hot Pressing" *Int. J. Refract. Met. Hard Mater.* 35, 32-40 (2012)

[10] J. K. Sonber, T. S. R. Ch. Murthy, C.Subramanian, R.K.Fotedar, R. C. Hubli and A. K. Suri; "Synthesis, densification and characterization of Boron Carbide", *Trans. Ind. Cerm. Soc.* 72[2], 100-107 (2013).

BARC NEWSLETTER
FOUNDER'S DAY SPECIAL ISSUE 2015

DEVELOPMENT OF OPTICALLY STIMULATED LUMINESCENCE PHOSPHORS AND DOSIMETRY SYSTEMS FOR PERSONNEL & ENVIRONMENTAL MONITORING AND RESEARCH APPLICATIONS

M.S.Kulkarni[1*], K.P.Muthe[2], Ratna P.[1], Munish Kumar[1], N.S.Rawat[1], S.N.Menon[1], B. Dhabekar[1], L.Paliwal[1], A.Soni[1], A.K.Singh[1], R.R.Bhingare[1], U.P.Gaonkar[1], D.R.Mishra[1] , Ajay Singh[2], S.Bhattacharya[2], S.K.Gupta[2]
[1]Radiological Physics and Advisory Division
[2]Technical Physics Division

Dr. M.S. Kulkarni and his team from Health, Safety & Environment Group received the DAE Group Achievement award for the Year 2013

Introduction

Luminescence is a phenomenon of emission of light by certain class of materials. Among the various categories of luminescence, themoluminescence (TL) and optically stimulated luminescence (OSL) are the ones in which emission of light takes place during stimulation of an irradiated material through thermal and optical means respectively. OSL is relatively new technique for radiation dosimetry that was originally developed for geological / archaeological dating [1]. Over several decades TL is being practiced as an established method for radiation dosimetry. However, of late, in the international scenario OSL based dosimety is being increasingly adopted in various branches of radiation dosimetry which includes personnel and environmental monitoring, medical dosimetry etc. The reason for this being several advantageous features of OSL over TL technique like fast and multiple readouts, absence (no) of thermal quenching, high sensitivity and dose re-estimation in a simple manner. OSL dosimetry thus is a viable alternative to the existing TL dosimetry program. Prompted by this, BARC has taken an initiative which has resulted into indigenous development of highly sensitive OSL phosphors like α-Al_2O_3:C, $LiMgPO_4$:Tb,B (LMP) and instrumentation for advanced OSL reader systems as well as new OSL techniques. This paper reports on some of these developments carried out in BARC in the field of OSL materials and associated instruments for their applications in personnel and environmental monitoring program and its current status.

Development of OSL phosphor Materials

The OSL phosphor material to be used for radiation dosimetry must have attributes like high sensitivity to ionising radiation, tissue equivalent atomic number, negligible post irradiation fading of signal and stability against environmental factors. Several oxide, phosphate and fluoro-silicate based OSL phosphors have been successfully synthesized using different techniques in BARC as well as in collaboration with universities, few to list are α-Al_2O_3:C, $LiAlO_2$:Mn/Ce/Tb, $Li_2B_4O_7$:Cu,Ag, YAG:C, Al_2O_3:Si,Ti, $LiMgPO_4$:Tb,B, SiO_2:Ag, $LiAl_5O_8$:Tb, α-Al_2O_3:B, M_2SiF_6, (M=Li,NaK), $CaSO_4$:Eu [2-12]. These materials were thoroughly investigated for their dosimetric performance using TL/OSL techniques. Besides TL/OSL characterization of these

materials, several spectroscopic techniques like photoluminescence (PL), optical absorption (OA) and electron paramagnetic resonance (EPR) were also used to understand their luminescence mechanisms.

Out of these phosphors, α-Al_2O_3:C and $LiMgPO_4$:Tb,B owing to their high OSL sensitivity and wide dynamic dose range were found to be most promising for applications in personnel & environmental monitoring and medical dosimetry.

α-Al_2O_3:C in particular, due to its ultra high sensitivity and desirable attributes like excellent thermo chemical stability and a favourable fading characteristics, has been widely accepted as reference OSL phosphor[13]. Conventional synthesis of this phosphor relies on Czochralski growth of alumina crystals in reducing environment of Carbon. This method however leads to a concentration gradient of carbon across the crystal volume. As a result, samples cut from different portions of the grown crystal exhibit variations in dosimetric performance [14].

In BARC, we have developed a cost effective method for the large scale preparation of highly sensitive dosimetric grade α-Al_2O_3:C phosphor [15]. In this method, high purity Al_2O_3 pellets were fused in vacuum induction furnace at about 2100 °C. Figure 1 shows the high temperature vacuum furnace set up used for this purpose. Fused alumina, figure 2 (a) thus obtained is pulverised and sieved to 75 to 100 µm grain size range fig. 2 (b). Figure 3 (a) and fig. 3(b) depict the TL and OSL response of the melt processed Al_2O_3:C phosphor and its comparison with the commercially available Al_2O_3:C phosphor.

Various dosimetric parameters *viz*. senstivity, batch homogenity, reproducbility, linearity, minium measurable dose (MMD) and energy response to photons and beta radiations were investigated on the developed phosphor and were found to be satisfactory. The fading studies at an absorbed dose (free in air) of 10 mGy performed up to a period of 95 days showed negligible (~ 2 %) loss of the OSL signal from Al_2O_3:C.

Fig. 1: Vacuum induction melting / casting furnace

Fig.2 (a): Melt processed Al_2O_3:C

Fig.2(b): Al_2O_3:C powder on pulverisation

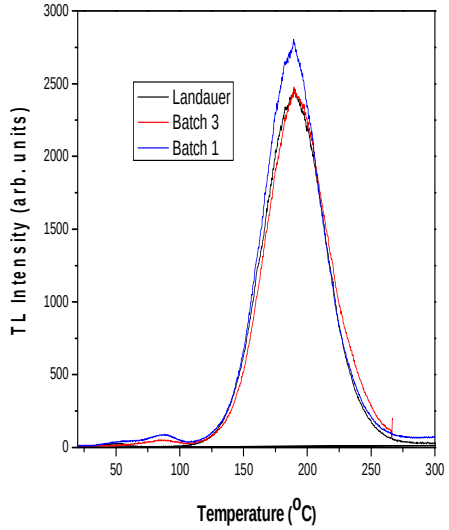

Measured TL parameters of dosimetric glow peak of α-Al_2O_3:C	190°C glow peak (Landauer)	194°C glow peak (BARC)
E_m (eV)	1.24	1.18
s (s^{-1})	1.02×10^{13}	2.54×10^{12}
ω	37.5	37.0
μ_g	0.44	0.45
b	1.21	1.25

Fig. 3 (a): TL glow curve of the melt processed Al_2O_3:C phosphor

The $LiMgPO_4$:Tb,B (LMP) phosphor was prepared by solid state reaction between LiOH, $Mg(NO_3)_2$:$6H_2O$ and $NH_4H_2PO_4$ in air. To dope the phosphor with Terbium and Boron, terbium oxide and boric acid were used as starting materials during the preparation of the phosphor [7]. For OSL measurements, discs made of phosphor uniformly mixed with Polytetrafluoroethylene in 1:3 ratio. Fig.4 (a) shows the TL glow curve of LMP along with the de-convoluted peaks. The glow curve exhibits three prominent, well separated TL peaks. The peak appearing around 230 ^oC is quite stable and is termed as ''dosimetric peak''. TL response of 230 ^oC peak of LMP is about 0.28 times that of the dosimetric peak of $CaSO_4$:Dy phosphor. The OSL sensitivity of LMP phosphor was found to be about 1.3 times to that of commercial Al_2O_3:C (fig 4 (b)). Various characterization tests were carried out on the LMP phosphor and the features are: detection threshold- 5 μGy; linear dose response - up to 1 kGy which is superior to Al_2O_3:C and

$CaSO_4$:Dy phosphor; reusability- at least up to 50 cycles and fading ~ 17 % in 20 days and stabilising thereafter. The phosphor can be used for personnel monitoring (low dose range) as well as for food irradiation.

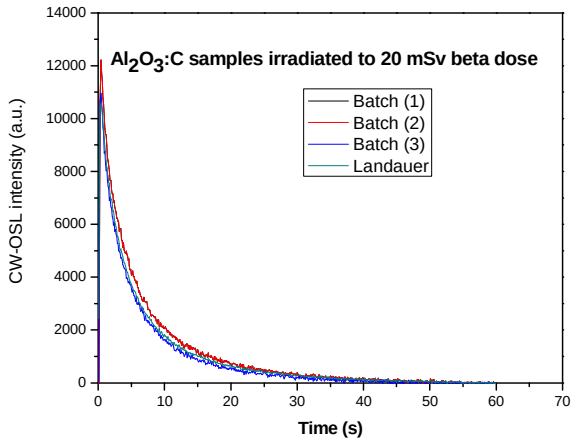

Fig. 3 (b): CW-OSL response of the melt processed Al_2O_3:C phosphor

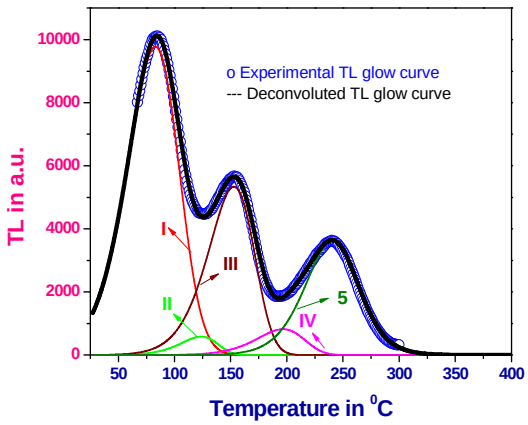

Fig 4 (a): TL glow curve of LMP. The peaks marked as I-V are the deconvoluted peaks.

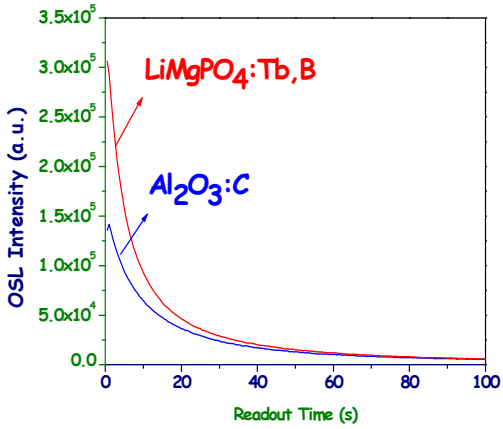

Fig. 4(b): CW-OSL curves of LMP & Al_2O_3:C

Development of OSL Dosimeters

α-Al_2O_3:C phosphor based dosimeters

α-Al_2O_3:C phosphor synthesized through melt processing technique was pulverized to a powder having grain size ranging from 75 -105 µm (figure 2). Thin dosimeter discs (fig. 5) of 7 mm

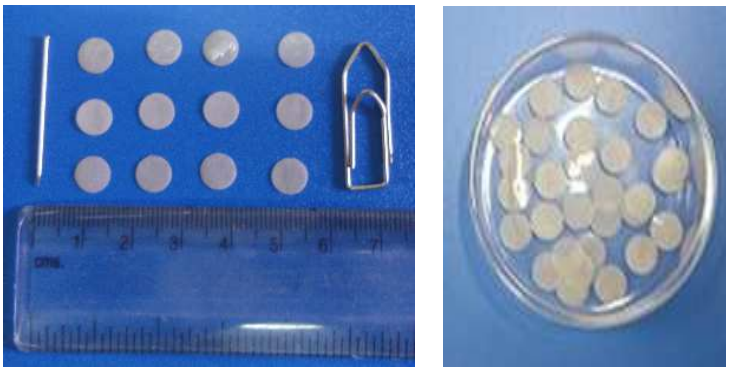

Fig. 5: Thin α -Al_2O_3:C dosimeter discs

diameter, 0.14 mm thickness and density ~25 mg/cm^2 were prepared by sandwiching the α-Al_2O_3:C powder between two thin transparent plastic films for their use in OSL dosimeter badge. Notably, these OSL discs being thin (0.14 mm), offer a distinct advantage over thick dosimeters particularly for the measurement of low enegy beta radiation. More than 12,000 such dosimeter discs were fabricated. The dosimetric characteristics of these OSL discs are given below:

i) Minimum measurable dose of 50 µGy using the indigenous reader systems (at the current stage of development).
ii) Dose Linearity from 50 µGy to 1 Gy.
iii) Fading in dark at room temperature is ~ 2 % in 3 months (~ 5 % in a year).
iv) Coefficient of variation $\left(\frac{\sigma}{\overline{D}}\%\right)$ among discs of a given batch within ± 5 % and batch homogeneity within ± 12 %.
v) Useful energy range for a) Photons is 5 keV to 3 MeV, b) Beta particles is 0.7 MeV to 3.54 MeV.

LMP based OSL dosimeter discs

The synthesized LMP phosphor (grain size ~ 50 µm) and high purity Teflon powder (7A grade, grain size ~ 53 µm)) in1:3 ratio was mixed thoroughly in liquid nitrogen. Dosimeter discs of diameter 10 mm and thickness ~ 0.4 mm were prepared from this mixture.

Various characterization tests were carried out on the LMP phosphor discs.

The results of this study indicated: detection threshold ~5 µGy; linear dose response - up to 1 kGy (fig. 6 a) ; reusability- at least up to 50 cycles, fading (post 24 hrs) ~ 17 % in 20 days (fig. 6 b). It is worth mentioning that neither established TL phosphors viz.,LiF:Mg,Ti, LiF:Mg,Cu,P and $CaSO_4$:Dy nor the widely used OSL phosphor like Al_2O_3:C possess linearity over such a wide range of doses.

Design of four element smart OSLD badge

A prototype smart OSL dosimeter (OSLD) badge based on thin α-Al_2O_3:C discs was designed and developed for DAE personnel and environmental monitoring applications. The OSLD badge is intended to measure X, β and γ radiation doses in field conditions. The prototype BARC OSLD badge consists of a four element OSLD card. The OSLD card is a 1.6 mm thick plastic card with four 1.0 mm deep, 7 mm diameter circular recessions to position the OSL dosimeter discs in the card. Four semitransparent Al_2O_3:C dosimeter disc (fig. 5) are placed in the recessions and locked using wire spring. A machine readable ID code in the form of 16x3 hole pattern is punched on the plastic card for the identification of the person using the OSLD. This OSLD card is inserted in a light tight black plastic cassette (containing energy compensation filters) to keep it under dark condition during use. The black plastic cassette is further inserted in to another transparent watertight plastic cassette which has a plastic clip for wearing on the body (figure 6).

Fig. 6: Prototype four element OSLD badge. (a) Plastic dosimeter card having built-in machine readable ID code which contains thin Al_2O_3:C OSL dosimeters and light-tight black cassette to house the plastic dosimeter card (b) OSLD badge with transparent plastic cover

Development of OSLD badge reader systems

Two semiautomatic versions of personnel monitoring OSLD badge reader systems (figure 7) working in reflection and transmission mode were designed and developed for the readout of the above mentioned four element OSLD badge. The electronic control system of both the version of the OSLD badge reader systems are based on 8051 core microcontrollers. The basic electronic hardware consists of optical stimulation source, light detection assembly (consisting of a PMT), high current driver circuit for the stimulation light source, current to frequency converter and optical power measurement unit. The reader is controlled through RS-232 serial interface and all the input parameters like stimulation light intensity, cycle time and EHT can be entered through PC. The optical stimulation of the OSLD cards is achieved using high power blue (470nm) LED clusters and work on continuous wave (CW) OSL mode of operation. User selectable variable stimulation (blue) light intensity upto ~100 mW/cm^2 at the sample position is provided in the reader system. After the read-out process is completed, the OSL data of each disc is stored on-

Fig. 7: Refletion and Transmission mode Semiautomatic OSLD badge reader systems

line into PC and can be accessed later for dose estimation. The reader has a number of self-diagnostic features to ensure a high degree of reliability.

The OSLD badge reader system was calibrated by recording OSL of the Al_2O_3:C discs exposed to known doses and the performance of the reader system was evaluated for various reader parameters. The reader systems cover a wide dynamic dose range of 20 µSv to 10 Sv with a MDL 50 µSv with the present α-Al_2O_3:C OSL dosimeters. Figure 7 shows reflection and transmission mode prototype OSLD badge reader systems. Figure 8 shows the variation in the OSL response for a set of 300 OSLD badges that were delivered an absorbed dose of 500 mR (5 mGy) from ^{137}Cs. The dose reproducibility of 60.7% badges was within ± 3%, 27.8 % within ± 5%, and the remaining within ± 8%. The intra card sensitivity variation is found to be well within the limits as stipulated in the IEC 61006 (2006) document.

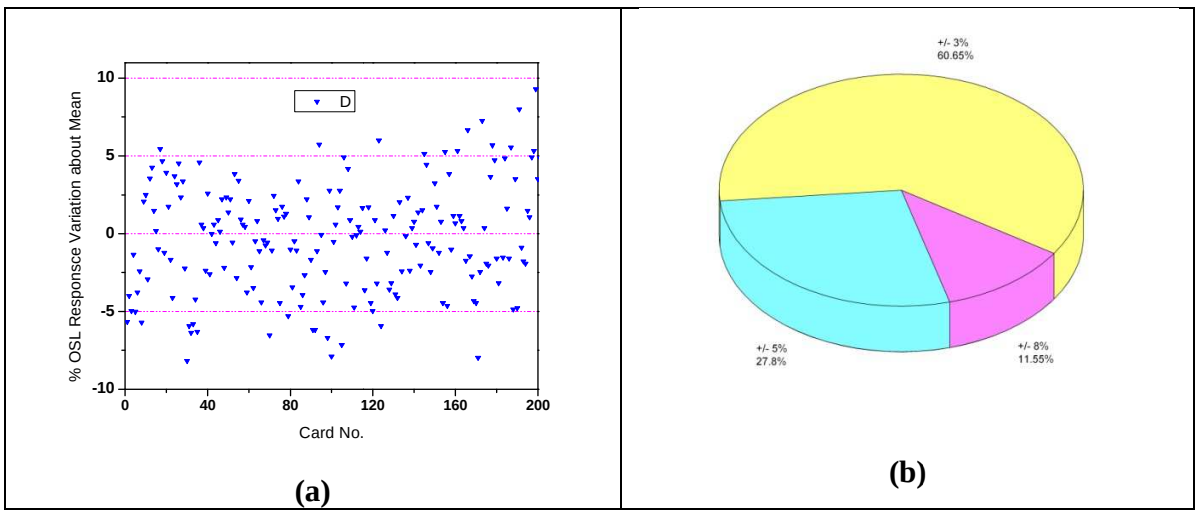

Fig. 8: Variation of OSL response for uniform dose of 500 mR of ^{137}Cs

Studies on Neutron Sensitive Dosimeters using α-Al_2O_3:C OSL Phosphors

Suitability of α-Al_2O_3:C phosphor (prepared using a melt processing technique) for personnel neutron monitoring was also investigated. Thin pallets of α-Al_2O_3:C powder mixed with ^{6}LiF, ^{7}LiF, high-density polyethylene (HDPE) and Teflon material were prepared. The pellets were arranged in two different pairs: α-Al_2O_3:C + ^{6}LiF / α-Al_2O_3:C + ^{7}LiF and α-Al_2O_3:C + HDPE / α-Al_2O_3:C + Teflon, for neutron dose measurement (in the monoenergetic neutron fields of 0.024 MeV to 14.8 MeV energy range and a field of a bare ^{252}Cf radionuclide neutron source) using Aalbedo and recoil proton techniques [16]. The OSL response of the Al_2O_3:C + ^{6,7}LiF dosimeter to radiation from a ^{252}Cf source was 0.21 (in terms of personal dose equivalent $H_p(10)$ and relative to radiation from a ^{137}Cs source). The OSL $H_p(10)$ response of the α-Al_2O_3:C + ^{6,7}LiF dosimeters was found to decrease by more than two orders of magnitude with increasing neutron energy, as known for TLD Albedo dosimeters. The OSL response of the α-Al_2O_3:C + HDPE / α-Al_2O_3:C + Teflon dosimeters was small (1% to 2%) in terms of Hp(10) and relative to radiation from a ^{137}Cs source, for neutron energies greater than 1 MeV. The α-Al_2O_3:C + ^{6,7}LiF OSL dosimeters will be useful alternative to TLD albedo dosemeters for personnel neutron monitoring.

Optical bleaching setup for fast resetting of large number of OSLD cards

The OSLDs needs to be optically reset before they are issueded to the users (like the TLDs which are annealed at ~ 230 °C for ressting the dose). Optical bleaching setup is necessary for erasing (resetting) left over dose from a large number of OSLD cards. For the fast and efficient erasing of large number of such OSLD cards an optical bleaching set up has been developed as shown in figure 9. It contains two LED panels each having 35 high power blue (470 nm) light emitting diodes (LED) arranged in a 7x5 matrix formation which uniformly illuminates area of 20x20 cm^2. The side panels of the bleaching setup is coated with silver paint which acts as a good reflector of blue light and further boost the optical bleaching of the OSLD's. The light intensity is programmed by controlling the current through each LED panel. The setup is capable of resetting fifty OSLD's at a time.

Fig. 9: Optical bleaching setup for resetting the OSLD badges

Field trials of OSL dosimeters

Extensive field trials of both Al_2O_3:C and LMP based OSL dosimeters were carried out for personnel and environmental monitoring applications. The Al_2O_3:C OSLDs were issued to the radiation workers in research (Dhruva) and power reactors (TAPS 1&2) along with the regualr TLD badges. Both TLD and OSLDs were issued in the begning of the service month and collected for readout at the end. This was done for a period of six months. The dose from the TLD badges were read in the TLDBR-7B badge reader system at TAPS and the OSLDs were read at RSSD, BARC[17]. Figure 10 depicts the dose estimates of both TLD and OSLDs. The comparitive study shows that the TLD and OSLD doses are in very good agreement. The OSLDs were also deployed along with TLD badges around BARC complex for a period of three months. The estimated dose of the environmental field test conducted around BARC complex using TLD and OSLD (figure 11) match within ±10%.

LMP phosphor based OSLDs were deployed along with the conventional $CaSO_4$:Dy based TLDs in the environs of proposed NPP in Jaitapur and Hissar as a part of pre–operational base

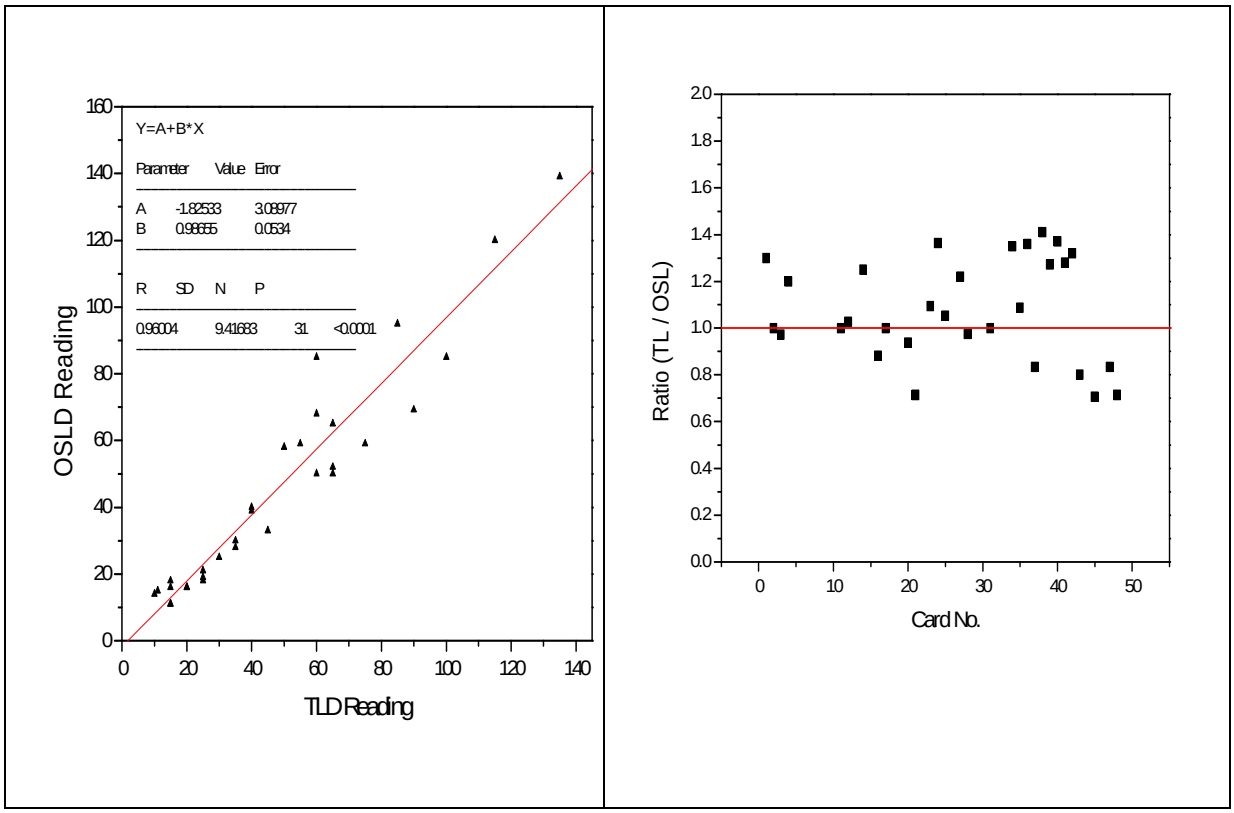

Fig. 10 (a): Comparison of the TLD and OSLD dose measured for TAPS 1&2
(b): Ratio of TLD to OSLD dose

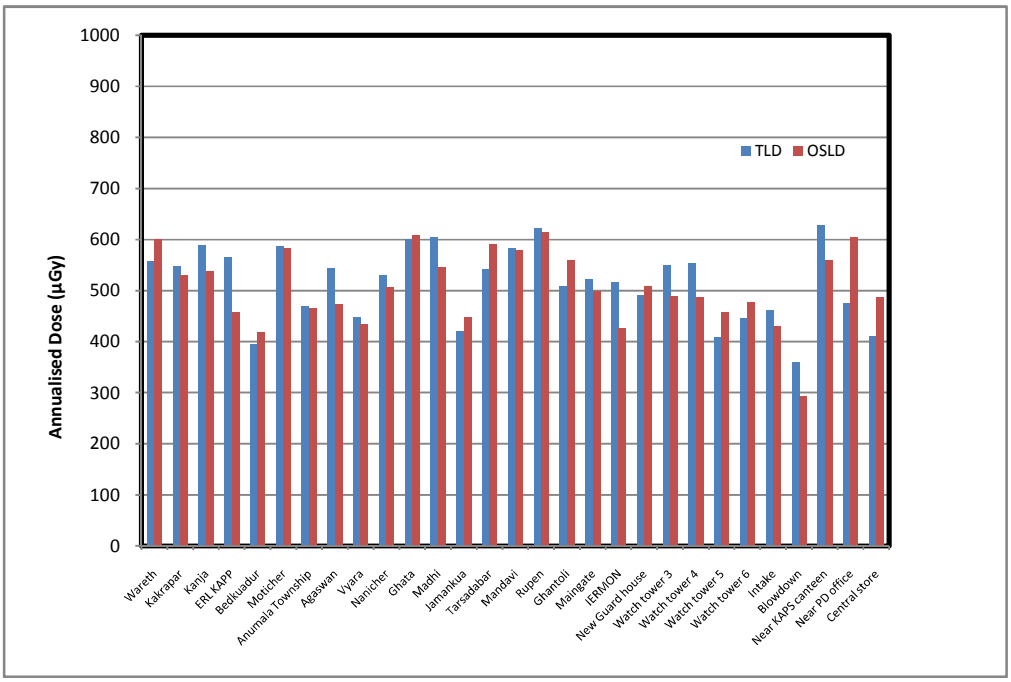

Fig. 11: Annualized doses in the environs of KAPS estimated by TLDs and LMP based OSLDs

line studies. In Jaitapur, the mean ratios of dose measured using TLDs to that of the dose measured using OSLDs were found to be 0.86 ± 0.12. In Kumharia, Hissar, the mean ratio of dose measured using TLDs to that of the dose measured using OSLDs was found to be 1.17 ± 0.22. The environmental gamma dose measured using OSLD's and TLD's in the environs of KAPS for a period of twelve quarters were found to be in very good agreement (fig. 11).

Multi-Sample TL-OSL Reader System

The commercially available automated TL and OSL reader systems used for luminescence dating and research applications can accommodate up to 80 samples at a time. The readout cycles in such reader systems are sequential i.e. only one disc is read at a given time. Luminescence dating requires extensive analysis of individual discs and hence the capabilities of large, automated, multi-sample readers are rarely used.

We have designed and developed a low cost multi-sample TL-OSL reader system which has facility for readout of eight samples in sequence in a programmed way. Such reader systems can be used in parallel and can increase the data throughput several fold. The Multi-Sample reader system (figure 12) has features for measurement of TL, OSL, elevated temperature OSL, isothermal TL/OSL modes. In OSL mode, continuous wave OSL (CW-OSL), Linearly Modulated OSL (LM-OSL) modes of operations have been provided.

Fig. 12: Multi sample integrated TL-OSL Reader system for luminescence dating and research applications

Two optical stimulation sources, blue ($\lambda_p \approx 470$ nm) and infrared (875 nm) are provided in the reader system. A pair of two high power blue light emitting diode (LED) clusters (placed in opposite to each other) provide up to 100 mW/cm^2 blue light intensity at the sample position. The infra red stimulation is carried out using a set of twenty high intensity infrared LED's (peak wavelength ~ 875 nm and $\Delta\lambda \approx 20$ nm) that are optically focused on the sample to deliver IR light intensity up to 100 mW/cm^2 at the sample position during the readouts. A precise temperature controller is provided in the reader system for the TL readouts of the samples. The temperature controller generates linear heating profiles from 0.5 to 40°C/s and can clamp temperatures up to 500°C. *The reader system has p*rovision for on plate irradiation of the samples using a 40 mCi ^{90}Sr/^{90}Y beta source. The user can specify heating / optical stimulation profiles for the TL or OSL measurements in the reader system.

Conclusions

OSL offers several advantages over conventionally used TL technique. Therefore, there is a worldwide paradigm shift from TL to OSL in the field of radiation dosimetry. In India, synthesis of sensitive indigenous OSL phosphor is a milestone towards reaping the benefits of OSL technique. Development of standard OSL phosphor Al_2O_3:C by indigenous technique and LMP, a new indigenous OSL phosphor together with associated instrumentation for reader system are the crucial steps in the direction of replacing existing TLD based personnel monitoring system with OSLD based countrywide personnel monitoring program of DAE.

References

1. Huntley D.J., Godfrey-Smith D.I. and Thewalt M.L.W. Optical dating of sediments. Nature 313 (1985), 105-107.

2. M.S.Kulkarni, D.R.Mishra, K.P.Muthe, Ajay Singh, M.Roy, S.K.Gupta and S.Kannan. An alternative method of preparation of dosimetric grade α-Al_2O_3:C by vacuum assisted post-growth thermal impurification technique. Radiat. Meas. 39/3 (2005), 277-282.
3. Bhushan Dhabekar, E Alagu Raja, Sanjeev Menon, T K Gundu Rao, R K Kher and B C Bhatt. J. Phys. D: Appl. Phys.41(2008) 115414 (6pp),
4. N.S.Rawat, M.S.Kulkarni, M.Tyagi, Ratna P., D.R.Mishra, S.G.Singh, B. Tiwari, A.Soni, S.C.Gadkari, S.K.Gupta. TL and OSL studies on lithium borate single crystals doped with Cu and Ag. Journal of Luminescence 132 (2012) 1969-1975.
5. M.S.Kulkarni, K.P.Muthe, N.S.Rawat, D.R.Mishra, M.B.Kakade, S.Ramanathan, S.K.Gupta, B.C.Bhatt, J.V.Yakhmi, and D.N.Sharma. Yttrium Aluminum Garnet (YAG:C) - A New Phosphor For Radiation Dosimetry. Radiation Measurements 43 (2008), 492-496.
6. B.C.Bhatt, P.S.Page, N.S.Rawat, B.S.Dhabekar, D.R.Mishra, and M.S.Kulkarni. TL, OSL and PL Studies in Al_2O_3:Si,Ti Phosphor. Radiation Measurements 43 (2008), 327-331.
7. B. Dhabekar, S.N. Menon, E. Alagu Raja, A.K. Bakshi, A.K. Singh, M.P. Chougaonkar and Y.S. Mayya. $LiMgPO_4$:Tb,B - A new sensitive OSL phosphor for dosimetry. NIMB 269 (2011) 1844-1848.
8. R.R.Patil, Rujuta Barve, S.V. Moharil, M.S.Kulkarni, B.C. Bhatt. Development of Ag doped crystalline SiO2 for possible applications in real-time in-vivo OSL dosimetry. Radiation Measurements 71 (2014) 208-211]
9. Indian Journal of Pure & Applied Phy ol. 47, June 2009, pp. 426-428, Thermoluminescence, optically stimulated luminescence and ESR studies on $LiAl_5O_8$:Tb. Dhabekar B., E Alagu Raja, T. K.Gundu Rao, et al. Environmental monitoring using $LiMgPO_4$:Tb,B based optically stimulated luminescence dosimeter. Radi. Prot. and Env. 36 **(** 2013) 146-149
10. Anuj Soni, K.P. Muthe, M.S.Kulkarni, D.R. Mishra B.C. Bhatt, S.K. Gupta, J.V. Yakmi, D.N. Sharma In-Vacuo thermal processing of α-Al_2O_3 Single Crystals in boron ambience and its implication on TL & OSL response. J. Luminescence 130 (2010) 1308 – 1312.
11. R.R. Patil, Rujuta Barve, M.S.Kulkarni, B.C Bhatt, S.V.Moharil. Synthesis and luminescence in some fluoro-silicates for the possible applications in OSL dosimetry. Physica B Condensed Matter 407 (2012) 629-634.
12. M.S.Kulkarni, R.R. Patil, A. Patle, N.S. Rawat, Ratna P., B.C.Bhatt, S.V.Moharil. Optically stimulated luminescence from $CaSO_4$:Eu - Preliminary results. Radiation Measurements 71 (2014) 95-98.
13. E. G.Yukihara and S.W. S.McKeever. Optically Stimulated Luminescence: Fundamentals and Applications, 2011 John Wiley & Sons Ltd. Publication
14. Akselrod A.E., and Akselrod M.S., 2002. Correlation between OSL and the distribution of TL traps in Al_2O_3:C. Radiat. Prot. Dosim., 100 (1-4) 217-220.
15. Patent Application No. US 2014/0209712/A1, dt. 31.7.2014 "Process for large- scale synthesis of optically stimulated luminescence grade α-Al_2O_3 based materials".
16. M.S.Kulkarni, M. Luszik-Bhadra, R.Behrens, K.P.Muthe, N.S.Rawat, S.K.Gupta, D.N. Sharma. Studies on new neutron-sensitive dosimeters using optically stimulated luminescence technique. Nucl. Instr. and Meth. in Phys. Rese. B 269 (2011) 1465-1470.
17. M. S. Kulkarni, Ratna P. and S. Kannan, A new PC based semi-automatic TLD badge reader system for personnel monitoring. Proc. IRPA Conf., Hiroshima, Japan, 14-19 May, 2000.

BARC NEWSLETTER
FOUNDER'S DAY SPECIAL ISSUE 2015

ON NUCLEAR SELL EFFECT AND ITS DAMPING WITH EXCITATION ENERGY

Prakash Chandra Rout
Nuclear Physics Division

Mr. Prakash Chandra Rout Received the INSA Young Scientist Award for the year 2014

Abstract

The shell effect and its damping over wide excitation energies have been deduced from an exclusive measurement of the neutron time of flight spectra with a large area (~1m^2) neutron detector array in the 7 Li breakup followed by fusion of triton with 205 Tl. A controlled measurement was also made with ^{nat}Ta where the shell effect of the residual nucleus is small (~2 MeV). The allowed values of the physical parameters, γ which relates the damping of the nuclear shell effect and the asymptotic nuclear level density parameter a, have been obtained for the first time in the Pb region. The measured values of these parameters will be very much useful in the context of the current research on nuclear astrophysics and synthesis of the supper heavy element.

Introduction

The observed magic numbers of nucleons (proton and neutron) in nuclei suggest they have shell structure analogous to the electronic shell structure in atoms. The nuclei with magic configuration have extra stability compared to the average behavior predicted by the liquid drop model (LDM). According to Strutinsky, the shell effect in a nucleus is considered as a small deviation from the uniform single particle energy distribution. The shell effect plays an important role in the explanation of the occurrence of super heavy elements, fission isomers and super-deformed nuclei. The shell effect also affects the nuclear level density (NLD). The total level densities of the nuclei at the closed shell configuration have several orders of magnitude smaller than that of off-shell nuclei at similar excitation energy. The nuclear level density makes a transition from the shell-dominated regime at low excitation energy to that of a classical liquid drop at high excitati . A direct measurement of the nuclear level density from the particle spectra can address the evolution of shell effect with excitation energy. The NLD, is a fundamental property of the atomic nucleus, defined as the number of energy levels per unit energy at an excitation energy E_X. It is an essential quantity for obtaining the thermodynamic properties of an excited atomic nucleus and also used for the calculations of reaction rates relevant to nuclear astrophysics, nuclear reactors, spallation neutron sources (see the cartoon inFig.1a). It is also, namely entropy, temperature and specific heat. The NLD was first calculated by Bethe using a non-interacting Fermi gas model where the single particle levels are equi-spaced and non-degenerate.

The analytic form of the NLD with respect to E_X deduced from Fermi gas model and the leading factor is $\rho(E_X) \sim e^{2\sqrt{(a\ Ex)}}$, where a is the level density parameter and is given by $a = \pi^2 g/6$, g is the sum of the neutron and proton single particle level density at the Fermi surface. The NLD, in general, depends on the mass number (A), excitation energy, angular momentum, parity, iso-spin, shell effect, paring and the collective motion. The NLD inferred from various measurements show that on an average the level density parameter a increases linearly with A as a $\approx$A/8 MeV^{-1}, which is like liquid drop behaviour of the nucleus. However, there is a significant deviation from this liquid drop value at shell closures and is the largest (a $\approx$ 26 MeV^{-1}) for the doubly magic nucleus ^{208}Pb. This shell effect on the NLD parameter is expected to wash out with excitation energy so that a approaches its liquid drop value at $E_X \geq 40$ MeV as shown in Fig.1b [34,]. There is no measurement in this important topic to address the washing out of the shell effect over a wide E_X range. This is because of the difficulty in producing the double closed shell nucleus at low EX where shell effect is pronounced using fusion of suitable projectile and target. We populated ^{208}Pb at low excitation energy using triton transfer or the breakup-fusion in the ^{7}Li induced reaction on ^{205}Tl and measured the neutron spectra from the ^{208}Pb in coincidence with the out-going alpha particles. A large area plastic scintillation detector array for the neutron measurement by time of flight technique(TOF) and a mini array of CsI(Tl) detectors for the charged particle measurement by Pulse shape discrimination(PSD), were set up for this exclusive measurement.

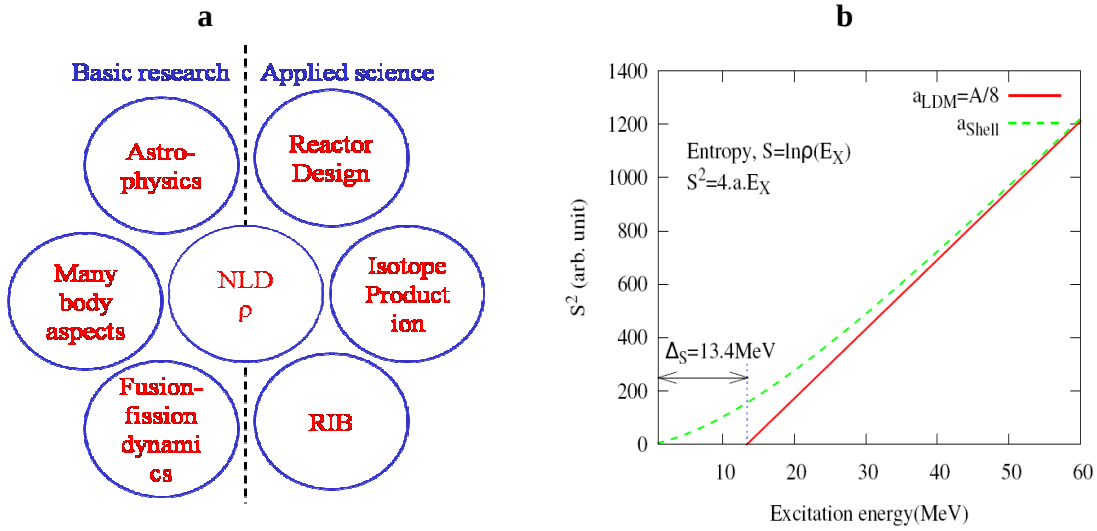

Fig. 1a: Scope of nuclear level density in pure and applied research, 1b: Plot,S^2 vs E_X , shows the washing out of shell effect with excitation energy in the doubly closed shell ^{208}Pb nucleus[3, 4]. The shell correction energy used for ^{208}Pb is -13.4MeV. The solid line is the asymptotic liquid drop behavior with a = A/8MeV $^{-1}$.

Neutron Detector array Large Area

p ,namely)particularly organic scintillators ,Hydrogenous mattertialslastic and liquid scintillators(have been widely used for neutron measurements by the TOF technique

because of their fast response. A long scintillator detectorcoupled to photomultiplier tube (PMT) at either ends generallyused to get position information from the timing signal from both the PMTs. A large area neutron detector array (~1×1m^2) has been setup for the fast neutron spectroscopyat the Mumbai Pelletron Linac Facility (PLF) [4]A photograph of the . on detector arrayThe neutr .2.neutron array is shown in the Figconsists of 16 plastic scintillator bars of square cross section. Each bar has a dimension 6 cm×6 cm×100 cm and is coupled to two 5 cm diameter XP2020 PMTs, one each at either end. The array can beused for fast neutron spectroscopy and also for any measurement in coincidence with neutrons.

The characterization of the plastic detector was done using radioactive sources and also for mono-energetic and continuum neutrons from produced in nuclear reactionusing beams from the PLF .The energy, time and position response has been measured for quasi-mono-energetic electrons using Compton tagging of scattered γ-rays and for mono-energetic neutrons using the ^{7}Li(p,n1)^{7}Be*(0.429 MeV) reaction at proton energies between 6.3 and 19 MeV. The array has been used to measure the evaporation neutron spectrum from 4 to 12 MeV in the reaction ^{12}C+ ^{93}Nb at E(^{12}C)= 40 MeV and the measured neutron spectrum compares well with the statistical model calculation. A Monte Carlo simulation algorithm has been developed in-house to simulate the neutron energy dependent efficiency of the array.

The Monte Carlo simulated efficiency of the plastic scintillator for the neutron detection agrees with that obtained from the ^{7}Li(p,n$_1$) measurements. Add-ons for the neutron detector array are: (a) Lead (Pb) sheets of total thickness 25 mm placed in front of the array to reduce the low energy-ray background while not considerably attenuating the neutrons from the target and (b) a 30cm thick shadow pyramid consisting of several plates of mild steel (MS) shield used to estimate the contribution due to the scattered neutrons.

Detector array (Tl)CsI

An array of 8 CsI(Tl) sintillationdetectors PIN-coupled to Siphotodiode (PD) and pre-T .d outamplifier for signal reahe array can be used for measurement oflight charged particles with a reasonably large efficiency.detector array mounted (Tl)A picture of the CsI The active area of each scintillator is .2.purpuse reaction chamber is shown in Fig-in a multi 2.5 cm × 2.5 cm and thickness of 1cm .The PD is effiecient and has good ,very compact stability andrequires less operatingvoltage .The detectors are covered with a 1μ m aluminised Mylar foil.

The standard pulse shape discrimination method is used for the particle identification by measuring the zero cross over timing (ZCT) of the amplifier bipolar pulse. These detectors have nonlinear energy response for various charged particles. The energy response of the CsI(Tl) detectors to-α particles has been measured from 8.5-40 MeV using a ^{229}Th source and the ^{12}C(12C, α)^{20}Ne reaction at E(^{12}C)=24MeV populating discrete states in ^{20}Ne. The energy non-linearity and the count rate effect on the PSD property have also been measured and it was found that the PSD deteriorates for count rate ≥3 kHzThe complete . .Mumbai ,characterization of the detector for the charged particle has been made at the PLF

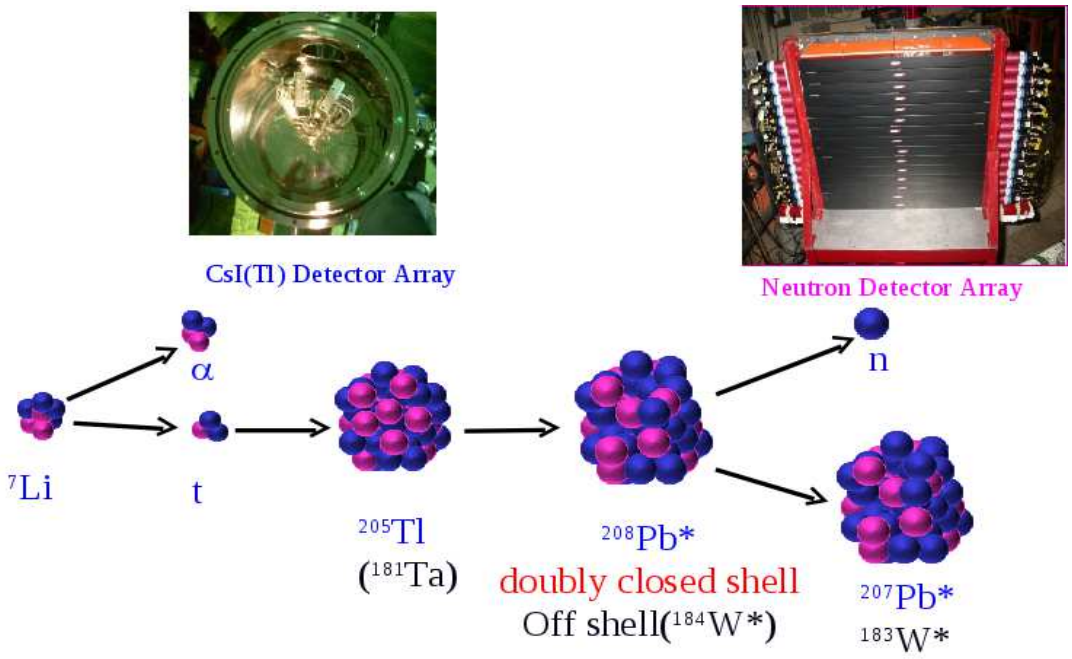

Fig. 2: Schematic of the reaction mechanism used to populate the nuclei of interest to address the damping of nuclear shell effect and the detector array used for the charged particle and neutron measurement

Measurement of the nuclear shell damping factor

The experiment was performed using a 30 MeV pulsed ^{7}Li beam (FWHM1~ .5 ns and period ~107 ns) at the Mumbai Pelletron Linac Facility (PLF). Self-supporting foils of 4.7 mg/cm^{2} ^{205}Tl (enriched to >99%) and 3.7 mg/cm^{2} ^{181}Ta (natural) were used as targets to populate ^{208}Pb and ^{184}W respectively. The schematic of the production mechanism along with particle detector array of the experimental setup is shown in Fig.2. A neutron detector array consists of 15 plastic scintillator of square cross section was used to measure the neutron spectra by TOF technique. Each scintillator has a dimension 6 cm×6 cm×100 cm and is coupled to two 2 inch diameter) photomultiplier tubes XP2020 PMTs(, one each at either end.

The array was placed at an angle of 90° to the beam direction and at a distance of 1 m from the target. An array of8 CsI(Tl) detectors of active area2.5 cm × 2.5 cm coupled to Si(PIN) photodiodes was used foralpha particles detector array was placed at (Tl)The CsI .detection backward angles (~126° -150°) and at a distance of 5 cm from the target. The standard pulse shape discrimination method is used for the particle identification by measuring the zero cross over timing (ZCT) of the amplified bipolar pulse with an in-house developed ZCT module.

The parameters (a) left (TL) and right (TR) timing of plastic scintillator with respect to the filtered RF (RF filtered by both the CsI(Tl) and plastic scintillator) using time to digital converter (TDC), (b) deposited charge from left (QL) and right (QR) PMTs with charge to digital converter(QDC), (c) time of CsI(Tl) detectors with respect to the filtered RF using a TDC, (d) energy of CsI(Tl) detectors and (e) ZCT of the CsI detector, were recorded in an event by event mode using a CAMAC based data acquisition system. The energy calibration of the CsI(Tl) detectors were made for α-particles from 8.5-25 MeV using a ^{229}Th source and the ^{12C}(12 C, α)^{20}Ne reaction at E(^{12}C) = 24 MeV. The calibration of energy deposited in the plastic detector was made using Compton tagged recoil electrons from ^{137}Cs and ^{60}Co γ-ray sources.

The time calibration of the TDC was done using a precision ORTEC time calibrator. The time walk correction was done to better than 0.25ns by inspecting the prompt gamma line in the 2D spectrum between the energy deposited in plastic and time of flight. The TOF, position information and geometric mean of the energy deposited for the neutron events in the plastic detector have been derived [5]. The geometric mean energy was used to put the electronic equivalent (E_{ee}) threshold on the TOF spectra. An increasing E_{ee} threshold was used with increasing neutron energy (decreasing TOF) to reduce the scattered neutron contribution to the main TOF spectra. The efficiency of the plastic detector as a function of incident neutron energy and energy threshold was calculated using a Monte Carlo simulation code. The efficiency corrected energy spectra of neutrons were derived from the TOF spectra. Typical evaporation spectra derived from the neutron TOF spectra for ^{208}Pb and ^{184}W are shown in Figs. 3(a) and (b), respectively.

Results and discussion

The projectedalpha spectra from two dimesion plot beween Energy of CsI detector and its ZCTpeak at 16.9 MeV(FWHM~4.5 MeV) with the 205Tl target and at 16.3 MeV(FWHM~4.2 MeV) with the Ta target. The nucleus ^{208}Pb produced in the excitation energy range 19 - 23 MeV corresponds to the gates onalpha energy spectrum beween13.5 and19.5 MeV .

The excited nucleus decays predominately by the neutron emission populating the residual nucleus in the E_X ~3 - 14 MeV. The statistical model(SM) analysis of the measured neutron spectra with Ignatyuk formulation of shell effect shows the expected large shell correction energy (~13.1MeV) for the nuclei in the vicinity of doubly magic ^{208}Pb and a small value (2.2 MeV) around ^{184}W (see figure: 3 (a-b)).

An exclusion plot between the damping parameter and the inverse level density parameter δa (= A/ã) has been made for the first time as shown in Fig. 3(c). It is observed that the acceptable range of δa lies between 8.0 and 9.5 MeV. The shell damping parameter γ constrained to ($0.060^{+.010}_{-0.020}$) MeV^{-1} [6, 7].

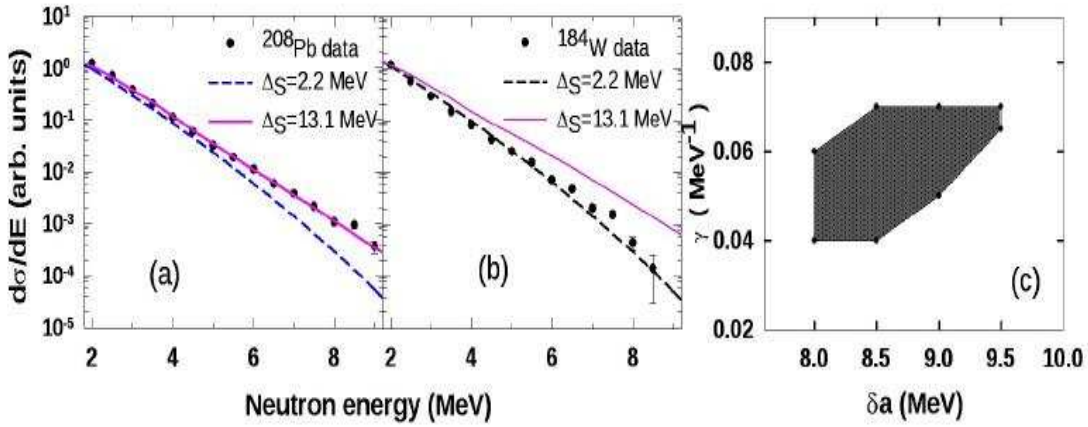

Fig. 3: (a) Neutron spectrum from 208 Pb at E_X =20.8 MeV and solid and dashed lines are the statistical model calculation using shell correction energy (ΔS) 13.1 and 2.2 MeV, respectively, for a=A/8.5 MeV−1 and γ=0.055 MeV^{-1} . (b) Same as (a) except for ^{184}W at EX =20.6 MeV and (c) the exclusion plot between δa (= $A\tilde{}$ a) and γ. The allowed values of *a* and γ are within the contour

Summary and future perspectives

The damping of the nuclear shell effect with excitation energy has been inferred from an exclusive measurement of the neutron spectra in the ^{7}Li breakup followed by fusion of triton with ^{205}Tl. The measured neutron spectra show a large shell effect in the vicinity of ^{208}Pb while small shell correction explains the neutron spectra from ^{184}W. A two dimensional plot between the parameter shell damping factor, γ and asymptotic nuclear level density parameter a, has been made for the first time and the physically allowed values are within the contour. The precision of the measurement of the damping factor can be improved by improving the detection techniques and also on data acquisition system to handle high count rate with less dead time.

The neutron detection can be improved using the liquid scintillation detector which has both good timing for TOF and pulse shape discrimination neutron and gamma separation. The charged particle detection can be made with Si-strip/CD detector for the excellent identification of the light charged particles and will be useful to estimate contribution from the other reaction mechanism. Similar measurement can be also be made in the nuclei where the shell effect is pronounced, for instances in ^{132}Sn(using rare isotope beams) and Pb-Po region. A precise measurement of the shell effect and its damping factor in the magic nuclei has important implication for current research in the nuclear astrophysics and synthesis of the super heavy element.

Acknowledgement

I thank all my collaborators for their help during the experiment. Special thanks to V. M. Datar, D. R. Chakrabarty for their valuable discussion during analysis and calculation.

References

[1] H. A. Bethe, Phys. Rev. 50, 332 (1936); Rev. Mod. Phys. 9, 69 (1937).
[2] A. Bohr, B. R. Mottelson, Nuclear Structure (Benjamin, New York,1969), Vol.1.
[3] V. S. Ramamurthy, S. K. Kataria, S. S. Kapoor, Phys. Rev. Lett. 25, 386 (1970).
[4] A.V. Ignatyuk et al., Yad. Fiz. 21, 485 (1975).
[5] P. C. Rout, D. R. Chakrabarty, V. M. Datar, Suresh Kumar, E. T. Mirgule, A. Mitra, V. Nanal, R. Kujur, Nucl. Instrum. Methods Phys. Res., Sect. A 598, 526 (2009).
[6] P. C. Rout, D. R. Chakrabarty, V. M. Datar, Suresh Kumar, E. T. Mirgule, A. Mitra, V. Nanal, S. P. Behera, V. Singh, Phys. Rev. Lett. 110, 062501 (2013).
[7] P. C. Rout' PhD thesis titled ‚Exploration of the Shell Effect on the Level Density Parameter near Doubly Closed Shell Nucleus A~208' Homi Bhabha National , .2014 ,Institute

BARC NEWSLETTER
FOUNDER'S DAY SPECIAL ISSUE 2015

HIGH LEVEL WASTE MANAGEMENT IN ASIA: R&D PERSPECTIVES

Sangeeta Deokattey[1], K. Bhanumurthy[2] and P.K. Wattal[3]
[1,2]Scientific Information Resource Division, [3] Process Development Division

This Paper received the Progress in Nuclear Energy Best Paper Award 2013 (for the year 2014) instituted by the Editors of the journal Progress in Nuclear Energy (Vol. 62, Jan. 2013, pp. 37-45).

Abstract

The present work is an attempt to provide an overview, about the status of R&D and current trends in HLW management in Asian countries. The INIS database was selected for this purpose. Appropriate query formulations on the database, resulted in the retrieval of 4322 unique bibliographic records. Using the content analysis, all the records were analyzed. Part One of the analysis details Scientometric R&D indicators, Part Two is a subject-based analysis, grouped under: A. Waste Processing B. Waste Immobilization C. Waste Disposal and D. Waste Packaging Materials. The results of this analysis are summarized in the study

Introduction

Asia is one of the fastest growing regions in the world in the area of nuclear power generation. According to the World Nuclear Association, in East and South Asia, there are 112 nuclear power reactors in operation, 37 under construction and firm plans to build a further 84 (at April 2010). Many more are proposed. The greatest growth in nuclear generation is expected in China, Japan, South Korea and India. Therefore, significant amounts of radioactive wastes will be generated in the coming years.

In 1994, IAEA instituted a revised waste classification system, according to which, there are three principal classes of radioactive waste.1. Exempt waste, 2. Low and intermediate level waste, and 3. High level waste. High Level Waste (HLW) management comprises a long term comprehensive strategy, involving solidification, interim storage, reprocessing, partitioning, packaging and ultimate disposal in a geological repository. All the member countries of IAEA are currently using a combination of waste processing methods to deal with solid, liquid as well as gaseous wastes.

Objective

The objective of the present study was to analyze the trends in R&D, in the area of HLW management in Asia.

Materials and Method

The INIS database was used for the purpose of analysis. It is the most comprehensive source of information, on Nuclear Science & Technology. One of the strengths of this database is the coverage of Non Conventional Literature (NCL), technical reports published by R&D institutions in the member countries of IAEA, which are not available through normal publishing channels.

The cut off period for inclusion of records in the study was December 2010. Appropriate query formulations (Table 1) on the database, resulted in the retrieval of 4322 unique records on HLW management in Asia.

Table 1: Query formulation and retrieval of records from the INIS database (1976-2010)

Search History

#15 #4 or #5 or #6 or #7 or #8 or #9 or #10 or #11 or #12
or #13 or #14 (4322 records)
#14 (#1 or #2) and Asia (673 records)
#13 (#1 or #2) and Egypt (13 records)
#12 (#1 or #2) and Vietnam (1 record)
#11 (#1 or #2) and Singapore (7 records)
#10 (#1 or #2) and Malaysia (1 record)
#9 (#1 or #2) and Indonesia (16 records)
#8 (#1 or #2) and Bangladesh (0 records)
#7 (#1 or #2) and Pakistan (10 records)
#6 (#1 or #2) and China (614 records)
#5 (#1 or #2) and Japan (3278 records)
#4 (#1 or #2) and India (457 records)
#3 #1 or #2 (24126 records)
#2 HLW (4664 records)
#1HIGH-LEVEL-RADIOACTIVE-WASTES' in DE* (22615 records)

(* The Descriptor field in the INIS database)

All the 4322 bibliographic records retrieved from the INIS database were downloaded. The content analysis method [1,2] was used to analyze the records. Content analysis method is a well-documented qualitative as well as quantitative research method. It is primarily concerned with the study of basic subject categories, which occur in any text or document. The researcher searches for structures and patterned regularities in the text and makes inferences on the basis of these regularities.

Analysis and Results

Fig. 1 shows the distribution of publications on HLW. From 1976 when the number of publications was 2, to 2008, when they increased hundred fold to 230, there has been a steady increase over the years. 2005 was the most productive year with a record number of 272 publications on HLW.

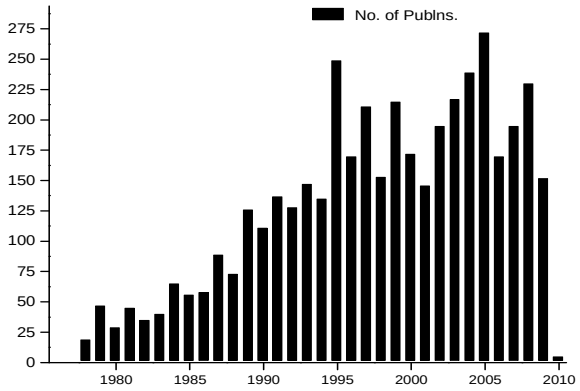

Fig. 1: Growth of Publications on HLW (INIS Database 1976-2010)

As for the type of publications on HLW downloaded from the INIS database, journal articles were predominant with 39% of the total retrieved records. Technical reports ranked second with 29%; Proceeding volumes, Books and Monographs 21%; Others 7%. Patents formed 2% of the retrieved records, which in itself is an indication of the strong R&D on HLW.

During the country-wise analysis (wherein the country of input of the publication is taken into consideration) it was observed, that Japan was the most productive country accounting for 56% of the total publications on HLW. USA ranked second with 11% of the publications; China was third with 9% and India ranked fourth with 8% of the publications on HLW. Fig. 2 gives an indication. Other countries and the IAEA contributed to the remaining 16% of the records. USA with 527 records, France with 120 records and Germany with 65 records formed a major portion of the retrieved records on HLW management in Asia.

On further analysis it was observed that this anomaly was due to corporate authorship of the retrieved bibliographic records. Several R&D institutions in USA such as the American Nuclear Society, US Dept. of Energy, Sandia National Laboratories, the American Institute of Physics, Materials Researh Society, US Nuclear Regulatory Commission, Idaho National Engineering Lab. and the Battelle National Pacific Labs, ASCE and ASME organized seminars, symposia, conferences and meetings on different aspects of HLW management.

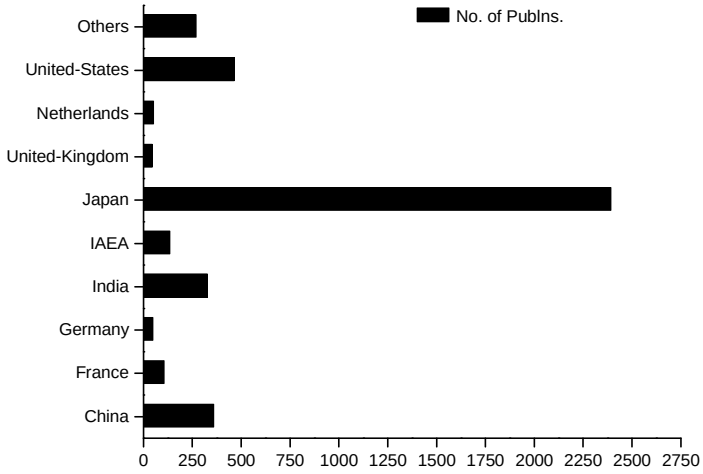

Fig.2: Country-wise breakup of Publications on HLW (INIS database 1976-2010)

Similarly in France, the Societe Francaise d'Energie Nucleaire (SFEN), OECD/NEA, ANDRA CNRS/IN2P3 and f were actively involved in sponsoring and arranging conferences and meets. In Germany R&D organizations such as GRS, BMWA, KFK and BFS were associated with organizing international symposia and seminars.

All the bibliographic records downloaded from the INIS database, were grouped under the following major areas, for the purpose of R&D mapping.

A. Spent Fuel Recovery and Partitioning
B. Waste Immobilization
C. Waste Disposal and
D. Waste Packaging Materials.

A. Spent Fuel Recovery and Partitioning

Japan

Japan has been and continues to be at the forefront of R&D in Waste processing technologies. The most widely used waste processing methods for high level liquid wastes (HLLWs) were Precipitation, Ion exchange and Solvent extraction (TRUEX (Transuranic waste extraction) process, DIDPA (Diisodecylphosphoric acid) process, DIAMEX (Diamide extractants) process, TRPO (Trialkylphosphine oxide) etc. One of the earliest reported studies was the extraction of lanthanoids(III) with di-isodecyl phosphoric acid from nitric acid solution in 1978. Other reported studies in the late 70's were solidification and partitioning experiments of high-level liquid waste; removal of

Cs, Sr, Ce, Eu and Tb into Na- and H-type zeolites particularly the distribution of cesium ion and the properties of ion exchange were studied in various kinds of zeolites, i.e. synthetic mordenite, natural mordenites and clinoptilolites. Zeolites are excellent inorganic ion exchangers with high stabilities to radioactive irradiation. Their ion exchange properties and thermal transformation were studied for the purpose of their application to the separation of cesium and strontium from HLLWs. Mordenite, one of the zeolites, selectively exchanged cesium ion with a high selectivity coefficient of more than 1000. Thus cesium ion can be preferentially exchanged into the mordenite even in the acid solution around pH 1, and separate it from other metal ions in HLLW. In the solvent extraction process, a survey and classification of extractants was undertaken, wherein, the extractants surveyed were classified into six groups; unidentate neutral organophosphorus compounds, bidentate neutral organophosphorus compounds, acidic organophosphorus compounds, amines and ammonium salts, N,N-disubstituted amides and the other compounds. Several experiments were carried out to test their extractability and radiation durability. Partitioning Studies carried out by JAERI, with DIDPA (diisodecyl phosphoric acid) were extensively reported Wherein was back-extracted from DIDPA solvent. Most of the experiments were carried out to select a suitable reagent for back-extraction of U (VI) extracted from 0.5M nitric acid with DIDPA. U, Pu, Np, Am and Cm in HLW were extracted simultaneously with DIDPA, and they were recovered from DIDPA with various reagents: nitric acid for Am and Cm, oxalic acid for Np and Pu, and sodium carbonate or hydrazine carbonate for U. Some partitioning studies were also reported using a novel silica-based CMPO extraction-resin as well as through TOGDA (N,N,N',N'-tetraoctyl-diglycolamide) a diglycolamide.A new separation process for Np, Pu and U using n- and iso-butyraldehydes as reductants for Np(VI) and Pu(IV), respectively, in the reprocessing was investigated. CRIEPI and JRC-ITU undertook a joint study on pyrometallurgical processing. The objective of this study was to demonstrate the capability of this type of process to separate actinide elements from spent fuel and HLLW.

As part of the long-term strategy for management of HLLW and its pretreatment, partitioning and transmutation studies [3] were first reported in Japan in the year 1979. In this study, separation between plutonium and uranium with the use of lactic and nitric acid mixed solution was achieved and transmutation of Cs-137 was carried out, by using a 10 GeV proton spallation reaction. In 1980, a chemical simulation study of mixed oxide targets for transmutating Am-241 with thermal neutron was carried out. At the same time, coprecipitation and volatilization methods were used to remove Tc and Ru. Radioactive ruthenium removal from liquid wastes of ^{99}Mo production process using zinc, charcoal mixture and ion adsorbents were also reported to treat HLLWs.Japan experimented with research on TRU incineration in a fusion reactor blanket. In the treatment of high-level waste discharged from nuclear fuel reprocessing plant. TRUs pose a major problem because of their long life and radioactive hazard. The TRUs are loaded in the blanket of a fusion reactor and are incinerated through fission reaction or nuclear transmutation, utilizing the abundant neutrons in a fusion reactor. The study was made on the modeling of Tokamak type fusion reactor, and the calculation of neutron fluxes and energy spectra in the fusion blanket and the group

constant for the burn-up calculation were done. The study was then made on the feasibility of incineration of TRU loaded in the fusion blanket by using one-group burn-up calculation. A conceptual study of actinide transmutation system with proton accelerator was undertaken and target thermal hydraulics and target neutronics calculations were performed. For treatment of solid wastes, under the Project OWTF (Oarai Waste reduction Treatment Facility) in JAEA (Japan Atomic Energy Agency) volume reduction of waste was carried out, by incinerating and melting treatments.

China

Nuclear energy is developing rapidly in China. More than 1000 tons of spent fuel will be discharged every year after 2020 in China. A feasible advanced nuclear fuel cycle has been proposed to tackle this problem, based on spent fuel reprocessing and high level waste partitioning through the PUREX, TRPO and An/Ln separation processes. These processes would reduce the quantity of Minor Actinides (MA) to about one-fifth of the original HLW even without MA transmutation. A compact tokamak transmutation reactor was designed and used for treatment of high level wastes focusing on neutronics, critical safety, heat transfer and optimization of material composition in several selected blanket designs. Several studies covered transmutation of actinides and fission products, and nuclear system analysis. These studies showed that a 1 GW(e) fusion transmutation reactor could detoxicate the nuclear wastes generated by 10 GW(e) normalized fission power plants. Another study involved minor actinides transmutation by Ultra Long Life Fast Breeding Reactor (ULLFBR). It demonstrated that loading MAs with optimum pattern in ULLFBR can achieve both high transmutation rate and good core performance.

India

Several waste processing methods are employed for the recovery of Uranium and Plutonium, waste volume reduction, recovery of other nuclides of commercial interest, effective separation of long-lived actinides and fission products and also to develop better extractants [4]. India has experimented with solvent extraction methods for a long time, using CMPO, DIDPA, TOGDA and TEGHDA. The Department of Atomic Energy, particularly BARC and IGCAR have been at the forefront of R&D on waste processing. One of the earliest reported studies on recovery of Americium-241 was in 1981. Extraction of actinides from high level waste streams of purex process using mixtures of CMPO and TBP in dodecane was first reported in 1984. Recovery of Technetium was experimented with an active carbon column. Adsorption behavior of Cs and Sr on a synthetic zeolite P was studied. Natural zeolites, clinoptilolite and mordenite, were converted into zeolite P with a high crystallinity, through hydrothermal treatment with NaOH solutions.Simultaneous spectrophotometric determination of iron, uranium and molybdenum in high level radioactive waste was done using a matrix computation method. Separation of transuranic elements based on DIDPA extraction and oxalic acid stripping was reported. Effect of gamma irradiation on some important extractants of divalent palladium was reported. Four reagents, tri-isobutylphosphine

sulphide (TIPS), alpha benzoin oxime (ABO), dioctylsulphide (DOS) and dioctylsulphoxide (DOSO), of relevance to the extraction and recovery of palladium from high radioactive waste solutions of PUREX origin, were irradiated at different gamma doses. A simple method for the recovery of ^{137}Cs and ^{90}Sr from fission product waste was done using ammonium molybdophosphate (AMP) and polyantimonic acid (PA). Resin column chromatography was used to recover palladium from simulated HLLW, in which separation of carrier-free ^{90}Y from high level waste by extraction chromatographic technique, using 2-ethylhexyl-2-ethylhexyl phosphonic acid (KSM-17) was reported. Spectrophotometer was used as a tool for the analysis of various species in radioactive liquid wastes. Monitoring of plutonium in high active waste streams of Purex process was carried out by alpha spectrometry. A method for determination of uranium and plutonium in high active solution by extractive spectrophotometry was developed. TOPO in xylene was used as an extractant for uranium and plutonium from irradiated plutonium carbide and uranium carbide. Partitioning studies in India concentrated on HLWs arising from reprocessing of PHWR fuels and FBR metallic fuels. IGCAR would be using the pyrochemical route to reprocess the waste. Development of the Diamex Process for treating PHWR HLLW and the use of N,N,N' ,N' -tetraoctyl-3-oxapentane-1,5-diamide impregnated magnetic particles for the uptake of lanthanides and actinides from nuclear waste streams were reported. A novel, simple technique based on Magnetically Assisted Chemical Separation (MACS) was developed for the uptake of lanthanides and actinides from pure nitric acid solutions as well as from Simulated Pressurized Heavy Water Reactor-High Level Waste (PHWR-SHLW). Development of long-lived radioactive nuclides transmutation technology with metallic fuel FBR, and analysis of radioactivity and decay heat of metallic fuel were carried out by IGCAR. A few studies were also reported on the development of pyrometallurgical partitioning of transuranium elements prior to transmutation in metallic fuel FBR. Another method of transmutation of fission products was reported with the use of an accelerator.

Three transmutation methods using an accelerator were reported: the proton method, the spallation neutron method and the mu CF method. Other studies on partitioning included: separation of radio cesium from acid-Purex solutions by sorption on granulated AMP; partitioning and recovery of neptunium from high level waste streams of PUREX origin using 30% TBP; degradation, clean-up and reusability of CMPO in HLW treatment for the partitioning of minor actinides; separation of carrier free ^{90}Y from Purex high active waste solutions using extraction chromatography; strontium extraction by dicyclohexano-18-crown-6; actinide partitioning from HLW in a continuous DIDPA extraction process by means of centrifugal extractors; solvent extraction of americium (VI) by tri-n-butyl phosphate; Ion-exchange selectivity of tertiary pyridine-type anion-exchange resin for treatment of spent nuclear fuels; degradation, cleanup, and reusability of octylphenyl-N,N'-diisobutylcarbamoylmethyl phosphine oxide (CMPO) during partitioning of minor actinides from high level waste (HLW) solutions; Recovery of actinides extracted by Truex solvent from high level waste using complexing agents; AKUFVE studies on extraction behavior of neptunium from simulated HLW solutions by 30% TBP; extraction behavior of neptunium from 3

M nitric acid as well as simulated pressurized heavy water reactor high level radioactive waste (PHWR-HLW) solution by 30% TBP/dodecane; partitioning of actinides from synthetic PHWR-HLW using trialkylphosphine oxide, Cyanex-923 with an aim to recover the actinides from high level waste solutions of Purex origin; thermodynamics of strontium extraction from nitric acid medium using substituted crown ether. Extraction of Sr(II) from 4.0 M nitric acid was carried out by di-t-butyl cyclohexano 18 crown 6 (DTBuCH18C6) in mixtures of n-octanol and n-butanol. N, N, N', N' tetrabutyl dodecyl malonamide (TBDDMA) was also studied as a novel extractant for actinide partitioning. Apart from TOGDA and TEGHDA, Pentaalkyl malonamides were also used as extractants for partitioning of technetium from high level nuclear waste solutions. Di(2-ethylhexyl)pivalamide (D2EHPVA): a selective extractant for uranium. Di(2-ethylhexyl)pivalamide (D2EHPVA, a branched chain amide) were used for the selective removal of U over Pu(IV) / Pu(III) and Np(V) / Np (IV) from HLW. Role of two reducing agents viz. hydroxyl amine nitrate (HAN) and hydrazine nitrate (HN) either alone or as mixture was evaluated for Np and Pu extractant under simulated high level waste conditions. Another amide, dimethyl dibutyl tetradecyl malonamide (DMDBTDMA) in dodecane was used, for the recovery of Am from fluoride waste solution. The extraction behaviour of heptavalent technetium from aqueous nitric acid as tracer and in the presence of simulated waste was studied over a range of acidity (1-6 M) using DMDBTDMA (N,N' dimethyl N,N' dibutyl tetra decyl malonamide) and TBDDMA (N,N,N'N' tetra butyl dodecyl malonamide) in n-dodecane as solvents. Large amounts of secondary wastes are also generated using solvent extraction methods. A new zero-emission separation process was reported, using a thermosensitive gel instead of the solvent extraction process, which is applicable to the partitioning and transmutation system of trivalent MAs in HLWs.

B. Waste Immobilization

Glass waste forms

Vitrification of nuclear wastes is attractive because of its flexibility, the large number of elements which can be incorporated in the glass, its high corrosion durability and the reduced volume of the resulting waste form. Vitrification involves melting of waste materials with glass-forming additives so that the final vitreous product incorporates the waste contaminants in its macro- and micro-structure. Hazardous waste constituents are immobilized either by direct incorporation into the glass structure or by encapsulation when the final glassy material can be in form of a Glass Composite Material (GCM). Both borosilicate and phosphate glasses are currently used to immobilize nuclear wastes, moreover in addition to relatively homogeneous glasses, novel GCMs are also used to immobilize waste streams.

Japan

Japan has been at the forefront of R&D in waste immobilization technologies. One of the earliest studies in 1978 reported the preparation of glass-metal composites

(particularly copper- glass mixtures) through pressure sintering, measurement studies of their thermal conductivities and microstructure were also reported. The late 1970's and early 80's saw a number of studies on vitrification technologies in Japan: characterization of borosilicate glasses containing simulated high-level radioactive wastes from PNC and their evaluation; study for the vitrification of high level liquid wastes by in-can melting process(1978); development of vitrification of high level liquid wastes by joule heated ceramic melter. (1979); pot vitrification of high-level radioactive waste; denitration and concentration of HLLW prior to vitrification (1979); mock-up tests for a hot vitrification system. (1980); melting of glass by direct induction heating in a ceramic container. (1981); vitrification tests by the use of glass bead-fed Joule-heated ceramic melters (1982); vitrification apparatus; design and performance test (1984). An advanced technology of SHTM (Super High Temperature Treatment Method) using an induction cold crucible for the treatment of fission products generated after the reprocessing of spent fuel was also proposed as the future stage in the vitrification process. All these experiments culminated in the design of the vitrification plant for HLLW generated from the Tokai Reprocessing Plant in 1986. The plant has a large shielded cell with low flow ventilation, and employed the rack-mounted module system and high performance two-armed servomanipulator system to accomplish the fully remote operations and maintenance. The vitrification of HLLW was based on the liquid-fed Joule-heated ceramic melter process. A computational fluid dynamics model of the melter was initially developed, to simulate the operation of actual melters.

India

Vitrification as a process for the management of high level liquid waste (HLLW) has been accepted worldwide including India. Vitrification process based on borosilicate matrices has evolved in India right from employing metallic melters in early eighties to currently deployed ceramic melters. Induction of cold crucible melters are also on the anvil for vitrification of HLLW from advanced fuel cycles. The Central Glass and Ceramic Research Institute (CGCGRI) was one of the first to experiment with vitrification of HLW in glass, in 1978. In contrast to normal practice of employing theoretical considerations, a scheme based on practical approach was evolved for the development of suitable glass. Thermal and radiation stability study of simulated high level vitrified waste products and corrosion evaluation of high temperature alloys in molten glass using neutron activation analysis method were done in 1981. Glass, ceramic and glass-ceramic matrices for high-level radioactive waste from fast reactors were also examined. The HLW from the reprocessing of fast reactor fuels contains higher concentrations of actinide elements and noble metals than that from thermal reactors. These elements have poor solubility in borosilicate glass, leading to phase segregation and consequent loss of chemical durability. Alternate glass and crystalline ceramic matrices thus need to be developed for the long-term disposal of fast reactor HLW. In this context, work was undertaken on simulated waste forms based on three different systems, viz., iron phosphate glass (IPG), SYNROC, and monazites. IPG is known to be a versatile host matrix for radioactive wastes. In India, extensive work was carried out on Borosilicate glasses and IPG in BARC and IGCAR. In addition to IPG,

studies on the thermo-physical properties of glass bonded ceramic waste form sodalite, were also carried out at IGCAR. This glass was used to immobilize simulated chloride waste from pyrometallurgical reprocessing.

China

Study on the leachability of simulated HLW-glass form, surface structure of leached HLW-glass forms and study on the devitrification behaviour of simulated HLW-glass forms were first reported by China in 1986. Other vitrification studies include analysis of simulated waste vitrification glass specimens by ICP/AES, performance studies for waste glasses and leaching test for BEL-15 vitrification waste form in simulated interstitial clay-water at high temperature. Apart from glass, another waste form study reported in the mid 80's was the Immobilization of simulated high level wastes into Alkali-Activated Slag Cement (AASC). A feasibility study on casting rock solidification of defence high level waste was also undertaken. A preliminary study on the formulation and technological process of casting rock solidification of defense HLW was carried out and the casting rock solidified product of defense HLW containing high contents of Na_2 and Al_2O_3 was prepared. The selected technological process was denitration-calcination-sintering. Temperature has strong effects on the leaching behavior of the 90-19/U simulated high-level waste glass form. Calculation of high temperature viscosity for simulated waste glasses as well as corrosion studies in simulated glasses were done.

Many countries have recognized vitrification as the suitable solidification method for conditioning high level radioactive waste before they are isolated from biosphere in geologic disposal. Several studies were undertaken on leaching behavior of a simulated HLW-glass (90Nd/10) under low oxygen repository condition during 1.5 years as well as unde repository condition in different kinds of geological media, such as granite, cement, bentonite, Fe_3O_4 , etc. Experimental results showed that glass had less mass loss in granite and more mass loss in bentonite after a two-year leaching test. SEM/XEDS analysis showed some element distributions on the leached specimen's surface, i.e., Na, Si and Mg elements were reduced on the specimen's surface; whereas Ba, Al, and Fe were enriched on the specimen's surface. Test on a new No.23 alloy steel to make melting pot for vitrification was also conducted. Efforts were made in the People's Republic of China to solidify HLLW by the Liquid-Fed Ceramic Melter process (LFCM) in the 1990's. This process was to be a continuous process with high throughput similar to the process followed in France.

Solidification of HLLW

Japan

Another alternative to vitrified solid which is acceptable and well characterized for storing radioactive HLLW with desirable long-term stability is ceramics. The earliest studies in 1978 reported the solidification of HLLW by the glass-ceramic process and

the sintering process. Glass-ceramic is a product obtained by the heat treatment of glass which is converted to thermodynamically stable state. The systems of glass-ceramics studied were diopside, celsian, perovskite, and eucryptite systems. A ceramic solidification system with natural zeolite was experimentally tested in 1979. Various compositions of glass-ceramics for the solidification of HLLW were studied and glass-ceramics in the diopside system were concluded to be the most suitable. Compared with the properties of HLW borosilicate glasses, those of diopside glass-ceramic were found to be almost equal in leach rate and superior in thermal stability and mechanical strength.

It was also found that the glass in this system could be crystallized simply by pouring it into a thermally insulated canister and then allowing it to cool to room temperature. Vitrified Waste Products made from simulated wastes were evaluated for their chemical durability, homogeneity, phase separation, thermal conductivity, viscosity, using nondestructive and other techniques. Safety evaluation of encapsulated vitrified products, was also carried out, using the Drop impact test of products. Borosilicate glass products containing simulated high-level waste were dropped onto an iron plate to examine mechanical strength against impact breakup.R&D on Storage and handling of vitrified waste products was also undertaken in Japan. A gamma-scanning system has been developed using an emission-computed tomography (E-CT) technique in order to detect the radioactive homogeneity of vitrified HLW forms, from which samples are provided for the performance tests under the long-term storage and disposal conditions in hot cells of the Waste Safety Testing Facility (WASTEF).

International Projects

JSS project

JSS (Japan, Sweden and Switzerland) undertook a joint study on the leaching properties of vitrified high-level waste subjected to ground disposal. It was initiated in 1981. The three countries are currently entrusting other nations with the reprocessing of their spent fuel. However, they will have to ultimately undertake the disposal of their own high-level wastes. JSS was therefore involved in the R&D for the JSS glass. A testing system was established to evaluate the leaching of radioactive glass. The leaching resistance of the simulated radioactive JSS glass prepared here was higher than that of any other simulated non-radioactive glass material reported elsewhere.

Japan-Australia co-operative programmeme on research and development of technology for the management of high level radioactive wastes

The R&D work carried out in the Co-operative Programmeme provides strong scientific evidence that the durability of ceramic waste forms is not significantly affected by radiation damage and that high loadings of actinide elements can be incorporated into specially designed ceramic waste forms.

Moreover, natural minerals have been shown to remain as closed systems for U and Th for up to 2.5 billion years. These results gave a boost to the development of second generation waste forms, such as SYNROC, to handle future waste which may not be suitable for vitrification

Other Waste Forms: Synroc

SYNROC (SYNthetic ROCk) is a titanate ceramic designed to immobilize the high level wastes arising from reprocessing of spent fuel from nuclear power reactors. Extensive investigations of the chemical and physical properties of SYNROC were carried out in Australia, between 1979 and 1983. SYNROC offers important advantages over borosilicate glass as a wasteform, both in terms of performance (resistance to groundwater leaching) and in achieving public acceptability.

Japan

R&D on high-level radioactive waste immobilization in synthetic minerals; Supercalcine and SYNROC was first carried out in Japan in 1981. Other studies followed: evaluation of fabrication condition of SYNROC by cold press and sintering method; fabrication parameters of SYNROC B (not contained simulated waste), SYNROC C 10 (with simulated waste of 10 wt%) and SYNROC C 20 (with simulated waste of 20 wt%) and their evaluation by cold press and sintering method. Another method reported for fabricating SYNROC was by Hot Uniaxial Pressing (HUP) method. SYNROC-B and -C samples were fabricated by HUP with variant conditions of sintering temperature, pressure and time.

China

Solidification of simulated trivalent actinides by SYNROC process was done. Zirconolite-rich ceramics and Perovskite-rich ceramics were fabricated for the incorporation of simulated trivalent actinide wastes, and the physical properties, XRD, SEM and durability tests were performed. The initial property tests indicate that the two SYNROC-type ceramics could immobilize the trivalent actinide wastes. Tc immobilization by using perovskite-rich and rutile-rich SYNROC was experimented upon. The simulated technetium separated from HLW was immobilized in perovskite-rich and rutile-rich SYNROC which contained 85wt% of perovskite or rutile and 20, 25, 30 or 35wt% waste loading, respectively. The SYNROC was prepared by hot pressing under reducing condition. Hollandite-rich SYNROC with different simulated ^{137}Cs separated from HLW was fabricated and tested. Radiation effects of pyrochlore-rich SYNROC by heavy-ion irradiation were studied. Heavy-ion irradiation is commonly used to study radiation damage of HLW forms, but S ion was never used before. In these investigations, 100 MeV ^{32}S ion produced by tandem accelerator was used, to study radiation effects on pyrochlore-rich SYNROC which contained simulated actinides. Solidification of simulated radioactive incineration ash with zirconolite and sphene SYNROC was done. Making use of cheap natural zirconite, $CaCO_3$ and TiO_2 as

raw materials, adopting high temperature solid-state reaction, the study of solidification of simulated radioactive incinerated ash was carried out with zirconolite and sphene using volume-density measurement, X ray diffraction (XRD) and scanning electron microscopy (SEM). Zirconolite and sphene could be synthesized and the simulated radioactive incineration SYNROC form could be sintered at the same time, which made the process technically feasible.

Indonesia

A comparative study on chemical resistivity of Glass and SYNROC that were loaded with HLW was carried out. A composition of high level liquid waste was simulated using Origen-2 referring to a PWR spent fuel with parameters such as burnup 45,000 of MWd/MtU, 4,5% enrichment, specific power of 38 MWd/MtU, and 4 years cooling time. The glass waste sample was made by adding a simulated high level waste into glass fritz and then heated at temperature of 1150^{o}C. Results showed that the leaching characteristics of both glass and SYNROC wastes tended to be similar. The higher the waste loading the higher the leaching rates, while the longer the leaching time, the lower the leaching rates. The leaching rates of SYNROC waste was about 10-20 times lower than that of glass waste.

Korea

Hollandite-rich SYNROC was used for immobilization of Sr/Cs separated from HLLW. SYNROC which comprised hollandite-rich ($Ba_{1-x}Cs_{2x}(Al_yTi_{2-y})Ti_6O_{16}$, 75wt. %), perovskite ($Ca_{1-x}TiO_3$, 15wt. %) and rutile ($TiO_2$,10wt. %) was devised for the immobilization of Sr/Cs (1:3, wt.%) separated from HLLW. Hollandite-rich SYNROC with different contents of Al element was fabricated, and its mineral phase assemblage and microstructure were determined by using XRD and SEM/EDS. The durability test was carried out by using MCC-1 method, the leachate was analyzed by using ICP/MS and ICP/AES. The results indicated that hollandite-rich SYNROC variants, was a suitable host for immobilization of Sr/Cs separated from HLLW.

International Projects on Waste Solidification and Immobilization

Vitrified Waste Coincidence Counter (VWCC)

Under an agreement between JNC and DOE, a vitrified waste coincidence counter (VWCC) capable of measuring the quality of nuclear material in vitrified waste was developed in cooperation with the Los Alamos National Laboratory (LANL), for the termination of safeguards of vitrified waste. The VWCC consists of a detector head (five He-3tubes shielded by lead, tungsten and polyethylene), two shiftresisters, a digital camera to photograph ID numbers and two computers. Measurements are taken and the data is stored automatically. The agencies are thus able to verify the termination of safeguards by checking data periodically.

International collaboration on nuclear waste solidification

A number of collaborative research projects between Belgium, Canada, France, Japan, Sweden, Switzerland, the United States, and the Federal Republic of Germany are now in progress to test the relative surface reactions or nuclear waste glasses under a variety of simulated repository conditions. Several glasses from these tests are also being evaluated in clay in Belgium. Comparisons of the simulated burial conditions with glasses containing radioactivity close to that expected for commercial operations at LaHague, France, are being made by a Japan-Sweden-Switzerland consortium, with collaboration from the Commissariat a l'Energie Atomique, Marcoule and the Hahn Meitner Institute, Berlin. These studies could lead to an international consensus on the relative performance of high-level waste forms including borosilicate glasses, waste packages and repository variables.

C. Waste Disposal

Japan

Once again Japan was in the lead in R&D on waste disposal. Most of the studies undertaken in Japan concentrated on experiments and computer simulations on design and development of HLW waste repositories. Since the 1970s, Japan has been conducting studies for geologic disposal of HLW. These were performed at the Tono mine and at the Horonube Underground Research Laboratory (Horonube URL).

a. Design studies, safety evaluation and performance assessment

Design study on a geological repository with respect to heat generated from high level radioactive waste forms was carried out; conceptual design of geological repositories for high level wastes was undertaken; experimental approach to performance of engineered barriers under repository conditions; development of computer codes for performance assessment of geological disposal system; study of deep cavern stability design method in radioactive waste repository.

An improved design of radwaste repository was also proposed based on the concept that with suitable engineering efforts, a well-harmonized design of the artificial-barrier system itself could reduce the potential radiological hazard of high-level radioactive wastes to an acceptable level. Key radionuclides and parameters that determine performance of geologic repositories for high-level radioactive wastes were investigated. An exploratory approach for scenario analysis in the performance assessment of geological disposal was also proposed.

b. In situ underground experiments

Thermal characteristics of rocks for high-level waste repository and solubility limited radionuclide transport through geologic media were undertaken in Japan in 1980. Heat transfer study around a high level radioactive waste repository was done and thermal

and mechanical effects of the high level radioactive waste on the rock mass for a repository were also studied. In the underground geological repository, buffer materials would be placed between a package and wall rock in a disposal pit. A bentonite powder produced in Japan was compacted in a test hole in-situ into 1.27 kg/cm^3 at 380 m below surface and heated with an electric heater for about 882 hours. The value of the obtained thermal conductivity of the buffer material was slightly larger than that of the laboratory data. A preliminary test on a bentonite/sand mixture was also undertaken.

International collaboration on Geologic Disposal

Under the joint international **Tunnel Sealing Experiment (TSX) Project,** between AECL, Canada and JNC, Japan, at the Underground Research Laboratory (URL) in Canada**, s**ealing technologies considered in the sealing concept were experimented upon. Sealing involves backfilling, plugging, grouting etc. The project mainly focused on plugging. R&D was carried out both on the mechanical plug and the hydraulic plug. The mechanical plug is the concrete plug, and the hydraulic plug is the clay-based plug. Pressurized water is injected in the pressure chamber installed between the concrete plug and the clay-based plug. The sealing performance of the clay was studied using water seepage from both the plugs. JNC also collaborated with the Lawrence Livermore National Laboratory on the near field performance assessmnt related to the geologic disposal of radioactive wastes. This project was initiated in 1999.

The Intraval Project

INTRAVAL project was started in Stockholm as an international effort toward validation of geosphere models. The project WAS initiated by the Swedish Nuclear Power Inspectorate (SKI) and was prepared by an ad hoc group with representatives from eight national and international organizations. The purpose of the project WAS to increase the understanding of how various processes and geohydrological structures of importance for the transport of radionuclides from a repository to the biosphere cOUL be properly described by mathematical models and how models developed for this purpose cOUL adequately simulate the nuclide transport during short as well as very long time periods.

c. Rock mechanical characterization

Survey on the characteristics of rock under low and high temperatures was undertaken. Particle motion induced by elastic waves radiating from subsurface, penny-shaped cracks and mapping of subsurface cracks were also studied. A Diffusivity Data Base (DDB) for major rocks was developed in Japan. In this database, 3 kinds of diffusion coefficients: effective diffusion coefficient (De), apparent diffusion coefficient (Da) and free water diffusion coefficient (Do) were treated. Rock was categorized into four kinds; acid crystalline rock, alkaline crystalline rock, sedimentary rock (argillaceous/tuffaceous rock) and sedimentary rock (psammitic rock/sandy stone) from the viewpoint of geology and mass transport.

d. Sorption, migration and groundwater chemistry

Studies on the behaviour of radionuclides in a saturated sandy layer were undertaken. The effect of pH on the transportation of long-lived radionuclides through a quartz sand column was studied. The movement of radionuclides through a sandy layer was also studied by mainly using the miscible displacement technique. Other radionuclide migration studies include: numerical model of radionuclide migration in geologic media; radionuclide transfer in underground media; evaluation method on ion exchange of radionuclides; migration of radionuclide through two-layered geologic media; adsorption kinetics of strontium and cesium cation on rock materials. intraparticle diffusion kinetics; effect of mineralization reaction on the radionuclide transport through geologic media; nuclide sorption on granite; three-dimensional groundwater flow and advection diffusion code for treating decay chain of radioactive materials by finite element method; fracture system of granite at the Tono Mine; evaluation of fracture characteristics at AN-1 (0-270 m) by borehole television system; Application of groundwater flow meter with single well to groundwater flow survey in fractured rock; study on radionuclide migration through a buffer material of the repository for high level nuclear waste; sensitivity analysis of radionuclide transport model using the Differential Algebra method; diffusion of the ^{241}Am -> ^{237}Np decay chain limited by their elemental solubilities in the artificial barriers of high-level radioactive waste repositories; sorption mechanism of Pu, Am and Se on sodium-bentonite; a new three-dimensional groundwater flow analysis system applying the element-free Galerkin method; experimental studies for sorption behavior of tin on bentonite and rocks and diffusion behavior of tin in compacted bentonite. Quantitative Assessment Radionuclide Migration Experimental Facility (QUALITY) was constructed, to investigate radionuclide migration behaviour under an aerobic condition. It became operational in 1999. This facility contains atmosphere controlled glove boxes to obtain basic data on radionuclide migration in engineered barrier materials and rocks on a laboratory scale.

e. Engineered Barrier Systems (EBS)

A sensitivity analysis was performed for assessing the effects of barriers, such as waste form, engineered barrier and geosphere, on the isolation system performance of the geologic disposal of high level wastes. Other studies focused on: preliminary analysis of engineered barrieer performances in geological disposal of high level waste; simulation of chemical reactions of released nuclides from high-level radioactive waste in engineered barrier; study on mechanical stability of engineered barrier system for deep geological isolation of high-level radioactive waste; Neptunium migration involving oxidation-reduction reactions in engineered barriers; studies on material properties and structural mechanics of engineered barriers for HLW geological isolation; verification of the safety analysis codes for geological disposal of high-level radioactive wastes; adsorption and diffusion experiments were conducted using Np-237 and Japanese bentonite (Kunigel V1) as buffer material of high-level radioactive wastes disposal system in order to verify the chemical transport model code GESPER; safety analysis of engineered barrier in geologic disposal of high-level waste; study on

vibration behaviours of engineered barrier systems. Prefabricated EBS modules (PEMs) to minimise the problems involved with handling compacted bentonite and ensuring that it was emplaced to established quality levels, was investigated in various national programmemes, for the disposal of both HLW and SF.

f. Backfill, Buffers and Cement

Backfill-waste interaction studies in repository simulating conditions were examined. Glass ceramic, supercalcine ceramic, sintered ceramic waste forms and their interactions with backfill were examined. Properties of bentonite clay and its performance assessment as buffer material in high-level waste geological disposal was studied. Various tests on buffer materials were performed; such as static and permeability sorption test; experiments on thermal conductivity; analysis of backfill performance of engineered barrier from view point of nuclide migration; evaluation of plutonium migration in artificial barrier (compacted bentonite) using leaching data of fully radioactive waste glass; comparison with leaching model and limited solubility model; permeation characteristics of compacted bentonite; diffusive behavior of water in compacted bentonite; performance test of waste package system with buffer material; Mechanical, thermophysical and hydraulic and swelling properties of buffer materials for repositories of high-level nuclear waste; studies of waste form and buffer material performance at the Japan Atomic Energy Research Institute and analysis on thermodynamics processes of buffer material in HLW deep geological repository. Study on the applicability of clay as backfill material in high level radioactive waste disposal was also conducted. A new manufacturing technique of synthetic buffer materials was developed. Another interesting study focused on the effects of bacteria on the corrosion behavior of carbon steel in compacted bentonite. As part of the evaluation of corrosion life of carbon steel overpack, experimental studies were performed on the effects of bacteria on the corrosion behaviour of carbon steel in compacted bentonite using iron bacteria (IB) as representative oxidizing bacteria and sulphur reducing bacteria (SRB) as representative reducing bacteria.

China

China has proposed a preliminary R and D programme for the deep geological disposal of high-level waste. The development strategy for high-level waste repository includes 3 stages: siting and site characterization, underground research laboratory for a site-specific study and building a repository. It is expected that a national geological repository will be built and put into operation during 2030-2040. The deep geological disposal method would be used. Analyses on the prospect of underground disposal for radioactive wastes from nuclear power plants in China and on the selection of geologic medium were initiated in 1984. The proposed site for the repository is the Beishan area in northwestern China.Other studies include: sorption of ^{237}Np, ^{239}Pu and ^{241}Am on bentonites and minerals; use of inorganic sorbents as backfill material for underground repositories; pre-selection of geological disposal reservoir sites of high-level waste in northern Sichuan-southern Shaanxi regions; study on the mechanic properties of high

dense bentonite buffer materials for disposal of high level radioactive waste; selection of backfill materials for the disposal of high level radioactive waste; modeling of water-glass and water-granite interaction.

Indonesia

A 1-D model for assessment of radionuclides migration in geological media for evaluating of safety performance of disposal of HLW was developed in Indonesia. A new strategy to dispose of high-level radioactive waste, was the use of an ocean-island approach. Indonesia which has more than 17000 islands, could dispose its proposed HLW in one of its remote islands.

Korea

The Korea Atomic Energy Research Institute (KAERI) has developed the preliminary disposal concept for high level wastes and subsequent total system performance assessment tools. To test the lithological suitability for HLW repository in Korea**,** **r**egional geologic conditions of Korea were studied with emphasis on rock mass and fracture system as a part of the research programme for high level radioactive waste disposal. With regard to the safety assessment of deep geological HLW repository, there could be several parameters of uncertainty. Dilution factor is considered as one of the parameters that has a large uncertainty. Under the assumption that PWR spent fuels are disposed of into deep geological repository, uncertainty analysis on dilution factor was performed.Another waste disposal concept, adapting room and pillar method, (which is a confirmed technique in mining and tunnel construction) was experimented in Korea. Important rock mechanics principals and in situ and laboratory tests for understanding the behavior of rock, buffer, and backfill as well as their interactions were reviewed. The Korea Underground Research Facility (KURF) is also under construction at KAERI, for in situ studies related to the validation of a HLW disposal system. For the safe construction and long-term researches at KURF, mechanical stability of the facility needs to be evaluated. A 3D mechanical stability analysis using the rock mass properties determined from various in situ as well as laboratory tests was carried out.

D. Waste Packaging Materials

Japan

Japan has conducted extensive studies on the design, safety analyses and tests of packagings for HLW and spent fuel transport/storage. Overpacks for high-level radioactive waste disposal in deep underground areas must prevent ground water contact with vitrified waste. To integrate the capability of overpack, corrosion-resistance, pressure-resistance, water tightness, air tightness and manufacturing properties need to be considered. Several materials were investigated, to develop overpacks. A conceptual design and fabrication of a full-scale ceramic overpack was undertaken; static fatigue behavior of ceramic materials as candidate overpack materials

was examined. A modeling study of general corrosion of copper overpack for geological isolation of high-level radioactive waste and an assessment of corrosion life of copper overpack were also performed. Other studies on overpacks include; use of Ti-alloys selections for titanium-complex overpack based on corrosion resistance; corrosion resistance of titanium alloy on the overpack for high-level radioactive waste disposal; conceptual design of overpack and experimental manufacture of titanium-carbon steel composite overpacks for geological disposal of high-level radioactive waste; trial manufacturing of copper-carbon steel composite overpack. Kobe Steel, Ltd. of Japan developed shielding materials of the 'kobesh' series, applicable for advanced transport packaging.

Silicon rubber base type 'kobesh SR-T01' is a material in which, from among the silicone rubber based neutron shielding materials, the hydrogen content is highest and the boron content is most optimized. Experimental results showed that the silicone rubber based neutron shielding material has good neutron shielding capability and high long-term fire resistance, and that it can be applied to the advanced transport packaging. For the final sealing technique of the overpack, carbon steel, one of the candidate materials for the disposal container in the geological disposal of high-level radioactive waste in Japan was used. Welding tests were conducted using TIG (GTAW), a typical arc welding process and electron beam welding (EBW), a high-energy beam welding process.

Conclusion

Japan's supremacy in R&D on HLW management can be gauged from the fact, that a total of 99 patents were filed between 1978 and 1999. The earliest patent (1978) detailed a method for processing high level radioactive liquid wastes containing sodium nitrate. Several others were on methods for processing, treating, storing and solidifying HLLWs. In the 1980s, in the area of waste glasses, the following patents were filed; methods were described for solidifying radioactive waste glass, using a cartridge; method of manufacturing borosilicate glass solidification products; process for producing sintered solidification product containing cesium and/or strontium as radioactive isotopes and method of using the sintered solidification product as large scaled RI cell by fabrication of the same. In the area of separation processes: method of recovering Ruthenium and a Ruthenium separation device from radioactive waste; method of cleaning volatile ruthenium; Technetium recovering method and device and a processing method of high level radioactive solution.

Other patents included: waste storage and materials for waste storage: dry-type storage facility for radioactive material; radioactive material dry storage facility and processing method for molten salt waste. India, particularly the institutions under DAE have established themselves in the field of process chemistry and waste reprocessing. China is the fastest developing country in the area of nuclear energy. In fact, the maximum number of new nuclear reactors would be commissioned in Asia in the next two

decades. All the Asian countries could cooperate in different core areas of their expertise, to make nuclear energy a more viable alternative.

References

[1] Krippendorff, K.: Content analysis: an introduction to its methodology. London, Sage, 1980.
[2] Molina, M.P.: Interdisciplinary approaches to the concept and practice of Written Text Documentary Content Analysis. (WTDCA), *Journal of Documentation*, 50(2), 1994, pp. 111-123.
[3] Actinide and fission product partitioning and transmutation: status and assessment report. Paris, NEA/OECD, 1999.
[4] Nuclear Fuel Cycle; BARC Highlights, Vol. 1, Mumbai, BARC, 2007.

BARC NEWSLETTER
FOUNDER'S DAY SPECIAL ISSUE 2015

RADIO-ADAPTIVE RESPONSE OF BASE EXCISION REPAIR GENES AND PROTEINS IN RESTING HUMAN PERIPHERAL BLOOD MONONUCLEAR CELLS EXPOSED TO GAMMA RADIATION

Sneh M. Toprani and Birajalaxmi Das*
*Low Level Radiation Research Section,
Radiation Biology and Health Sciences Division

Ms. Sneh Toprani, was awarded the Young Scientist Award at the International Conference on Radiation Biology, 12th Biennial Meeting of ISRB, New Delhi , Nov.11-13, 2014

Abstract

Ionizing radiation (IR) induces several isolated and clustered DNA lesions in human cells at high dose exposures. These damages, if mis-repaired or unrepaired may affect the integrity of the genome. Depending upon the type of lesions, various DNA repair pathways gets activated to repair the damages. For instance, single strand breaks (SSBs) and base damages are repaired by base excision repair (BER) or nucleotide excision repair pathway (NER), whereas complex lesions such as DNA double strand breaks (DSBs) are repaired through non-homologous end joining or homologous recombination pathway. DNA DSBs are highly deleterious and but base damages and single strand breaks cannot be underestimated as they are associated with many types of cancers and neurological disorders. In the present study, attempt has been made to study the role of BER genes and proteins in radio-adaptive response, if any, in resting human peripheral blood mononuclear cells (PBMCs). Venous blood samples were collected from twenty random healthy individuals with written informed consent. Dose response, time dependent changes and radio-adaptive response at the level of DNA damage, transcription and protein expression were studied in PBMCs exposed to gamma radiation. Dose response study was carried out in PBMCs exposed between 0.1 Gy to 2.0 Gy at 0 and 4 h post irradiation. Post irradiation changes in PBMCs exposed to 1.0 Gy and 2.0 Gy were studied up to 240 min. Radio-adaptive response was studied in PBMCs exposed to a priming dose of 0.1 Gy followed by a challenging dose of 2.0 Gy after 4 h post irradiation. Our results have shown a significant ($p \leq 0.05$) dose dependent increase in the percentage of DNA in tail (%T) in PBMCs of 20 individuals studied. At transcriptional level, LIGASE3, MBD4 and LIGASE1 showed significant up regulation ($p \leq 0.05$) at 4 h post irradiation. Radio-adaptive response study showed significant reduction in percentage of DNA in tail. Both at transcript and protein level APE1, FEN1, LIGASE1, OGG1 showed significant up-regulation ($p \leq 0.05$). In conclusion, BER genes and proteins have shown involvement in radio-adaptive response which has important biological significance in human.

Introduction

Humans are continuously exposed to both natural and man-made sources of ionizing radiation (IR) in their daily life, which include natural background, occupational, medical and radio-therapeutic doses of radiation. It is widely accepted that IR at high doses is detrimental to human health. However, the effect of low and moderate doses of IR is inconsistent and inconclusive. In recent years, a number of epidemiological studies are conducted in human population to delineate the effect of low doses of IR (1-3). At the same time, efforts have been made worldwide to generate radiobiological data on in human cells, tissues and organisms exposed to IR. In addition, it is also important to understand the biological mechanisms occurring in human cells exposed to low to moderate doses of IR. The Linear No Threshold (LNT) hypothesis is well debated as the data for low-dose exposures were extrapolated from high acute-dose exposures. The mechanism of carcinogenesis at low-dose radiation exposures is not yet clearly understood. Hence, it is essential to conduct dose response and radio adaptive response (RAR) studies in human cells to understand the biological mechanisms including various pathways of DNA repair involved in the interaction of IR (4). RAR is a phenomenon where a small dose (priming) of radiation reduces the response/effect to a subsequent larger (challenging) dose (5-8). It is assumed that RAR may be either due to enhanced repair of DNA damage or protection against the adverse effects induced by high challenging doses (9). Thus it is important to understand the repair of DNA damages produced by IR at low to moderate doses of exposure in human cells *ex vivo*. Low linear energy transfer (LET) radiation such as gamma radiation deposits ~70% of the energy that induces isolated lesions, which add to the oxidative burden of the cell (10). IR induces isolated DNA lesions, DNA protein cross links and clustered DNA damages that include bi-stranded clusters such as double-strand breaks (DSBs) or non-DSB-clustered damage. In mammalian cells, gamma radiation induces around 850 pyrimidine lesions, 450 purine lesions, 1000 single strand breaks (SSBs) and 20–40 DSBs/cell/Gy (10-11). However, the efficient DNA repair machinery in human constantly repairs various DNA lesions through biochemical and molecular pathways to maintain the genome integrity (12). If the damages are unrepaired or mis-repaired, it may lead to alteration in transcription and protein expression profile and activation of cell cycle check points. It may also lead to cell death (apoptosis) and mutagenesis (13-15).

A typical therapeutic dose of around 2.0 Gy/fraction of gamma radiation produces ~3000 DNA lesions per cell exposed, a level of damage far lower than the level of up to 50000 lesions produced daily through reactive oxygen species (ROS). It is known that DNA DSBs are highly deleterious and at the same time, the cytotoxic and mutagenic nature of SSBs, oxidised bases and abasic sites cannot be underestimated as they have been associated with many cancers, neurodegenerative disorders and age-related diseases (16-17). BER pathway plays an important role in the removal of these damages, which are formed either spontaneously or by chemical reactions or ROS generation. It maintains the genomic integrity and prevents mutations associated with a common product of oxidative damage to DNA (18-19).

BER pathway involves various steps for damage removal, which includes excising the damaged moiety, incision of the abasic site, replacing the excised nucleotide and sealing the nicks as shown in figure 1.

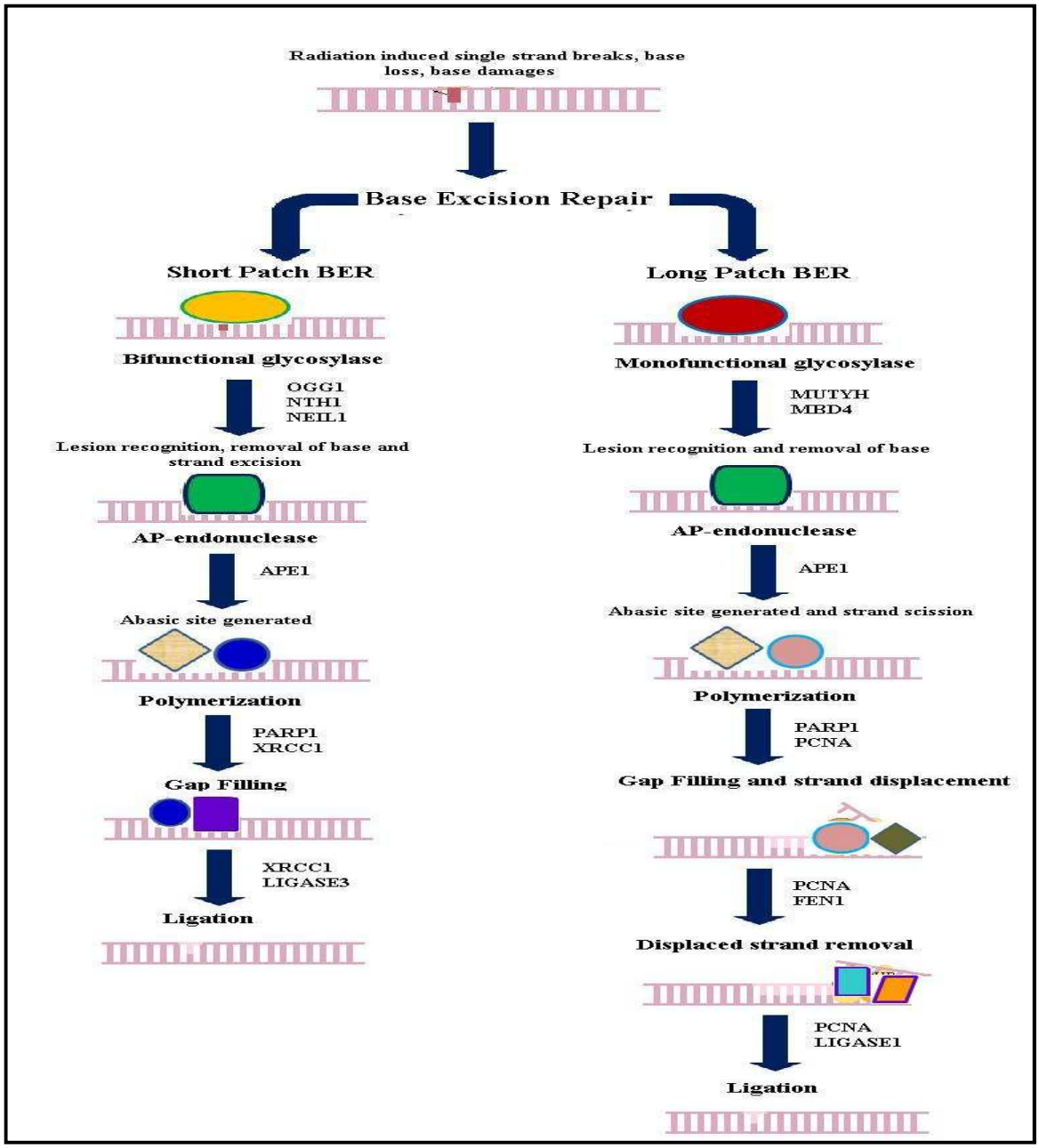

It is initiated by DNA glycosylases that are either mono-functional or bi-functional in nature based on their catalytic mechanism and ability to execute AP lyase strand cleavage activity (20-21). Mono-functional glycosylases (MBD4, MUTYH, etc.) generate abasic sites, wherein the bi-functional glycosylases (OGG1, NTH1 and

NEIL1) exhibit base excision activity and harbour the capacity to incise at the abasic site to create a SSB (22-23). AP sites are further processed by APE1 (24-25). BER is operated through two different sub-pathways (short and long patch) depending on the type of damage. The genes involved in short-patch BER pathway are XRCC1 (X-ray cross-complementing factor 1) and DNA LIGASE3, whereas in long-patch BER pathway, PCNA (proliferating cell nuclear antigen), FEN1 (Flap endonuclease 1) and DNA LIGASE 1 are involved (26-27). In addition, there are other factors such as poly (ADP-ribose) polymerase 1 (PARP1) that is known to repair single-strand DNA nicks and even involved in recruiting other BER proteins onto the damaged site (28).

However, the determining factor for the activation of both the sub-pathways is not known yet. It is also not clear whether both the sub-pathways work simultaneously or in an independent manner.There is sufficient evidence that the effect of radiation is qualitatively and quantitatively different at low to moderate doses as compared to high-dose exposures. The dose, dose rate and time period between priming and challenging dose are crucial for a cell to induce RAR. Besides these factors, humans also display a high degree of inter-individual variation that may play an important role in radio-adaptive response as it is dependent on the radio-sensitivity of an individual. Considering all these factors, induction of repair processes and protection of radiation-induced damage by the RAR in human cells are very complex.

RAR have been demonstrated *in vitro* and *in vivo* using various end points such as cellular damage, cell lethality, chromosomal aberrations, mutation induction, radio-sensitivity and DNA repair. It is not yet clear at what relevant dose and dose rate RAR is functional in humans. Olivieri *et al*. (29), have shown a reduced frequency of chromosome aberrations in peripheral blood lymphocytes cultured in the presence of [3H] thymidine followed by X-ray exposure. There are studies showing the involvement of DNA repair mechanisms such as nucleotide excision repair (NER) and non-homologous end joining (NHEJ) in mammalian cells but no DNA repair genes/enzymes have been directly implicated to this response (30-32). Our group has demonstrated active involvement of NHEJ and BER genes and proteins in repairing radiation-induced damage in G0/G1 stage of human peripheral blood mononuclear cells (PBMC) up to 4 h (30, 33-34). RAR has been demonstrated when both the conditioning and challenge doses are applied at late stages (S/G2 phases) of the cell cycle. Human PBMC are in the resting stage (G0/G1) of the cell cycle and are considered to be highly sensitive and thus an ideal choice to study *ex vivo* exposure. In the present study, an attempt has been made to find out the involvement, if any, of BER genes and proteins in RAR, in resting human PBMC exposed to gamma radiation.

Materials and methods

Sample collection and Irradiation

Venus blood samples were collected from twenty random, normal and healthy individuals (Age range: 25 to 40 years) in EDTA containing vacutainers with written

informed consent which was approved by Medical ethic committee, BARC, Mumbai. All the individuals included in this study are non-smokers and having no chronic illness. Approximately, 12.0 ml of venous blood was collected from each individual, PBMCs were isolated through density gradient centrifugation and divided into different aliquots (~ 1 X 10^6 cells/ml) for further experiments. PBMCs were re-suspended in RPMI-1640 medium (Hi-Media Pvt. Ltd., Mumbai) containing 10% fetal bovine serum (FBS), 2.0 mM L-glutamine and mixture of antibiotics. These were exposed to different doses of gamma irradiation (0.1, 0.3, 0.6, 1.0 and 2.0 Gy) using ^{60}CO source (Bhabhatron II, Panacea Medical Technologies, Banglore, India).

Dose response study

PBMCs were irradiated at different doses of radiation between 0.1 to 2.0 Gy. DNA damage was quantified immediately after irradiation. For gene expression analysis, one set was processed immediately after irradiation (0 h) and the other set was processed after 4 h of incubation at 37°C.

Repair kinetics or post irradiation experiments

PBMCs were irradiated at 1.0 Gy and 2.0 Gy and incubated at different time intervals up to 240 min. Aliquots of PBMCs were collected at various time intervals of post irradiation for gene and protein expression studies.

Radio-adaptive response study

PBMCs were irradiated at a priming dose of 0.1 Gy followed by a challenging dose of 2.0 Gy after an incubation of 4 h at 37°C (primed cells). Along with this, aliquots for priming dose and challenging dose alone (non-primed cells) were also collected. Un-irradiated PBMCs were simultaneously processed as a control along with the irradiated samples for all the above experiments.

DNA damage measurement using comet assay

DNA damage and its repair kinetics were studied in irradiated PBMCs using alkaline single cell gel electrophoresis (comet assay) as per the protocols described by Singh et al., 1998 (35). SYBR Green I stained slides in duplicates were analysed in fluorescent microscope. About 100 cells (50 cells from each slide) were randomly selected and quantified with the TriTek Comet Score FreeWare^{TM}version 1.5 and DNA damage in terms of percentage of DNA in tail (%T) was calculated.

Gene expression analysis

Total RNA was extracted from irradiated PBMCs and was reverse transcribed to cDNA. Analysis of gene expression pattern of the BER genes [short patch (*OGG1, NTH1, NEIL1, XRCC1,* and *LIGASE3*), regulatory (*APE1, PARP1)* and long patch (*MUTYH,*

MBD4, PCNA, FEN1 and *LIGASE1*)] was carried out using real time quantitative-polymerase chain reaction (RT q-PCR). Melting curve analysis was also done to ensure the specific amplified product of interest.

Protein expression analysis

BER protein expression was studied using Western blot. Nuclear extracts were obtained from control and irradiated PBMCs at 30 min post irradiation. Electrophoresis was carried out using 100µg of protein per sample on SDS-polyacrylamide gels using specific antibodies. β-actin was used as a loading control.

Statistical analysis

The level of significance was set at $p \leq 0.05$ for all statistical analysis. Regression analysis was performed in order to see the correlation between irradiated and control samples for DNA damage. Paired 't' test was performed to find out the significant difference between irradiated and un-irradiated samples for DNA damage, gene expression and protein expression analysis.

Results

DNA damage, repair kinetics, gene and protein expression profile were studied in gamma irradiated PBMCs of twenty individuals at different doses up to 2.0 Gy. In addition, adaptive response study was done in PBMCs of these individuals with a priming dose of 0.1 Gy followed by a challenging dose of 2.0 Gy with incubation of 4h.

Dose response study at the level of DNA damage, transcription and protein expression

Quantitation of DNA damage in terms of percentage of DNA in tail (%T) was done using alkaline comet assay at various doses (0.1, 0.3, 0.6, 1.0, 2.0 Gy) of gamma radiation along with un-irradiated control as shown in figure 2.

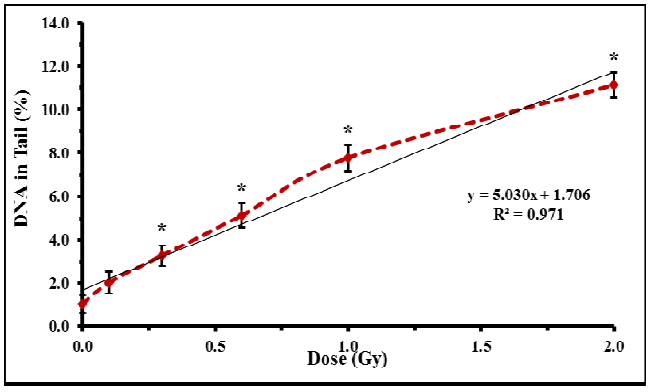

Fig. 2: Dose response study in PBMCs of twenty individuals using alkaline comet assay. Mean percentage of DNA damage in tail (%T) in PBMCs exposed to different doses of radiation (0.1, 0.3, 0.6, 1.0 and 2.0 Gy).

Our results have shown a significant ($p \leq 0.05$) dose dependent increase in the percentage of DNA in tail (R^2 = 0.971) from 0.3 Gy to 2.0 Gy. No significant difference was observed in mean percentage of DNA damage in tail (%T) at 0.1 Gy as compared to un-irradiated control. Approximately, 11.0 % of DNA in tail was observed at the highest dose (2.0 Gy) studied. Dose response of BER genes was analysed in PBMCs exposed to different doses between 0.1 to 2.0 Gy at 0 h and 4h post irradiation (figure 3).

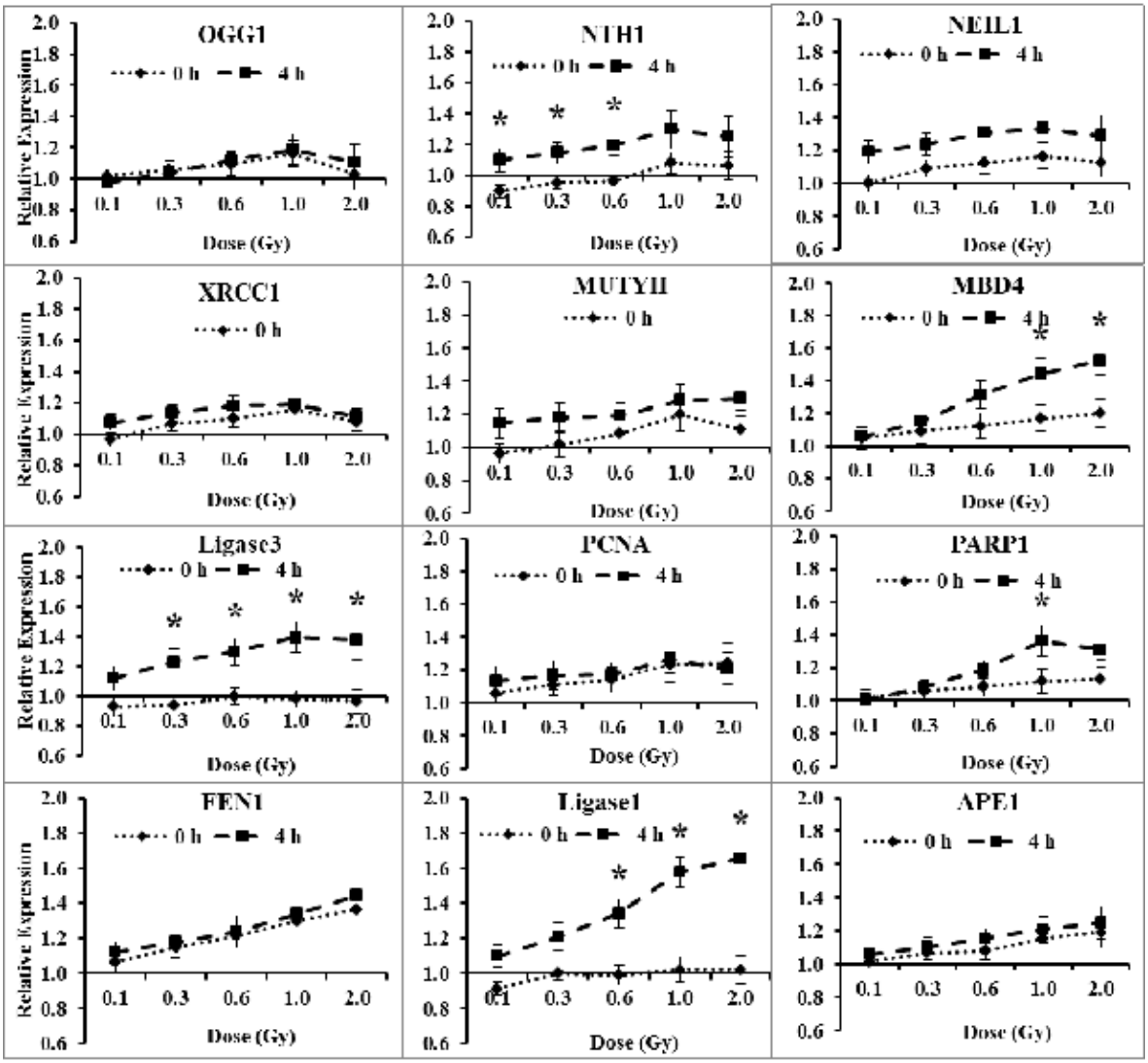

Fig. 3 Average relative gene expression of BER genes in PBMCs of twenty individuals exposed to different doses (0.1, 0.3, 0.6, 1.0 and 2.0 Gy) of radiation at 0 h and 4 h in post irradiation. (*p<0.05)

The relative expression of genes involved in short patch (*OGG1*, *NTH1*, *NEIL1*, *XRCC1*, *LIGASE3*), regulatory (*APE1*, *PARP1*) and long patch (*MUTYH*, *MBD4*, *PCNA*, *FEN1* and *LIGASE1*) were analysed with respect to beta actin. Short patch genes

such as *OGG1, XRCC1, NEIL1* and regulatory gene *APE1* did not show any significant up regulation at the level of transcription 4 h post irradiation. *NTH1 and LIGASE3* showed a significant increase ($p<0.05$) in expression at lower doses up to 0.6 Gy. *PARP1* showed significant increase in expression at 4 h post irradiation at 1.0 Gy. *MBD4* showed significant dose dependent increase in expression whereas *LIGASE1* showed a significant increase in expression after 0.6 Gy at 4 h post irradiation.

Dose response study of BER proteins in PBMCs exposed to various doses between 0.1 Gy to 2.0 Gy showed short patch BER proteins such as XRCC1, OGG1 and LIGASE3 were significantly up regulated upto 0.6 Gy (figure 4). APE1 showed dose dependent increase in protein expression, whereas PARP1 showed increased expression at 0.6 Gy (1.4 fold) and 1.0 Gy (1.8 fold) as compared to control. Similarly, long patch BER proteins such as MUTYH showed no change in protein expression as compared to control, whereas MBD4 showed ~ 2.7 fold increased expression up to 2.0 Gy. PCNA showed a marginal change in protein expression whereas FEN1 protein was up regulated from 0.3 Gy to 2.0 Gy (ranging from 1.5 to 2.1 fold). LIGASE1 showed dose dependent increase in protein expression with a maximum of ~2.0 fold increase at 2.0 Gy as compared to control.

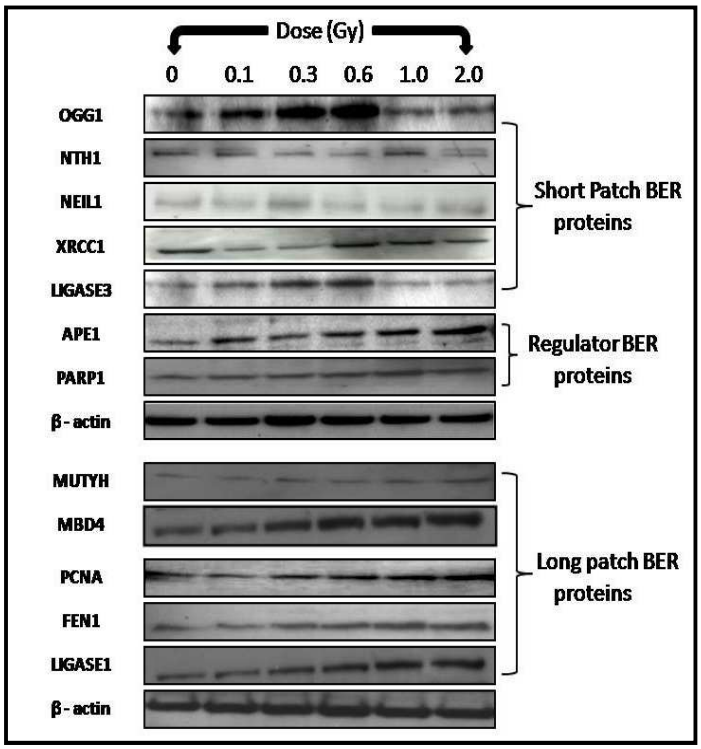

Fig. 4: A representative image of Western blot of an individual showing expression profile of BER proteins in PBMCs exposed to different doses of radiation (0.1, 0.3, 0.6, 1.0 and 2.0 Gy) along with the unirradiated control

Repair kinetics and post irradiation changes at transcript and protein expression level:

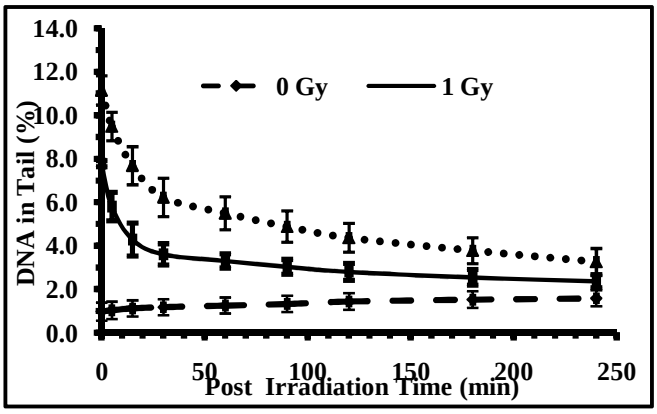

Fig.5: Repair kinetics of DNA strand breaks in PBMCs of twenty individuals at different post-irradiation time intervals (0 min, 5 min, 15 min, 30 min, 60 min, 90 min, 120 min, 180 min and 240 min) for 1.0 Gy and 2.0 Gy along with control using alkaline comet assay

Repair kinetics was studied at 1.0 Gy and 2.0 Gy along with un-irradiated control at different time intervals up to 240 min in irradiated PBMCs for 20 individuals using alkaline comet assay as shown in figure 5.

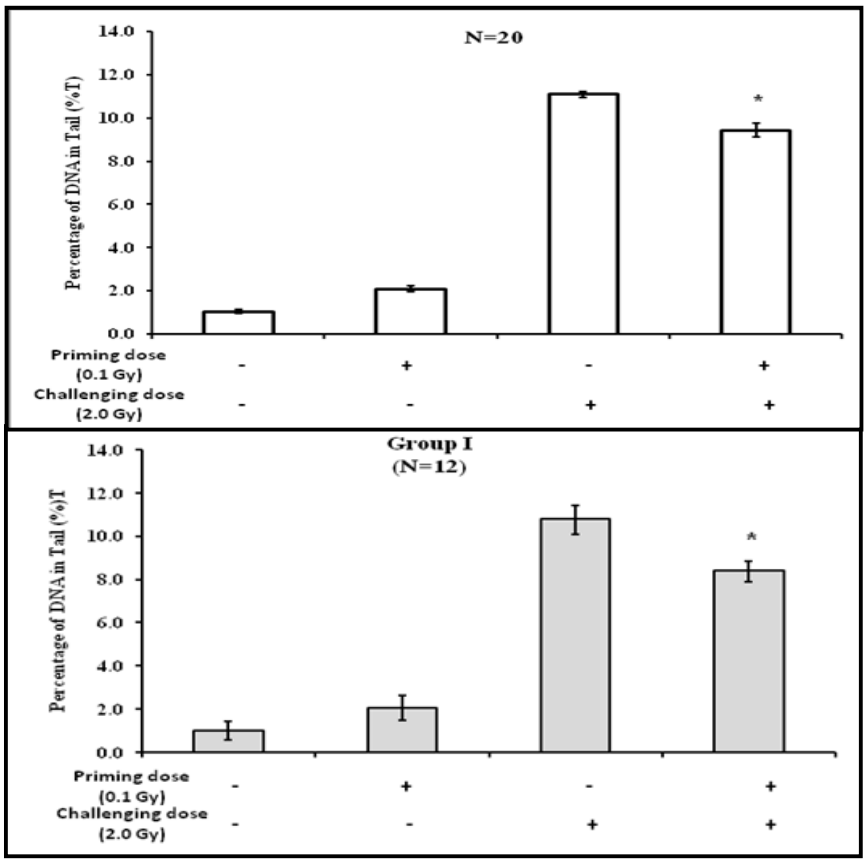

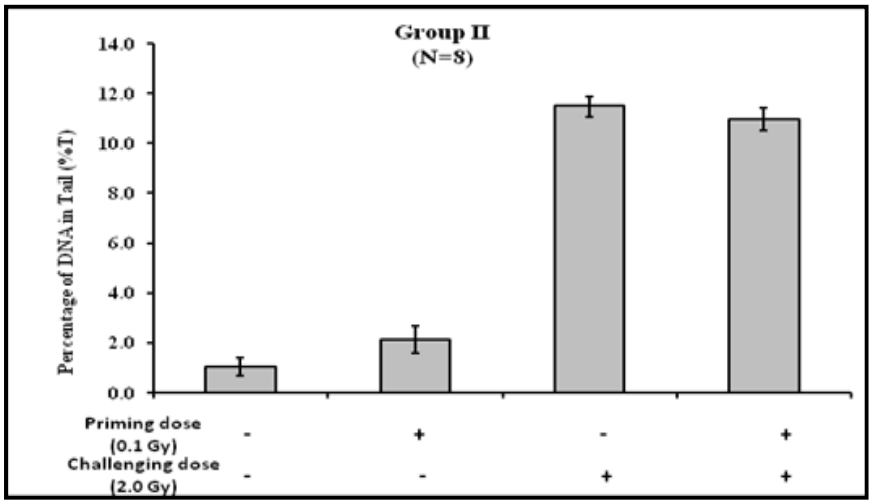

Fig. 5: Mean percentage of DNA in tail (%T) in PBMCs exposed to a priming dose of 0.1 Gy followed by a challenging dose of 2.0 Gy after 4 h post irradiation.

At 1.0 Gy, the mean percentage of DNA in tail was approximately 7.5% and approximately, 50% of DNA in tail was repaired at 30 min. At 2.0 Gy, percentage of DNA in the tail was approximately 11%, whereas approximately 50% of DNA in tail was repaired at 60 min. The residual damage at both the doses after 240 min was in the range of ~10-30 %.Transcription profile of BER genes was studied in PBMCs exposed to 1.0 Gy and 2.0 Gy at different time intervals up to 240 min for 20 individuals. Short patch BER genes such as *OGG1, NTH1, NEIL1* and *XRCC1* showed no change in expression with post irradiation time points whereas *LIGASE3* showed an increase in expression at 1.0 Gy and 2.0 Gy up to 240 min. Regulatory BER genes such as *APE1* and *PARP1* showed no change in expression with time. Similarly, long patch genes such as *PCNA, MUTYH* and *FEN1* showed no significant change in expression up to 240 min at both the doses. At 1.0 Gy and 2.0 Gy, *MBD4* and *LIGASE1* showed a significant increase ($p \leq 0.05$) in expression up to 240 min.

Protein expression profile was studied for BER proteins at 1.0 Gy and 2.0 Gy with various time intervals up to 240 min. At 1.0 Gy, OGG1 showed an increase in protein expression upto 60 min. XRCC1 showed increased expression only at 240 min for 1.0 Gy and 2.0 Gy (~2.7 fold). At 1.0 Gy, LIGASE3 showed no change in protein expression, while increase in expression upto 240 min was observed at 2.0 Gy (2.0 to 2.5 fold). APE1 showed increased expression with time (2.3 to 3.0 fold at 1.0 Gy and 2.0 Gy), whereas PARP1 showed an increase in protein expression upto 60 min at 1.0 Gy and 2.0 Gy. However, MUTYH showed no change in expression both at 1.0 and 2.0 Gy. At 1.0 Gy, MBD4 and LIGASE1 showed an increased expression upto 60 min, whereas PCNA and FEN1 showed increased protein expression at 120 min and 240 min. At 2.0 Gy, MBD4, PCNA and FEN1 showed no change in expression, whereas LIGASE1 showed an increase in expression upto 240 min.

Radio-adaptive response study at the level of DNA damage, transcript and protein expression

Adaptive response study was carried out in PBMCs of twenty individuals and end points such as DNA damage, gene and protein expression were studied. DNA damage quantitation in terms of DNA damage in tail (%T) was carried out in PBMCs exposed to a priming dose of 0.1 Gy followed by challenging dose of 2.0 Gy after 4h (Figure 5).

A significant reduction ($p \leq 0.05$) was observed in % T among the individuals studied. The mean %T was 11.07 % at 2.0 Gy, which was reduced to 9.42 % in samples receiving a priming dose of 0.1 Gy followed by a challenging dose of 2.0 Gy after 4 h. Further stratification of samples into two groups revealed that twelve individuals (Group I) were showing a significant reduction ($p \leq 0.05$) in the mean %T. Among these individuals the mean %T was 10.78 % at 2.0 Gy, which was reduced to 8.39 % in primed cells. However, eight individuals (Group II) showed marginal reduction in mean %T. Among these individuals, the mean %T was 11.49 % at 2.0 Gy, which was reduced to to 10.97 % in primed cells.

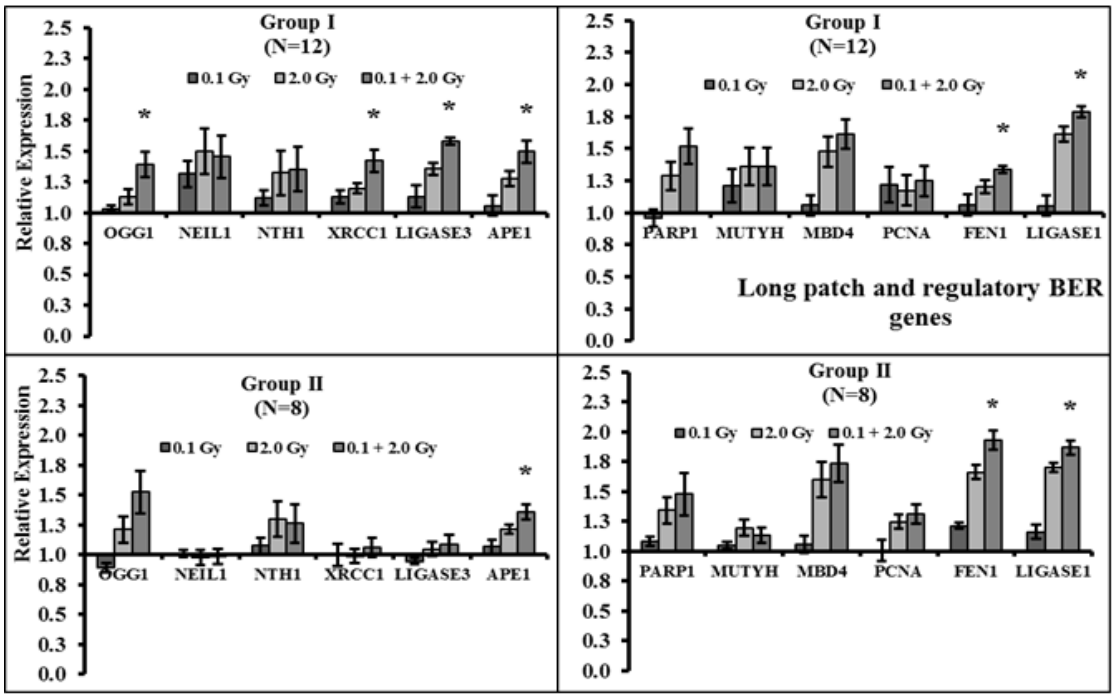

Fig. 6 Transcription profile of BER genes in Group I (N=12) and Group II (N=8) individuals in primed and non-primed PBMCs.

The relative expression of twelve BER genes was also studied in both the groups (Group I and Group II) as shown in figure 6. Group I individuals revealed that *OGG1*, *XRCC1*, *LIGASE3*, *APE1*, *FEN1* and *LIGASE1* showed a significant increase in expression in primed cells as compared to 0.1 Gy or 2.0 Gy (non-primed) alone.

However, no significant increase was observed for *NEIL1, NTH1, PARP1, MUTYH, MBD4* and *PCNA* in primed and non-primed cells. *APE1, FEN1* and *LIGASE1* showed significant increase in expression in primed cells as compared to 0.1 Gy and 2.0 Gy (non-primed) in both the groups. In Group I, the protein expression profile of OGG1, XRCC1, APE1 and LIGASE3 was significantly ($p \leq 0.05$) increased in primed cells as compared to control (un-irradiated), 0.1 Gy and non-primed cells. Similarly, long patch BER protein such as MBD4, FEN1 and LIGASE1 showed a significant increase in protein expression in primed cells as compared to 0.1 Gy, 2.0 Gy (non-primed cells) and un-irradiated control. However, no change in protein expression was observed for NTH1, NEIL1, PARP1, MUTYH and PCNA in this group. In Group II, OGG1, APE1, MBD4, FEN1 and LIGASE1showed significantly increased ($p \leq 0.05$) upregulation in primed cells as compared to 0.1 Gy, 2.0 Gy (non-primed cells) and un-irradiated control. No significant change was observed for proteins such as NTH1, NEIL1, XRCC1, LIGASE3, PARP1, MUTYH and PCNA in primed cells as compared to 0.1 Gy, 2.0 Gy (non-primed cells) and un-irradiated control. Interestingly, LIGASE3 showed significant ($p \leq 0.05$) reduction in expression in primed cells as compared to 0.1 Gy, 2.0 Gy (non-primed cells) and un-irradiated control. The protein expression profile at 2.0 Gy was observed to be significantly increased for MBD4 and FEN1 as compared to 0.1 Gy and 2.0 Gy. In summary, the protein expression profile of OGG1, APE1, MBD4, FEN1 and LIGASE1 showed significantly increased expression in primed cells in both the group of individuals (Group I and Group II) (figure 7).

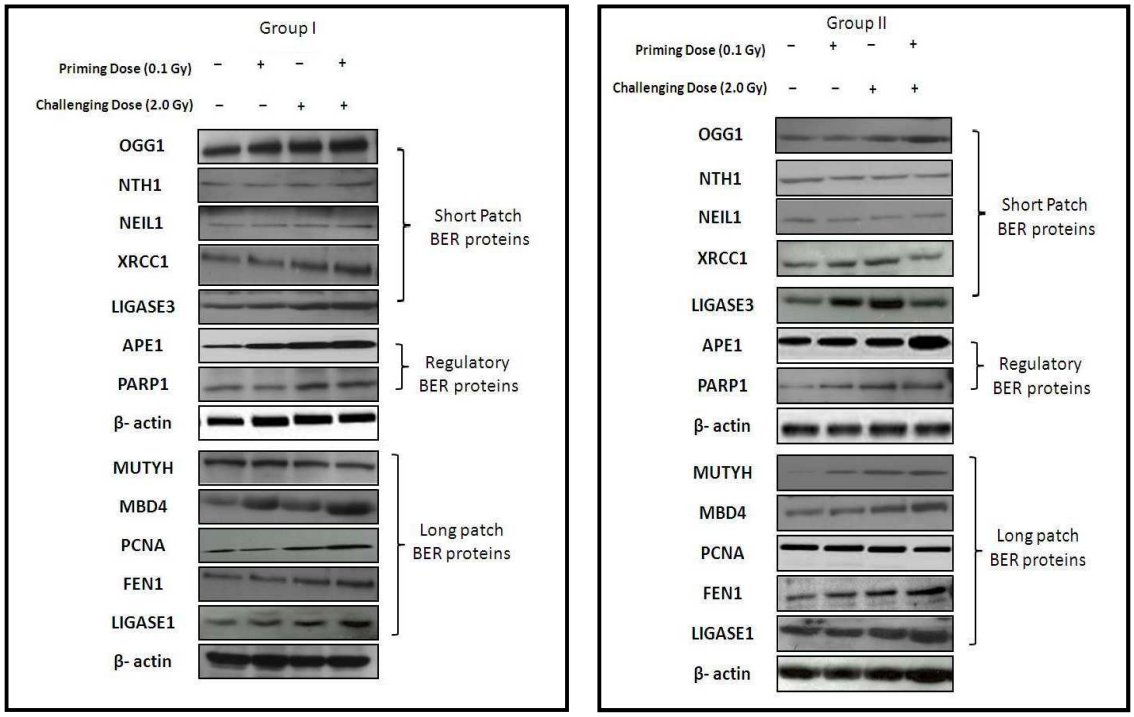

Fig.7: Representative Western blot images showing expression profile of BER proteins in PBMCs irradiated at various doses (0.1, 0.3, 0.6, 1.0 and 2.0 Gy) along with control in Group I and Group II individuals

Discussion

Understanding the DNA repair mechanisms at low and moderate doses of IR exposures has immense implications to human health. RAR maintains the genetic integrity by protecting the cells from adverse effects of radiation exposure. However this phenomenon is highly variable depending upon the time, type of tissue or cells and the amount of exposure. RAR studies have been conducted in several biological systems *in vitro* and vary with the stage of the cell cycle at which the cells are irradiated. RAR is not instantaneous after a low dose exposure but requires about 4–6 h to develop full activity against a challenging dose exposure. Complexity of RAR in eukaryotic cells depends on time schedule, dose, cell type, experimental condition, priming dose, cell cycle, physiological status of the donor and inter individual variation. One of the observations in RAR is individual variation towards radio-sensitivity. Induction of DNA repair resulting in an adaptive response is only visible through a narrow window of dose. There is lack of information in human PBMCs at G0/G1 regarding the involvement of specific genes and proteins in RAR, although the role of non-homologous end joining (NHEJ) and Nucleotide Excision Repair (NER) pathway has been reported (30-32).In present study, we have observed a dose dependent increase in percentage of DNA in tail (%T) between 0.3 to 2.0 Gy. Repair kinetics study at 1.0 Gy and 2.0 Gy clearly indicated both fast and slow repair kinetics of DNA strand breaks and revealed that approximately 50 % of damaged DNA was repaired at 30 min and 60 min for 1.0 Gy and 2.0 Gy respectively. Inter-individual variation was observed with no distinct pattern.

IR induced DNA Damage Response (DDR) also lead to alteration of gene expression profile in human cells (34,36). Our results showed dose and time dependent transcriptional changes of BER genes such as *MBD4, LIGASE1* and *LIGASE3*. *MBD4* is involved in DNA demethylation, wherein the degree of differential methylation varies with radiation dose and time. Significant up regulation of MBD4 at the level of transcription and protein expression with radiation dose and time points studied is supportive of the above facts. Similarly, significant up regulation of *LIGASE1* (long patch BER) and *LIGASE3* (short patch BER) with respect to dose and time points studied indicated both short and long patch BER pathways are active in resting PBMCs exposed to gamma radiation.

PCNA and MUTYH did not show any change in expression at transcript and protein level across all the doses studied. However, regulatory BER proteins such as APE1 and PARP1 showed significantly increased expression profile up to 4 h indicating their role in activating SSBs repair and recognition of BER components. Interestingly, we have observed that short patch BER proteins such OGG1, XRCC1 and LIGASE3 showed significant up regulation at lower doses up to 0.6 Gy, while long patch BER proteins such as MBD4, FEN1 and LIGASE1 were significantly up regulated at higher doses studied ($\geq$ 1.0 Gy). The possible explanation could be lower induction of DNA damage favours short patch BER pathway to be more active as complex lesions are comparatively less at low doses exposures $\leq$ 0.6 Gy. At the same time, increased

expression of long patch BER protein at doses ≥1.0 Gy, perhaps indicating that lesions are more complex thus activating induction of increased fold of expression of long patch BER proteins.

Adaptive response study was carried out in resting human PBMCs exposed to gamma radiation at a priming dose of 0.1 Gy followed by challenging dose of 2.0 Gy at 4h post irradiation and different endpoints such as DNA damage, the expression of BER genes and proteins were studied. Interestingly, variation in DNA damage among the twenty individuals was observed. Individuals belonging to Group I (N=12) showed significant reduction of DNA damage (%T) whereas individuals belonging to Group II (N=8) showed marginal reduction in DNA damage (%T) though not significant. At transcript level, Group I individuals showed significant up regulation of short patch BER genes (*XRCC1* and *LIGASE3)* in primed cells, whereas no significant change was observed in Group II individuals. This is a major difference between Group I and Group II individuals at transcript level. At transcript level, long patch BER genes have not shown distinct differences between the two groups. At protein level, short patch BER proteins (OGG1, XRCC1 and LIGASE3) and regulatory protein (APE1) showed significantly increased protein expression in primed cells of Group I individuals. Among Group II individuals, only APE1 showed increased protein expression profile.Another interesting observation at protein level is that short patch repair proteins showing significant adaptive response among Group I individuals. At the same time, Group II individuals showed increased expression of most of the long patch repair proteins including LIGASE1, suggesting the role of long patch repair proteins in RAR observed in Group II individuals.

Conclusion

In conclusion, the present study demonstrated active role of BER genes and proteins in radio-adaptive response in human PBMCs at G_0/G_1. The dose at which short-patch and long-patch repair pathway gets activated is an important finding in this study which needs to be further investigated in cellular extracts and stimulated lymphocytes. It would be very interesting to extend further research with chronic doses of radiation. The extent of RAR in humans not only depends on dose or dose rate but even on the heterogeneity among the individuals exhibiting this response, which remains still unresolved. A deeper understanding of the radio-adaptive response and the interplay of all the repair pathways such as BER, NHEJ and NER is needed before estimating risk of low dose of IR for humans.

Acknowledgements

The authors wish to thank the volunteers who have participated in the study. We are thankful to the volunteers who have participated in the study. We profusely thank Ms Prabhu J. A. and Mr Sangram Kamble for helping us in collecting the blood samples from BARC dispensary, Trombay, Mumbai. We thank Mr. Sanjay Shinde and Mr.

Manjoor Ali for assisting in irradiation of samples. The fellowship of Ms. Sneh Toprani from Department of Atomic energy is highly acknowledged.

References

[1] Jaikrishan G, Sudheer KR, Andrews VJ, Koya PKM, Madhusoodhanan M ,Jagadeesan CK and Seshadri M. 2013. Study of stillbirth and major congenital anomaly among newborns in the high-level natural radiation areas of Kerala, India, J. Community Genet., **4** : 21–31.

[2] Tao Z, Y. Zha, S. Akiba, Q. Sun, J. Zou, J. Li, Y. Liu, H. Kato, T. Sugahara, L. Wei, Cancer mortality in the high background radiation areas of Yangjiang, China during the period between1979 and 1995, J. Radiat Res, 41 Suppl: 31-41.

[3] Nair RRK, Rajan B, Akiba S, Jayalekshmi P, Nair MK, Gangadharan P, Koga H, Morishima T, Nakamura S and Sugahara T. 2009. Background radiation and cancer incidence in Kerala, India – Karunagapally cohort study. Health Phys., 96: 55–66.

[4] Morgan WF, W.J. Blair WJ. 2013. Issues in low dose radiation biology: the controversy continues. A perspective, Radiat Res, 179 : 501-510.

[5] Wolff S, Afzal V, Jostes R. and Wiencke J. 1993. Indications of repair of radon-induced chromosome damage in human lymphocytes: an adaptive response induced by low doses of X-rays. Environ. Health Perspect.,101: 73–77.

[6] Shadley J. 1994. Chromosomal adaptive response in human lymphocytes.Radiat. Res., 138 : S9–S12.

[7] Wojcik A and Streffer C. 1994. Adaptive response to ionizing radiationin mammalian cells: a review. BiolZentralbl., 113: 417–434.

[8] Wolff S. 1998. The adaptive response in radiobiology: evolving insightsand implications. Environ. Health Perspect., 106 : 277–283.

[9] Mitchel REJ. 2006. Low doses of radiation are protective in vitro andin vivo: evolutionary origins. Dose Response, 4 : 75–90.

[10] United Nations Scientific Committee on the Effects of Atomic Radiation, 2000.Report to the General Assembly, With Annexes. United Nations Sales PublicationE.00.IX.3. United Nations, New York.

[11] Lomax M, Folkes L and O'Neill P. 2013. Biological consequences ofradiation-induced DNA damage: relevance to radiotherapy. Clin. Oncol., 25 : 578–585.

[12] Sancar A, Lindsey-Boltz A, Unsal-Kacmaz K and Linn S. 2004. Molecular mechanisms of mammalian DNA repair and the DNA damagecheckpoints. Annu. Rev. Biochem., 73 : 39–85.

[13] Lindahl T. 1993.Instability and decay of the primary structure of DNA.Nature, 362 : 709–715.

[14] Abraham R .2001. Cell cycle checkpoint signaling through the ATM andATR kinases. Genes Dev., 15 : 2177–2196.

[15] Schonthal A. 2004. Checkpoint Controls and Cancer, Vol. 280. HumanaPress Inc., Totowa, New Jersey, USA.

[16] Watson J, Baker T, Bell S, Gann A, Levine M and Losick R. 2004. Molecular Biology of the Gene, 5th edn. CSHL Press, New York, USA.

[17] Wilson D, III and Bohr V. 2007. The mechanics of base excision repair,and its relationship to aging and disease. DNA Repair (Amst.), 6 : 544–559.

[18] Izumi T, Wiederhold LR, Roy G, Roy R, Jaiswal A, Bhakat KK, Mitra S and Hazra TK. 2003. Mammalian DNA base excision repairproteins: their interactions and role in repair of oxidative DNA damage.Toxicology, 193 : 43–65.

[19] David S, O'Shea V and Kundu S. 2007. Base-excision repair of oxidativeDNA damage. Nature, 447 : 1038.

[20] Cunningham R.1997. DNA glycosylases. Mutat. Res., 383: 189–196.

[21] Lindahl T, Karran P and Wood R. 1997. DNA excision repair pathways.Curr. Opin. Genet. Dev., 7 : 158–169.

[22] Wood, R. 1996. DNA repair in eukaryotes. Annu. Rev. Biochem., 65: 135–167.

[23] Singer B and Hang B. 1997. What structural features determine repairenzyme specificity and mechanism in chemically modified DNA? Chem.Res. Toxicol., 10 : 713–732.

[24] Sheila D, O'Shea VL and Kundu S. 2007. Base-excision repair of oxidativeDNA damage. Nature, 447 : 941–950.

[25] Dianov G . 2011. Base excision repair targets for cancer therapy. Am.J. Cancer Res., 1 : 845–851.

[26] Seeberg E, Eide L and Bjoras M. 1995. The base excision repair pathway.Trends Biochem. Sci., 20 : 391–397.

[27] Maynard S, Schurman SH, Harboe C, de Souza-Pinto NC and Bohr VA. 2009. Base excision repair of oxidative DNA damage and associationwith cancer and aging. Carcinogenesis, 30 : 2–10.

[28] Parsons J. 2005. Poly (ADP-ribose) polymerase-1 protects excessiveDNA strand breaks from deterioration during repair in human cell extracts. Febs J., 272 : 2012–2021.

[29] Olivieri G, Bodycote J, Wolff S. 1984. Adaptive response of human lymphocytes tolow concentrations of radioactive thymidine, Science, 223 : 594–597.

[30] Shelke S and Das Birajalaxmi. 2015. Dose response and adaptive response of non-homologous end joining repair genes and proteins in resting human peripheral blood mononuclear cells exposed to γ radiation. Mutagenesis. 30 (3) : 365-379.

[31] Klammer H, Kadhim M and Iliakis G. 2010. Evidence of an adaptive response targeting DNA nonhomologous end joining and its transmission to bystander cells. Cancer Res., 70 : 8498–8506.

[32] Hafer K, Iwamoto KS, Iwamoto KK, Scuric Z and Schiest RH. 2007. Adaptive response to gamma radiation in mammalian cells proficient and deficient in components of nucleotide excision repair. Radiat.Res., 168 : 168–174.

[33] Toprani SM and Das B. 2015. Role of base excision repair genes and proteins in gamma irradiated resting human peripheral blood mononuclear cells. Mutagenesis. 30 (2): 247-61.

[34]Toprani SM and Das B. 2015. Radio-adaptive response of base excision repair genes and proteins in human peripheral blood mononuclear cells exposed to gamma radiation. Mutagenesis, 30 : 663–676.

[35] Jain V, Das B, and Seshadri M. 2011. Transcriptional expression of H2B, CTP synthase and PLK3 genes in whole blood exposed to ^{60}Co gamma radiation. International Journal of Low Radiation, 8 (1): 55-65.

[36] Saini D, Shelke S, Vannan A, Toprani S, Jain V, Das B, and Seshadri M. 2012. Transcription profile of DNA damage response genes at G_0 lymphocytes exposed to gamma radiation. Molecular and Cellular Biochemistry, 364: 271–281.

BARC NEWSLETTER
FOUNDER'S DAY SPECIAL ISSUE 2015

PARA ENCODED ON CHROMOSOME II OF DEINOCOCCUS RADIODURANS INVOLVES IN CELL DIVISION REGULATION THROUGH NUCLEOID OCCLUSION MECHANISM

Kruti Mehta-Modi and H.S. Misra
Molecular Biology Division

This paper received the A. Krishnamurthy Award at the Meeting of the Society of Biological Chemists, India, (SBCI) Bhubaneswar, Dec. 18-21, 2014

Abstract

Deinococcus radiodurans is a multipartite genome containing bacteria known for its extreme tolerance to DNA damaging agents. This bacterium when exposed to such agents it undergoes a cell cycle arrest during which it repairs its genome. The regulation of this arrest with respect to chromosome segregation and cell division is worth investigating. We have been actively involved in understanding the basic process of cell division and chromosome segregation and their role in bacterial response to DNA damage. In this work, we characterized an actin-like genome partitioning protein encoded on secondary chromosome II (named it ParA2) for its role in cognate chromosome maintenance in D. radiodurans. We observed that ParA2 in the absence or with lower stiochiometric ratio of its cognate partner ParB2 play a regulatory role in cell division through a process very similar to nucleoid occlusion. When ParB2 was provided in trans it presumably resumed its normal function and its inhibition of cell division was not observed. These results suggest a conditional regulatory role of ParA2 in cell division depending upon its need in ParB2 mediated genome maintenance in D. radiodurans.

Introduction

An accurate duplication and transmission of genetic information is a fundamental attribute of the life and that determines the successful inheritance of different phenotypes into daughter cells. In bacteria, the genome partitioning occurs mainly by pushing or pulling of duplicated genome toward the cell poles [1]. This involves three core components like *cis*-element that functions like centormere in bacteria, a centromere binding protein and an actin homologue of bacterial ATPase. *Deinococcus radiodurans* R1 is a Gram positive bacterium that shows extraordinary tolerance to different DNA damaging agents [2]. This bacterium also has peculiar cytogenetic features. It has multipartite genome system comprise of chromosome I (ChrI), chromosome II (ChrII) and plasmids [3]. Each of these genome elements is present in multiple copies. Genome of this bacterium encodes putative ParA and ParB types proteins located on each of the four genome elements. The *cis* elements are not known in the genome of this bacterium. Understanding the function of 'Par' proteins would be a step forward in knowing the mechanism(s) of chromosome segregation in this bacterium harboring complex genome. Recently, chromosome I partitioning system has been characterized [4] and cell division proteins like FtsZ and FtsA have been characterized in vivo and in vitro [5,6]. The work received this award was on characterization of ParA2 and parB2 roles in chromosome II partitioning during cell division.

ParA2 is characterized as a DNA binding ATPase

Multiple sequence alignment of ParA2 with other ParA-type proteins using CLUSTAL X program showed that ParA2 contains the typical A, A′ and B components of Walker motifs that are found in P-loop ATPases. Unusually, it was found that ParA2 is missing one of the largely conserved lysine at the beginning of the Walker A motif, which was also conserved in ParA encoded on chromosome I of D. radiodurans. Phylogenetic analysis indicated that ParA2 is evolutionarily different from other chromosomal type ParAs including ParA1 of *D. radiodurans* and it was placed between chromosomal type ParAs and other small ATPases involved in regulation of bacterial cell division. Recombinant ParA2 was purified and its identity was further confirmed by mass spectrometry.

The purified ParA2 showed both DNA binding (Fig. 1a) and ATPase activities (Fig.1b). The DNA binding efficiency of ParA2 increased further in the presence of ATP, and its ATPase activity was stimulated with DNA. These results suggested that ParA2 is evolutionarily different from other bacterial ParAs and is a DNA-binding ATPase.

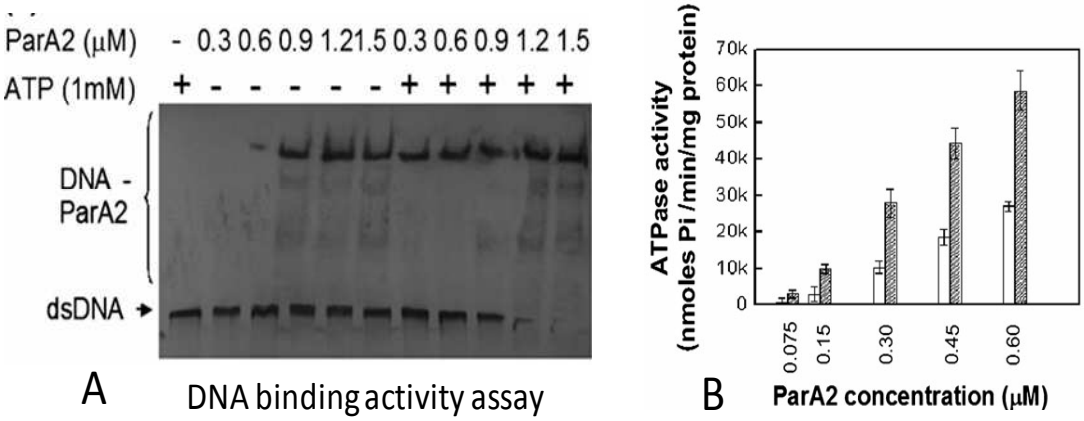

Fig. 1: ParA2 activity characterization. Purified recombinant ParA2 was checked for DNA binding activity (A) in the presence and absence of ATP. Similarly, its ATPase activity was measured with increasing concentration of protein (B)

ParA2 localizes on nucleoid and causes cell elongation

ParA2-CFP was expressed in E. coli AB1157 on pA2CFP plasmid and cells were examined under fluorescence microscope. Results showed cell elongation and localization of multiple spots of ParA2-CFP on false blue coloured DAPI-stained nucleoid spread throughout the cell (Fig 2). Effect of ParA2 on growth and cell division was monitored in *E. coli*. Transgenic *E. coli* expressing ParA2 showed a significant reduction in colony forming units (CFU) as compared to untransformed cells and the cells expressing ParA1on multicopy plasmid [4]. Nearly no effect in optical density at 600 nm while several-fold decrease in CFU in the cells expressing ParA2 could be attributed to the continued increase in cell volume but inhibition of the cytokinesis.

These results indicated that ParA2 co-localizes with nucleoid in *E. coli* and is most likely affecting cell division in *E. coli*. Since, FtsZ is key player in bacterial cell division, the possibility of ParA2 overexpression making FtsZ inefficient was hypothesized. However, we observed that FtsZ expressing on plasmid did not rescue the ParA2 effect in ParA2 over-expressing *E. coli* cells and recombinant FtsZ activity was not affected by ParA2 in vitro. These results suggested that the increase in cell length and decrease in CFU per mL of cells expressing ParA2 seems to be due to ParA2 effect on cell division in *E. coli* and its direct effect on FtsZ function is less supported.

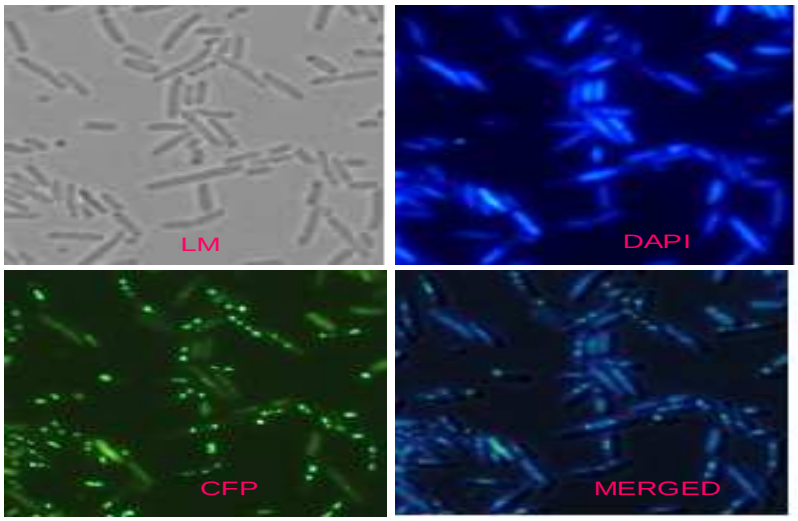

Fig.2: Cellular localization of ParA2 in transgenic *Escherichia coli*. The *E. coli* cells expressing ParA2 –CFP fusion was observed under fluorescence microscope using normal mode (LM), excited for DAPI emission (DAPI) and fluorescence protein (CFP). These images were merged (Merged) to find out if green fluorescent ParA2-CFP is localized on DAPI stained nucleoid

ParA2 complemented known nucleoid occlusion function in *E. coli*

Binding of ParA2 with nucleoid and its effect on inhibition of cell division are the functions known also for nucleoid occlusion proteins such as SlmA in E. coli [7] and 'Noc' in Bacillus subtilis [8]. These proteins are known to inhibit cell division by bringing nucleoid occlusion to the vicinity of FtsZ ring formation. Therefore, the possibility of ParA2 inhibiting cell division either by nucleoid occlusion or by affecting DNA replication and genome segregation could be hypothesized. ParA2 was expressed in E. coli strain TB85 (ΔslmA) and E. coli strain TB86 (ΔminCDEΔslmA) cells, and the effect of ParA2 on growth characteristics of these mutants were examined. The slmA mutant expressing ParA2 grew similar to mutant control, while ParA2 could help slmAminCDE double mutant to recover its growth defect in rich medium (Fig. 3) and produce asymmetric cell division generating high frequency of minicells. Double mutants expressing ParA2 produced 19.24±2.12% minicells as against 5.12±1.26% in control without ParA2. Asymmetric cell division has been observed in *E. coli* cells lacking MinCDE system.

This indicated that ParA2 expression could make slmAminCDE double mutants similar to min CDE single mutants, implying the complementation of Slm A loss in the double mutant. These results may, therefore, suggest that ParA2 effect on cell division is most likely by affecting genome compaction, a process integral to nucleoid occlusion mechanisms operated by two distinctly different proteins SlmA in *E. coli* and 'Noc' in *B. subtilis*.'

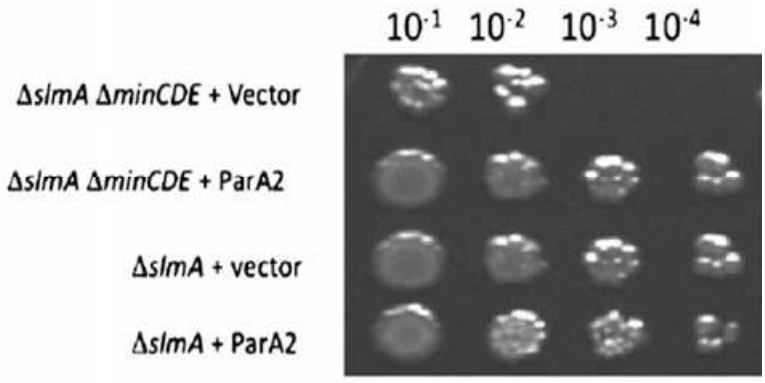

Fig 3: Functional complementation of SlmA (a nuceloid occlusion protein) loss by ParA2 in *E. coli*. ParA2 was expressed in trans into slmA mutant (ΔsmlA+ParA2) and slmAminCDE mutant (ΔslmAΔminCDE +ParA2) and growth characteristic was compared with these mutants harboring vector as control

E. coli expressing ParA2 showed cell elongation which was not observed when either ParA1 was expressed or cells harbor vector as control. This indicated the functional difference of ParA2 from ParA1 and seems to specific effect of ParA2.This was probed further and observed that ParA2 localized on nucleoid and able to interact nonspecifically with DNA *in vitro*. The mechanism underlying cell division inhibition by ParA2 was investigated and observed that ParA2 could rescue the growth defect in *minCDEslmA* double mutant and thereby produced a phenotype that was specific to minCDE system implying that ParA2 could complement double mutant for *slm*A phenotype but not minCDE phenotype. Thus in conclusion, ParA2 is a DNA binding protein which might play an indirect role in spatial regulation of FtsZ function in *D. radiodurans.*

References

[1] Adams, D.W. and Errington, J. "Bacterial cell division: assembly, maintenance and disassembly of the Z ring". *Nature Reviews in Microbiology* 7 (2009):642–653.

[2] Misra, H. S. Rajpurohit, Y. S. and Kota, S. "Physiological and molecular basis of extreme radioresistance in *Deinococcus radiodurans*". *Current Science* 104 (2013):194-205.

[3] White, O., Eisen, J.A., Heidelberg, J.F., Hickey, E.K., Peterson, J.D., Dodson, R.J., et al. "Genome sequence of the radioresistant bacterium *Deinococcus radiodurans* R1". *Science* 286(1999):1571–1577.

[4] Charaka, V, K. and Misra, H.S. "Functional characterization of the role of the chromosome I partitioning system in genome segregation in *Deinococcus radiodurans*". *Journal of Bacteriology* 194 (2012):5739-5748.

[5] Modi, K.M. Tewari, R. and Misra, H.S. "FtsZDr, a tubulin homologue in radioresistant bacterium *Deinococcus radiodurans* is characterized as a GTPase exhibiting polymerization/depolymerisation dynamics in vitro and FtsZ ring formation in vivo". *International Journal of Biochemistry and Cell Biology* 50 (2014):38-46.

[6] Modi, K. and Misra, H.S. Dr-FtsA, an actin homologue in *Deinococcus radiodurans* differentially affects Dr-FtsZ and Ec-FtsZ functions in vitro. *PLoS One* 9 (2014):e115918.

[7] Bernhardt, T.G. and de Boer, P.A. "SlmA, a nucleoid-associated, FtsZ binding protein required for blocking septal ring assembly over chromosomes in *E. coli*". Molecular Cell 18 (2005): 555–564.

[8] Wu, L.J. and Errington, J. "Coordination of cell division and chromosome segregation by a nucleoid occlusion protein in *Bacillus subtilis*". *Cell* 117 (2004) : 915–925.

BARC NEWSLETTER
FOUNDER'S DAY SPECIAL ISSUE 2015

INFLUENCE OF LANTHANUM SITE DEFICIENCY ON PHASE STABILITY AND ELECTRICAL CONDUCTIVITY OF $(LA_{0.75}SR_{0.25})_{1-X}CR_{0.5}MN_{0.5}O_{3-\Lambda}$ IN AIR AND HYDROGEN ATMOSPHERE

Jyothi Sharma[a], T.Mahata[a], R.C. Hubli[b], P.K. Patro[a], R.K. Lenka[a], Deep Prakash[a], P.K. Sinha[a]
[a]Powder Metallurgy Division, [b]Materials Processing Division

This paper received the Best Poster Presentation Award at the DAE-BRNS 5th Interdisciplinary Symposium on Materials Chemistry (ISMC-2014), Mumbai, Dec.9-13, 2014

Abstract

A-site-deficient LSCM perovskite oxides of compositions $(La_{0.75}Sr_{0.25})_{1-x}Cr_{0.5}Mn_{0.5}O_{3-\delta}$(x=0.0, 0.05, 0.10), were prepared by gel combustion method, employing citric acid as complexing agent and fuel. The calcined (900°C) LSCM powders were predominantly composed of perovskite phase for all the three compositions. Low intensity peaks of secondary phase(s) were observed in the XRD patterns of calcined powders. However, these phases disappeared on sintering and the sintered LSCM samples consisted of single perovskite phase. The perovskite phase purity is retained in the sintered samples even after treatment in hydrogen atmosphere at 900°C. The electronic conductivity decreases with increasing A-site deficiency in oxidizing atmosphere in the lower temperature range. Above 750°C the electrical conductivity of La-site deficient (x = 0.05) LSCM was found to be more than stoichiometric LSCM composition. The conductivity of LSCM in reducing atmosphere is about two orders of magnitude lower than that in oxidizing atmosphere. Also the conductivity decreases significantly with increase in La-site deficiency. The results have been analyzed through defect chemical relationships.

Keywords: LSCM, Combustion Synthesis, Phase stability, Electrical Conductivity, Defect Chemistry

Introduction

Perovskite structured alkaline earth metal doped lanthanum manganite ($LaMnO_3$) and lanthanum chromite ($LaCrO_3$) have been reported to be used as cathode and interconnect material in solid oxide fuel cellrespectively [1-4]. Alkaline earth metal doping in A-site of the perovskite structure leads to increase in electrical conductivity. Sr-doped $LaMnO_3$ (LSM), a state of art cathode material, has high electrical conductivity but is not stable in reducing atmosphere. On the other hand, Sr-doped $LaCrO_3$ (LSC) has high stability in reducing environment but has moderate electrical conductivity. In tubular design of SOFC operating at higher temperature the most commonly used interconnects are $LaCrO_3$ based ceramics. Partial substitution of chromium by manganese in LSC increases the electrical conductivity. Manganese substituted LSC of composition $La_{0.75}Sr_{0.25}Cr_{0.5}Mn_{0.5}O_{3-\delta}$ (LSCM) has been reported to be used in solid oxide fuel cell as both cathode and anode material because of its stability in both oxidizing and reducing atmospheres [5,6]. LSCM can be considered as a solid solution of

$La_{1-x}Sr_xMnO_3$ (LSM) and $La_{1-x}Sr_xCrO_3$ (LSC). Sinterability of LSCM is reported to be better compared to LSC and therefore use of LSCM can be advantageous in fabrication of cells.

For long term use of LSCM as a SOFC component (either cathode, anode or interconnect) compatibility with other cell components is an important aspect. In YSZ electrolyte based SOFC it is likely that LSCM will be in contact with YSZ. In case of LSM, a common cathode material with YSZ electrolyte, formation of electrically resistive phases like La_2ZrO_7 and Sr_2ZrO_7 has been reported [7,8]. Lanthanum site deficiency has been reported to be useful to avoid formation of zirconates. Thus it will be of technical importance to study the effect of A-site deficiency on electrical conductivity and phase stability of $(La_{0.75}Sr_{0.25})_{1-x}Cr_{0.5}Mn_{0.5}O_{3-\delta}$. In the present study, LSCM powders with different extent of A-site deficiency have been synthesized via gel combustion method using citric acid as chelating agent. These compositions were investigated for their phase stability and electrical properties in both oxidizing and reducing atmosphere.

Experimental

LSCM perovskite oxides with A-site deficiency were prepared by gel combustion method, employing citric acid as complexing agent and fuel [9,10]. The starting materials for the synthesis of LSCM were lanthanum nitrate [$La(NO_3)_3 \cdot 6H_2O$, purity: 99.9%], strontium nitrate [$Sr(NO_3)_2$, purity 99.99%], chromium nitrate [$Cr(NO_3)_3 \cdot 9H_2O$, purity: 99.99%] and manganese acetate[$Mn(CH_3COO)_2.4H_2O$, purity 99.99%].Stock solutions (1M) of the above salts were prepared and mixed in required molar ratio for the preparation of LSCM of different compositions. Citric acid was added to the mixed solution in a ratio of 0.708 mole per mole of LSCM. The resulting solution was dehydrated slowly on a hot plate forming viscous gel which subsequently formed a solid foamy product. On continuation of heating, spontaneous combustion took place within the foamy product.The combustion synthesized powders were finally calcined in air at 900^{o}C, 3h to remove the residual carbonaceous matter.

X-ray diffraction (XRD) patterns of the calcined powder were recorded using an X-Ray diffractometer (INEL, France) withCuK_α radiation from 20-80^{o}C. The calcined powder was de-agglomerated by wet milling in a planetary ball mill. The milled powders were uniaxially pressed at 150 MPa pressure to form pellets (15 mm dia. x ~1.5 mm ht.) and bar shaped specimens (20mm L × 5mm W × 5mm H). Sintering of the green compacts was carried out at 1350^{o}C, 3h in static air. X-ray diffraction (XRD) patterns of the sintered samples were recorded. Green pellets as well as sintered pellets were fired in flowing humidified (3 wt% H_2O) hydrogen gas for 3h. XRD patterns of these samples were recorded after exposure in hydrogen atmosphere.

Four probe dc technique was used to measure the conductivity of the rectangular bar shaped sintered samples. The setup for electrical conductivity measurement is shown in Fig. 1. Electrical measurements were taken in oxidizing (air) environments while heating in the temperature range from 650 to 900^{o}C. At 900^{o}C the environment was changed from oxidizing to reducing atmosphere by flowing argon gas initially for 10 minutes and subsequently flowing humidified (3 wt% H_2O) hydrogen gas. The samples were held in reducing environment for 3h and thereafter electrical measurements were taken during cooling in the temperature range 900 – 650^{o}C. The electrical conductivity data were taken at every 50^{o}C interval after holding for more than 20 min at each temperature to equilibrate thermally until no significant change in measured value was observed.

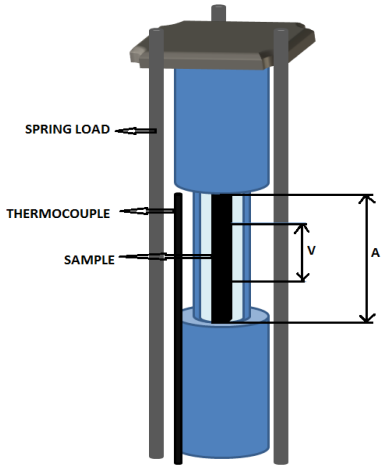

Fig. 1: Setup for electrical conductivity measurement

Results and Discussion

Phase stability of calcined LSCM powders

The XRD patterns of combustion synthesized $(La_{0.75}Sr_{0.25})_{1-x}Cr_{0.5}Mn_{0.5}O_{3-\delta}$ powders(x=0, 0.05, 0.10) after calcination at 900°C are shown in Fig.2.The XRD patterns have been analyzed using JCPDS (# 04-013-5403) database of crystal structures. All the major peaks correspond to the perovskite LSCM structure. Low intensity peaks may be attributed to the formation of mixed oxide phases of various compositions locally. In our experiments calcined powders were milled and compacted and thereafter exposed to reducing atmosphere at 900°C, 3h. This condition is more severe than exposing sintered pellets in reducing atmosphere. XRD patterns of porous unsintered LSCM samples of all the three compositions after exposure to reducing atmosphere is shown in Fig. 3.

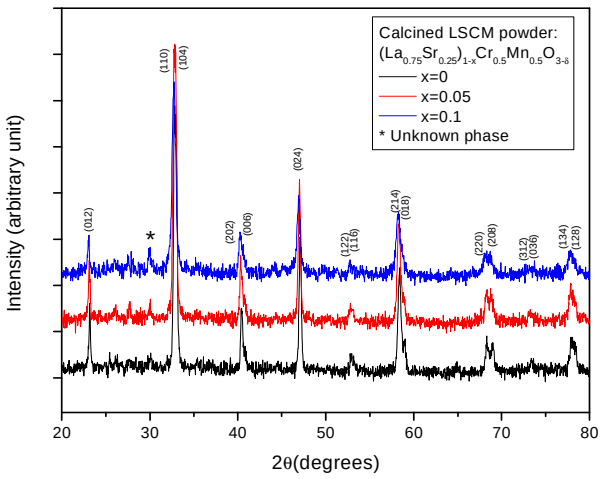

Fig. 2: XRD patterns LSCM powders calcined at 900°C

All the major peaks correspond to perovskite structure. In all the three compositions a low intensity peak (marked by '*')of secondary phase at ~31°2θ has been observed. The low intensity extra peak at round 31° 2θ) in hydrogen treated LSCM sample has been reported in literature[11,12]. It is reported to be originating from the decompositionof the perovskite-like oxide to a K_2NiF_4-like phase (Ruddlesden–Popper (R–P) phase) or ordering of the perovskite structure[11]. M. Oishialso observed R–P phase, i.e., $(La,Sr)_2MnO_4$, for LSCM quenched from 900 °C ata P_{O_2} of 9.9×10^{-21}atm[12].Overall the results indicate that A-site deficiency has no significant influence on the stability of perovskite phase of LSCM.

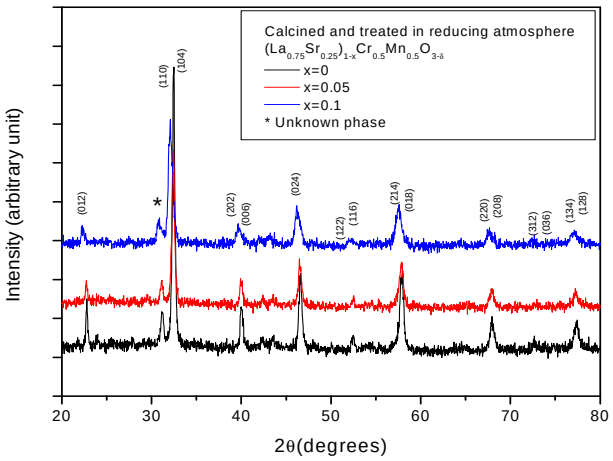

Fig.3: XRD patterns of calcined LSCM powders after exposure to hydrogen atmosphere at 900°C

Phase stability of sintered LSCM

The XRD patterns of sintered $(La_{0.75}Sr_{0.25})_{1-x}Cr_{0.5}Mn_{0.5}O_{3-\delta}$with x=0, 0.05, 0.10 are shown in Fig. 4.

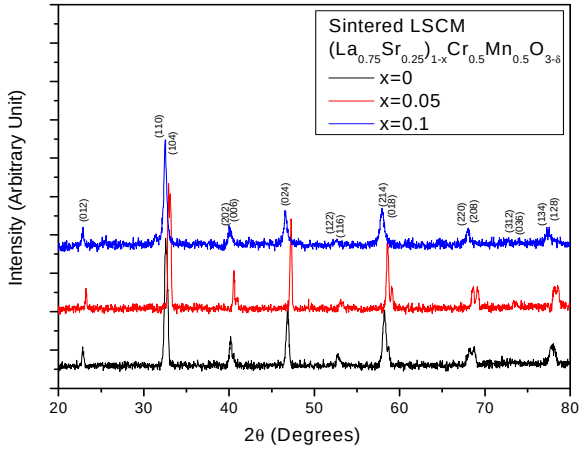

Fig. 4: XRD patterns of LSCM powders sintered at 1350°C, 3h

All the peaks could be assigned to pure perovskite structure. Low intensity extra peaks observed in the XRD patterns of calcined powders have disappearedin the XRD patterns of sintered samples. The XRD patterns of the sintered LSCM samples after exposure in hydrogen atmosphere is shown in Fig. 5. The XRD results have been compared with LSCM sample sintered in air. The perovskite phase purity is retained in the sintered samples of all the three compositions even after exposure in hydrogen atmosphere at 900^{o}C and no effect of site deficiency has been observed.

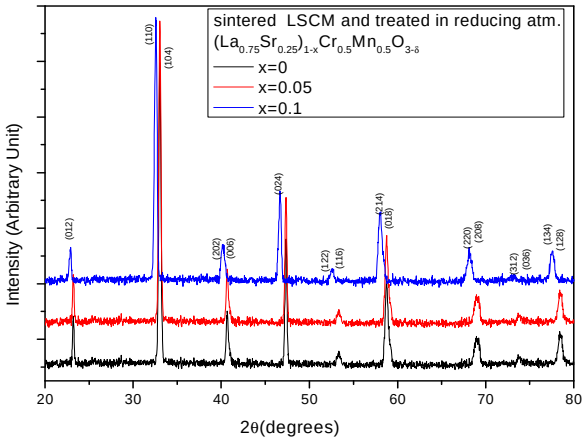

Fig.5: XRD patterns of sintered LSCM after exposure to hydrogen atmosphere at 900^{o}C

Electrical conductivity in oxidizing atmosphere: Effect of A-site deficiency

The electrical conductivity in $La_{0.75}Sr_{0.25}Cr_{0.5}Mn_{0.5}O_3$ is primarily due to Sr^{2+} substitution in La^{3+} sites. The following defect reactions are possible when SrO is added in the $LaMO_3$ (here, M = Mn, Cr) perovskite structure.

$$2\,SrO \leftrightarrow 2Sr'_{La} + V_{\ddot{O}} + 2O_O^{\times} \quad \ldots\ldots\ldots (1)$$
$$SrO \leftrightarrow Sr'_{La} + M_{\dot{M}} + O_O^{\times} \quad \ldots\ldots\ldots (2)$$

Thus the negatively charged Sr'_{La} can be charge compensated by either formation of oxygen vacancy or through $Mn^{3+} \rightarrow Mn^{4+}$ and/or $Cr^{3+} \rightarrow Cr^{4+}$ transition. The later leads to the formation of electronic hole, a p-type charge carrier. Under oxidizing atmosphere (P_{O_2}>10^{-8} atm), oxygen deficiency is expected to be negligible, therefore, all charge compensation occurs via formation of electronic holes.

The electrical conductivity in LSCM is due to small polaron hopping of the charge carriers localized at Mn and Cr sites.The electrical conductivities of $(La_{0.75}Sr_{0.25})_{1-x}Cr_{0.5}Mn_{0.5}O_{3-\delta}$ samples (with x = 0.0, 0.05 and 0.10) as a function of temperature are shown in Fig. 6 in the form of Arrhenius plot.It is observed that in the lower temperature range as the La-site deficiency level increases, the electrical conductivity decreases.Above 750^{o}C the electrical conductivity of La-site deficient (x = 0.05) LSCM was found to be more than stoichiometric LSCM composition. La-site deficiency in LSCM can be expressed by the following defect chemical reaction.

$$2La_{La}^{\times} + 3O_O^{\times} \leftrightarrow 2V_{La}''' + 3V_{\ddot{O}} \quad \ldots\ldots\ldots (3)$$

The presence of strong negatively charged V_{La}'''sites is likely to influence the movement of positively charged carriers through defect association. At higher temperature and in oxidizing atmosphere the following defect reaction is expected to be prevalent.

$$V_{\ddot{O}} + \frac{1}{2}O_2 \leftrightarrow O_O^{\times} + M_M^{\circ} \quad \ldots\ldots\ldots\ldots\ldots (4)$$

Therefore, hole concentration increases at higher temperature and this leads to increase in the electrical conductivity in the La-site deficient LSCM at higher temperature region. The activation energies have been calculated to be 0.26, 0.34 and 0.36 eV for $(La_{0.75}Sr_{0.25})_{1-x}Cr_{0.5}Mn_{0.5}O_{3-\delta}$ samples with x = 0.0, 0.05 and 0.10 respectively. Higher activation energy in La-site deficient LSCM is due to the activation barrier caused by defect association with negatively charged V_{La}'''sites.

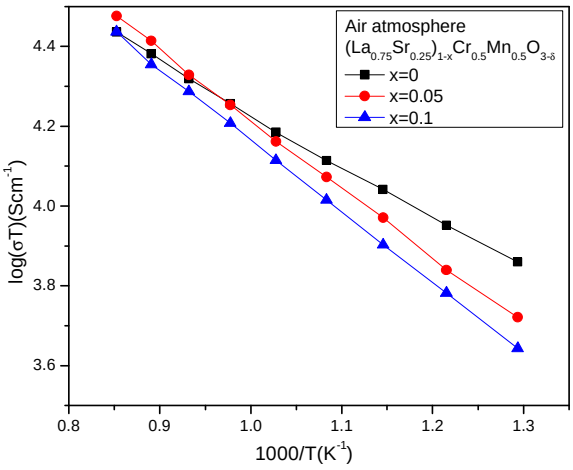

Fig. 6: Electrical conductivity of different LSCM compositions in air

Electrical conductivity in oxidizing atmosphere: Effect of A-site deficiency

The electrical conductivities of $(La_{0.75}Sr_{0.25})_{1-x}Cr_{0.5}Mn_{0.5}O_{3-\delta}$ samples (with x = 0.0, 0.05 and 0.10) in humidified hydrogen atmosphere as a function of temperature are shown in Fig. 7 in the form of Arrhenius plot. The conductivity of LSCM in reducing atmosphere is about two orders of magnitude lower than that in oxidizing atmosphere. Also the conductivity has been found to decrease significantly with increase in La-site deficiency. Under reducing condition the defect reaction (1) becomes dominant. In other word, the lattice oxygen transforms into a doubly charged oxygen vacancy consuming two electronic holes. The defect chemical reaction between the defect species and the surrounding atmosphere can be described as:

$$O_O^{\times} + 2M_M^{\circ} \leftrightarrow \frac{1}{2}O_2 + V_O^{\circ\circ} + 2M_M^{\times} \quad \ldots\ldots\ldots (5)$$ where, M= Mn, Cr.

Therefore, hole concentration effectively decreases in reducing atmosphere. This phenomenon decreases the electrical conductivity significantly. La-site deficiency further aggravates the hole conduction by increasing the activation barrier as discussed earlier.In reducing atmosphere the defect chemical reaction (4) is not feasible and conductivity of La-site deficient LSCM always remains lower than stoichiometric LSCM composition. The activation energies have been calculated to be 0.58, 0.74 and 0.78eV for $(La_{0.75}Sr_{0.25})_{1-x}Cr_{0.5}Mn_{0.5}O_{3-\delta}$ samples with x = 0.0, 0.05 and 0.10 respectively in reducing atmosphere. High activation energy for electrical conductivity in reducing atmosphere is due to the activation barrier caused by large concentration of oxygen vacancies. Increase in activation energyin La-site deficient LSCM is attributed to defect association with negatively charged V_{La}'''sites.

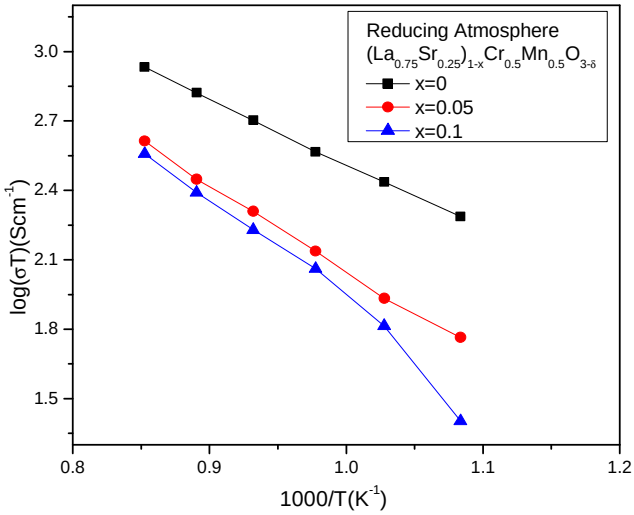

Fig. 7: Electrical conductivity of different LSCM compositions in reducing atmosphere

Conclusions

Pure perovskite structured phase has been obtained in the sintered LSCM having different levelof La-site deficiency. The perovskite phase remains stable after exposure in humidified hydrogen atmosphere at 900°C in all the three compositions of LSCM $(La_{0.75}Sr_{0.25})_{1-x}Cr_{0.5}Mn_{0.5}O_{3-\delta}$(x=0.0, 0.05, 0.10). The electrical conductivity is influenced significantly with the atmosphere as well as lanthanum site deficiency. The electrical conductivity in hydrogen atmosphere is about two orders of magnitude lower than that in air atmosphere. The conductivity in general decreases with increase in lanthanum site deficiency. However, at higher temperature and in oxygen atmosphere the conductivity of La-site deficient LSCM exceeds that of stoichiometric LSCM.

References

[1] San Ping Jiang, J Mater Sci, 43 (2008) 6799–6833.
[2] V. S. Reddy Channu, Rudolf Holze , Edwin H. Walker, New Journal of Glass and Ceramics, 3 (2013) 29-33.

[3] W.Z. Zhu, S.C. Deevi, Materials Science and Engineering, A348 (2003) 227-243.
[4] San Ping Jiang, Li Liu, Khuong P. Ong, Ping Wu, Jian Li, JianPu, Journal of Power Sources 176 (2008) 82–89.
[5] J.C. Ruiz-Morales, J. Canales-Vazquez, J. Pena-Martinez, *Electrochim. Acta*, 52 (2006) 278.
[6] S. Tao, J.T.S. Irvine, *J. Electrochem. Soc.* 151 (2004) A252.
[7] 0.Yamamoto, Y. Takeda, R. Kanno, and M. Noda, "Perovskite-Type Oxides as Oxygen Electrodes for High-Temperature Oxide Fuel Cells," Solid State lonics, 22 (1987) 24146.
[8] H. Yokokawa, N. Sakai, T. Kawada, and M. Dokiya. "Thermodynamic Analysis on Interface between Perovskite Electrode and YSZ Electrolyte," Solid State lonics, 40/41 (1990) 398401.
[9] J.G.M. Furtado and R.N. Oliveira, *RevistaMateria.* 13 (2008) 147.
[10] I. Jitaru, D. Berger, V. Fruth, A. Novac, *Ceramics International*. 26 (2000) 193.
[11] J.C. Ruiz-Morales, J. Canales-Vazquez, D. Marrero-Lopez, J.T.S. Irvine, P. Nunez, *Electrochim. Acta*, 52 (2007) 7217.
[12] M. Oishi, K. Yashiro, K. Sato, J. Mizusaki, T. Kawada, *J. Solid State Chem.*, 181 (2008) 3177.

BARC NEWSLETTER
FOUNDER'S DAY SPECIAL ISSUE 2015

AN INSIGHTS INTO THE ELECTROCATALYSIS OF U(VI) ON GOLD NANOPARTICLES (AUNPS)

Saurav K. Guin[1,*], Parvathi K.[2,3], Arvind S. Ambolikar[1], Jisha S. Pillai[1], Dilip K. Maity[2,3], S. Kannan[1], Suresh K. Aggarwal[1]

[1] Fuel Chemistry Division, [2] Homi Bhabha National Institute, [3] Theoretical Chemistry Section

This paper received the First Prize in the Poster Presentation at the International Conference "ECHEMS 2014: Electrochemistry in Molecular Understanding" held at Wells, UK, June 17-20, 2014

Abstract

Gold nanoparticles (AuNPs) of controlled dimension are prepared on glassy carbon electrode from the solution of 1 mM $HAuCl_4$ in 0.1 M HCl by electrochemical route without using any additional size-directing reagents. The electrochemistry of U(VI)/U(IV) redox couple in 1 M H_2SO_4 is studied by cyclic voltammetry, differential pulse voltammetry and electrochemical impedance spectroscopy experiments. It is evidenced that AuNPs catalyses the redox reaction of U(VI)/U(IV). The quantum mechanical calculation unravels the mechanism of electrocatalytic reduction of uranyl ($U^{VI}O_2^{2+}$) sulphate redox species on AuNPs. The higher density of states of 5d band of AuNPs and its strong interaction with the LUMO(U-5f) of $[U^{VI}O_2(\eta^1\text{-}OSO_3)(\eta^2\text{-}O_2SO_2), 2H_2O]^{2-}$ catalyzes the heterogeneous electron transfer reaction between AuNPs and uranyl ($U^{VI}O_2^{2+}$) sulphate redox species. This is the first report on the involvement of the 5f-orbital of actinyl ion in the electrocatalytic electron transfer reaction.

Introduction

Bulk gold is highly stable in corrosive environments and it rarely shows low catalytic activity for most of the reactions. Therefore, bulk gold metal has not drawn any attention in catalysis. On the contrary, supported gold nanoparticles (AuNPs) offer excellent electrochemistry compared to bulk counterpart because of their high effective surface area, high rate of mass transport through convergent diffusion and electrocatalytic action at the nano-surfaces. Recently, AuNPs have exhibited high electrocatalytic activity for CO oxidation [1] and oxygen reduction [2, 3]. Interestingly, the oxygen reduction on AuNPs occurs in the potential range -0.5 to -0.15 V vs. Ag/AgCl (saturated KCl) reference electrode,[2] which is in similar range of reduction potential of the uranyl ($U^{VI}O_2^{2+}$) complex to U(IV) complex in sulphuric acid medium on mercury pool electrode [4]. Due to the health and environmental hazards of mercury, efforts are being put on the development of the suitable alternative electrodes for the replacing mercury. Therefore, it is of interest to explore the applicability of AuNPs for the electrochemical reduction of U(VI) in 1 M H_2SO_4.Eventually, this is the part of the first report on the electrocatalysis of $U^{VI}O_2^{2+}$ in 1 M

H_2SO_4 at AuNPs supported on glassy carbon electrode (AuNPs/GC) as evidenced from cyclic voltammetry (CV), differential pulse voltammetry (DPV) and electrochemical impedance spectroscopy (EIS) experiments [5]. The electrocatalytic mechanism was investigated at molecular level by correlating the electrochemical results with the quantum chemical calculations.

Experimental

The chemicals of highest available purity are used without any further purification. All the solutions are prepared using ultra pure water (Milli-Q, Millipore, 18.2 MV cm). The electrochemical experiments are performed at room temperature (T = 294 K) in a conventional three-electrode cell by using Autolab PGSTAT 30 and CHI-760D electrochemical workstations. A commercial glassy carbon (GC) (w = 3 mm) or gold (Au) (w = 2 mm) or AuNPs/GC electrode is used as the working electrode, Ag/AgCl/KCl (saturated) ($E_{Ag/AgCl}$ = +0.197 V vs. standard hydrogen electrode) is used as the reference electrode and a platinum wire acts as the counter electrode. All the potentials quoted are with respect to the Ag/AgCl reference electrode. Prior to perform the electrochemical experiments, the working solution is purged with high purity nitrogen for 15 min to remove the dissolved oxygen from the solution. The polishing of GC and Au electrodes in between the experiments is carried out by using alumina slurries with different powders of size down to 0.05 mm. After each polishing, the electrode is thoroughly rinsed with water and sonicated in ultrapure water in an ultrasonic bath for 30 min to remove any adsorbed substances from the electrode surface. Electrochemical simulation software is used to evaluate the kinetic parameters of the electrode reaction corresponding to the reduction of U(VI) in 1 M H_2SO_4. The AuNPs/GC is synthesised by multiple galvanostatic pulse strategy as reported by Guin et al. [6] This template free electrosynthesis route produces AuNPs with controlled particle size dispersion without employing any surface stabilizing agent.

The geometry of the most probable species of U(VI) in 1 M H_2SO_4 is optimized by applying a popular nonlocal correlated hybrid density function, namely, B3LYP. Gaussian type atomic basis functions, 6-31+G(d) are adopted for O and S atoms while for U atom, SARC-ZORA basis sets are used for all the calculations.[7] This particular basis set for U is obtained from Extensible Computational Chemistry Environment Basis Set Database, Pacific Northwest National Laboratory.[8] The minimum energy structure is found by applying quasi-Newton-Raphson based algorithm. All these calculations are carried out applying GAMESS suit of ab-initio program for electronic structure calculation.[9] Vibrational analysis of U(VI)-species is performed to ensure the true minima and to assess the effect on the actinyl bond due to changes in the number of equatorial ligands. Changes to the thermal contributions and zero point energies are negligible and, therefore, are not included in the final results.

Results and Discussion

Fig. 1 shows the scanning electron microscopic (SEM) image of the electrochemically synthesized tapped hemispherical AuNPs of diameter 350-400 nm and height 25-30 nm. The

synthesized AuNPs shows narrow particle size distribution confirming the ability of the template free electrosynthesis route in controlling the dimension of the nanoparticles though in the absence of the size controlling physical/chemical agents.

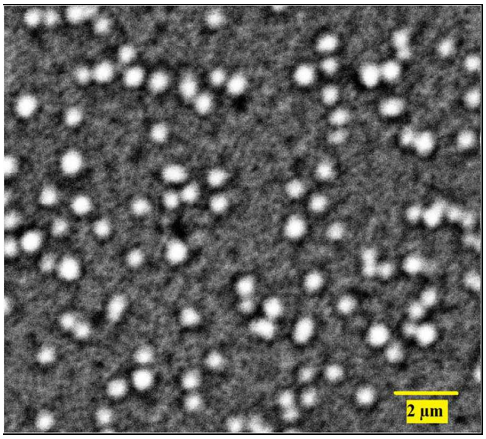

Fig. 1: SEM image of AuNPs/GC at 25000X. [5]

The DPV of 5 mM U(VI) in 1 M H_2SO_4 on (i) GC, (ii) Au and (iii) AuNPs/GC at 10 mV pulse amplitude is shown in Fig. 2. The cathodic peak of U(VI) on GC is observed at -0.494 V with a peak current density of -17.8 mA cm^{-2}. The cathodic peak potential is shifted to -0.191 V and -0.129 V on Au and AuNPs/GC, respectively. The peak current density increases to -30.4 and -82.4 mA cm^{-2} on Au and AuNPs/GC, respectively. Fig. 2 indicates that the energy barrier of the electron transfer reaction from the electrode to U(VI) centre is significantly minimized at AuNPs/GC. Therefore, AuNPs/GC acts as a catalyst for the electrochemical reduction of U(VI) in 1 M H_2SO_4. Further, the significant enhancement of the cathodic peak current of U(VI) at AuNPs/GC draws analytical importance for the quantitative measurement of U(VI). The evidence of electrocatalytic reduction of U(VI) is also supported by the cyclic voltammograms (Fig. 3).

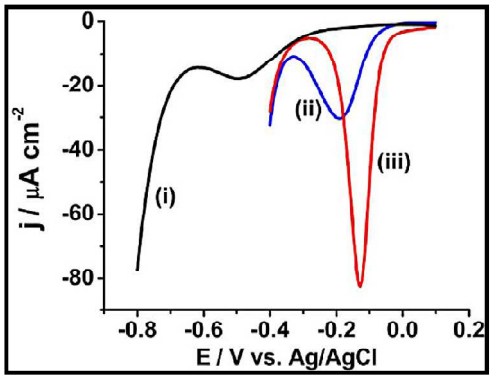

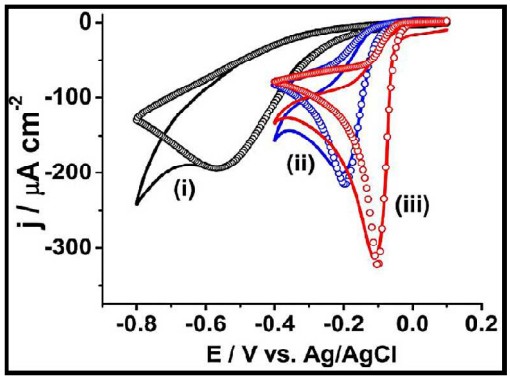

Fig. 2: DPV of 5 mM U(VI) in 1 M H_2SO_4 on (i) GC, (ii) Au and (iii) AuNPs/GC at 10 mV pulse amplitude.[5]

Fig. 3: Cyclic voltammogram of 5 mM U(VI) in 1 M H_2SO_4 on (i) GC, (ii) Au and (iii) AuNPs/GC at a scan rate (n) of 10 mV s^{-1}. The solid lines and circles represent the experimental data and fitted curves respectively

The detailed voltammetric analysis revealed that the electrochemical reduction of U (VI) in 1 M H_2SO_4 happens at Au electrode through a mixed adsorption-diffusion mechanism and the contribution of adsorption increases in AuNPs/GC. Further, the variation of the current function with respect to the scan rate indicates that the extent of reduction of U(VI) in 1 M H_2SO_4 through electrochemical-chemical (EC) mechanism increases at Au and AuNPs/GC. $U^{(VI)}O_2^{2+}$ is reduced to $U^{(V)}O_2^{+}$ (Eq. (1))

$$2U^{(VI)}O_2^{2+} + 2e^- = 2U^{(V)}O_2^{+} \quad (1)$$

In acidic solution, $U^{(V)}O_2^{+}$ disproportionates into $U^{(VI)}O_2^{2+}$ and $U^{(IV)4+}$ (Eq. (2)).

$$2U^{(V)}O_2^{+} + 4H^{+} = U^{(VI)}O_2^{2+} + U^{(IV)4+} + 2H_2O \quad (2)$$

From the shapes of the CVs (Fig. 3), it can be speculated that under strongly acidic conditions (i.e. 1 M H_2SO_4), reaction (2) occurs so fast that at the potential corresponding to reaction (1), the $U^{VI}O_2^{2+}$ ion is reduced completely to $U^{(IV)4+}$ at the vicinity of the electrode according to overall Eq. 3.

$$U^{(VI)}O_2^{2+} + 2e^- + 4H^{+} = U^{(IV)4+} + 2H_2O \quad (3)$$

Since, U(IV) is stable in 1 M H_2SO_4 and the oxidation of U(IV) involves the formation of two U=O bonds, which occurs much slowly with respect to the recommended time frame of the electrochemical potential sweep at the electrode. Therefore, $U^{(VI)}O_2^{2+}/U^{(IV)4+}$ shows irreversible redox behavior and no oxidation peak of uranium (IV) is observed in anodic scan direction irrespective of the scan rates. Further the cathodic peak of uranyl is better defined with AuNPs/GC than with Au or GC electrode compared to the background hydrogen evolution peak and thus the selectivity of the U(VI) reduction is improved at AuNPs/GC. The onset reduction potential (E_c) of U(VI) to U(V) are appeared at -0.278, -0.108 and -0.101 V at GC, Au and AuNPs/GC, respectively. The systematic decrease of Ec from GC to AuNPs/GC suggests that the energy of the virtual state ($E_{VS\text{-}LUMO}$) of the electron transfer from the electrode to U(VI) systematically decreases from GC to AuNPs/GC. The $E_{VS\text{-}LUMO}$ is calculated as -4.372, -4.549 and -4.542 eV vs. vacuum for GC, Au and AuNPs/GC, respectively. The rate of electron transfer reaction from the electrode to U(VI) is calculated as 3.5×10^{-5}, 5.0×10^{-5} and 5.4×10^{-5} cm s^{-1} for GC, Au and AuNPs/GC, respectively, by fitting the experimental CV with the calculated CV for combined reaction (1) and (2). Interestingly, the charge transfer coefficient (α; symmetry factor of the transition state) improves from 0.13 at GC to 0.50 at Au and 0.90 at AuNPs/GC. Therefore, it can be speculated that the rate as well as the symmetry of the potential energy barrier of the heterogeneous electron transfer reaction from electrode to U(VI) follows the order GC < Au < AuNPs/GC.

There are two common possibilities to get enhanced current of the electrochemical reaction at the modified electrodes with nanoparticles; (1) enhancement in the overall surface area of the electrode because of the higher surface-to-volume ratio of the nanoparticles; and (2) presence of higher number of synthetic defects or active sites on the nanoparticles.

In these cases, nanoparticles modified electrode is expected to show electrocatalytic action irrespective of the redox system.

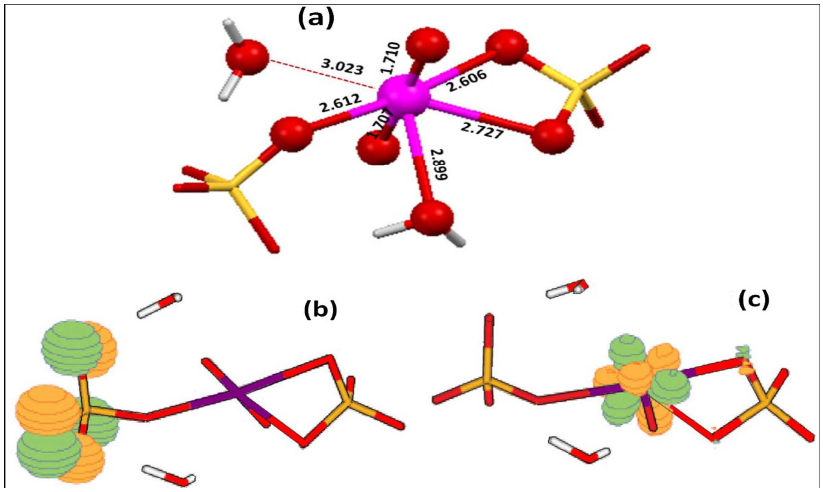

Fig. 4: (a) Optimized structure (b) HOMO & (c) LUMO of hydrated $[U^{VI}O_2(\eta^1\text{-}OSO_3)(\eta^2\text{-}O_2SO_2), 2H_2O]^{2-}$. The bond distances given are in Å. HOMO is comprised of lone pair from oxygen atoms of SO_4^{2-} group which acts as monodentate ligand whereas LUMO is made of 5f $z(x^2\text{-}y^2)$ orbital of U. [5]

Therefore, the CV and EIS experiments were performed at GC, Au and AuNPs/GC electrodes with an electrochemically reversible probe, i.e. $K_3[Fe(CN)_6]/K_4[Fe(CN)_6]$ redox couple. No appreciable change in the peak current densities and peak potentials is observed for these electrodes. It may rule out the first possibility. Further, no appreciable change in the charge transfer resistance is observed between Au and AuNPs/GC for $K_3[Fe(CN)_6]/K_4[Fe(CN)_6]$. It may rule out the second possibility. The electrocatalysis can also be defined by the decrease in the height of the activation barrier of the electron transfer reaction. Further, a change in the energy of the virtual states as well as the contribution of adsorption of U(VI) at the electrodes is discussed in the earlier paragraph. calculated to be most stable and thus predominant species under studies (Fig. 4).Therefore, quantum mechanical calculations is performed for understanding the electrocatalysis of U(VI) by AuNPs/GC at molecular levels. $[U^{VI}O_2(\eta^1\text{-}OSO_3)(\eta^2\text{-}O_2SO_2), 2H_2O]^{2-}$ is The energies of the highest occupied molecular orbital (HOMO) and lowest unoccupied molecular orbital (LUMO) are calculated as -7.01 eV and -5.84 eV vs. vacuum, respectively. More interestingly HOMO is comprised mostly of O(p) orbitals of monodentate sulfate; whereas LUMO is comprised of U[5f $z(x^2\text{-}y^2)$] orbital. It shows that an interaction between filled p orbital of oxygen atom of sulphate with that of vacant f orbital of U(VI) ion, indicating the f orbital participation in bonding. The density of states (DOS) of the sp-band of GC depends on the energy range and it is very low (~2.2×10^{-3} states/eV) i.e. below -0.1 V vs. Ag/AgCl. Therefore, the heterogeneous rate of electron transfer to U(VI) was found to be the lowest at GC due to the low DOS. Further, the weak interaction of LUMO (consisting of U-5f orbital) of $[U^{VI}O_2(\eta^1\text{-}OSO_3)(\eta^2\text{-}O_2SO_2), 2H_2O]^{2-}$ with carbon sp-band creates a virtual energy state at -4.372 eV vs. vacuum, as discussed earlier, for the heterogeneous electron transfer reaction to take place (Fig. 5a). The weak absorption of $[U^{VI}O_2(\eta^1\text{-}OSO_3)(\eta^2\text{-}O_2SO_2),$

$2H_2O]^{2-}$ on GC surface results into lowest charge transfer coefficient of the reaction as evidenced from the electrochemical experiments. On the other hand, gold has a DOS of 0.28 states/eV and this value is relatively constant with energy. Therefore, the heterogeneous rate of electron transfer to U(VI) increased at Au. The Fermi energy of Au is -5.31 eV vs. vacuum and the centre of 5d band of Au is situated at -9.01 eV vs. vacuum. The metal 5d band interacts comparatively strongly with the LUMO (U-5f orbital) of $[U^{VI}O_2(\eta^1\text{-}OSO_3)(\eta^2\text{-}O_2SO_2), 2H_2O]^{2-}$ creating VS-LUMO at -4.549 eV vs. vacuum (Fig. 5b).Moreover, the better adsorption of $[U^{VI}O_2(\eta^1\text{-}OSO_3)(\eta^2\text{-}O_2SO_2), 2H_2O]^{2-}$ on Au improves the charge transfer coefficient of the cathodic reaction. The DOS is not only expected to be increased for AuNPs/ GC, but the energy level of its 5d band is also expected to be changed. Therefore, the contribution of adsorption of $[U^{VI}O_2(\eta^1\text{-}OSO_3)(\eta^2\text{-}O_2SO_2), 2H_2O]^{2-}$ on AuNPs/GC is increased due to the increase of the DOS at AuNPs and more interaction of the U(VI)-LUMO(5f) with the Au-5d band of AuNPs. This phenomenon was indirectly supported by the energy of the VS-LUMO (at -4.542 eV vs. vacuum) and the highest observed value of the charge transfer coefficient at AuNPs/GC (Fig. 5c).

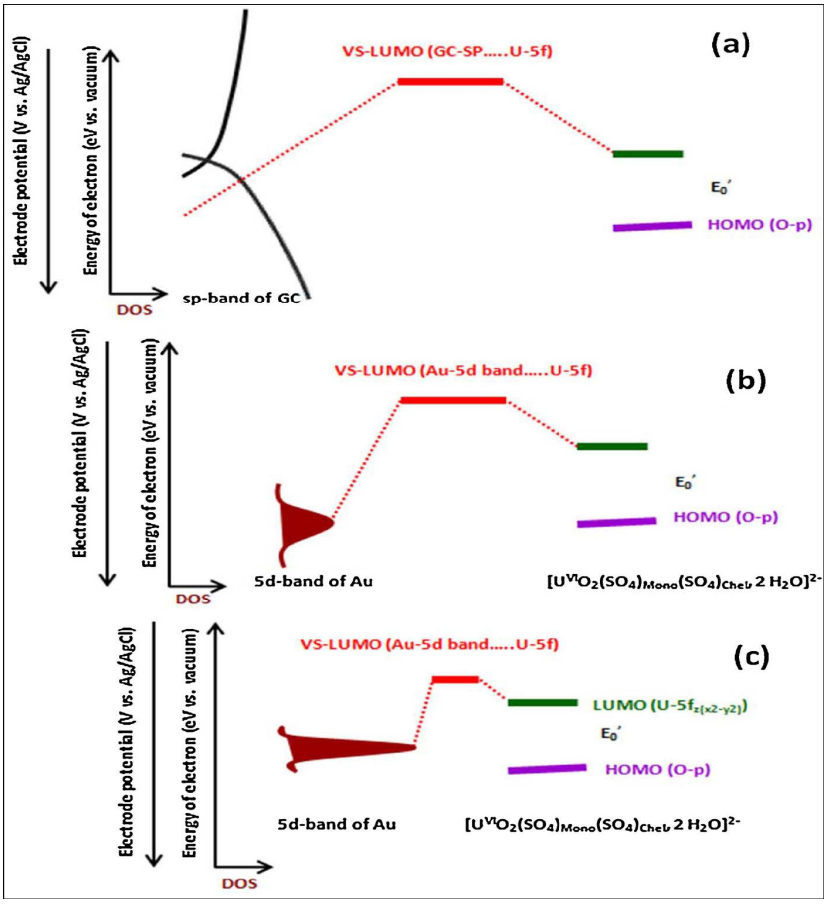

Fig. 5: The representation (not in absolute scale) of the interaction of LUMO with the electronic bands of (a) GC, (b) Au and (c) AuNPs/GC. VS-LUMO represents the virtual state of LUMO after interacting with the electronic bands of electrode [5]

Conclusion

The present study unravels, for the first time, the electrocatalytic action of AuNPs for the reduction of actinyl complexes (more precisely uranyl complexes). The CV, DPV and EIS reveals that AuNPs/GC is a superior electrocatalyst compared to Au or GC for reduction of $U^{VI}O_2^{2+}$ in 1 M H_2SO_4. The highest observed value of the charge transfer coefficient and rate of electron transfer at AuNPs are proposed because of the highest density of states of 5d band of AuNPs and its better interaction with the LUMO contributed by U-5fz(x2-y2) orbital of $[U^{VI}O_2(\eta^1\text{-}OSO_3)(\ \eta^2\text{-}O_2SO_2),\ 2H_2O]^{2-}$, predominant stable species of $U^{VI}O_2^{2+}$ in 1 M H_2SO_4. This is the first report on the participation of the 5f-orbital of actinyl ion in electrocatalysis.

References

[1] A. Herzing, C. J. Kiely, A. F. Carley, P. Landon, G. J. Hutchings, *Science* **321** (2008) 1331.
[2] W. Chen, S. Chen, *Angew. Chem. Int. Ed.* **48** (2009) 4386.
[3] Hvolbaek, T. V. W. Janssens, B. S. Clausen, H. Falsig, C. H. Christensen, J. K. Norskov, *Nanotoday* **2** (2007) 14.
[4] K. -U. Din, J. Kuta, L. Pospisil, *Electrochim. Acta* **22** (1977) 1109.
[5] S. K. Guin, Parvathi K., A. S. Ambolikar, J. S. Pillai, D. K. Maity, S. Kannan, S. K. Aggarwal, *Electrochim. Acta* **154** (2015) 413.
[6] S. K. Guin, J. S. Pillai, A. S. Ambolikar, A. Saha, S. K. Aggarwal, *RSC Adv.* **3** (2013) 17977.
[7] D.A. Pantazis, F. Neese, *J. Chem. Theory Comput.* **7** (2011) 677.
[8] K. L. Schuchardt, B. T. Didier, T. Elsethagen, L. Sun, V. Gurumoorthi, J. Chase, J. Li, T. L. Windus, *J. Chem. Inf. Model.* **47** (2007) 1045.
[9] W. Schmidt, K. K. Baldridge, J. A. Boatz, S. T. Elbert, M. S. Gordon, J. H. Jensen, S. Koseki, N. Matsunaga, K. A. Nguyen, S. J. Su, T. L. Windus, M. Dupuis, J. A. Montgomery, *J. Comput. Chem.* **14** (1993) 1347.

BARC NEWSLETTER
FOUNDER'S DAY SPECIAL ISSUE 2015

CONTAINMENT STUDIES FACILITY: EXPERIMENTS AND ANALYTICAL STUDIES

Anu Dutta, I. Thangamani, V.M. Shanware, K.S. Rao, B. Gera, A. Ravi Kiran, P. Goyal, Pavan K. Sharma, Vishnu Verma, M.K. Agrawal, S. Ganju and R.K. Singh
Reactor Safety Division

This paper received the Best Poster Paper Award at the Conference "New Horizons in Nuclear Reactor Thermal Hydraulics and Safety", Mumbai, Jan.13-15, 2014

Abstract

The Containment Studies Facility (CSF) is a test facility which has been set up at BARC for carrying out experiments related to nuclear reactor containment. It consists of a containment model and a pressure vessel (or PHTM vessel). Containment thermal hydraulic experiments were carried out in CSF for 50bar and 75bar blowdown conditions for simulating containment pressure and temperature transients following pipe break, simulating LOCA/MSLB. Pressure, temperature and other transient parameters were recorded during the experiments. The experimental results were compared with outputs of modeling carried out using various codes like RELAP, ASTEC and CONTRAN etc. The details of the experimental and analytical studies conducted in the CSF are presented in this paper.

Introduction

In Indian Pressurized Heavy Water Reactor (IPHWR), containment building is the last safety barrier for preventing the consequences of accident such as LOCA/Main Steam Line Break (MSLB). In case of LOCA, high enthalpy steam is discharged into the containment atmosphere and the containment pressure and temperature start rising. The containment building itself acts as a passive heat sink and heat transfer to containment takes place by way of convection and condensation. The condensation heat transfer in containment is a complex phenomenon and depends upon many parameters [1,2]. In order to generate large data base for validating the mathematical modelling using various codes like, RELAP[3], ASTEC[4] and in-house CONTRAN [5,6] and also to resolve the issues related to suitable condensation models, blowdown experiments were carried out in CSF [7].

Brief Description of Experimental Facility

The experimental facility consists of a pressure vessel (PHTM) simulating the primary heat transport system and a concrete containment model. A blow down pipe connects the

pressure vessel to the containment model. The arrangement is shown schematically in Figure 1. A brief description of each of the components of the facility follows.

Containment Model

The containment model is a cylindrical structure with an ellipsoidal dome, made out of reinforced cement concrete (RCC) and inside wall surface is coated with epoxy painting. The outer diameter of the model is 6.9 m and its height is 10.95 m.This facility is approximately 1:200 volumetrically scaled down model of the standardized 220MWe IPHWR [3]. The scaled down model simulates geometrically all the major compartments in IPHWR viz. fuelling machine vaults, pump room vaults, boiler room, dome region, vent annulus, suppression pool etc. The containment model consists of two floors and a basement. The two floors constitute the volume–V1 that contains 6 rooms (from Room R1 to R6) in total and the basement forms the volume–V2 (refer Figure 1). The suppression pool is also a part of the basement. Volumes–V1 & V2 are connected by vent pipes or downcomers submerged in the suppression pool.

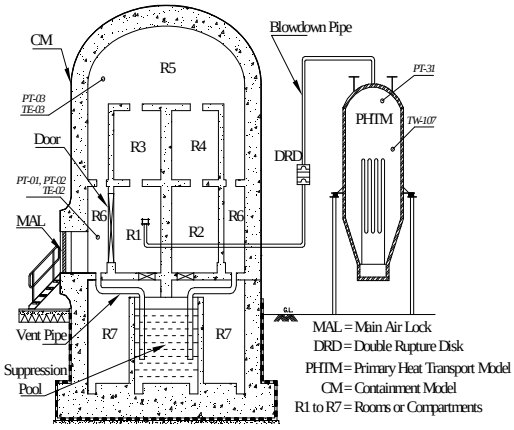

Fig. 1: Schematic diagram of Containment Studies Facility

Primary Heat Transport System (PHTM)

The function of PHTM system is to simulate the LOCA/MSLB by discharging high enthalpy steam (i.e. mass and energy) into the containment model. The PHTM system consists of a pressure vessel, feed and bleed system, heater unit, blowdown pipe line and other associated equipments to generate steam at prescribed conditions. A 1 m^3carbon steel pressure vessel is designed for the maximum operating pressure of 100bar and equipped with safety systems such as rupture disk, safety relief valves etc. for safe operation.

The volume of pressure vessel evaluated based on cumulative mass and energy discharge required to simulate LOCA in IPHWR. The pressure vessel has submerged U type heater pins for generating steam at desired pressure. Feed and bleed system is provided to perform the function of supplying and removing process water from the vessel for maintaining

desired operating conditions. Apart from that the feed and bleed system can create saturated or sub-cooled blowdown conditions in the vessel.

Piping and Instrumentation

The pressure vessel is connected to the containment model by a discharge pipe of 50mm NB size. A Double Rupture Disc (DRD) with suitable operating mechanism is mounted on this pipe. The blow down could be initiated by causing rupture of these rupture discs.The process instrumentation for the CSF mainly consists of pressure, temperature and level measurements at various locations on the PHTM and CM for the requirement of transient data recording. Apart from this, safety related instruments and controls for pressure and temperature are also provided in PHTM and CM. The pressurization process status of PHTM vessel is monitored using an Industrial PC based Data Acquisition System (DAS), which has 256 channels with a scanning speed of about 10,000 samples/s and an overall accuracy of about ±0.1% of full scale. A paperless recorder is also deployed to continuously monitor the important parameters such as PHTM pressure, level etc.Once the pre-set operating conditions are established in the PHTM, blow down into CM can be initiated. This event simulates LOCA or MSLB accident, due to pipe line rupture, in a typical PHWR reactor containment. A schematic diagram of the blow down initiating mechanism along with Dual Rupture Disc (DRD) assembly is shown in the Figure 2.

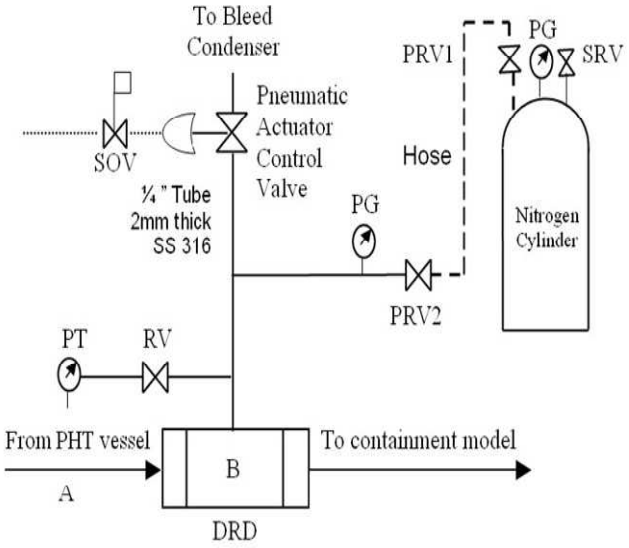

Fig. 2: Blow down initiating mechanism

The DRD assembly consists of two rupture disks which are kept in series and the rupture disk ratings are chosen 3/4 of the test blowdown pressure. The upstream side of the DRD assembly is connected to PHTM vessel, the downstream is connected to CM and the inter-space between two rupture disks is pressurized to half of test blowdown pressure using a separate nitrogen cylinder. The blowdown process is initiated by depressurization of inter-space between the rupture disks with the help of pneumatically operated fast acting control

valve.In Containment Model, each compartment is provided with a pressure, relative humidity, room and wall temperature measurements and each junction between the compartments is provided with a junction flow meter. In vapor suppression pool, the level variation and associated loads generated during the flow of air-steam mixtures through pool water are measured using submersible pressure transducers.

Experimental and Analytical Studies

Initially the PHTM vessel is filled with de-mineralised (DM) water up to desired level. A Double Rupture Disk (DRD) assembly, which is fixed with two suitable rupture disks in series, has been used for initiating blowdown. The DM water in PHTM vessel is heated, using heater banks, to generate steam to the test pressure and temperature and then it is allowed to blowdown into V1 volume of containment model by rupturing the rupture disks in DRD assembly. The analysis was carried out in two steps. In first step, the PHTM vessel along with blowdown pipe and DRD assembly are modeled using thermal hydraulic code RELAP5/Mod3.2. Since instruments to measure the steam blowdown rate and its enthalpy are not installed in the experimental set up, RELAP5/Mod3.2 code was used to calculate it indirectly. The obtained blowdown data were then used as input for the second step, in which, the ASTEC and in-house CONTRAN codes use the blowdown data for calculating containment model transient parameters like compartment pressure, temperature, wall temperature, junction flow rate etc. Figure 3 represents the flowchart of method of analysis. The PHTM vessel, blowdown pipeline, DRD assembly and the containment model were modelled using RELAP5 code, in which, the entire system is divided into a series of nodes or control volumes connected together via junctions.

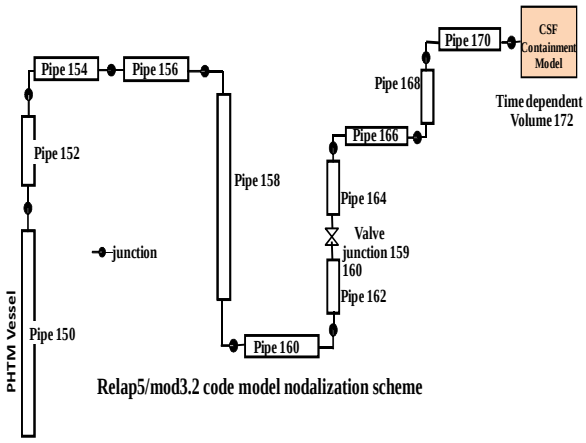

Fig. 3: RELAP5/mod3.2 code model nodalization configuration of scheme represents PHTM vessel and blowdown pipe

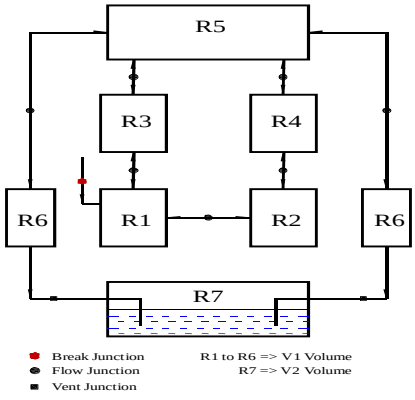

Fig. 4: Seven volume containment model

In containment thermal hydraulics, the containment model is divided into seven compartments (i.e. nodal volumes) and the configuration is shown in figure 4, in which all the rooms in V1 volume is considered as separate compartments and are connected

by flow junctions. R1 & R2 represents the break compartment and from R6, the volume V2 (R7) is connected vent junction represents the vent pipes to suppression pool.PHTM vessel and blowdown pipe dimensions, heating rate, thermo-physical properties of the associated materials and initial water level, initial pressure and temperature in PHTM vessel are the inputs for RELAP5 code.

Geometrical details, initial conditions in the containment and the thermo physical properties of structural materials were some of the inputs. Blowdown mass and energy discharge rate from pressure vessel to containment model is evaluated using RELAP 5/Mod3.2 thermal hydraulic code for the initial vessel operating pressure of 50bar and 75bar. The blowdown mass and energy discharge data were then used as inputs to CONTRAN code.

Results and Discussion

The calculated vessel pressure, temperature and level transients during both 50 bar and 75 bar blowdown using RELAP5/Mod3.2 code is compared with the experimental values are shown in the figures 5 to 10. The measured data and the RELAP5 predictions are matching very closely, however in temperature predictions, the experimental value (i.e. Thermocouple reading) gives the local temperature of the two phase mixture whereas the RELAP prediction gives the average temperature of the particular control volume. Mass blow down rate variations with respect to time for 50 bar and 75 bar blowdown pressures (figures 11 & 14) are evaluated using RELAP code which are the major input for containment thermal hydraulic calculations using CONTRAN code.

The containment pressure and temperature variation, following blowdown, is strongly depends on condensation heat transfer coefficient of steam over concrete wall structures in presence of non-condensables. In this analysis, the correlations for evaluating condensation heat transfer coefficient are diffusion, Tagami and Uchida model [7].Figures 12 and 15 show the containment volume V1 pressure variation with respect to time for 50bar and 75bar blowdown pressures respectively.

The V1 volume pressure variations are evaluated using CONTRAN code for different condensation models (Tagami, Uchida and Diffusion models) and ASTEC code which are then compared with the experimental values. The peak pressure obtained using CONTRAN code for Tagami, Uchida and Diffusion condensation models, for 50 bar blowdown pressure, are 1.08kg/cm^2-g, 0.83kg/cm^2-g and 0.79kg/cm^2-g respectively and ASTEC code predicts 0.83kg/cm^2-g and the peak pressure obtained in experiment is around 0.82kg/cm^2-g.

Similarly the peak pressure obtained using CONTRAN code (for Uchida condensation model) and ASTEC code, for 75 bar blowdown pressure, are 1.01kg/cm^2-g and 1.00kg/cm^2-g respectively and the peak pressure obtained in experiment is 0.986kg/cm^2-g.

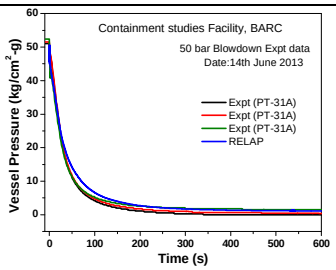

Figure-5: PHTM vessel pressure variation for 50bar blowdown expt.

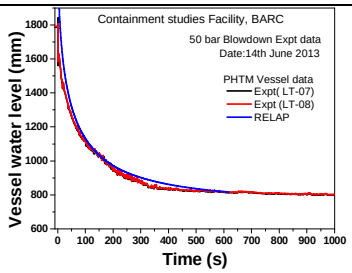

Figure-6: Water level variation in PHTM vessel for 50bar blowdown expt

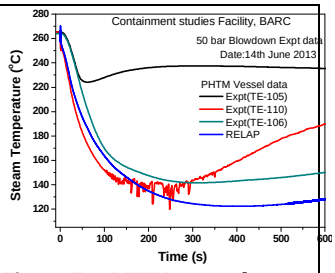

Figure-7: PHTM vessel steam temperature variation for 50bar expt.

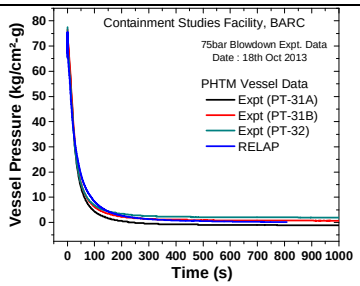

Figure-8: PHTM vessel pressure variation for 75bar blowdown expt.

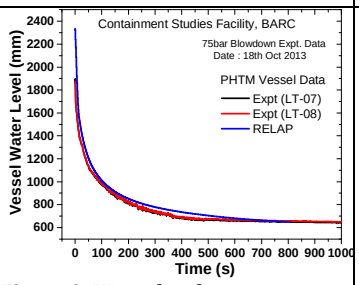

Figure-9: Water level variation in PHTM vessel for 75bar blowdown expt

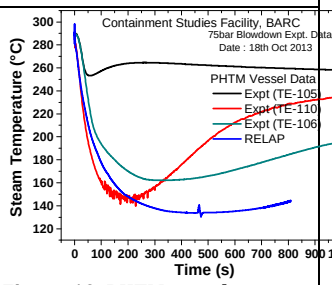

Figure-10: PHTM vessel steam temperature variation for 75bar expt.

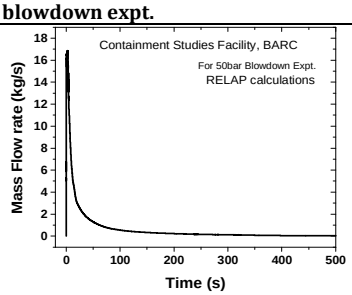

Figure-11: Blowdown discharge rate Vs time. (50bar).

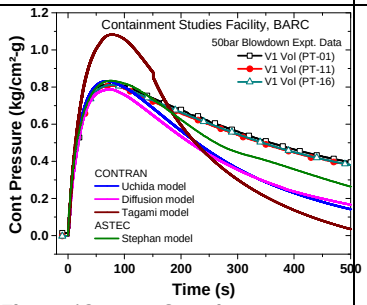

Figure-12: Containment pressure (V1 vol) variation (50bar Expt).

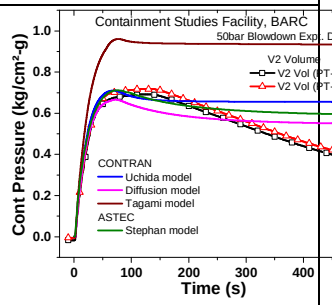

Figure-13: Containment pressure (V2 vol) variation (50bar Expt).

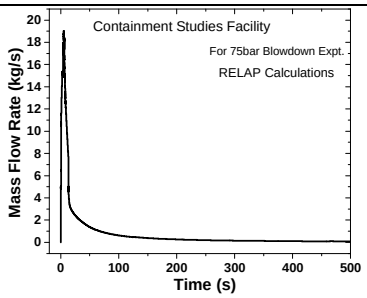

Figure-14: Blowdown discharge rate Vs time. (75bar).

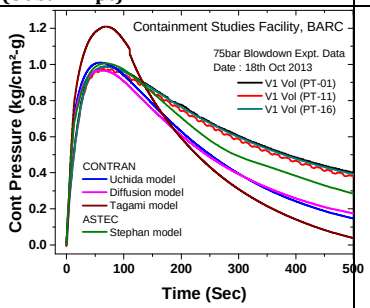

Figure-15: Containment pressure (V1 vol) variation (75bar Expt).

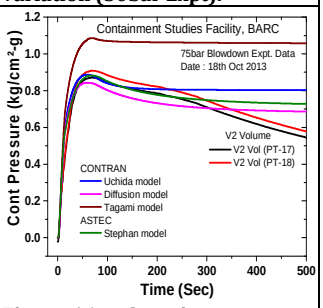

Figure-16: Containment pressure (V2 vol) variation (75bar Expt).

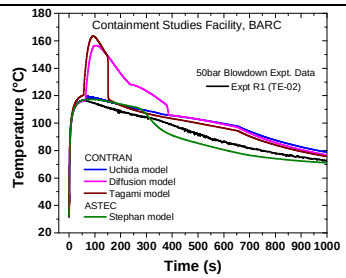

Figure-17: Temperature variation in R1compartment (50bar Expt.).

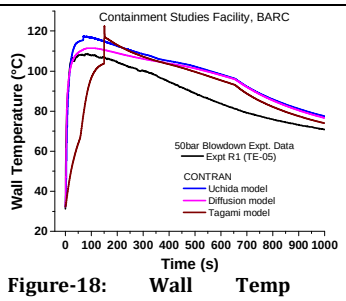

Figure-18: Wall Temp variation ofR1 compartment (50 bar Expt).

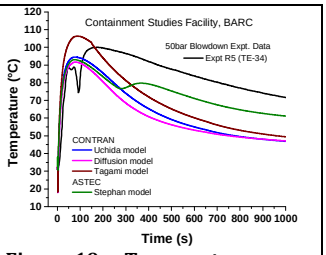

Figure-19: Temperature variation in R5 compartment (for 50 bar Expt).

Figures 13 and 16 show the containment volume V2 pressure variation with respect to time for 50bar and 75bar blowdown pressures respectively. The peak pressure obtained using CONTRAN code (for Tagami, Uchida and Diffusion condensation models) and ASTEC code, for 50 bar blowdown pressure, are 0.96kg/cm²-g, 0.71kg/cm²-g, 0.67kg/cm²-g and 0.71kg/cm²-g respectively and for 75 bar blowdown pressure, are 1.08kg/cm²-g, 0.89kg/cm²-g, 0.84kg/cm²-g and 0.88kg/cm²-g respectively. The peak pressure obtained in experiment for 50bar and 75bar blowdown pressures are 0.72kg/cm²-g and 0.91kg/cm²-g respectively.Figures 17 and 20 show the R1 compartment temperature variation after 50bar and 75bar blowdown pressures respectively.

The peak temperature obtained using CONTRAN code (for Tagami, Uchida and Diffusion condensation models) and ASTEC code, for 50 bar blowdown pressure, are 163.6°C, 119°C, 156.5°C and 117.2°C respectively at R1 compartment and for 75 bar blowdown pressure are 152.1°C, 122°C, 121°C and 120.1°C respectively at R1 compartment. The peak temperature obtained in experiment for 50bar and 75bar blowdown pressures are 116.4°C and 134°C respectively. Similarly the temperature variations in R5 and R7 (V2 volume) compartments are shown in figures 19 and 24 for 50bar blowdown pressure and figures 22 and 27 for 75bar blowdown pressure. Wall temperatures variations by the predictions of code and measured values R1, R5 and R7 compartments are shown in figures 18, 23 & 25 for 50bar blowdown pressure and figures 21, 26 & 28 for 75bar blowdown pressure. Junction flow variation calculated by CONTRAN code and measured values, between the compartments in containment model, are shown in figures 29 to 34 for 50 and 75bar blowdown pressure.

Conclusions

Two blowdown experiments each at 50bar and 75bar were carried out in CSF and excellent repeatability in the measured values have been observed in all the parameters of PHTM vessel and containment model. Mathematical modelling of blowdown part was carried out using RELAP and containment calculations were performed using ASTEC and CONTRAN codes. Measured PHTM vessel pressure, temperature and level transients are consistent with the calculated values using RELAP code. The peak pressure and peak temperature values and its time of occurrence in containment model are close to the calculated values using CONTRAN and ASTEC codes. However, both codes predict early containment depressurization due to condensation but experiment shows slow depressurization. This is

the major issue to be addressed otherwise prediction of radioactivity release, in long term, by codes would be under estimated.

References

[1] Carbajo, J.J., 1981. "Heat transfer coefficients under LOCA conditions in containment buildings", Nucl. Eng. Des. 65, 369–386.
[2] Almenas, K., 1982. "Heat transfer from saturated and superheated atmospheres for containment analysis", Nucl. Eng. Des. 71 (July (1)), 1–14.
[3] Allison, C. M., RELAP/MOD3.2 Code Manual, NUREG/CR-5535, INEL -95/0174, 1995.
[4] J.P. Van Dorsselaere, S. Pignet, C. Seropian, T. Montanelli, P. Giordano, F. Jacq, B. Scwhinges, "Development and assessment of ASTEC code for severe accident simulation", NURETH-11, Avignon, France, October 26, 2005.
[5] Haware, S. K., Markandeya, S. G., Ghosh, A. K., and Venkat Raj,V., January 1994, "Assessment of multi-compartment containment analysis computer code CONTRAN with the experiments on containment response during LOCA conditions", First ISHMT-ASME Heat and Mass Transfer Conference and 12th National Heat and Mass Transfer Conference, BARC, Bombay, India.
[6] Haware, S. K., Ghosh, A. K., Venkat Raj,V., and Kakodkar, A., Oct 1994, "Analysis of CSNI Benchmark test on containment using the code CONTRAN" 3rd Int. Conference on Containment Design and Operation, Vol-2, Toronto, Ontario.
[7] I.Thangamani, Anu Dutta, Vishnu Verma, R.K.Singh and A.K. Ghosh, "Analysis of CSF Model for a Simulated Loss of Coolant Accident Conditions", 20th National and 9th International, ISHMT-ASME Heat and Mass Transfer Conference, paper no. 10HMTC246, January 4-6, 2010, Mumbai, India.

BARC NEWSLETTER
FOUNDER'S DAY SPECIAL ISSUE 2015

NEUTRON DIFFRACTION AND REVERSE MONTE CARLO SIMULATION STUDY OF $M_{1.5}[Cr(CN)_6]\bullet zH_2O$ (M = Fe,Co,Ni) PRUSSIAN BLUE ANALOGUES MOLECULAR MAGNETS

Pramod Bhatt and S. M. Yusuf
Solid State Physics Division

This paper received the Best Poster Award at the 7th India-Singapore Symposium on Experimental Condensed Matter Physics (2014), Mumbai, Feb. 24-26, 2014

Introduction

Molecular magnets of transition metal cyanides, known as Prussian blue analogues (PBAs) form a unique class of materials because of their interesting physical properties and possible wide technological applications. PBAs possess many interesting multifunctional properties, such as magnetic pole inversion, photo-magnetic behavior, zero/ negative thermal expansion, spontaneous magnetization, and slow magnetic relaxation, etc [1, 2]. The possible technological applications of PBAs are in the field of ion sensing [3], hydrogen storage [4], memory storage [5], biomedical [6] and photo switching based electronic devices [7]. The PBAs are commonly represented by a formula $A^{II}_k[B^{III}(CN)_6]_l{\cdot}zH_2O$ where A and B ions are transition metal ions, and are periodically arranged. The crystal structure of such compounds is shown in figure 1. The A ions exhibit high spin state and located at the 4a (0, 0, 0) crystallographic position, whereas B ions have low spin state occupying the 4b (½, ½, ½) crystallographic position in the cubic structure of the compound. The water molecules reside at 24e (x, 0, 0) coordinated as well as interstitial 8c (1/4, 1/4, 1/4) and 32f (x, x, x) sites.

Two types of water molecules (coordinated and non-coordinated) are present in PBA compounds depending on their stoichiometry. When k/l = 1, no $[B(CN)_6]$ vacancies exist, thus only non-coordinated water molecules occupy the interstitial positions. However, when k/l >1, $[B(CN)_6]$ vacancies are present in the compound, and both types of water molecules, (coordinated and non-coordinated) are present. The coordinated water molecules reside at empty nitrogen sites. The stoichiometries and valence modulation of the A and B ions lead to change in their magnetic properties, such as magnetic exchange interaction, ordering temperature T_C, saturation magnetization (M_S), coercive field (H_C) and remanence (M_R) [8-19]. Moreover, doping of alkali ions, and by using external stimuli like light, pressure and heat, one can also modulate the physical properties. The presence of water molecules and $[B^{III}(CN)_6]$ vacancies causes structural disorder in the compounds and thus hinders their magnetic properties [13]. It is, therefore, very important to make a quantitative investigation of the structural disorder in such compounds. In order to study the structural disorder, we have carried out reverse Monte Carlo (RMC) simulation study on the neutron diffraction data of the

$M_{1.5}[Cr(CN)_6]\cdot zH_2O$ (M = Fe, Co and Ni) compounds [13]. All the compounds are synthesized using co-precipitation method at room temperature. The chemicals {M(II)Cl_2 (M = Fe, Ni), Co(II)$(NO_3)_2\cdot 6H_2O$ and $K_3[Cr(CN)_6]$} were reagent grade, and used as received from Sigma-Aldrich. For the synthesis of $M_{1.5}[Cr(CN)_6]\cdot zH_2O$, the required amounts of 0.15 Mol and 0.1 Mol aqueous solutions (10 ml each) of MCl_2 and $K_3[Cr(CN)_6]$, respectively, were prepared and heated separately up to 40°C for 15 min.

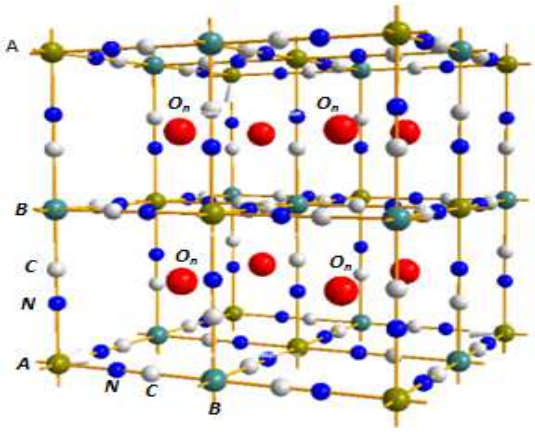

Fig. 1: Crystal structure of $A^{II}_k[B^{III}(CN)_6]_l\cdot zH_2O$ PBAs. The non-coordinated oxygen molecules are denoted by O_n, and reside at the interstitial sites 8*c* (1/4, 1/4, 1/4). Another non- coordinated site 32*f* (x, x, x) is not shown for clarity

The prepared $FeCl_2$ solution is thereafter mixed with the rapidly stirred aqueous solution of $K_3[Cr(CN)_6]$ and heated up to 60°C for 15 min. The precipitate of the required composition was formed. The precipitate was filtered, and washed many times with doubly distilled water and ethanol, and finally allowed to dry in air. The neutron diffraction patterns were recorded at 300 and 6 K using the five linear position-sensitive detectors based neutron powder diffractometer-II (wavelength, λ=1.249 Å) at the Dhruva reactor, Trombay. We have used the RMCPOW program [21-22] to analyze the diffuse scattering in the neutron diffraction data of $M_{1.5}[Cr(CN)_6]\cdot zH_2O$ compounds.

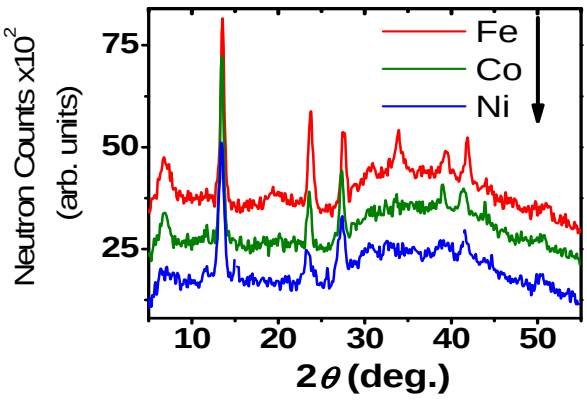

Fig. 2: Measured neutron diffraction patterns of $M_{1.5}[Cr(CN)_6]\cdot zH_2O$ (M= Fe, Co and Ni) PBAs at 300 K

Figure 2 shows neutron diffraction patterns of $M_{1.5}[Cr(CN)_6]\cdot zH_2O$ (M = Fe, Co, Ni) compounds at 300K. The diffraction patterns, for all compounds show well defined crystalline Bragg peaks over the modulated backgrounds suggesting that a large amount of diffuse scattering is present in the neutron diffraction patterns.

In order to determine the atomic positions, and lattice constants of the unit cell for these compounds we have fitted the neutron diffraction patterns using the Rietveld refinement method (FULLPROF program)[23-24]. Figure 3 presents Rietveld refined neutron diffraction patterns of $M_{1.5}[Cr(CN)_6]\cdot zH_2O$ (M = Fe, Co, Ni) compounds at 300 and 6 K. It is evident from the derived results that all compounds are in single crystalline phase with facecentered cubic (*fcc*) structure of space group *Fm3m*. The lattice constants are found to be ~10.18 (9), 10.38 (3), and 10.51 (8) Å for $Fe_{1.5}[Cr(CN)_6]\cdot zH_2O$, $Co_{1.5}[Cr(CN)_6]\cdot zH_2O$ and $Ni_{1.5}[Cr(CN)_6]\cdot zH_2O$ compounds, respectively.

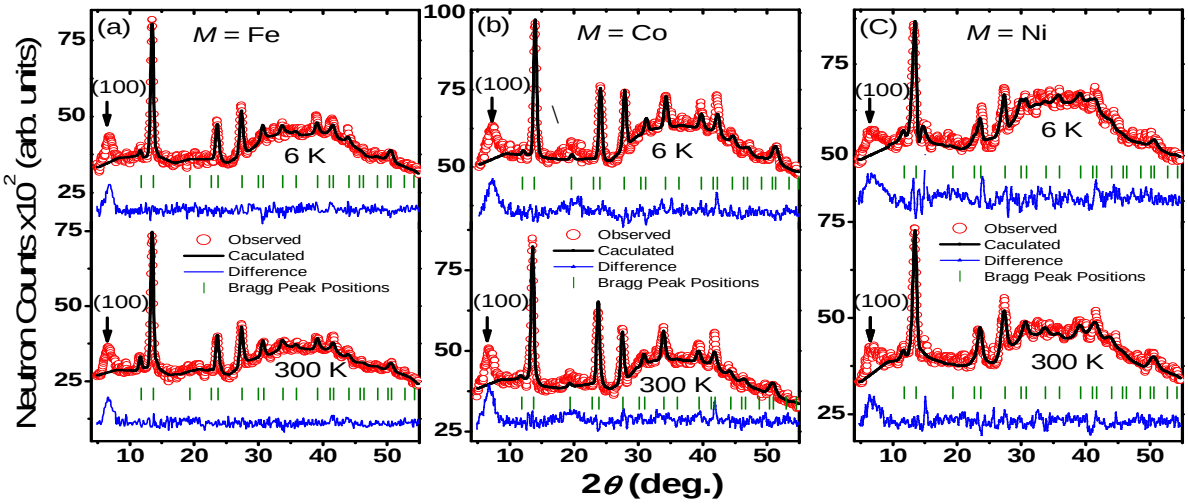

Fig. 3: Rietveld refined neutron diffraction patterns for $M_{1.5}[Cr(CN)_6]\cdot zH_2O$ compounds at 300 and 6 K {where M= Fe (a), Co (b) and Ni (c)}

It is interesting to see that the Bragg peak (100), marked by arrow is forbidden in the fitting of the diffraction patterns with *Fm3m* space group (Figure 3). The forbidden peak could be due to the structural disorder present in the compound. Moreover, the modulated background in the diffraction patterns also suggests a diffuse scattering. Therefore, the presence of diffuse scattering and forbidden Bragg peak (100) infers that there is an inherent structural disorder in the compounds.

It has also been found that the neutron diffraction patterns recorded at 6 K do not show any observable enhancement in the intensity of the fundamental nuclear Bragg peaks (due to the expected magnetic ordering) because the diffuse scattering contribution is substantially larger than the magnetic contribution. Figure 4 shows the RMC fitted neutron diffraction patterns for the $M_{1.5}[Cr(CN)_6]\cdot zH_2O$ compounds.

We have used the RMCPOW program, based on RMC simulations to quantify the diffuse scattering caused by the structural disorder (due to water molecules and $[B^{III}(CN)_6]$ vacancies) present in the compound. Generally Rietveld refinement method, used for refinement of the diffraction patterns, does not have any provision to provide any information of diffuse scattering. Such information is considered as a background by this Rietveld refinement method.

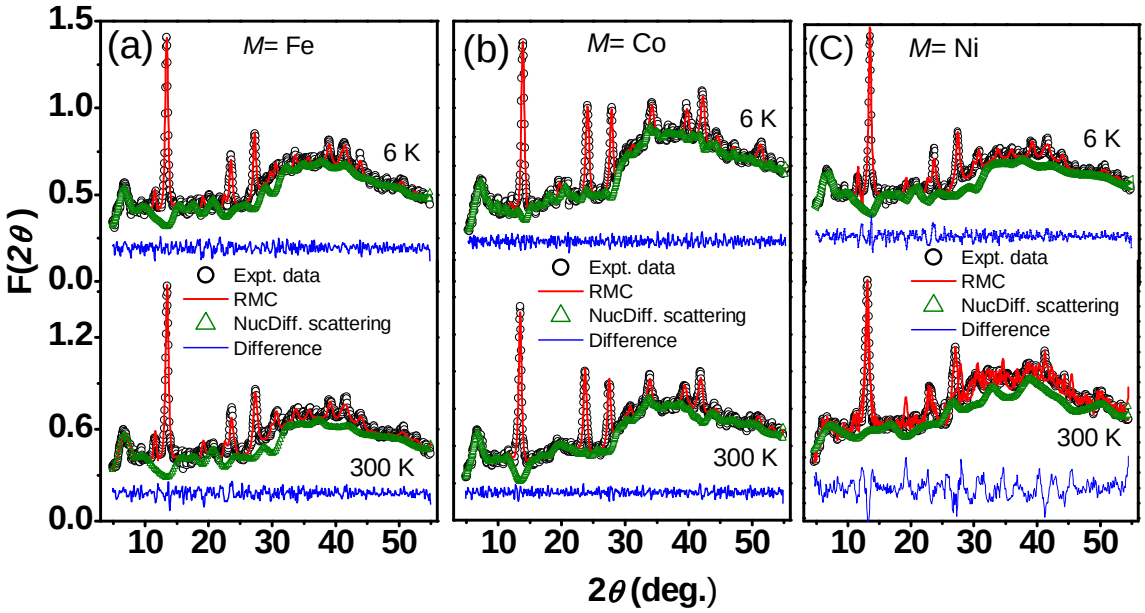

Fig 4: RMC fitted neutron diffraction patterns (300 K and 6 K) of $M_{1.5}[Cr(CN)_6]\cdot zH_2O$ compounds {where *M*= Fe (a), Co (b) and Ni (c)}. *F*(2θ) is the total scattering contribution of neutron diffraction patterns.

Therefore, we have used the RMC simulation method where, the parameters derived from the Rietveld analysis of neutron diffraction pattern have been used as inputs for this program. Figure 4 shows the fitted RMCPOW patterns of neutron diffraction data for all compounds at two different temperatures (300 and 6K). F(2θ), the sum of the scattering amplitudes from all the atoms is plotted as a function of 2θ. It is interesting to note that the forbidden Bragg peak (100) in the Rietveld fitted neutron diffraction patterns (Figure 3) has been fitted well by employing the RMC program for all patterns (Figure 4). This confirms that the Bragg peak (100) is due to inherent structural disorder present in these compounds. In order to further quantify disorder, we have carried out partial pair correlation function {g(r)} analysis for all compounds. The partial pair correlation function is important for finding the local crystal structure of the compound. It gives probability of the centre of an atom at given distance from the center of another atom.

Figure 5 shows the partial pair correlation functions g(r) for the coordinated (O_c), and non-coordinated (O_n) oxygen atoms at 300 K and 6 K for $M_{1.5}[Cr(CN)_6]\cdot zH_2O$

compounds (*M*= Fe, Co and Ni). Based on the input parameters used for the RMCPOW calculation, it is clearly seen that,the coordinated–noncoordinated (O_c–O_n) oxygen molecules are periodically arranged over the range up to ~18 Å in the configuration cell. The partial pair correlation functions obtained after the RMC analysis show confinement of oxygen atoms within the short distance for all compounds. The confinement of oxygen atoms is maximum for the case of $Fe_{1.5}[Cr(CN)_6]\cdot zH_2O$. The maximum number of oxygen pairs lie within a distance ~ 4 Å for all compounds. The confinement of oxygen atoms within the short distance of ~2-4 Å clearly suggests clustering of non-coordinated oxygen (O_n) around the coordinated oxygen (O_c) atoms.

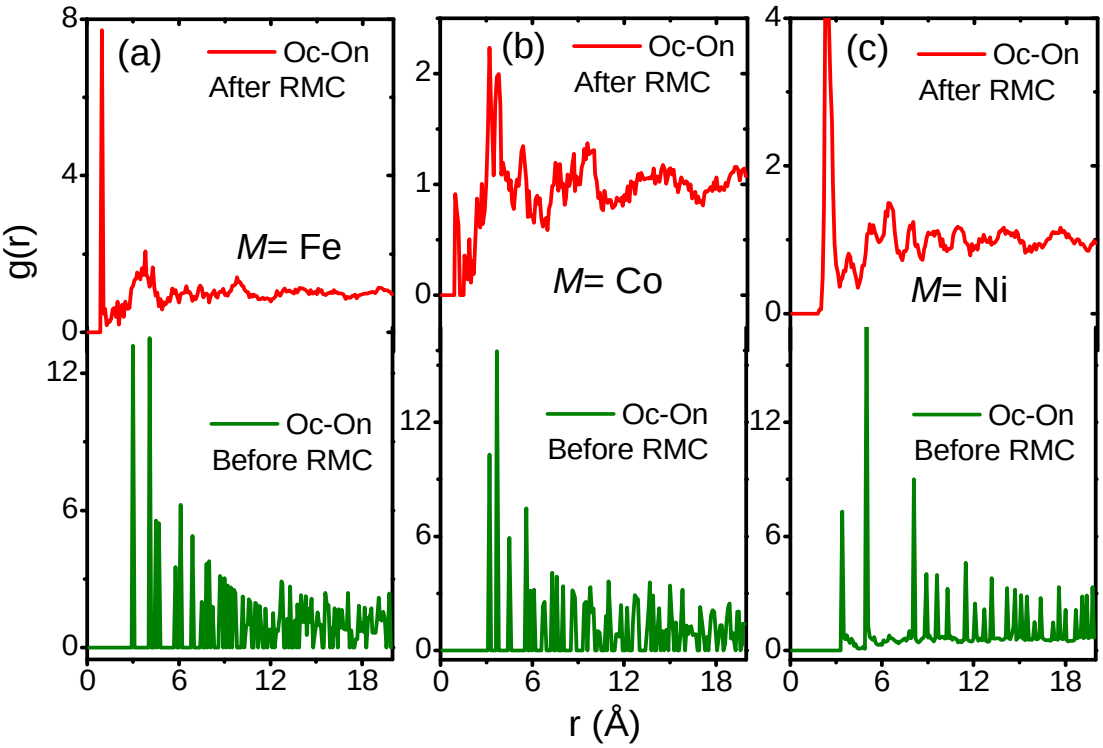

Fig. 5: The oxygen atoms partial pair correlation function g(*r*) with distance *r* at 300 K for $M_{1.5}[Cr(CN)_6]\cdot zH_2O$ compounds {where *M*= Fe (a), Co (b) and Ni (c)}. The O_c—O_n denotes the coordinated—noncoordinated oxygen atoms before and after the RMC simulation

Figure 6 shows distribution of oxygen atoms before and after RMC analysis in a two dimensional plots for all $M_{1.5}[Cr(CN)_6]\cdot zH_2O$ compounds {where *M*= Fe, Co and Ni}. It is seen that, before RMC simulation, the densities of the oxygen atoms are minimum and periodically distributed, shown by the yellow color intensity. However, after RMC analysis, it has been observed that the density of the oxygen atoms is maximum at the center (red color) and it decreases towards the periphery (cyan color) suggesting oxygen clustering present in the compounds.

The oxygen clustering is very prominent for $Fe_{1.5}[Cr(CN)_6]\cdot zH_2O$ compound suggesting a large amount of local structural disorder in the $Fe_{1.5}[Cr(CN)_6]\cdot zH_2O$ compound. Similar oxygen clustering has been observed for the $Co_{1.5}[Cr(CN)_6]\cdot zH_2O$ and

$Ni_{1.5}[Cr(CN)_6]\cdot zH_2O$ compounds however not that prominent as compared to that for the $Fe_{1.5}[Cr(CN)_6]\cdot zH_2O$ compound. In summary, we have carried out detailed structural disorder investigation of Prussian blue analogues $M_{1.5}[Cr(CN)_6]\cdot zH_2O$ (M = Fe, Co and Ni) using a reverse Monte Carlo simulation on the powder neutron diffraction data and propose that, The water molecules and the $[Cr(CN)_6]$ vacancies are mainly responsible for the structural disorder. Moreover, a clustering of the non-coordinated oxygen atoms around the coordinated oxygen atoms has also been ascertained by the RMC analysis.

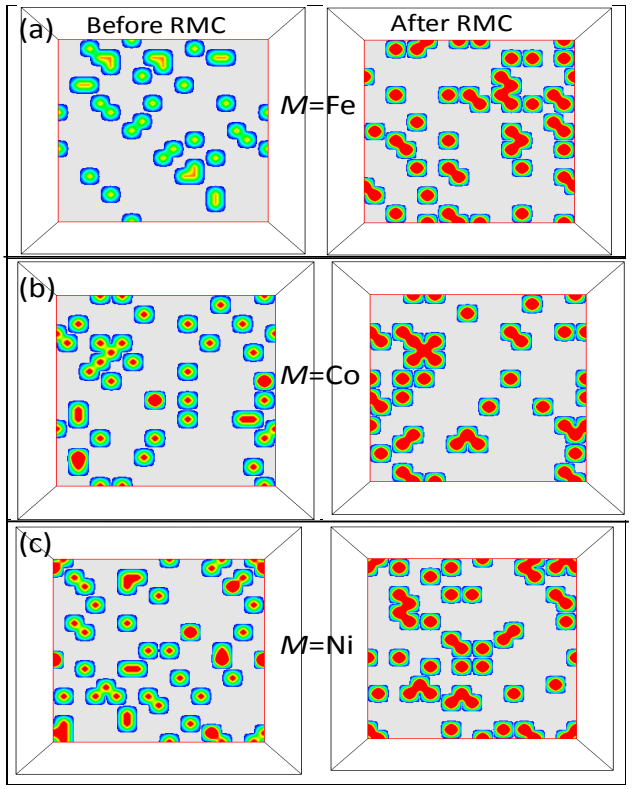

Fig. 6: The distribution and arrangements of oxygen atoms before and after the RMC simulation for $M_{1.5}[Cr(CN)_6]\cdot zH_2O$ {where M= Fe (a), Co (b) and Ni (c)} compounds in 2-d plane. The density of the oxygen atoms is maximum at the center (24*e* crystallographic site), and decreases towards the periphery

The authors would like to thank Dr. A. Das for his help in neutron diffraction measurements.

References

[1] H. Tokoroa, S.-i. Ohkoshi, *Dalton Trans.* **40**, 6825, (2011).
[2] S. I. Ohkoshi, Y. Abe, A. Fujishima, K. Hashimoto, *Phys. Rev. Lett.* **82**, 1285 (1999).
[3] A. Karyakin, Electroanalysis **13**, 813, (2001).

[4] S. S. Kaye, J. R. Long, J. Am. Chem. Soc. **127**, 6506, (2005).
[5] S. Ferlay, T. Mallah, R. Ouahès, P. Veillet & M. Verdaguer Nature, 378, 701 (1995).
[6] F. Ricci, G. Palleschi, Biosens. Bioelectron **21** 389–407 (2005).
[7] M. K. Carpenter and R. S. Conell J. Electrochem. Soc. 137, 2464-2467 (1990).
[8] N. Thakur, S. M. Yusuf, P. L. Paulose, L. Keller, J. Appl. Phys. **111**, 063908 (2012).
[9] N. Thakur, S. M. Yusuf, J. V. Yakhmi, Phys. Chem. Chem. Phys, **12**, 12208, (2010).
[10] P. Bhatt, S. M. Yusuf, M. D. Mukadam and J. V. Yakhmi, J. Appl. Phys. **108**, 023916 (2010)
[11] P. Bhatt, S. M. Yusuf, R. Bhatt, G. Schuetz, J Solid State Electrochem. **17**, 1285 (2013).
[12] P. Bhatt, S. M. Yusuf, R. Bhatt and G. Schuetz, Appl Phys A **109**, 459 (2012).
[13] P. Bhatt, N. Thakur, M. D. Mukadam, S. S. Meena and S. M. Yusuf, J. Phys. Chem. C, **117**, 2676 (2013).
[14] Kumar, S. M. Yusuf, L. Keller, and J. V. Yakhmi, Phys. Rev. Lett. **101**, 207206 (2008).
[15] S. M. Yusuf, A. Kumar, and J. V. Yakhmi, Appl. Phys. Lett. **95**, 182506 (2009).
[16] S. M. Yusuf, N. Thakur, A. Kumar, and J. V. Yakhmi, J. Appl. Phys. **107**, 053902 (2010).
[17] Kumar, S. M. Yusuf, L. Keller, Phys. Rev. B **71**, 054414 (2005).
[18] Kumar, S. M. Yusuf, L. Keller, J. V. Yakhmi, J. K. Srivastava, P.L.Paulose, Phys.Rev.B **75**, 224419 (2007).
[19] Kumar, S. M. Yusuf, Physics Reports **556**, 1-34, (2015).
[20] S. M. Yusuf, N. Thakur, M. Medarde, L. Keller, J. Appl. Phys. **112**, 093903 (2012).
[21] R. L. McGreevy, L. Pusztai, Mol. Simulation **1**, 359-367 (1988).

BARC NEWSLETTER
FOUNDER'S DAY SPECIAL ISSUE 2015

STUDIES ON α-Al_2O_3:C BASED OSL BADGE FOR EYE LENS MONITORING IN INDIA

Munish Kumar[1], M. S. Kulkarni[1], Ratna P.[1], Amit Bhatnagar[2], Sunil Kumar Singh[1], Kamaldeep[2],C. Sunil[3], K. Biju[3], S.D.Sharma[1], S. M. Tripathi[1], N. Gaikwad[1], Sunil K. Yadav[2],A. A. Shanbhag[3], K. P. Muthe[4], D.A.R. Babu[1] and D. N. Sharma[#]

[1]Radiological Physics and Advisory Division, [2]Radiation Safety Systems Division, [3]Health Physics Division, [4]Technical Physics Division, [#]

This paper received the Best Poster Presentation Award at 31th National Conference on Advances in Radiation Measurement Systems and Techniques, Mumbai, March 19-21, 2014

Abstract

A prototype two element eye lens dosimeter badge based on highly sensitive α-Al_2O_3:C optically stimulated luminescence (OSL) phosphor was designed, developed and tested in laboratory and field conditions. The badge consists of a plastic card in which two thin α-Al_2O_3:C OSL discs are placed. The OSL dosimeters when inserted in the plastic card are covered with two different filters made of i). 0.3 mm thick Cu (1st disc) and ii). Teflon having thickness of 1.35 mm (2nd disc). The OSLD badge is useful for monitoring doses from photons and beta particles. In this paper, theoretical results obtained using Monte Carlo calculations on the energy response of α-Al_2O_3:C based disc dosimeters under various filter combinations are presented. In addition, results of experimental studies performed using eye lens dosimeter badge are reported. In view of various advantages like multiple readout facility, less processing time, very good beta response; the OSL based Eye Lens Dosimetry system is likely to be used for monitoring applications in near future.

Introduction

Ionizing radiations *viz.* beta particles, photons (X and gamma rays) and neutrons contribute towards the doses received by the occupational radiation workers. For strongly penetrating radiation (*i.e.* photons >15 keV and neutrons of all energy), the quantity to be measured is personnel dose equivalent $H_p(10)$ whereas for weakly penetrating radiations (*i.e.* beta particles and photons having energy < 15 keV), $H_p(0.07)$ is defined. For monitoring the doses to the eye lens, the quantity personal dose equivalent $H_p(3)$ is defined as the dose equivalent in tissue at 3 mm depth in the phantom. It may be noted that the beta particles and low energy photons (X-rays) are potential contributors towards the dose to the eye lens although the contribution from high energy photons and neutrons is not ruled out. This is due to fact that the beta

particles and low energy photons have smaller range and deposit more dose at 3 mm depth compared to the dose deposition from high energy photons and neutrons at the same depth. Normally, beta particles having $E_{max} \geq 0.7$ MeV contribute towards dose to the eye lens as the range of beta particles with $E_{max} < 0.70$ MeV is < 3 mm. In the recent International Commission on Radiological Protection (ICRP) recommendations, the equivalent dose limit (yearly) for the lens of the eye has been reduced from 150 mSv to 20 mSv (not exceeding 50 mSv in a single year) for occupational workers [1]. In view of this, the eye lens dosimetry is likely to receive more attention than before [2] and the monitoring of eye lens doses may be essential in those situations where probability of receiving higher doses to the eye lens is not ruled out. In the present paper, results of theoretical and experimental studies pertaining to design and development of eye lens dosimeter are presented.

Materials and methods

The choice of the α-Al_2O_3:C detector material was made based on the criteria applicable for selection of OSL phosphor for monitoring applications as well as the ready availability of this phosphor. α-Al_2O_3:C OSL discs having thickness of 0.14 mm (25 mg/cm^2) and diameter ~ 7 mm prepared by sandwiching α-Al_2O_3:C phosphor having grain size >75 - <105 µm between two thin transperent films are studied and explored for their use in the design of eye lens dosimeters.

a. Theoretical studies

i) Photon energy response studies for bare α-Al_2O_3:C based disc dosimeters

Monte Carlo simulations were carried out to obtain the relative dose response of the α-Al_2O_3:C detector with respect to the dose to tissue using FLUKA Monte Carlo code [3-4]. The dose response of the Al_2O_3 detector was estimated by simulating mono-energetic parallel photon beams of varying energies; 10 keV to 1.5 MeV falling on the bare detector. The statistical error in the simulations was within ± 3%. The results are shown in (Fig. 1a)

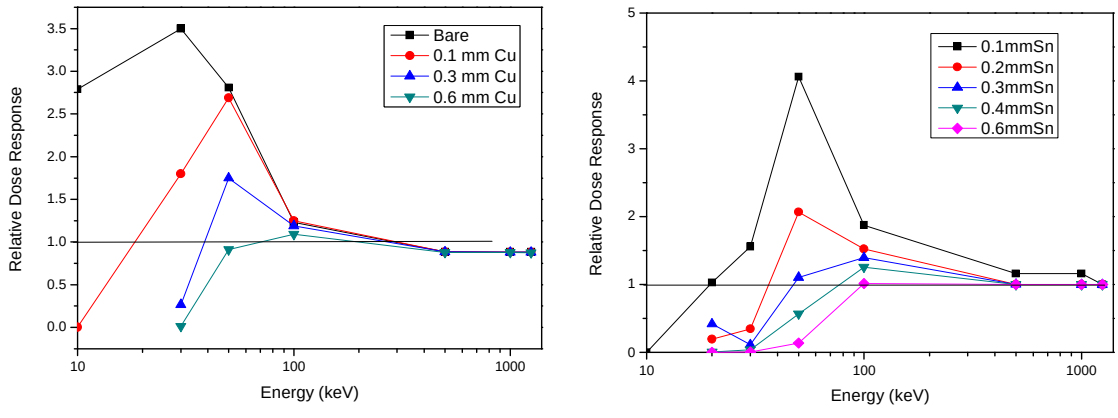

a **b**

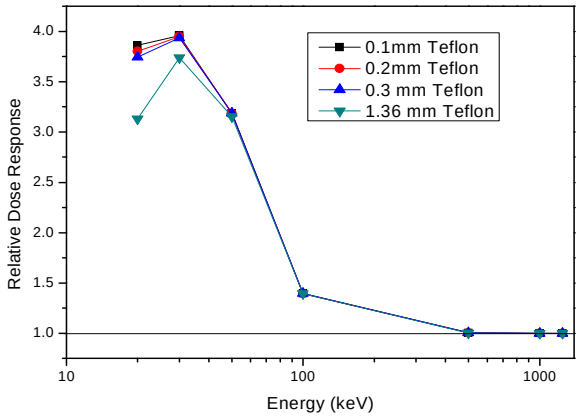

c

Fig. 1: The relative energy response of α-Al_2O_3 detector with respect to water as afunction of incident photon energy for various thicknesses of copper filter(a), tin filter (b) & Teflonfilter (c). The energy response of bare α-Al_2O_3 disc isalso shown

ii) Photon energy response studies for α-Al_2O_3:C OSL discs under energy compensation filters

Studies were performed by evaluating the response of α-Al_2O_3:C based OSLD's under different thickness of aluminum (Al), copper (Cu), tin (Sn) and Teflon. The metal filters were selected so as to correct the over-response of the α-Al_2O_3:C based OSLD's especially for lower energy photons. Studies were also performed to study the response of α-Al_2O_3:C based OSLD's under various thicknesses of Teflon as a buildup material. Results are shown in Figs. 1a-1c [5].

b. Experimental studies

i) Energy response studies

Energy response studies for α-Al_2O_3:C based OSL disc dosimeters (bare & under filters) were performed for x, gamma and beta radiations. Irradiations were performed using X-ray machine (model YXLON MG325) in narrow beam geometry at a distance of 2 m from focal spot of X-rays. The dosimeters were kept at a height of 1.5 m from ground to reduce the scattering effect. Narrow beams used in above study were N-15, N-40, N-80, N-100, N-120, N-150, N-200 and N-250 and had average energy ~10.7 keV, 33 keV, 63 keV, 82 keV, 100 keV, 123 keV, 167 keV and 213 keV respectively.
In addition, the irradiations were also carried out by using ^{241}Am (60 keV), ^{137}Cs (662 keV) and ^{60}Co (1.25 MeV) photon sources. A build-up of 3 mm and 5 mm was provided using Perspex sheets for ^{137}Cs (662 keV) and ^{60}Co (1.25 MeV) photon sources, respectively, for achieving electronic equilibrium. Studies were also performed with ^{90}Sr/^{90}Y beta source. Results of the experimental study are shown in (Fig. 2 a) whereas in (Fig. 2b), the ratio of the response of OSL disc under Teflon to Cu filter is shown.

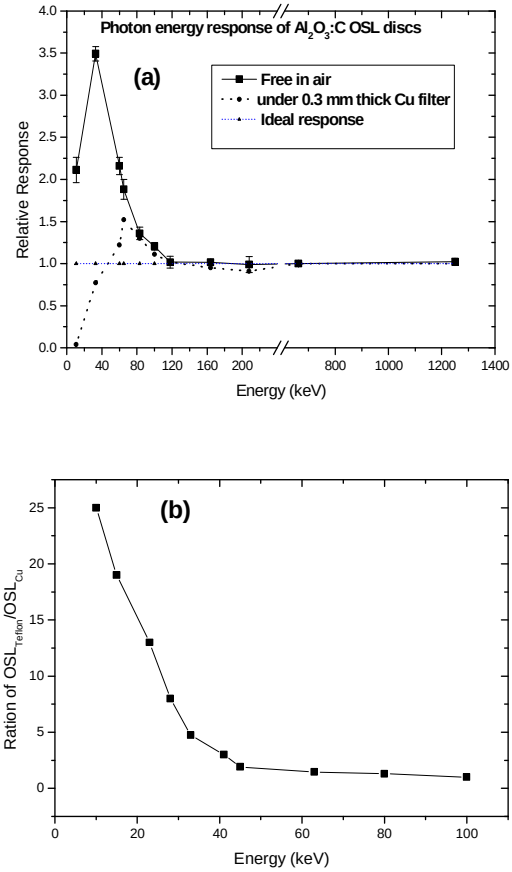

Fig. 2: (a) Experimental energy response (free in air) of the α-Al_2O_3:C OSL discs for photons. The response (free in air) of α-Al_2O_3:C OSL discs for photons under 0.3 mm thick Cu filter is also shown. (b) Ratio of OSL response of α-Al_2O_3:C OSL discs with 1.35 mm Teflon filter to that under 0.3 mm Cu filter

For the readout of OSLD cards, the OSL reader system was operated in the continuous wave OSL (CW-OSL) mode at 20 mW cm^{-2} with blue (470 nm) light stimulation. Two high power LEDs (blue, ~470 nm) placed at an angle of 45° with respect to the sample holder are used as stimulation light source in the reader system. A GG-435 colour glass filter was fixed in front of the blue LEDs to cut off the stimulation wavelengths below 435 nm. An UG-1 colour glass filter is placed in front of the PMT (Electron Tube, 9125B) to prevent the scattered stimulating light from reaching the PMT [6].

ii) MMD and mutliple readout studies

The background contribution arising due to the dark current, scattered stimulation light and its dependence on stimulation power was accounted for the OSLD badge reader system prior to the evaluation of MMD for eye lens dosimeter badge. In addition the

possibility of multiple readout including the dependence of MMD on readout number was explored. Results are shown in (Figs. 3a-3c)[7].

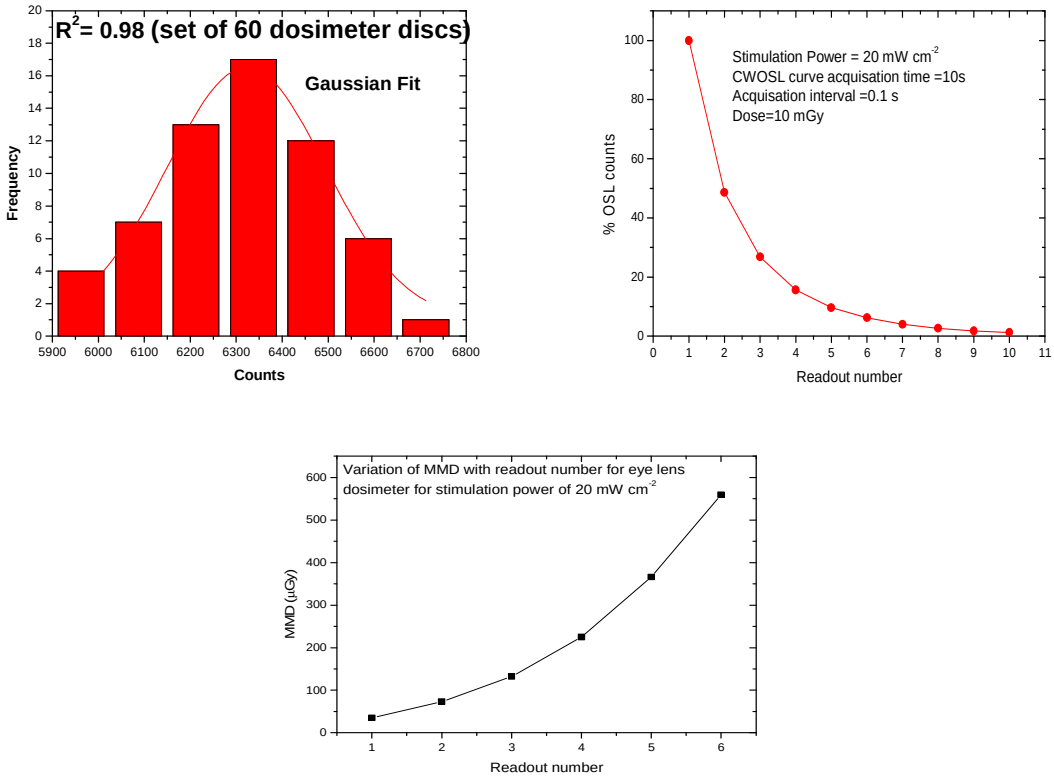

Fig. 3: (a) Variation of background signal/counts, (b) Variation of OSL counts with readout number & (c) Variation of MMD with the readout number for α- Al_2O_3:C dosimeter discs

Results and discussion

It may be noted from theoretical and experimental studies that α-Al_2O_3:C OSL disc exhibits maximum response of 3.49 at photon energy of ~33 keV whereas for photon energies beyond 80 keV, the response is nearly independent of photon energy.

Fig. 4: (a) Two element α-Al_2O_3:C dosimeter card, (b) eye lens dosimeter badge & (c) Proposed eye lens dosimetry badge showing the two element OSL card along with plastic cassette and energy compensating filters

From theoretical and experimental studies, Cu and Teflon having thickness of 0.3 mm and 1.35 mm were found to be optimized filter thicknesses in the design of two element eye lens dosimeter. The designed card, cassette and badge is shown in Fig. 4. The ratio of the response of OSL under Teflon to Cu filter is a measure of the average energy of the photons and the ratio varies from 25 at 10.7 keV to 1.3 at 80 keV. Beyond 80 keV, the ratio of the response of OSL under Teflon to Cu filter is < 1.3 and energy discrimination is not possible.

The readout of the OSL disc below the Teflon filter can be directly correlated to $H_p(3)$ for photons (> 80 keV) and same holds true for beta particles having maximum beta energy beyond 0.7 MeV. However, for photon energy (< 80 keV), the response correction is required which is obtained by using the ratio of the readout of the disc under Teflon filter to that under metal filter. It is also worth mentioning that water filled cylindrical phantom having diameter and height of 20 cm each was used for calibration and measurement of $H_p(3)$. The MMD was found to be ~35 µSv. It was found that the MMD increases with the readout number and it may be possible to perform multiple readouts up to 5-10 times for doses incurred up to 10 mGy.

Conclusions

Two element eye lens dosimeter badge using α-Al_2O_3:C phosphor has been designed and developed and is useful for monitoring doses from photons and beta particles in terms of $H_p(3)$. The badge is capable of measuring photons from 10 keV-1.25 MeV and beta particles from 0.8 MeV-3.54 MeV. The MMD using the eye lens dosimeter badge was found to be ~35 µSv. The satisfactory performance of the two element eye lens dosimeter badge along with its attractive features like multiple readout, less processing time, very good beta response uniquely position it for monitoring the eye lens dose.

Acknowledgements

The authors would like to thank Dr. K. S. Pradeepkumar, Associate Director, HS&EG & Head, RSSD, BARC for valuable suggestions. Authors are also thankful to Health Physicists/RSO's of Dhruva Reactor - RMC – RMD Facilities; BARC & RRCAT, Indore, TMH, Breach Candy, Jaslok, Hinduja, Nanawati, Holy Spirit and Jupiter hospitals for their valuable cooperation during field trials.

References

[1] International Commission on Radiological Protection (ICRP), *Statement on tissue reactions*, ICRP 4825-3093-1464, April 2011.
[2] Dietze G., Radiation Protection in Nuclear Medicine (*Edited by:* Mattsson S. and Hoeschen C.), Springer, 33, 2013.
[3] Fasso, A. Ferrari, A.Ranft, J. Sala, P.R. CERN-2005-10. INFN/ TC_05/11, SLAC-R-773 (2005).

[4] Battistoni, G. Muraro, S. Sala, P.R. Cerutti, F. Ferrari, A. Roesler, S. Fasso, A. Ranft, J., AIP Conf. Proc. 896, 31-49 (2007).
[5] Ratna P., Gaonkar U. P., More Vinay and Kulkarni M. S., Proc. IARPNC-2012, Mangalore University, March 15-17, 2012.
[6] M. S. Kulkarni, Munish Kumar, P. Ratna, K. P. Muthe *et al*., *Rad. Prot. and Environ.*, 37 (2014) 106.
[7] Munish Kumar, M. S. Kulkarni, Ratna P., A. Bhatnagar *et al*., *Rad. Prot. and Environ.*, 37 (2014) 89.

BARC NEWSLETTER
FOUNDER'S DAY SPECIAL ISSUE 2015

LOW RESOLUTION SYBR GREEN DYE BASED MELT PROFILING FOR ANALYSIS OF STMS AND SCAR MARKERS IN PLANTS

G. Vishwakarma[1], R.P. Sanyal[2], A. Saini[2], N. Jawali[2], S.G. Bhagwat[1] and B. K. Das[1*]
[1]Nuclear Agriculture and Biotechnology Division,
[2]Molecular Biology Division

This paper received the Best Poster Award at the National Symposium on ' Crop Improvement for Inclusive Sustainable Development', Ludhiana, Nov. 7-9, 2014

Introduction

Wheat is the third most important cereal crop globally after maize and rice, and second most important in India after rice. It contributes maximum calories and protein to world diet than any other crop (1). Wheat breeding has improved significantly and the modern day wheat cultivars are far better in terms of yield and quality compared to their ancestors. Wheat breeding has several challenges ahead like durable resistance to diseases, better quality grain, enhanced tolerance to changing climate and higher yields in marginal and stressed land (2). Such a scenario has led wheat breeders to shift towards new molecular biology and genomics tools to assist in their breeding programs.

DNA based molecular markers are one of the most widely used genomic tools by wheat researchers for screening large populations in a very short time (3). DNA markers give researchers the advantage of screening the germplasm even in the absence of a phenotypic screening facility or when phenotypic screening is laborious and time consuming. Extensive research has been carried out in the area of molecular markers and as a result different types of molecular markers have been developed for wheat and other important crops. Sequence Characterized Amplified Regions (SCARs) and Sequence Tagged Microsatellite Sites (STMS) are two of the most popular DNA markers used in plant breeding (4). Both being single locus marker, have the advantage of easy and convenient screening.

SCAR markers are very convenient for ascertaining presence or absence of a particular trait and hence, have found wide spread use globally. SCAR markers are used in large breeding projects for gene pyramiding, characterization of alien translocations, linkage mapping and many other applications (5). Similarly, STMS markers are also very useful as they have added advantage of being co-dominant in nature and highly polymorphic within a species. STMS markers have vast areas of application like marker assisted selection, linkage analysis, phylogenetic studies, DNA fingerprinting etc (6).Both SCAR and STMS markers are usually screened using gel based analytical methods based on agarose or polyacrylamide gel electrophoresis. However, such methods are cumbersome and laborious, hence can be used

only for few samples (7). With advancement in molecular biology and genomics new technologies like capillary electrophoresis, automated bio-analyzer systems and fluorescence based detection, have been suggested as a replacement of regular gel-based methods. However, currently the cost and infrastructure involved in these methods is very high and not suitable for breeders. Thus simple, time saving and cost effective methods as an alternate to gel-based screening are highly desirable.

Fluorescent DNA binding dye have been extensively used in molecular biology for nucleic acid studies in areas of expression analysis, transgenic detection, nucleic acid characterization (GC content) etc. SYBR Green dye in particular is widely used in PCR based assays to monitor reaction progress and product specificity (8). Melt curve assay are DNA dissociation studies done to characterize DNA for its GC content. Melt curve assays using fluorescent dyes drastically increase the resolution of amplicon detection, which has reached today even up to single base pair with improved dyes. Hence, dye based DNA melting curve analysis can be used for ascertaining presence or absence of a specific amplicon in a gel-free manner. In this study, we demonstrated utility of SYBR Green dye based melt curve analysis for analyzing SCAR and STMS markers in wheat, in a rapid and gel-free manner.

Material and Methods

Seven SCAR markers viz. *Sr24*, *Sr26*, *Sr31*$^{+}$, *Sr31*$^{-}$, *Pina*, *Pinb* and *Glu-D1d* related to stem rust resistance and quality traits of wheat were screened using SYBR Green based melting curve analysis in Indian wheat varieties (Table 1).

Table 1: List of wheat genotypes used for screening SCAR markers

S. No.	Gene/ Locus	Genotypes
1	*Sr24*	Vaishali, Vidisha Kalyan Sona[a]
2	*Sr26*	Kite, Flinder, Harrier, King, Jabiru, Takari Kalyan Sona[a]
3	*Sr31*	PBW343 Kalyan Sona[a]
4	*Pina*[b]	Agra Local, Sonalika, Flinder, Kite, Harrier, Jabiru
5	*Pinb*[b]	HUW206, Kanchan, PBW343, MACS2496, Vidisha, Kalyan Sona[a]
6	*Glu-D1d*	PBW343, Kalyan Sona[a]

([a]: non-carriers of respective genes; [b]: *Pina* carriers were used as non-carriers of *Pinb* and vice versa)

In addition, 45 STMS markers belonging to A, B and D genome of *Triticum aestivum* L. were analyzed in 12 wheat genotypes (Kalyansona-1, Sonalika, C-306, TWM-89, Vaishali, Kite, Flinder, HW-2021, NIAW-917, PBW-343, Chinese Spring, LWH) using SYBR Green based melt curve assay.All the markers were PCR amplified on Mastercycler ep Realplex^4 PCR machine (Eppendorf, Germany) using previously reported cycling conditions. Briefly, PCR mix consisted of 2-5 picomoles of each primer, 250 µM of each dNTP, 50-100 ng of genomic DNA, 2.5 µl of 10X buffer (15 mM Tris-Cl pH 9.0, 50 mM KCl, 0.01% gelatin) and 1.0 unit of *Taq* DNA polymerase along with SYBR green dye at 1X final concentration. Post PCR melting curve analysis was performed with a ramp rate of 3.5°C min^{-1}. The raw melting curve analysis data was converted to the negative first derivative as a function of temperature to identify maximum intensity changes (represented as peak curves) using the Eppendorf Mastercycler ep realplex software (Ver 2.2).

Results

SCAR and STMS markers could be successfully amplified in PCR reactions with sizes matching with reported sizes (Fig. 1).

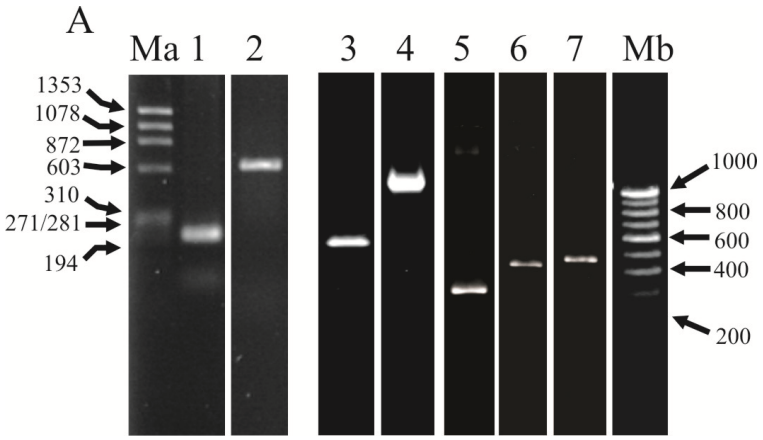

Fig. 1: PCR amplified SCAR markers from representative wheat genotypes analzyed on agarose gel: Lane 1: *Sr26* (207 bp), Lane 2: *Sr24* (607 bp), Lane 3: *Sr31*$^+$ (576 bp, indicates presence of *Sr31* gene), Lane 4: *Sr31*$^-$ (~1100 bp, indicates absence of *Sr31* gene), Lane 5: *Pina* (330 bp), Lane 6: *Pinb* (447 bp), Lane 7: *Glu-D1d* (478 bp). Lane Ma indicates DNA marker ØX174 DNA (*Hae*III digest) and Mb indicates 100 bp DNA ladder

Amplification of these markers in the presence of SYBR Green dye was optimized and clean amplification were obtained for each marker. Unique melt curve profiles for individual SCAR and STMS markers were generated. SCAR markers had following Tm *Sr26* (207 bp, T_m: ~81°C), *Sr24* (607 bp; T_m: ~85°C), *Sr31*$^+$ (576 bp, T_m: ~90°C), *Sr31*$^-$ (~ 1100 bp, T_m: ~83°C), *Pina* (~330 bp, ~92°C), *Pinb* (~447 bp, ~92°C), and *Glu-D1d* (~478 bp, ~93°C) (Fig. 2, A-D). STMS markers showed clean amplification and could be screened for presence or absence in all the cases. In some examples STMS markers alleles could be distinguished based on melting curve profile.

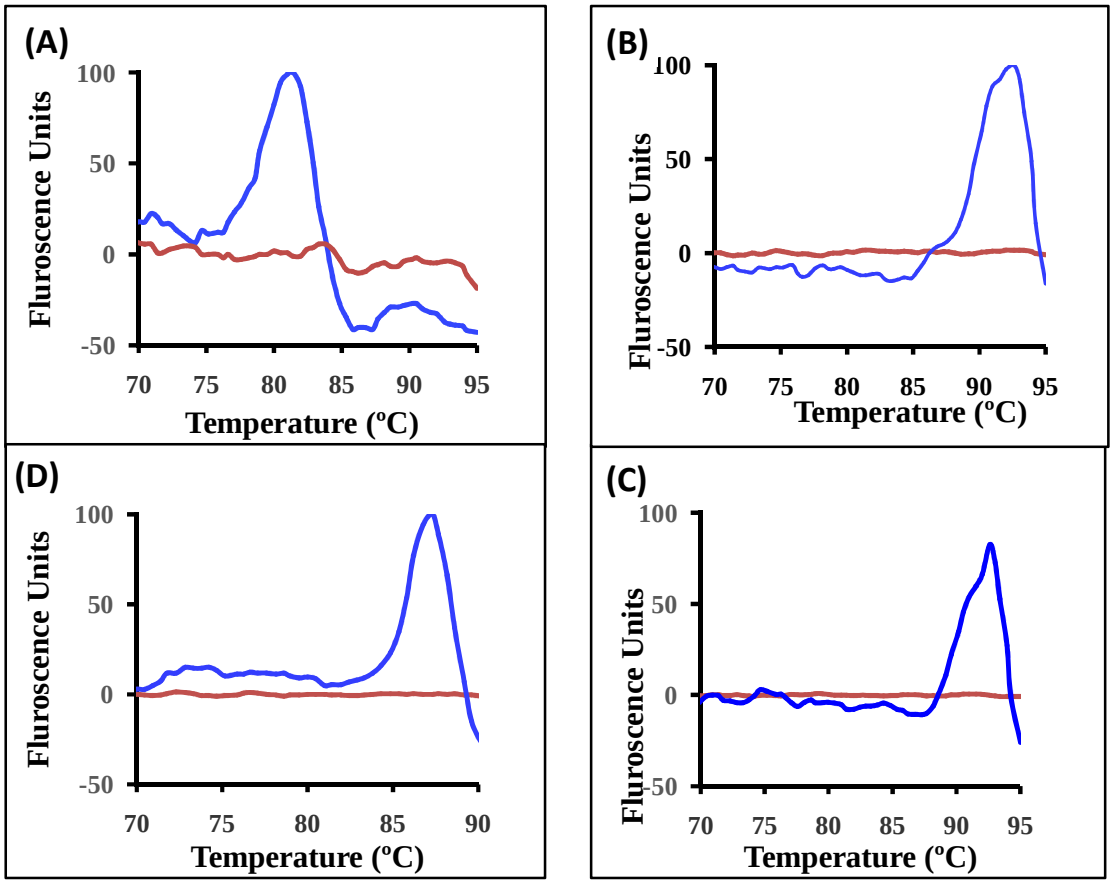

Fig. 2: SYBR Green dye based melt-profiles of SCAR markers linked to the following genes: (A) *Sr26*, (B) *Sr31*$^{+}$, (C) *Pina*, and (D) *Glu-D1d*. Blue profiles indicate presence of a marker while red profiles indicate absence

Discussion

DNA based molecular markers are extremely useful in Marker Assisted Selection (MAS) especially in case of traits where phenotype based screening is not possible or very cumbersome. Single locus markers such as SCAR and STMS are convenient to use and hence, widely used for MAS. However, both SCAR and STMS markers are routinely screened using gel (agarose and polyacrylamide gel) based electrophoresis methods. Gel based methods limit the throughput and ease of screening especially in case of large experimental population (9). SYBR Green based melt curve analysis provides an alternative method for quick and cost effective screening of single locus markers without modifications in existing standard protocols and without use of additional proprietary kits.SYBR Green is a fluorescent DNA binding dye widely used in quantitative PCR experiments for monitoring reaction progression and amplicon specificity using melting (dissociation) curve analysis (10). In MAS, usually large number of population has to be screened for specific locus using

SCAR, STMS or other markers. Gel-free and economical methods for screening large populations are highly desirable.

SYBR Green incorporated in regular PCR mix could amplify and detect specific amplicons in the current study. All seven SCAR markers yielded clean melt profiles the carrier and non-carrier genotypes could be screened without ambiguity.Similarly, around 45 STMS markers also yielded clean melt profiles. STMS melt profiles could easily distinguish the presence or absence of the allele and to some extent even allelic variants of the locus. The method has an advantage over other methods since screening was done using regular PCR reagents and previously reported primers and conditions.We have also optimized multiplex detection of two SCAR markers, two STMS markers, and two different alleles of same STMS markers.

Amplicons having very distinct melting temperature (Tm) could be easily detected by multiplexing on the basis of melt curve assay. However, SYBR Green being a low resolution dye cannot discriminate clearly amplicons with very close Tm, and hence for such cases other more sensitive methods like HRM must be used. Multiplex based screening of these markers drastically reduces the cost and time involved in screening and reduces the work load.The SYBR Green based melt curve approach was found to be ~ 20% cheaper than agarose gel based method which is routinely used for marker detection. In addition, it is much cheaper than other commercially available technologies like capillary electrophoresis, probe based SNP typing, and HRM curve based methods. Hence, SYBR Green dye based low resolution melt curve assay can provide an alternative to regularly used gel based methods.

References

1. http://faostat.fao.org
2. Chatrath R, Mishra B, Ferrara GO, Singh SK, Joshi AK (2007) Challenges to wheat production in South Asia, Euphytica 157(3): 447-456.
3. Gupta PK, Rustgi S, Sharma S, Singh R, Kumar N, Balyan HS (2003) Transferable EST-SSR markers for the study of polymorphism and genetic diversity in bread wheat. Mol Gen Genomics 270: 315-323.
4. Mienie CM, and Pretorius AE (2013) Application of marker-assisted selection for ahFAD2A and ahFAD2B genes governing the high-oleic acid trait in South African groundnut cultivars (*Arachis hypogaea* L .). African J. Biotechnol. 12(27): 4283-4289.
5. Gupta PK, Langridge P and Mir RR (2009) Marker-assisted wheat breeding: present status and future possibilities. Mol. Breed. 26(2): 145-161.
6. Lalitha Sunil Kumar, 2009/1999) DNA markers in plant improvement: An overview, Biotechnology Advances, 17: 143-182.
7. Collard BC and Mackill DJ (2008) Marker-assisted selection: an approach for precision plant breeding in the twenty-first century, Phil. Trans. R. Soc. B, 363, 557-572.
8. Mendes RE, Kiyota KA, Monteiro J, Castanheira M, Andrade SS, Gales AC, Pignatari AC, Tufik S (2007) Rapid detection and identification of metallo-beta-lactamase-encoding genes by multiplex real-time PCR assay and melt curve analysis. J. of Clinical Microbiology, 45(2) 544-547.

9. Ma W, Zhang Wand Gale KR (2003) Multiplex-PCR typing of high molecular weight glutenin alleles in wheat. Euphytica 134: 51-60.
10. Varga, A., and D. James. 2006. Real-time RT-PCR and SYBR Green I melting curve analysis for the identification of Plum pox virus strains C, EA, and W: effect of amplicon size, melt rate, and dye translocation. J. Virol. Methods 132(1-2): 146-153.

BARC NEWSLETTER
FOUNDER'S DAY SPECIAL ISSUE 2015

RADIATION CROSSLINKED GRAPHENE/POLYMER NANOCOMPOSITES FOR CONTROLLED OROTRANSMUCOSAL DELIVERY OF DOXYCYCLINE

Jhimli Paul Guin, C. V. Chaudhari, K. A. Dubey, Y. K. Bhardwaj, L. Varshney
Radiation Technology Development Division

This paper received the Best Poster Award (Second Prize) at the DAE-BRNS 5th Interdisciplinary Symposium on Materials Chemistry, Mumbai, Dec.9-13, 2014

Abstract

This study reports development of novel graphene reinforced interpenetrating networks of carboxymethyl cellulose (CMC) and polyvilyl alcohol (PVA) for controlled drug release applications. The nanocomposites were made through solution blending and sonication assisted dispersion technique. Different crosslinking densities were imparted in nanocomposites using different doses of high energy radiation. The elastic modulus of the polymer composites increased by four folds with increasing the graphene content from 1 wt% to 3 wt%; however, no significant change in the elastic modulus was observed on further increase in graphene concentration. Mass uptake kinetics changed significantly; though, the transport mechanism was found to be anomalous in all the nanocomposites with increase in radiation dose. With the addition of 3 wt% graphene, there was a marginal increase in the time for 60% drug release (T_{60}). However, T_{60} increased by 100 % with an increase in radiation dose from 25 kGy to 150 kGy, suggesting suitability of these matrices in controlled drug release applications.

Introduction

Controlled and targeted drug delivery is a major challenge faced in achieving therapeutic success, greatly affecting therapeutic efficacy and patient compliance [1-2]. Polymers, both synthetic and natural, are extensively explored for such applications, and constant drug release. Graphene, due to its exceptional properties, is actively researched for modulating drug release kinetics as well as for matrix reinforcement [3-4]. Polyvinyl alcohol (PVA) is a hydrophilic polymer having good water swelling, mechanical and physical characteristics [5]. It has been extensively explored for different pharmaceutical applications. Carboxymethyl cellulose (CMC), on the other hand, is a derivative of cellulose; it has excellent water uptake and mucoadhesive characteristics. PVA/CMC blends therefore can be used to tailor different drug release and mucoadhesive behvaiour. High energy radiation is an additive free tool to crosslink different polymer matrices [6-7].It is clean, room temperature and environment friendly method. PVA and CMC both can be crosslinked by high energy radiation and are explored for different biomedical applications [6].This study reports for the first time the effectiveness of gamma radiation synthesized PVA/CMC/graphene interpenetrating

polymer nanocomposites for the controlled release of an antibiotic drug, doxycline.Preliminary efforts were made to analyze the effect of graphene content and radiation dose on the release behvaiour of doxycline. Mechanical and swelling behvaiour of matrices were also investigated to understand effect of graphene on the matrix reinforcement which is expected to help in the development of the mucoadhesive buccal drug delivery systems.

Material and methods

CMC (Mol. weight = 2,50,000 D) and PVA (Mol. weight = 85,000 D) were procured from M/s SD Fine India. Doxycycline and graphene powder (purity 95%, sheet thickness: 3-6 nm, average surface area: >200 m^2/gm, aspect ratio: 70, specific gravity: 2 gm/cc) were purchased from Aldrich and Otto Chemie Pvt Ltd, Mumbai, India, respectively. Double distilled water was used for preparing solution and swelling studies.

Synthesis of PVA/CMC nanocomposites

10 wt% and 5 wt% PVA and CMC aqueous solutions were prepared in double distilled water at 80 ^{o}C. Different fractions of graphene were incorporated in PVA/CMC solution mixture. The homogeneous graphene-polymer mixture was transferred to petri dishes, and exposed for different gamma radiation doses using a gamma chamber 5000 (GC-5000) under inert atmosphere to yield crosslinked polymer nanocomposites. The dose rate of the GC was ascertained to be 1.2 kGy/h by Fricke dosimetry prior to irradiation.

Physico-mechanical properties

The thickness of the samples were determined to the nearest of 0.01 mm. The tensile strength and elongation at break of the sample of thickness 0.1 mm were measured using a universal testing machine supplied by M/s HEMETEK, Mumbai, INDIA at crosshead speed of 10 mm/min at room temperature.

Drug release studies

The PVA/CMC nanocomposites of known dried weight were immersed in known volume of 10 mM Doxycycline solutions for 24 h with continuous stirring, until equilibrium was reached. The samples were dried and drug release kinetics from those was followed spectrophotometrically using a calibration curve for doxycycline. Available standard procedure was followed for buffer solution, calibration curves, drug loading and drug release kinetics measurements.

Results and discussion

Effect of graphene on elastic modulus

Figure 1 shows the effect of graphene on the elastic modulus of PVA/CMC blends. Elastic modulus increased with the addition of graphene up to 3 wt% and there was no

further increase in the elastic modulus at 5wt% graphene loading. In the present system, there was fourfold increase in the elastic modulus with an increase of graphene content 1 wt% to 3 wt% graphene. This suggests significant reinforcement of the matrix; though, a slight decrease in modulus was observed on further increase in graphene content. Several studies have reported decrease in mechanical properties on higher loading of nanoparticulate fillers and have attributed this phenomenon to the agglomeration of nanofillers in the matrix [4,6].

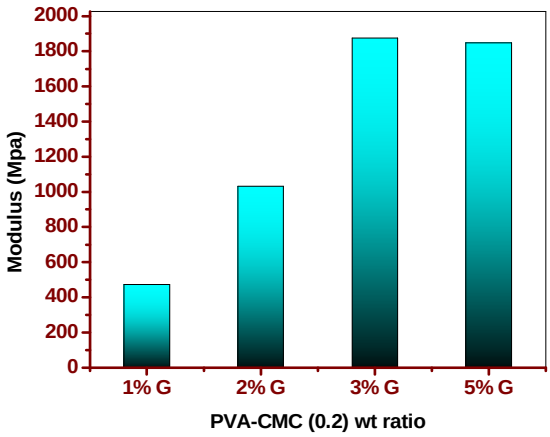

Fig. 1: Effect of graphene on the elasticmodulus of PVA/CMC nanocomposites

Effect of graphene content and radiation dose on mass uptake kinetics

Mass uptake kinetics of the PVA/CMC nanocomposites with (Gr 5%) and without graphene (Gr 0%) is shown in (Figure 2.) Mass uptake increased with time and attains equilibrium; the diffusion kinetics was determined using the mass uptake equation as mentioned below (equation (1))

$$\frac{M_t}{M_\infty} = kt^n \qquad (1)$$

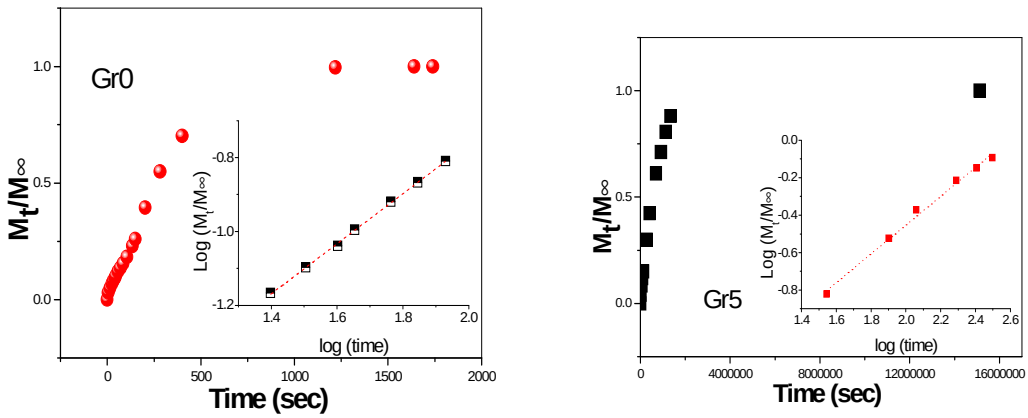

Fig. 2: Water uptake kinetics of the PVA/CMC composites with different radiation doses (graphene content 3 wt%)

where M_t and M_∞ are mass uptake at time t (in seconds) and equilibrium, k and n are constants. The initial data up to 60% uptake was fitted to the equation and the value of constants was evaluated. The value of n was 0.67 for Gr 0% and 0.77 for Gr 5%. Both matrices followed anomalous diffusion, though, with the addition of graphene, deviation from Fickian transport increased. Shen et al have investigated effect of graphene on the swelling properties of acrylic acid and demonstrated that solvent transport mechanism is nearly Fickian and there was a reduction in equilibrium degree of swelling [4]. They also reported increase in n value with the addition of graphene. The slight disagreement between our results and their results might be due to the fact that they have used in-situ polymerization which is expected to have better interaction between filler and polymer matrix. However, this strategy is difficult to implement in polymers which are derived from natural sources such as CMC. Zhang et al have explored graphene oxide/ polyacrylamide / sodium carboxymethylcellulose nanocomposite and also reported reduction in n value, supporting our results [3]. High energy radiation had profound effect on the diffusion kinetics (Figure 3).

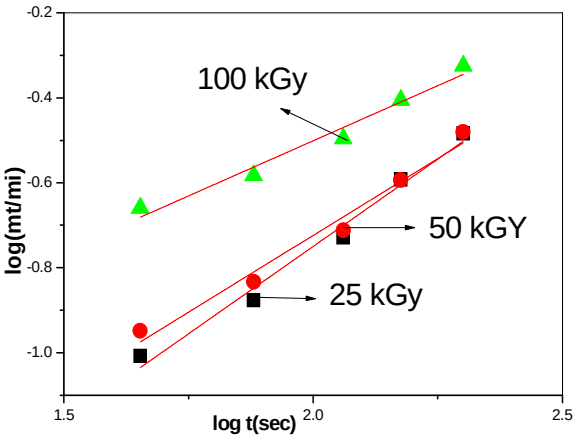

Fig. 3: Water uptake kinetics of the PVA/CMC composites with different radiation doses (graphene content 3 wt%)

At 25 kGy, the solvent diffusion kinetics was very fast which decreased substantially on irradiating the matrix to 150 kGy. The n value was found to be 0.823, 0.723 and 0.512 at 25 kGy, 75 kGy and 150 kGy, respectively. These results can be attributed to the changes in crosslinking density with increase in radiation dose. Since PVA forms crosslinked network on irradiation, the diffusion and relaxation of polymer chains might reduce, profoundly affecting mass uptake kinetics.

Effect of radiation dose and graphene on drug release kinetics

Figure 4 shows effect of radiation dose on the drug release kinetics. It can be seen that in all cases the drug release increases with time and attains a plateau. The

nanocomposites irradiated to 150 kGy had the slowest release whereas the release was highest in the nanocomposites irradiated to 25 kGy.

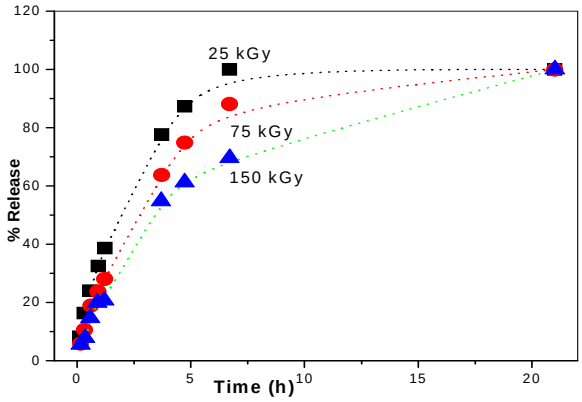

Fig. 4: Effect of different radiation doses on doxycyline release [Graphene 3wt%]

The time for T_{60} was determined to be 2.67 hrs, 3.49 hrs and 4.58 hrs for 25 kGy, 75 kGy and 150 kGy, respectively. To further evaluate the drug release process, the kinetics of drug release was studied using following relation (2)

$$C_t / C_\infty = kt^n \quad (2)$$

where C_t and C_∞ are the cumulative drug concentration at time t and at equilibrium. n, k′ are constants related with the type and rate of drug release. The value of n was calculated as 0.59, 0.67 and 0.68 respectively (Figure 5).

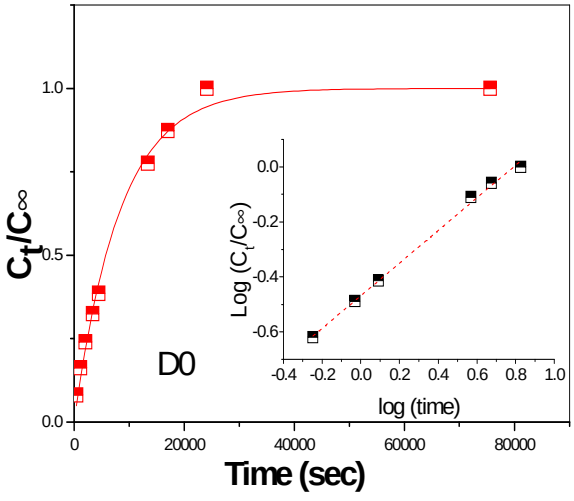

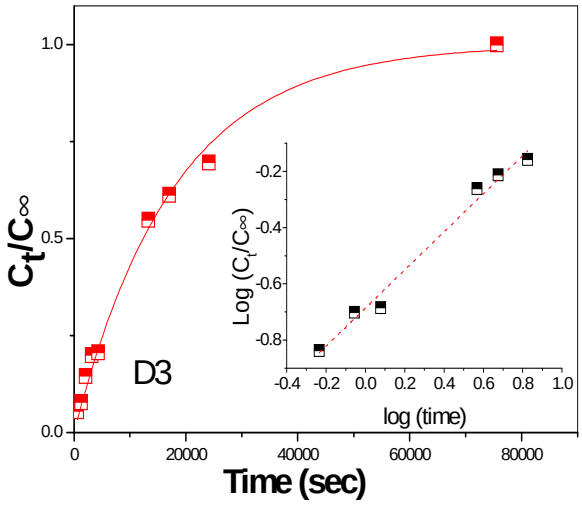

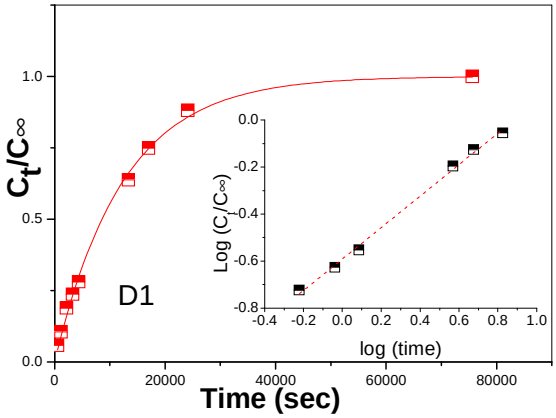

Fig. 5: Effect of different radiation dose on doxycyline release kinetics [Graphene 3 wt%]

This suggests that drug release process is anomalous in all the samples. Radiation induced increase in the crosslinking density can be ascribed to the observed retardation in the drug release kinetics [10]. Effect of graphene on the drug release kinetics is presented in (Figure 6.)

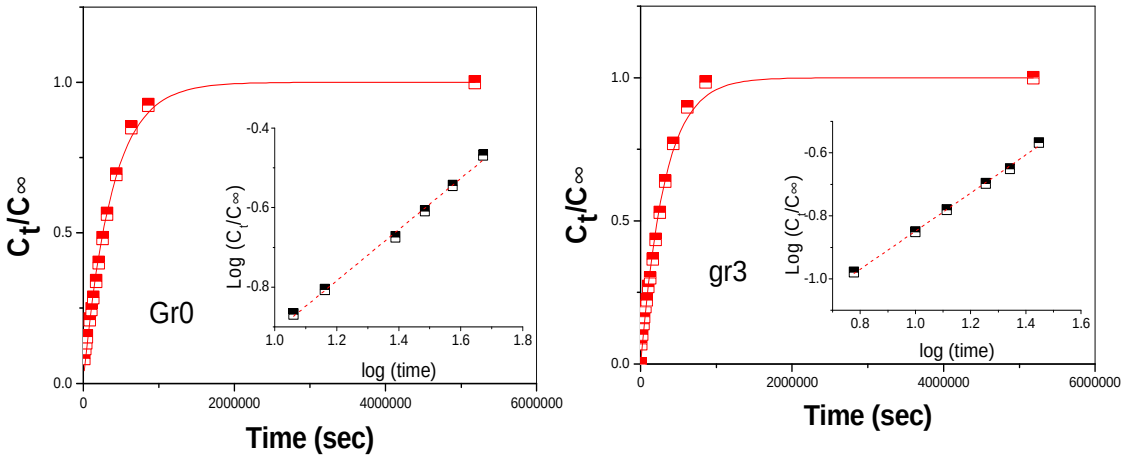

Fig. 6: Effect of different graphene on doxycyline release kinetics [Dose 100 kGy].

It was found that graphene had little effect on the drug release kinetics; T_{60} increased from 1.3 hrs to 1.75 hrs and the n value changed from 0.64 to 0.61 with the loading of 3 wt% graphene (Table 1).

Table 1: **Drug release kinetics parameters of the PVA/CMC nanocomposites**

Sample/parameter	Gr 0%	Gr 3 wt%	25 kGy	75 kGy	150 kGy
Time for 60% drug release	1.3 hrs	1.75 hrs	2.62 Hrs	3.46 Hrs	4.45 hrs
n	0.64 4	0.60 5	0.59 4	0.66 8	0.67 8

This is a peculiar finding, as nanoparticles are widely reported to affect the drug release behvaiour. The observed behvaiour can be attributed to the fact that graphene does not affect the crystallinity of the system and the weight fraction of graphene is too low to impart steric hindrance.

Nonetheless, reinforcement without significant affect on the drug release kinetics is desirable in several applications; particularly in cases where matrices with mechanical strengths are desired, at the same time, it is expected that nanofillers are not affecting the drug release behvaiour such as mucoadhesive matrices, implants, patches or stimuli-sensitive drug release formulations.

Conclusion

The results suggest that graphene reinforced PVA/CMC blends can be used in controlled drug release applications by imparting different doses of high energy radiation. Graphene significantly enhanced the elastic modulus of the blends; it however had a marginal effect on the drug release behvaiour. Radiation dose affects T_{60} profoundly and leads to 100% increase in $T_{60,}$ with an increase of dose from 25 kGy to 150 kGy. Mass uptake results suggest anomalous diffusion in all the samples. These results highlight that PVA/CMC/graphene nanocomposites can be used to develop high performance scaffolds, implants, mucoadhesive patches and controlled drug release formulations.

References

[1.] Salehi R, Rasouli S, and Hamishehkar H. *International Journal of Pharmaceutics* 2015;487(1:274-284.
[2.] Singh SK, Yadav AK, Prudhviraj G, Gulati M, Kaur P, and Vaidya Y. *European Journal of Pharmaceutical Sciences* 2015;73:72-80.
[3.] Zhang H, Zhai D, and He Y. *RSC Advances* 2014;4:44600-44609.
[4.] Shen J, Yan B, Li T, Long Y, Li N, and Ye M. Soft Matter 2012;8(6):1831-1836.
[5.] Islam MS, Rahaman MS, and Yeum JH. Carbohydrate Polymers 2015;115(0):69-77.
[6.] Dubey KA, Chaudhari CV, Rao R, Bhardwaj YK, Goel NK, and Sabharwal S. Journal of Applied Polymer Science 2010;118(6):3490-3498.
[7.] Dubey KA, Bhardwaj YK, Rajkumar K, Panicker L, Chaudhari CV, Chakraborty SK, and Sabharwal S. Journal of Polymer Research 2012;19(5).
[8.] Shen J, Yan B, Li T, Long Y, Li N, and Ye M. Soft Matter 2012;8(6):1831-1836.
[9.] Zhang H, Zhai D, and He Y. RSC Advances 2014;4(84):44600-44609.
[10.] Cirillo G, Spataro T, Curcio M, Spizzirri UG, Nicoletta FP, Picci N, and Iemma F. Materials Science and Engineering: C 2015;48(0):499-510.

BARC NEWSLETTER
FOUNDER'S DAY SPECIAL ISSUE 2015

FEMTOSECOND COHERENT ANTI-STOKES RAMAN SPECTROSCOPY (FS-CARS) WITH NITROBENZENE AND NITROMETHANE

Vinu V. Namboodiri[a], Mohammed Ahmed[a], G. Krishna Podagatlapalli[b] and Ajay K. Singh[a]
[a]Radiation & Photochemistry Division
[b]Advanced Centre of Research in High Energy Materials, University of Hyderabad

This paper received the Best Poster Award at DAE-BRNS Theme Meeting on Ultrafast Science (UFS) 2014 Manipal, Oct. 30-Nov. 1, 2014

Abstract

Over the past few decades, time-resolved coherent anti-Stokes Raman scattering (CARS) has evolved as a versatile tool for studying dynamical processes with pico/femtosecond time resolution. In this contribution, we describe the development of an experimental facility for the time-resolved coherent anti-stokes raman scattering spectroscopy and its application to study the vibrational dynamics of molecules containing nitro (NO_2) group. CARS experiments were carried out in neat liquids of nitrobenzene, nitromethane and their mixture. The CARS transient shows rich beating structure corresponding to frequencies as high as 10 THz*. The fourier transform of the transient allows accurate determination of the vibrational energy differences.*

Introduction

Coherent Raman spectroscopic techniques are now widely being used as an alternative to conventional Raman spectroscopy due to its high signal levels and coherent nature of the signal[1]. Coherent anti-Stokes Raman scattering (CARS) is one of the coherent Raman techniques that has evolved as a versatile technique for material characterisation and imaging in various areas of science.

Though experimentally complex compared conventional Raman, the high signal levels and natural rejection of fluoroscence eliminates the most common factors plaguing the applicability of conventional Raman spectroscopy.

Additionally, CARS using ultrashort pulses makes time-resolved measurements of ultrafast dynamical processes possible[2]. The broad spectral width of femtosecond pulses enables simultanoeus excitation of multiple vibrational modes. In this contribution we describe the experimental facility for time-resolved CARS using femtosecond laser pulses and results of time-resolved measurements of vibrational dynamics in nitrobenzene and nitromethane. Many of the high energy materials contain

nitro groups and the aim of the CARS experiment was to explore the applicability of CARS in deciphering the vibrational dynamics of high energy materials.

Materials and Methods

The experimental setup for CARS is described in detail elsewhere[3]. Briefly, the pump, Stokes and probe pulses for the CARS experiment were derived form two optical parametric amplifiers (TOPAS, Light Conversion) both pumped by $800\,nm$, $1\,mJ$ pulses of width $\sim 50\,fs$ from an amplified femtosecond laser system (Amplitude Technologies, Trident-M, $1\,KHz$). The pump and probe pulses were of the same wavelength and was derived from one of the OPA outputs using a 50/50 beam splitter. The pump and stokes wavelengths were $590\,nm$ and $635\,nm$ respectively and were tuned to a wavenumber difference of $1200\,cm^{-1}$. The broad spectral width of the pulses enabled excitation of Raman modes within a region of $\pm 500\,cm^{-1}$ from the centre of excitation. The three beams were arranged in folded-BOXCARS geometry[4] for ensuring phase matching and focussed onto the sample using a lens of 10 cm focal length. The spatially seperated CARS signal from the sample is collinated using another lens (f=10 cm) and sent to a spectrometer (ANDOR Shamrock) attached with a TE cooled CCD (ANDOR Newton). The time delay between the pulses were adjusted using computer controlled linear translation stages (Newport ILS 150) mounted with retroreflecting mirros. Neat liquids of nitromethane and nitrobenzene were used for the experiments.

Results and Discussion

CARS on Nitrobenzene

e time-resolved CARS transient of nitrobenzene is shown in figure 1. The transient shows well defined beating structure arising due to the excitation of different vibrational modes which fall within spectral width of the excitation pulses. A frequency slice of the transient is shown in figure 2a and shows the fast modulations of the CARS signal arising due to the beating between the different excited vibrational modes. The frequency difference between the beating vibrational modes can be determined from the fourier transform of the transient which is shown in Figure 2b.

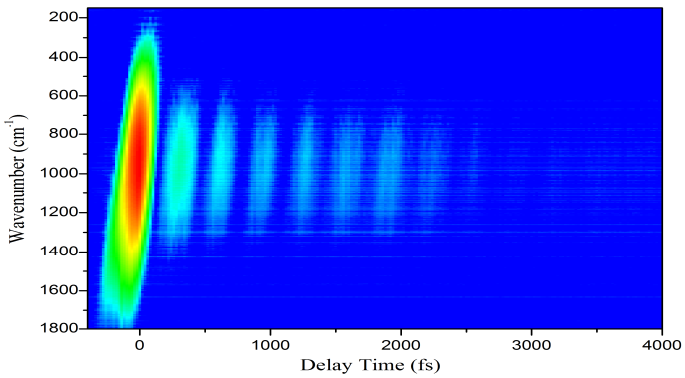

Fig. 9: Time and frequency resolvedCARS spectrum of nitrobenzene

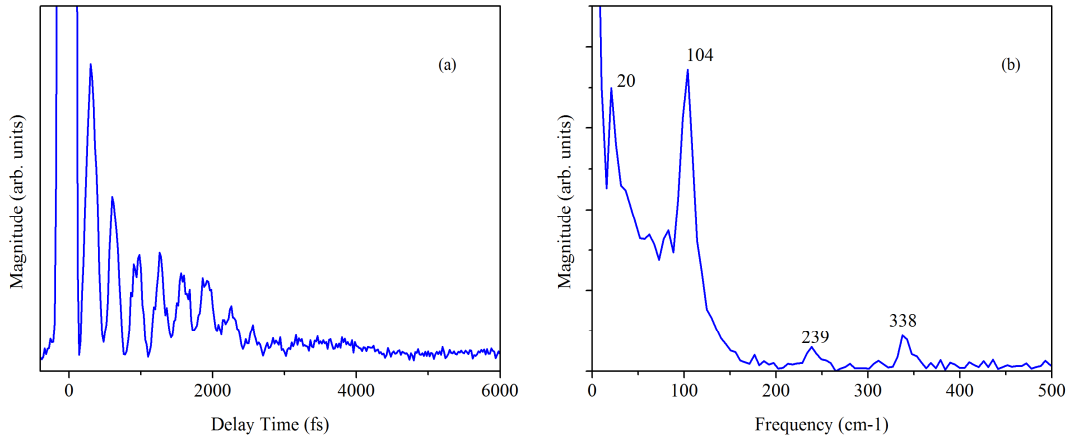

Fig. 10: a) Time resolved CARS transient showing rapid modulations (spectral slice). b) FFT corresponding to the transient showing the beat frequencies

The beat frequencies seen in the fourier spectrum shows peaks at wave number positions $20\ cm^{-1}, 103\ cm^{-1}, 238\ cm^{-1}$ and $337\ cm^{-1}$. These peaks correspond to the frequency difference between the $853\ cm^{-1}, 1003\ cm^{-1}, 1022\ cm^{-1}, 1107\ cm^{-1}$ and $1347\ cm^{-1}$ vibrational modes of nitrobenzene. The highest beat frequency of $337\ cm^{-1}$ between the nitrobenzene vibrational modes at $1003\ cm^{-1}$ and $1347\ cm^{-1}$ corresponds to a frequency of 10.1 THz. This is indicative of the high temporal resolution of the experiment which enables probing of terahertz phenomena with appreciable accuracy.

CARS on Nitromethane and Mixture

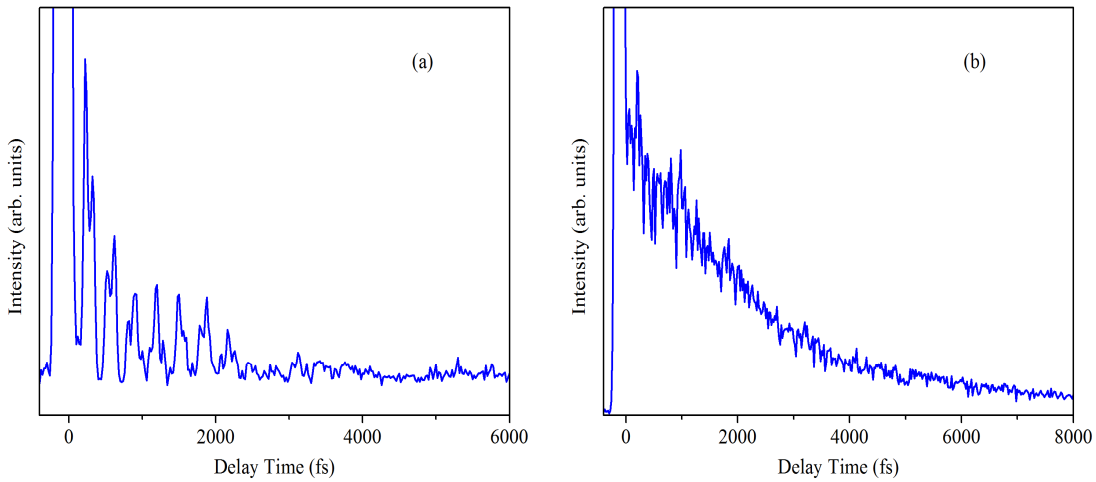

Fig. 11: a) CARS transient from 1:1 (by volume) mixture of nitromethane and nitrobenzene. b) CARS transient from pure nitromethane

Similar experiments were carried out in nitromethane and a mixture of nitromethane and nitrobenzene (1:1 v/v). The nitromethane CARS transient is dominated by a single Raman mode at 917 cm^{-1} and hence did not show any beating structure (figure 3b) where as the CARS transient of the mixture showed modulations of the CARS signal (figure 3a) similar to the case of nitrobenzene. Fourier analysis of the CARS transient of the mixture showed an additional beat frequency component at 86 cm^{-1} (figure 4) which arises from the beating between the vibrational modes of nitromethane (917 cm^{-1}) and nitrobenzene (1003 cm^{-1}).

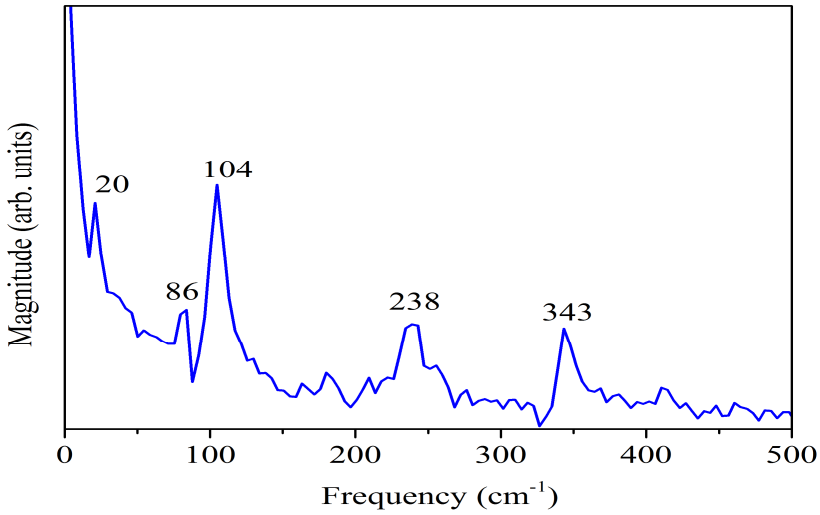

Fig. 12: FFT of the CARS transient of mixture

The presence of additional frequency components in the CARS transient can be used as a signature to identify components in a mixture. Further analysis is being carried out to extract the dephasing time of different participating vibrational modes and to analyse how the dephasing times are influenced in a mixture.

References

[1]. Eesley G. L. "Coherent Raman Spectroscopy". *J. Quant. Spectrosc. Radiat. Transfer* 22 (1979): 507.
[2]. Zinth W., Polland H.-J., Lauberau A. and Kaiser W. "New results on ultrafast coherent excitation of molecular vibrations in liquids". *Appl. Phys. B.* 26 (1981): 77.
[3]. Namboodiri V., Guleria A., Singh A.K. and Sarkar S.K. "Coherent anti-Stokes Raman Scattering Spectroscopy Using Shaped Ultrashort Laser Pulses". *ISRAPS Bullettin*. 26 (2014): 45.
[4]. El F. "Coherent anti-Stokes Raman scattering: Spectroscopy and microscopy" *Vibr. Spectrosc*. *55*, (2011):1.

BARC NEWSLETTER
FOUNDER'S DAY SPECIAL ISSUE 2015

EFFECTIVE ELIMINATION OF MEMORY EFFECT OF BORON IN ICPMS USING A SPRAY CHAMBER COATED WITH SILICONIZING FLUID

K. Chandrasekaran and D. Karunasagar
National Centre for Compositional Characterization of Materials

This Paper was given the Best Poster Award at the 12th Ismas Triennial International Conference on Mass Spectrometry (12th Ismas-Tricon-2013), Goa, March 4-8, 2013

Introduction

The high sensitivity of inductively coupled plasma-mass spectrometry (ICP-MS) makes this technique suitable for reliable and rapid boron determinations. However, determination of boron at ultratrace levels by ICP-MS is often plagued by significant memory effect. Boron is known to stick to the glass wares in the sample introduction system of ICPMS*[1]*.

This necessitates long washing times after every sample run to eliminate the memory from affecting the subsequent samples.Many methods have been reported in the literature to minimize memory effects of boron *[2, 3, 4]*. Sun *et. al. [5]* had examined the memory effect of boron using different diluents/rinse solutions – water, nitric acid, Triton X-100, ammonia and mannitol.

A combination of ammonia and mannitol, when used as both diluent and flush solution, gave reduced memory effect and low background in the determination of boron by ICPMS in biological fluids. However, use of mannitol-ammonia mixture as diluent for the sample in their study resulted in significant overlap of 12C+ peak on 11B+ peak; hence 10B+, the isotope with lesser abundance had to be used for quantification of boron concentration, resulting in a loss of sensitivity. Sun *et. al. [5]* and Al-Ammar *et. al. [6]* had reported that a primary source of the memory effect was the volatilization of sample droplets giving rise to boric acid in the spray chamber. In order to eliminate the memory effect, a small amount of ammonia gas was also introduced into the nebulizer gas flow *[6]*.

We have reported earlier a flow-injection ICPMS method for the determination of boron isotope ratio *[7]*, wherein the introduction of microlitre volume of sample in flow injection analysis (FIA) helps in the reduction of memory effect when compared to direct solution nebulization. In the present work, the combined use of a spray chamber coated with a siliconizing fluid and the use of a low flow-rate nebulizer has minimized/eliminated the memory effect of boron during direct solution nebulization. The results of this study are discussed below.

Experimental

Instrumentation

A VG Plasmaquad 3 Inductively Coupled Plasma-Quadrupole Mass Spectrometer (VG Elemental, Winsford, Cheshire, UK) situated in a class 100 laboratory was used in this study.A micro-flow nebuliser - SeaSpray™ [AR35-1-USS0.4] - was used for sample introduction through a water cooled (1°C) Scott type double-pass spray chamber. Parameters such as plasma rf power, nebulizer gas flow and lens voltages were optimized daily by aspirating a 10 µg L-1 boron solution prepared from boric acid in 5% HNO3 passed at a flow rate of 200 µL min-1. The reagents were introduced using a peristaltic pump (REGLO *Digital* MS-4/12, ISMATEC, Switzerland).

Coating the spray chamber

The interior walls of the (Scott type double pass, water cooled) quartz spray chamber used in the sample introduction system in ICP-QMS, was coated with a hydrocarbon soluble siliconizing fluid –5% (v/v) dimethyl dichlorosilane in carbon tetrachloride. About 10 mL of the solution was poured into the spray chamber, slowly rotated to completely wet the whole inner surface and this was continued for 15 min. Any traces of liquid were drained and the spray chamber was air dried and then heated using an IR lamp for 30 min.

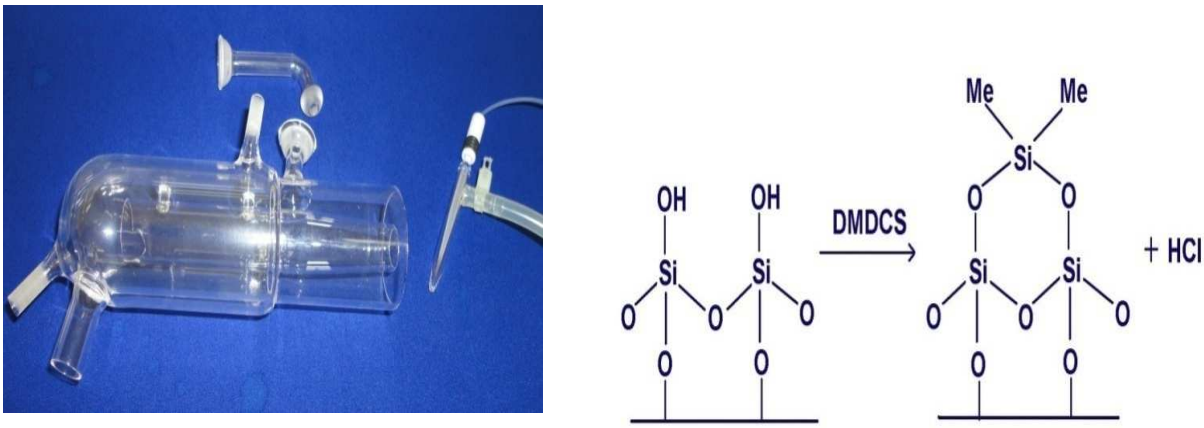

Fig. 1: Profile showing the effect of coating the spray chamber on the memory between two successive samples with sample concentration of boron varying between 140-600 µg L−1 in different water samples

Results and Discussion

Surface treatment with siliconizing fluids helps to reduce adsorption of polar compounds, proteins and trace metals onto glass surfaces *[8]*. The dimethyldichlorosilane deactivates the silanol (Si-OH) groups on the glass surface, resulting in a hydrophobic surface that resists nonspecific binding. The effectiveness of

the spray chamber coating was evaluated by analyzing a set of water samples (groundwater and wastewaters) (SAM1-SAM9 in Fig. 1) with concentration ranging from 140–600 µg L-1. The concentrations were so chosen to see the effectiveness of the coating in eliminating the memory effect. A rinse solution of 5% (v/v) HNO3 was used for washing between two successive samples. The rinse solution was passed at the maximum speed of the peri-pump during washing. After a wash for 30-40 s, the boron signal of the rinse solution equals the value measured at the beginning of the experiment (Fig. 1), whereas in the absence of coating the spray chamber with siliconizing fluid, the time taken for eliminating the memory effect of boron with the same rinse solution is > 200 s. The samples and the rinse solution were analyzed alternately for their boron content, every 3 min. Results of this experiment are tabulated in (Table 1.)

Table 1: Elimination of boron memory effect by coating the inner walls of the spray chamber with siliconizing fluid and using 5% (v/v) HNO3 as rinse solution

Time of measurement (min)	**Concentration of boron in rinse solution (µg L-1) (n = 3)**	**Concentration of boron in sample solution (µg L-1) (n =)**
0	9.0 ± 0.4	
3		169 ± 0.7
6	9.2 ± 0.2	
9		203 ± 2.5
12	8.9 ± 0.1	
15		355 ± 2.7
18	11.1 ± 0.2	
21		352 ± 2.6
24	10.7 ± 0.5	
27		564 ± 2.8
30	10.6 ± 0.7	
33		310 ± 3.1
36	11.2 ± 0.3	
39		143 ± 1.9
42	11.6 ± 0.8	
45		204 ± 1.2
48	10.9 ± 0.9	
51		288 ± 2.0
54	11.3 ± 0.5	

The concentration of boron in the rinse solution was initially determined to be 9.0 ± 0.4 µg L-1. As may be seen from the table, at the end of 1 hour of sample analysis, the concentration of boron in the rinse solution has increased by only 2 µg L-1 and had stabilized close to 11 µg L-1. This demonstrates that the contribution due to memory effect is not significant in the coated spray chamber despite the wide variation in the concentration of boron in the water samples.

Comparison with other methods

The use of mannitol *[5]* and ammonia *[6]* as diluents has resulted in loss of sensitivity of boron. In addition, the use of mannitol by Sun *et. al. [5]* , gave rise to a huge

interference on the most abundant isotope of boron – 11B+ due to 12C+ and therefore 10B+ was required to be used for quantification. In the present study the combined use of nitric acid and coated spray chamber, did not show any spectral interference on both the isotopes of boron (10B+ and 11B+), that might have arisen had there been leaching of the coating material. This shows that the spray chamber coating was stable throughout the experiment. The 10B/11B isotope ratio recorded throughout the experiment matched with natural isotopic ratio. Hence either isotope can be used for quantification of boron in various types of water. In the present study both, coating of spray chamber with siliconizing fluid and the use of low flow-rate nebulizer, had helped in minimizing/eliminating memory effect of boron.

Conclusion

The coating of the spray chamber with a siliconizing fluid results in a fast wash-out of boron memory between two successive samples by direct solution nebulization.

References

[1] K. E. Jarvis, A. L. Gray and R. S. Houk, (1997), *Handbook of Inductively Coupled Plasma Mass Spectrometry*, Blackie Academic & Professional, London.

[2] N. I. Ward, F. R. Abu-Shakra and S. F. Durrant, *Biol. Trace Element Res.* **26** (1990) 177.

[3] F. G. Smith, D. R. Wiederin, R. S. Houk, C. B. Egan and R. E. Serfass, *Anal. Chim. Acta* 248 (1991) 229.

[4] S. Assad, R. K. Gupta and R. M. Barnes, *Spectrochim. Acta Part B* 54 (1999) 1077.

[5] D. H. Sun, R. L. Ma, C. W. McLeod, X. R. Wang and A.G. Cox, *J. Anal. At. Spectrom.* 15 (2000) 257.

[6] Al-Ammar, E. Reitznerová and R. M. Barnes, *Spectrochim. Acta Part B* 55 (2000) 1861.

[7] K.Chandrasekaran and D. Karunasagar, *11th ISMAS-Triennial International Conference on Mass Spectrometry* (2009).

[8] www.thermo.com/eThermo/CMA/PDFs/Various/File_52881.pdf, Thermo Fisher Scientific Inc. *(2008) 21.*

BARC Newsletter
Founder's Day Special Issue 2015

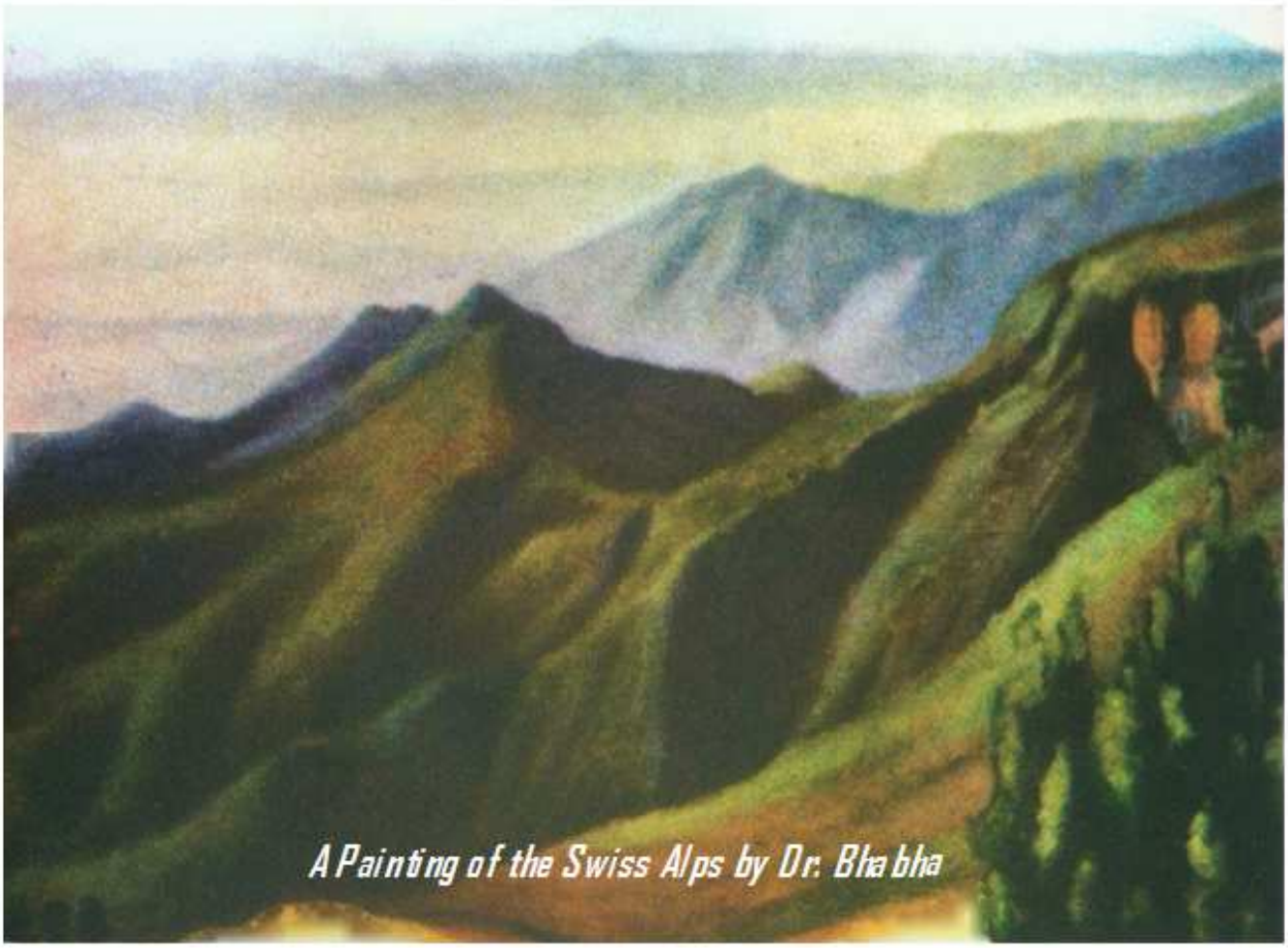

A Painting of the Swiss Alps by Dr. Bhabha

Published by
Scientific information Resource Division
Bhabha Atomic Research Centre
2015